JAERI-Review
97-015

JAERI-Review--97-015

JP9804024

TIARA Annual Report 1996

November 1997

Advanced Radiation Technology Center

日本原子力研究所
Japan Atomic Energy Research Institute

本レポートは，日本原子力研究所が不定期に公刊している研究報告書です。
入手の問合わせは，日本原子力研究所研究情報部研究情報課（〒319-11 茨城県那珂郡東海村）あて，お申し越しください。なお，このほかに財団法人原子力弘済会資料センター（〒319-11 茨城県那珂郡東海村日本原子力研究所内）で複写による実費頒布をおこなっております。

This report is issued irregularly.
Inquiries about availability of the reports should be addressed to Research Information Division, Department of Intellectual Resources, Japan Atomic Energy Research Institute, Tokai-mura, Naka-gun, Ibaraki-ken, 319-11, Japan.

編集兼発行　日本原子力研究所
印　　刷　いばらき印刷㈱

JAERI-Review 97-015

TIARA Annual Report 1996

Advanced Radiation Technology Center

Takasaki Radiation Chemistry Research Establishment
Japan Atomic Energy Research Institute
Watanuki-cho, Takasaki-shi, Gunma-ken

(Received October 1, 1997)

This annual report describes research activities which have been performed with the JAERI TIARA (Takasaki Ion Accelerators for Advanced Radiation Application) facilities from April 1, 1996 to March 31, 1997.

Summary reports of 88 papers and breaf discriptions on the status of TIARA in the period are contained. A list of publications, the type of research collaborations and organization of TIARA are also given as appendices.

Keywords: JAERI TIARA, Ion Accelerators, Solid State Physics, Radiation Effects in Materials, Materials for Space, Semiconductors, Organic Materials, Inorganic Materials, Nuclear Fusion Reactor, Functional Materials, Radiation Chemistry, Radiation Biology, Nuclear Medicine, Biotechnology, Radioisotope Production, Nuclear Chemistry, Radiation Shielding, Materials Analysis, Accelerator Technology, Safety Control

---

(Eds.) Ryuichi TANAKA, Hideki OMICHI, Isamu NASHIYAMA, Hiroshi NARAMOTO, Takeshi SUWA, Yousuke MORITA, Akio TORAISHI, Hiroshi WATANABE, Yasuo KUSAMA, Denjiro NEMOTO and Sohei OKADA

原研イオン照射研究施設（ＴＩＡＲＡ）平成８年度年次報告

日本原子力研究所高崎研究所
放射線高度利用センター

(1997年10月１日受理)

本年次報告は、原研イオン照射研究施設で、1996年４月１日から1997年３月31日までの間に行われた研究活動の概要をまとめたものである。

１）宇宙用半導体、２）バイオテクノロジー、３）放射線化学および有機材料、４）無機材料、５）材料解析、６）核化学およびラジオアイソトープ製造、７）加速器施設の放射線遮蔽、８）加速器技術 の８部門にわたる88編の研究報告に加えて、施設の運転・利用状況、公表された文献、企業・大学等との研究協力関係、研究開発・施設運営組織を収録する。

高崎研究所：〒370－12　群馬県高崎市綿貫町1233

PREFACE

This report covers research and development activities which have been conducted with TIARA (Takasaki Ion Accelerators for Advanced Radiation Application) during the period from April 1996 until March 1997, and also gives an outline of the operation of TIARA in the same period.

All accelerators of TIARA, i.e. the AVF cyclotron, the 3MV tandem accelerator, the 3MV single-ended accelerator and the 400kV ion implanter, have been operated steadily since their construction were completed in 1993, and have supplied the beam-time to the research programs as had been recognized in advance by the TIARA General Program Committee. In the same time, available species and energy ranges of ions have been widened to meet requests from users, and the quality of ion beams have been improved gradually.

In accelerator technology, single ion technique for local hit on a semiconductor device and a living cell has been developed by using 15 MeV heavy ion microbeams from the tandem accelerator. Acceleration technique of cocktail ions has been also developed for quick change of ion species, extracted from the AVF cyclotron, with mass to charge ratios approximately of 4 and 5. In radiation shielding for accelerator facilities, the results of new measurement were reported for charged particle emmission data, neutron activation cross sections and fission reaction rate in polyethylene using a quasi-monoenergetic neutron source.

In the field of radiation effects on semiconductor devices for space, testing of single-event upsets (SEU) in commercial memory devices has been performed using the newly developed cocktail ion acceleration, and a technique for mapping of SEU sensitive areas in these devices was developed by the use of a scanning heavy-ion micro-probe.

In biotechnology, several characteristic mutants were selected from the plant seeds irradiated by ion beams. The effectiveness of ion beams as a mutagen was revealed. In addition, it was found from the experiments of penetration controlled irradiation that a marker gene could be inserted to the tobacco pollen which was incubated with DNA solution following irradiation with low energy ion beams.

The main scientific activities in the field of inorganic materials and ion beam analysis have been directed to the combined research between materials processing and surface analysis and to expoloratory study of new analytical techniques by considering the ion-solid interactions. The ion beam processing itself has also changed from the simple implantation experiment into the employment of radiation effects on quasi-stable states, and the special interests appeared in materials-designing of intended structure utilizing the above elementary processes.

Ion beam irradiation effects of polymer materials were investigated on the point of linear energy transfer (LET) and the products analysis were carried out for double bond and free radicals induced by ion irradiation, and the resultant change of mechanical properties as tensile strength and

the LET dependency was compared.

In nuclear chemistry and radioisotope-production, production methods of positron emitters were developed for use in plant study. The positron emitters ^{11}C, ^{13}N, ^{18}F and ^{48}V have been used as labeled compounds like $^{11}CO_2$ and ^{11}C-methionine. Using an isotope separator on-line (ISOL), the atomic masses of $^{126,127,128}La$ produced in the $^{nat,94}Mo(^{36}Ar, 3pxn)$reactions were determined by observing their β^+-ray maximum energies.

To promote the operation efficiency of research experiment, the way of beam-time allotment for the cyclotron was improved from the day-unit system to the hour-unit system, and the operation time of electrostatic accelerators was extended till late at night. The effective operation of the cyclotron was also made possible by development of the cocktail beam acceleration technique, by which one accelerated ion is quickly changed to other ion with almost same mass-to-charge ratio.

The management of TIARA have been smoothly performed on the basis of activity of the TIARA General Program Committee. A new beam-time allotment system which reflects results of evaluation of experimental subjects was approved by the committee, and the priority system is applied from F.Y.1997.

The reception of users, general management of facilities, safety management of the radiation controlled areas, supports on utilization of facilities, and other duties have also been practicized smoothly; A computer code system to calculate induced radioactivity, IRAC, have been developed and practically used for the evaluation of radiation safety in irradiation experiments.

The Sixth TIARA Research Review Meeting was held on June 16 and 17 1997 at Takasaki, of which subjects were reported in this issue. 11 oral and 69 poster papers, and one invited lecture were presented in addition to a topical session (on high-energy cluster ions and their interaction with matter). 267 persons participated the meeting. In contrast with the earlier meetings, numerous results of TIARA utilization were presented, suggesting the TIARA is now becoming a fruitfull facility.

We owe the progress mentioned above to advices of the Consultative Committee for the Research and Development of Advanced Radiation Technology, the Consultative Committee for the JAERI-Universities Joint Research Project, the TIARA General Program Committee, and their subcommittees.

田中隆一

Ryuichi Tanaka
Director
Advanced Radiation
Technology Center,
Takasaki Radiation Chemistry
Research Establishment

Contents

1. Semiconductors for Space

1.1 Development of a collimated swift heavy-ion microbeam

I. Nashiyama, T. Hirao, T. Hamano, H. Itoh, and T. Ohshima
Department of Materials Development, JAERI

1. Introduction

A microbeam of energetic ions is a powerful tool to irradiate a tiny specimen in a positioning accuracy better than a few micrometer. This technique is especially useful for investigating mechanisms and sensitive areas of Single-Event Effects (SEE) in semiconductor devices. An ion microbeam is formed by either applying a micro-aperture or focusing an ion-beam using electromagnetic lenses. Though it is simple and convenient, the minimum beam size we can obtain using micro-aperture method is 10 μm at the best, because probability that incident ions are scattered at the inside wall of the aperture increases markedly with decreasing the aperture size. Whereas, a beam size in a few micrometer can be achieved by the focusing method so far as the energy purity of the ions is sufficient.

Therefore, when ion positioning accuracy better than 10 μm is needed, a focused ion microbeam has been conventionally used, where electrostatic tandem or single-ended accelerators are used because of their very high energy purity and beam emittance. In most cases, unfortunately, their beam energy is not high enough for SEE experiments. For example, the 3 MV tandem accelerator of TIARA provides heavy-ion beams with the maximum energy of 18 MeV and their ranges are too short to be applied to the SEE experiments on modern LSI memory devices, because their chip surfaces are covered with a thick passivation layer.

For an accurate analysis of SEE mechanism, we need heavy ions with LET higher than 20 MeV mg/cm^2 and ranges above 40 μm in silicon. To meet these requirements, we are developing a new technique to form heavy-ion microbeams with energies of a several hundreds of MeV.

In this paper, we present a new technique to form a microbeam of energetic cyclotron ions and some preliminary experimental results.

2. Reduction of Edge-scattering

In developing a microbeam of very high energy heavy ions from the cyclotron, we use the micro-aperture method, since the electromagnetic focusing method can not be applied to a cyclotron ion beams because of their insufficient energy purity. Since the beam energies are extremely high, we need a micro-aperture in a very thick metal plate, e.g. a 50 μm thick tantalum plate is necessary to stop all the energetic incident ions within the plate. Therefore, it is indispensable to reduce the edge scattering effect in applying the micro-aperture method.

To reduce the edge scattering, we combines a micro-aperture with a highly collimated ion beam. In the case of a micro-aperture with 1 μm diameter and 50 μm thickness, beam divergence less than 0.15 degree is needed so that the probability of the edge-scattering is kept less than 10^{-3}.

3. Collimation of Ion Beam

A 330 MeV Ar-ion beam from the AVF cyclotron was collimated using a pair of double slits (1 mm x 1 mm) placed along the beam line with 11.24 m distance each other [1]. The angular divergence of the beam obtained by this collimation method is geometrically calculated to be 0.01 degree.

In order to measure the angular divergence of the ion beam, we used the channeling effect in a thin silicon surface barrier detector (SSD). A dip curve around the <111> axis is shown in Fig. 1, where the pulse-height window is fixed to the value corresponding to the energy which the random ions dissipate in the SSD. From this result, we have obtained the angular divergence of 0.17 degree (FWHM). Considering the theoretical angular half width of the <111> axial channeling of 330 MeV Ar-ion in silicon is 0.09 degree [2], we can say that the half angle of the beam divergence is less than 0.01 degree, which is almost equal to the half angle of the beam divergence calculated geometrically from the sizes of the x-y slits and their distance. Energy spectrum of the collimated beam is shown in Fig. 2.

4. Alignment

The collimated 330 MeV Ar-ion beam is incident normally on the micro aperture with 50 μm diameter and 100 μm thickness. An energy spectrum of the ions passing through the micro-aperture was measured by a partially depleted silicon surface barrier detector placed behind the micro-aperture.

The result is shown in Fig. 3. A peak at 176 channel corresponds to the ions passed through the micro aperture without scattering. Below the peak, there exists significant spread of the yield due to the ions scattered at the edge of the micro-aperture. Such edge-scattering is mostly caused by poor angular alignment of the micro-aperture. Therefore, more precise angular and positional alignment is required.

5. Summary

A method to develop a cyclotron heavy-ion microbeam is presented, which is based on the combination of a micro-aperture and a highly collimated ion beam to eliminate the edge scattering.

A collimated 330 MeV Ar-ion beam with the beam divergence less than 0.01 degree is developed using a pair of double slits installed on HE-2 beam line.

6. Reference

1) Nashiyama, et al. "Collimation of Heavy Ion Beam Produced by Cyclotron for Single-Event Measurements", JAERI-Review 95-019, 8 (1995).
2) B.R. Appleton and G. Foti, in "Ion Beam Handbook for Material Analysis", Ed. J.W. Mayer and E. Rimini (Academic Press, New York, 1977), Chap. 3.

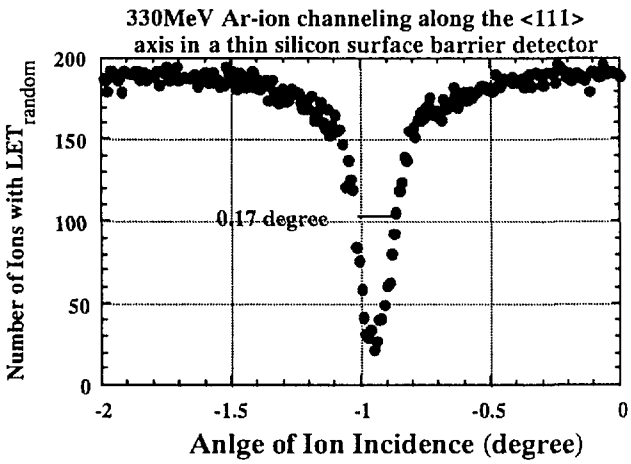

Fig. 1 Dip curve of 330 MeV Ar-ions passing through a 50 μm thick silicon surface barrier detector.

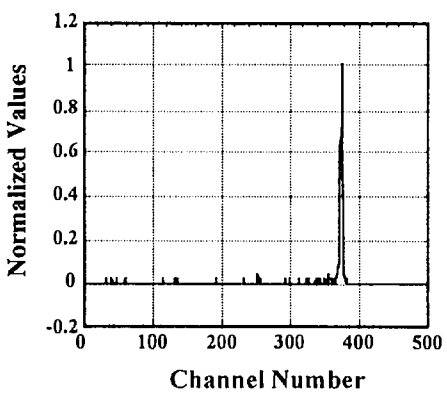

Fig. 2 Energy Spectrum of the collimated 330 MeV Ar-ion beam.

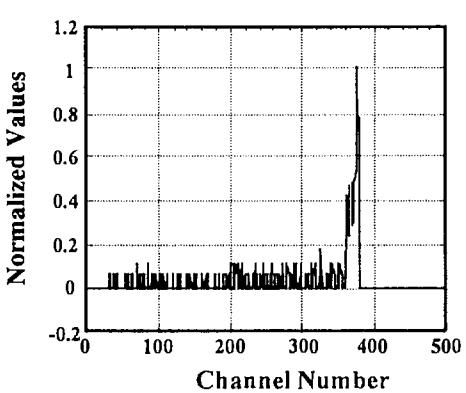

Fig. 3 Energy Spectrum of the collimated 330 MeV Ar-ion beam after passing through a micro-aperture of 50 μm in diameter and 100 μm in thickness.

1．2 Electrical Characteristics of Large Fluence 3MeV or 10MeV Proton Irradiated Space Silicon Solar Cells

Sumio MATSUDA, Tadashi HISAMATSU, Osamu KAWASAKI, Tetsuya NAKAO,
Yousuke MORITA*, Takeshi OHSHIMA* and Isamu NASHIYAMA*
National Space Development Agency of Japan (NASDA)
Department of Materials Development, JAERI*

1. Introduction

Radiation tolerance is one of the important characteristics for space solar cells. It has been evaluated generally using 1MeV electrons with fluence up to 1×10^{16} p/cm^2 and 10MeV protons with fluence up to 1×10^{13} p/cm^2. However, recently we found that the space silicon solar cells irradiated with larger fluence electrons or protons showed anomalous degradation behavior which could not be predicted with previous data. That is, a sudden drop of electrical performance in the larger fluence region and a slight increase of short circuit current Isc, just before the sudden drop of performance.[1),2)] We have studied the degradation mechanism in various aspects and already reported the electrical characteristics of 1MeV-electron-irradiated cells and 10MeV-proton-irradiated cells[3)], and proposed the models for explaining this anomalous degradation[4),5),6),7)]. As a part of these studies, we have also investigated the electrical characteristics of degraded cells due to the proton irradiation with various energy.

In this paper, we compare the electrical characteristics of 3MeV-proton-irradiated cells and 10MeV-proton-irradiated cells and discuss the irradiation effect with the displacement damage dose.

2. Experiments

Samples are Si BSFR cells (2×2cm^2 50μm thick) manufactured by SHARP corporation. Figure 1 shows the structure of the cell. The substrate is a boron-doped p-type single crystal silicon with resistivity of about 10Ωcm. For the front surface, a thin n^+ layer is formed by a phosphorous diffusion. For the rear surface, a thin p^+ back-surface-field layer is formed by a boron diffusion. Metallurgical electrodes are deposited on each side and an anti-reflective coating is deposited on the front surface.

Proton irradiation was carried out using the tandem accelerator for 3MeV protons and the AVF cyclotron for 10MeV protons at JAERI Takasaki. The protons with energy of 3MeV or 10MeV go through the solar cells (50μm) because the projection ranges of those protons in Si are deeper than 50μm. Electrical performance, dark I-V characteristics and C-V characteristics were measured at room temperature after annealing at 60℃ for 24 hours for stability of the performance.

3. Results and Discussion

Figure 2 (a)～(d) show the fluence dependence of remaining factors of cell performance (normalized electrical performance). Similar to 10MeV proton irradiation, the anomalous degradation behavior is found in large fluence region of 3MeV proton irradiation.

Figure 3 and 4 show the fluence dependence of the reverse saturation current density I_0 and the series resistance R_{se} derived from the dark I-V measurement results, respectively. In both energy conditions, the increase of the I_0 and the R_{se} with the increase of fluence are found. Figure 5 and 6 show the fluence dependence of the diffusion voltage V_d and the carrier density in substrate p derived from the $1/C^2$–V plots of C-V measurement results, respectively. In both energy conditions, the decrease of the V_d and the p with the increase of fluence are found.

We compare the 3MeV-proton-irradiation results with the 10MeV-proton-irradiation results in terms of displacement damage dose, i.e. the absorbed energy spent for atomic displacement. The displacement damage dose is calculated as the product of fluence and nonionizing energy loss (NIEL). The NIEL value in Si of 3MeV-protons are 3.15×10^4 (eV•cm^2•atm/g) and that of 10MeV protons are 1.06×10^4 (eV•cm^2•atm/g). Thus, for the same fluence, the displacement damage dose of 3MeV proton irradiation is about 2.97 times larger than that of 10MeV proton irradiation. So, we multiply the fluence values of the 3MeV proton's data by 2.97 and draw curves in Figures 2 ～ 6

with broken lines. These broken lines seems to agree approximately with 10MeV proton's data except for large fluence region near 10^{14} p/cm^2.

In conclusion, it became clear that 3MeV-proton-irradiated space silicon solar cells showed similar anomalous degradation behavior which was found in solar cells irradiated with 10MeV protons, however the fluences at which the anomalous degradation occurred were different. This difference can be explained approximately in terms of displacement damage dose. However, discrepancy can not be ignored in large fluence region around 10^{14} p/cm^2. We will investigate the proton-induced defects and the relation between proton energy and the cell structure in detail.

[1] Y. Yamamoto, O. Kawasaki, S. Matsuda and Y. Morita: Proceeding of the European Space Power Conference, Poitiers, France, 4-8 September 1995, esa SP-369, (1995), p573-578.
[2] O. Kawasaki, S. Matsuda, Y. Morita, T. Ohshima and I. Nashiyama: JAERI TIARA Annual Report 1994 (Vol.4), April 1994-March 1995, JAERI-Review 95-019, (1995), p11-13.
[3] T. Hisamatsu, O. Kawasaki, S. Matsuda, T. Nakao and Y. Wakow: Technical Digest of 9th International Photovoltaic Science and Engineering Conference, Nov.11-15 1996, Miyazaki, Japan, p633-634.
[4] M. Yamaguchi, S. T. Taylor, M.-J. Yang, S. Matsuda, O. Kawasaki, T. Hisamatsu: Jpn. J. Appl. Phys. Vol.35 (1996) pp.3918-3922.
[5] M. Yamaguchi, S. J. Taylor, S. Matsuda and O. Kawasaki: J. Appl. Phys., 80, (9),1 November 1996, p4916-4920.
[6] T. Ohshima, Y. Morita, I. Nashiyama, O. Kawasaki, T. Hisamatsu, T. Nakao, Y. Wakow and S. Matsuda: 33rd Annual International Nuclear and Space Radiation Effects Conference, Indian Wells, California, July 15-19, 1996, G-2.
[7] Y. Morita, T. Ohshima, I. Nashiyama, Y. Yamamoto, O. Kawasaki and S. Matsuda: J. Appl. Phys. 81 (9), 1 May 1997.

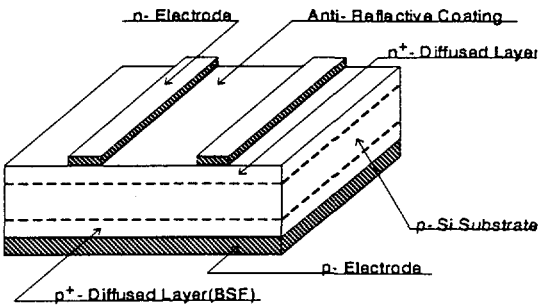

Fig.1. Structure of Si BSFR cell.

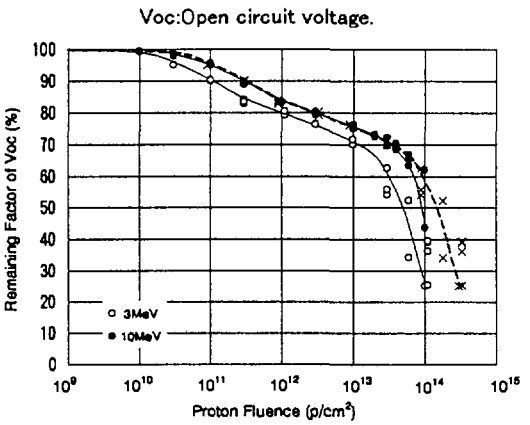

(a)

Fig.2. Degradation of proton irradiated Si BSFR cells.

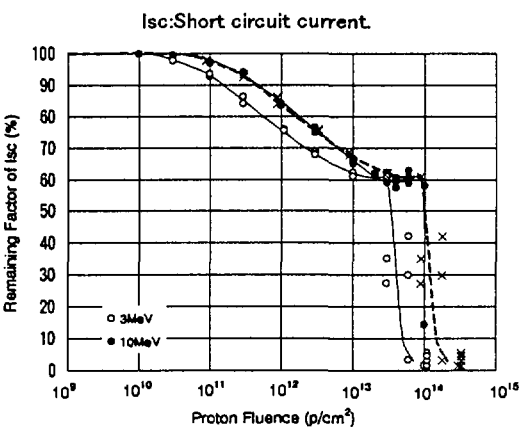

(b)

Fig.2. Degradation of proton irradiated Si BSFR cells.

FF:Fill factor.

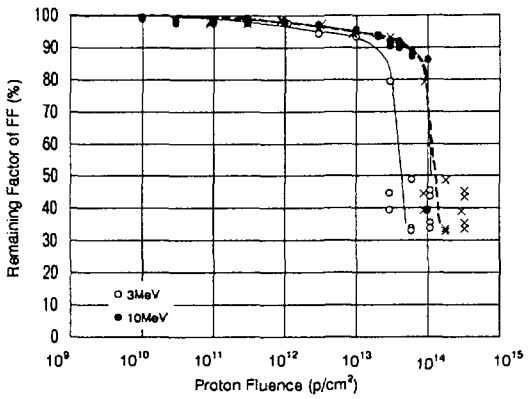

(c)

Fig.2. Degradation of proton irradiated Si BSFR cells.

Pmax:Maximum power.

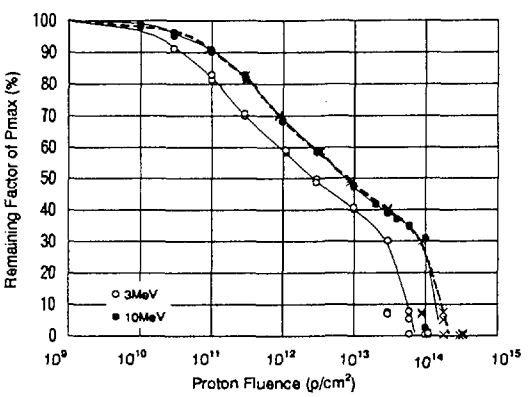

(d)

Fig.2. Degradation of proton irradiated Si BSFR cells.

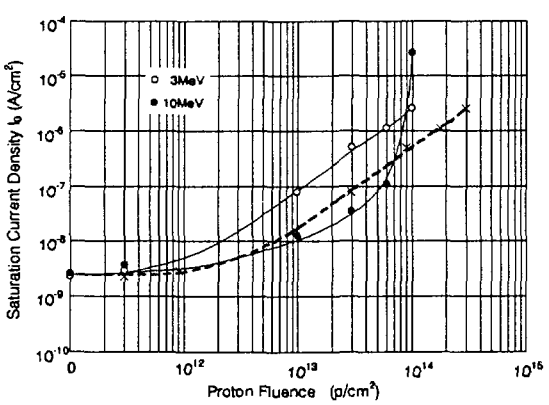

Fig.3. Proton fluence dependence of saturation current density I_0.

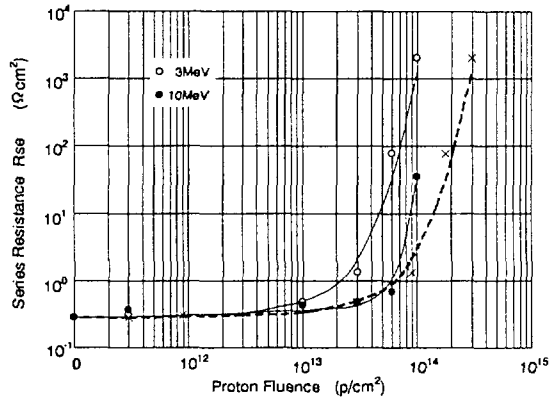

Fig.4. Proton fluence dependence of series resistance Rse.

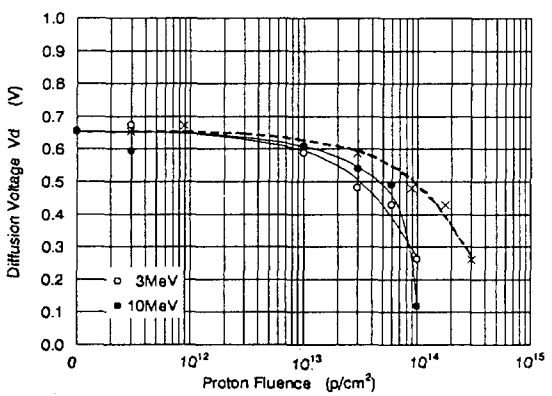

Fig.5. Proton fluence dependence of diffusion voltage Vd.

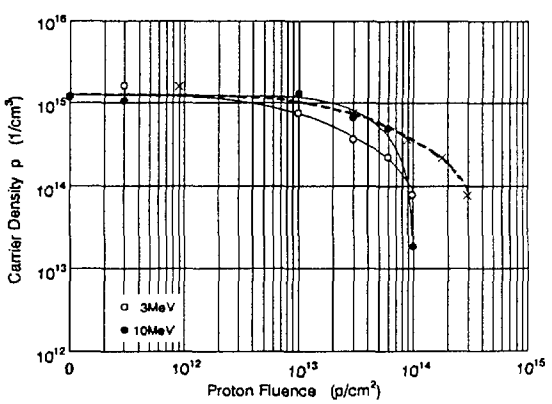

Fig.6. Proton fluence dependence of carrier density p.

In Fig.2～Fig.6, broken lines show the 3MeV proton irradiated data whose fluence are multiplied by 2.97.

1.3 Evaluation of Single-Event Upset Tolerance on 64Mbit DRAM and 16Mbit DRAM

N. Nemoto, H. Shindou, K. Matsuzaki, T. Akutsu, S. Matsuda, T. Hirao*, H. Itoh*, I. Nashiyama*

National Space Development Agency of Japan(NASDA)
* Department of Materials Development, JAERI

ABSTRACT

In recent years, reduction in the mission cost is regarded as one of the most important matters, and thus much effort has been made to reduce the cost of electronic components used in spacecrafts without diminishing their performance. On this policy, there has been a growing interest in space application of commercial devices such as highly integrated memory ICs because of low prices and high performance of such devices. To ensure success in this application, it is indispensable to investigate radiation effects, e.g., single-event and total-dose effects, on commercial devices precisely. In the present study, we have evaluated single-event upset (SEU) tolerance for 1Mbit, 4Mbit SRAM and 16Mbit, 64Mbit DRAM by irradiation of high energy heavy ions such as 175MeV-$Ar^{8+}$and 450MeV-Xe^{23+}. We observed these SEU tolerance in space.

1. Introduction

High radiation tolerance and reliability are required for spacecrafts equipped with semiconductor devices, which are exposed to high energy particles such as solar protons and galactic cosmic rays. From this reason, semiconductor devices used in spacecrafts have been designed and fabricated according to severe specifications. This fact boosts the device cost and also prolongs the development time of qualified devices. Recently in order to decrease the cost of space craft and to increase performance, designer wants to design the space craft with commercial devices. Radiation tolerance and reliability are a problem which must be solved before commercial devices such as highly integrated memory ICs and Microprocessor Unit will be used for the space craft.

It is necessary for these device to do screening test and/or increasing reliability and radiation experiment. In National Space Development Agency of Japan (NASDA), we are discussing about how to use commercial device for space application. Figure 1 shows one of an idea for screening process of commercial devices for space application. In the first screening which is preliminary examination, reliability and radiation tolerance of every commercial devices which is interested in by a system designer are estimated from design and structure of each devices. Irradiation experiment is performed by using californium 252. From these result, if there is a possibility for space usage, then these device are examined in detail. In the second screening, radiation test is performed by using high energy heavy ions from an cyclotron to clear the single-event effects. Reliability is estimated by thermal stress, thermal shock and so on. Then we decide that we can use this commercial device for space application or not.

In the present study, we have evaluated Single-event upset (SEU) characteristics for recent commercial memory ICs by irradiation of high energy heavy ions in order to predict their SEU rate in actual space.

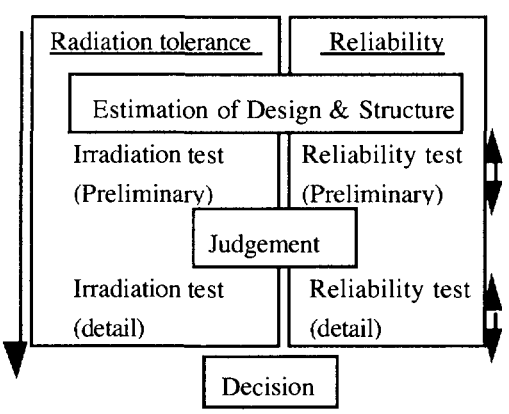

Figure 1. Commercial device screening process for space application

2. Experiment

2.1 Sample

The sample used for our SEU tests were commercial 16Mbit DRAMs, 64Mbit DRAMs, 1Mbit SRAMs and 4Mbit SRAMs. Figure 2 shows Memory cell cross-section of 16Mbit DRAM. This memory device technology are shown in table 1[1]. In this memory device, memory cell capacitor which value is 27fF was performed over the bitline. The value of capacitor is so big that SEU is not occurred by impingement of alpha ray.

Cross-section of 64Mbit DRAM are shown in figure 3[2]. This memory cell also use Capacitor over bitline technology. Table 1 also shows 64Mbit DRAM process technology.

Table 1. 16Mbit and 64Mbit DRAM process technology[1), 2)]

		16Mbit DRAM	64Mbit DRAM
Structure		N well CMOS 2 aluminum layer	3 stacked well CMOS 2 aluminum layer
channel length	PMOS	0.9μm	0.7μm
	NMOS	0.7μm	0.5μm
Gate oxide layer		140Å	110Å
Memory cell	size	3.075μm²	1.25μm²
	structure	Stack (Capacitor Over Bit-line)	
	Capacity	27fF (t_{oxeff}=50Å)	25fF (t_{oxeff}=50Å)
Supply voltage		5.0 ±0.5 V	3.3 ±0.3 V

These process technology data of 16Mbit DRAM and 64Mbit DRAM suggest radiation tolerance. For example, memory cell capacitor has a relationship with a critical charge of SEU occurred. And gate oxide layer thickness is important parameter for total dose effects. But usually it is difficult to get these information. It is well known that general commercial device user can not know the process technology. And commercial devices are often changed process technology of without notice. In the present case, we can not know the process technology data of 1Mbit SRAMs and 4Mbit SRAMs.

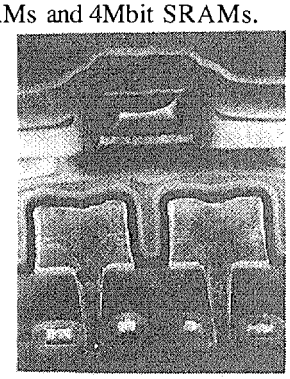

Figure 2. Memory cell cross-section of 16Mbit DRAM[1)]

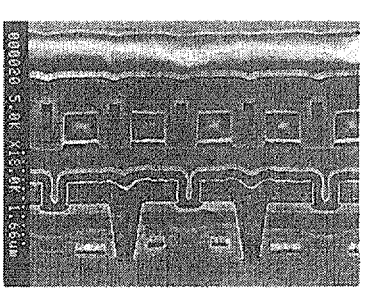

Figure 3. Memory cell cross-section of 64Mbit DRAM[2)]

2.2 Irradiation test

16Mbit DRAMs, 64Mbit DRAMs, 1Mbit SRAMs and 4Mbit SRAMs were irradiated with high energy heavy ions such as 120MeV Ne^{6+}, 322MeV-Kr^{17+}, 520MeV Kr^{20+} and 450MeV Xe^{23+} by using an AVF cyclotron in JAERI Takasaki.

Using these high energy heavy ions, the memory devices were irradiated directly and in a defocused mode. To obtain the SEU cross-section, both the number of memory bits in which upset occurred and total ion fluence were measured. From the SEU measurements under several irradiation conditions, we obtained the SEU cross-section as a function of LET in silicon. We varies irradiation angle and supplied voltage of memory. It is well known that there is a relationship between irradiation angle θ and LET in silicon, and cross-section σ. The equation is as follow:

$$LET_{eff} = \frac{LET}{\cos\theta} \quad , \quad \sigma = \frac{\sigma_{eff}}{\cos\theta} \qquad (1)$$

Where LET_{eff} is effective LET, σ_{eff} is effective cross-section.

3. Result and discussion

The LET dependence of the SEU cross-section for 16Mbit DRAMs and 64Mbit DRAMs are shown in figure 4. Data of 1Mbit SRAM and 4Mbit SRAM are shown in figure 5. These result are fitted by using weibull distribution[3)]. Fitting result are also shown in figure 4 and 5.

The threshold LET and the saturated cross-section are derived from the SEU cross-section vs. LET[4)], which are shown in table 2. 16Mbit DRAMs from 3 different companies were tested and results were compared. It is found that threshold LET was almost the same. But saturated cross-section was not the same. The difference between these device is about an order of magnitude. This result can be explained by difference of process technology and structure. This result suggests that it is important to know each device SEU tolerance which we want to use in space application.

Comparing with 16Mbit DRAMs and 64Mbit DRAMs which was made by same company, the threshold LET was found to decrease from 4.1 to 2.4(MeV/(mg/cm²)). The saturated cross-section decreased also from 1.6×10^{-7} to 3.0×10^{-8}(cm²/bit). These results can be explained by the decrease of memory cell capacity and cell size. It is well known that there is correlation between saturated cross-section and memory cell size, and also between critical charge and memory capacitor. In the table 1, memory cell capacitors of 16Mbit DRAM and 64Mbit DRAM are almost same. So threshold LETs are almost the same.

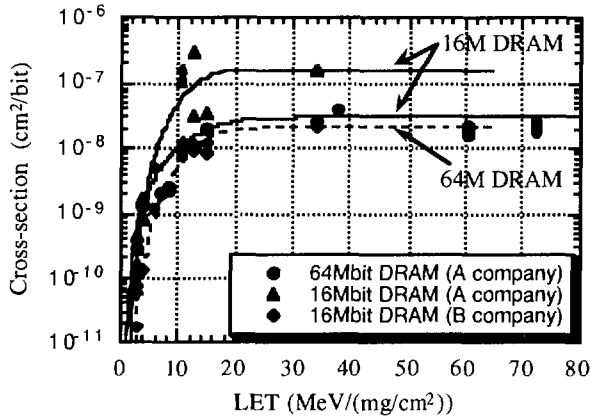

Figure 4. LET vs. cross-section of 16Mbit DRAM and 64Mbit DRAM

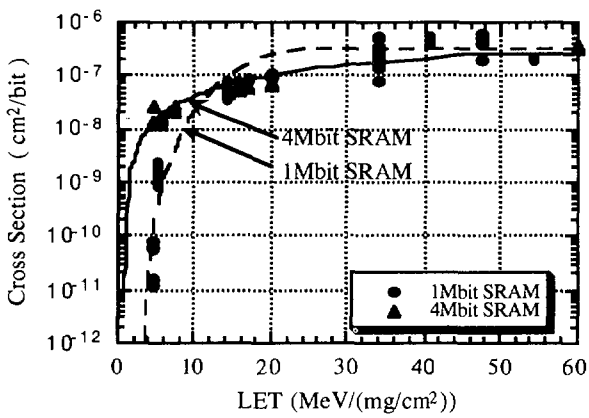

Figure 5. LET vs. cross-section of 1Mbit SRAM and 4Mbit SRAM

Table 2. Threshold LET and Saturated Cross-section

	Threshold LET (MeV/(mg/cm^2))	Saturated cross-section (cm^2/bit)
1Mbit SRAM	7.1	3.3×10^{-7}
4Mbit SRAM	2.5	4.2×10^{-7}
16Mbit DRAM (A company)	4.1	1.6×10^{-7}
16Mbit DRAM (B company)	4.2	2.1×10^{-8}
64Mbit DRAM (A company)	2.4	3.0×10^{-8}

In comparing same company made 1Mbit SRAMs and 4Mbit SRAMs, the saturated cross-section was almost the same. But the threshold LET decreased from 7.1 to 2.5(MeV/(mg/cm^2)). From this result, radiation sensitive area which has correlation with saturated cross-section does not change widely regardless of process technology improvement. From the decrease in the threshold LET, we can say that improvement of process technology causes decrease in critical charge of the SRAM device.

From these result, it is suggested that the threshold LET of the DRAMs is not change much in spite of memory process technology improvement. But in the SRAMs, it decreases. This difference may be caused by memory structure. Memory capacitor of DRAMs are made using capacitor over bitline which is stack cell technology. But it is difficult for memory cell of SRAMs to use same technology. Because a SRAM memory cells does not have a memory capacitor. It has only a flip-flop circuit.

4. Conclusions

We have evaluated SEU tolerance for recent commercial memory ICs by irradiation of high energy heavy ions in order to predict their SEU tolerance in actual space. The threshold LET and the saturated cross-section are derived from the SEU cross-section vs. LET. From these result, it is obtained that:

1. 16Mbit DRAM has higher radiation tolerance compared with 4Mbit SRAM made the same process technology.
2. Improving process technology, upset rate of SRAM increases. On the other hand, in DRAM it decreases.
3. The SEU cross-section of 16Mbit DRAMs differ by company

5. Acknowledgment

The authors would like to thank the Ryouei Technica Corporation and NEC people for their help in performing high energy heavy ion irradiation and for many discussions throughout the course of this experiment.

References

1. Shigeru Koshimaru, Seiichi Hannai, et al., 1993, 2nd Generation 16Mbit DRAM, NEC Technology Journal, 90-92.
2. Akihiko Kagami, Shyuichi Tsukada, et al., 1995, Development of 64Mbit DRAM (2nd Generation), NEC Technology Journal, 11-15.
3. E. L. Petersen et al., 1992, Rate Prediction for Single Event Effects, IEEE Trans. Nucl. Sci. NS-39, 1577-1599.
4. I. Naito et al., 1993, An Evaluation of the Single Event Upset Effect by Heavy Ion on SRAM for Space Application, JAERI TIARA Annual Report (vol. 3), 8-9

1.4 Measurement of SEU sensitive area of a random access memory

Toshio Hirao, Tsuyoshi Hamano, Takuro Sakai and Isamu Nashiyama
Department of Materials Development, JAERI

1. Introduction

Single-event upset (SEU) is triggered when an amount of electric charges induced by energetic ion incidence exceeds a value known as a critical charge in a very short time period. In order to solve this problem and develop single-event free devices, it is important to clarify the mechanisms of the SEU, e.g., the transportation of charges induced in devices by ion irradiation. Nuclear microprobe techniques have been applied for the first time to SEU-transient current measurements[1,2,3] and then expanded to SEU mapping in SRAM[4,5] and DRAM chips [6,7] and ion-beam-induced-current (IBIC) measurements [5,6].

In the present work, we apply microbeams of oxygen and silicon ions in order to measure sensitive area in SRAM. We have obtained detailed information about the sensitive areas of SEU.

2. Experimental

Experiments were performed by using a focused heavy-ion microbeam apparatus installed on a beam line of 3 MV tandem accelerator at JAERI Takasaki. We used a NCMOS 256 kbit (4 bit x 64 word) SRAM. Figure 1 shows the schematics of experimental set up.

The size of whole bit-cell array of the SRAM was measured to be 2.6 mm x 6 mm by using an optical microscope, and the number of the bits are 256 bits on a row and 1024 bits on a column. So, a bit-cell size is calculated to be 10.3 μm x 5.9 μm. The, SEU threshold LET of this SRAM is known to be 6.4 MeV cm^2/mg.

The energy and the specie of an ion beam were selected so that its LET in Si is larger than the SEU threshold LET.

We used a 15 MeV O^{4+} microbeam whose size determined by SEM is 1 μm in diameter, and whose LET in Si is 6.9 MeV cm^2/mg which is high enough to cause upsets[6]. The beam current was weakened to be 100～1000 ions/sec in order to avoid radiation damage.

The position of the microbeam irradiation was determined by using a long distance microscope and a secondary electron imaging technique. Irradiation time is controlled by using an electrostatic fast beam switch which consists of a pair of parallel electrodes, a high voltage power supply and a pulse generator.[7]

2. Result and Discussion

On an area of 31 μm x 15 μm of the bit-cell array, pin-point irradiation was made by shifting the microbeam at horizontal intervals of 1.6 μm and at vertical intervals of 1.9 μm. In Figure 2, irradiation points where SEU occurred are indicated with ●. Figure 2 shows irradiation points for "1" to "0" upset. Total numbers of upset points are 72 and 94 for "1" to "0" and for "0" to "1" upset, respectively.

Figure 3 is an enlarged map of the area enclosed by the rectangle frames. Symbols of (0▶1),(1▶0) and (0▶1,1▶0) mean the modes of the upset occurred at the same bit. The hatched rectangular area corresponds to the area of the single bit-cell derived from Figure 2. From this map, one can say that the hatched rectangular area is approximately the same as the calculated bit-cell size (10.3 μm x 5.9 μm).

The up-set sensitive areas are 21.4 μm^2 and 19.2 μm^2 for the up-set modes of ("0" to "1") and ("1" to "0"), respectively. The upset-cross-section(σ_1) can be calculated to be 20.3 x 10^{-8} cm^2/bit by taking the average. Whereas, the up-set cross-section (σ_2) obtained by using Kr and Ar ions from AVF cyclotron is 3.2 x 10^{-8} cm^2/bit.

Therefore, σ_1 is about an order of magnitude larger than σ_2.

This difference is not understood well at present. Further investigation is needed.

4. Conclusion

By applying oxygen ion microbeams combined with SRAM read-write system, we have measured single-event soft-error maps with about 2 μm resolution.

The sensitive areas of SEU induced by the heavy ion incidence on the SRAM are successfully obtained by mappingg.

References

[1] I. Nashiyama et al., IEEE Trans. Nucl. Sci. NS-40(1993) 1935-1940

[2] T. Hirao et al., Nucl. Instrum. Methods in Phys, Res. B104,

[3] T. Hirao et al., TIARA ANUAL REPORT (Vol. 1~5)

[4] K.H.Horn et al., IEEE Trans. Nucl. Sci. NS-39, 7 (1992)

[5] S.Metzger et al., IEEE Trans. Nucl. Sci. NS-41,589(1994)

[6] H.Sayama, M. Takai et al., Jpn. J. Appl. Phys. 31, 4541(1992)

[7] M. Takai et al., Nucl. Instr. and Methods B77, 344(1993)

[8] K.H.Horn et al., Nucl. Instr. and Methods B77, 355(1993)

[9] T. Kamiya, M. Utsunomiya, E. Minehara, R. Tanaka, and I. Ohdomari, Nucl. Instr. and Meth.B64(1992) 362

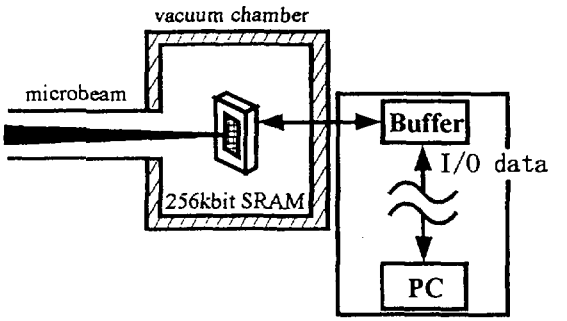

Fig.1 Schematic diagram of SRAM read-write system. SEU is measured by this system and data are stored in PC.

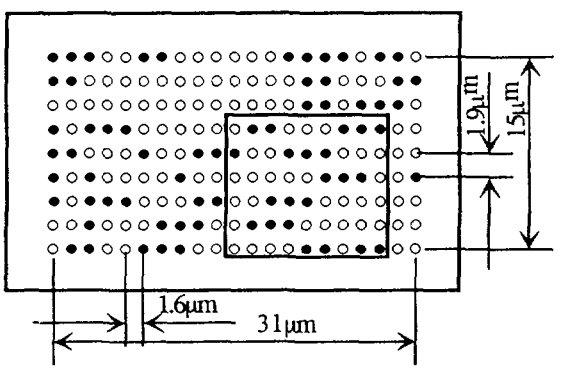

Fig.2 Upset bit map. In this map, irradiation points where "1" to "0" upset occurred indicated with ●.

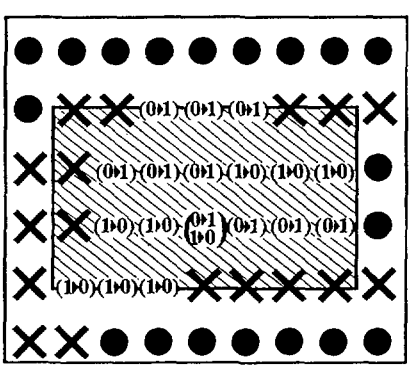

Fig.3 An enlarged map of the area enclosed by rectangle frames in Fig.2. Symbols of (0 ▶ 1), (1 ▶ 0) and (0 ▶ 1, 1 ▶ 0) mean the upset mode. Hatched rectangular area corresponds the calculated single bit-cell of 10.3μm x 5.9μm.

1.5 Production of point defects in silicon carbide semiconductor by irradiation of high energy ions

Hisayoshi Itoh, Takeshi Ohshima, Toshio Hirao and Isamu Nashiyama
Department of Materials Development, JAERI

1. Introduction

Energetic particles like electrons and ions are known to create defects in solid due to the direct collision of particles with lattice atoms. In recent years, the production and annealing of point defects due to electronic excitation induced by energetic particles have been found in some kinds of metal.[1] Based on this fact, it can be speculated that the same phenomena take place in semiconductors. Very little is, however, known about the effects of electronic excitation on the production and annealing of defects in semiconductors. Since ion-beams are commonly used in the fabrication processes of semiconductor devices, the studies of point defect introduced in semiconductors by ion irradiation are important from technological as well as physical points of view.

We deal with cubic silicon carbide (3C-SiC) in this study because it is a promising material for high-power, high-frequency, and radiation-resistant devices. In previous papers[2,3], we showed the formation of silicon vacancies in 3C-SiC by irradiation of 120MeV-Ne^{6+}. In this paper, we evaluate the displacement of silicon atoms in 3C-SiC subjected to irradiation of several high-energy heavy-ions based on the results of electron spin resonance (ESR) measurements and a Monte Carlo simulation. We also discuss the effects of electronic excitation on annealing of point defects.

2. Experimental

Single crystalline 3C-SiC films with a thickness of ≈30μm were epitaxially grown on Si substrates by chemical vapor deposition using SiH_4-C_3H_8-H_2. After the growth, the Si substrates were etched off with an HF-HNO_3 solution. These films were irradiated with 175MeV-Ar^{8+}, 330MeV-Ar^{11+}, and 120MeV-Ne^{6+} at fluences up to $10^{14}/cm^2$ using an AVF cyclotron in JAERI Takasaki. Temperature of the samples is estimated to be kept below 100°C during the irradiation. In order to characterize point defects in the irradiated samples, ESR measurements were performed at RT. The spin number of paramagnetic defects was determined within an accuracy of a factor of 2 by using DPPH and Mn^{2+} in MgO as spin standards.

3. Results and Discussion

The spin density of silicon vacancies generated in thin 3C-SiC films by irradiation of 120MeV-Ne^{6+}, 330MeV-Ar^{11+}, or 175MeV-Ar^{8+} was obtained as a function of ion fluence from ESR measurements.[2] The number of silicon atoms displaced by irradiation of an ion was derived from the fluence dependence of the spin density of silicon vacancies, and the results are shown in Table I. The numbers of silicon and carbon atoms displaced by an ion were also calculated using the Monte Carlo simulation (TRIM-95). In this simulation, we used a

Table I The number of atoms displaced in SiC by ion irradiation. The results obtained experimentally and calculated numerically are shown. Stopping power of each ion calculated for SiC is also indicated.

Ion Species	Stopping Power (MeV/mg/cm²)			Displacement Measured (/ion)	Displacement Calculated (/ion)		
	Total	Electron	Nuclear	Si	Total	Si	C
120MeV-Ne	4.973	4.970	2.8×10^{-3}	47.0	304	169	135
330MeV-Ar	11.538	11.531	6.5×10^{-3}	43.9	647	359	288
175MeV-Ar	15.561	15.550	11.4×10^{-3}	280.5	4175	2319	1856

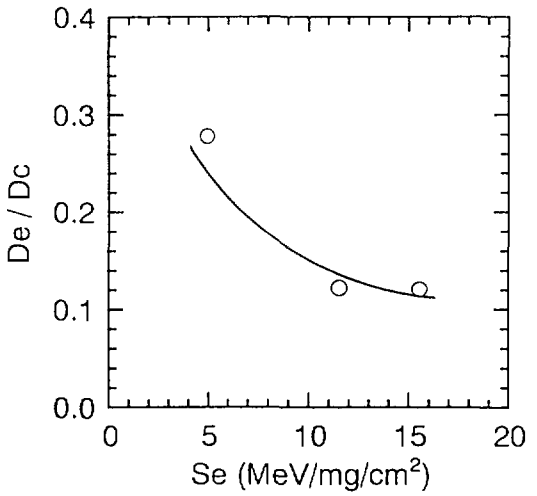

Fig.1 The ratio of the displacement of silicon atoms obtained experimentally (De) to that calculated numerically (Dc) as a function of electronic stopping power (Se) for 3C-SiC irradiated with 120MeV-Ne, 330MeV-Ar, and 175MeV-Ar ions.

displacement energy of 23eV and a lattice binding energy of 6.7eV. The calculation results are represented in the same table. In every case, the number of displacement of silicon atoms obtained experimentally is much less than that calculated numerically. It is expected from this difference that silicon vacancies produced primarily are partially annealed during ion irradiation. It was found that silicon vacancies in 3C-SiC were annealed at a stage of 750°C.[3,4] This fact suggests strongly that silicon vacancies themselves are immobile during the irradiation. Thus, it is most likely that the partial annealing of silicon vacancies during irradiation is caused by interactions between silicon vacancies and the other point defects such as interstitials.

The ratios of the displacement of silicon atoms per ion obtained experimentally (De) to that calculated numerically (Dc) are estimated to be 0.278, 0.122, and 0.121 for 120MeV-Ne, 330MeV-Ar, and 175MeV-Ar ion irradiation, respectively. The values of De/Dc are plotted in Fig.1 as a function of electronic stopping power (Se). The concentration of displaced silicon atoms, i.e., the density of silicon vacancies is suggested to decrease with increasing Se. This can be interpreted by the supposition that the interactions between silicon vacancies and interstitials are enhanced due to electronic excitation induced by irradiation. In order to clarify the effects of electronic excitation on annealing of point defects in 3C-SiC, further investigations are necessary.

4. Summary

We have performed ESR measurements of single crystalline 3C-SiC films irradiated with 120MeV-Ne^{6+}, 330MeV-Ar^{11+}, and 175MeV-Ar^{8+}. The number of silicon atoms displaced by a heavy ion was estimated from the spin density of silicon vacancies. Comparison between the number of displacement of silicon atoms obtained experimentally and that calculated theoretically using TRIM-95 suggests partial annealing of silicon vacancies during the irradiation. This annealing is probably due to the interactions between silicon vacancies and the other point defects like interstitials. It is also suggested that these interactions are enhanced due to electronic excitation induced by irradiation.

References

1) A. Iwase and T. Iwata, Nucl. Inst. & Methods Phys.Res. B90, 322 (1994).
2) H. Itoh, T. Ohshima, T. Hirao, and I. Nashiyama, in JAERI-Review 1996, (TIARA Annual Report-1995).
3) H. Itoh, A. Kawasuso, T. Ohshima, M.Yoshikawa, I.Nashiyama, S.Tanigawa, S. Misawa, H. Okumura, and S. Yoshida, to be published in phys. stat. sol. (a) Vol.162 (1997).
4) H.Itoh, N.Hayakawa, I.Nashiyama, and E.Sakuma, J.Appl.Phys.66, 4529 (1989).

1.6 ESR Studies of High-Energy Phosphorus Ion Implanted Diamond Crystals (II)

J. Isoya, S. Wakoh, M. Matsumoto Y. Morita* and T. Ohshima*
University of Library and Information Science, * Department of Material Development, JAERI

1. Introduction

Boron-doped diamond crystals are *p*-type semiconductors with the acceptor level of 0.37 eV. With a wide energy gap, a high thermal conductivity, a high mobility for both electrons and holes, and a high radiation hardness, diamond is a promising material for electronic devices for high-speed, high-power applications and for those used in a harsh environment. However, applications of diamond for active devices in electronics are severely limited, since synthesis of *n*-type semiconducting diamond has not been established, yet.

Phosphorus is among those impurities expected as potential candidates of *n*-type dopants of diamond. We have been searching a condition for doping of phosphorus by using high energy (9-21 MeV) ion implantations. By using high energy ions, the implants are located in the regions far from the surface. Since the slow-down processes of the implants create lattice damages, annealing which reduces the radiation damages and induces activation to drive the implant into the required lattice site is critically important in ion implantation doping. Since diamond is a metastable state of carbon at ambient pressures, both the implantation conditions and the annealing conditions need to be carefully chosen. We use electron spin resonance (ESR) method to characterize the radiation damages and, hopefully, to identify the local structure of the implanted ions.

In diamond implanted with heavy ions at room temperature, the ESR signal assigned to be arising from the randomly-oriented dangling bonds (broken bonds) in the amorphous phase is, usually, the only feature observed as the implantation-induced ESR signal before heat treatment.[1,2] By decreasing the fluence (< ~4×10^{14} ions/cm^2), we observed ESR signals of point defects in addition to that of dangling bonds. In the high energy implantations, it has been found that, under low fluences (< ~1×10^{15} ions/cm^2), the paramagnetic dangling bonds are created with a rate of 2.5×10^2 spins/ ion. At high fluences, the increase of the number of spins of the dangling bonds exhibits a tendency of saturation, reflecting the collapsing of microscopic amorphous particles into larger amorphous islands, and eventually, into a continuous amorphous layer. The degree of the amorphization is also manifested in the linewidth and the temperature dependence of the linewidth of the ESR signal of dangling bonds.

In the case of implantation at room temperature, even at low fluences, isolated microscopic amorphous particles are formed.[3] The reduction of the formation of the amorphous phase should be achieved by using implantations at high temperatures. In the present work, implantations at high temperatures have been carried out.

2. Experimental

High-pressure synthetic diamond crystals of type IIa were irradiated with phosphorus ions from a 3MV tandem accelerator. Diamond crystals which contain least amount of impurities belong to type IIa. The samples had a shape of regular plate, with a size of $3\times3\times1$ mm^3 with the wider plane being (100). The ion beam was scanned over an area of 2×2 cm^2. Implantation was performed along the [100] axis. For hot implantation, the samples were mounted on a molybdenum hot plate. The ESR spectra were recorded on a Bruker ESP300 X-band spectrometer by

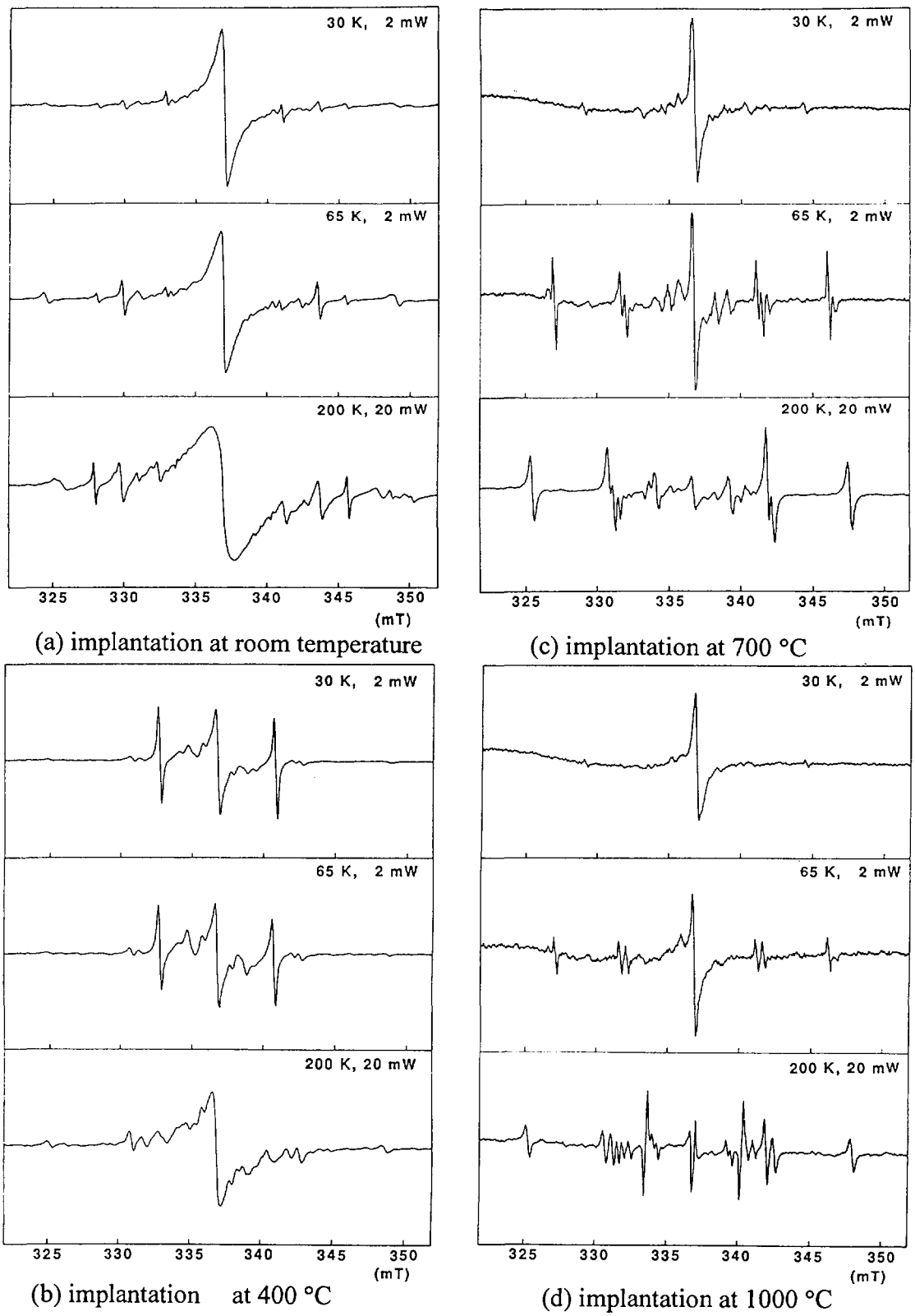

Fig.1 ESR spectra (B//[100], 293 K, 9.44 GHz) of high pressure synthetic diamond crystals of type IIa implanted with phosphorus ions at nine different energies in the range from 9 to 21 MeV with a fluence of 4×10^{12} ions/cm^2 at each energy.

using an Oxford Instrument ESR-900 to control the sample temperature.

3. Results and Discussion

In our present work, we used a low fluence at which the amorphous phase is formed as isolated amorphous particles for implantation at room temperature. The growth of the amorphization through overlap of ion tracks is manifested as the motional narrowing of the ESR signal of dangling bonds.[3] In the case of implantation at room temperature, for high fluences, the linewidth of the ESR signal of dangling bonds is smaller than that of dangling bond of amorphous carbon (*a*-C) and its temperature dependence is small.[3] With a fluence lower than $\sim 4\times10^{13}$ ions/cm^2, the linewidth of dangling bonds increases markedly with the increase of temperature. The depth profile of implanted ions varies with the energy of implantation. Since the lattice damages are mostly created in the region where implanted ions come to rest, it is expected that implanting a crystal at various energies should give a lower density of the radiation damages than implanting the same total number of phosphorus ions at one energy.[4] Irradiation was carried out at nine different energies from 9 to 21 MeV, with a fluence of 4×10^{12} ions/cm^2 at each energy. By implanting each crystal at various energies, a relatively good S/N of ESR signals is achieved, while keeping the low density of radiation damages.

The ESR spectra of type-IIa synthetic crystals implanted with high energy phosphorus ions at various target temperatures (room temperature, 400 °C, 700 °C, and 1000 °C) are shown in Fig.1. For the implantation at room temperature, the linewidth of the ESR signal of dangling bond increases with the increase of temperature (ΔH_{pp}=3.65 mT at room temperature), which is likely to be unique to small isolated amorphous particles embedded in the crystalline lattice.[3] In the case of implantation at 400 °C, the presence of the ESR signal of dangling bonds (the signal at g=2.0026 with the linewidth 0.64 mT at 200 K) indicates that the amorphous phase was formed. The linewidth of the ESR signal of dangling bonds of implantation at 400 °C is smaller than that of implantation at room temperature. It is likely that the structure of the small isolated amorphous particles depends on the temperature at which they are formed.

After implantation at 700 °C and after that at 1000 °C, the ESR signal of dangling bond was not observed. In diamond, the vacancy which is formed as radiation damages is mobile at ~600 °C. While the lattice vacancies have been identified by ESR, there is no direct experimental information of isolated self-interstitial which must be formed as the Frenkel partner to the lattice vacancy in the radiation-damage experiments. It is generally presumed that the self-interstitial is mobile below room temperature. Considerable reduction of the formation of the amorphous phase requires a target temperature higher than the migration temperature of the vacancy.

In Fig. 1, ESR signals from several kinds of point defects are observed. Detailed ESR measurements of single crystal rotation to clarify whether phosphorus is associated with any of these point defects or not are under way.

The synthetic type-IIa diamond crystals used in the present work were supplied from Sumitomo Electric Industries. Our project is being carried out as collaboration with Dr. H. Kanda (NIRIM).

4. References

1) P. R. Brosius *et al*, Phys. Stat. Sol. 21, 677-683 (1974)
2) M. Teicher et al, J. Appl. Phys. 53, 1467-1469 (1982)
3) J. Isoya *et al*, Rad. Phys. Chem. in press.
4) J. Isoya *et al*, Diamond Relat. Mater., 6, 356-360 (1997)

2. Biotechnology

(continued to the next page)

2.1 Development of gene transfer technique for pollen using the penetration-controlled irradiation with ion beams

A.Tanaka, H. Watanabe, Y. Hase*, M. Inoue*, M. Kikuchi, Y. Kobayashi and S. Tano**
Department of Radiation Research for Environment and Resources, JAERI, *Department of Agriculture, Kyoto Prefectural University, **Advanced Science Research Center, JAERI

1. Introduction

Agrobacterium-mediated DNA transfer technique and direct gene transfer into protoplasts on the basis of the electroporation technique have been frequently used for the gene transfer methods in plants. However, *Agrobacterium*-mediated DNA transfer technique is hardly adapted to mono-cotyledonous plants. Laborious preparation of protoplasts and its cultures are needed for the direct gene transfer technique. These deficiencies found in gene transfer techniques will be largely overcome if pollen could be used as a DNA vector. However, several difficulties will also presented in this approach. One of major problems is pollen-specific envelop which is hard to pass for exogenous DNA [1].

We have previously established the penetration-controlled irradiation with ion beams for the biological study [2]. When dry pollen were exposed to He or C ions with shallow penetration-depth (e.g. 4 μm depth in the case of He ions), the leaky pollen, which was thought to be a physical lesion in the pollen envelop induced by ion beams, was efficiently produced [2]. Furthermore, only a few number of varied plants have been obtained from the crosses using the irradiated pollen with shallow penetration-depth, whereas a number of varied plants were observed in the case using the irradiated pollen with deep penetration-depth [3]. These results suggest that gene transfer into pollen and subsequent normal plants would be acquired by taking advantage of the penetration-controlled irradiation with ion beams.

In this study, we examined efficiencies of gene transfer into the ion-irradiated pollen. Especially, combined effects of ion fluence, DNA concentration and penetration-depth of ions on transient GUS gene expression were investigated.

2. Materials and Methods

2.1. *Ion beam irradiation*

Irradiation apparatus for Cell (IAC) [4], which has been connected to a beam line of 3 MV tandem accelerator, was used for the penetration-controlled irradiation. Dry pollen of tobacco (*Nicotiana tabacum* L. cv Bright Yellow 4, 20 μm in thickness) was monolayered on plastic plate and irradiated with 6 MeV He^{2+} ions. The penetration-depth of ions into a target was controlled by the distance between the beam-window and the target as described by Tanaka et al. [2].

2.2 *Germination assay*

The irradiated pollen were collected and put on the agar nutrient medium (1 % agar, 10 % sucrose, 100 ppm boric acid). After incubated in the dark for 24 h at 25°C, germination rates were measured.

2.3. *Transient GUS assay*

For transient GUS assay, the irradiated pollen were collected into a plastic tube, and incubated in 10 μl of DNA solution (0~100 μg/ml pBI 221 containing the CaMV 35S promoter, GUS coding region and NOS terminator, 10 % sucrose, 100 ppm boric acid) for 1 h at r.t. The solution was then put on the agar nutrient medium, and incubated in the dark for 24 h at 25°C. Histochemical GUS assay of pollen were performed by replacing the culture solution with a solution of 3 mM X-Gluc in 50 mM NaH_2PO_4, 10 mM EDTA at 25°C for up to 4 days. The percentage of the number of pollen in which GUS activity were observed against total number of pollen tested was measured as GUS expression rate.

3. Results and Discussion

3.1. *Effect of the penetration-controlled irradiation on germination*

Table 1 shows the result of germination rates after irradiations with

Table 1 Germination rate (%) after penetration-controlled irradiation with He ions

Ion fluence (p/cm^2)	Control	Penetration depth in pollen (μm)		
		2	4	6
0	57±8.3	—	—	—
4×10^{9}	—	31±4.5	24±5.7	48±4.6
4×10^{10}	—	21±2.9	12±1.0	23±2.7
4×10^{11}	—	17±3.7	0.1±0.1	1.3±0.2

Values represent the mean± SD.

penetration-controlled He ions. In the case of the irradiation with a fluence at 4 X 10^{9}, little inhibition of germination was observed in the irradiation with 6 μm penetration-depth. As ion fluence increased, however, pollen germination was more inhibited. In the case of the irradiation with a fluence at 4 X 10^{11}, most of pollen could not germinate. Thus, irradiated pollen with a fluence less than 4 X 10^{11} seems to be suited for gene transfer.

Concerning the effect of penetration-depth, the irradiation with 4 μm penetration-depth was most effective compared with 2 μm or 6 μm penetration-depth. We previously showed that leaky pollen, which seemed to be caused by a physical lesion in the pollen envelop, were most induced by the irradiation with 4 μm penetration-depth [2]. Therefore, the effective inhibition of germination observed in the irradiation with 4 μm penetration-depth would be resulted from physical lesions of pollen envelop.

3.2. *Effects of the ion fluence and DNA concentration on transient GUS activity*

In order to obtain an effective transformation into subsequent plant by the use of irradiated and transformed pollen as a DNA vector, it should be needed for a combination of three key points; effective transformation into pollen, little-damaged pollen irradiated with ions and minimum DNA content enough to be transformed.

Fig. 1 shows the results of histochemical GUS assay when ion fluence and DNA concentration altered. GUS activity was observed in the unirradiated control, and increased as DNA concentration increased. Higher GUS activity rate was obtained in pollen those were irradiated with 4 X 10^{9} at 4 μm penetration-depth and treated with 50 μg/ml DNA concentration, compared with unirradiated pollen. No increase was

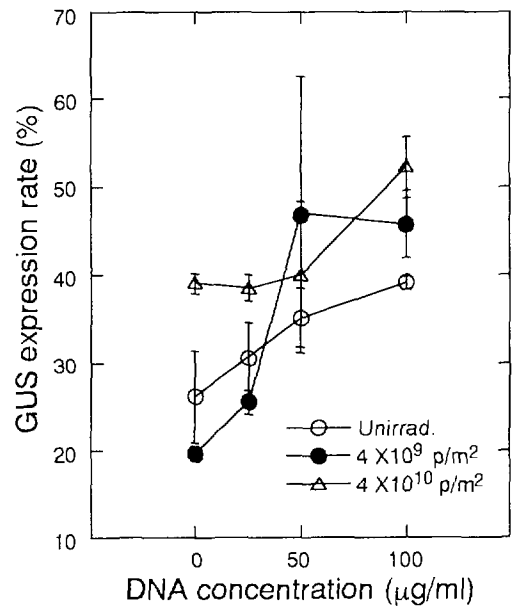

Fig. 1 Transient GUS expression rate as a function of DNA concentration.
Pollen were irradiated with He ions with 4 μm penetration-depth, and were incubated with DNA solution.

observed in DNA concentration at 100 μg/ml compared with at 50 μg/ml. In the case of the irradiation with a fluence at 4 X 10^{10}, high and constant levels of GUS activity rate were observed in treatments with DNA solution at 0-50 μg/ml.

Existence of endogenous GUS or GUS-like reaction has been reported in tobacco pollen [5,6]. This suggests that GUS activity observed in pollen treated with non-DNA containing solution will be an endogenous GUS activity. It is indicated, therefore, that the net GUS activity introduced from pBI221 containing GUS gene should be a subtraction GUS expression rate in the pollen treated with non-DNA containing solution from total GUS expression rate. Considering this

Table 2 GUS expression rate (%) in pollen irradiated with penetration-controlled He ions

Ion fluence (p/cm^2)	Unirradiated control		Penetration depth in pollen (μm)		
	− DNA	+ DNA	2	3	4
0	24.2 ± 1.1	31.3 ± 1.9	—	—	—
4×10^9	—	—	37.7 ± 2.7	36.8 ± 3.2	55.1 ± 3.2
4×10^{10}	—	—	35.2 ± 7.5	49.6 ± 6.6	35.2 ± 4.2

Values represent the mean ± SD.

matter, our results will indicate that the pollen which is irradiated with a fluence at 4 X 10^9 and treated with DNA at 50 μg/ml are most effectively transformed.

3.3 *Effects of the penetration-depth of ions and ion fluence on transient GUS activity*

As described above, penetration-depth of ions in pollen is one of major keys to pollen transformation. Table 2 shows the effects of penetration-depth of ions in pollen and ion fluence on transient GUS expression rate. In the case of irradiations with a fluence of 4 X 10^9, pollen irradiated with 4 μm penetration-depth yielded highest GUS expression rate. The net GUS expression rate introduced from exogenous GUS gene will be estimated to be approx. 31 %, in contrast with 7 % in the case of the unirradiated control. On the contrary, in the case of irradiations with a fluence of 4 X 10^{10}, pollen irradiated with 3 μm penetration-depth yielded high GUS expression rate. The lower GUS expression rate observed in the irradiation with 4 μm penetration-depth at a fluence of 4 X 10^{10}, compared with at a fluence of 4 X 10^9, will be resulted from a lowering of germination rate, that is, pollen activity. It should be noted that a combination of penetration-depth and ion fluence is important for a efficient gene transfer into pollen. These results will indicate that ion-irradiation with 4 μm penetration-depth or shallower depth is enough to introduce exogenous DNA into pollen if ion fluence will sufficient for enlargement of permeability of pollen envelop for DNA uptake.

4. References

[1] I. Potrykus (1990) in *Bioactive compounds from plants*, Wiley, Chichester (Ciba Foundation Symp. 154) 198-212

[2] A. Tanaka, H. Watanabe, T. Shimizu, M. Inoue, M. Kikuchi, Y. Kobayashi, S. Tano (1997) *Nucl. Instr. and Meth. in Phys. Res. B*, In press

[3] A. Tanaka, T. Yamashita, S. Tano, M. Kikuchi, Y. Kobayashi, H. Watanabe (1995) *TIARA Ann. Rep.*, 5: 29-31

[4] M. Kikuchi, A. Tanaka, Y. Kobayashi, R. Nozawa, H.Watanabe (1992), *TIARA Annual Report* 1: 159-162

[5] S. Kosugi, Y. Ohashi, K. Nakajima, Y. Arai (1990) *Plant Science*, 70:133-140

[6] J. E. Wilkinson, D. Twell, K. Lindsey (1994) *Plant Science*, 97: 61-67

2.2 Analysis of carbon ion- and electron-induced mutations in *Arabidopsis thaliana*

Naoya Shikazono, Yukihiko Yokota*, Atsushi Tanaka, Hiroshi Watanabe and Shigemitsu Tano
Advanced Science Research Center, JAERI, * Beam Operation Co. Ltd.

1. Introduction

High linear energy transfer (LET) radiation such as ion particles causes localized, dense ionization within cells compared to low LET radiation such as X-rays or γ-rays [1]. Based on microdosimetric and radiobiological considerations, it is proposed that high LET radiation would predominantly produce double strand breaks with damaged end groups whose repairability would be low [2,3]. Therefore, it seems plausible that high LET radiation would be able to generate large genetic changes more frequently than low LET radiation.

In plants, some investigations on the molecular nature of mutations induced by X-rays, γ-rays and fast neutrons have been carried out along with the isolation of genes. Although rearrangement types of mutations were observed in several genes, it was shown that these radiations frequently induced deletions whose lengths were larger than several thousand base pairs. Recently, Bruggemann et al. [4] reported that 13 out of 18 long hypocotyl 4 (*hy4*) mutants of *Arabidopsis* induced by fast neutrons carried deletions larger than 5 kb. However, there are few investigations in plants on the type of mutation induced by high LET ion particles. Only Mei et al. [5] reported that a rearrangement was induced in the semi-dwarf mutant of rice by argon ions, using a random genomic clone as a probe.

In order to investigate the molecular nature of mutations induced by high LET radiation in plants, a comparison was made between DNA fragments amplified by the polymerase chain reaction (PCR) from carbon ion- and electron-induced *Arabidopsis* mutants. The PCR analysis indicated that one of the characteristics of the carbon ion mutagenesis was the frequent induction of rearrangements rather than deletions. Furthermore, to clarify the molecular nature of mutations induced by carbon ions in more detail, nucelotide sequences of the *GL1* locus from the wild type and from one of the carbon ion-induced *gl1* mutant were determined. It was indicated from the comparison of the nucleotide sequence that complex rearrangements were induced by carbon ion-irradiation.

2. Materials and methods

2.1. Plant material

Plants of *Arabidopsis thaliana* ecotype Columbia were grown on rock wool at temperatures around 25 °C in an air-conditioned greenhouse, and were subirrigated at 3- or 4-day intervals with 0.03% HYPONeX (HYPONEX Co. Ltd., USA). Seeds of the mutants used for the complementation test were provided from the Nottingham Arabidopsis Stock Center (NASC).

2.2. Irradiation and mutant isolation

Irradiation of dry seeds was carried out as previously described [6]. The energy of carbon ions was 220 MeV and the mean LET within the seeds was calculated to be 113 keV/μm by the computer program OSCAR, which was developed by Hata and Baba [7]. The energy of electrons was 2MeV and the mean LET was calculated to be 0.2 keV/mm. The dry seeds were irradiated with a dose of 150 Gy for carbon ions and 750 Gy for electrons. Irradiated M1 seeds (14,400 for carbon ions and 9600 for electrons) were sown and selfed to obtain M2 seeds. *gl*, *tt*, *hy* mutants were screened from 52407 M2 plants derived from carbon ion-irradiated M1 and from 44009 M2 plants derived from electron-irradaited M1. For the complementation test, *gl* mutant lines were crossed with *gl1-1*, *gl2-1* and *gl3-1* mutants, and *tt* mutant lines were crossed with *tt3-1*, *tt4-1*, *tt5-1*, *tt6-1* and *tt7-1* mutants.

2.3. DNA extraction and molecular analysis

Genomic DNA was extracted from the mutants of M3 generation following the procedure described by Konieczny and Ausubel [8]. Primers for PCR were designed using the computer software Genetyx Mac ver. 7.3 (Software Development Co. Ltd., Japan). The amplified DNA fragments were analyzed by agarose gel electrophoresis in TAE buffer and were visualized by ethidium bromide staining. For further analysis, *Hin*d III restricted fragments containing the *GL1* locus from wild type and from one of the *gl1* mutant induced by carbon ions were cloned into pUC18. Sub-

sequently, both fragments were sequenced by dideoxy termination method.

3. Results and Discussion

Mutation frequencies per locus per diploid cell per dose for carbon-induced *tt*, *gl*, and *hy* were 3.4×10^{-6}, 1.8×10^{-6}, 2.3×10^{-6}, respectively and for electron-induced *tt*, *gl*, and *hy*, mutation frequencies were 0.14×10^{-6}, 0.25×10^{-6}, and 0.14×10^{-6}, respectively (Table 1). It was indicated from the present result that mutation frequencies by carbon ions were 7 fold to 24 fold higher than those by electrons.

Comlementation analysis revealed that 4 mutant lines, composed of two *gl1* mutants and two *tt4* mutants, were induced by carbon ions, and 5 mutant lines, composed of three *gl2* mutants, one *tt3* mutant and one *tt4* mutant, were induced by electrons.

The results of the PCR analysis at the 4 loci, of which mutants were induced in the present study, is schematically shown in Fig. 1. An analysis of a *gl1* mutant induced by carbon ions (panel A a) demonstrates that a break occurred at exon 3 between primer 5 and 4 and then either the upstream or downstream region was inverted or translocated. In the other *gl1* mutant induced by carbon ions (panel A b), no DNA fragment was amplified. This result indicated that this mutant carried either a deletion larger than 3.1 kb or a rearrangement. In the case of rearrangement, it is presumed that 2 breaks (one between primer 3 and 5 and the other between primer 4 and 6) occurred, and the regions seperated by those breaks underwent inversions or translocations. Panel B shows the results of 3 lines of *gl2* mutant, which are all induced by electrons. Two of these lines (a and b) showed no detectable changes in number or size of the amplified DNA fragments, suggesting that point-like mutations were generated in these mutants. In the residual *gl2* mutant (c), the result indicated that a break occurred at exon 3 between primer 6 and 4 and that either inversion or translocation took place. Panel C shows the result of a *tt3* mutant induced by electrons. Since no detectable change was observed, it was estimated that a point-like mutation occurred in this mutant. The result of *tt4* mutants are presented in panel D. In the case of the *tt4* mutant induced by carbon ions (a), it was revealed that a break within exon 2 (between primer 7 and primer 8) occurred and that either the upstream or downstream fragment underwent inversion or translocation. The residual *tt4* mutants (b and c), one induced by carbon ions and the other induced by electrons, may both carry point-like mutations. Supposing the carbon ion-induced *gl1* mutant which showed no detectable PCR fragments arose from rearrangements, 3 out of 4 mutants induced by carbon ions and 1 out of 5 mutants induced by electrons resulted from rearrangements. These results implyed that, rather than large deletions, rearrangements were frequently generated among mutants induced by carbon ion irradiation in *Arabidopsis*.

Comparing the nuceotide sequences of the *GL1* locus from the wild type and from the carbon induced mutant (Fig. 1, Panel A a) revealed that a break occurred at exon 3, 91 bp upstream from the 3' end (Fig. 2). Downstream sequences from the break were identical between the mutant and the wild type. In the mutant, unknown fragment of 107 bp in length was inserted upstream of the break. Further upstream of the 107 bp insertion, 3' flanking region of *Atpk7* gene was found to be joined. These results imply that complex rearrangements occurred after carbon ion irradiation.

The conclusion that carbon ions mainly induced rearrangements in *Arabidopsis* shows a clear contrast to the results of mammalian cells in which the majority of large genetic changes induced by high LET radiation were deletions. Further analyses at the sequence level to elucidate the repair process of induced damage in *Arabidopsis* are now in progress.

References

1. Kraft, G., Kramer, M. and M. Scholz (1992), Radiat. Environ. Biophys., 31, 161-180.
2. Hagen, U. (1994), Radiat. Environ. Biophys., 33, 45-61.
3. Goodhead, D. T. (1995), Radiat. Environ. Biophys., 34, 67-72.
4. Bruggemann, E., Handwerger, Essex, C. and G. Storz (1996), Plant J., 10, 755-760.
5. Mei, M., Deng, H., Lu, Y., Zhuang, C., Liu, Z., Qiu, Q., Qiu, Y. and T. C. Yang (1994), 10, 363-372.
6. Tanaka, A., Shikazono, N., Yokota, Y., Watanabe, H. and S. Tano (1997), , Int. J. Radiat. Biol., in press.
7. Hata and Baba (1988) , JAERI-M,88-184.
8. Konieczny, A. and F. M. Ausubel (1993), Plant J., 4, 403-410.

Table 1. Mutation frequencies for mutants induced by carbon ions and electrons

Mutagen	Loci	Number of M1 seeds	Number of M2 plants	Number of mutants	Mutation frequency /locus/cell/ dose (Gy) ($\times 10^{-6}$)
carbon ions 150Gy	*TT3,TT4,TT5, TT6,TT7*	14400	52407	29	3.4
	GL1,GL2,GL3, TTG	14400	52407	12	1.8
	HY1,HY2,HY3, HY4,HY5,HY6	14400	52407	23	2.3
electrons 750Gy	*TT3,TT4,TT5, TT6,TT7*	9600	44009	5	0.14
	GL1,GL2,GL3, TTG	9600	44009	7	0.25
	HY1,HY2,HY3, HY4,HY5,HY6	9600	44009	6	0.14

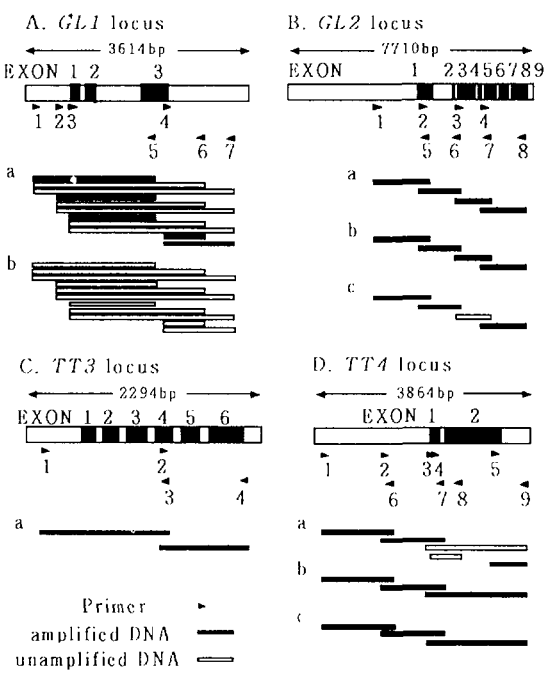

Figure 1. Schematic representation of the results of the PCR analysis of the mutants. The number of base pairs that was sequenced and the location of exons and primers are presented at each locus. DNA fragments which were amplified are shown as black boxes, whereas DNA fragments which were not are shown as white boxes. Panel A: *gl1* mutants induced by carbon ions (a, b); Panel B: *gl2* mutants induced by electrons (a, b, c); Panel C: *tt3* mutant induced by electrons (a); Panel D: *tt4* mutants induced by carbon ions (a, b) and by electrons (c).

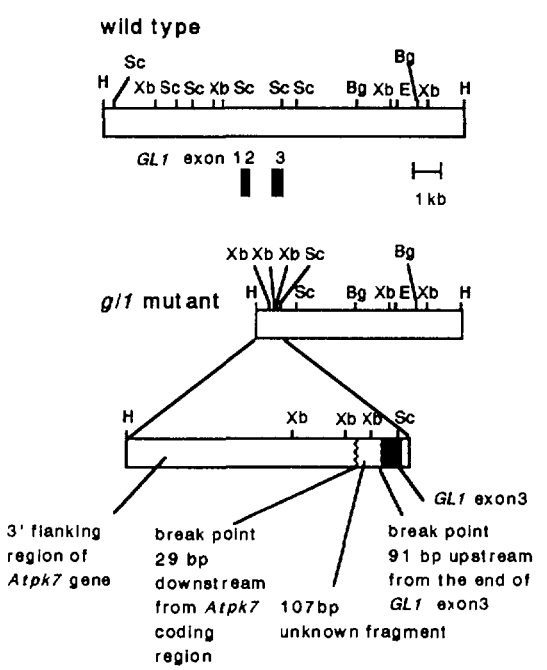

Figure 2. Schematic representation of the *GL1* locus in the wild type and in the carbon-induced mutant (Fig. 1, Panel A a). The position and size of the exons are shown beneath the wild type DNA fragment. The restriction enzyme sites are indicated. H=*Hin*dIII, Sc=*Sca*I, Xb=*Xba*I, Bg=*Bgl*II, E=*Eco* RI.

2.3 Influence of LET on Repair of DNA Double-Strand Breaks in *Deinococcus radiodurans*

Y. Kobayashi, M. Kikuchi, A. Tanaka and H. Watanabe.
Department of Radiation Research for Environment and Resources, JAERI.

1.Introduction

It is widely accepted that the cellular response to ionizing radiation is mainly determined by damage to DNA. Especially, the induction of double strand breaks (DSBs) in DNA has been considered to be a predominant determinant of radiotoxicity, because the patterns of DSBs/LET response for normally radioresistant cells are comparable to the shape of the LET response for cell lethality[1]. Increases in LET were assumed to cause increases in the extents of damage associated with DSBs in DNA. As the cells with normal resistance to sparsely ionizing radiation seemed to be able to repair efficiently other forms of DNA damage, those changes were supposed to be accompanied by decreasing abilities of cells to recover from radiation damage. Therefore the induction of DSBs has been thought to contribute significantly to the RBE value of a given radiation.

A maximum of the RBE for inactivation of mammalian cells has been observed around 100 keV/μm[2,3]. However, recent data of DSBs yields in cells obtained with protons, α-particles and heavier ions demonstrate that the yields of DSBs do not vary significantly with increasing LET over a range where RBE varies widely[4-9]. To explain these LET effects, it is assumed that radiations of differing qualities produce different complexities of lesions which are currently not distinguished in the current assays used to measure DSBs. High-LET-specific-damage such as clustered lesions, that is, more complex DSBs occurring in the LET range of enhanced biological efficiency, are considered as the dominant damage of DNA for cell lethality[10,11]. Accordingly, the maximum of the RBE around 100 keV/μm is likely due to lower repairability of DSBs induced in the LET range, rather than higher yields of DSBs.

Deinococcus radiodurans[12] can repair all DNA lesions including DSBs induced with doses up to 5 kGy[13,14]. This extraordinary radiation resistant bacterium is also resistant to heavy ion irradiation and the survival curve had a large shoulder[15-17]. Those facts suggest that this bacterium can also repair DSBs induced by heavy ions.

Therefore we have studied the inactivation of *Deinococcus radiodurans.* caused by heavy ions; and we have already demonstrated that all survival curves were characterized by a large shoulder of the curves and no final slopes at the exponential part of survival curves for heavy ion irradiation were steeper than that for 2.0 MeV electron irradiation[18,19]. The plots of relative biological effectiveness (RBE) versus linear energy transfer (LET) showed no obvious peaks suggesting that this bacterium can repair not only DSBs but also clustered damage in DNA which may be induced by heavy ions. Then we analyzed the induction of DSBs in genomic DNA of *D. radiodurans* and the repair process during post-irradiation incubation. Using a pulsed-field gel electrophoresis (PFGE) technique, we detected the reappearance of ladder pattern of genomic DNA digested with a restriction enzyme *Not* I before PFGE analysis to study the LET dependence of the DNA rejoining process.

2.Experimental

(1) *Cell material*

Deinococcus radiodurans R_1 strain was cultivated in TGY liquid medium (0.5% Bacto-Tryptone, 0.3% Bacto-Yeast extract, Difco Laboratories; 0.1% glucose, pH 7.0) with shaking at 30°C for 24 hrs. The cells were harvested in the stationary phase, and then washed and resuspended with 0.1 M sodium phosphate buffer (PB), pH 7.0. To examine the survival responses 1×10^3-1×10^4

cells were settled on a membrane filter (pore size 22 μm, diameter 47 mm, Millipore Corporation) and the filters were placed on PB agar plates (10 mM sodium phosphate buffer, pH 7.0, containing 2% Bacto-Agar, Difco Laboratories). For PFGE analysis of DSBs induction and rejoining of DNA, 3×10^8 cells were settled on the membrane filter as a monolayer.

(2) *Irradiation method*

The cells on the membrane filters were irradiated in the atmosphere using the method of track segment experiment with 25 MeV/u $^4He^{2+}$ and 18 MeV/u $^{12}C^{5+}$ ions from the AVF cyclotron at TIARA. The particle fluence was determined by microscopic counting of etched particle tracks on track detector CR-39. To convert particle fluence to dose in Gy, the following relationship was used:

$$\text{Dose [Gy]} = 1.6 \times 10^{-9} \times \text{LET [keV/μm]} \times \text{Fluence [particles/cm}^2\text{]}$$

Dose uniformity of scanned ion beams was checked with radiochromic dosimeter (RCD) or track detector. LET values were calculated with ELOSS code developed in JAERI. The cells were also irradiated with 2.0 MeV electron beams from a Cockcroft-Walton accelerator.

(3) *Analysis of surviving fractions*

After irradiation, the membrane filters were transferred onto TGY agar plates and surviving colonies were counted after 3 days incubation at 30°C. Dose response curves for inactivation of *D. radiodurans* R_1 were obtained by plotting the fraction of surviving colonies versus particle fluence and radiation dose. From the final slope of the curves, cross sections ($\sigma = 1/F_{37}$) were determined for inactivation. To obtain the values of RBE, inactivation constants (D_0) and 10% surviving dose (D_{10}) were calculated for both heavy ions and electrons taking into account the corresponding LET.

(4) *Post-irradiation incubation*

After irradiation, the membrane filters were transferred onto TGY agar plates and incubated at 30°C to induce DNA repair enzymes. Then the filters were transferred onto TGY agar plates containing 100 μg/ml of chloramphenicol (CP) to inhibit protein synthesis, and incubated at 30°C to continue DNA repair process without allowing the cells to restart their growth. To determine the total needed time to complete the repair process, the incubation time on the CP-containing TGY agar plate was changed after a constant CP-free window sufficient to induce repair enzymes.

(5) *Pulsed-Field Gel Electrophoresis (PFGE)*

The irradiated cells were embedded in agarose plugs and incubated in lysis buffer as previously described[18,19]. The agarose plugs were cut into 4.5 mm length. Genomic DNA in a plug piece was digested with 30 units of *Not* I restriction endonuclease at 37°C for more than 10 hrs. Then PFGE was performed as previously described[18,19] with a transverse alternative field electrophoresis system, GeneLine™ (Beckman). The agarose gels were stained with 0.5 μg/ml of ethidium bromide (EtBr) for 1 hr and destained twice in distilled water. The ladder pattern of DNA fragments were photographed on the ultraviolet transilluminator.

3.Results and Discussion

The genomic DNA of *D. radiodurans* cells was cleaved into large fragments with the restriction enzyme *Not* I after post-irradiation incubation, and the fragments were separated and detected using PFGE. Figure 1 shows the reappearance of ladder pattern of DNA fragments during post-irradiaton incubation accompanied with rejoining process of DNA DSBs induced by irradiation with 2 kGy of 18 MeV/u $^{12}C^{5+}$ ions. Incubation time was prolonged from 2.5 hrs to 5.5 hrs, and the total needed incubation time to complete the repair process was estimated at 4 hrs according to the reappearance of DNA banding pattern shown in Figure 1.

Figure 2 shows the total repair time necessary for the rejoining of DSBs after irradiation with 2 kGy of 2 MeV electrons (LET=0.3 keV/μm), 25 MeV/u $^4He^{2+}$ ions (LET=9 keV/μm) and 18 MeV/u $^{12}C^{5+}$ ions (LET=120 keV/μm). The longer repair time was needed after the higher LET irradiation at the equal dose in Gy, although the RBE for cell killing after irradiation with $^4He^{2+}$ was equal to the RBE for electrons, and the RBE

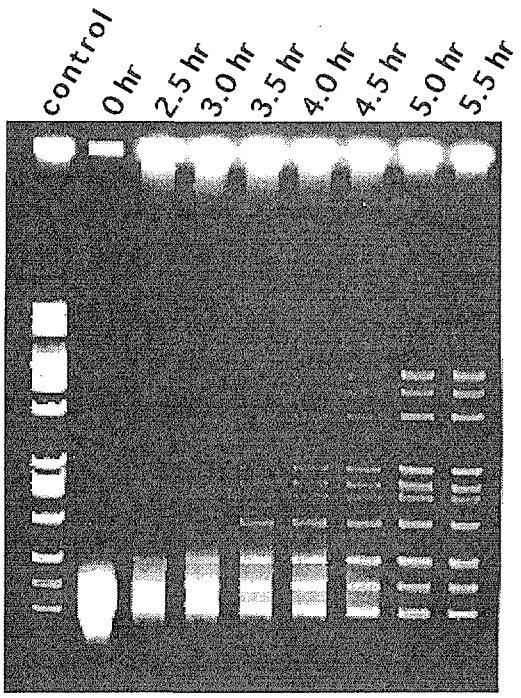

Figure 1. PFGE analysis of the rejoining of radiation induced DSBs during post-irradiation incubation: Normal banding pattern of genomic DNA of *D. radiodurans* digested with restriction enzyme *Not* I (control), time course of the DSBs rejoining during post-irradiation incubation after irradiation with 2 kGy of 18 MeV/u $^{12}C^{5+}$ ions (0 to 5.5 hr).

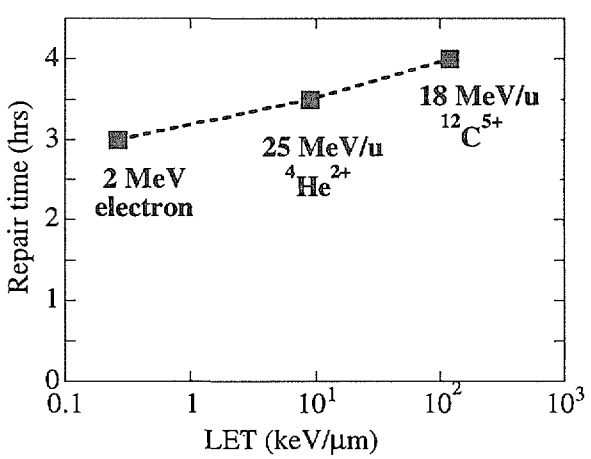

Figure 2. Total repair time including the CP-free window necessary for the rejoining of DSBs induced in *D. radiodurans* genomic DNA after irradiation with 2 kGy of 2 MeV electrons, 25 MeV/u $^4He^{2+}$ ions and 18 MeV/u $^{12}C^{5+}$ ions.

for $^{12}C^{5+}$ ions was lower than those RBE values[18,19]. This result indicates that it takes longer time to repair DNA lesions induced by .higher LET heavy ions compared with low LET electrons even for *D. radiodurans*, although the DNA lesions are finally to be repaired completely and furthermore higher LET heavy ions have lower RBE values.

References

(1) J.T. Lett, *Radiat. Environ. Biophys.*, **31**, 257-277 (1992)
(2) G. W. Barendsen. and H. M. D. Walter, *Radiation Research*, **18**, 106-119 (1963)
(3) E. A. Blakely, *Radiat Environ Biophys.*, **31**, 181-196 (1992)
(4) K. M. Prise *et al.*, *International Journal of Radiation Biology*, **58**, 261-277 (1990)
(5) M. Belli, *et al.*, *International Journal of Radiation Biology*, **65**, 529-536 (1994)
(6) T. J. Jenner, *et al.*, *International Journal of Radiation Biology*, **61**, 631-637 (1992)
(7) M. Löbrich, *et al.*, *Radiation Research*, **139**, 142-151 (1994)
(8) G. Taucher-Scholz, *et al.*, *Radiat Environ Biophys.*, **34**, 101-106 (1995)
(9) J. Heilman, *et al.*, *International Journal of Radiation Biology*, **68**, 153-162 (1995)
(10) K. M. Prise, *et al.*, *International Journal of Radiation Biology*, **66**, 537-542 (1995)
(11) D. T. Goodhead, *et al.*, *International Journal of Radiation Biology*, **65**, 7-17 (1994)
(12) B. W. Brooks, *et al.*, *International Journal of Systematic Bacteriology*, **31**, 353-360 (1981)
(13) S. Kitayama and A. Matsuyama, *Biochem. Biophis. Res. Commun.* **33**, 418-422 (1968)
(14) S. Kitayama and A. Matsuyama, *Agr. Biol. Chem.* **35**, 644-652 (1971)
(15) D. L. Dewey, *International Journal of Radiation Biology*, **16**, 583-592 (1969)
(16) M. Kikuchi, *et al.*, *JAERI TIARA Annual Report 1992* ,(**2**), 34-37 (1993)
(17) Y. Kobayashi, *et al.*, *TIARA Annual Report 1994* (**4**), 44-46 (1995)
(18) Y. Kobayashi, *et al.*, *TIARA Annual Report 1995* (**5**), 35-37 (1996)
(19) Y. Kobayashi, *et al.*, *JAERI-Conf 97-003: 7th International Symposium on Advanced Nuclear Energy Research*, 68-72 (1997)

2.4 Microbeam System for Local Irradiation of Biological Systems

Y. Kobayashi, M. Taguchi and H. Watanabe
Department of Radiation Research for Environment and Resources, JAERI.

1.Introduction

Recently laser microbeam irradiation has been used for cell biology and developmental biology, however ion microbeam has not been applied. Therefore we have designed and installed a microbeam apparatus at TIARA to develop a novel cell manipulation technique, which is called Cell Surgery technique [1,2]. To investigate the effect of local irradiation of heavy ions on various biological system, *e.g.* fertilized eggs of insect and meristematic tissue of plant, the energy of the ions must be high enough to penetrate the region of interest in the target. Therefore the apparatus has been connected to a vertical beam line of AVF cyclotron giving heavy ion beams ranging from 12.5 MeV/u ^{4}He to 11.0 MeV/u ^{40}Ar. This particle spectrum covers an LET range between 14-1800 keV/μm. The beams have been collimated to about 10 μm in diameter using a set of apertures.

2.Outline of Microbeam System for Local Irradiation

The apparatus has been installed under the vertical beam line of AVF cyclotron. This microbeam system has two vacuum chambers, connected to each other with an isolation gate valve and a conductance pipe, and two sets of pumps for differential vacuum pumping to pass the ions from the second chamber into the air through an aperture on the microprobe. Electrical status signals are given by a main control unit which supervises the vacuum system, positions of collimators and the status of Faraday cups. CCD-camera image of beam spot on beam monitors can be observed from a neighboring room. Almost all functions of this microbeam system can be controlled by both local control unit beside the apparatus and remote control unit from a neighboring room.

Figure 1(A) shows a schematic diagram of the biological microbeam system. Heavy ion beams from the AVF cyclotron are introduced to the first chamber through a bending magnet and a pair of beam steering magnets. The shape and the position of the beam spot can be observed with beam monitor 1. Two aluminum collimators with 5 mmϕ aperture and 0.5 mmϕ aperture, respectively, are set in the first chamber. The lower collimator with 0.5 mmϕ aperture is set on the micropositioning X-Y stage 1. The intensity of the ion beams through the collimators can be measured with the Faraday cup 1 and 2, respectively.

The ion beams through the first chamber are introduced to the second chamber passing through the isolation gate valve. After adjustment of the position of the beam spot on the beam monitor 2, the ion beams are extracted from the second chamber into the air with a microaperture in a tantalum disk perforated using a spark erosion method. The microprobe is attached to the tilt-adjuster and fixed on the micropositioning X-Y stage 2, which is connected to the second chamber with a flexible bellows.

The alignment of the beam is achieved by the use of the beam steering magnet system upstream of the vertical beam line and two sets of micropositioning X-Y stages in the apparatus. The intensity and the energy of ion beams on the target micropositioning stage or after penetrated the target are measured with a plastic scintillator, CR-39 track detector and solid-state detector (SSD) in the atmosphere.

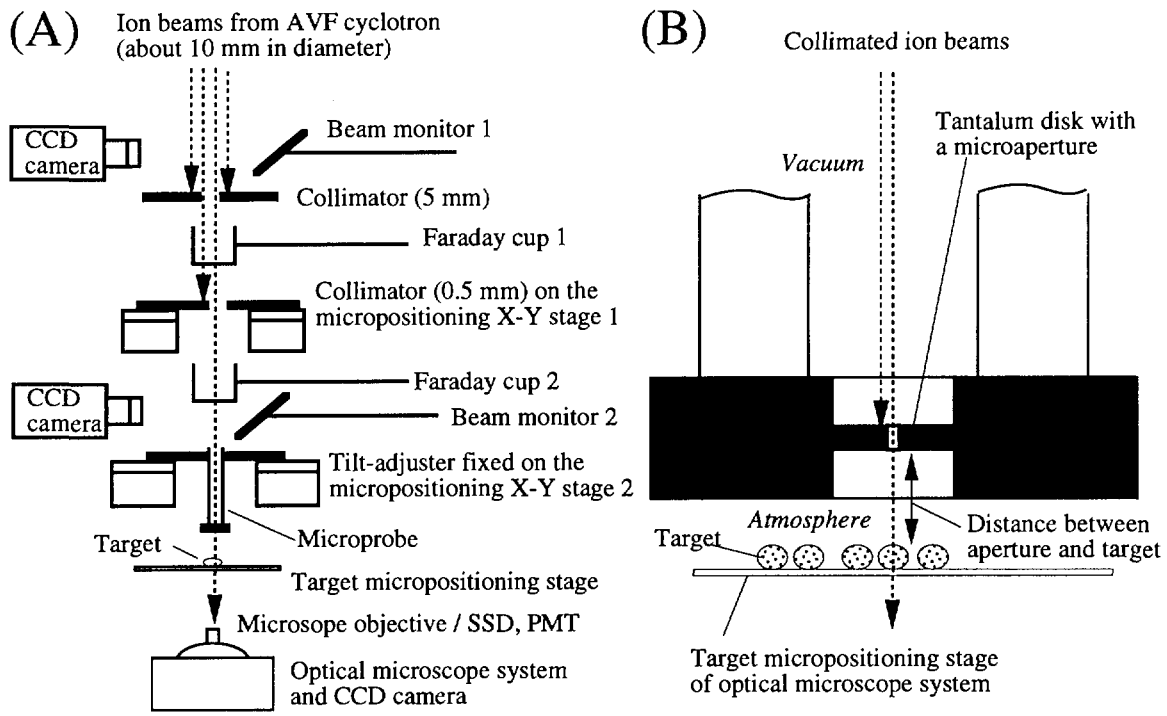

Figure 1. Schematic diagram of microbeam system for local irradiation installed under the vertical beam line of AVF cyclotron at TIARA. **(A)** Beam collimation system of the microbeam apparatus. Heavy ion beams introduced from the AVF cyclotron are about 10 mm in diameter at the Beam monitor 1. **(B)** Detailed view of the end of the microprobe. Sizes of microapertures of available microprobes are 10 to 250 μm in diameter.

During irradiation, the biological target can be observed with optical microscope system under the microprobe. The X-Y stage 2 and the whole optical microscope system are held with an anti-vibration damper. Almost all functions of optical microscope system, *e.g.* focus, lighting, objective and stage positioning can be controlled from a neighboring room. Detailed view of the end of the microprobe is shown in Figure 1(B). The minimum aperture size of available microprobe is about 10 μm in diameter.

3.Spatial Distribution of Etched Ion Tracks on the Target

To characterize the collimated ion beams passing through the microaperture, intensity and energy of the ions were measured with a plastic scintillator and a photomultiplier, and with solid-state detector. The particle fluence at the target position was also determined by electron microscopic counting of etched particle tracks on track detector CR-39 exposed to the ion beams on the target micropositioning stage. The particle fluence determined with a track detector corresponded with that measured with a scintillator and a solid-state detector. Obtained beam flux was about 1-10^5 ions/sec.

Figure 2(A) shows spatial distribution of etched ion tracks on CR-39 exposed to collimated 17.5 MeV/u ^{20}Ne ions at distances of 1 mm and 5 mm between aperture and target. Microprobes with apertures of 40, 90 and 250 μmϕ on 0.5 mm-thick tantalum disk, respectively, were used. Normalized particle fluence was flat in the "core" region around a center of beam distribution. The size of the core was equal to the size of the microaperture. On the CR-39 exposed to ions at a distance of more than 1 mm, two

components of halo were observed outside of the core; "inner halo" where a ratio of particle fluence decreases with a steep slope from 1 to about 10^{-2}, and "outer halo" with a gradual distribution of widely scattered ions. At every exposure, the ratio of particle fluence in halo was decreased to 10^{-2} at about 25 μm of radial distance from the edge of the core.

The width of inner halo increased as the ion path through air became longer (Figure 2B). It suggests that the size of inner halo may reflect the divergence of ion beams passed through the microaperture.

References

[1] Y. Kobayashi, M. Taguchi, S. Okumura and H. Watanabe, *JAERI TIARA Annual Report*, 1995 (Vol.5), 38-40 (1996).

[2] Y. Kobayashi, H. Watanabe, M. Taguchi, S. Yamasaki and K. Kiguchi, *Proceedings of the 12th Symposium on Microdosimetry*, (Oxford, U.K., September 29-October 4, 1996), in press.

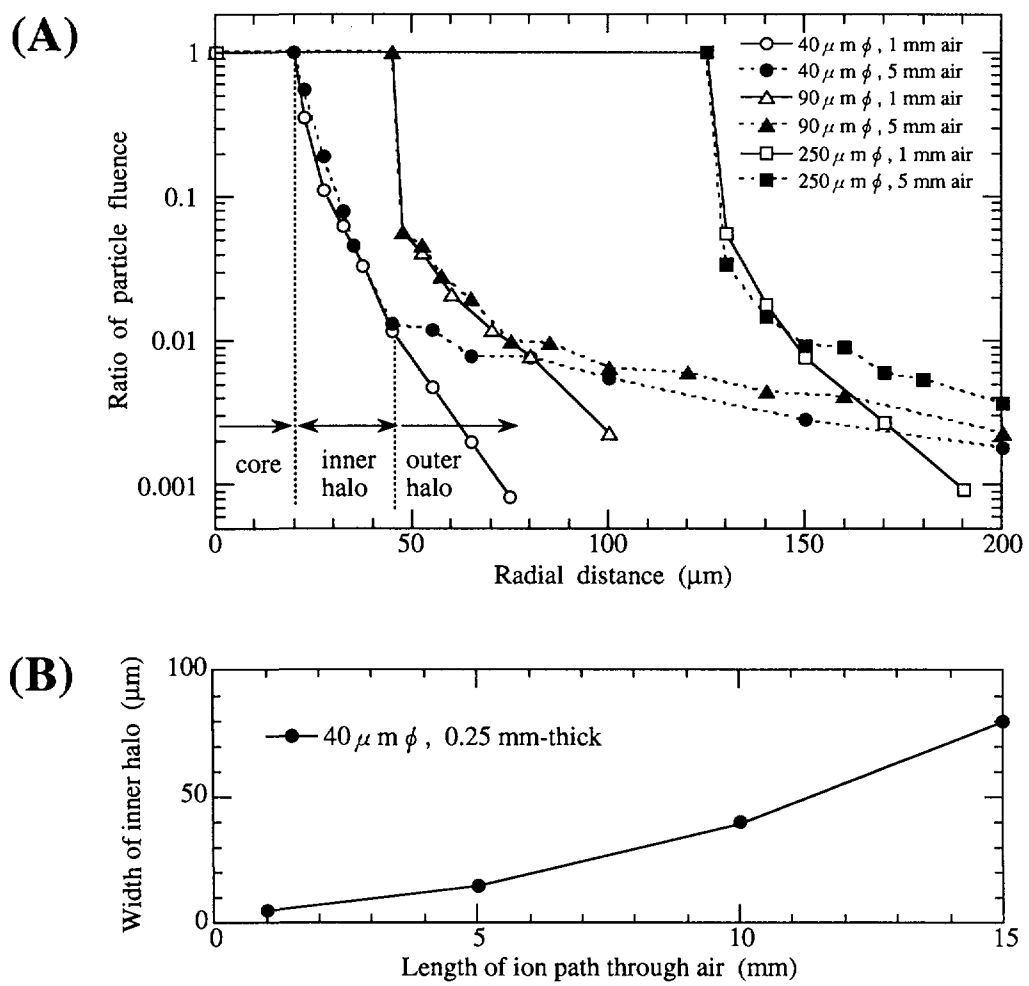

Figure 2. Effect of diameter of microaperture and air gap (distance between aperture and target) on spatial distribution of etched 17.5 MeV/u Ne ion tracks on track detector CR-39. **(A)** Spatial distribution of etched ion tracks relative to a center of beam distribution collimated with 0.5 mm-thick tantalum microaperture. **(B)** Width of the inner halo around the core of beam distribution collimated with a 0.25 mm-thick tantalum microaperture as a function of the length of ion path through air (air gap).

2.5 Molecular Weight Distribution of Fragments from Polynucleotide Irradiated with Heavy Ions

R.Watanabe, M.Taguchi, Y.Kobayashi,
A.Tanaka, H.Namba and H.Watanabe
Department of Radiation Research for Environment and Resources, JAERI

1. Introduction

DNA damages induced by high-LET radiations were suggested to be more stable and unrepairable than those induced by low-LET radiations. Such damages are called clustered damages [1] or locally multiply damaged sites [2]. These damages are considered to be one of the most relevant forms of damage in a cell after irradiation. However, it has not been observed that the difference of DNA damages depend on the radiation LET. Quality of DNA damages can be related to the spatial distribution of ionization or excitation on DNA. It is suggested that there is a high probability of small fragments being produced (over the range of 1-15bp) in DNA with high LET irradiation as a result of densely induced DNA strand breaks [3].

We tried to detect the small fragments expected to be induced after irradiation with ion beams. Single stranded polythymidylic acid (poly(dT)) in solid state was chosen as a simple model system to study the relationship between spatial distribution of strand breaks and ionizations. Poly(dT) samples were irradiated with heavy ions and electrons. The ratio of the fragments shorter than 30 nucleotides to total fragments was obtained by using high performance liquid chromatography(HPLC).

2. Materials and methods

Poly(dT) was purchased from Pharmacia Co. Ltd. in freeze-dried form, and dissolved in distilled water at the concentration of 2 mg/ml. Fifty μl aliquots of the solution were dried in the 4 mm x 8 mm area on glass plates. The thickness of the dried poly(dT) sample was about 1.5 μm. Fig.1 shows the unit structure of poly(dT), which is one of the DNA unit structure, 2' deoxythymidine-5'monophosphate (dTMP).

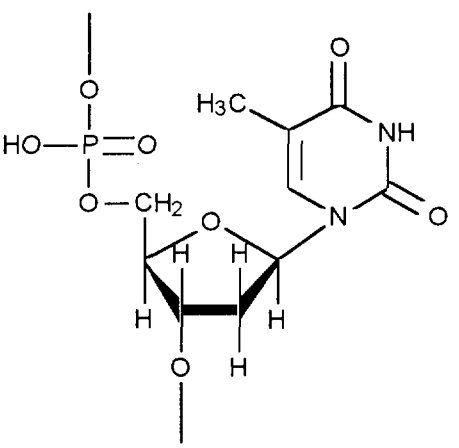

Fig.1 Unit structure of poly(dT). (2' deoxythymidine-5' monophosphate (dTMP)).

The samples were irradiated in the air with 17.5 MeV/n neon ions (350 MeV $^{20}Ne^{8+}$) and 18.3 MeV/n carbon ions (220 MeV $^{12}C^{5+}$) from the AVF cyclotron in TIARA facility. Irradiations were also performed with 2.0 MeV electron beams (EB) from a Cockcroft-Walton accelerator for comparison with the ion beams.

Irradiated samples were dissolved in the distilled water, and analyzed by HPLC. The various lengths of fragments of the polynucleotide were separated each other

using anion exchange column (Shodex DEAE-420N). Quantitative monitoring was performed by a UV absorption flow monitor at 260 nm. The wavelength was chosen to favor the UV absorption of thymine moiety.

3. Results and discussion

Released thymine and polynucleotide fragments of various lengths were obtained as radiation induced products from poly(dT). Fig. 2 shows the HPLC chromatogram of poly(dT) irradiated with carbon ions. The shorter fragments are eluted at earlier retention time.

The fragments shorter than 30 nucleotides (30mer) were separated clearly each other on the chromatogram. Fig.3 shows the chromatogram of poly(dT) irradiated with neon ions. The large peak of each fragment shows a fine structure consist of small four peaks. It means that each fragment contains at least four different chemical structures. The structure was also observed in other cases we investigated.

The amount of thymine and all fragments increased linearly with the increase of dose. The production efficiency of thymine, fragments shorter than 30mer, and total fragments from poly(dT) were estimated from the slope of the dose-response curves. Relative yields of the products per absorbed dose were shown in Table 1. The values were normalized with the yield of the total fragments induced by the electron beams. With respect to different radiation quality, no significant difference was observed in the yields of thymine and the fragments per absorbed dose.

Table 2 shows the relative yields of these products irradiated with the ion beams and electron beams per incident particle. The values in the table 2 were also normalized with the yield of total fragments induced by the electron beams. The order of the product yields was Ne > C > EB. LET of neon ions, carbon ions and electron beams in poly (dT) are 315 keV/μm, 106 keV/μm and 0.25 keV/μm, respectively. The production efficiency per particle for the base release and the fragmentation increase with the LET. However, the ratios of the yields of the fragments shorter than 30mer to those of the total fragments were around 0.1 in all radiations with different LET values. This indicates that the strand breaks may be induced at random on poly(dT) in solid state regardless of the radiation LET. In this study, the spatial distribution of ionization or excitation was not correspond to the quality of radiation induced products.

References

[1] J.F.Ward, Radiat. Res., **104**, S103-111(1985).

[2] D.T.Goodhead et al., Int. J. Radiat. Biol., **63**, 543-556(1993).

[3] K.M.Prise, Int. J. Radiat. Biol., **65**, 43-48(1994).

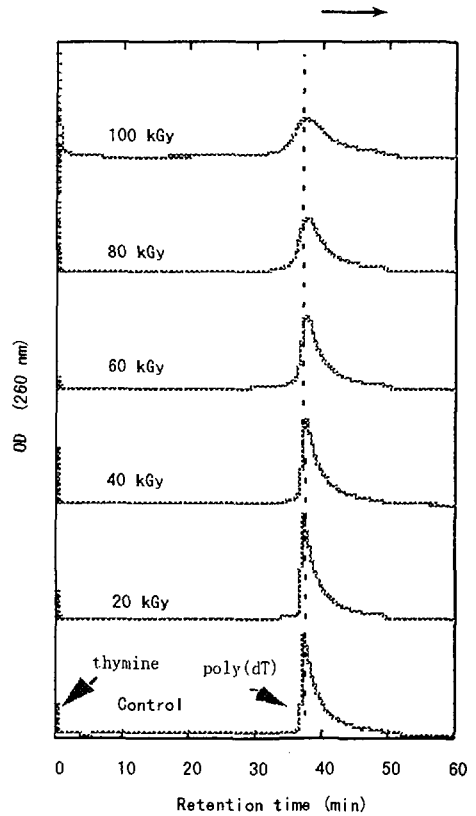

Fig.2 HPLC chromatogram of poly(dT) irradiated with carbon ions.

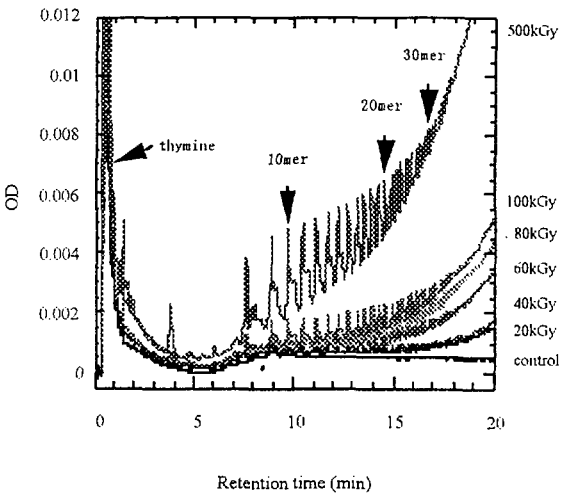

Fig.3 HPLC chrtomatogram of poly(dT) irradiated with neon ions. Radiation induced fragments(shorter than 30 mer) were separated each other.

Table 1 Relative yields of radiolytic products from poly(dT) irradiated with ion beams and electron beams per absorbed dose. The values were normalized with the yield of products induced by electron beams.

	Thymine	Fragments (< 30mer)	Total fragments	Fragments (< 30mer) / Total fragments
350 MeV $^{20}Ne^{8+}$	0.03	0.1	1	0.1
220 MeV $^{12}C^{5+}$	0.04	0.1	0.9	0.1
2 MeV EB	0.03	0.1	1	0.1

Table 2 Relative yields of radiolytic products from poly(dT) irradiated with ion beams and electron beams per incident particle. The values were normalized with the yield of total fragments induced by electron beams.

	Thymine	Fragments (< 30mer)	Total fragments	Fragments (< 30mer) / Total fragments
350 MeV $^{20}Ne^{8+}$	40	160	1600	0.1
220 MeV $^{12}C^{5+}$	20	70	600	0.1
2 MeV EB	0.03	0.1	1	0.1

2.6 Decolorization of dark brown pigments in distillery slop by mutant strains of *Aspergillus usamii* induced by ion beam irradiation

M. Takigami and H. Ito
Department of Radiation Research for Environment and Resources, JAERI

1. Introduction

The dark brown pigments contained in distillery slop are hardly decomposed by usual biological treatments such as the activated sludge process. To develop a biological treatment, screening of microorganisms has been carried out by many research scientists.[1-7] Some of the microorganisms effectively decolorized the dark brown pigments, however, they had the disadvantages that they need long time to decompose the pigments or they cause diseases to the domestic animals when the fermented products are fed to the animals.

Therefore, screening of the microorganisms to decompose the dark brow pigments in distillery slop was carried out by the authors. Among 24 strains examined, *Aspergillus usamii* seemed to be promising because it needs only 2-3 days to decompose the pigments and it does not produce anything toxic. The fermented products might be used as animal feed. To obtain mutant strains which have higher ability to decompose the dark brown pigments, spores of *Aspergillus usamii* were subjected to the ion beam irradiation.

2. Experimental

(i)Microorganisms

The fungus used in this study was *A. usamii*. IFO 4388. It was incubated on Difco Potato dextrose agar slants at 30℃.

(ii)Sample preparation

The fungus was incubated on Potato dextrose agar plates at 30℃ for 1 week and the spores suspended in distilled water were collected by centrifugation at 5000 rpm for 15 min, and then washed once with 1% peptone solution. After washing, the spores were resuspended in the solution containing 1% sodium glutamate, 2% peptone, 2% glycerol and 2% poly(vinyl alcohol). Then the spores were filtered on Millipore membrane filter with the pore size of 0.22μm.

The spores on the membrane filter were freeze-dried and the membrane filter was sealed in poly(vinylidene chloride) film with a thickness of 10μm, and subjected to C^{5+} ion beam irradiation.

(iii)Irradiation

The samples were irradiated with 220MeV C^{5+} ion beam from AVF cyclotron at Advanced Radiation Technology Center, JAERI Takasaki.

(iv)Plating and screening

The irradiated samples were inoculated on potato dextrose agar plates after keeping the irradiated samples at 4℃ for 2 days.

The plates were incubated at 30℃ for 7 days and the number of colonies was counted. Some of the colonies were picked up and transferred to potato dextrose agar slants and incubated for 7 days.

The mutant strains subjected to the following experiments are shown in Table 1.

(v)Decolorization of distillery slop

The spores on the slants were inoculated in distillery slop diluted to 8 times which contains $NaNO_3$ 3.0 g, KH_2PO_4 1.0 g, K_2HPO_4 0.5 g, $MgSO_4$ 0.5 g, $FeSO_4$ 0.01 g, and glucose 2.0 g per liter. The pH of the medium was adjusted to 5.0 by NaOH aqueous solution. The shaking flasks containing medium and spores of fungi were set to a

Table 1 Mutant strains used for experiments

Strain	Dose (kGy)	Symbol used in Figures 1 and 2
UC-2	0	●
U2-1	0.2	△
U2-2	0.2	▲
U5-3	0.75	□
U6-2	1.0	■

reciprocal shaker and incubated at 30℃ with 120 oscillations per min. After incubation, the fungi were filtered with No. 2 filter paper and the filtrate was subjected to the following experiments. The fungi was thoroughly washed with distilled water, freeze-dried and weighed.

(vi)pH measurement

pH of the medium after incubation was measured by a Beckman f100 ISFET pH Meter.

(vii)Non-volatile dissolved mass

Ten ml of filtrate was freeze-dried and weighed.

(viii)Decolorization yield

The degree of decrease of optical densities in absorbance at 660, 600, 570, 520, 500, 460, 440 and 420 nm after dilution with 0.1M acetate buffer (pH5.0)[1] compared to those of the blank solution was measured and the values were averaged to give decolorization yield.

(ix)COD measurement

COD (Chemical Oxygen Demand) of the filtrate was measured following the JIS K0102.

3 .Results and Discussion

The change of pH of the medium during incubation is shown in Figure 1. The pH values of the medium, in which U2-1 and U6-2 strains were incubated, increased from the initial value of the medium by 1 day incubation, then decreased drastically and showed minimum value when incubated for 2 days, and increased slightly by further incubation. These two strains showed comparatively low pH values.

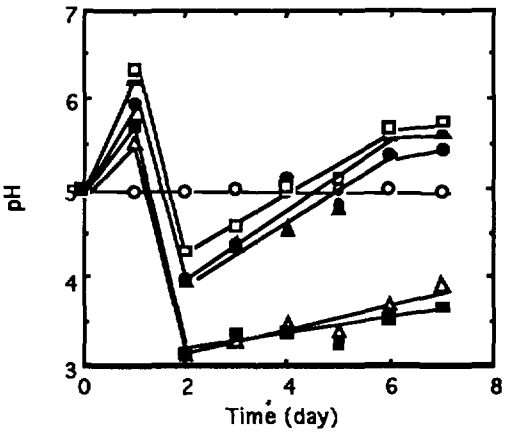

Fig. 1 Change of pH of medium during incubation of fungi. ○: Blank

However, in other strains, the pH values increased from the initial value by 1 day incubation, then decreased and increased again by further incubation. Ohmomo et al. reported that enzymes isolated from a strain of *Coriolus versicolor* decolorized dark brown pigments in distillery slop and produced lactic acid.[3] Therefore, the decrease of the pH values of medium during decolorization is explained by the production of lactic acid. When UC-2, U2-1, U5-3 and U6-2 strains were inoculated in the medium which did not contain dark brown pigments, the change of pH values in the medium showed same tendency with that in the medium containing dark brown pigments. The medium of UC-2 and U5-3 became dark when incubated for a long time even if the medium did not contain distillery slop, while those of U2-1 and U6-2 were not colored. Therefore, it is inferred that the mutant strains such as U2-1 and U6-2 lost the ability to produce dark brown pigments.

As shown in Figure 2, decolorization yield of the distillery slop showed maximum value by 2-3 days incubation and decreased by further incubation for all the strains.

From the results of Figures 1 and 2, it is inferred that mutant strains with high decolorizing ability show low pH values of medium after incubation. The products given by the decomposition of

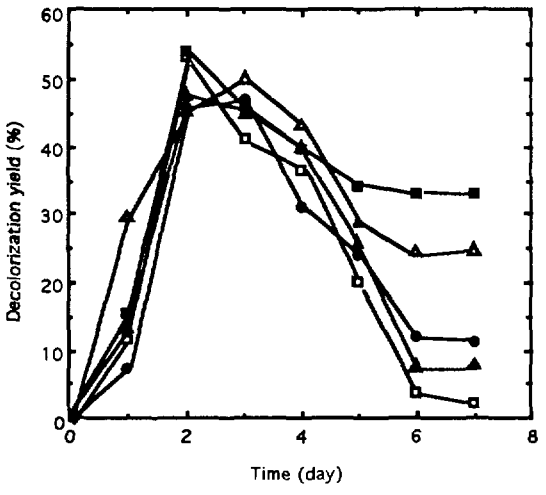

Fig. 2 Decolorization of distillery slop by fungi.

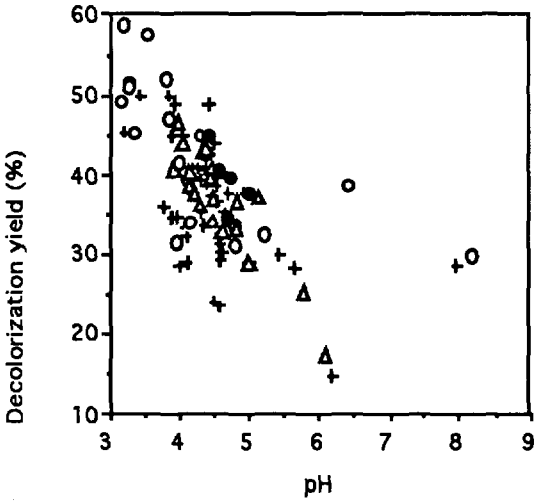

Fig. 3 Relation between pH of medium and decolorization yield. ○: mutants by C^{5+} irradiation, no ability to produce pigments; +: mutants by C^{5+}, produce pigments, △: mutants by gamma-rays irradiation; ●: parent strain

dark brown pigments can be used as the raw materials to synthesize dark pigments. So that the mutant strains such as UC-2 and U5-3 utilize organic acid to synthesize pigments and increase the pH values of medium, while the mutants such as U2-1 and U6-2 have lost the ability to synthesize pigments.

Dry weight of fungi increased and non-volatile dissolved mass in medium and COD decreased by incubation for 3 days, however, further incubation did not cause any change in all the strains examined.

The relation between pH of medium and decolorization yield by mutant strains induced by C^{5+} and gamma-irradiation is shown in Figure 3. From the graph it can be said that mutant strains which give lower pH values of medium have higher decolorizing ability. Some mutant strains which were obtained by ion-beam irradiation and lost the ability to produce pigments showed higher decolorizing activity (about 60%) than parent strain (35-45%) and those obtained by gamma-irradiation. So that ion beam irradiation onto fungi gives useful mutant strains more effectively than gamma-rays irradiation.

Potato dextrose agar plates with pH indicator were proved to be effective for the screening of mutant strains with high ability to decolorize distillery slop.

References

1) I. Aoshima, Y. Tozawa, S. Ohmomo and K. Ueda, Agric. Biol. Chem., **49**(7), 2041-2045(1985)
2) S. Ohmomo, I. Aoshima, Y. Tozawa, N. Sakurada and K. Ueda, Agric. Biol. Chem., **49**(7), 2047-2053(1985)
3) S. Ohmomo, I. Aoshima, Y. Tozawa and K. Ueda, Agric. Biol. Chem., **49**(9), 2767-2768(1985)
4) S. Ohmomo, Y. Kaneko, S. Sirianuntapiboon, P. Somchai, P. Atthasampunna and I. Nakamura, Agric. Biol. Chem., **51**(12) 3339-3346(1987)
5) S. Silianuntapiboon, P. Somchai, S. Ohmomo, and P. Atthasampunna, **52**(2), 387-392(1988)
6) M. Murata, N. Terasawa and S. Homma, Biosci. Biotech. Biochem., **56**(8), 1182-1187(1992)
7) N. Terasawa, M. Murata and S. Homma, J. Food Sci., **61**(4) 669-672(1996)

2.7 Studies on the leaf primordium development in tobacco seedlings exposed to ion beam

Y.Hase,M.Inoue,A.Tanaka[2],H.Watanabe[3] and S.Tano[2]
Department of Agriculture,Kyoto Prefectural University,
Advanced Science Research Center,JAERI[2],
Department of Radiation Research for Environment and Resources,JAERI[3]

Introduction

When plant seeds are exposed to radiations at different stages during the germination period, characteristic chimera is formed, depending on developmental stage. On the basis of chimera formation on subsequent growth, e.g., shape, size and/or position, number of initial cells at the exposure time, process of cell differentiation and organogenesis can be analyzed.

Ion beam has a higher LET, as compared to that of gamma-rays, and the penetration depth can be controlled. It is expected that ion beam can induce a novel mutation differing from that with gamma-rays, and also that ion beam can be used as a tool for cell surgery.

We are continuing to analyze the cell differentiation and organogenesis during the course of embryo formation and development in plants .

In this study, the leaf primordium development was analyzed in tobacco seeds exposed to ion beam at different stages during the germination period. Formation and pattern of mutated leaf-sectors appearing on the subsequent growth were determined. Number of initial cells in the leaf primordium and their developmental pattern were discussed.

Materials and Methods

Two cultivars, Consolation402 and NC402 of *Nicotiana tabacum* L., were used as parents for obtaining the material seeds. Those parents are isogenic for the gene controlling leaf color. Crosses between Consolation402 (*ygyg*, yellow-green leaf) and NC402 (*YgYg*, dark-green leaf) were performed. Heterozygous (*Ygyg*, dark-green leaf) seeds were used in the present experiments.

Dry seeds were exposed to 220MeV C^{5+} beam of 0-40Gy from AVF cyclotron and also irradiated with 0-100Gy of ^{60}Co gamma-rays. The seeds were allowed to germinate and to grow in a growth chamber at about 25℃ under light condition. Sectors appearing in the 1st to the 5th leaf were observed. Frequency of plants with sectors was recorded.

Seeds presoaked for 0, 24 and 72 hour were exposed to C^{5+} beam with dose of 5-20, 5 and 4 Gy, respectively. Sectors in the 1st to the 5th leaf were recorded, and relative ratio of sectorial area in individual leaf was measured. Referring to the sector formation, developmental pattern of initial cells in the 2nd to the 5th leaf primordium was discussed.

Results and Discussion

Survival rates of dry seeds exposed to C^{5+} beam and irradiated with gamma-rays were shown in Fig.1. C^{5+} beam was about ten times more effective on the reduction of survival rate than gamma-rays.

There were three types of sector color; yellow-green, yellow and light-green. Frequencies of plants with sectors were shown in Table1. The frequency ranged from 3.1×10^{-2} to 5.2×10^{-2}. Yellow-green sector and yellow sector were obtained only in C^{5+} beam regime except for C^{5+}-40Gy. However, the frequency in C^{5+}-40Gy was higher than that in the other regime. After gamma irradiation, only light-green sector was obtained at the frequency of 3.7×10^{-2} and 4.6×10^{-2}.

From the relative ratio of sectorial area, number of initial cells present in the leaf primordium were estimated. In the present experiment, each plant with sectors had only one type of sectorial color. Considering this fact, it could be thought that sectors appearing on the same plant were derived from one initial cell mutated. If each initial cell contributes equally to the subsequent growth, the relative ratio of sectorial area to whole area in the developed leaf reflects number of initial cells present in a leaf primordium at the time of exposure. For example, if sectorial area is one fourth, it is conceivable that a leaf primordium consists of four initial cells. From this point of view, the ratio of sectorial area in the individual leaf was calculated, and the reciprocal value of the ratio was used as a number of initial cells composing a leaf primordium at the time of exposure. As shown in Table2, the primordium of the 1st, 2nd and 3rd leaf in dry seeds consisted of about 7 initial cells. On the other hand, there were 2 and 1 cell in the 4th and the 5th leaf primordium, respectively. After 24hour-imbibition, the 4th leaf primordium was composed of 5 cells, but 1 cell in the 5th. In 72hour-imbibed seeds, number of cells in the 4th and the 5th leaf primordium increased to 10 and 5, respectively.

From the results on sector formation observed here, developmental pattern in the 2nd to the 5th leaf was also ascertained in relation to initial cells of individual leaf-primordium in dry seeds(Fig.2).

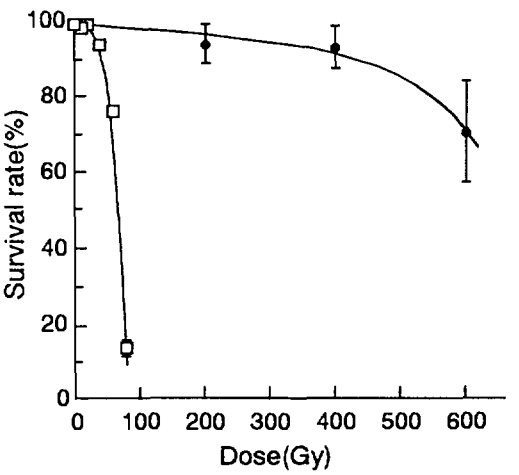

Fig.1 Effect of C^{5+} beam and gamma -rays on survival of *N. tabacum* dry seeds.

□ ;C^{5+}beam, ● ;gamma ray.

Table1 Frequency of plants with sectors in the 1st to the 5th leaf

Radiation	No. of plants observed	No. of plants with sectors	No. of plants sectorial color		
			yellow-green	yellow	light-green
control	321	0	0	0	0
C^{5+} – 5 Gy	295	11	4	1	6
C^{5+} – 10Gy	293	9	5	0	4
C^{5+} – 20Gy	372	13	5	2	6
C^{5+} – 40Gy	327	17	0	0	17
γ ray – 50Gy	108	5	0	0	5
γ ray – 100Gy	108	4	0	0	4

Table2 Number of initial cells present in a leaf primordium, estimated by relative ratio of sectorial area in the 1st to the 5th leaf

Leaf \ Time after imbibition	not imbibed (dry seed)	24hr after imbibition	72hr after imbibition
1st leaf	7.3±3.5 (2)	—	—
2nd leaf	6.8±1.5 (20)	—	—
3rd leaf	7.0±2.0 (13)	4.6±1.5 (6)	—
4th leaf	1.6±0.3 (3)	5.1±2.1 (4)	9.8±5.1 (3)
5th leaf	1.0 (1)	1.0 (1)	5.0±3.1 (3)

Each value is mean ± S.E.. Value in parenthesis is number of plants with sectors in each leaf.

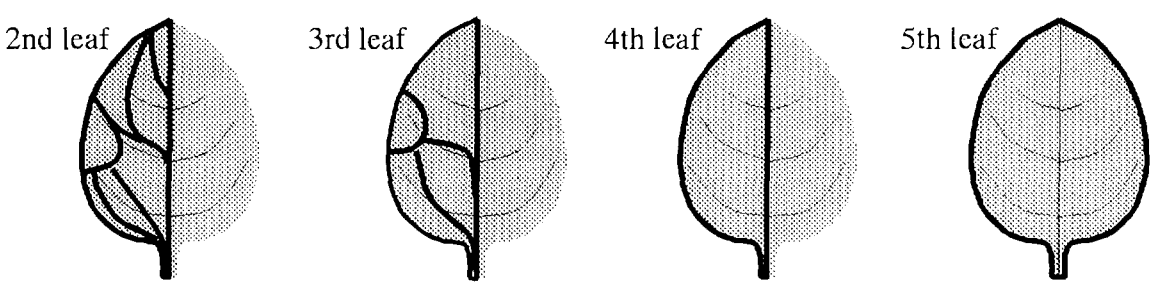

Figure2 Developmental pattern in the 2nd to the 5th leaf.
Each zone enclosed by bold line in individual leaf means a cell group derived from one initial cell of leaf primordium in dry seeds.

2.8 Effect of Cosmic Radiation on *Escherichia coli* Cells and Plasmid DNA Experimented by AVF Cyclotron in TIARA Facility

Kazuki Harada, Yurino Obiya, Yuki Ozaki, Tatsuo Nakano,
Masahiro Imamura[1], Masato Imamura[2],
Akihisa Takahashi[3], Xinjiang Wang[3], Takeo Ohnishi[3],
Yasuhiko Kobayashi[4], Masahiro Kikuchi[4], Hiroshi Watanabe[4]

Div. of Mol. Life Sci., PL Botanical Inst., PL Gakuen Women's Jr. College,
[1]Dept. of Radiology, Kansai Medical Univ.,
[2]3rd Dept. of Int. Medicine, Kansai Medical Univ.,
[3]Dept. of Biology, Nara Medical Univ.,
[4]Biotec. Lab., JAERI/Takasaki

1. Introduction

We have been investigating the effects of heavy ion beams generated from AVF cyclotron on *Escherichia coli* DNA deficient mutants and plasmid DNA in addition to radioresistant bacterium, *Deinococcus radiodurans* in "TIARA Cooperative Research" in succession to "The Inter-University Collaborative Research Project with JAERI". On September in 1996, these biological samples were loaded in Space Shuttle in order to research the effect of cosmic radiation including high-energy heavy particles (HZE particles) on survival and mutation frequency of *E. coli* derivatives of the KMBL3835 (*trpE9777*) and *pol*^{ts} (*pol*$^{+}$ and *exo*$^{-}$, *recA*^{ts}), and on DNA strand break and point mutation (hot spot) of DNA molecular level of plasmid pKmK8 DNA. This space experiment using Space Shuttle "Atlantis" was called "Phase 1 Space Radiation Environment Measurement Program" in NASA Shuttle/Mir Mission No. 4 (S/MM-4, STS-79). In this study, we mainly reported the new detecting methodology of short DNA fragments due to pKmK8 DNA strand breaks caused by low dosage of cosmic radiation during space shuttle flight. The reaction of 5' end labeling reaction of [γ-^{32}P] with T4 polynucleotide kinase (PNK) was utilized as this new methodology.

2. Experiments

The pKmK8 DNA is the plasmid of 7.6 kbp length with *crp* gene which serves as a mutagenesis target (Fig. 1).

This plasmid as well as *E. coli* mutant cells was irradiated with neon ion beams ($^{20}Ne^{8+}$ of 350 MeV; LET = about 320 keV/μm) generated from AVF cyclotron at TIARA in JAERI/Takasaki. The ion beam dose-response survival curve of the plasmid using *E. coli* KY30 strain was experimented.

After then, the plasmid pKmK8 DNA and *E. coli* cells in liquid were placed on the paper disk and membrane filter, respectively, dried in a desiccator, and the dried biological samples on the disks and the filters were packed in autoclaved polypropylene bags, which were heat-sealed to prevent contamination[1]. These biological samples were placed in Radiation Dosimeters comprised an aluminum dosimeter pack with small physical radiation dosimeters. These Dosimeters were attached to the Realtime Radiation Monitoring Device II (RRMD II) (Fig. 2) and the other equipments. The same Dosimeters were left on earth in NASA John F. Kennedy Space Center (KSC) in Florida, USA, as the control.

The Space Shuttle "Atlantis" (OV-104) was launched on September 16, 1996, docked to Russian Space station Mir, and then separated from Mir, landed 10 days

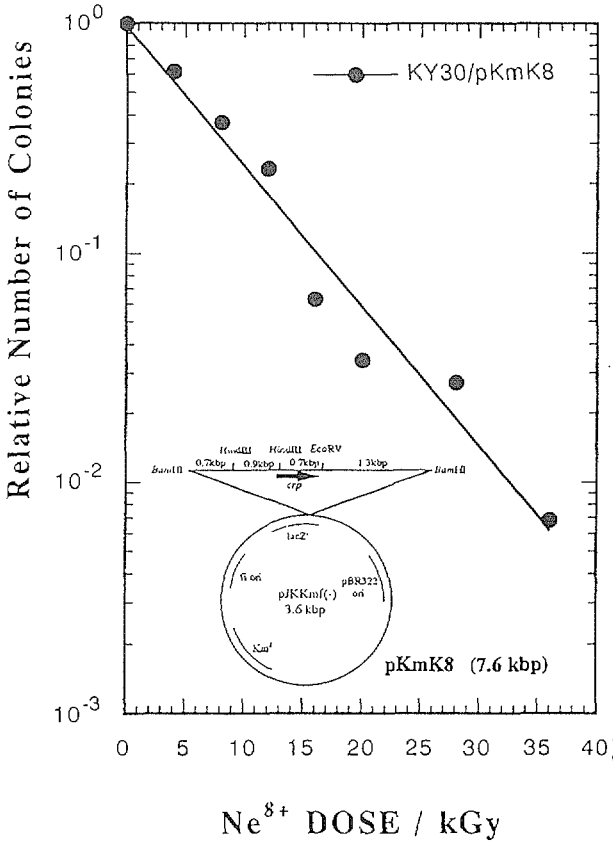

Fig. 1 Diagram of the Plasmid pKmK8 DNA Used for the Electrophoresis Experiments and Dose Response Survival Curve of the Plasmid Exposed to Neon Ion Beams in TIARA.

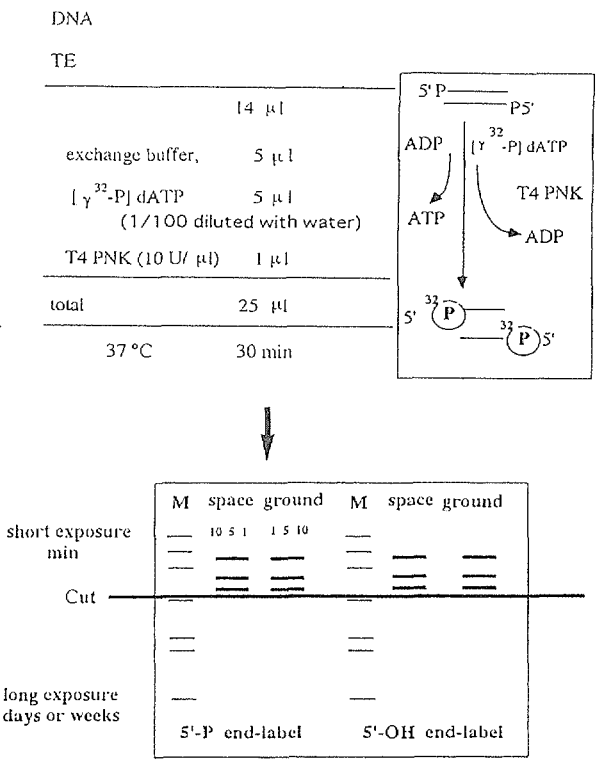

Fig. 3 Schematic Protocol of the Detecting Method of the Short DNA Fragments from End Breaks of Plasmid pKmK8 by the [g-^{32}P], T4 PNK and Autoradiography.

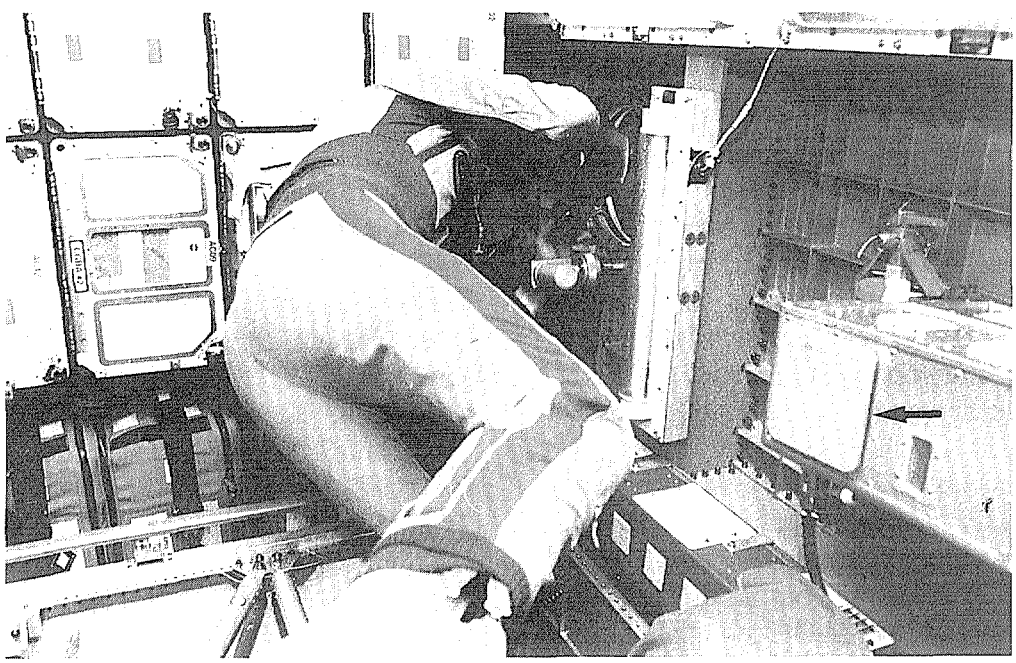

Fig. 2 Photograph of Radiation Dosimeter (Arrow) Attached to the RRMD II in Spacehab of Space Shuttle "Atlantis" during S/MM-4 (Courtesy of NASA).

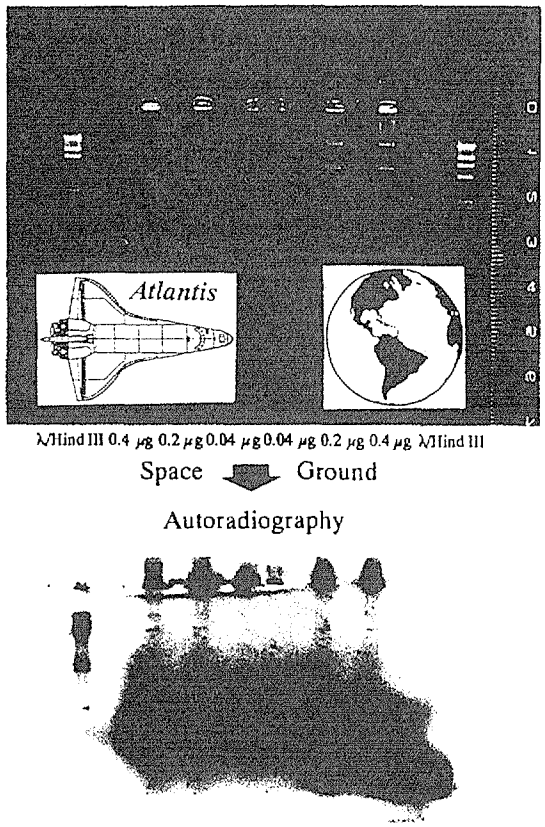

Fig. 4 Electrophoresis and Auto-radiography Patterns of Short DNA Fragments from End Breaks of Space and Ground pKmK8 Plasmid Samples by Exchange Reaction for 5'-P Ends.

later. The orbit was circular at an altitude of 250 to 400 km and the orbital inclination was 51.8 degrees. Astronauts who carried out the space experiment were J. Apt and C. E. Walz (NASA Mission Specialists).

After "Atlantis" returned to earth, the drastic molecular damage of plasmid pKmK8 DNA was measured using an agarose electrophoresis method. Furthermore, as shown in the schematic protocol of Fig. 3, the short DNA fragments from end breaks of pKmK8 were analyzed using [γ-^{32}P] end labeling reaction with T4 PNK and the autoradiography. The 5'-P end labeling was carried out at the exchange reaction, and the 5'-OH end labeling at phosphorylation reaction.

3. Results and Discussion

The survival curve of plasmid pKmK8 DNA using *E. coli* KY30 strain showed the exponential decreasing pattern, and indicated 16 kGy of D_{10} value (Fig. 1). The agarose electrophoresis experiment showed that no drastic DNA breaks of the pKmK8 DNA occurred in any sample in space or on earth (Fig. 4)[2]. Because it would be the reason that the average absorbed dose rate of cosmic radiation was a few 38 μGy/day (297.3 μSv/day) at the altitude of 400 km and the orbital inclination of 51.6 degrees[2] in comparison with large 16 kGy of D_{10} value of pKmK8 plasmid. Then, we tried to detect the short DNA fragments from end breaks of pKmK8 using [γ-^{32}P], T4 PNK and autoradiography (Fig. 3). We surely found the short fragments from space sample DNA, however, there also were short fragments in ground sample, unfortunately (Fig. 4). From now, though we must remove the background of short fragments from ground DNA sample, this new method will useful of detection of minor DNA damage caused by low dose cosmic radiation.

4. Acknowledgments

We are grateful to Prof. Koichi Takimoto (Yamaguchi University) for providing us with plasmid pKmK8 DNA and to Mrs. Noriko Shindo (M. A.) for her constantly kind encouragement during this study. The results are obtained in part from the joint NASA and NASDA RRMD program.

5. References

1) K. Harada, Y. Obiya, T. Nakano, M. Kawashima, T. Miki, H. Watanabe, Y. Kobayashi, K. Okaichi, T. Ohnishi, C. Mukai and S. Nagaoka, *Oncol. Rep.*, **4**, 691-695 (1997).

2) T. Doke, H. Watanabe, K. Harada and F. Tomita, in "STS-79 Shuttle/Mir Mission 4, Realtime Radiation Monitoring Device (RRMD) Experiment Quick-Look Reports", National Space Development Agency (NASDA), 1996, pp. 1-20.

2.9 Effects of Local Irradiation of Heavy Ion Microbeam on the Embryogenesis in the Silkworm, *Bombyx mori*

K.Kiguchi*, S.Yamasaki*, Y.Kobayashi** and H.Watanabe**
*Faculty of Textile Science and Technology, Shinshu University,
**Department of Radiation Research for Environment and Resources, JAERI.

1.Introduction

A novel microbeam system connected to the vertical beam line of AVF cyclotron have been installed at TIARA in JAERI-Takasaki. The heavy ion beams with different LETs can be collimated to the minimum about 10 μmø in diameter using a set of various microapertures. The main purpose of this system is to study the biological effects of HZE particles in spaceflight environment. However, it is also considered to be useful as a tool of cell surgery for analyses of the embryogenesis, growth and differentiation in various animal and plant cells or tissues.

The silkworm, *Bombyx mori*, is one of ideal experimental insects, owing to its well documented genetics, embryology and physiology. Recently, the silkworm eggs were irradiated with a scanning UV-laser microbeam to prepare a fate map. When irradiated at the fertilization stage, localized cuticle defects are induced in the integument of the resultant larvae, in spite of absence of nuclei or cells at the irradiated sites[1]. Here we report the effect of heavy ion microbeam irradiation to *Bombyx* eggs, which were significantly different from the one of UV-laser microbeam.

2. Experiments

The larvae of *Bombyx pnd* mutant (pigmented non-diapausing egg) were reared on a commercial artificial diet (Yakult) . As *pnd* mutant embryos do not enter embryonic diapause, this mutant is particularly convenient for studying embryogenesis[2]. Egg collection was made on a cellophane paper or on a polyester film for 20 minutes. Irradiation experiments were done at two different developmental stages: one is the before fertilization stage (BFS, within 2 hours after oviposition) , and the other is the cellular blastderm stage (CBS, about 12-13 hours after oviposition at 25℃) . Eggs were overall exposed to 18.3 MeV/u carbon ions from AVF cyclotron, or locally irradiated by the collimated beams with a 250 or 1400 μmø aperture. After the irradiation, the treated eggs were kept at 25℃ for 10-12 days, and morphology of the hatched larvae or unhatched embryos was examined under the dissecting microscope.

3. Results and Discussion

1) Effect of overall irradiation

First, effects of overall irradiation of heavy ion beams were examined for the comparison. Using the irradiation apparatus for plant seeds, BFS and CBS eggs were exposed to carbon ions at the dose range of

0.1 - 50 Gy. As shown in Fig.1, the hatchabilities were clearly inhibited at almost same particle fluence (4.3×10^7 p/cm^2) in both stage eggs. The inhibition of hatchability of the BFS eggs may be due to damaging male and female pronuclei by the irradiation. When dissected the unhatched eggs, partial fragments of embryo were observed in some of the eggs irradiated at CBS, suggesting that the radiosensitivity to the heavy ion beams is different depending on the cycle of nuclear division.

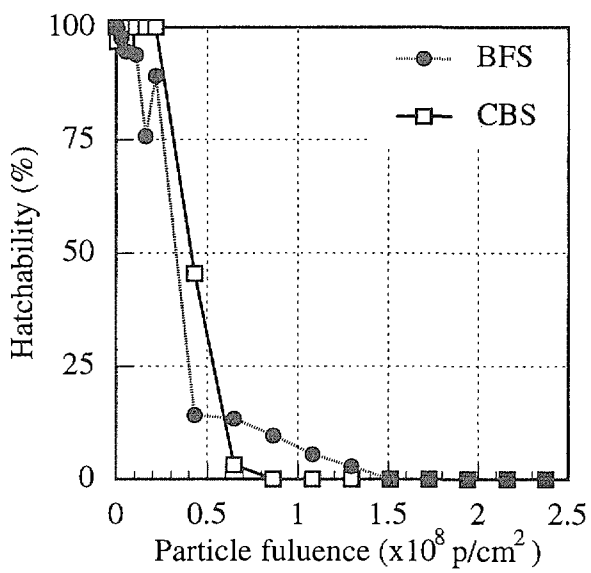

Fig.1 Effects of overall irradiation on the hatchability in the silkworm, *Bombyx mori*.

2) Effect of local irradiation

Next, effects of local irradiation were investigated using two kinds of aperture. When anterior half of the BFS eggs were irradiated with 1400 μmø aperture (see Fig.2) , none of eggs showed any sign of blastderm formation. By contrast, most eggs irradiated their posterior half at BFS looked to develop normally and no perceptible abnormality was observed in the hatched larvae.

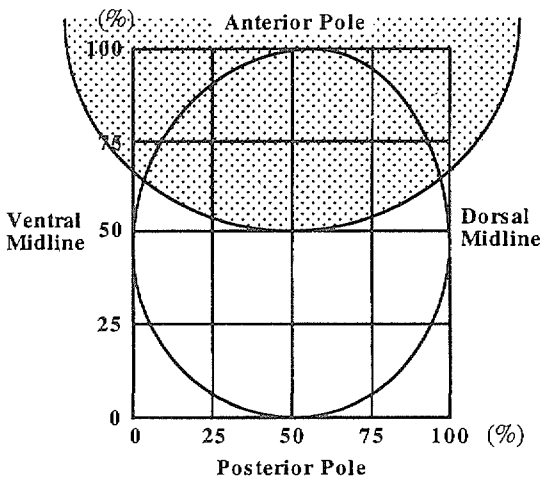

Fig.2 An example of area irradiation using a 1400 μmø aperture.

On the other hand, when anterior half of CBS eggs were irradiated, partial embryos lacking the head region were induced. Irradiation to the posterior half resulted in the pronounced abnormal embryos lacking tail and abdominal segments (Fig.3).

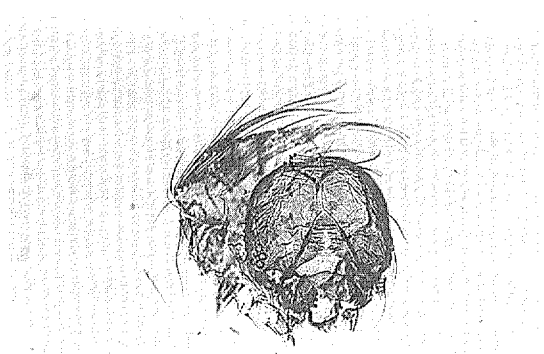

Fig.3 A partial embryo lacking tail and abdominal segments.

Effects of spot irradiation were also examined at fluence (2.7×10^9p/cm^2) using a 250 μmø aperture (Fig.4). When the beam spot was exposed to the anterior region of a BFS egg, where male and female pronuclei exsist, serious inhibition of embryonic

development was induced. However, irradiation to the region with no nucleus did not induce any visible effects in the treated eggs. Irradiation to the CBS eggs brought about various abnormal embryos including deletion, duplication and fusion *etc.* as seen in Figs.5 and 6.

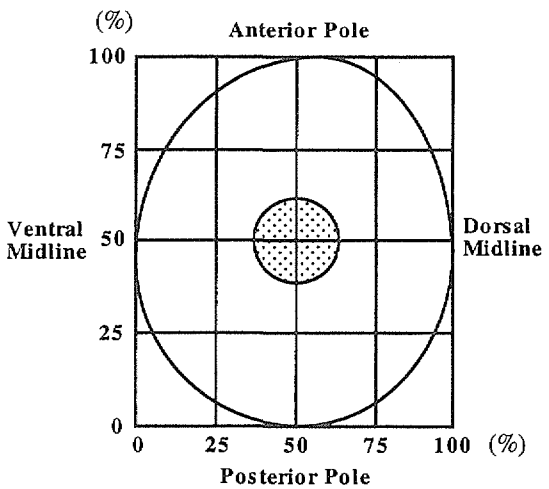

Fig.4 An example of spot irradiation using a 250 μmø aperture.

Although the data have not been sufficient yet to draw an accurate conclusion, it is obvious that the biological effect of heavy ion microbeam are significantly different from the one of UV-laser microbeam. Irradiation of UV-laser to *Bombyx* eggs at BFS resulted in the cuticle defects in the hatched larvae, in spite of absence of nuclei or cells at the irradiated sites (Myohara, 1994) . UV-laser is likely to affect not only nucleic acids but also proteins, while the primary targets of heavy ion microbeam seem to be nuclei or DNA, since visible effects were induced only when irradiated to the sites where nuclei exsist.

From these findings, it is considered that the microbeam system established is a quite useful tool for cell-targeting radiosurgery, which might be one of excellent methods for study on cell determination and differentiation mechanism in various living organisms.

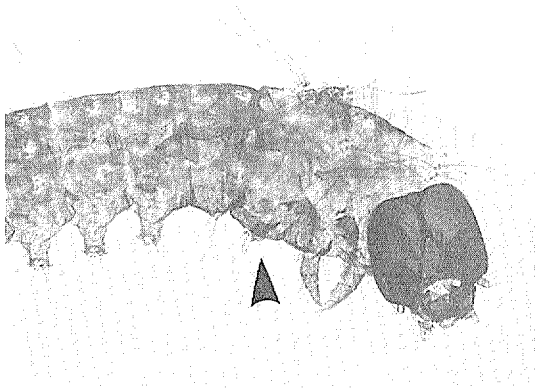

Fig.5 Deletion of thoracic legs (arrow) induced by spot irradiation (250 μmø) at the position of 50% egg width and 50% egg length.

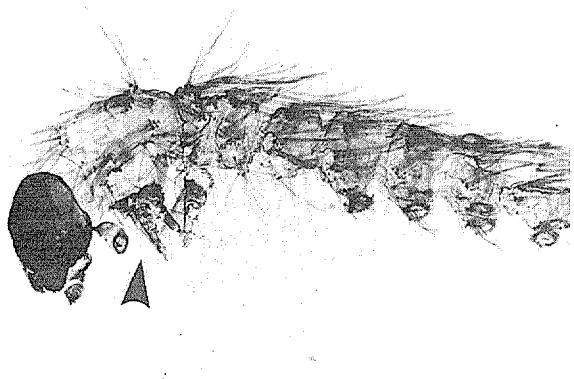

Fig.6 Fusion of thoracic legs (arrow) induced by spot irradiation (250 μmø) at the position of 25% egg width and 50% egg length.

4. References

1) M. Myohara, Deveropment 120, 2869-2877 (1994)

2) Nagy *et al.* Deveropmental Biology 165, 137-151 (1994)

2.10 Enlargement of Potential Chimera on Chrysanthemum Mutants Regenerated from $^{12}C^{6+}$ Ion Beam Irradiated Explants

S. Nagatomi[1], A. Tanaka [2], H. Watanabe [2] and S. Tano [2]
Institute of Radiation Breeding, NIAR[1]
Takasaki Establishment, JAERI [2]

I. Introduction

In mutation breeding of agricultural crops, a combined method of irradiation with in vitro culture is valid to enhance mutation frequency, and to enlarge the mutation spectrum[2]. The method also permits to obtain a homohiston mutant from single cell by means of cell culture techniques.

On the other hand, more than 80% of mutagens used for registered mutant varieties in the world are gamma ray and x ray. Novel mutagen, therefore, has been required for effective mutation induction and broadening mutation spectrum in plant mutation breeding. Ion beams which has a property of higher LET than gamma rays and X ray, may affect on biological effect and mutation induction. The present studies have been conducted to elucidate biological effects and mutation induction of the ion beams on two representing crops, chrysanthemum and rice. Previously, we reported that the RBE of $^{12}C^{6+}$ ion beam relative to gamma ray was estimated to be 4.5 and the specific flower color mutants with complex and stripe types, which was not obtained by gamma ray, were induced with the ion beam. In this report, using those specific flower color mutants, mutation was induced by means of in vitro culture of the floral organs without mutagenic treatment so as to investigate potential chimera formation.

II. Experimental methods

The explants of floral petals and buds excised from a chrysanthemum cultivar, "Taihei" (Pink flower), were plated on aseptic media in petri dish. Those cultured materials were irradiated with $^{12}C^{6+}$ ion beam of 220 Mev from the AVF cyclotron in JAERI. After irradiation, the cultured materials were transferred to new callus media for callus proliferation. The regenerated plants were obtained from the callus. The flower color and shape of regenerated plants were investigated in the field nursery in the Institute of Radiation Breeding.

Fifteen flower color mutants selected on field nursery were used as the explant sources. The segments of floral petal and receptacle were cultured on aseptic media for callus proliferation and the induced callus were transferred to the regeneration media. Totally 2220 regenerated plants were established for investigation of flower color mutation in the field nursery.

III. Results and discussion

Flower color of the fifteen mutant lines used as the experiment were categorized into three types; Pink for one mutant; White for 2; Complex for 12. The results investigated on mutation induction of the regenerated plants, showed that 165 mutants were recognized on 2,220 plants being 7.4% of mutation rate. Table 1 shows mutants were induced on seven lines, which mutation rates are ranging from 0.2% to 23.1%. All of the mutant inducing lines were fallen into the complex type.

The line 94C-13 showing the highest mutation rate induced mutants with floral petal shrinking and shortage derived from both floral petal and receptacle, and had highly mutable characteristics in floral petal morphology

(Fig. 1). The lines, 94C-1, 94C-4 and 94C-8, produced complex type mutants with different flower color. The line 94C-14, being a whitish pink flower petal with yellow stripe, induced yellow and/or light yellow flower color mutants commonly having yellow stripe. The yellow stripe of those mutants after organ culture suggested to cause by not periclinal chimera but a mutable factor.

Conclusively, the complex type mutants specifically induced by the ion beam were proved to be not complex chimera but stable homohiston mutants. The high relative biological effect of the ion beam on explant tissues and cells may lead to those complex type mutants, so that they can be used for experimental materials to elucidate mutation induction mechanism of the ion beam. Especially, the highly mutable lines 94C-13 and 94C-14 are remarkable as the fundamental materials for the mutation mechanism.

It is noted that $^{12}C^{6+}$ ion beam can be utilized as a new mutagen possessing different effect from gamma ray. Further investigations on the mutagenesis of the other ion beams on crops are in progress.

References

1)S. Nagatomi et al., Breed. Sci., 46(Suppl.1), 62 (1996).
2)S. Nagatomi and E. Miyahira, ibid., 44 (Suppl.1), 292 (1994).
3) S. Nagatomi et al., TIARA Ann. Rep., 5: 50-52 (1996).
4) S. Nagatomi, Seminar for Regional Cooperation in Asia, Bangkok. p. 24-32 (1996).

Table 1. Flower color mutation of regenerated plants from floral organ culture of flower color mutant lines induced by 12C8+ ion beam.

Line	Fl. color	Explant	No. plant	No.mutant	Mutat.(%)	Mutated character				
						Yellow	L. yellow	Complex	Shurink	Short
94C-1	LY/LP	F	59	6	10.2			6		
		R	60	8	13.3			8		
94C-2	W	F	10	0	0					
94C-3	LY/LP	F	75	0	0					
		R	89	0	0					
94C-4	LY/LP	F	59	5	8.5			5		
94C-5	P	F	20	0	0					
94C-6	W	F	10	0	0					
94C-7	LY/LP	F	70	0	0					
94C-8	LY/LP	F	55	1	1.8			1		
		R	160	5	3.1			5		
94C-9	LY/VLP	F	54	0	0					
		R	30	0	0					
94C-10	Y/O	F	103	1	1					1
		R	35	0	0					
94C-11	LP,VLP	F	11	0	0					
		R	20	0	0					
94C-12	Y/VLP	F	59	0	0					
		R	20	0	0					
94C-13	Y/VLP	F	453	107	23.6				107	
		R	53	10	18.9				10	
94C-14	LP,LP/Ys	F	248	21	8.5	16	5			
94C-15	Y/O	F	254	1	0.4					
		R	197	0	0					
Total/Average			2,220	165	7.4	16	5	25	117	1

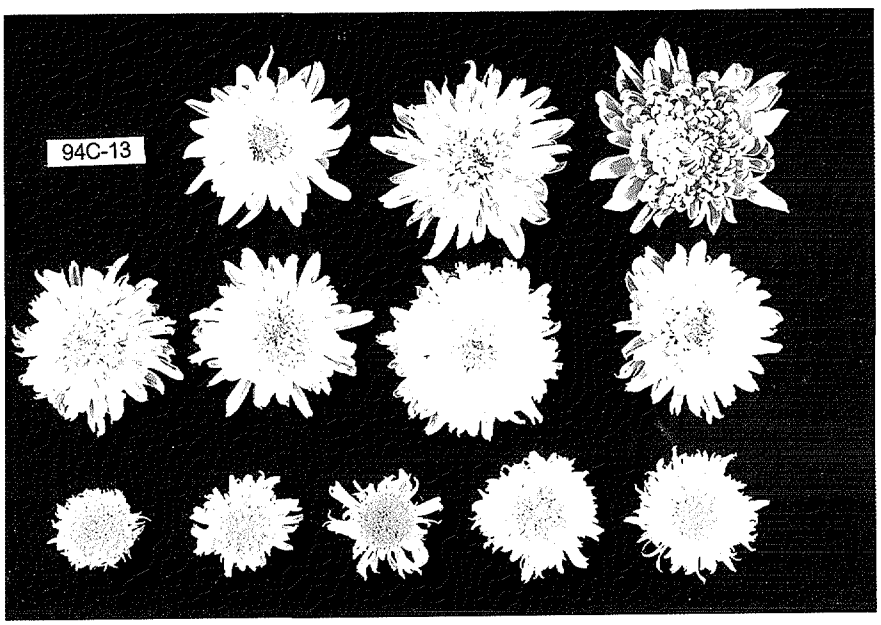

Fig. 1. Flower shape mutants of regenerated plants from floral organ culture of mutant line, 94C-13 induced by 12C8+ ion beam

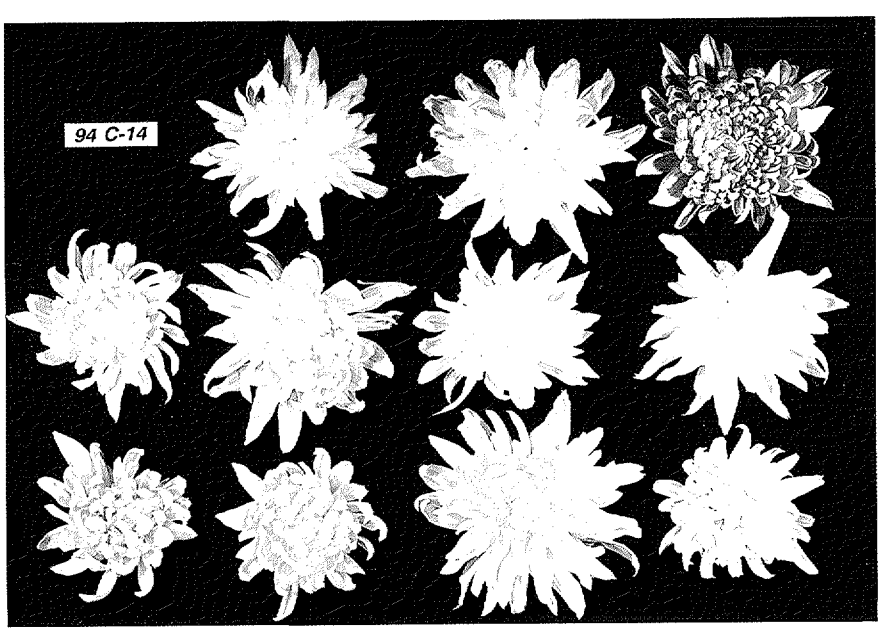

Fig. 2. Flower color mutants of regenerated plants from floral organ culture of mutant line, 94C-14 induced by 12C8+ ion beam

2.11 Analysis of Carbon Translocation in Plants Using Positron-Emitting Tracer

T. Kume[1], S. Matsuhashi[1], H. Ito[1], G. W. Roeb[2], N. S. Ishioka[3], A. Osa[3], H. Matsuoka[3], T. Sekine[3] H. Uchida[4], A. Tsuji[4], H. Nakanishi[5], N. Bughio[5] and S. Mori[5]
Dept. Radiat. Res. Environ. Resources, JAERI[1], KFA, Germany[2], Hamamatsu Photonics Co[3]., Dept. Radioisotopes, JAERI[4], Dept. Appl. Biol. Chem., University of Tokyo[5]

Introduction

Positron emission tomography (PET) has been utilized for diagnosis in nuclear medicine. Short life positron-emitting radionuclides such as ^{11}C (half life 20.4 min), ^{13}N (10.0 min), ^{18}F (110 min) have been used for *in vivo* studies of whole plant transport. To take advantage of PET in studies of physiological functions of plants *in vivo*, we have developed a special "Positron-Emitting Tracer Imaging System" (PETIS) which can be used to obtain a dynamic image of plant transport.

In the present study, the translocation of ^{11}C-labeled compounds introduced into plants was dynamically followed by the positron imaging system.

Experimental

The system (PETIS) used in this experiment consisted of two-dimensional block detectors (4.8 x 5.0 cm square) which were composed of a $Bi_4Ge_3O_{12}$ scintillator array coupled to a position sensitive photomultiplier tube (PS-PMT; Hamamatsu R3941-2). The plant samples are placed at midposition between the two planer detectors and the annihilation γ -rays from positron emitting tracer were detected in coincidence (Fig. 1). $^{11}CO_2$ gas was produced from the reaction ^{14}N (p, α)

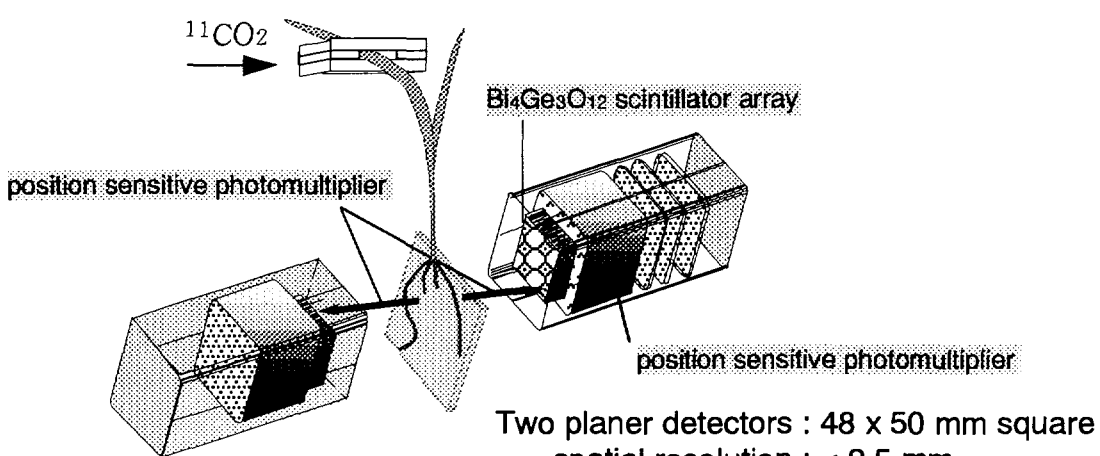

Fig. 1. Scheme of positron-emitting tracer imaging system

^{11}C by bombarding N_2 gas with 1.0 μ A of 20 MeV proton from TIARA AVF cyclotron.

Results and Discussion

1. Translocation of photosynthetic products

The $^{11}CO_2$ gas was circulated for 20 minutes using a specially designed application unit to the leaf. The $^{11}CO_2$ gas supplied to the leaves of wheat was absorbed and the photosynthetic ^{11}C-products were translocated to the root. Figure 2 shows the image of ^{11}C activity accumulated for 90 min and the time-activity curves. The clear images of ^{11}C in roots were observed by PETIS and the import of labeled carbon into the roots could be detected about 30 min after the $^{11}CO_2$ gas supply. The results of the PETIS analysis reflect the amount and the time course of carbon movement within individual roots. The high accumulation of ^{11}C labeled products was observed at the tip of young roots where the photosynthetic products were used up to balance the energy for root growth. The ^{11}C accumulation in old root (No. 4 in Fig. 2) was lower than that in young root (No. 2 in Fig. 2). The image taken by Bioimaging Analyser (BAS) after the PETIS analysis for 90 min gives an overview about the distribution of the ^{11}C activity. It confirms the high carbon accumulation in the tip of the young roots. It is considered that the result is the first data showing the images of translocation of carbon in an intact plant.

The effect of light conditions on the translocation of photosynthetic products were investigated using $^{11}CO_2$. The translocation of ^{11}C compounds into a young leaf (No. 3 in Fig. 3) kept in dark was observed in a short time and it was higher in dark than in light. The translocation of ^{11}C into the other leaves was hardly observed. Whereas , it was observed that the accumulation in an ear of wheat was faster in light.

2. Translocation of ^{11}C-methionine

The demand of methionine under Fe-limited conditions is suggested to be higher in roots as the mugineic acids is synthesized from methionine in roots. In the present study, we used ^{11}C-methionine, which was synthesized from $^{11}CO_2$. ^{11}C-methionine was supplied to the leaves of barley and measured the translocation rate of methionine from leaves to roots in Fe-deficient plants. Methionine was translocated downward rapidly (within 1 h). It was accumulated at the base of leaves (discrimination center) and was hardly translocated to the roots. A considerable amount of methionine was re-translocated to the new leaves and tillers. This may be the first trial to measure the translocation rate of amino acid in a whole plant (Fig. 4).

The results show that the system is effective in observing the uptake and transport of ^{11}C labeled compounds in plants and is useful for the study of physiological functions of plants.

References

Kume T, Matsuhashi S, Shimazu M, Ito H, Fujimura T, Adachi K, Uchida H, Shigeta N, Matsuoka H, Osa A and Sekine T 1997 Appl. Radiat. Isoto. in press.

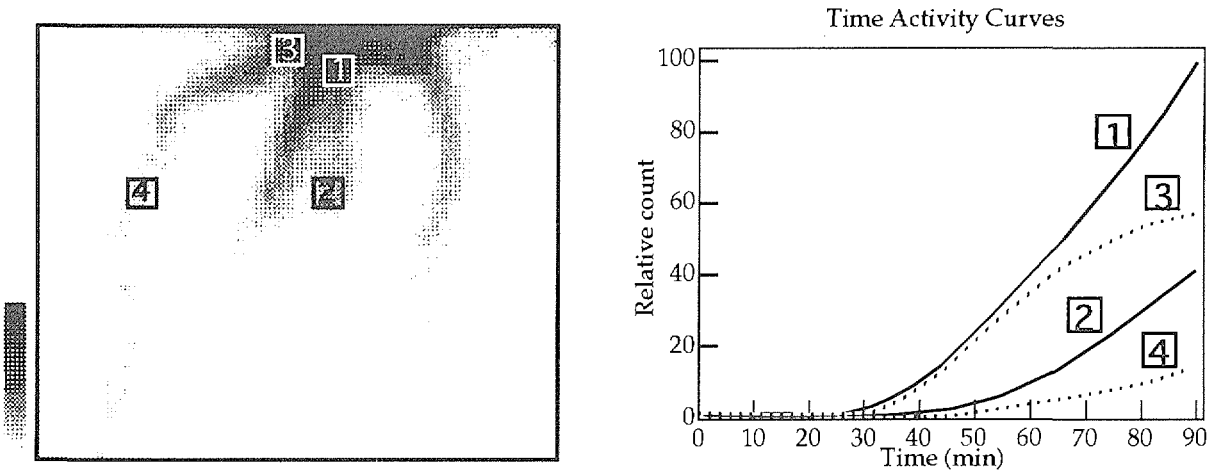

Fig. 2. Translocaton of ^{11}C photosynthetic products in wheat to the roots from leaves supplied with $^{11}CO_2$ gas

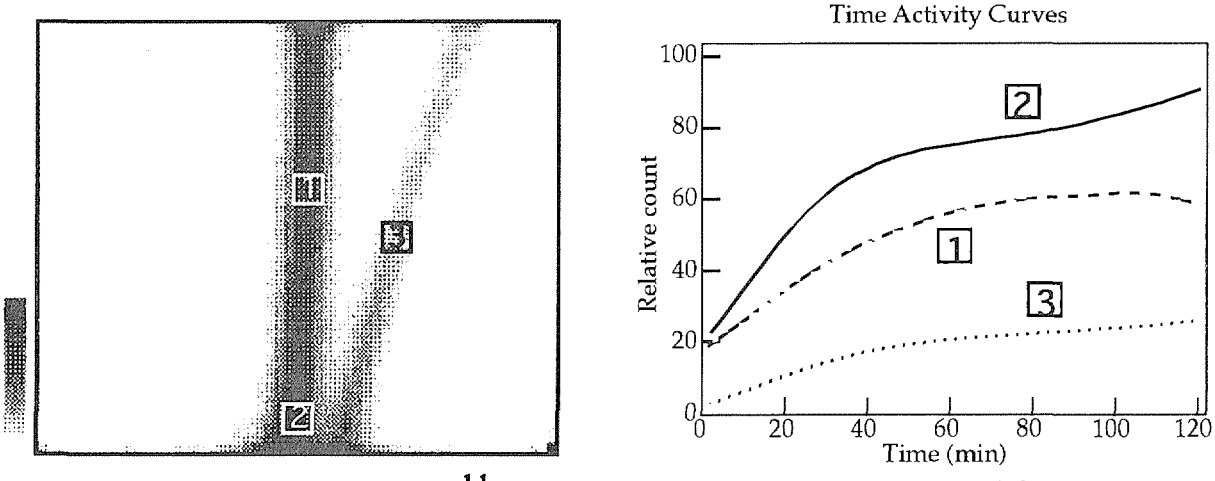

Fig. 3. Translocaton of ^{11}C photosynthetic products in wheat to a youg leaf in dark from the leaves supplied with $^{11}CO_2$ gas

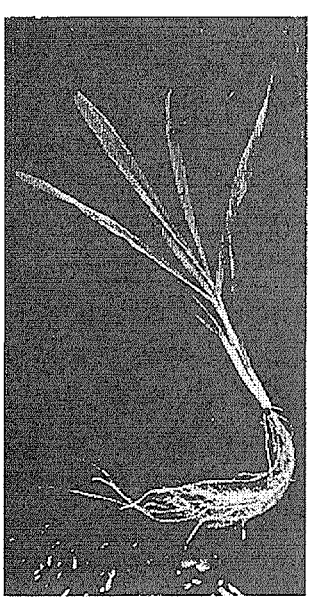

Photograph of whole plant

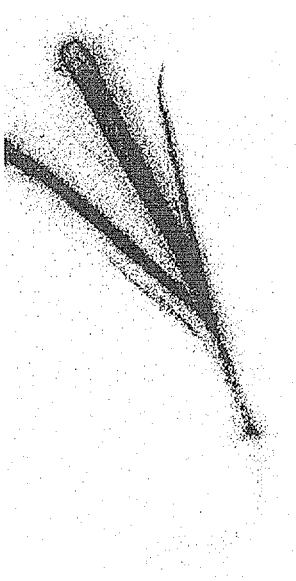

Image obtained by BAS

Fig. 4. Translocaton of ^{11}C-methionine supplied from the leaves of Fe-deficient barley

2.12 Induction of Mutation in Tobacco by Ion Beam Irradiation - Effects of ion beams on germination rate, survival rate and morphology -

Tomonori SUZUKI, Hiroshi TANAKA, Toshiake MATSUZAKI,
Atsushi TANAKA* and Hiroshi WATANABE**
JAPAN TOBACCO INC., Leaf Tobacco Research Laboratory,
*Advanced Sci. Rec. Center at Takasaki, JAERI,
**Department of Radiation Research for Environment and Resources, JAERI

Introduction

Ion beams have a higher LET than X and gamma rays. The irradiation of ion beams has high potential of inducing mutant plants with novel characters which might be impossible to obtain by commonly used mutagens. Tobacco yellow spotted streak disease caused by potato virus Y is one of the serious diseases in tobacco cultivation and only limited sources of resistance for the disease are available now. The final goal of this study is to develop novel resistant lines by ion irradiation. In this paper, we report the effects of ion irradiation to tobacco seeds on the germinability of the seeds, survivability of germinated plants and morphological changes in grown plants.

Materials and Methods

Six tobacco lines were used in this study: F_1 plants from crosses of Coker 319 × VAM; Coker 319 × Perevi; Burley 21 × VAM and Burley 21 × Perevi; inbred plants of Coker 319; and Burley 21. Coker 319 and Burley 21 are commercial cultivars susceptible to the disease. VAM and Perevi are resistant source lines to the disease. The ion beams used were $^{12}C^{5+}$ and $^{4}He^{2+}$ with the doses of 10 - 160 Gy and 10 - 700 Gy, respectively. Ions were irradiated to 200 seeds of each of these lines. Then numbers of germinated seeds and numbers of plants survived at the more than five leaf stage were recorded. Visible morphological mutations were investigated and mutation rates were measured.

Results and Discussion

The germination rates of F_1 seeds irradiated with $^{12}C^{5+}$ were 10 - 20% lower than non-irradiated seeds of corresponding lines with the doses of 40 - 60 Gy and they were almost none with the dose of 100 Gy (Fig. 1). In contrast, germination rates of Coker 319 seeds and Burley 21 seeds irradiated with $^{12}C^{5+}$ were 10 or 60% lower than non-irradiated seeds with the dose of 100 Gy and they were almost none at the dose of 140 Gy (Fig. 1). The survival rates of four lines irradiated with $^{12}C^{5+}$ were 10 - 20% lower than non-irradiated plants with the dose of 20 Gy and they were almost none in six lines with the dose of 80 Gy (Fig. 2).

The germination rates of six lines irradiated with $^{4}He^{2+}$ were 10 - 50% lower than non-irradiated seeds with the dose of 400 Gy and were almost none with the dose of 600 Gy (Fig. 3). The survival rates of six lines irradiated with $^{4}He^{2+}$ were 20 - 60% lower than non-irradiated plants with the dose of 200 Gy and were almost none with the dose of 400 Gy (Fig. 4).

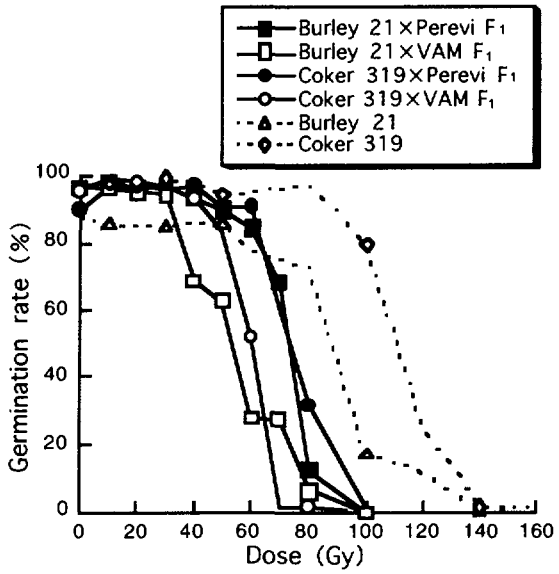

Fig.1 Germination rate of tobacco seeds irradiated with $^{12}C^{5+}$.

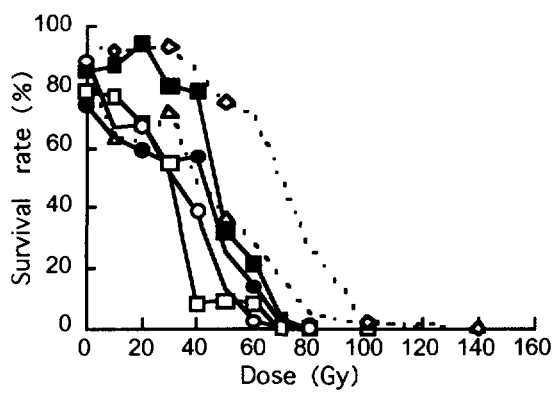

Fig. 2 Survival rate of tobacco grown from seeds irradiated with $^{12}C^{5+}$.

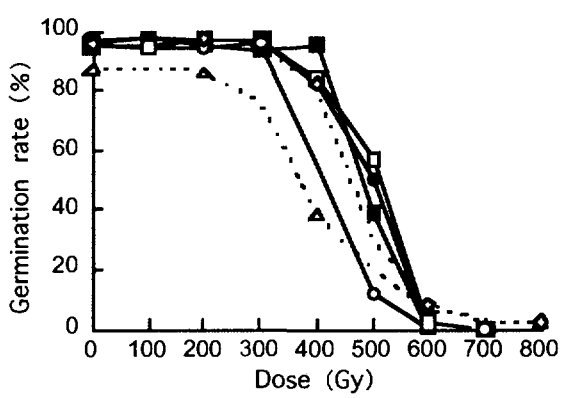

Fig. 3 Germination rate of tobacco seeds irradiated with $^{4}He^{2+}$.

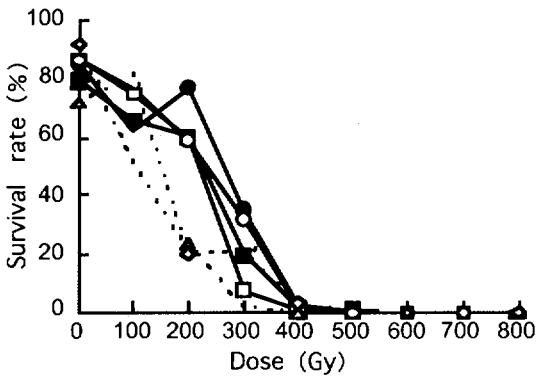

Fig. 4 Survival rate of tobacco grown from seeds irradiated with $^{4}He^{2+}$.

Mutation rates by $^{12}C^{5+}$ irradiation were 0 - 7.7% with the dose of 10 Gy, about 50% with 30 - 40 Gy and almost 100% with 60 Gy in some lines (Table 1). Mutation rates by $^{4}He^{2+}$ irradiation were about 5% with the dose of 100 Gy, about 50% with the dose of 300 Gy and 100% with the dose of 400 Gy in some lines (Table 2).

It is concluded from these results that the doses best for obtaining yellow spotted streak disease-resistant plants with minimum mutation in other characteristics will be 20 - 40 Gy of $^{12}C^{5+}$ or 100 - 200 Gy of $^{4}He^{2+}$. In these irradiation conditions, the rate of visible morphological mutation was low.

To achieve the final goal of this study, there will be the need of irradiating a larger amount of tobacco seeds with ion beams at the conditions described above and of assaying the plants grown from the irradiated seeds for the resistance to the disease.

Table 1 Number of mutants with $^{12}C^{5+}$ irradiation

Dose (Gy)	Number of mutants*					
	Burley 21 ×Perevi F1	Burley 21 ×VAM F1	Coker 319 ×Perevi F1	Coker 319 ×VAM F1	Burley 21	Coker 319
10	0/171**	2/155	9/130	5/138	3/138	14/183
20	10/181	14/143	21/122	24/144	4/58	7/43
30	36/154	14/110	52/126	40/123	22/133	36/127
40	84/163	9/23	79/117	53/97	30/81	37/86
50	58/84	12/21	42/59	35/47	42/96	20/33
60	33/48	12/27	36/42	7/7	31/48	15/23
70	5/10	0/0	6/6	0/0	—	—
80	0/0	0/0	1/1	0/0	4/6	5/6
100	0/0	0/0	0/0	0/0	1/1	0/0
120	—	—	—	—	0/0	0/0

* : Mutants are plants with narrow leaves or chlorophyl deficiency in leaves.
** : No. of mutants / No. of survived plants.
— : not tested.

Table 2 Number of mutants with $^{4}He^{2+}$ irradiation

Dose (Gy)	Number of mutants*					
	Burley 21 ×Perevi F1	Burley 21 ×VAM F1	Coker 319 ×Perevi F1	Coker 319 ×VAM F1	Burley 21	Coker 319
100	7/132**	8/150	27/125	2/154	6/163	14/102
200	25/121	16/120	56/155	35/118	5/47	16/40
300	9/39	7/14	44/70	30/65	3/5	19/42
400	2/3	2/2	5/6	2/4	0/0	6/7
500	2/2	0/0	0/0	0/0	0/0	0/0
600	0/0	0/0	0/0	0/0	0/0	0/0
700	0/0	0/0	0/0	0/0	0/0	0/0

* : Mutants are plants with narrow leaves or chlorophyl deficiency in leaves.
** : No. of mutants / No. of survived plants.

3. Radiation Chemistry / Organic Materials

(continued to the next page)

3．1 The Distribution of Chemical Reaction in Polyethylene Induced by Ion-beam Irradiation

Y. Hama, T. Takano, K. Inoue, M. Kitoh, H. Kudoh*,
M. Sugimoto* and T. Seguchi*
Advanced Research Institute of Science and Engineering,
Waseda University, *Department of Material Development,
JAERI.

1. Introduction

We have studied on the effects of heavy ion-beam irradiation on some polymers. [1)-2)] The profile of the change of some chemical structures along the path of ion-beam could be obtained by micro-FT-IR measurement. The profile obtained resemble that of the stopping power calculated by TRIM code. The position of the peak and the range, however, has been reported to be different between both profiles. We have noted that the differences could be caused by the complicated chemical reaction in polymer solid and the incomplete algorithm in the TRIM calculation for polymer materials. In order to make the TRIM code for polymers better, it would be important to obtain the detailed informations on the process of the chemical reactions induced by ion-beam irradiation. This paper concerns the process of chemical reactions in polyethylene induced by ion-beam irradiation.

2. Experimental

The sample used in this work was a low density polyethylene (LDPE) of 2mm thick. Irradiation was carried out in vacuum at room temperature by 10 MeV H^+, 20 MeV He^{2+}, 220 Mev C^{5+} and 350 MeV Ne^{8+}, respectively, from AVF cyclotron (TIARA). The fluence and the absorption dose were estimated by the beam current and the stopping power calculated by TRIM code.

After irradiation, the sample was exposed to air and sliced along the pathway of the beam to obtain a thin film for the micro-FT-IR measurement.

3. Results and discussion.

(i) Chemical species induced by irradiation.

The predominant changes of chemical structure induced by ion-beam irradiation were creation of cross-linkings and trans-vinylene groups (964 cm^{-1}). In addition, the amount of end-vinyl (910 cm^{-1}), vinylidine (890 cm^{-1}), and carboxylic acid (1716 cm^{-1}, 3400 cm^{-1}) groups which are included slightly respectively in the virgin sample were caused to change by irradiation.

(ii) Cross-linking.

The gel fraction of LDPE irradiated to the fluence of about 10^{12} (ion/cm^2) by 220 Mev C^{5+} or 350 Mev Ne $^{8+}$ reached easily 90%. This could be corresponded to the effect of γ-irradiation.

(iii) Trans-vinylene group.

The depth profile of the absorption due to trans-vinylene induced by 220 MeV C^{5+} is shown in Fig.1, together with those of end-vinyl and vinylidine and the stopping power calculated by TRIM code, in which the absorption of unirradiated region are took as the base line. The trans-vinylene was predominant product also on γ-irradiation, giving the constant depth profile. The trans-vinylene would be induced by the elimination reaction of hydrogen molecule or the alkyl radical migration to encounter each other.

(iv) End-vinyl group.

As shown in Fig.1, the depth profile of the end-vinyl group is similar to that of the trans-vinylene. The absorption intensity, however, is less than that of the virgin sample in the region which the stopping power is lower. This was observed on all ion-beam irradiation, though on H^+ - and γ-irradiation the absorption intensity was less than the virgin sample over whole regions. This indicates that the recovery of the absorption intensity of end-vinyl is not dependent of the absorbed dose but the LET. This would be an evidence of LET effect for polymer irradiated by ion-beams.

The consumption of the end-vinyl groups results in the creation of branching by double bond opening. On the other hand, the increment of the end-vinyl groups in the region of high LET may be due to the decomposition of the trans-vinylene groups.

(v) Vinylidine group.

The vinylidine groups were consumed on irradiation of all ion-beams and γ-rays over most of the irradiated region. The absorption due to these groups began to recover toward the original one at near the range of the ion. The vinylidine groups should be consumed through the cross-linking reaction. This is supported by many works on the photodegradation of polyethylene.

(vi) Carboxylic acid group.

The absorptions due to the carbonyl group and hydroxyl group were observed slightly at around 1716 cm^{-1} and 3400 cm^{-1}, respectively. It may be reasonable that the absorption of the carbonyl group is attributed to the component included in the carboxylic acid since the absorption appears at 1716 cm^{-1}. It is concluded that those groups come from the reaction of the allyl radical which is rather stable at room temperature in vacuum with oxygen molecule when the irradiated sample was exposed to air.

(vii) Fluence and stopping power dependence of species.

Figs. 2 and 3 show the fluence and the stopping power dependences, respectively, of the species induced by irradiation, except the carboxylic acid group. Both absorptions of the trans-vinylene and the end-vinyl increase with the fluence or the stopping power. On the other hand, the absorption of the vinylidine reaches constant value lower than that of the virgin sample with the fluence or the stopping power.

4. Conclusion.

The effects of the fluence and the LET on the chemical reaction induced in LDPE by various ion-beams irradiation were investigated. On irradiation by low LET beam such as H^+, the reaction induced is similar to that of γ-irradiation. However, on irradiation of high LET ion-beams heavier than H^+ ion, the LET effects are found on the reaction in which the trans-vinylene converts to the end-vinyl through the main chain scission.

References.

1) Y.Hama et al., Radiat. Phys. Chem., **48**(5), 549 - 554(1996)

2) M.Sugimoto et al., Proceedings of the 7th International Symposium on Advanced Nuclear Energy Research, JAERI-Conf 97-003, 269(1997)

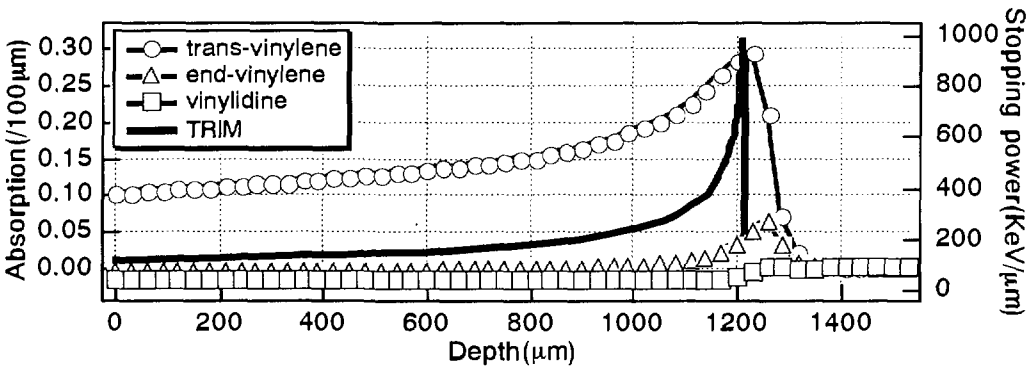

Fig. 1. Depth profiles of the species induced by 220 MeV C^{5+} irradiation and the stopping power calculated by TRIM code.

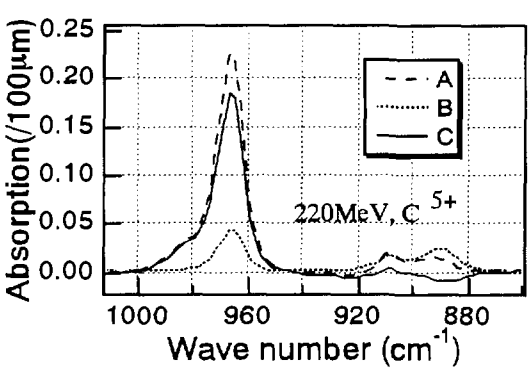

Fig.2. Fluence dependence of species at 90μm from the surface. A: 1.14 x10^{13} (ions/cm^2), B: 1.10 x 10^{12}(ions/ cm^2), C: subtracted spectrum; (A – B).

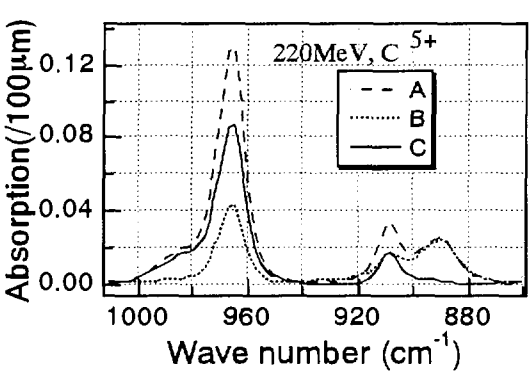

Fig.3. Stopping power dependence of species irradiated to 217 kGy. A: 1230 μm, B: 90 μm, C:subtracted spectrum; (A – B)

3．2 LET Effects of Ion Beam Irradiation on Poly(di-n-hexylsilane)

S. Seki, K. Kanzaki, Y. Kunimi, Y. Yoshida, S. Tagawa, H. Kudoh, M. Sugimoto, T. Seguchi
The Institute of Scientific and Industrial Research, Osaka University.
Takasaki Radiation Chemistry Institute, JAERI

Introduction

It has been suggested that spatial distribution of deposited energy by charged ions has played a significant role in the chemical reactions occurred in the target materials. Models of the energy distribution was proposed experimentally and theoretically as "Ion Track" and "Penumbra" models by Magee et al., , Varma et al., Wingate et al. and Wilson. In spite of the theoretical modeling effort, the size of ion tracks has not shown good agreement with the values of intratrack reaction radius that was experimentally obtained by the analysis of irradiation products(Kurshev et al. and Koizumi et al.). Thus the theoretically predicted energy distribution was not the universal function that was able to apply for the elucidation of ion beam induced reaction systems.

Ion beam irradiation and its induced modification have been vigorously investigated for polymer materials because ion irradiation has been expected to cause heterogeneous and peculiar reaction based on the high dense excitation. It enables to develop novel reaction system leading to new materials which can not be obtained by bulk chemical reactions. Puglisi et al., Licciardello et al. and Calcagno et al. reported the effects of ion beam bombardment to polystyrene. Irradiated polystyrene showed aggregation of molecules and crosslinked. The molecular weight distribution changed anomaly with the ion irradiation, which was ascribed to the intratrack reaction.

Polysilane derivatives have attracted great interest as a new category of polymer materials. We have already reported on reactive intermediates of polysilane derivatives irradiated by ion, electron and g-rays. Predominant reactive intermediates in polysilane derivatives were assigned to silyl radicals showing great stability in comparison with carbon centered alkyl radicals. The ion beam irradiation effects on polysilanes also reported in the previous study. Reactions in the polymers were drastically changed with the energy deposition rate of incident particle ; LET of radiation sources. Polymers were crosslinked for high LET ion beam irradiation in spite of predominant main chain scission reaction for low LET radiation. The difference in radiation induced reactions was ascribed to a variation of density of stable reaction intermediates ; silyl radicals generated by radiation. In the present study, it is discussed that molecular weight distribution of polysilanes was extraordinary changed with ion beams. Both main chain scission and crosslinking reactions of polysilanes are able to regard as reactions occurred in ion tracks ; intratrack reactions. The observation of molecular weight distribution makes it enable to estimate the size of each ion track in the polymer materials.

Experimental

Poly(di-n-hexylsilane) ; PDHS was prepared by the reaction of di-n-hexyl-dichlorosilane with sodium in refluxing toluene. The samples had their molecular weight of 1.1×10^4 and 5.6×10^5, respectively, determined by polystyrene calibration standards. The polymer films were irradiated in a vacuum chamber ($< 5 \times 10^{-6}$ Torr) by 2 MeV H^+ and He^+ ion beams from a Van de Graaff accelerator at the Research Center for Nuclear Science and Technology, University of Tokyo. Temperature was controlled at 295 K and 340 K. Irradiation was also carried out at Japan Atomic Energy Research Institute, Takasaki Radiation Chemistry Laboratory using several ion beams from TIARA cyclotron accelerator in a vacuum chamber ($< 5 \times 10^{-6}$ Torr) at room temperature. After irradiation, molecular weight distribution of irradiated PDHS films was measured by GPC system. The loss of kinetic energy of ions in traversing polymer films was estimated by the TRIM 91 code.

Results and discussion

It was already confirmed that the polymer gel was generated for several kinds of a few MeV order ion beams. According to the statistical theory of crosslinking and scission of polymers induced by radiation, the behavior of gelation is expressed by the following equation (Charlesby-Pinner relationship),

$$s + s^{1/2} = p_0/q_0 + m / q_0(M_n)_0 D,$$

$$s = 1 - g,$$

where p_0 is the probability of scission, q_0 the provability of crosslinking, s the sol fraction, g the gel fraction, m the molecular weight of a unit monomer, $(M_n)_0$ the number average molecular weight before irradiation, and D is absorbed dose. And then, each G-value is related to the values of p_0 and q_0 as follows,

$$G(x) = 4.8 \times 10^3 \times q_0$$

$$G(s) = 9.6 \times 10^3 \times p_0$$

where G(x) is the G-value of crosslinking and G(s) is the G-value of main chain scission. The evaluation was carried out for the crosslinking behavior of PDHS upon irradiation of high LET ion beams as summarized in Table 1.

Table 1 The Behavior of Poly(di-n-hexylsilane) for the Various Radiation Source

Radiations	LET (eV/nm)	Gelation Doses (MGy)	G(x)	Type
160MeV O^{6+}	3.0	3.1	0.71	Crosslink
225MeV O^{7+}	2.3	3.4	0..62	Crosslink
2MeV He^{+}	1.8	3.3	0.67	Crosslink
220MeV C^{5+}	1.1	2.9	0.78	Crosslink
20MeV He^{2+}	0.35	5.4	0.19	Crosslink
2MeV H^{+}	0.17	6.8	0.12	Crosslink
20MeV H^{+}	0.027	——	0.029	Main Chain Scission
45MeV H^{+}	0.014	——	——	Main Chain Scission
Co^{60} γ-rays	0.002-0.003	——	0.014	Main Chain Scission

For 20 MeV H^+ ion beam, the shoulder in the low molecular weight region (around 10^4) raises with the irradiation, which is proof of the main chain scission. The G values of crosslinking and main chain scission are also evaluated by the next formula in this case of high energy proton irradiation. Then,

$1/M_n = 1/(M_n)0 + (p0 - 0.5q0)\ D/m,$

$1/M_W = 1/(M_W)0 + (0.5p0 - q0)\ D/m$

The crosslinking G values in Table 1 were also obtained by the calculation for main chain scission reactions caused by lower LET ion beams than 1 eV/Å.

However, the ion beam induced molecular weight change are quite unique in both cases in comparison with γ-rays which cause simple increase of poly-dispersion. It is considered that the ion beam irradiation is heterogeneous, and the reactions bringing molecular weight change are occurred at the inside of ion trucks along the ion projectiles. It is assumed that the two peaks have logarithmic Gaussian ; $DF_1[M_1,s]$ and $DF_2[M_2,s]$ with same deviation as distribution functions for the analysis. A model distribution function is obtained by the linear

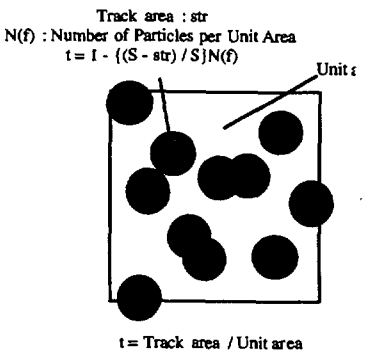

Fig. 1. Schematic view of ion tracks at the surface of a thin polymer film.

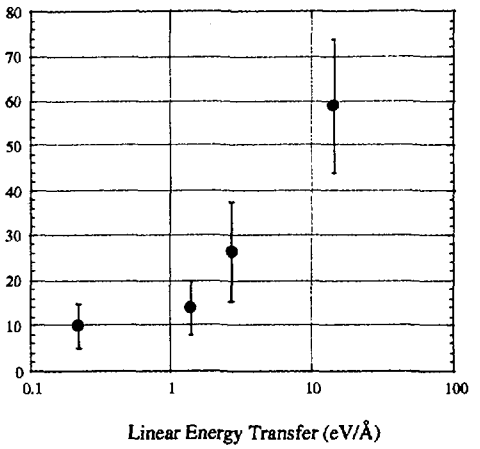

Fig. 2 The relationship between the track radius (reaction radius in PDHS) and linear energy transfer : LET.

combination of two functions using a parameter t.

$$DF = t \cdot DF_1 + (1-t) \cdot DF_2 \quad 0 \bullet t \bullet 1 \ (1)$$

Weight and number average molecular weight ; Mw, Mn of the distribution are obtained by next equations.

$$Mw = \frac{\sum M^2 \cdot DF}{\sum M \cdot DF} = \frac{\sum M^2 \cdot t \cdot DF_1 + \sum M^2 \cdot (1-t) \cdot DF_2}{\sum M \cdot t \cdot DF_1 + \sum M \cdot (1-t) \cdot DF_2}$$

$$Mn = \frac{\sum M \cdot DF}{\sum DF} = \frac{\sum M \cdot t \cdot DF_1 + \sum M \cdot (1-t) \cdot DF_2}{\sum DF} \quad (2)$$

In this analysis, parameter t means the ratio of the ion track volume to total volume of polymer film. The polymer films used in this experiment was thin enough to regard the ion tracks as cylindrical, thus t can be estimated the ratio of covered area by ion tracks to film surface. The relationship between parameter t and fluence of ion beams is simulated as shown in Fig. 1. According to statistical theory, next expression of a form is obtained.

$$t = 1 - \{(S - s_{tr}) / S\}^{N(f)} \quad (3)$$

Thus, obtained changes in Mn and Mw are simulated by the models as shown in next equations.

$$Mw = \frac{[1 - \{(S-s_{tr})/S\}^{N(f)}] \sum M^2 \cdot DF_1 + \{(S-s_{tr})/S\}^{N(f)} \sum M^2 \cdot DF_2}{[1 - \{(S-s_{tr})/S\}^{N(f)}] \sum M \cdot DF_1 + \{(S-s_{tr})/S\}^{N(f)} \sum M \cdot DF_2}$$

$$Mn = \frac{[1 - \{(S-s_{tr})/S\}^{N(f)}] \sum M \cdot DF_1 + \{(S-s_{tr})/S\}^{N(f)} \sum M \cdot DF_2}{\sum DF} \quad (4)$$

Molecular weight dispersion : Mw/Mn shows obvious change with increasing ion fluence. Mw / Mn shows maximum value at a fluence, therefore the value of (S - s_{tr}) / S can be optimized using equation 4. The optimization reveals cross section of a ion track leading to the radius of the track. For 2 MeV He^+ ion beam irradiation for PDHS, the calculated value of the radius becomes 59 ± 15 Å. The calculated results show good agreement with ion beam induced changes in Mn and Mw respectively. Fig. 2 shows changes of Mw and Mn of PDHS by the irradiation. This mean of simulation can be applied

for the trace of molecular weight distribution changes observed as main chain scission. For other ion beam sources, the same simulation is carring out to elucidate the track radius of the incident ions.

Conclusion

Irradiation of MeV order ion beams caused heterogeneous reactions of crosslinking and main chain scission in PDHS films. Ion beams with high LET (> 1 eV/Å) caused mainly crosslinking reaction in spite of predominant reaction of main chain scission for lower LET ion beams. The molecular weight distribution ion beam track radius (ion beam induced reaction radius).

Acknowledgements

The authors thanks to Dr. T. Kozawa at ISIR Osaka University and Mr. M. Narui and Mr. T. Omata at the University of Tokyo for their experimental supports. This work was supported in part by Universities-JAERI Collaborative Project Program.

References

Calcagno, L., Percolla, R., Foti, G. (1994) Nucl. Instr. Meth. Phys. Res. **B91**, 426.

Charlesby, A. (1954) Proc. R. Soc. London Ser. A, **222**, 60

Charlesby, A. (1954) Proc. R. Soc. London Ser. A, **224**, 120.

Charlesby, A., Pinner, S. H. (1959) Proc. R. Soc. London Ser. A, **249**, 367.

Koizumi, H., Ichikawa, T., Yoshida, H., Namba, H., Taguchi, M., Kojima, T. (1996) Nucl. Instr. Meth. Phys. Res. B **117**, 431

Kouchi, N., Tagawa, S., Kobayashi, H., Tabata, Y. (1989) Radiat. Phys. Chem. **34**, 453.

Kurshev, V. V., Koizumi, H., Ichikawa, T., Yoshida, H., Shibata, H., Yoshida, Y., Tagawa, S. (1994) Radiat. Phys. Chem. **44**, 521

Licciardello, A., Puglisi, O., Calcagno, L., Foti, G. (1988) Nucl. Instr. Meth. Phys. Res. **B32**, 131.

Licciardello, A., Puglisi, O. (1994) Nucl. Instr. Meth. Phys. Res. **B91**, 436.

Miller, R. D.; Michl, J. (1989) Chem. Rev. **89**, 1359

Puglisi, O., Licciardello, A. (1994) Nucl. Instr. Meth. Phys. Res. **B91**, 431.

Seki, S., Tagawa, S., Ishigure, K., Cromack, K. R., Trifunac. A. D. (1996) Rad. Phys. Chem. **47**, 217.

Seki, S., Ando, M., Yamaki, T., Nakashiba, Y., Asai, K., Ishigure, K., Tagawa, S. (1995) J. Photopolym. Sci. Technol. **8**, 89.

Seki, S., Shibata, H., Yoshida, Y., Ishigure, K., Tagawa, S. (1996) Rad. Phys. Chem. in press.

Varma, M. N., Baum, J. W., Kuehner, A. J. (1975) Radiat. Res. **62**, 1.

Varma, M. N., Baum, J. W., Kuehner, A. J.. (1977) Radiat. Res. **70**, 511.

Varma, M. N., Baum, J. W. (1986) Radiat. Res. **81**, 355.

Wingate, C. L., Baum, J. W. (1976) Radiat. Res. **65**, 1.

Wilson, W. E. (1994) Radiat. Res. **140**, 375.

3．3 Radical formation in the radiolysis of solid adipic acid by heavy ions

Hitoshi Koizumi, Mitsumasa Taguchi*, Hideki Namba*,
Tsuneki Ichikawa, and Hiroshi Yoshida
Graduate School of Engineering, Hokkaido University,
*Department of Radiation Research for Environment and Resources, JAERI

1. Introduction

Chemical effects of energetic heavy ions differ from that of γ-rays and fast electrons. This effects arises from high local dose in the ion tracks. It can be utilized for material modification and fabrication of micro structure. It is important to know how the chemical effects depends on ion beams and on materials . It will be helpful to develop new applications of the ion beams.

We have already reported radical formation in ion-irradiated solid alanine[1-4]. The yield of radicals depends on ion beams. The dependence of the yield can be explained by local dose in the ion tracks and dose-yield relationship for γ-irradiated alanine. In this report, we have examined radical formation in the radiolysis of adipic acid by heavy ions. The purpose is to examine how the radical yield in ion-irradiated solids depends on the solids.

2. Experimental

Adipic acid (stated purity >98.5%) was supplied by Kanto chemicals. Films made of adipic acid and polyethylene as binder were used for ion-irradiation. Polyethylene powder was supplied by Merck (for spectroscopy, Uvasol). 50 wt% : 50 wt% mixture of adipic acid and polyethylene were pressed into film of ca. 0.5 mm thick under vacuum at 135 °C. For γ-irradiation, powder of adipic acid is sealed in a high-purity quartz tube under high vacuum.

The ion beams of 175 MeV $^{40}Ar^{8+}$, 220 MeV $^{12}C^{5+}$, and 350 MeV $^{20}Ne^{8+}$ from the cyclotron of the JAERI TIARA were used for the ion irradiation. The ion irradiation was carried out under vacuum at ambient temperature. The thickness of the piled films for the ion irradiation is sufficiently larger than the range of the ion beams. γ-irradiation was carried out with a ^{60}Co source at Hokkaido University.

Radicals were observed with an X-band ESR spectrometer. The amount of the radicals was determined by double integration of ESR spectra using TEMPO as a reference.

3. Results and Discussion

The radical yield (number of radicals per ion) in the adipic acid films irradiated with 220 MeV C^{5+} ions is shown in Fig. 1. The radical yield is constant below a critical fluence of 10^{11} ions cm^{-2}, and it decreases above the fluence with increasing the ion fluence. This arises from the overlap of the ion tracks: the radical decreases in the overlap region through combination reaction of the radicals and the reaction of the radical

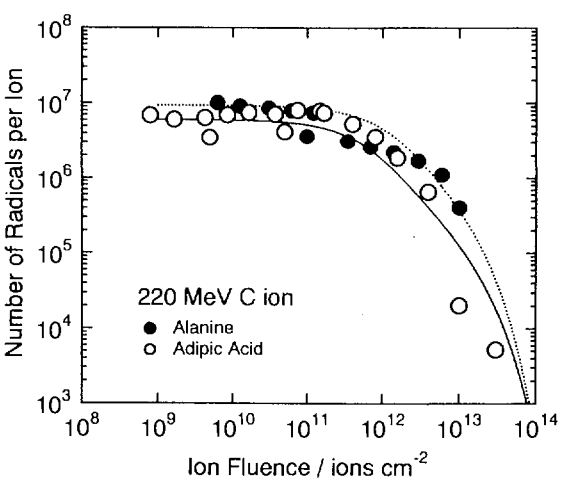

Fig.1. Radical yield in adipic acid / polyethylene films (-○-) and in alanine film dosimeter (-●-) irradiated with 220 MeV C^{5+} ions as a function of ion fluence.

with short-lived intermediates[1-4]. The G-value for the radical formation is obtained from the constant yield at the low fluences; It is 5.6 for the C ion irradiation. This value is calculated on the basis of absorbed 100 eV energy by adipic acid.

The radical yields in the adipic acid films irradiated with 350 MeV Ne^{8+} ions and with 175 MeV Ar^{8+} ions are shown in Figs. 5 and 6, respectively. The critical fluence for the Ne ions is 10^{11} ions cm^{-2}, and that for the Ar ions is $5x10^{11}$ ions cm^{-2}. The G-value for the radical formation is obtained to be 2.3 for the Ne ions, and 0.65 for the Ar ions.

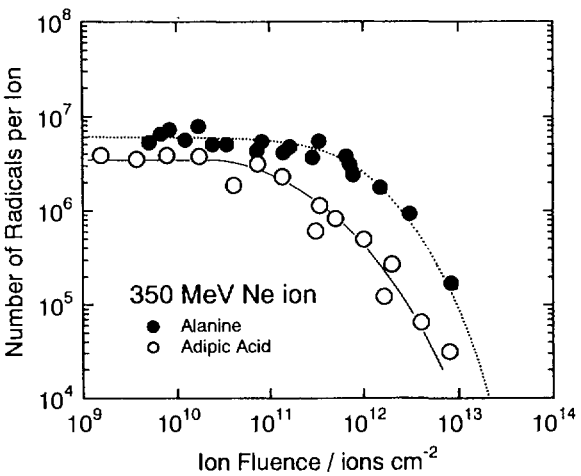

Fig.2. Radical yield in adipic acid / polyethylene films (-○-) and in alanine film dosimeter (-●-) irradiated with 350 MeV Ne^{8+} ions as a function of ion fluence.

The G-values of the radical formation in adipic acid and alanine are shown in table 1. The relative yields for ion-irradiations to the yield for γ-irradiation are compared. The values of the relative yield for 220 MeV C^{5+} and 350 MeV Ne^{8+} ions are similar in both the solids. However, the G-values by 175 MeV Ar^{8+} are much different: the value for adipic acid is 1/3 of that for alanine.

The difference in the yield for adipic acid and alanine will be ascribed to that in dose-yield relationship for the radical formation. The yield of trapped radicals in ion-irradiated solids is affected by the dose-yield relationship at the high doses, which is determined by the efficiency of the destruction reactions of the radicals, as well as by dose distribution in the ion tracks. LET in adipic acid and alanine are of similar values. The dose distribution in the ion tracks will be similar in both the solids. On the other hands, the dose-yield relationship for adipic acid differs from that for alanine.

The radical concentrations in γ-irradiated adipic acid and alanine are plotted as a function of dose in figure 4. The efficiency of the radical formation in adipic

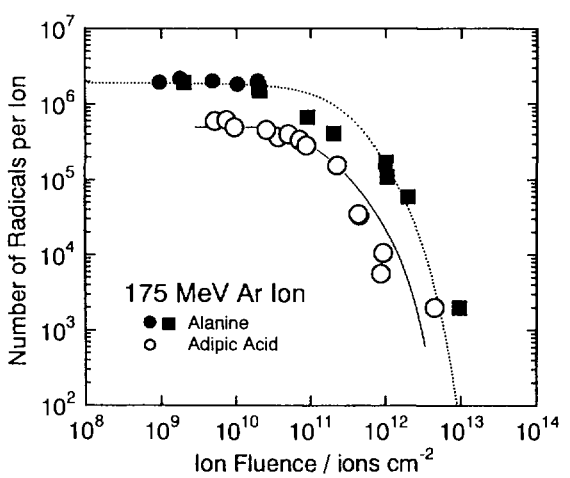

Fig.3. Radical yield in adipic acid / polyethylene films (-○-) and in alanine film dosimeter (-●-) irradiated with 175 MeV Ar^{8+} ions as a function of ion fluence.

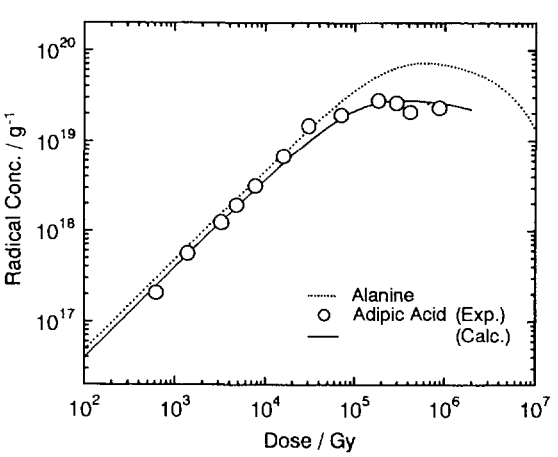

Fig.4. Radical concentration in γ-irradiated adipic acid (-○-) and in γ-irradiated α-alanine(----).

Table 1. The G-values for the radical formation in adipic acid and in alanine by γ- and ion-irradiations.

Ion	Energy /MeV	G-value[a] Adipic acid radicals (100eV)$^{-1}$	rel.	DL-α-Alanine[b] radicals (100eV)$^{-1}$	rel.
^{60}Co γ-ray		6.3	1.0	7.7	1.0
C	220	5.6	0.89	8.3	1.1
Ne	350	2.3	0.37	2.9	0.38
Ar	175	0.65	0.10	2.3	0.30

[a] The G-values are calculated based on the radiation energy absorbed by adicpic acid or DL-α-alanine.
[b] references 2.

acid decreases from lower dose than in alanine. The maximum concentration in adipic acid is less than half of that in alanine.

The radical yields for both the solids are plotted as a function of dose. The yields are normalized at the low doses where the yields are independent of the dose. The yield for adipic acid decreases more steeply than that for alanine. The difference in the yields for the two solids increases from 10 kGy to 1 MGy. The local dose in the ion tracks for 220-MeV C^{5+}, 350-MeV Ne^{8+}, and 175-MeV Ar^{8+} ion irradiations increases in this order. The larger difference in the G-values for the Ar ion than that for the other ions is explained by the higher dose in the ion tracks.

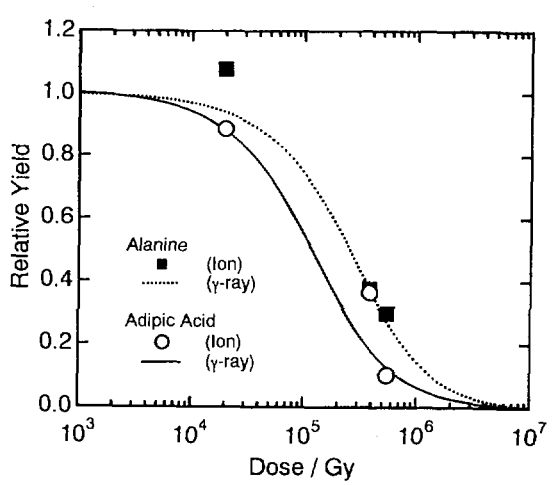

Figure 5. Radical yields for g-and heavy ion-irradiations: radical yield for the g-irradiation of DL-a-alanine (----) and adipic acid (——) as a function of dose, radical yields for the heavy ion irradiations of alanine (■) and adipic acid (○)

The radical yields for the ion irradiations are plotted at average doses in the ion tracks. The average doses are determined to reproduce the G-values of alanine for the ion irradiations[2]. The yields for the ion irradiation of adipic acid are plotted at the same average doses for alanine. They correlate well with the curve for γ-irradiation. The radical yields both in adipic acid and in alanine are mainly determined by the dose-yield relationship at high doses. The effects of ion irradiation will be estimated with dose-yield relationship for low-LET radiation and with dose distribution in the ion tracks.

4. References

1) H. Koizumi et al. Nucl. Instrum. Meth. B 117:269-274 (1996).
2) H. Koizumi et al. Nucl. Instrum. Meth. B 117:431-435 (1996).
3) H. Koizumi, T. Ichikawa and H. Yoshida. Appl. Radiat. Isot. 47:1205-1209 (1996).
4) V.V. Krushev et al. Radiat. Phys. Chem. 44: 521-526 (1994).

3．4 Ion Beam Radiolysis Using the JAERI-AVF Cyclotron

- The Time Resolved Luminescence Measurement of Dilute Benzene Solution in Cyclohexane -

H. Namba, M. Taguchi, Y. Aoki* and Y. Matsumoto

Department of Radiation Research for Environment and Resources, JAERI
** Department of Materials Development, JAERI*

Ⅰ. Introduction

The effects of radiation depending on its quality has been one of the important subjects in radiation chemistry. It is known as "LET effects" and the quality of radiation is indicated often by the LET value. The "LET effects" are involved in luminescence processes of scintillators and also in evaluation of influence of radiation on human bodies in various radiation environments such as space and so on. The origin of the LET effect is believed to be the amount of deposited energy in a small volume by radiation, that is energy density, because the reactive species produced become to interact with each other more and more with increasing the energy density. It is noted that the LET is a one-dimensional parameter, while the parameter which substantially influences the difference of radiation effects, is three-dimensional energy density.

In order to investigate the origin of the LET effect, we have started a study of ion beam radiolysis using the JAERI-AVF cyclotron in 1994. The first year, we have constructed systems for time-resolved luminescence measurement to follow the reaction process of one of the reactive species, excited states[1]. In 1995, a method for irradiation of liquid samples has been developed. Using these systems we pointed out that the reaction rate of benzene excimers in liquid and in solid irradiated with high LET heavy ions are quite different from those measured in the electron irradiation with low LET[2]. This year, ion beam induced fluorescence of a dilute solution of benzene in cyclohexane was measured to follow the changes in the density of the reactive species with time for estimation of the energy density deposited in materials by high-energy heavy ions.

Ⅱ Experimental

Solutions were prepared with benzene (UVASOL, Merck) and cyclohexane (spectroscopy grade, Dotite) without further purification and poured into sample cells reported the last year. Ions used for irradiation were 220MeV $^{12}C^{5+}$ and 330MeV $^{40}Ar^{11+}$ from the JAERI-AVF cyclotron. Fluorescence from the samples under irradiation was measured by a photon counting method with a photomultiplier tube (H3177, HAMAMATSU) described peviously.

Ⅲ. Results and Discussion

Since the mole fractions of cyclohexane (CH) are 99.6% for a 40mM solution and 99.9% for a 10mM solution, most of the deposited energy should be absorbed by CH. After passing through a 5 μm Havor foil (8.3g/cm^3, main components are Co(42.5%), Cr(20%), Ni(13%), Fe(17.9%), W(2.8%)) at the entrance of the cell, the energy incident on the solutions can be estimated about 217MeV for ^{12}C and 294MeV for ^{40}Ar ions. Fig.1 shows the stopping power as a function of depth in cyclohexane for a 220MeV C incident ion. The projected ranges are estimated about 1.47mm and 170μm for 217MeV ^{12}C and 294MeV ^{40}Ar, respectively and the depth-mean stopping powers are listed in Table 1. Fig. 2 shows the time profiles of benzene fluorescence from the 40mM solution observed at three kinds of wavelength. Two fluorescent components, fast and slow with different spectra, are clearly seen in the profiles of solution irradiated with 217MeV ^{12}C ions. West and Miller[3] have reported a similar work on benzene fluorescence using MeV proton and helium ion beams. In their study, the decay curves were analyzed in terms of ion

track expansion by molecular diffusions and in order to explain the faster decay part, the "dynamic quenching" due to transient species like radicals was introduced. However, the time profiles in this study are difficult to explain with the "dynamic quenching." Those seem to be superimposition of the fast and slow components. The time resolution was about 3-5 nsec in this study and the decay constant of the fast component was always shorter than the resolution. The constants of slow components obtained from the time profiles are seen in table 1. The slow component might be ascribed to the singlet excited states of benzene molecules because of the spectral region (λ_{max} ~ 285 nm) of the fluorescence. The decay constant is dependent on the stopping power and shorter than the intrinsic decay constant (26 nsec[3]), which means that the excited states can possibly react with some species in the time scale of several tens nsec. It is very curious that the slow component showed single exponential decay and also showed a LET dependence, because a single exponential decay means a pseudo 1st order reaction in which the concentration of the counterpart to the excited states seems constant. On the other hand, the LET dependence means the difference depending on the local energy density deposited around ion trajectories, that is the local density of reactive species produced by irradiation. In appearance, these are inconsistent with each other. Hence, in order to understand the chemical reaction under ion irradiation, further efforts to improve the time resolution of our system for analysis of reaction behaviors of fast component and more detailed investigation on the fluorescence decay under irradiation of ions with various stopping power values, are needed.

References

1) Y. Aoki, M. Taguchi, H. Namba, R. Watanabe, Y. Matsumoto, K. Kimura and K. Ushida, JAERI-TIARA Ann. Rep. 1994 (Vol.4) 62 (1995).
2) Y.Aoki, M.Taguchi, H. Namba, R. Watanabe, and Y. Matsumoto, JAERI-TIARA Ann. Rep. 1995 (Vol. 5) 71 (1996).
3) J.H. Miller and M.L. West, J. Chem. Phys., 67, 2793 (1977) : M.L. West and J.H. Miller, Chem. Phys. Lett., 71, 110 (1980).

Table 1
The ion irradiation conditions, sample, ion, energy, stopping power(SP) and the decay constant of slow component(see text).

Sample	Ion	Energy	SP (eV/A)	Decay const. (nsec)
40mM benzene in cyclohexane	$^{12}C^{5+}$	217MeV	15.0	15.8 ± 0.1
10mM benzene in cyclohexane	$^{40}Ar^{11+}$	294MeV	176.3	12.6 ± 0.2

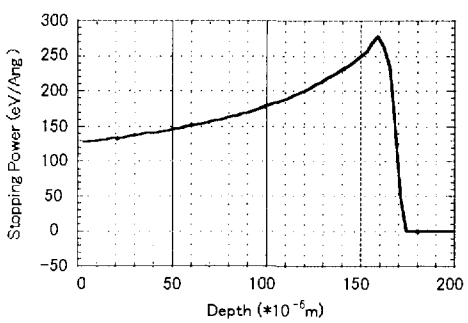

Fig. 1 Stopping power for 200MeV $^{12}C^{5+}$ ion in a 40mM benzene solution in cyclohexane.

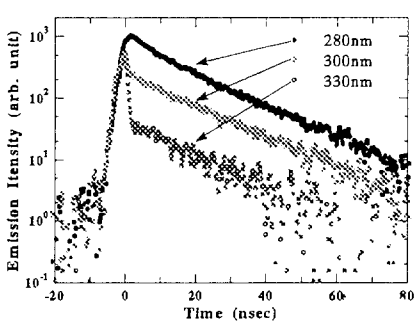

Fig. 2 The time profiles of benzen fluorescence from a 40mM benzene solution in cyclohexane irradiated with 220MeV $^{12}C^{5+}$ ion pulse observed at 280nm, 300nm, 330nm.

3.5 Radiation Effects of Ion Beams on TCNB in PVA Films(V)

M.Taguchi[1], M.Moriyama[2], Y.Matsumoto[2], H.Namba[1],
Y.Aoki[3] and H.Hiratsuka[2]
Department of Radiation Research for Environment and Resources, JAERI[1]
Department of Chemistry, Gunma University[2]
Department of Materials Development, JAERI[3]

1.Introduction

Heavy ions accelerated to high energy deposit a large volume of kinetic energy in a spatially confirmed region called track along its trajectory in a target material. The radius of the region depends mainly on the kind of the ion accelerated and on the target material. The distribution of the deposited energy in the region has been theoretically estimated by simple equations with a parameter of LET, linear energy transfer[1]. However, the region where chemical reactions occur effectively, is not the same as the estimated ones derived from the theoretical considerations and gives a different radius of the track. The former is called "chemical track" and we have estimated it experimentally for 1,2,4,5-tetracyanobenzene (TCNB) in poly(vinyl alcohol) (PVA) film irradiated with heavy ions. As a results, the radius of the chemical track is found to be related to LET values and then the energy density.

2.Experimental

PVA films doped with TCNB was used as a sample here. Those were prepared with TCNB (purity 98%, Tokyo Kasei Organic Chemicals) and PVA powder (degree of polymerization 1400, Koso Chemical Co.). The concentration of TCNB in PVA film was about 13 mM. The size of the film was 40 mm^2 x 200 μm thick. Ion irradiation with Ne^{8+}(350 MeV) and C^{5+}(220 MeV) ions from the AVF cyclotron (TIARA facility) was carried out in the Experimental Apparatus for Basic study of Radiation Chemistry with Heavy Ions (EA-BRACHI)[2-4] which is connected to AVF cyclotron at the port of HX1. The DC beam current was about 200 pA typically. UV-VIS absorption spectra were recorded by the on-line measurement system[5]. The energy of the ion was attenuated by a stack of Mylar (polyester) film having thickness 100 μm or Kapton (polyimide) film of 7.5 μm in thickness for the irradiation. The attenuated energy of the ions and LETs in the sample were calculated by IRAC code[6].

3.Results and Discussion

Figure 1 shows the fluence dependence of the yield of TCNB anion radicals produced by C and Ne ion irradiation as a parameter of ion energies. TCNB anion radical has a typical absorption band at 464 nm. The yields of TCNB anion radical were derived from the differences of the absorbance between before and after the irradiation. The changes in the yield were simulated with the radius of the chemical track as a parameter under an adequate assumption described in the previous report[1]. The simulated curves were satisfactorily fit to the experimental results. The radii obtained in such a way are plotted as a function of LET in Figure 2. The radius of the chemical track becomes bigger with increasing the LET value in both cases of C and Ne ion irradiations. The energy density around the ion trajectory was estimated by simple formulas[1]. The energy densities at the chemical track radius determined experimentally was identically about $5x10^3$ eV/nm^3. It means that the production of TCNB anion radical occurs in the limited region whose energy density above $5x10^3$ eV/nm^3.

References

1. J. L. Magee and A. Chatterjee, J. Phys. Chem., **84**, 3529 (1980).
2. M. Taguchi, H.Namba, Y.Aoki, R. Watanabe, Y. Matsumoto and H. Watanabe, JAERI Tech., 96-046.
3. M. Taguchi, Y. Aoki, H. Namba, R. Watanabe, Y. Matsumoto and H. Hiratsuka, Nucl. Instr. Meth. B, in press.
4. H. Namba, Radioisotopes, **44**, 69 (1995).
5. M. Taguchi, Y. Matsumoto, H. Namba, Y. Aoki, R. Watanabe, and H. Hiratsuka, JAERI TIARA Annual Report, **5**, 73 (1995).
6. S. Tanaka, M. Fukuda, K. Nishimura, W. Yokota, T. Kamiya, H. Watanabe, T. Shiraishi, K. Hata and N. Yamano, TIARA Annual Report, **1**, 76 (1992).

Table 1 Characteristic of the ion used and the radius of the chemical track.

Ion	Energy/MeV	LET/keV/μm	Radius/nm
C	220	134	20
C	195	155	28
C	166	185	30
C	132	247	35
Ne	350	411	25
Ne	316	464	30
Ne	279	548	32

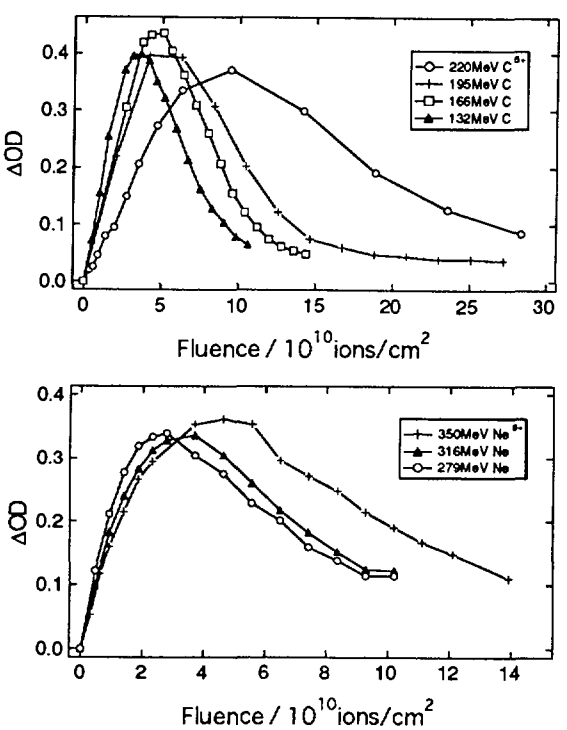

Fig. 1 The fluence dependence of differential absorbance of poly(vinyl alcohol) film doped with 1,2,4,5-tetracyanobenzene at 464 nm between before and after the irradiation with C ions and Ne ions of different energies.

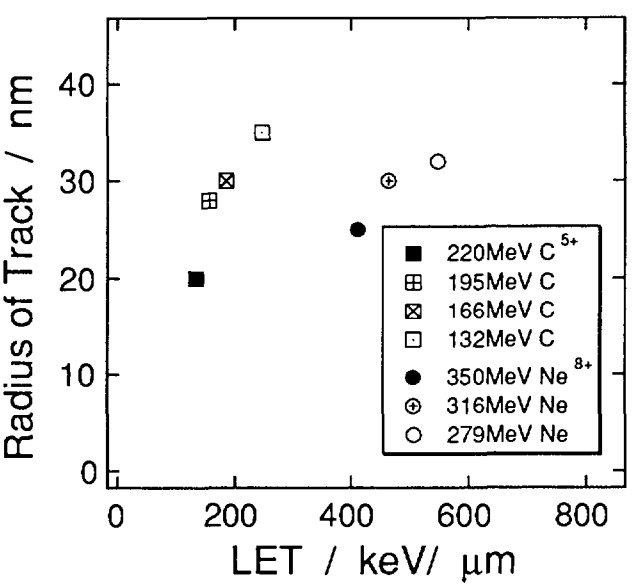

Fig. 2 Relationships of LET and radii of the chemical track for 1,2,4,5-tetracyanobenzene anion radical formation by C and Ne ions.

3．6 Fluorescence of Gaseous Nitrogen Irradiated with High Energy Ar ion

M.Taguchi[a], H.Namba[a], Y.Aoki[b], K.Furukawa[c] and S.Ohno[d]

[a]Department of Radiation Research for Environment and Resouces, JAERI,

[b]Department of Materials Development, JAERI

[c]Department of Chemistry and Fuel Research, JAERI,

[d]Institute of R&D, Tokai University

1.Introduction

We have been studying on spatial distribution of energy deposited by high energy heavy ions traveling through matters, which gives the nature of ion irradiation effects, such as in chemical reactions and in defect formation. Until the last year, using a movable ionization chamber, we have measured the amount of ionization yields in Ar gas to deduce the distribution of an absorbed dose in water by a density correction method. Water is among the most important substances from the point of view of microdosimetry relateing to health physics, because it is the main component of living bodies. The experimental results showed a steep decrease in dose with radial distance from the incident ion beam. However the decreasing curve has a little deviation from the theoretical estimation of r^{-2} dependence. At the second stage of this study, we have examined to measure excited states during ion irradiation. Excited states, as well as ionized species, contribute to chemical reactions induced by ion irradiation. In the present report, the excited states produced in gaseous nitrogen irradiated with 330 MeV Ar^{11+} ions are identified and their kinetic behavior was studied.

2.Experimental

Ion irradiation and fluorescence measurement were performed at the beam port of HX-1 of the AVF cyclotron facility in JAERI-Takasaki, which is called the Experimental Apparatus for Basic study of Radiation Chemistry with Heavy Ions (EA-BRACHI)[1-4]. The energy and the kind of ion which was used in this study were 330 MeV Ar^{11+}. The pressure of nitrogen gas was controlled to 98, 293 and 593 Torr at ambient temperature, using pressure sensors (MKS Baratron 122A and 127A) and a throttling valve(MKS253A-2-4CF-2). LETs of Ar with the incident energy of 330MeV in the target gas were calculated to be less than 1.65 eV/nm by the IRAC code[5]. The fluorescence of the excited nitrogen molecules were measured in the UV and VIS region (260 - 440 nm). A streak camera (HAMAMATSU C3610) was used in focus mode to get the fluorescence spectra and a single photon counting system with a photomultiplier tube (HAMAMATSU H3177) for the lifetime mesurement. Figure 1 shows the simple diagram of the single photon counting system. The repetition frequency of 330MeV Ar^{11+} pulses from the cyclotron in normal operation was substantially 14MHz.

3.Results and Discussion

Figure 2 shows the fluorescence spectrum of nitrogen gas irradiated with 330MeV Ar^{11+} ions. Several emission lines are clearly seen in the spectrum at 298, 316, 337, 358, 376, 391 and 428nm. Similar bands of nitrogen have been observed by Panta et al. in the electron irradiation experiment[6]. According to their spectral identification, all these fluorescence band measured here could be ascribed to either the second positive transitions of nitrogen molecules or the first negative transitions of nitrogen molecular ions, which are indicated in Fig. 2. The (0,0) transition of the first negative system of nitrogen molecular ion observed at the wavelength of 391.4 nm has an excitation cross section proportional to the total ionization cross

section[7]. Therefore, the analysis of this transition may be important to evaluate the yields of total ion pairs, which corresponds to the ionization measurements performed previously. On the other hand, the (0,0) transition of the second positive system of nitrogen molecules observed at 337.1 nm($C^3\Pi_u$-$B^3\Pi_g$) is known to be induced exclusively by low energy electrons[8]. Thus it is suitable for estimation of the contribution to the energy deposition from the low energy electrons. The fluorescence time profiles of the second positive transition of nitrogen molecules and the first negative transition of nitrogen ions were recorded at 98 Torr pressure as shown in Fig. 3 with using the interference filter of 338 and 429 nm, respectively. To obtain the time profile of the first negative transition of nitrogen+, the fluorescence of 429 nm was monitored because the first negative(0,0) band overlaps with the second positive(0,2) band at 376 nm. The time profiles of the fluorescence were dependent on the gas pressure. The decay curves decreased faster with increasing gas pressure.

Reference

1. H.Namba, Y.Aoki, M.Taguchi and K.Furukawa, TIARA Annual Report 1,163(1992).
2. M.Taguchi, H.Namba, Y.Aoki, R.Watanabe, Matsumoto and H.Watanabe, JAERI Tech., 96-046.
3. H.Namba, Radioisotopes, 44,69(1995).
4. M.Taguchi, Y.Aoki, H.Namba, R.Watanabe, Y.Matsumoto and H.Hiratsuka, Nucl.Instr.Method B, in press.
5. S.Tanaka, M.Fukuda, K.Nishimura, W.Yokota, Kamiya, H.Watanabe, T.Shiraishi, K.Hata and N.Yamano, TIARA Annual Report, 1,76(1992).
6. P.P.Panta, A.G.Chmielewski, Z.A.Zimek, M.Paduch and K.Tomaszewski, Radiat.Phys.Chem.,46,1259-1262(1995).
7. W.L.Borst and E.C.Zipf, Phys.Rev., A1,834-840(1970).
8. M.Imai and W.L.Borst, J.Chem.Phys., 61,1115-1117(1974).

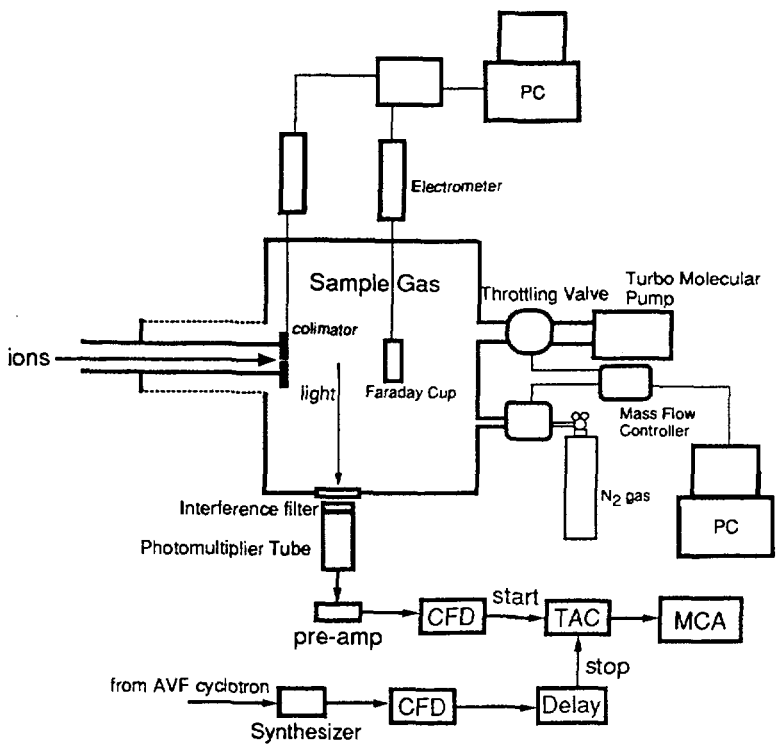

Fig. 1 Schematic presentation of the experimental apparatus for the irradiation with Ar ions and the detection of the fluorescence from gaseous nitrogen.

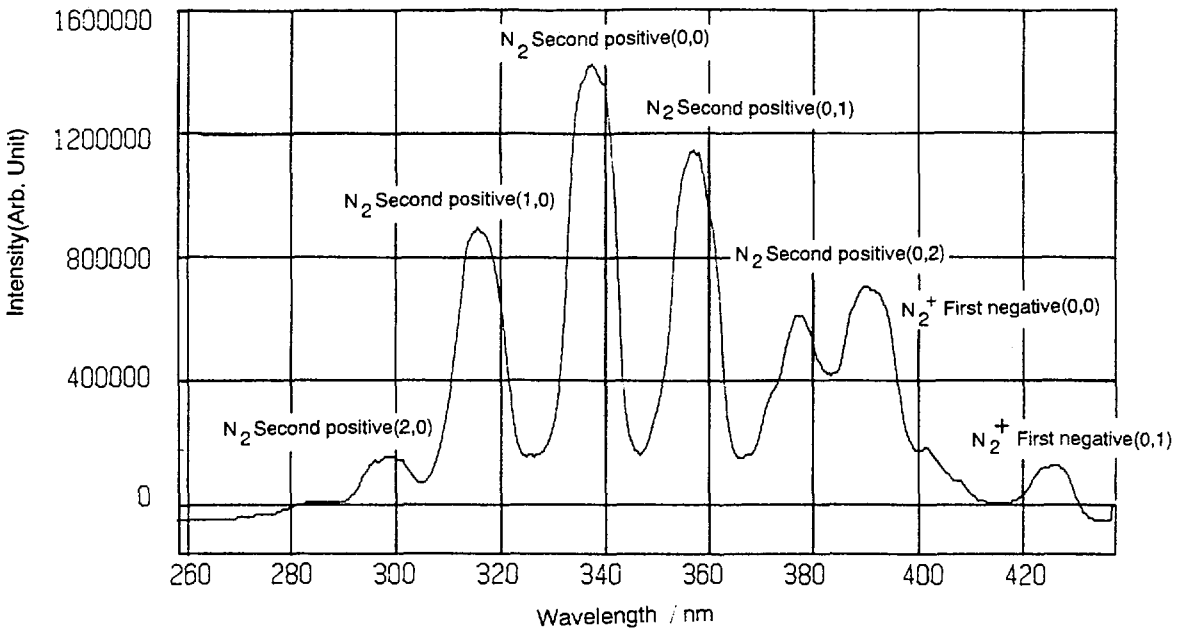

Fig. 2 Fluorescence spectrum of gaseous nitrogen irradiated with 330 MeV Ar^{11+} ions.

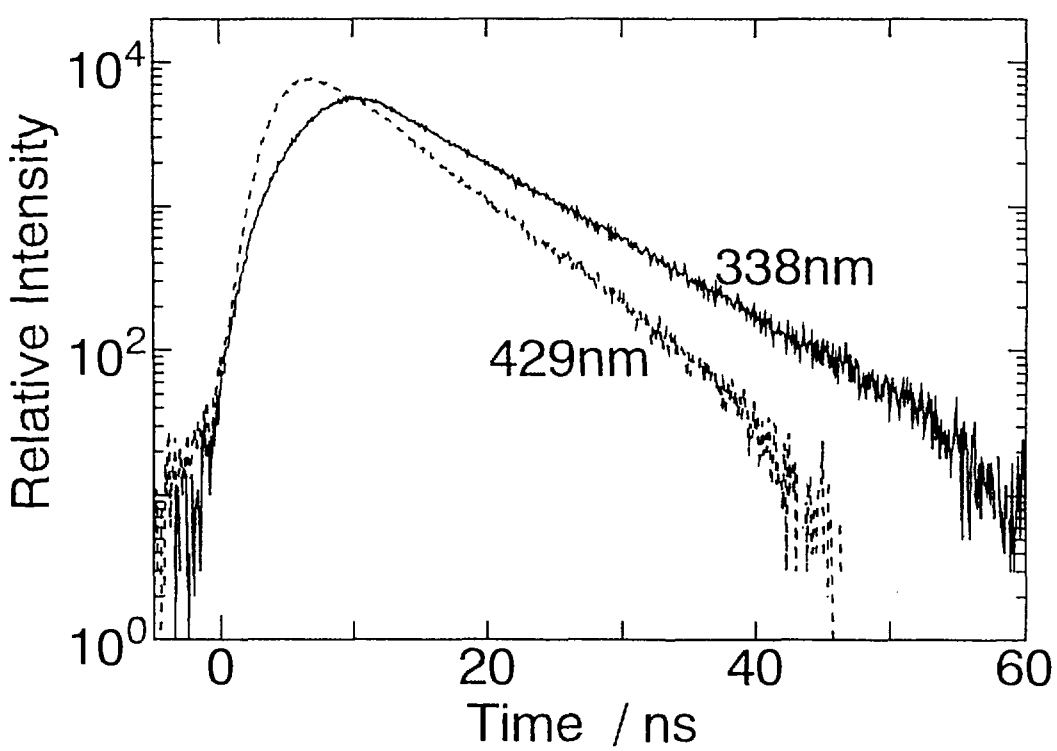

Fig. 3 Time profiles of 338 and 429 nm fluorescence of gaseous nitrogen irradiated with Ar

3．7 Dosimetry Systems For Characteristics Study of Thin Film Dosimeters (II)

T. KOJIMA, *H.SUNAGA, H.TAKIZAWA, H.TACHIBANA
Advanced Radiation Technology Center, TRCRE, JAERI

1. Introduction

Reliable dosimetry method to estimate absorbed dose and its distribution in interested materials is necessary for interpretation or comparison of radiation effects on polymers, semiconductors, and biological materials.

The thin film dosimeters of about 10 to 200 μm in thickness such as cellulose triacetate(CTA) dosimeter and alanine film dosimeter, have been well-characterized for $^{60}Co\,\gamma$ rays and 0.15-3 MeV electron beams. Their dose response characteristics study is required for application of these dosimeters to ion beam dosimetry. Development of precise beam monitoring technique was also indispensable to control dosimeter irradiation .

2.Experimental

The simultaneous irradiation technique of a Faraday cup, a calorimeter and film dosimeters was developed using the wide-uniform fluence irradiation field of 100x100 mm^2 with scanning ion beams of 5-20 MeV/amu provided from the TIARA AVF cyclotron. The Faraday cup (suppression voltage:−100V) and the total absorption calorimeter[(the specific heat capacity of aluminum(Al) as an absorber: Ca(t)=0.8612+0.00126t (t= 10-40 ℃)] are exposed to ion beams passing through 3-mm thick Al slit plate with the aperture of ϕ30 mm^2(7.07 mm^2), as shown in Fig.1. The thin film dosimeters mounted on the slit plate are irradiated in vacuum of 10^{-5}Pa with current/ charge measurement using the Faraday cup. This method allows us to minimize uncertainty due to instability of beam current.

Irradiation using 50 MeV $^4He^{2+}$, 330 MeV $^{40}Ar^{11+}$ and 520 MeV $^{84}Kr^{20+}$ with the current of 0.20 nA/cm^2 for each ions was performed additionally to the previous experiments[1].

Fluence values in terms of measured integrated charge were about 40-550 nC/ϕ30 mm^2, which resulted into temperature rise of about 4 Celsius in calorimeter absorber within 30-200 sec. These fluence values were compared with calculated values Φ using the following formula: $\Phi = \Psi / E$, where Ψ is the energy fluence derived from calorimeter measurement and E is the nominal energy given from cyclotron operation parameters.

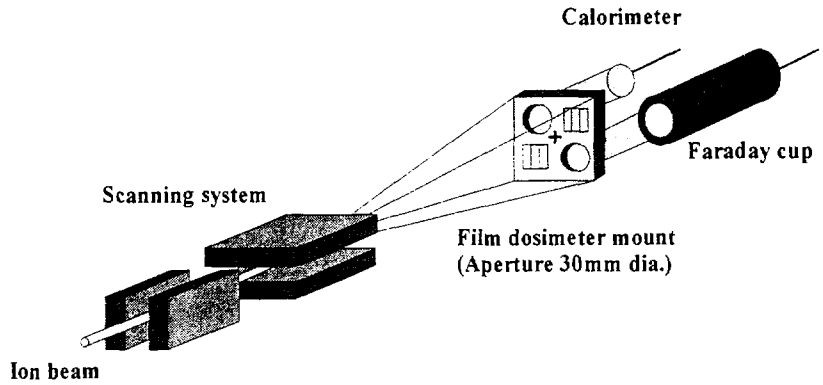

Fig.1 Schematic diagram of the simultaneous irradiation of a Faraday cup, a total absorption calorimeter, and film dosimeters in wide uniform fluence radiation field.

Table 1 Uncertainties in fluence measurement

ion beams	energy*1 (MeV)	measured charge*2 (nC)	fluence ratio*3	v.c.*4 (%)
$^{1}H^{+}$	20(20)	780-1,900	1.056	±0.8
$^{4}He^{2+}$	20(5)	390-540	1.073	±3.0
	50(12.5)	360-550	0.993	±1.3
$^{12}C^{5+}$	220(18.3)	160-300	0.991	±1.4
$^{16}O^{6+}$	160(10)	150-200	1.040	±1.3
$^{20}Ne^{8+}$	350(17.5)	110-140	0.997	±4.7
$^{40}Ar^{11+}$	330(8.3)	200	1.043	±0.3
$^{84}Kr^{20+}$	520(6.2)	40	1.001	±1.8

*1 nominal energy of incident ions(MeV/amu).
*2 integrated charge measured in the area of ϕ 30mm^2(7.07mm^2).
*3 the fluence ratio of the measured ones to those estimated based on the nominal energy.
*4 variation coefficients at a 68% confidence level which were estimated from at least three repeating measurements.

3.Results and discussion

Table 1 tabulates the ratio of measured fluence and estimated value based on the nominal energy, and the variation coefficients among at least three repeating fluence measurements. The ratios are in the range 0.991-1.073(average:1.024) and variation coefficients are within ±2%(1σ) for studied ion beams. The uncertainty in fluence measurement mostly meets ± 5% precision required in dosimetry for radiation effect studies on polymers under consideration of original uncertainty in film dosimeter systems. The overestimation of about 2% in fluence suggests the need of accurate measurement of current/charge lower than 0.1 nA/cm^2 or 5 nC/cm^2, and checking of uncertainty in nominal energy values of the cyclotron[2].

On the basis of this real-time current/charge monitoring, dose response characteristics of several film dosimeters were studied preliminarily for ion beams of 5-20 MeV/amu with mass collision stopping power for film dosimeters ranging about 20-30,000 MeV/g/cm^2 in linear dose range of 10- 200 kGy for CTA and 2-10 kGy for other films.

Dose responses in terms of dosimeter response(e.g. optical density change) per unit dose were plotted against mass collision stopping power values of incident ion beams. Absorbed dose in dosimeter materials was calculated as the product of fluence measured by the Faraday cup and mass stopping power derived by OSCAR code[3] based on Ziegler's tables[4]. Dose responses were normalized to those for 20 MeV $^{4}He^{2+}$.

Relative dose response for all the dosimeters decreases with increase of mass stopping power at above 100 MeV/g/cm^2, for instance, about 0.6 at about 1,000 MeV/g/cm^2. For higher LET radiation with shorter penetration such as $^{40}Ar^{11+}$ and $^{84}Kr^{20+}$, evaluation of LET dependence may have much uncertainties because of dose saturation characteristics in high energy deposition localized along the ion pass. Development of accurate dose profile estimation, experimentally and theoretically, and dose response characteristics in detail are necessary for reliable discussion on the LET dependence of dose responses.

4.References

1)T.Kojima et al.: JAERI TIARA Annual Report 1995, No.5, JAERI-Review 96-017, p.79-80(1996)
2)T.Kojima et al.: received by *Radiat.Phys. Chem.*(1997)
3)K.Hata and H.Baba: JAERI-M 88-184(1988)
4)J.F.Ziegler, J.P.Biersack and U. Littmark : "The stopping power and range of ions in solids",Vol.1(Permagon Press, Oxford, 1985).

3.8 Changes of Mechanical Properties of Polymer Materials by High Energy Ion Irradiation.

Hisaaki Kudoh, Masaki Sugimoto and Tadao Seguchi
Department of Materials Development, JAERI

1. Introduction

Polymer materials applied for space or fusion reactors are subjected to high energy ions and neutrons. The changes in mechanical properties of polymers upon the radiation are essential to evaluate and select the materials. It has been found that proton irradiation effects on mechanical properties of polymers differ little from gamma rays or electron beam irradiation effects as a function of dose[1]. For better understanding, it is necessary to examine whether the LET (linear energy transfer) effects on mechanical properties appear or not for high LET radiation. In this work, changes in mechanical properties of polymers are studied by He, Ne, and Xe ion irradiations.

2. Experimental

Polymer materials used are medium density polyethylene (MDPE, 150 μm thick) and polymethylmethacrylate (PMMA, 3 or 2 mm thick). Ion irradiation was carried out by an AVF cyclotron accelerator in TIARA under vacuum. Ions were He^{2+} (50 MeV), Ne^{8+} (350 MeV) and Xe^{23+} (450 MeV). The stopping powers and penetration ranges based on TRIM 95 code[2] are shown in Table 1. For MDPE, stopping powers of Ne^{8+} and Xe^{23+} are larger by $1.6x10^3$ and $4.4x10^4$ times than that of 2 MeV electron (ICRU 37[3]). For PMMA, these ions stop at the inside of specimen. The spot beam of about 10 mm diameter was scanned at 50 Hz in horizontal direction and 0.5 Hz in vertical direction on 80-100 cm^2 area of specimen at the currents of 100 nA for He and Ne, and 20 nA for Xe ions. Tensile tests were carried out at room temperature for MDPE (dummbell) at a crosshead speed of 200 mm/min, and three-point bending tests were carried out for PMMA at a crosshead speed of 2 mm/min with a span/thickness ratio of 16.7.

Table 1 Stopping power (S: keV/μm, at surface) and range (R: μm) of ions (TRIM 95 code).

Ion	PE		PMMA	
(MeV)	S	R	S	R
He (50)	$1.5x10^1$	$1.8x10^3$	$1.8x10^1$	$1.5x10^3$
Ne(350)	$2.9x10^2$	$7.2x10^2$	$3.4x10^2$	$6.1x10^2$
Xe(450)	$9.1x10^3$	$5.9x10^1$	$1.1x10^4$	$5.2x10^1$

3. Results and Discussion

Figure 1 shows the changes in elongation at break in tensile tests for MDPE as a function of dose, together with the previous result[1] for H^+ (10 MeV). The dose was the product of fluence and average stopping power in MDPE for each ion. Elongation at break decreases with dose in all the cases, and the decay curves are almost the same when compared with dose. It means less LET dependence on the change of elongation despite of a large difference in the stopping power. In a case of Xe^{23+} (450MeV) irradiation, the specimen is thicker than the penetration range, in other words, the ion doesn't penetrate the 150 μm thick specimen. Therefore, the change in elongation is plotted as a function of fluence. The elongation halved at a fluence of around 4 x 10^{10} ions/cm^2, which equals to about 520 kGy, if dose is averaged in the penetration range. The change of elongation could not be compared directly with the cases of other ions because of a large difference in depth dose profile. When thinner specimens are used and the dose distribution is small throughout the specimen, the decay behavior in Xe ion would become the same with other ions.

Figure 2 shows the changes in flexural strength of PMMA as a function of the dose averaged from the surface to the end of penetration range. Flexural strength decreases with dose for all the ions. PMMA specimen is also thicker than the range and dose distribution in the polymer is not homogeneous, then the dose is averaged in the range by the calculation with TRIM code. The flexural strength depends on the direction of stress to specimens. When the flexural stress is added to the irradiated side where the compresive stress is induced, the flexural strength decreased slightly. However, the strength decreased much, when the flexural stress is added to the opposite side of specimen where the tensile stress is induced. The data in Fig. 2 are for the test that the stress is added to the opposite side of ion irradiation. Though decrease in strength is not sufficient, the irradiations of Ne and Xe give a similar deterioration as a function of the dose. On the other hand, the irradiation of He gives a less deterioration. However, it is not likely plausible at present to discuss LET effects because the distribution of dose in depth direction is different among the ions (LET).

The decrease of elongation for PE is caused by radiation induced crosslinking, and the decrease of flexural strength for PMMA by chain scission[4]. The change of mechanical peroperties would be closely related to the probability of crosslinking or chain

scission of polymers. Our results indicate that these probabilities don't depend clearly on LET of radiation. LET is defined as the energy deposition per penetration length along the path of ion in material. For polymer materials, the chemical reactions as crosslinking or chain scission would be induced even in the rather long distance from the ion path by the energy transfer. Then, the density of these chemical reaction sites would be low, compared with the initial energy deposition of ion with high LET.

4. Conclusion

Tensile test on MDPE shows little LET dependence up to high LET of Ne^{8+} 350 MeV (in average, 303 keV/μm for 150 μm thick specimen). For PMMA, it is necessary to establish a correlation between inhomogeneous degradation and mechanical properties to discuss the LET dependence. If degradation behavior is analyzed with considering depth dose profile, the irradiations of Ne and Xe might give a similar behavior with γ rays.

References

1) H. Kudoh *et al.*, TIARA Annual Report, vol. 3, page 79 (1994)

2) J. F. Ziegler *et al.*, "The stopping power and ranges of ions in matter", vol. 1 (Pergamon press, Oxford, 1985)

3) ICRU report 37, Bethesda, Mary Land, USA (1984)

4) A. Chapiro, "Radiation Chemistry of Polymeric Systems", (Interscience Publishers, New York, 1962).

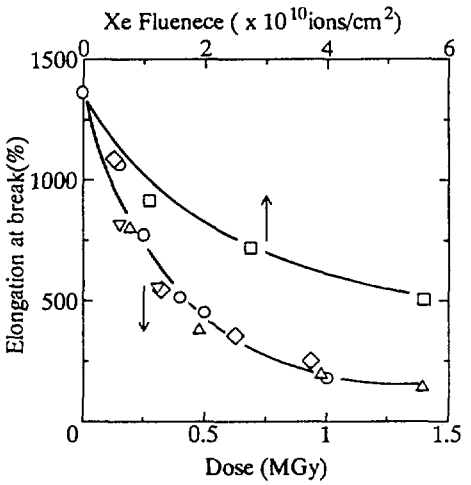

Fig. 1 Change in elongation at break in tensile test of MDPE by ion irradiations. [○ :e^- (2MeV), △ :H^+ (10MeV), ◇ :He^{2+} (50MeV), ▽ :Ne^{8+} (350MeV), □:Xe^{23+} (450MeV).]

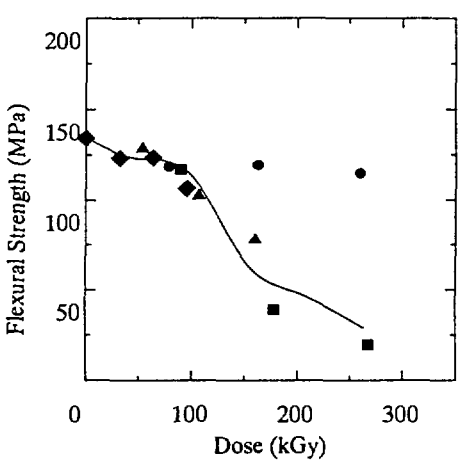

Fig. 2 Change in flexural strength of PMMA measured with irradiated side under tensile stress. Dose is averaged in the range. [●:He^{2+} (50MeV), ▲:Ne^{8+} (350MeV), ◆ :Xe^{23+} (450MeV), Solid line : γ rays.]

3．9 Heavy Ion Irradiation Effects on Optical Properties of Polymer Materials.

Noboru KASAI, Hisaaki KUDOH, and Tadao SEGUCHI
Department of Materials Development, JAERI

1. Introduction.

Polymer materials called engineering plastics have excellent thermal, optical, and mechanical properties, and are expected for use as temperature controlling material or optical reflector in a space satellite. There, the materials are exposed to high energy radiation such as electrons, protons and heavy ions under high vacuum, and the characteristics of the materials would degrade. Radiation resistance of the polymers, especially against ion irradiation, is of critical importance in the environment. Poly-ether-ether-ketone (PEEK) and poly-ethylene-naphthalete (PEN) films containing aromatics were irradiated by heavy ions, and the changes in optical properties such as light transmittance at a certain wavelength were investigated. In our previous report[1], decrease in transparency was appreciably larger by Ni^{4+} (15 MeV) irradiation at Tandem accelerator, in comparison with that by electron beam. In this report, effects of various ion species and influence of dose rate (ion beam current) were studied.

2. Experimental.

Materials are poly-ether-ether-ketone (PEEK, 6 μm thick), and poly-ethylene-naphthalete (PEN, 1 μm thick). Electron beam (EB, 2 MV) irradiation was carried out under vacuum. The ion energy, the stopping power and the penetration range are shown in Table 1. Irradiations of Ni^{4+}, Fe^{4+}, and Si^{4+} were carried out with Tandem accelerator under vacuum, where polymer film was put on a cylindrical holder made of Al, rotated at 120 rpm, and moved repeatedly along the rotational axis at a speed of 120 cm/min. Irradiations of Ar^{8+} and Xe^{23+} were carried out with Cyclotron accelerator by beam scanning. The dose of ion irradiation was evaluated as a product of fluence and stopping power from TRIM code. The dose of electron beams was evaluated by CTA film dosimeter. Light transmittance (absorption) spectra were obtained by an UV spectrometer at room temperature in the wavelength range of 200-900 cm^{-1}.

Table 1. Ion Energy (E), Stopping power (S, averaged in 6 μm thickness) and range (R) for PEEK.

Ion	E(MeV)	R(μm)	S(keV/μm)
Ni^{4+}	15	6.4	$2.31x10^3$
Fe^{4+}	15	6.6	$2.31x10^3$
Si^{4+}	15	8.0	$2.28x10^3$
Ar^{8+}	175	58.6	$2.59x10^3$
Xe^{23+}	450	51.0	$1.14x10^4$
e^-	2	8 mm	0.234

3. Results and Discussion.

(1) Depth profiles and LET effects.

Figure 1 shows depth profiles of absorbance (optical density, OD) and stopping power by TRIM code for PEN film, where Ni^{4+} (15 MeV) was exposed to a stack of 1 μm thick films, and the OD was measured at 400 nm. Stopping power by TRIM code changes with depth, and gives the same depth profile as dose. The two profiles are identical, indicating that the OD change per dose is independent of stopping power in the range from the first layer to the sixth layer, approximate 40-400 eV/A (400-4000 keV/μm).

(2) Dependence of OD change on dose rate and ion species.

Figure 2 shows the OD change of PEEK film at 400 nm as a function of dose for various ions.

(a) Effect of dose rate.

The effect of dose rate was investigated by changing rotor diameter and rotor speed for Ni^{4+} ion irradiation. By increasing the scanned area and scanning rate, the average dose rate could be decreased to one twentieth. As shown in the figure, the low dose rate irradiation gave a less OD change. Since irradiation was carried out in the absence of oxygen, this dose-rate dependent coloration would be due to beam heating, as seen in the case of EB irradiation[2]. For better understanding, however, characteristics of the new irradiation apparatus should be clarified and taken into account.

(b) Effect of ion species.

Figure 2 also shows that, even in the lower dose rate cases, the coloration is enhanced upon Ni^{4+} (15 MeV) ion irradiation, compared to EB. To investigate the effect of accelerated ion species, Ni^{4+} (15 MeV), Fe^{4+} (15 MeV), and Si^{4+} (15 MeV) ions from Tandem, and Ar^{8+} (175 MeV) and Xe^{23+} (450 MeV) ions from Cyclotron were irradiated on PEEK. They (except for Xe) give almost an equal stopping power in 6 μm thick PEEK film, and Xe gives a higher stopping power more than four times, as shown in Table 1. The OD changes in Figure 2 resulted in two groups; one is for three ions from Tandem, and the other for two ions from Cyclotron, respectively. Since three ions from Tandem give an equal stopping power and the same coloration

sensitivity, the irradiation effects per dose would depend on mainly stopping power. However, Ar caused a less coloration than the three ions, though Ar gives a similar stopping power as them. We are currently considering that this observation reflects difference in irradiation and cooling procedures (temperature controlling procedure during irradiation to avoid heating).

References

1) N. Kasai, T. Arakawa, and T. Seguchi, TIARA Annual Report, vol. 5, 82 (1996)

2) N. Kasai, T. Arakawa, and T. Seguchi, JAERI-conf 97-003, 277 (1997).

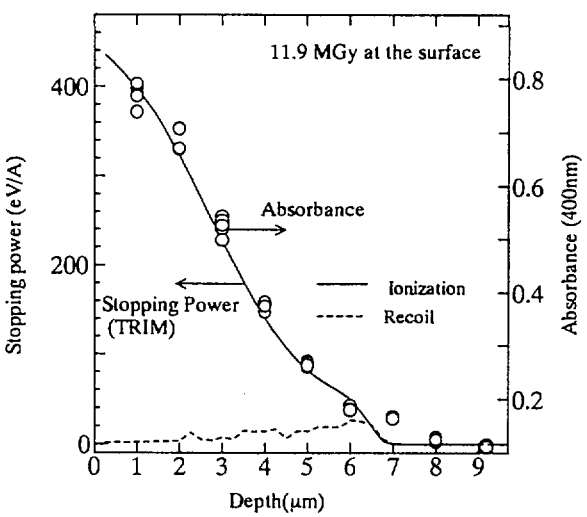

Figure 1. Depth profiles of absorbance at 400 nm and stopping power of PEN (a stack of 1 μm thick films) by Ni^{4+} (15 MeV) irradiation.
(○:Absorbance of PEN at 400nm, solid line : stopping power by ionization, broken line : stopping power by recoil.)

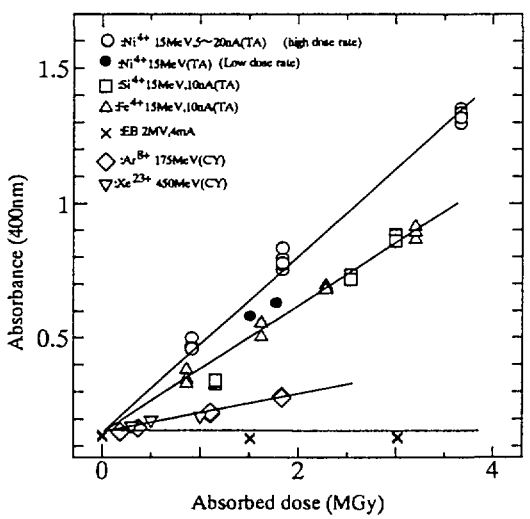

Figure 2. Change in absorbance at 400 nm of PEEK (6 μm thick) film for various ions and dose rates.
(○ :Ni^{4+} 15MeV at high dose rate, ●:Ni^{4+} 15MeV at low dose rate, □:Si^{4+} 15MeV, △:Fe^{4+} 15MeV, ×:EB 2MV, ◇:Ar^{8+} 175MeV, ▽:Xe^{23+} 450MeV)

3.10 Closure Characteristics of Ion-track Pores with a thermo-responsive Function by Size Exclusion Method

Masaru Yoshida, Masaharu Asano, Takeshi Suwa, Ryoichi Katakai*,
Nicole Reber**, Johann Vetter**, and Reimar Spohr**
Department of Material Development, JAERI, 1233 Watanuki-Machi,
Takasaki, Gunma 370-12,Japan, *Department of Chemistry,
Faculty of Engineering, Gunma University, Kiryu,Gunma 376,
Japan, and **Gesellschaft für Schwerionenforschung mbH,
Planckstrasse 1, D-64291 Darmstadt, Germnany

I. Introduction

In recent years, much atention has been directed towoards the development of polymer hydrogels capable of undergoing large volume changes due to such an external stimulus as temperature[1-4]. It enables the transformation of chemical into mechanical energy, leading to responsive systems. Hydrogels consist of a three dimensional network of long polymer chains immersed in an aqueous solution. The characteristics of the hydrogel are defined by the interaction between the solution and the polymer chains. Their properties can be tailored according to the specific needs by balancing the hydrophilic and hydrophobic side chains of the polymer network. Multi-responsive hydrogels belong to the calss of intelligent materials, which are able to respond to external conditions, similar to biological membranes or technological ecosystems. Hydrogels are used for chromatography, electrophoresis, and controlled release of drugs. The surface grafting onto the wall of etched single pore enables the realisation of mechanically stable, responsive ion track pores with well defined switching temperature at which a drastic change of the membrane permeability occurs.

II. Experimantal

The preparation of ion track membranes with a thermo-responsive function is as follows. The poly(ethylene terephthalate) (PET) with a thickness of 19 μm was irradiated with exactly one ^{197}Au ion with a specific energy of 11.6 MeV/u, then ethced in 5M aqueous solution of sodium hydroxide leading to a cylindrical pore of 2.9 μm diameter and 17.8 μm thickness, and grafted at 25°C with a dose of 10 kGy by γ-rays from a ^{60}Co source, in 10% aqueous solution of N-isopropyl acrylamide (NIPAAm), giving 8% grafting.

For conductivity measuements[5], the membrane is placed between two chambers filled with electrolytes of known specific conductivity. After applying a voltage the current is measured as a function of temperature. To take into account the changes of the specific conductivity due to temperature changes and to be able to compare the different solutions the current is normalized to the specific conductivity of 0.1M potassium chloride (KCl) at a temperature of 20°C.

$$I_{norm} = \frac{I}{\kappa(T)} \kappa_0$$

where I_{norm} is the normalized current, I is the measured current, $\kappa(T)$ is the specific conductivity of the solution at temperature T, and κ_0 is the specific conductivity of 0.1M KCl at 20°C (κ_0 = 11.5 mS/cm).

In the swollen state, gels grafted onto the

pore wall have a dispsed reticular structure and are therefore permeable, though reduced for the small electrolyte ions or small molecules. Organic molecules will be excluded from the pore it they are larger than the mean mesh size. In this case, the specific conductivity inside the pore is increased comapred to the outside, because of the increased electorolyte concentration inside the pore. On the other hnad, in the shrunken state of the gel the transport of ions and molecules is carried out through the free volume indpendent of their molecular weight, as the specific conductivity is the same inside and outside the pore.

The systematic study of the closure characteristics was carried out with a mixture of 90% 0.1M potassium chloride and 10% polyethyleneglycol (PEG) with molecular weights of 60-35,000. The permeation of organic molecules through the thermo-responsive pore and the efficiency of the pore as chemical valve was determined. The PEG chains are entangled spheres, with a diameter corresponding to the molecular weight of the respective PEG[6]. A crucial question for this thermally controllable valve is, if in the closed state organic molecules can be hindered to penetrate through the membrane, e.g. the degree of closure.

III. Results

Figure 1 shows current versus temperature for a mixture of PEG and 0.1M potassium chloride. The normalized current in the open ed state is practically identical, namely about 8 nA, as in the measurement with pure potassium chloride because the transport of ions and molecules is carried out through the free volume of the pore. In the closed state the normalized current depends on the effective diameter (molecular weight) of the PEG molecules reflecting their size exclusion from the polymer network. In this case, the electrolyte concentration inside the pore is increased in comparison on the bulk liquid outside. This result in an increased specific conductivity and, consequently in an increased current. The shift of the phase transition temperature is attributed to such interactions as van der Waals and hydrogen bond b etween the PEG molecules and the polymer network. It is known that polar molecules like PEG alter the hydration structure, e.g. by breaking some of the hydrogen bonds.

Figure 2 shows the mean normalized current as a function of the size of the PEG molecules in the closed state at a temperature of 21.5°C. The mean value of the mesh size can be determined from the inflection point of the fit. It is 1.17 ± 0.035 nm. PEG molecules larger than 2 nm are completely blocked from entering and passing through the membrane in the closed state, in contrast to observations with a multi-porous responsive membrane. The bottom line shift is attributed to the interaction of the smaller and therefore penetrating PEG molecules with the polymer network as stated above.

IV. Conclusion

The experiments with a mixture of PEG and electrolyte prove that the responsive pore represents a thermally controllable vale, hermetically closing for organic molecules larger than 2 nm. In the closed state, the gel blocks the pore and a complete exclusion of PEG with molecular weights above 2000 is achieved.

V. References

1. M. Yoshida, H. Omichi, H. Kubota, R. Katakai, *J. Intelligent Mater. Sys. Struc.* **4**, 223 (1993)
2. C. Li, Z. Hu, and Y. Li, *J. Chem. Phys.*, **100**, 4645 (1994)
3. K. Kubota, S. Fujishige, and I. Ando, *J. Phys. Chem.*, **94**, 5154 (1990)
4. N. Nagaoka, M. Yoshida, M. Asano, P. Apel, H. Kubota, and R. Katakai, *Pharm. Sci.*, **2**, 265 (1996)
5. N. Reber, H. Omichi, R. Spohr, M. Tamada, A. Wolf, and M. Yoshida, *NIM B*, **105**, 275 (1995)
6. S. Kuga, *J. Chromat.*, **206**, 449 (1981)

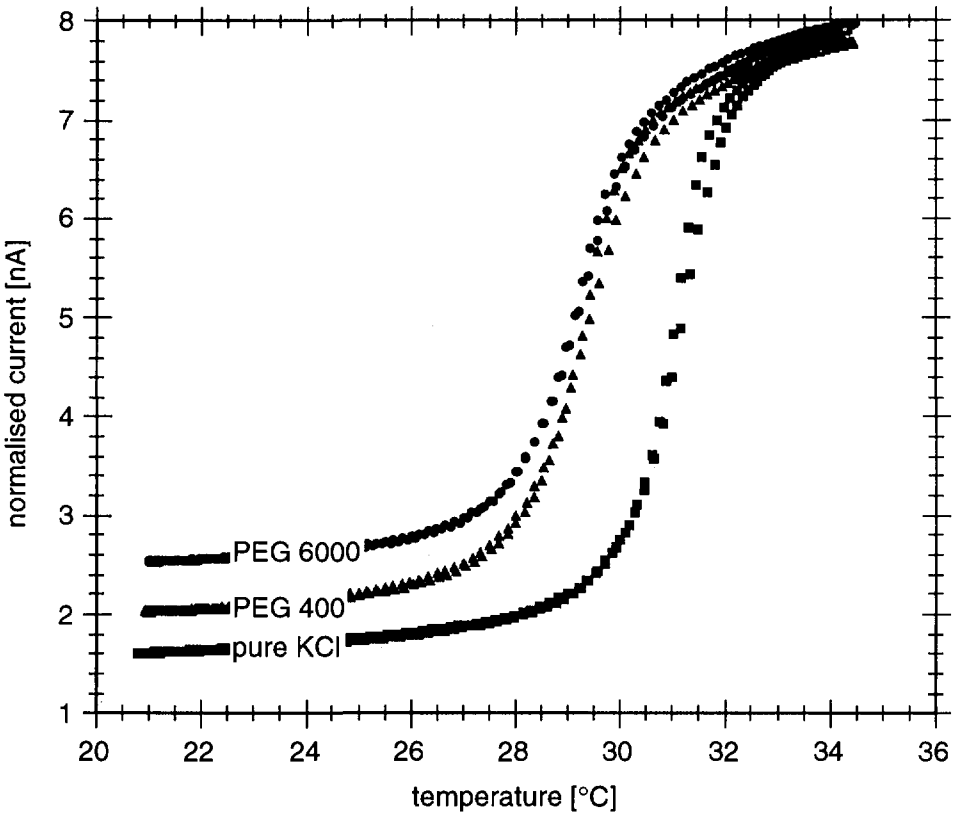

Figure 1 Current characteristics of a grafted single ion track in various solutions normalized to the same bulk conductivity

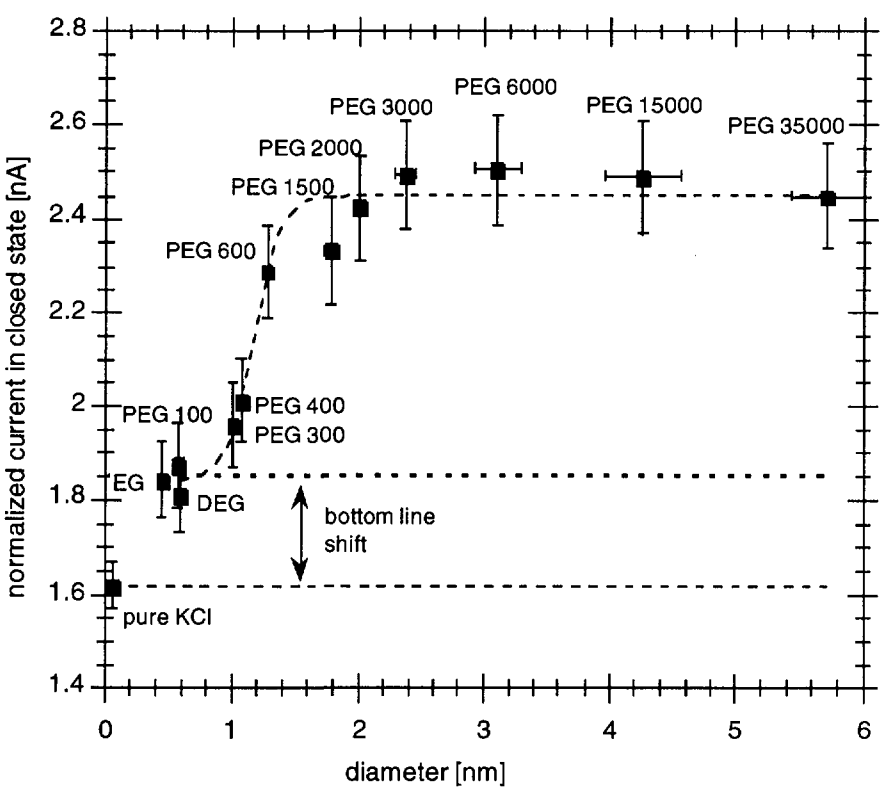

Figure 2 Size exclusion of PEG molecules.

3．11 LET effect of ion irradiation on photo stimulated luminescence

M. TAKEBE, K. ABE, T. HAMANO, Y. MURAKAMI, T. SUZUYA,
*T. KOJIMA, *T. SAKAI

Graduate School of Engineering, Tohoku University
* Advanced Radiation Technology Center, TRCRE, JAERI

1. Introduction

We have investigated excitation spectra of the imaging plate (Fuji Photo Film Co. Ltd., type BAS 3000UR, hereafter IP) for various ion beams and found the change in the spectra according to the range of radiations. Further analysis revealed that the differences of the spectra are attributed to the blue dye containing phosphor which is added in the IP for improvement of spatial resolution of photo stimulated luminescence(PSL). The blue dye prevents red light from penetrating the IP and attenuates the intensity of the PSL stimulated with red light. That is, the PSL intensity induced with red light decreases, when the IP is irradiated with longer range ion beams. On the other hand, the PSL intensity induced with blue light is less influenced by ion beam ranges. The difference in the PSL intensities stimulated with red and blue light, dye effect in other expression, leads us to distinguish the ranges of ion beams[1-3]. Our preliminary experimental results, however, suggest that the dye effect did not enable us to interpret fully the difference of excitation spectra of the IP for very high LET ion beams. Then, we started to study the LET effect on the IP using high LET ion beams such as Ne, Ar and Kr.

2. Experimental

An original imaging plate is of 5"x5" in area size and cut into 2x5cm^2 pieces as the IP samples. The IP samples were irradiated up to a few μ C/cm^2 at room temperature in vacuum with ion beams of 350 MeV $^{20}Ne^{8+}$, 330 MeV $^{40}Ar^{11+}$ and 520 MeV $^{84}Kr^{20+}$ which were provided from the TIARA AVF cyclotron. The ion beams were scanned homogeneously in the 10x10 cm^2 area at the current density of 20 nA/cm^2 covering whole area of the IP samples. The IP samples were kept in dark during irradiation and covered with aluminum foil after the irradiation to avoid exposure of unintended light. The PSL intensity decreases after irradiation and then seems to be settled down. Excitation spectra of the IP samples were measured 24hrs after irradiation to minimize the fading effect.

We constructed a simple apparatus for excitation spectra measurement which consists of a 40W tungsten lamp, a monochromater, a photomultiplier tube(PMT) and a personal computer(PC). The tungsten lamp light is guided to a monochromater changing its wavelength with a PC. The IP samples are exposed to the monochromated light through a low pass filter. The PSL light emitted from the IP samples is focused on the PMT surface through a 390 nm band pass filter.

The excitation spectra of the irradiated IP samples were measured over the wavelength range of 450 nm to 750 nm in 5 nm steps with accumulation time of 1s at each wavelength.

3. Results and Discussion

The measured excitation spectra are illustrated in Fig. 1 after normalization of the PSL intensity to that at 500 nm, associating with the result of 10 MeV alpha. All the spectra show two peaks at around 500 and 600 nm. The ratios of peak intensity at 600 nm to that at 500 nm

seem to increase with increase of the LET of the ion beams. The PSL ratios, however, vary with the range of ion beams in the IP because of the blue dye additive in the IP, that is dye effect. In order to discriminate the dye effect, we evaluated the PSL ratios on the basis of the TRIM code assuming the dependence of PSL intensities on the deposit energy in the IP and using the absorption coefficients of the light to the IP which were derived from our previous experiment[3]. To the contrary for proton beams and gamma rays, the differences between the experimental PSL ratios and the calculated ones are appreciable for higher LET radiations and seem to increase with the LET.

The LET of the charged particle varies according to the track of the ion beams in the IP. The LET increases generally along the track. For the sake of simplicity, we estimated the average LET value by dividing the integrated LET value along the ion beam track with the range. The differences in the PSL ratio between the experimental and calculated ones are plotted in Fig.2 as a function of the average LET. It is clearly shown that the difference increases with the average LET value of the ion beams. The dye effect is already corrected for the calculated PSL ratios, therefore, the differences can be interpreted only as the LET effect on the PSL intensity. It may be concluded that the intensity of the PSL induced with a longer wavelength light decreases in comparison with that induced with a shorter one when the IP is irradiated with high LET ion beams.

The mechanism of the differences caused with the high LET beams can be preliminarily discussed as following considerations. The electron trap sites may be divided roughly into two parts which belongs to the site excited with a shorter wavelength light or the site excited with a longer wavelength light. There are two possible explanations: (1) the sites excited with the longer wavelength light are assumed to have the shorter life and decrease immediately after

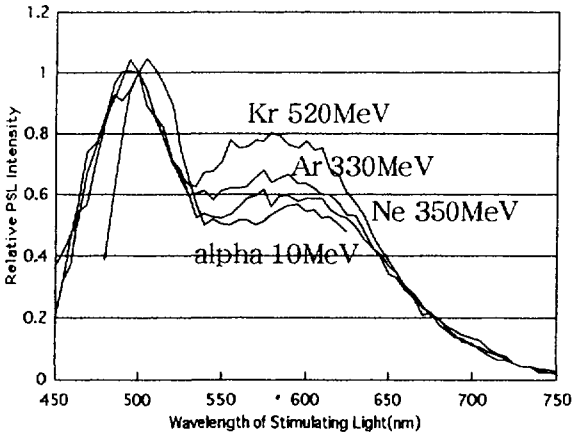

Fig. 1. Excitation Spectra of IP irradiated by vaious ion beams.

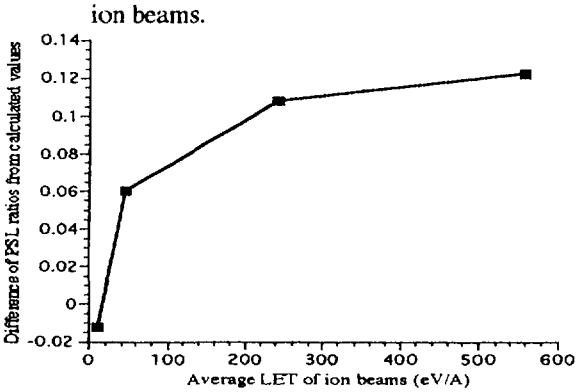

Fig.2 Differences in PSL between experimental and calculated values.

irradiation, (2) the initial distribution of electrons in traps is different with the LET of ion beams. Extensive investigation is still necessary to elucidate the mechanism. New applications of the IP to variety fields can be expected on the basis of further study on the PSL characteristics for high LET radiations .

4. References

1) M. Takebe, K. Abe, *Nucl.Instr. and Meth.*, **A345**, 606(1994).
2) M. Takebe, K. Abe, M. Souda, Y. Satoh, Y. Kondo, *Nucl.Instr. and Meth.*, **A359**, 625 (1995).
3) M. Souda, K. Abe, Y. Kondo, Y. Satoh, and M.Takebe, Extended Abstracts (The 56th Autumn Meeting, 1995), The Japan Society of Applied Physics, No.1, p.35 (in Japanese).

4. Inorganic Materials

(continued to the next page)

4. 1 Transport Properties of Pyrolytic Carbons Irradiated with 2-MeV Electrons

A. Iwase*, N. Ishikawa* Y. Chimi,* T. Iwata* and T. Nihira**

*Advanced Science Research Center, JAERI
** Faculty of Engineering, Ibaraki University

1. Introduction

It is well known that poorly graphitized pyrolytic carbons (referred to P. C. hereafter) show the peculiar galvanomagnetic behaviors; the negative magneto-resistance even at 100K and the Hall coefficient inversely proportional to the magnetic field strength at high field[1,2] These properties have been discussed in terms of lattice defects (disorder) and the two-dimensional character of P. C.[1-3]. Our previous report shows that the negative magneto-resistance of P. C. is enhanced by electron irradiation[4]. This paper reports the effects of electron irradiation on the Hall coefficient and zero field electrical resistivity at 30 K.

2. Experimental Procedure

P. C. specimen with a shape of 10x2x0.28 mm^3 was irradiated with 2-MeV electrons to the fluence of $3.1x10^{17}/cm^2$ at 30 K. The Hall voltage and zero field resistivity were measured as a function of electron fluence.

3. Results and Discussion

Figures 1 and 2 show the zero field electrical resistivity, ρ_0, and the Hall coefficient, R_H, respectively, as a function of electron fluence. The Hall coefficient was obtained from the low field Hall voltage. With increasing the electron fluence, ρ_0 decreases and R_H increases. As the concentration of defects induced by irradiation is only up to ~6 at. ppm, the changes in ρ_0 and R_H are mainly due to the change in the concentration of carriers (electrons and holes). In P. C., It is believed that a shift of the Fermi level can be induced by relatively small amount of defects. This shift may decrease the concentration of electrons and increase that of holes, resulting in the decrease of ρ_0 and increase of R_H. The relationship between the above behaviors of ρ_0 and R_H and the enhancement of negative magneto-resistance by irradiation remains uncertain.

References

[1] K. Yazawa, J. Phys. Soc. Japan, 26(1969) 1407.

[2] K. Yazawa, J. Chim. Phys. 64(1967) 961.

[3] V. Bayot, L. Piraux, J-P. Michenaud and J-p. Issi, Phys. Rev. B40(1989) 3514.

[4] A. Iwase et al. TIARA ANNUAL REPORT 1995 p. 91 (1996).

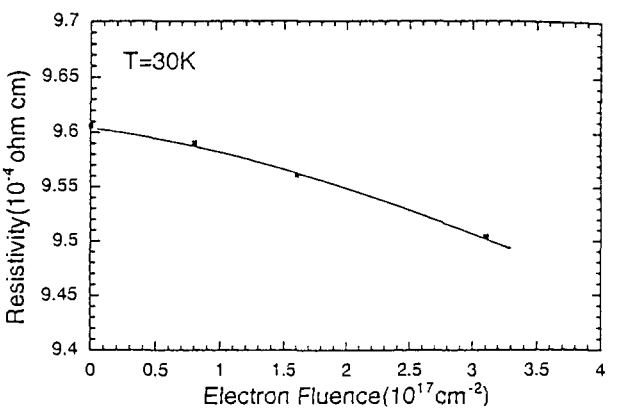

Fig. 1 Zero field electrical resistivity of P.C. as a function of electron fluence

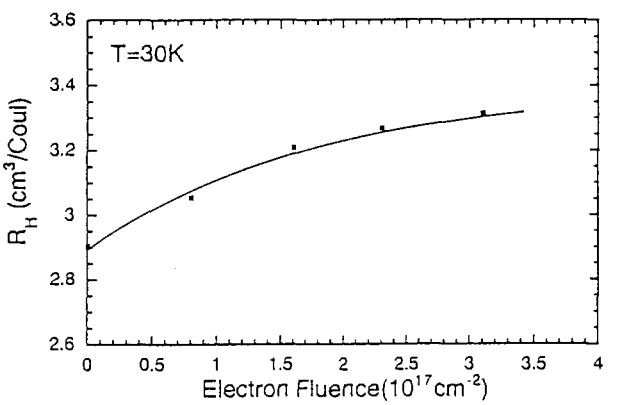

Fig. 2 Hall coefficient of P. C. as a function of electron fluence

4.2 Investigation of the resonant vibration modes of self interstitial atoms in Cu by low temperature specific heat measurement

M.Watanabe, A.Iwase, N.Ishikawa and Y.Chimi
Advanced Science Research Center, JAERI

Introduction

Some theories predict the resonant vibration modes due to self interstitial atoms in metals, which has a large amplitude and a low frequency. To verify the existence of these modes, we measured the specific heat of electron-irradiated Cu at low temperatures.

Experimental

The specimen used in this work was a Cu single crystal with a shape of 12×12×0.5 mm^3. The irradiation with 2-MeV electrons to the dose of 7.7×10^{17}/cm^2 and 1.2×10^{18}/cm^2 at 19K and at 95K, respectively, was performed by using the low temperature irradiation facility interfaced to TIARA 3MV single-ended accelerator. The aperture of 6×6 mm^2 was used to define the electron beam. Before and after irradiation, we measured the specific heat of the specimen under the adiabatic condition between 2K-20K.

Results and discussion

Figures.1 and 2 show the difference in the specific heat between before and after irradiation at 19K and 95K, respectively. The shape of peaks for 95K irradiation is not largely different from that for 19K irradiation. Even after annealing at 100K theses peaks do not disappear completely. If these peaks were caused by the vibration of self interstitial atoms, they would disappear after 100K annealing. Therefore, in order to relate the change in specific heat to the vibration mode of interstitial atoms, more detailed experiments are indispensable.

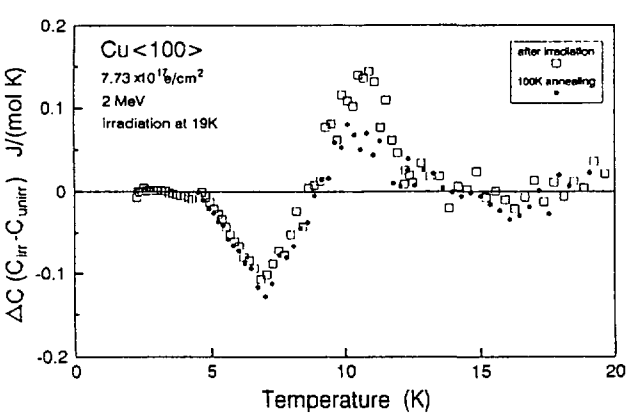

Fig.1. Specific heat after irradiated the dose of 7.7×10^{17}/cm^2 at 19K and 100K annealing.

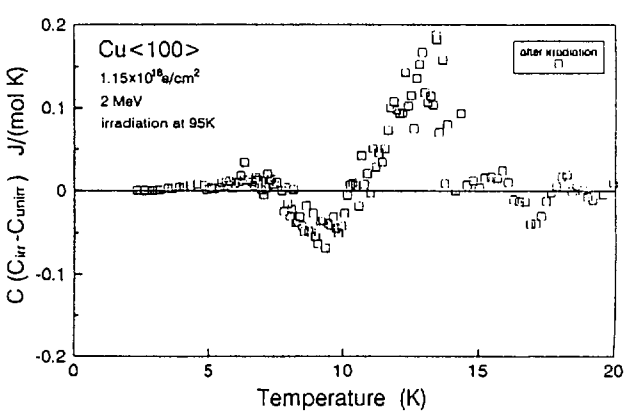

Fig.2. Specific heat after irradiated the dose of 1.2×10^{18}/cm^2 at 95K.

4.3 Low temperature irradiation and in-situ measurement of resistivity in high-Tc superconductors irradiated with energetic ions and electrons

N. Ishikawa, Y. Chimi, A. Iwase, K. Tsuru*, and O. Michikami**
Advanced Science Research Center, JAERI, *NTT Basic Research Laboratories, **Iwate University

1.Introduction

When high-Tc superconductors are irradiated with energetic ions or electrons, incident charged particles deposit energy elastically to a sample, and consequently lattice defects are produced. In order to estimate defect concentration created by irradiation, we have to estimate defect production cross section, σ_d, by which defect density can be estimated from ion-fluence. However, since high-Tc superconductors are composed of several elements, it is not straightforward to estimate σ_d value. One of the available methods for estimating σ_d value may be the TRIM. calculation code programmed be J. F. Ziegler[1]. Since the calculation of defect production cross section using TRIM for high-Tc superconductors is not fully tested, it is necessary to test the validity of σ_d value estimated by TRIM calculation. If TRIM calculation is proven to be applicable to ion-irradiated high-Tc superconductors, the estimation of σ_d value for electron irradiation become possible. In this study, high-Tc superconductor $EuBa_2Cu_3O_y$ (EBCO) was irradiated with ions. Resistivity change which corresponds to defect concentration was measured as a function of fluence, and the validity of σ_d value calculated by TRIM has been verified for ion-irradiation. Irradiation experiment was also performed for EBCO irradiated with electrons. Based on the result for ion-irradiation experiment and the TRIM calculation, σ_d value for electron irradiation was estimated.

2. Experiment

$EuBa_2Cu_3O_y$ thin films were prepared by magnetron sputtering method. The sample thickness was 300nm. Tc was about 84K. For ion irradiation 1MeV He ion, 1MeV C ion, 1MeV Ne ion, 2MeV Ar ion were used. For electron irradiation 2MeV electron was used. The samples were irradiated at 100K along c-axis of the samples, and in-situ measurement of resistivity at 100K as a function of fluence were performed.

3.Results and Discussion

In Fig.1 resistivity change normalized by the resistivity for unirradiated sample, $\Delta\rho/\rho_0$, was plotted as a function of ion-fluence Φ. Different slopes of the curves were observed, reflecting each ion-irradiation having a different σ_d value. By using TRIM σ_d value for each irradiation was estimated, and calculated dpa was estimated by multiplying ion-fluence with the calculated σ_d value. In Fig.2 $\Delta\rho/\rho_0$ was plotted against the calculated dpa. This figure shows that $\Delta\rho/\rho_0$ can be scaled with the calculated dpa within the error of 20%. This result implies TRIM calculation of σ_d value is reliable within the error of 20%. Fig.3 shows the slope of $\Delta\rho/\rho_0$ against Φ at $\Phi=0cm^{-2}$, $(d(\Delta\rho/\rho_0)/d\Phi)_{\Phi=0}$, plotted as a function of

the calculated σ_d. This figure shows $(d(\Delta\rho/\rho_0)/d\Phi)_{\Phi=0}$ varied linearly against the calculated σ_d value within the error of 20%. This result also shows estimation of σ_d value using TRIM is reliable within the error of 20%. From the result for ion-irradiation the relation between $(d(\Delta\rho/\rho_0)/d\Phi)_{\Phi=0}$ and the calculated σ_d value was found to be

$$(d(\Delta\rho/\rho_0)/d\Phi)_{\Phi=0} = k\,\sigma_d, \quad (1)$$

where $k \sim 2.6\times10^{-2}$. Using this relation, the σ_d value for electron irradiation can be estimated. In Fig.4 shows $\Delta\rho/\rho_0$ as a function of fluence for electron irradiation. From this figure, $(d(\Delta\rho/\rho_0)/d\Phi)_{\Phi=0}$ can be estimated to be $1.8\times10^{-20}\mathrm{cm}^{-2}$. Therefore, from the formula (1) σ_d can be estimated to be $7\times10^{-23}\mathrm{cm}^2$. In Fig.5 the process for the estimation of σ_d value for electron irradiation was illustrated.

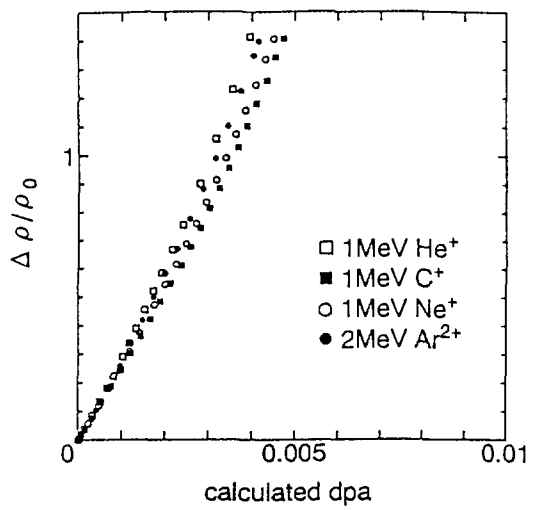

Fig.2
$\Delta\rho/\rho_0$ plotted against the calculated dpa. for ion-irradiation

Reference
1)J. F. Ziegler, Handbook of Stopping Cross-Sections For Energetic Ions in All Elements (Pergamon, New York, 1980).

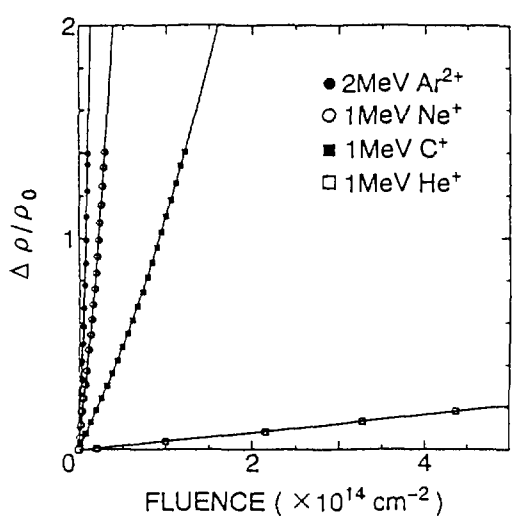

Fig.1
Resistivity change normalized by the resistivity for unirradiated sample, $\Delta\rho/\rho_0$, plotted as a function of ion-fluence Φ.

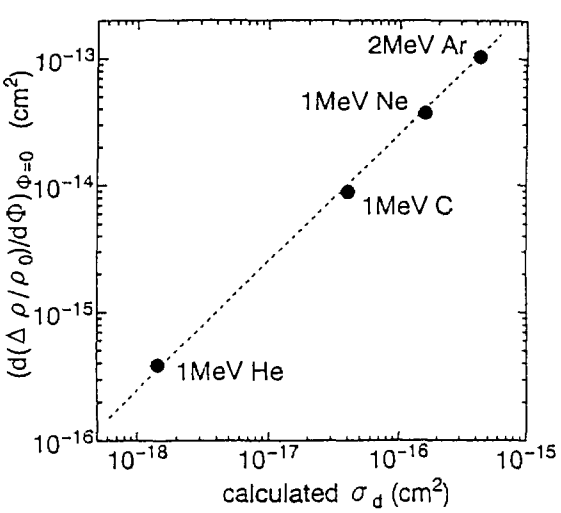

Fig.3
The slope of $\Delta\rho/\rho_0$ against Φ at $\Phi=0\mathrm{cm}^{-2}$, $(d(\Delta\rho/\rho_0)/d\Phi)_{\Phi=0}$, plotted as a function of the calculated σ_d. The relation between $(d(\Delta\rho/\rho_0)/d\Phi)_{\Phi=0}$ and the calculated σ_d value was found to be $(d(\Delta\rho/\rho_0)/d\Phi)_{\Phi=0} = k\,\sigma_d$, where $k \sim 2.6\times10^{-2}$.

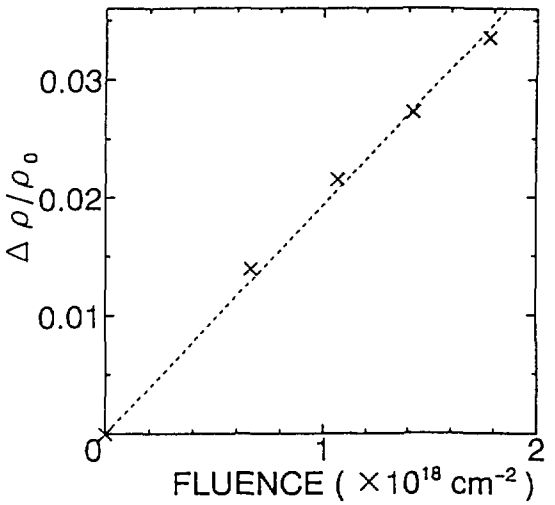

Fig.4
$\Delta\rho/\rho_0$ as a function of fluence for electron irradiation. $(d(\Delta\rho/\rho_0)/d\Phi)_{\Phi=0}$ can be estimated to be $1.8\times10^{-20}cm^{-2}$.

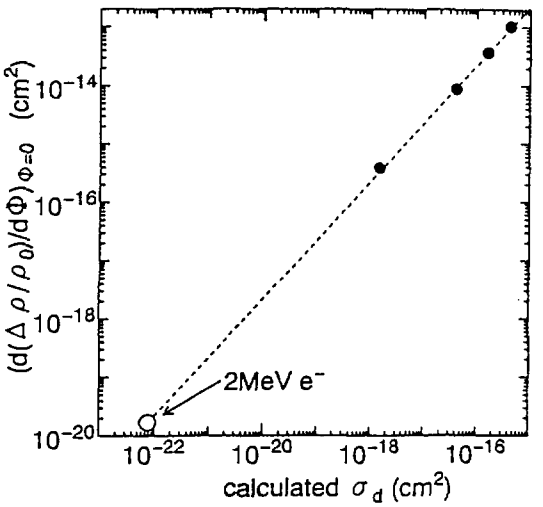

Fig.5
Same plot as Fig.3. From $(d(\Delta\rho/\rho_0)/d\Phi)_{\Phi=0}=1.8\times10^{-20}cm^{-2}$ obtained for electron irradiation, σ_d value for electron irradiation can be estimated to be $7\times10^{-23}cm^2$.

4.4 Effect of Low Temperature Irradiation on Elastic Property of Nanocrystalline Au

H.Tanimoto, H.Fujita, S.Sakai, H.Mizubayashi and A. Iwase*
Institute of Materials Science, University of Tsukuba, *Advanced Science Research Center, JAERI

1. Introduction

The polycrystalline materials with a ultra-fine grain size of about 10 nm (nanocrystalline (*n*-) materials) are expected to exhibit new properties different from those of the polycrystalline materials because of the very small grain size and increased ratio of atoms at the grain boundaries.[1] Most of *n*-materials are prepared by compacting ultra-fine particles formed by an inert gas condensation method. Recently, a gas deposition method has been developed to draw a fine-circuit pattern of ultra-fine particles utilizing the jet flow.[2] We have applied it to prepare *n*-Au[3,4] and investigated their physical properties. One of current topics on *n*-metals is whether as grown dislocations are existing in *n*-metals or not. Our preliminary 20 MeV proton irradiation experiment on *n*-Au[5] showed no dislocation pinning in the low dose range and a strong modulus defect in the high dose range. To pursue the further insight into these items, we carried out the internal friction (Q^{-1}) measurement on both the *n*-Au and polycrystalline (poly-) Au specimens after low temperature irradiation.

2. Experimental

Ultra-fine Au particles formed by the inert gas evaporation method in a evaporation chamber filled with 1000 Torr He gas were transferred to a deposition chamber kept at 0.1 Torr He pressure through a thin stainless steel tube by the pressure difference, and then jetted out from a nozzle toward a glass substrate at room temperature. The *n*-Au ribbons of 20 mm long, 0.8 mm wide and 0.005 mm thick were patterned by moving the substrate. The mean grain size evaluated from the scanning tunneling microscope images is about 20 nm. The *n*-Au ribbons detached from the substrate by using a razor were used for the irradiation experiment. A 5N poly-Au wire (0.8 mm ϕ and 15 mm long) was shaped to a thin reed leaving one end thick by a press machine and then annealed at 873 K for 30 min in 10^{-6} Torr after chemical etching. The grain size of the annealed poly-Au is more than 2 μm.

The 20 MeV proton irradiation at 1.5 K and the 2.5 MeV electron irradiation at 5 K were carried out using the tandem accelerator at University of Tsukuba and the single-ended accelerator at Japan Atomic Energy Research Institute, Takasaki, respectively. During irradiation and warm-up after irradiation, the resonant frequency (f, where $f^2 \sim E$ and E is the dynamic Young's modulus) and Q^{-1} were measured using the flexural vibration of the reed ($f \sim 150$ Hz), where the measurements of f, Q^{-1} and temperature were automatically repeated in every 30 s. The irradiation at low temperatures and the subsequent warm-up run were repeated with increasing C_{FP}. The concentration (C_{FP}) of Frenkel-pairs introduced by irradiation was estimated from the dose (2.8×10^{14} p/cm^2 = 1 ppm C_{FP} for 20 MeV proton and 2.8×10^{16} e/cm^2 = 1 ppm C_{FP} for 2.5 MeV electron[6]).

3. Results and Discussion

Figure 1 shows an example of the f and Q^{-1} spectra observed on the poly-Au specimen after low temperature 20 MeV proton irradiations. In the poly-Au specimen before irradiation, the well-defined internal friction peaks are observed at around 60 and 100 K which are called as the Niblett-Wilks and Bordoni peaks, respectively, and attributed to dislocation motions.[7] During the irradiation at 1.5 K in the low dose range, f at 1.5 K increases and Q^{-1} at 1.5 K decreases. Since the self interstitial atom (SIA) in Au is believed to be mobile at 0.3 K,[8] the observed changes in f and Q^{-1} is surmised to be due to dislocation pinning by SIAs. During warm up

after irradiation, the further increase in f and the further decrease in Q^{-1} are observed at around 15 K, suggesting dislocation pinning due to SIAs released from traps. Both the Niblett-Wilks and Bordoni peaks become to be suppressed with increasing irradiation dose. The results observed at the low dose range clearly demonstrate that dislocations in Au can be pinned down by SIAs. In the high dose range (the third irradiation with C_{FP} of 11 ppm) after the completion of dislocation pinning, a small decrease in f with increasing C_{FP} was observed. This decreased in f is surmised to reflect the so-called bulk effect which is the decrease in the elastic modulus ($\Delta E/E$) due to accumulation of SIAs. In the present measurements, $(\Delta E/E)/C_{FP}$ was observed to be about -14, which is comparable with the values reported in bulk pure metals after irradiation.

Figure 2 shows an example of the f and Q^{-1} spectra in the n-Au specimen observed after 2.5 MeV electron irradiation with C_{FP} of 2.9 ppm at 5 K. In contrast to the f and Q^{-1} spectra in the poly-Au specimen after irradiation, both the f and Q^{-1} in the n-Au specimen are hardly modified in the low dose range, suggesting that the dislocation density in the n-Au specimen is negligibly low and the internal friction peaks observed at around 50 K and 95 K are not of dislocation motions. On the other hand, in the high dose range, f shows a strong change with increasing dose (see Fig.3), but the Q^{-1} spectrum remains almost unchanged. These features are very similar to those found in the n-Au specimens after 20 MeV proton irradiation.[5]

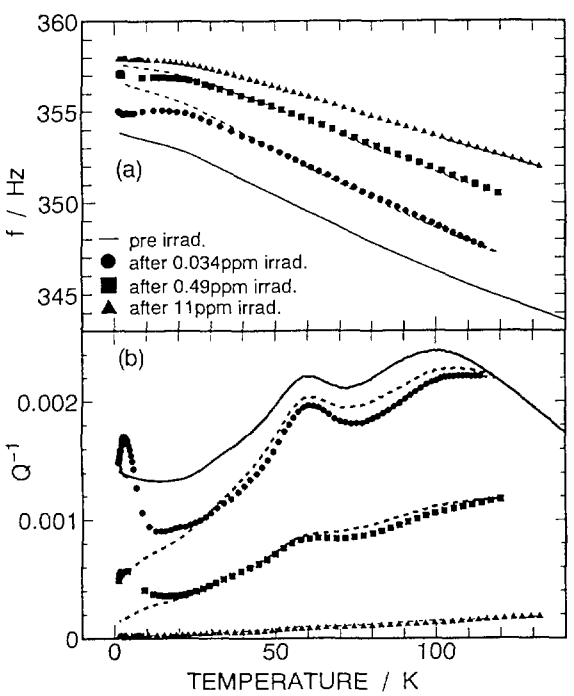

Fig.1 (a) Change in the resonant frequency (f) observed for the poly-Au specimen during warm-up (symbols) and subsequent cool-down (dashed lines) after 20 MeV proton irradiations. The data observed before irradiation are also shown by the solid lines. (b) Similar to (a) but the internal friction (Q^{-1}) is plotted.

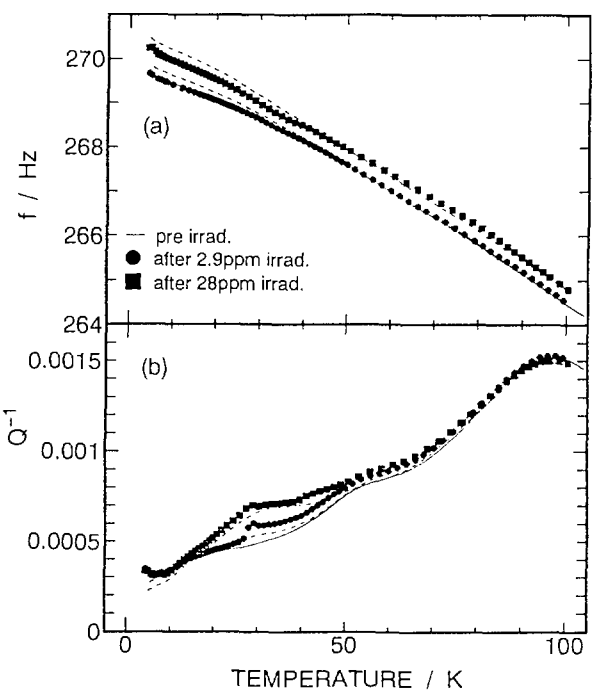

Fig.2 (a) Change in f observed for the n-Au specimen during warm-up (symbols) and subsequent cool-down (dashed lines) after 2.5 MeV electron irradiations. The data observed before irradiation are also shown by the solid lines. (b) Similar to (a) but Q^{-1} is plotted.

Figure 3 shows the normalized change in the elastic modulus, $\Delta E/E$, by the accumulation of irradiation induced defects, here C_{FP}, observed in the *n*-Au specimens after 20 MeV proton irradiation at 1.5 K. During the irradiation, E shows a decrease at the early stage of the irradiation which is followed by an increase at the later stage. The magnitude of $(\Delta E/E)/C_{FP}$ found in the *n*-Au specimens is, in general, larger by about one order than the bulk effects found in the poly-Au specimens. Such a strong change in E found in the *n*-Au specimens suggests that the grain boundary structures in *n*-Au are modified by the irradiation-induced point defects. Moreover, the fact that the decrease in E at the early stage of irradiation is followed by the increase in E at the later irradiation stage, suggests that the effects of irradiation induced point defects on the grain boundaries are not monotonous, they are different among various types of grain boundaries, or both. We surmise that the concept of the deformable unit proposed to explain the elastic property of amorphous alloys[9] is partly applicable to explain the present elastic response observed in the *n*-Au specimens.

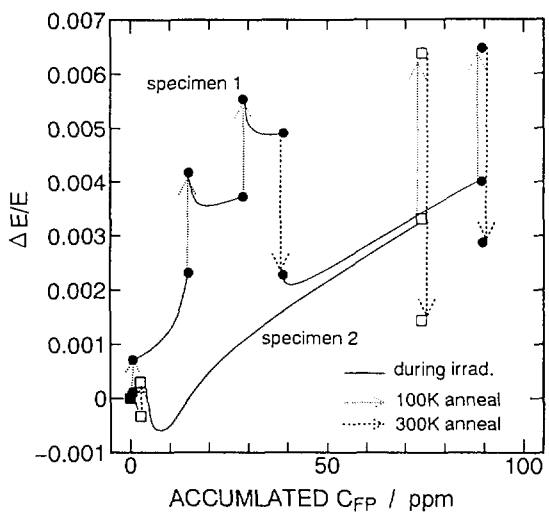

Fig.3 Change in the normalized E at 1.5 K ($\Delta E/E$) by 20 MeV proton irradiation (solid lines) and the successive warm-ups (dashed arrows).

The present work demonstrates that the characteristic elastic property found in the *n*-Au specimens are not due to dislocation motions but reflect the property of the grain boundaries, and that the grain boundaries can be modified by low temperature irradiation. To clarify the properties of the grain boundaries in *n*-Au, the further study is now in progress.

4. References

1) R.Birringer and H.Gleiter, "Advances in Materials Science and Engineering", Ed. by R.W.Cahn, Pergamon Press, New York, 1988, p.339.
2) E.Fuchita, K.Setoguchi, I.Katsu, R.Mizutani and M.Oda, Proc. 8th Int. Microelectronics Conf. (IEC 94), Omiya, Japan April 20-22, (1994). : E. Fuchita, M.Oda and C.Hayashi, Materia Japan, 34(1995)455.
3) S.Okuda, F.Tang, H.Tanimoto and Y.Iwamoto, J. Alloy and Compounds, 211/212 (1994) 494.
4) F.Tang, H.Tanimoto and S.Okuda, Nanostruc. Mater., 6(1995)563.
5) H.Tanimoto, H.Fujita, H.Mizubayashi, Y.Sasaki, E.Kita and S.Okuda, Mat. Sci. Eng. A, 217/218 (1996)108 : H.Tanimoto, H.Fujita and H.Mizubayashi, J de Physique III, 6(1996)C8-285-C8-288.
6) P.Jung, "Landolt-Bornstein Numerical Data and Functional Relationships in Science and Technology, New Series vol.25: Atomic defects in Metals", Ed. by H.Ullmaier, Splinger- Verlag, Berlin, 1991, p.12.
7) G.Fantozzi, C.Esnouf, W. Benoit and I.G.Ritchie, Prog. Mater. Sci., 27(1982)315.
8) H.Schroeder and B.Stritzker, Rad. Effect, 33(1977)125.
9) H.Mizubayashi, M.Kaida, S.Otsuka and S.Okuda, Acta Metall., 42(1994)2099.

4.5 Effect of Synergistic Irradiation of Triple Beam on Dislocation Structure in Austenitic Stainless Steel

S. Hamada, Y. Miwa and A. Naito
Dept. of Material Science & Engineering, JAERI

1. Introduction

The irradiation environments for structural materials of fusion reactors would be characterized by heavy displacement damage, a large amount of hydrogen and helium atoms produced by nuclear transmutations. It has been reported that synergistic effects of displacement damage and helium atoms lead significant influence on various mechanical properties. In order to clarify the role of helium on correlation between microstructural evolution and mechanical properties in austenitic stainless steels, dual beam irradiation experiments using both heavy and helium ions have been carried out [1-3]. On the other hand, it has been considered that effects of hydrogen on them is small in comparison with the effects due to helium. Actually, in the triple beam irradiation of an austenitic stainless steel at the elevated temperature beyond 923K, the synergistic irradiation effects of hydrogen and helium on microstructural evolution have been reported to be modest[4,5]. It is, however, known that hydrogen leads significant embrittlement below 573K [6]. This seems to suggest some effects of hydrogen on microstructural evolution in the fusion reactor-relevant irradiation conditions at medium and low temperatures.

The objective of this study is to investigate the synergistic irradiation effects of hydrogen and helium on the microstructural evolution in an austenitic stainless steel below 673K, which is relevant to water-cooled fusion reactors such as ITER (international thermonuclear experimental reactor), by the irradiation experiments using triple beam of nickel, hydrogen and helium ions.

2. Experimental

The material used in this study is a titanium-modified austenitic stainless steel (JPCA). The main chemical composition in wt% is Fe-16Ni-14Cr-0.25Ti-2.5Mo. Disks of 3 mm in diameter with 0.25 mm in thickness of this material were solution-annealed for 1 hour at 1323K. The irradiation was carried out with the triple beam irradiation facility in TIARA of JAERI[7]. Samples were simultaneously irradiated with 12.0 MeV Ni^{3+} and 1.0 MeV He^{+} and 350 keV H^{+} ions in the temperature range of 573 - 673 K. The energies of helium and hydrogen ions were selected so as to be injected at same depth. The theoretical depth profiles of displacement damage produced by nickel ions and the concentrations of both helium and hydrogen injected in 316 stainless steel were calculated using the TRIM code 89[8] with threshold energy of 40 eV.

After the irradiation, the specimens to carry out TEM (transmission electron microscope) observation of a cross sectional view normal to the incident surface were prepared from the irradiated samples. Nickel was electroplated on both sides of an irradiated sample to a thickness greater than 3 mm. The electroplated sample was sliced into 0.2 mm thick sheet using a low speed diamond saw, and cut into 3 mm disc. Then it was electropolished to perforation. The detailed procedure is described elsewhere[9]. The cross sectional microstructures were observed with a 2000-FX TEM operated at 200 kV.

3. Results and discussion

The cross-sectional dislocation structures in JPCA irradiated with triple beam are shown in fig. 1. The irradiation condition is as follows : JPCA irradiated with triple beam to 56 dpa, 20570 appm H and 11270 appm He in the depth of 1.6 μm at 573-673K. In the case of triple beam irradiation, high density of dislocation loops and lines were also observed from the depth of 0.5 μm to the projected range of nickel ion. However, the region of lower dislocation density in comparison with that in the shallower or deeper region than it existed in the region from 1.2 μm to 1.5 μm in depth in the triple beam irradiation as shown in fig. 1. The region of lower dislocation density observed in fig. 1 could be considered to correspond to the region where both hydrogen and helium atoms accumulated. As a result of strong interaction among dislocations, hydrogen and helium atoms, the region of lower dislocation density would have appeared in the specimen irradiated with the triple beam. Unless the strong interaction exist in the region where hydrogen and helium were

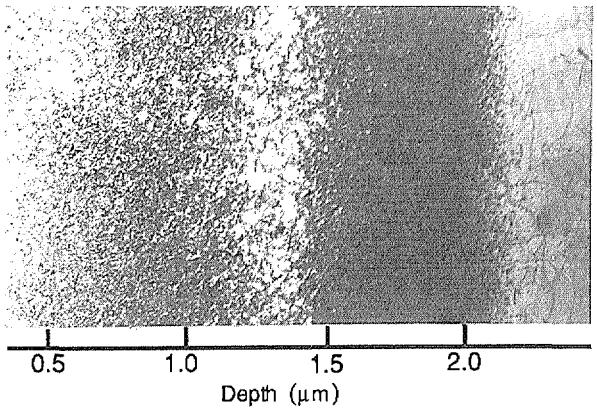

Fig. 1 Depth profile of dislocation structures in JPCA irradiated with triple beam. The incident ions traveled from left to right in the micrograph.

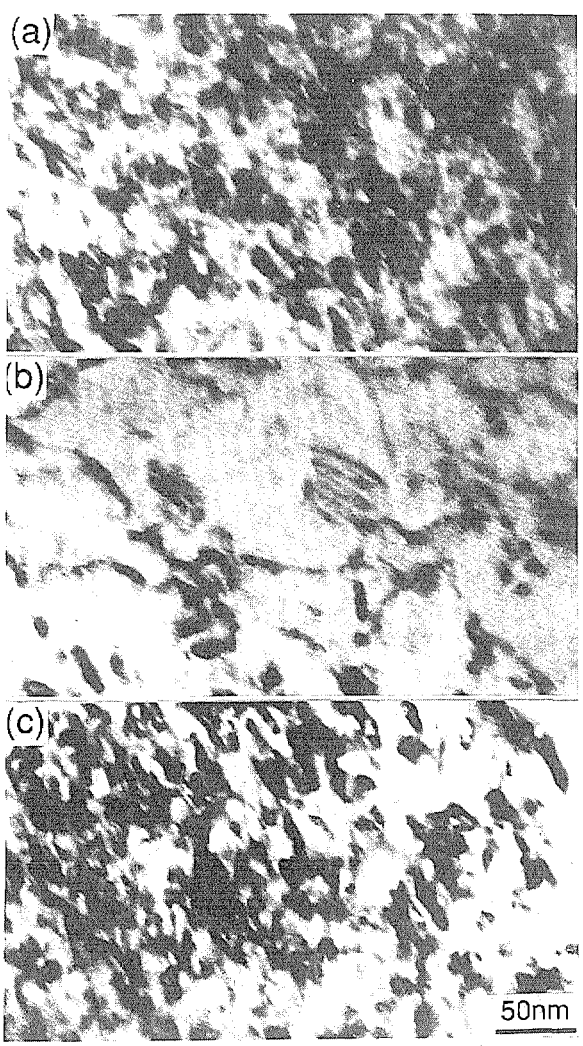

Fig. 2 Difference in the distribution of dislocation structures observed in the region of each depth (a) 0.8-1.0μm, (b) 1.1-1.3μm, (b) 1.4-1.6μm.

simultaneusly implanted, the high dislocation structures would distribute in the entire region consisted of dislocation loops and lines. However, the character of dislocation structure depends on each region. High number density of dislocation loops dominates in the regions of 0.8 to 1.0 μm and 1.4 to 1.6 μm in depth (fig.2(a) and 2(c)), while dislocation lines are mainly found in the region of 1.0 to 1.4 μm in depth, which is considered to correspond to the

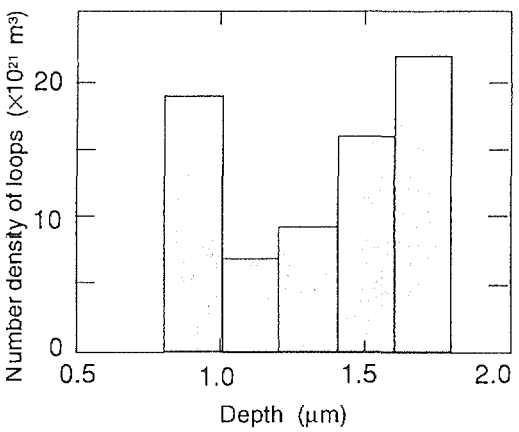

Fig. 3 Depth profile of the number density of dislocation loops in the range of 0.8 to 1.8 μm in depth.

region where hydrogen and helium atoms accumulated (fig. 2(b)). Fig. 3 shows depth distribution of the number density of dislocation loops in the range of 0.8 to 1.8 μm in depth in fig. 2. The number densities were measured in the region of 75-130 nm in thickness in the foil. The sizes of loops were not so chaged in each region and about 10 to 20 nm in diameter. The number density of them varies in this depth range : While the loop density in the region of 0.8 to 1.0 μm in depth and beyond the depth of 1.4mm was about 2.0×10^{22} m^{-3}, it decreased into 7 to 9 x 10^{21} m^{-3} in the region of 1.0 to 1.4 μm in depth. This indicates that the number density of dislocation loop decreases in the region where hydrogen and helium were simultaneously implanted. As mentioned above, it was characterized that the number density of dislocation loops was lowered in the region where hydrogen and helium atoms were simultaneously injected with the triple beam in the temperature range of 573-673K, in comparison with that in the region irradiated to similar displacement damage level without injection of helium and hydrogen atoms in the same specimen. This phenomenon seems to be due to strong interaction among defects produced by displacement, helium and hydrogen atoms.

It has been reported that dislocation and hydrogen show the strong interaction in iron and steels[6] and the dislocation traps hydrogen to bow and easily move under stress[10]. Dislocation loops produced during irradiation in the region where hydrogen and helium atoms were simultaneously injected, might trap hydrogen to grow and coalesce to dislocation lines. The internal stress necessary to drive dislocation might be provided by a number of atoms injected and accumulated during irradiation. Eventually, the number density of dislocation loops would decrease and some dislocation lines would remain in the specimen.

4. Summary

An austenitic stainless steel was simultaneously irradiated with triple beam of nickel, helium and hydrogen ions to 58 dpa, 20500 appm He and 11000 appm H at 573 - 673 K. Microstructural evolution due to the triple beam irradiation was revealed from the cross sectional view normal to the irradiation surface using a TEM. Main result obtained is summarized as follows;

Simultaneous irradiation of hydrogen, helium and nickel ions makes the number density of dislocation loops lower in comparison with structure consisting of dislocation lines dominantly.

5. References

1) G. Ayrault et al., J. Nucl. Mater. 104 (1-3): 1035 (1982).
2) N. Sekimura et al., J.Nucl.Mater. 122 (1- 3): 322 (1984).
3) J. Tenbrink et al., J.Nucl.Mater. 140 (3): 274 (1986).
4) K. Farrell et al., Scripta Met. 12:1121 (1978).
5) K. Farrell and N.H. Packan, J.Nucl.Mater. 85 & 86:683 (1979).
6) J.P. Hirth Metall. Trans. A, 11A: 861 (1980).
7) S. Hamada et al., JAERI-Review 94-005, TIARA ANNUAL REPORT (vol. 3):105 (1993).
8) J.F. Ziegler et al., The Stopping and Range of Ions in Solids, Pergamon Press, New York : (1985).
9) S. Hamada et al., J. Nucl. Mater. 114: 338 (1983).
10) R.E. Miner et al., Acta Met. 24:233 (1976).

4．6 Effects of dual and triple beam irradiation with H, He and O-ions on damage structures in Al_2O_3

Y. Katano, T. Nakazawa, D. Yamaki, T. Aruga, and K. Noda
Department of Materials Science and Engineering, JAERI

1. Introduction

Alumina(Al_2O_3) has been proposed for electrical insulators and diagnostic materials in fusion reactors, because of its excellent electrical and optical properties[1]. The synergetic effects of atomic displacement damage with H and He atom production, under fusion reactor neutronic environments, have been studied by ion irradiation techniques [2-5], but have not been clarified yet.

In the present study, we have examined damage structures in Al_2O_3 irradiated with triple and dual ion beams, and also after a subsequent annealing at a high temperature, by cross-sectional transmission electron microscopy (TEM).

2. Experimental procedure

The materials used in this study were single crystal alumina (α-Al_2O_3) in a shape of disk of 0.2 or 0.5mm in thickness and 10mm in diameter with surface perpendicular to the (0001) axis. The procedures for the sample preparation and irradiation have been reported elsewhere[5]. Samples were irradiated with either triple ion beams (H^+, He^+ and O^{2+}) or dual ion beams (H^+ and O^{2+}) up to ion fluences of 1.5~7.6x10^{20}ion/m^2 at 923K. Table 1 summarizes the irradiation conditions examined and respective damage parameters determined by TRIM89 code[6].

After irradiation, cross sectional TEM observation was performed for the as-irradiated samples and those annealed for 1h at 1273 K, using a JEM-2000FX electron microscope operating at 200kV.

3. Results and discussion

3.1 *Microstructures after triple and dual beam irradiation*

As has been already reported[5], the cross-sectional damage microstructures of Al_2O_3 irradiated with triple(H^+, He^+ and O^{2+}) beams (total peak damage of 3.6 dpa) at 923K were observed to be extended from the ion-incident surface to a depth of 1.8μm . Cavities were formed in the restricted region of depths from 1.2 to 1.7μm.

The depth-dependent microstructure of Al_2O_3 irradiated with dual(H^+ and O^{2+}) beams (total peak damage of 10.6 dpa) at 923K is shown in fig.1. The depth profile of the cavity formation is apparently seen to be very similar

Table 1 Irradiation conditions and corresponding damage parameters obtained by TRIM calculations.

Ion beams	Energy/Ion (MeV)	Flux (10^{16} ions/m^2s)	Fluence (10^{20} ions/m^2)	Calculated value (TRIM)			
				Damage peak depth (μm)	Peak damage (dpa)	Average projected range (μm)	Peak ion concentration (at.%)
Triple	0.25 H^+	3.6	2.3	1.35	0.04	1.38	1.8
#94-05	0.6 He^+	2.4	1.5	1.34	0.3	1.39	0.9
	2.4 O^{2+}	3.3	2.1	1.34	3.3	1.41	1.3
Dual	0.25 H^+	4.0	5.0	1.35	0.09	1.38	3.9
#95-11	2.4 O^{2+}	6.0	7.6	1.34	10.5	1.41	3.0

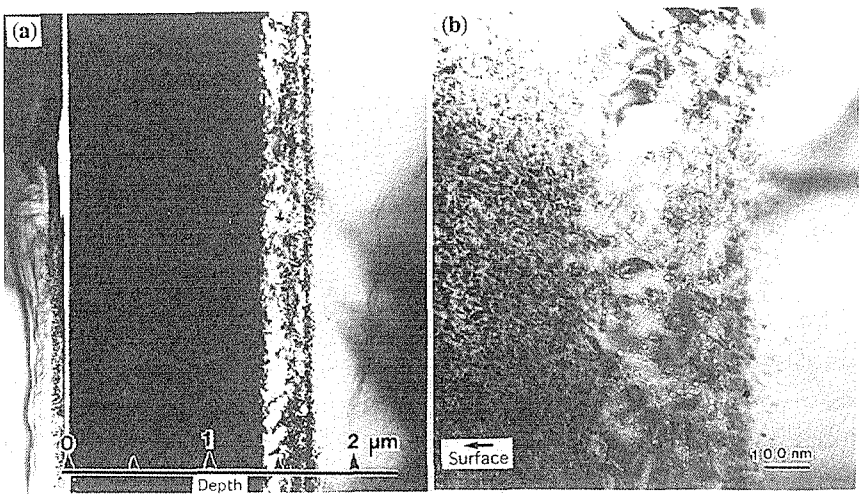

Fig.1. Cross-sectional damage structures in Al_2O_3 irradiated with dual beams at 923K, (a) dislocation component and (b) a typical cavity component around the ion ranges.

to that observed in the triple beam irradiated sample[5]. That is, irregular shaped cavities are formed around 1.2~1.3 μm in depth. However, tiny cavities smaller than 5 nm are formed in the region of smaller depths down to 0.5 μm. In fig. 3(a,b), the depth profiles of the number density and average sizes for cavities observed in the both samples are compared with the predicted depth profiles of damage parameters, dpa, H, He and O ion concents (fig.3(c)).

The fact that cavities are formed in the more restricted region of depths in the triple beam irradiated sample than those observed in the dual beam (H^+ and O^{2+}) irradiation, implies that He atoms play a role of trapping the radiation produced point defects which would enhance the nucleation of defect clusters, thus lowering the mobility of the point defects.

3.2 *Microstructures after post-irradiation annealing*

The microstructures observed in the annealed sample after triple beam irradiation are shown in fig.2. The dislocation loops are annealed remarkably, for a region of depths of 0~0.8 μm (fig.2(a)). On the other hand, a zone with a high density dislocation loops and denuded zone appears around depths of 0.8~1.0 μm and 1.0~1.4 μm, respectively, Furthermore, dislocations grown to long the

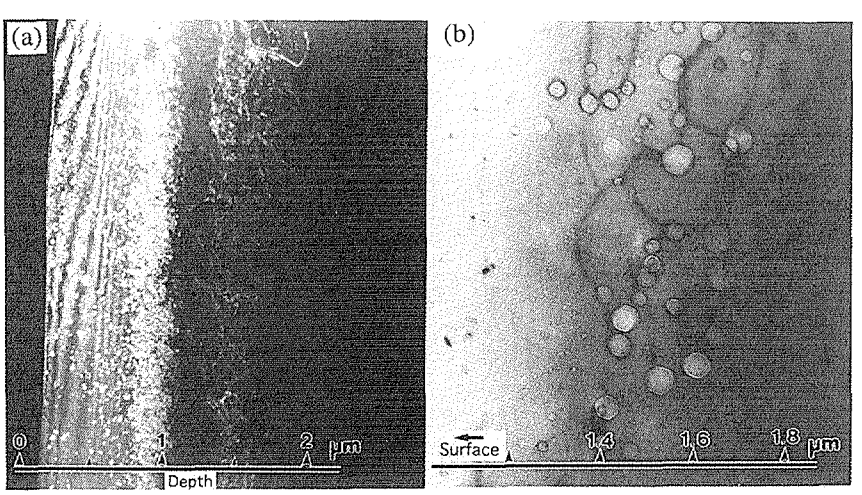

Fig.2. Damage structure in Al_2O_3annealed for 1h at 1273 K after triple beam irradiation at 923K: (a) dislocation component and (b) a typical cavity component around the ion ranges.

segments in the region of 1.5-2.0 μm in depths. Cavities extraordinarily grown to 70~80 nm at the maximum size, which are observed to be facetted to form a hexagonal shape, are formed for a region of depths of 1.3~1.7 μm(fig.2(b)). Moreover, irregularly shaped cavities smaller than 20 nm are formed for a region of depths of 0.7~1.1 μm, where no cavity was discernible in the as-irradiated sample.

Upon annealing the dual beam irradiated sample for 1h at 1273K, damage structures appear very similar to those observed in the triple beam irradiated and subsequently annealed sample; remarkable annealing of dislocation loops for a region of depths of 0~0.5 μm, a zone of high density dislocation density, denuded zone, and dislocation lines grown to long segments in a relatively high density up to a depth larger than 2 μm, furthermore, large cavities grown to 80 nm at the maximum size in a region of depths of 1.4~1.8 μm.

The appearance of very similar structures for dislocations and cavities in both the annealed samples signifies that co-existence of He atoms no longer influences the structural evolution during the annealiat 1273K, but the changes in the structures during the annealing would be determined by the accumulated density of the radiation-produced defects.

In summary, similar dislocation structures mainly consisting of loops evolved in the both single crystal Al_2O_3 irradiated with triple and dual beams at 923 K. The depth profile of cavity density for the triple beam irradiation appeared in a more restricted region of depths around the damage peak. The development of similar structures for dislocations and cavities occurred diring annealing for 1h at 1273K in the both samples, which revealed that coexistence of He atoms no longer influences the microstructural evolution during annealing at this temperature.

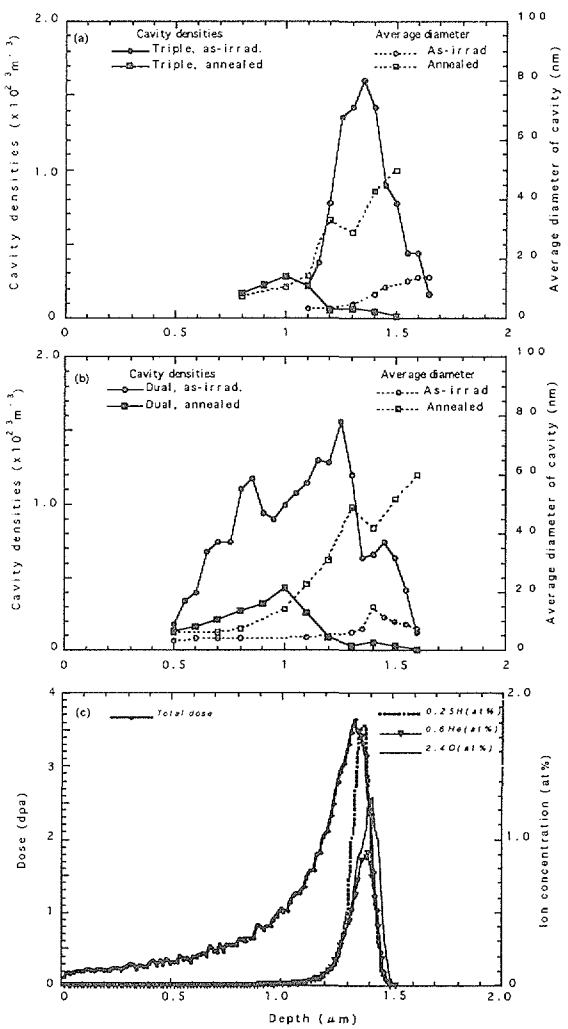

Fig.3. Depth profiles of cavity formation behaviors measured densities and average diameter of cavity in the Al_2O_3 after irradiation and subsequent annealing (a) triple beam, (b) dual beam irradiation, and (c) depth profiles of damage parameters for triple beam irradiation.

Reference

[1] R.E. Gold, E.E Bloom, F.W. Clinard Jr., D.L. Smith. R.D. Stevenson and W.G.Wolfer, Nucl. Technol./Fusion **1** (1989) 161.
[2] S.J. Zinkle, J. Nucl. Mater **219** (1995)113.
[3] Y, Katano, H. Ohno and H. Katsuta, J. Nucl. Mater. **155-157** (1988) 366.
[4] Y. Katano, T. Nakazawa, D. Yamaki, T. Aruga, K. Hojou, K. Noda, Nucl. Instr & Meth. B **116** (1996) 230.
[5] S.J. Zinkle. Nucl. Inst. and Meth. in Phys. Res. B**91** (1994) 234.
[6] J.F. Ziegler, J.P. Biersak and U.L.Littmark, The stopping and Range of Ions in Solids (Pergamon, New York, 1985).

4．7 Effect of minor elements on damage structure in ion-irradiated austenitic stainless steels

Y. Miwa, T. Tsukada, S. Hamada, A. Naito and H. Tsuji
Department of Materials Science and Engineering, JAERI

1. Introduction

Since austenitic stainless steels show a good corrosion resistance in high temperature water environment, they are used generally as in-core structural materials in light water reactors, and also planned to be used as structural materials of a water-cooled fusion reactor, such as the International Thermonuclear Experimental Reactor. In these reactors, however, the material tends to degrade due to stress corrosion cracking (SCC), resulting from coincidence effects of energetic particle irradiation, high temperature water environment including both radicals and active molecules, and static and/or dynamic loading. This SCC was termed Irradiation-Assisted SCC (IASCC). IASCC is one of the degradation problems affecting plant economics, reliability, and safety. IASCC is affected via changes in mechanical properties (radiation hardening, creep etc.), material microchemistry and so on. These changes were related to the microstructural change which was influenced by chemical composition, for example impurities and minor elements. In this experiment, effects of those elements on microstructural evolution in model steels ion-irradiated were studied.

2. Experimental procedure

The materials used in this experiment are a solution-annealed, high purity austenitic stainless steel and some similar steels doped with Si, P, S, C, C/Ti, and Si/P/S/C/Ti. The chemical composition of these steels is listed in Table 1. Disk specimens with 3 mm diameter were cut from these steels, and then irradiated at about 573 K by using 12 MeV Ni^{3+} from the 3 MV tandem accelerator in TIARA. Total ion fluence was about 3.8×10^{19} ions/m^2, and depth profiles of incident Ni ion and produced displacement were shown in Fig.1. Those profiles were calculated by using TRIM-85 computer code[1] with displacement energy of 40 eV. After the irradiation, transmission electron microscopy was performed at areas irradiated to about 1 displacement per atom (dpa).

3. Results and discussion

Figure 2 shows electropolished surfaces irradiated to about 1 dpa in C-doped and Si/P/S/C/Ti-doped alloys. No etch pits were observed along the grain boundaries except for C-doped alloy, though some etch pits were observed along the flaws of mechanical pol-

Table 1 Chemical composition of materials tested (mass%)

	C	Si	Mn	P	S	Cr	Ni	Ti	Al	N
high purity alloy	0.003	0.01	1.36	0.001	0.0014	18.17	12.27	0.01	0.16	0.001
Si-doped alloy	0.003	0.69	1.36	0.001	0.0014	18.01	12.24	0.00	0.10	0.001
P-doped alloy	0.006	0.03	1.40	0.017	0.0011	18.60	12.56	0.01	0.11	0.002
S-doped alloy	0.002	0.03	1.41	0.001	0.0318	18.32	12.47	0.01	0.07	0.001
C-doped alloy	0.098	0.03	1.39	0.001	0.0020	18.30	12.50	0.00	0.11	0.002
C/Ti-doped alloy	0.099	0.03	1.39	0.001	0.0017	18.50	12.47	0.31	0.11	0.002
Si/P/S/C/Ti-doped alloy	0.107	0.72	1.41	0.019	0.0356	18.66	12.68	0.29	0.10	0.003

ishing in Si/P/S/C/Ti-doped alloy. The result shows that addition of C alone degraded the corrosion resistance of the grain boundary in the high purity alloy.

Figure 3 shows microstructures of (a) C/Ti-doped alloy, (b) Si-doped alloy, and (c) C-doped alloy. As seen in Fig. 3, highly dense and fine defects were observed homogeneously except for Si-doped alloy. In Si-doped alloy, those defects developed preferentially near the grain boundaries and dislocations existed before irradiation. In C-doped alloy, $M_{23}C_6$ type carbide was observed at the grain boundaries. Precipitates including $M_{23}C_6$ were not observed in C undoped alloys, C/Ti-doped alloy or Si/P/S/C/Ti-doped alloy which contained about 0.1 mass% carbon as same as C-doped alloy. This result of precipitation observation is in agreement with the result of preferential grain boundary attack observed only in C-dpoed alloy. Therefore these precipitates at the grain boundaries degraded the corrosion resistance of the grain boundaries. Precipitation of $M_{23}C_6$ might be suppressed by addition of Ti controlling the diffusivity of carbon by TiC forming. However, TiC was not observed in either C/Ti-doped or Si/P/S/C/Ti-doped alloy.

Figure 4 shows Frank loops observed in the high purity alloy, Si-doped alloy, and P-doped alloy, respectively. Relatively larger Frank loops were observed in the high purity alloy. By addition of Si, the size and the number density of the Frank loops appear to decrease, as seen in Fig. 4(b). By addition of other elements,the number densities of Frank loops increase as shown in Fig 4(c) which indicates the case of P-doped alloy. Similar effects of impurities and minor elements on dislocation evolution were observed in the same alloys neutron-irradiated at about 513 K to the same dose level of about 1 dpa[2]. In those alloys, addition of Si suppressed development of Frank loops, and addition of C increased the number density of Frank loops. However, there are two differences in microstructures between ion-irradiated and neutron-irradiated materials. Precipitate was not observed in any nuetron-irradiated alloys. Effect of Si in decreasing the number density of Frank loops in nuetron-irradiated alloy was much stronger than that in ion-irradiated alloy. These differences of microstructural characterisitics between ion- and neutron-irradiated materials might be influenced by the differences of primary knock-on atom (PKA) energy spectrum and dpa rate. As previously reported[3], relatively low energy PKAs (~500 eV) were mainly produced in ion irradiated alloys, whereas high energy PKAs (~5 keV) were produced in neutron irradiated alloys. According to Hinisch[4], the fraction of free point defects per unit displacement with low energy PKA was larger than that with high energy PKA as the PKA energy decreased from 30 keV. Therefore the number of free point defects produced in ion irradiated alloys was larger than that in neutron irradiated alloys. Since these free point defects aggregated and grew to defects cluster, like Frank loops, it could be considered that a larger number of free defects in ion-irradiated material promoted the development of the defects in spite of the same dose level in both ion- and neutron-irradiated materials.

References

(1) J. F. Ziegler et al.,"The Stopping and Range of Ion in Solids" Vol.1, PREGAMON PRESS (1985)
(2)Y. Miwa et al., J. Nucl. Mater. 233-237 (1996), p.1393
(3)Y. Miwa et al., JAERI TIARA annual Report 1995 (Vol.5), p.105
(4)H. L. Heinisch, J. Nucl. Mater. 117 (1983), p.461.

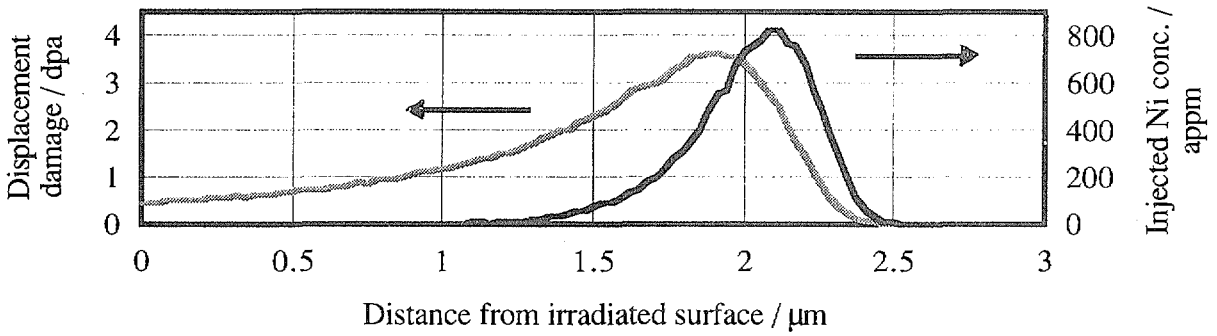

Figure 1 Calculated depth profile of displacement and injected Ni^{3+} ion using TRIM-85 computer code.

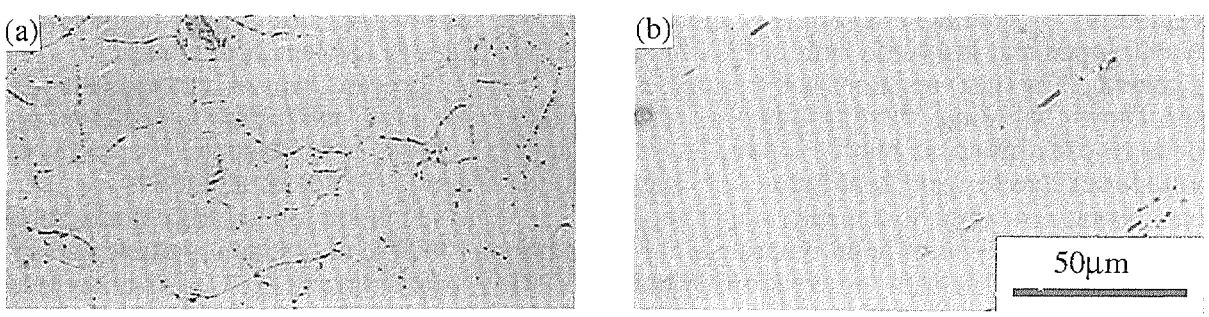

Figure 2 Electochemically polished surfaces of (a) C doped alloy and (b) Si/P/S/C/Ti doped alloy. These surfaces were in regions irradiated up to about 1dpa.

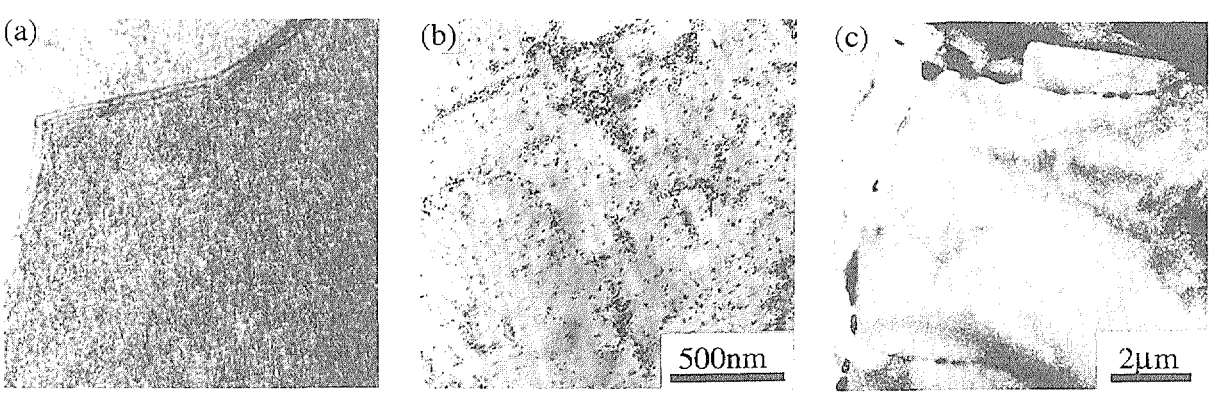

Figure 3 Microstructures of (a) C/Ti doped alloy, (b) Si doped alloy, and (c) C doped alloy.

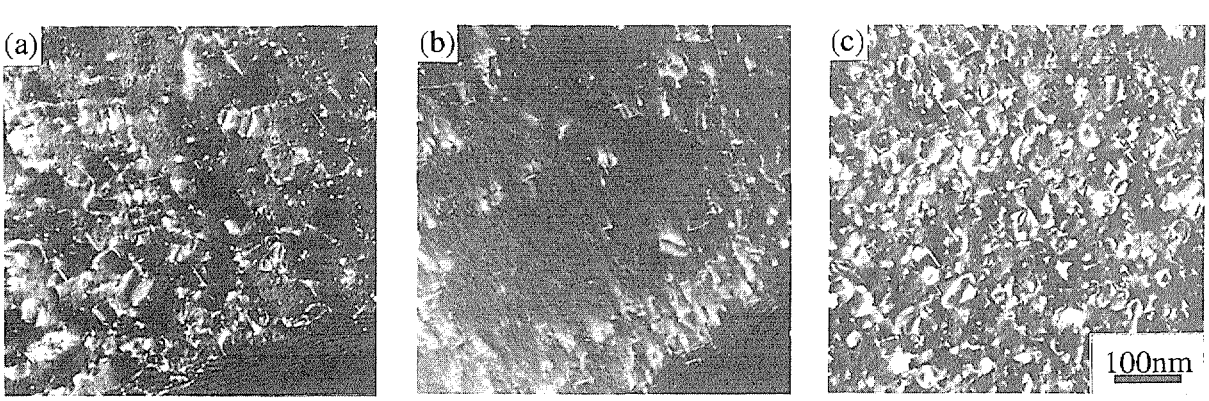

Figure 4 Frank loops of (a) high purity alloy, (b) Si doped alloy, and (c) P doped alloy.

4.8 Microstructures of austenitic stainless steel irradiated by 50 MeV He ion

Y. Miwa, T. Tsukada, Y. Nakamura*, S. Hamada and H. Tsuji
Department of Materials Science and Engineering, JAERI
* Advanced Radiation Technology Center, JAERI

1. Introduction

Repair and replacement of irradiation-degraded and damaged components by welding are planned during the operational life of light water reactors and a fusion reactor. The weldability of irradiated materials is affected by entrapped and insoluble helium[1,2], which is generated by (n,α) reactions and tritium decay. During welding, the entrapped helium tends to precipitate as bubbles along grain boundaries due to weld heat input, and may lead to weld cracking. So it is important to understand the behavior of helium during welding, the effect of helium on weldability and mechanical properties of the welds.

In this preliminary experiment, the effect of helium implantation on microstructure of austenitic stainless steel was studied. A special apparatus for high-energy-helium implantation was equipped for this experiment.

2. Irradiation apparatus

An irradiation apparatus was installed in Light Ion Room No.2 of cyclotron facility in TIARA. Details of the apparatus were reported elsewhere[3]. This apparatus with an energy degrader and X-Y beam scanners makes it possible to implant helium ions in any regions of specimens. This energy degrader which locates in front of target specimens consists of two wheels which have aluminum foils of different thickness; one has 20 foils from 5 to 25 μm every 1 μm and the other one has 30 foils from 20 to 600 μm every 20 μm. Schematic illustration is shown in Fig. 1. These tandem wheels rotate independently or synchronously. Incident ions lose their energy as passing through these foils of any given thickness, and stop at the aimed ranges. By controlling this energy degrader, several irradiation modes are available. In Fig. 2, three examples of irradiation mode are illustrated; (a) ion-penetration mode, (b) uniform implantation mode and (c) selected area implantation mode. In ion-penetration mode, incident ions pass through the targets, so only displacements were produced in the targets. In uniform implantation mode, incident ions were homogeneously implanted across the targets' depth. While incident ions were implanted in the selected regions, for example, the interfaces of composite materials in selected area implantation mode.

This apparatus was evacuated with both rotary vane pump and turbo molecular pump, and the pressure in the apparatus were reduced to the order of 10^{-5} Pa for about 6 h.

The specimen temperature during heat input of 100 W/cm^2 (incident particle energy: 50 MeV, beam current: 4μA, irradiation area: 2cm^2) was kept below about 323 K using water-cooled irradiation stage and water cooling system.

3. Experimental procedure

High purity model austenitic stainless steel was used in this experiment. The chemical composition by mass was 0.003% C, 0.01% Si, 1.36% Mn, 0.001% P, 0.0014% S, 12.27% Ni and 18.17% Cr. This alloy was a solution-annealed stainless steel. He^{2+} ions with 50 MeV from a cyclotron accelerator were irradiated into φ3 mm disks and miniature tensile specimens by using the irradiation apparatus. In this experiment, type (a) and (b) irradiation modes were utilized. In ion-penetration mode, specimens were irradiated to dose levels of 9×10^{-4} displacement per atom (dpa) and 4×10^{-3} dpa without using the energy degrader. While in uniform implantation mode, He was implanted up to the concentration of 30 appm by using a 20 μm step energy degrader . The specimen temperature during irradiation was about 323 K. After the irradiation, transmission electron microscopy was performed.

4. Results and Discussion

Figure 3 shows microstructures of irradiated specimens; (a) and (b) are He ion penetrated specimens damaged to 9×10^{-4} dpa and 4×10^{-3} dpa, respectively, and (c) is 30 appm

He uniformly implanted specimen. A few of very fine defects were observed in the He implanted specimen. Bubbles were not observed in any specimens. As irradiation temperatures were too low to create He bubble and damage levels were also too low to grow dislocation loops, irradiation induced defects did not develop in these specimens. Future investigation on the nucleation and growth of He bubbles with post-irradiation heat treatment is planned.

Reference
(1) K. Tsuchiya et al., J. Nucl. Matter. 233-236(1996)218-223
(2) C. A. Wang et al., J. Nucl. Matter. 233-236(1996)213-217
(3) Y. Nakamura et al., TIARA annual report 1995 (Vol.5), p.232.

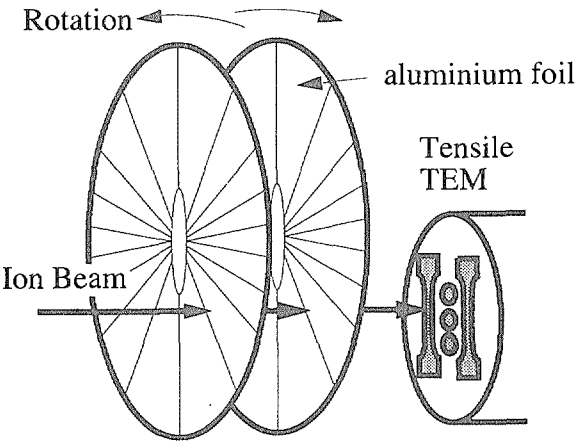

Figure 1 Energy degrader with tandem wheels.

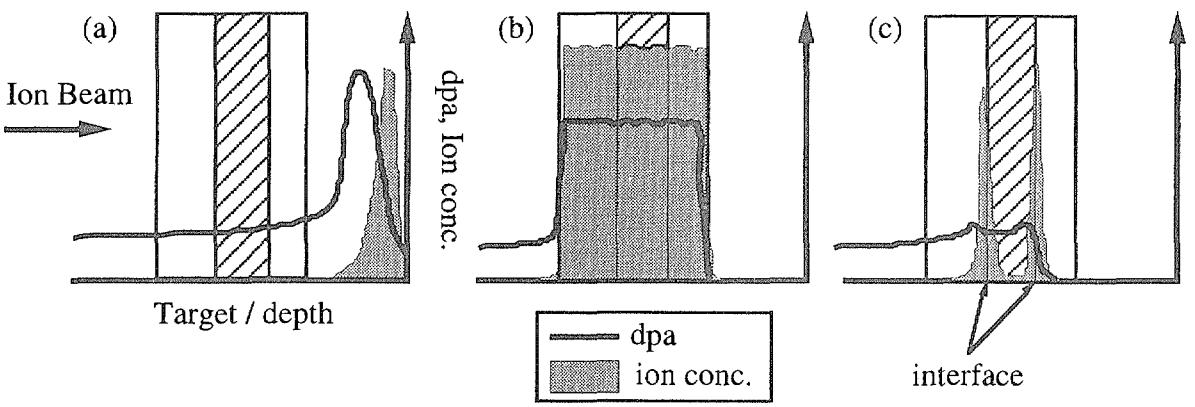

Figure 2 Schimatic diagrams of irradiation mode
(a) ion penetraion mode, (b) uniform implantation mode, and (c) selected area implantation mode

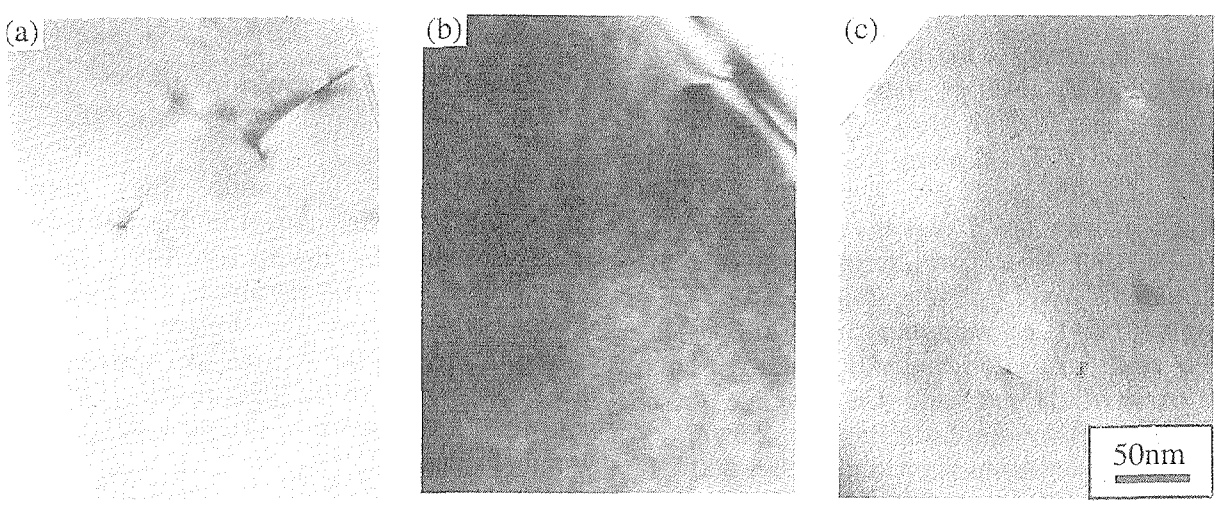

Figure 3 Microstructures of (a) He penetrated specimen damaged to 9×10^{-4} dpa, (b) He penetrated specimen damaged to 4×10^{-3} dpa, and (c) 30 appm He uniformly implanted specimen.

4.9 Effects of Phosphorus on Damage Structure and Hardening of Ion-Irradiated Ultra-High-Purity Iron

A. Naito*1, S. Jitsukawa*1, A. Hishinuma*1, S. Hamada*1, Y. Miwa*1 and K. Abiko*2
*1) Department of Materials Science and Engineering, JAERI.
*2) Tohoku University.

1. Introduction

Embrittlement caused by neutron irradiation is a critical problem for structural materials of nuclear power plants. The irradiation forms defect clusters which act as obstacles for gliding dislocations, and then the material irradiated often shows hardening with ductility loss. Phosphorus is known to enhance the radiation-induced embrittlement of iron-based alloys or ferritic steels [1, 2, 3].

In this study, specimens of ultra-high-purity iron doped with phosphorus were irradiated by 11.3 MeV Fe-ion. Their damage structures were examined by a transmission electron microscope (TEM), and the hardening was measured by ultra-microhardness test to evaluate the effect of phosphorus on microstructure and hardness.

2. Experimental

The materials used are ultra-high-purity iron doped with 0, 0.05 and 0.3 wt% phosphorus. TEM disk specimens were irradiated at 473 K using 11.3 MeV Fe^{3+} to a dose of 7 dpa with a dose rate of 1 x 10^{-3} dpa/s at the peak damage region. Fig. 1 shows the depth profile of displacement damage level and implanted Fe^{3+} concentration calculated with TRIM-85 code. The mean projected range of implanted ions is around 2.3 μm, and the damage peak locates slightly shallower depth of 2.0 μm.

TEM observation was done with a 200 kV JEOL-2000FX using cross-section method to examine the microstructure along the specimen depth.

Ultra-microhardness test was done on the irradiated surface at room temperature to a load of 0.98 N using a Vickers pyaramid indenter. The relationship between a load and an indentation depth was recorded continuously during loading and unloading.

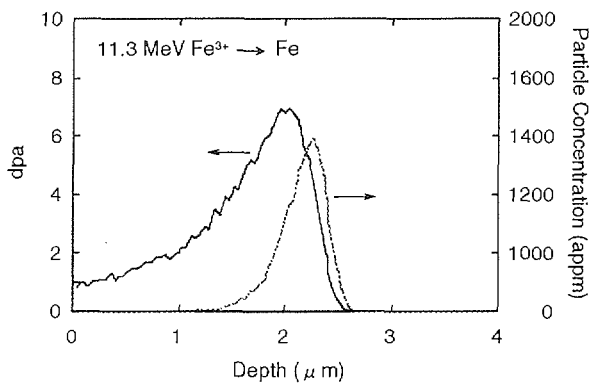

Fig. 1 Depth profile of displacement damage level and implanted Fe^{3+} concentration calculated with TRIM-85 code.

3. Results and Discussion

TEM observation

Microstructures around the mean projected range are shown in Fig. 2. Defect clusters, which seems to interstitial loops are observed in each specimen. The loops in Fe specimen are distributed relatively nonuniformly. The degree of uniformity becomes higher with phosphorus content, and finer loops are distributed with higher number density.

The depth dependence of number density

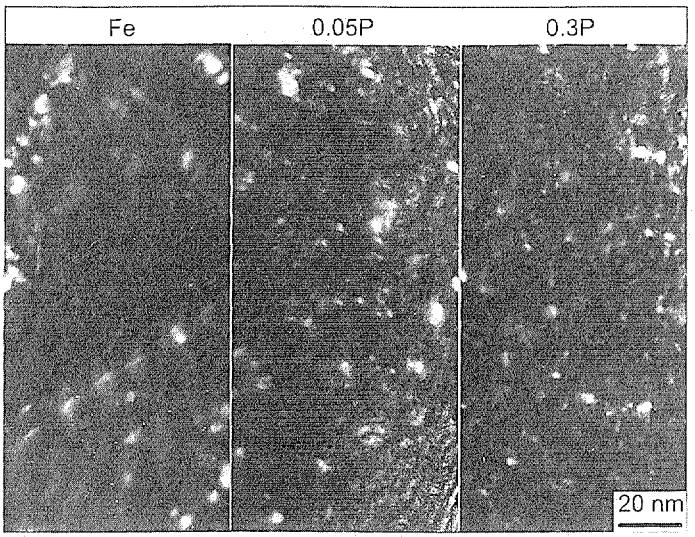

Fig. 2 Microstructures observed in each specimen irradiated with 11.3 MeV Fe^{3+} to 7 dpa at 473 K.

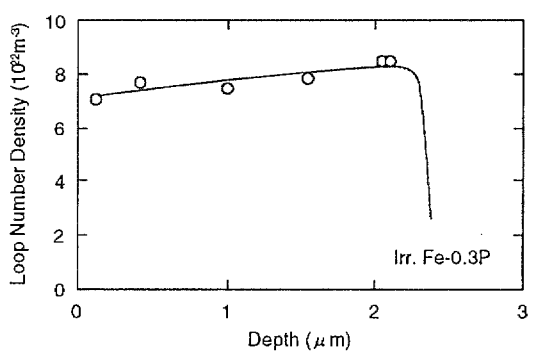

Fig. 3 Depth dependence of number density of loops formed in 0.3P specimen.

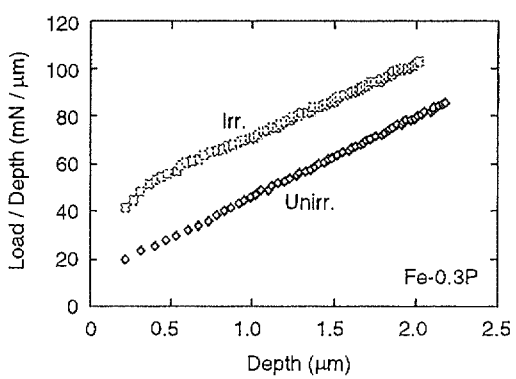

Fig. 5 Ultra-microhardness results for unirradiated and irradiated 0.3P specimens.

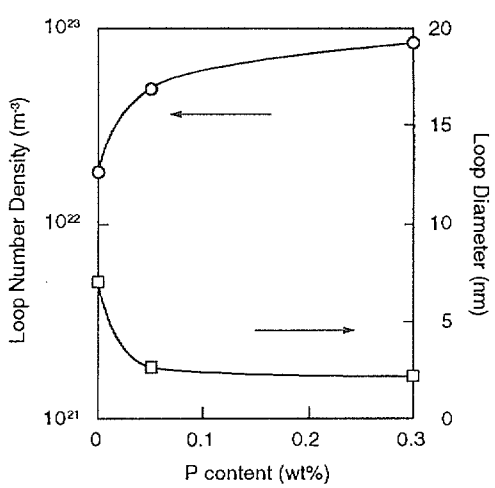

Fig. 4 Phosphorus content dependence of the number density and the diameter of loops.

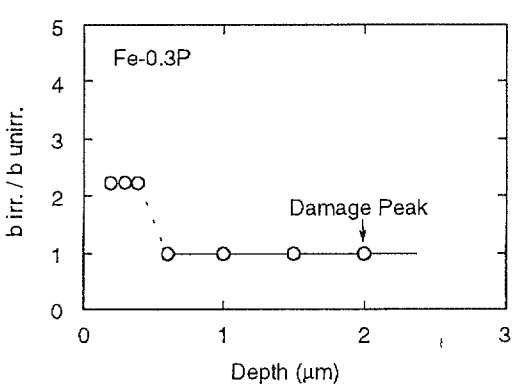

Fig. 6 Ratio of both the hardnesses of irradiated and unirradiated 0.3P specimens.

of loops formed in 0.3P specimen is rather small as shown in Fig. 3. The value of number density shows a maximum at the depth of 2 μm corresponding to the damage peak. On the other hand, the depth dependence of size is also small. These tendencies are similar to Fe and 0.05P specimens.

Fig. 4 shows the phosphorus content dependence of the number density and the diameter of loops. The number density of the order of $10^{22}m^{-3}$ increases with phosphorus content, and the diameter of the order of several nm decreases.

Ultra-microhardness test

Fig. 5 shows ultra-microhardness results for unirradiated and irradiated 0.3P specimens. Gradients of these lines correspond to the hardness of the specimen. The unirradiated specimen exhibits a constant gradient. The irradiated specimen exhibits a larger gradient to a depth of about 0.4 μm, and at the deeper region it exhibits the approximately same gradient with that of the unirradiated specimen. Namely the irradiated specimen shows hardening to the about 1/5 depth of the damage peak, and at the deeper region it shows the approximately same hardness for the unirradiated specimen.

The ratio of both the hardnesses is shown in Fig. 6. The hardness of the irradiated specimen is 2.2 times as large as that of the unirradiated specimen. However for Fe and 0.05P specimens, irradiation hardening is not detected. Hardening estimated from microstructural data and ultra-microhardness are summarized in Table 1.

4. Summary

① Phosphorus addition brings about increase in number density and decrease in size of defect clusters. The defect clusters are possibly interstitial loops.
② The depth dependence of distribution of the loops is rather small.
③ Irradiation hardening was detected for 0.3P specimen by ultra-microhardness test, however it was not detected for Fe and 0.05P specimens. 0.3P specimen exhibits maximum hardening estimated from microstructural data.
④ No agreement between ultra-microhardness and TEM result was obtained.

5. References

[1] J. R. Hawthrne : Nuclear Engineering and Design, 89 (1985) 223.
[2] G. E. Lucas, G. R. Odette, R. Maiti and J. W. Sheckherd : ASTM STP 956 (1987) 379.
[3] M. G. Burke, S. P. Grant and M. K. Miller : Proceedings of the Fourth International Symposium on Environmental Degradation of Materials in Nuclear Power Systems – Water Reactors (1989) 2

Table 1 Hardening estimated from microstructural data and ultra-microhardness.

	Microstructural Examination		Hardness
	$\sqrt{N_l d_l}$	$\Delta\sigma_y = \frac{\sqrt{3}Gb\sqrt{N_l d_l}}{3}$	
Fe	$1.14 \times 10^7\ m^{-1}$	151 MPa	zero incrase
0.05P	$1.14 \times 10^7\ m^{-1}$	151 MPa	zero incrase
0.3P	$1.34 \times 10^7\ m^{-1}$	178 MPa	$2.2 \times H_{unirr.}$ (corresponding to ~500 MPa increase)

4.10 Micro-Polycrystalline Formation of Fe-Cr-W Alloys under Fe^+ Ion Irradiation

E. Wakai, H. Abe*, A. Hishinuma, Y. Miwa, H. Naramoto*, and K. Abiko**

Department of Materials Science and Engineering, JAERI, *Department of Materials Science, JAERI, **Institute for Materials Research, Tohoku Univ.

1. Introduction

For the application of Fe-Cr-based alloys to industrial materials and/or nuclear materials, the embrittlement due to α'-precipitates[1-4] and sigma[5,6] phases is especially important problems. The sigma formation is closely related to formation of carbides which likely work as nucleuses for the sigma phase. Recent studies[8,9] show that the ductilities of the Fe-Cr alloys with relatively high chromium content (18 and 50%) are improved by purification, especially by the reduction of interstitial impurities such carbon and nitrogen atoms, and even in the Fe-50Cr annealed at 700 °C for $1x10^3$ hr, no formation of sigma phase is confirmed[8]. However, tensile strengths of high-purity Fe-Cr alloys are relatively low, and additional alloying elements such as tungsten and molybdenum are need for the applications.

The phase transformation under irradiation occurs, however, often at different temperatures and at different solute content as compared with the ordinary phase diagrams[10,11]. Therefore, to examine the phase stability during irradiation is very important for the application to nuclear materials such as structure materials.

The purpose of this study is to investigate the phase stability of the Fe-50Cr-W (W = 0-8 wt%) alloys under self-ion irradiation.

2. Experimental

The specimens used are high-purity Fe-50Cr, Fe-50Cr-5W, and Fe-50Cr-8W alloys. The high-purity alloys were prepared from high-purity metals of 99.995 mass% iron, of 99.98 mass% chromium, and of 99.98 mass% tungsten in a high vacuum of 10^{-6} Torr in a high-frequency induction furnace. Further details of the preparation could be found elsewhere[8, 12]. Chemical compositions of these alloys are given in Table 1. The specimens were normalized at 1050 °C for $1.8x10^3$ s in a high-purity Ar atmosphere, then forged and rolled to sheets of 0.2-mm. After that, the specimens again heated at 1050 °C for $1.8x10^3$ s in a vacuum followed by air-cool to obtain large grain sizes with a single α-ferrite phase. TEM specimens with standard 3-mm diameter were thinned using an automatic Tenupol electropolishing unit. The irradiations were performed with 300 keV Fe^+ ions at temperatures ranging from 400 to 800 °C in a transmission electron microscope operated at 200 kV, and the microstructural evolution and phase stability were investigated by in situ observation. The irradiations were performed up to 1.7×10^{21} ions/m^2 for 1.2×10^3 s, and the damage peak level is about 190 dpa. The peak depth positions of damage and Fe^+ ion are about 60 and 100 nm, respectively. The depth distributions of damage and Fe^+ ion were calculated by TRIM-code.

The thermal effects of microstructual evolution on the alloys were also examined for the specimens annealed at 700 °C for $1x10^3$ hr, because α-phase in the alloys is unstable at the temperature ranges of the irradiation.

3. Results

Dislocation loops were formed in the Fe-50Cr alloy at lower temperatures than about 650 °C, but no formation of precipitates were observed in matrix and on the loops. Fig. 1(a) shows a microstructure formed in the alloy at 700 °C by the irradiation, and a boundary was seen in nearly parallel to specimen edge. The evaporation began to occur at 600 °C, and it increased with the temperature.

The dislocation loops were formed in the Fe-50Cr-5W alloys at lower temperatures than about 720 °C. The evaporation began to occur at 650 °C, and violently occurred at 700 °C. Fig. 1(b) shows the microstructures formed at 700 °C by the irradiation. In the specimen edge, the shape is changed by evaporation. Micro-crystallines are formed near the edge in the thinner regions, and many dislocations tangled are in the thicker regions. The grain size of the micro-polycrystalline is about 100 nm, and the phase is also different from the matrix, sigma, and α' phases. Although the irradiation continued furthermore, no micro-crystalline was observed in thicker region, because of high evaporation rate. No formation of the micro-polycrystalline and other

Table 1. Chemical compositions of high-purity specimens used

	Fe	Cr	W	C	N	O	S
	mass%			massppm			
Fe-50Cr	Bal.	49.9	0.00	12.1	10.8	73.9	6.2
Fe-50Cr-5W	Bal.	50.0	5.09	14.1	7.1	57.5	4.8
Fe-50Cr-8W	Bal.	49.8	8.10	11.3	6.7	53.7	3.6

phases were observed at lower temperatures than 670 °C. The micro-crystallines are also formed in the Fe-50Cr-8W alloy at 700 °C at 85 dpa, and the alloy irradiated to 190 dpa are shown in Fig. 1(c). Figure 2 shows a sequence of the microstructures formed by the Fe^+ ion irradiation at 670 °C in the Fe-50Cr-8W alloy. In Fig. 2(a), the thickness fringe seen is formed by a reflection of $\mathbf{g} = 200$ near $\mathbf{z} = <001>$, and the extinction distance corresponding to the reflection is about 50 nm. After the irradiation at 8.5 dpa (60 s), many dislocation loops were formed as shown in Fig. 2(b), and the loops tangled at 19 dpa (120 s). As the irradiation proceeded up to 85 dpa (600 s), micro-crystallines were formed near specimen edge in very thin regions, as shown in Fig. 2(c). The micro-crystalline has also a different phase from the matrix and sigma. After that, the micro-polycrystallines were furthermore formed in the thicker region, and the grains with small size were observed at 115 dpa, as seen in Figs. 2(d). In Fig. 2(e), the micro-crystallines with small size are growing. The micro-polycrystalline formation are not observed at 800 °C and also at lower than 600 °C. The evaporation began to occur at 670 °C. Dislocation loops were also formed at lower temperatures than 750 °C, but no formation of precipitates were observed in matrix and on the loops.

4. Discussion

The foil thickness in the boundary between the first micro-crystalline and the second one from the edge is evaluated as 55 nm, which is obtained from the thickness fringe as shown in Fig. 2. The thickness is thinner than the range of the injected-ions, i.e., 100 nm, and it is nearly same with that of the damage peak, i.e., 60 nm. Therefore, the micro-crystallines appear to be formed by the damage. In the specimens annealed at 700 °C, no formation of micro-polycrystalline was confirmed. Accordingly, the micro-polycrystallines formation in the Fe-Cr-W alloys are formed by the irradiation, and the process accompanies with the phase transformation.

The precipitates of α' and sigma phase which exist in phase diagrams are not observed in this experiments of the Fe^+ ion irradiation. However, in the previous works [9, 10] on electron and neutron irradiation of Fe-Cr alloys with high chromium contents, α'-precipitates were formed on dislocation loops, and the number density of precipitates under 1 MeV electron irradiation was higher than that under fast neutron irradiation. The cause of the difference of precipitate amounts and no formation of precipitates appears to depend on the cascade size due to incident particles with high energy, because the smallest size of cascade is electron irradiation experiment, and the largest one is Fe^+ ion irradiation. Therefore, the formation of precipitates on the loops and in matrix would be very difficult under Fe^+ ion irradiation.

5. Summary

The phase stability and microstructural evolution of the Fe-50Cr-W (W= 0-8 wt%) under 300 keV Fe^+ ion irradiation has been investigated at temperatures ranging from 400 to 800 °C up to 190 dpa. The results obtained are described as follows:

(1) Dislocation loops are observed in the Fe-50Cr, -5W, and -8W alloys at lower temperatures than 650, 720, and 750 °C, respectively.

(2) No formation of α' and sigma phases are observed in all alloys during the irradiation.

(3) The evaporation in the Fe-50Cr, -5W, and -8W alloys begins to occur at 600, 650, and 670 °C, respectively, and it occurs violently in the Fe-50Cr alloy.

(4) Micro-polycrystallines are formed in the Fe-50Cr-5W and Fe-50Cr-8W alloys at 670 and 700 °C by the irradiation. The micro-polycrystalline has a different phase from the matrix, sigma, and α'.

6. References

1) R. M. Fisher et al., AIME Trans. 197: 690-696 (1953).
2) P. J. Grobner, Metall. Trans. 4: 251-258 (1973).
3) E. C. Bain and W. E. Griffiths, Trans. Amer. Inst. Min. Met. Eng. 75: 166-173 (1927).
4) M. J. Marcinkowski and D. S. Miller, Phil. Mag. 7: 1025-1032 (1962).
5) E. O. Hall and S. H. Algie, Metall. Reviews 11: 61-88 (1966).
6) K. Abiko, Proc. Ultra High Purity Base Metals, Ed. K. Abiko et al., The Japan Institute of Metals, Sendai (Japan) : 522-523 (1994).
7) G. T. Jones et al, J. Iron and Steel Institute, September: 953-958 (1967).
8) K. Abiko, Physique (IV)5, C7: 77-84 (1995).
9) E. Wakai et al, Physique (IV)5, C7: 277-286 (1995).
10) E. Wakai et al, Phys. stat. sol. (a) 160: 441-448 (1997).
11) P. Dubusson et al., J. Nucl. Mater. 205: 178-184 (1993).
12) S. Takaki et al, Physique (IV)5, C7: 159-164 (1995).

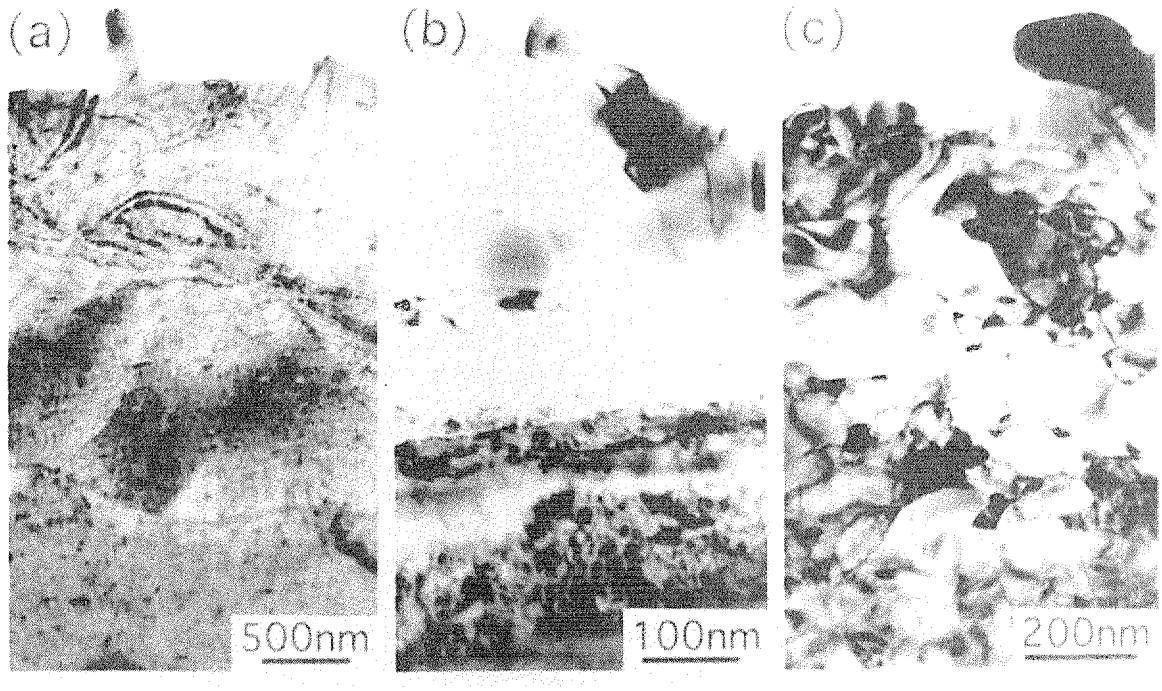

Figure 1 Fe-50Cr, Fe-50Cr-5W, and Fe-50Cr-8W alloys irradiated at 700 °C by 300 keV Fe^+ ions to 1.7 x 10^{21} ions/m^2 (190 dpa).

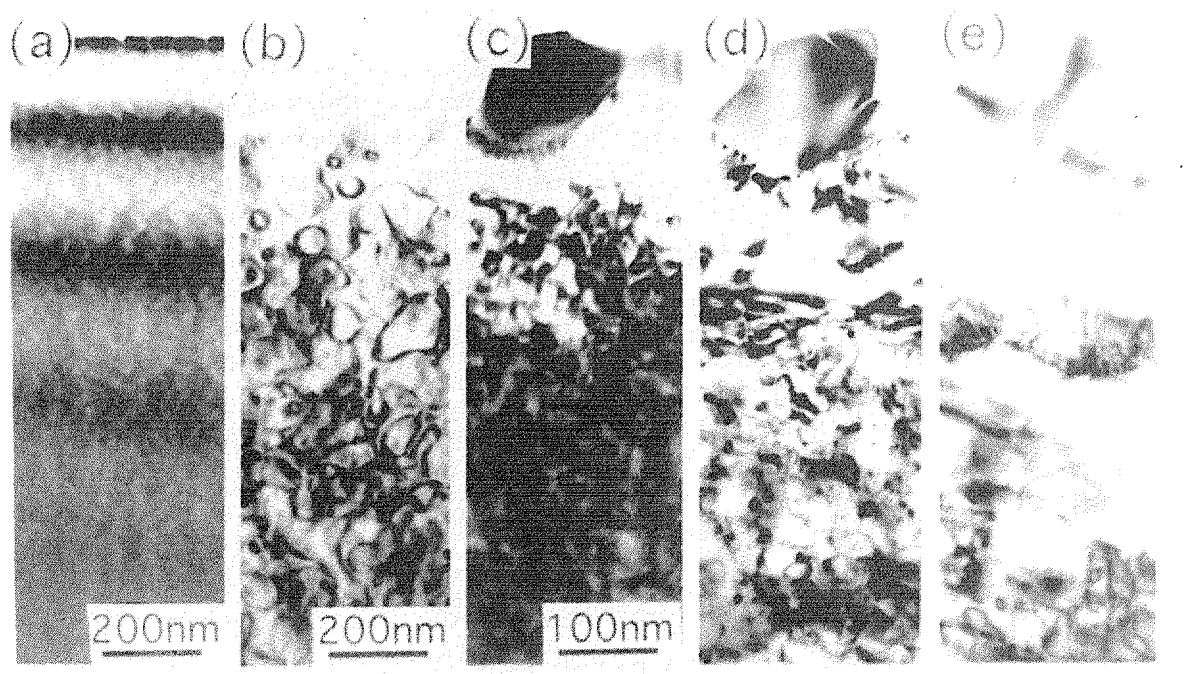

Figure 2 Microstructural evolution of Fe-50Cr-8W alloy irradiated at 670 °C with 300 keV Fe^+ ions. From left to right: (a) before irradiation, (0 dpa); (b) dislocation loops formed, 8.4 x 10^{19} ions/m^2 (8.5 dpa), (c) micro-polycrystalline near the specimen edge, 8.4 x 10^{20} ions/m^2 (85 dpa), (d) and (c) micro-polycrystallines proceeded to thicker regions, 1.1 x 10^{21} and 1.3 x 10^{21} ions/m^2 (115 and 135 dpa), respectively.

4.11

Microstructural Studies of Ion-Irradiated Ceramic Materials

H. Saka, K. Kuroda, N. Noda*, Y. Katano* and T. Nakazawa*
School of Engineering, Nagoya University and
*Department of Materials Research, JAERI

Introduction

Many kinds of ceramic materials are considered to be used in fusion reactors. Improvement of resistance to irradiation degradation of ceramic materials is desired for development of fusion reactors. AlN is a candidate material for insulator and RF window in fusion reactors. Characteristic feature of the irradiation damage in fusion reactor irradiation conditions is to accompany generation of helium gas due to nuclear reactions between the component atoms and high energetic neutrons. The helium gas has a large influence on the dimensional instability characteristics such as swelling through the formation of bubbles as well as displacement damage due to energetic neutrons. Therefore investigations of the effects of displacement per atom (dpa) and generated helium gas are important for development of irradiation resistance performance of the ceramic materials under fusion reactor conditions. In this study, radiation damages of AlN irradiated with protons, helium ions and oxygen ions were investigated to get fundamental information for improvement of resistance to irradiation degradation.

Experimental

The specimens used were sintered AlN. The specimens were irradiated at 928K with triple ion beams. Oxygen ions with an energy of 2.4MeV, helium ions with 0.45MeV and protons with 0.25MeV irradiated simultaneously. The fluence of each ion was about 3x 10^{20} ions/m^2.

The irradiated specimens were sectioned perpendicularly to the surface with a diamond saw and polished mechanically down to the thickness of about 0.03mm. The slice mounted on a single hole grid was further thinned by a focused ion beam (FIB) system. Tungsten was deposited before FIB fabrication to prevent the near surface structure from Ga ion etching. Two trenches were milled away in such a way that a thin wall is left behind between the two trenches, the wall being thin enough to be electron-transparent when tilted by 90 degrees. The specimens thus prepared were examined in either a JEOL JEM-200CX or a Hitachi H-800 electron microscopes at accelerating voltage of 200kV.

Results and discussion

The recess with an area 10x5 micrometer squares was fabricated to electron transparency in 3 hours by FIB system. This area is wide enough for the whole depth of the irradiated region to be observed.

Figure 1 shows a typical example of near surface microstructure of the irradiated specimens. Two bands of strain contrasts are observed in the region of about 1.8 and 1.3 micrometer away from the surface. The decrease in contrast of bend contours at the bands indicates that the ion irradiation lowered degree of crystallinity. Figure 2 shows the dpa depth profiles calculated using the TRIM98 code. This indicates the depths of the maximum dpa were about 1.7 micrometer for oxygen ions and protons and 1.3 micrometer for helium ions, being in good agreement with the damage distribution observed in Fig.1. At higher magnification the dark-field micrograph of the damaged region in Figure 3 shows high density of small defects induced by the ion beam irradiation.

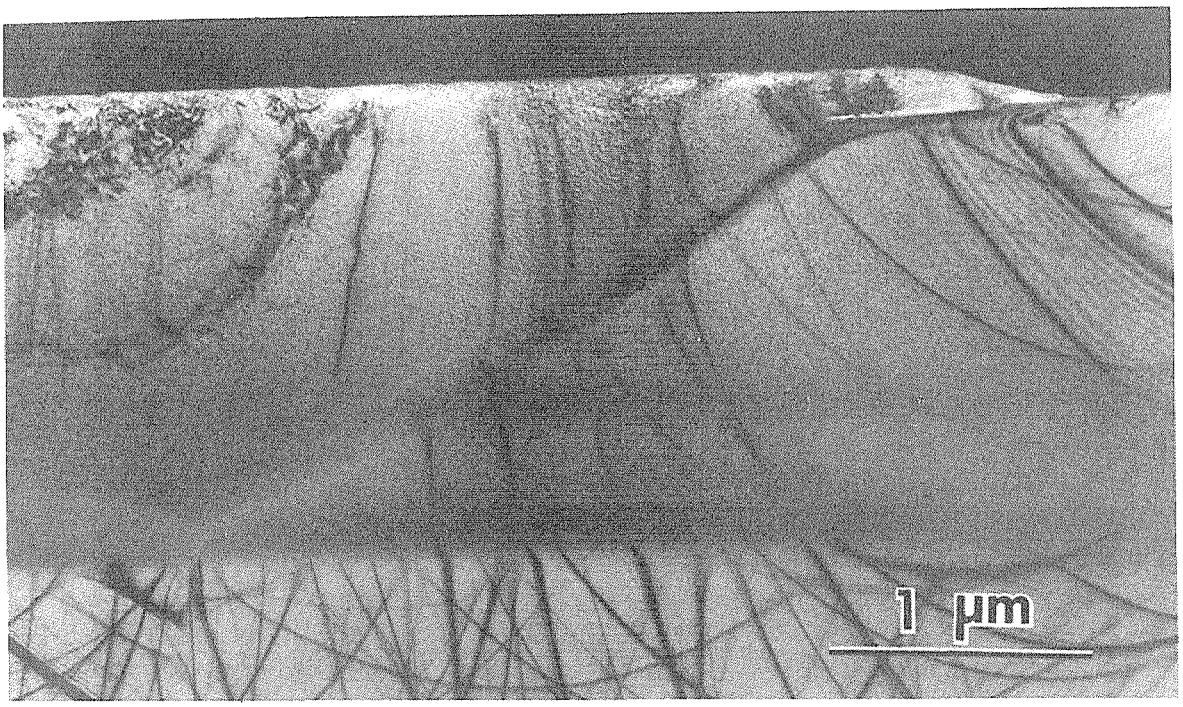

Figure 1 Cross-sectional TEM micrograph of AlN irradiated with oxygen ions, helium ions and protons.

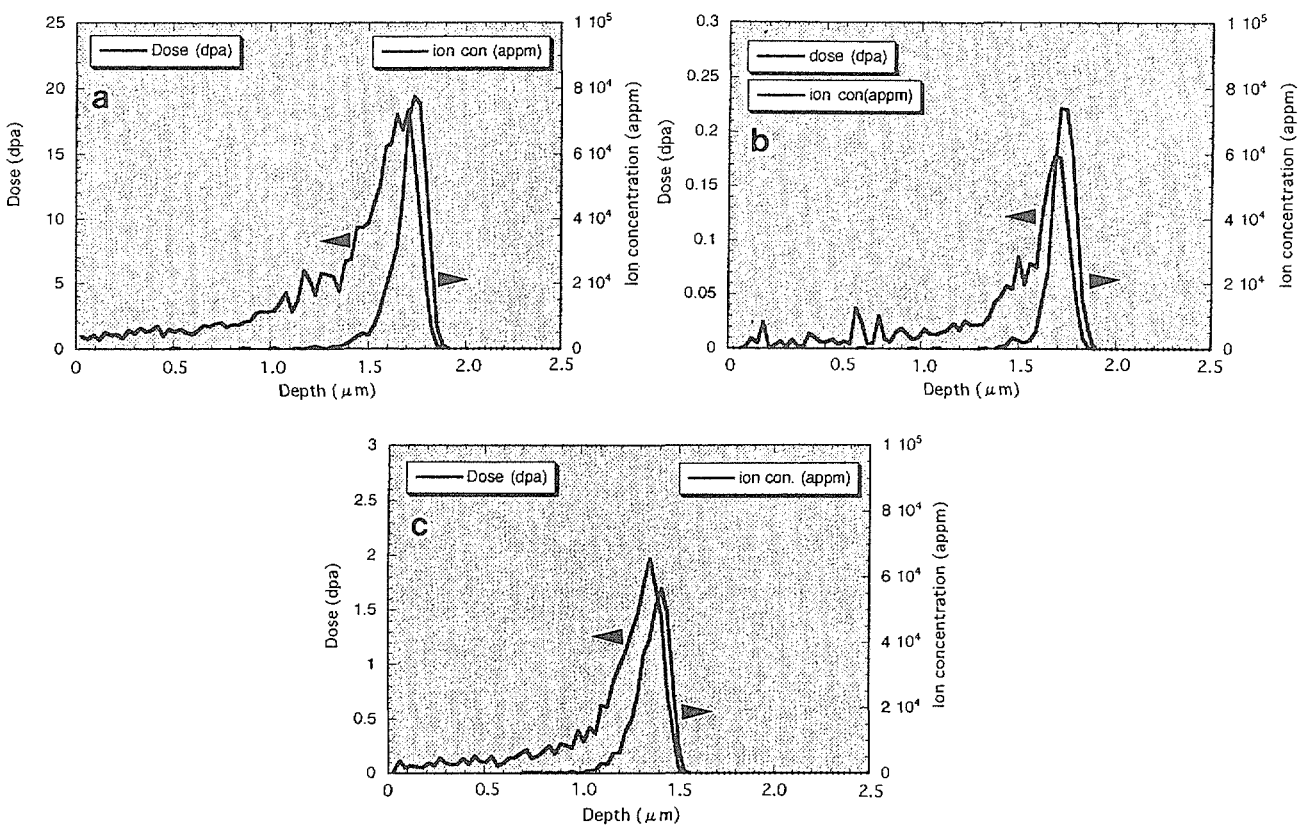

Figure 2 Dpa and ion concentration profiles calculated as function of depth (x, μm) using TRIM 98 code for 2.4MeV O+ (a), 250keV H+ (b) and 450keV He+ (c).

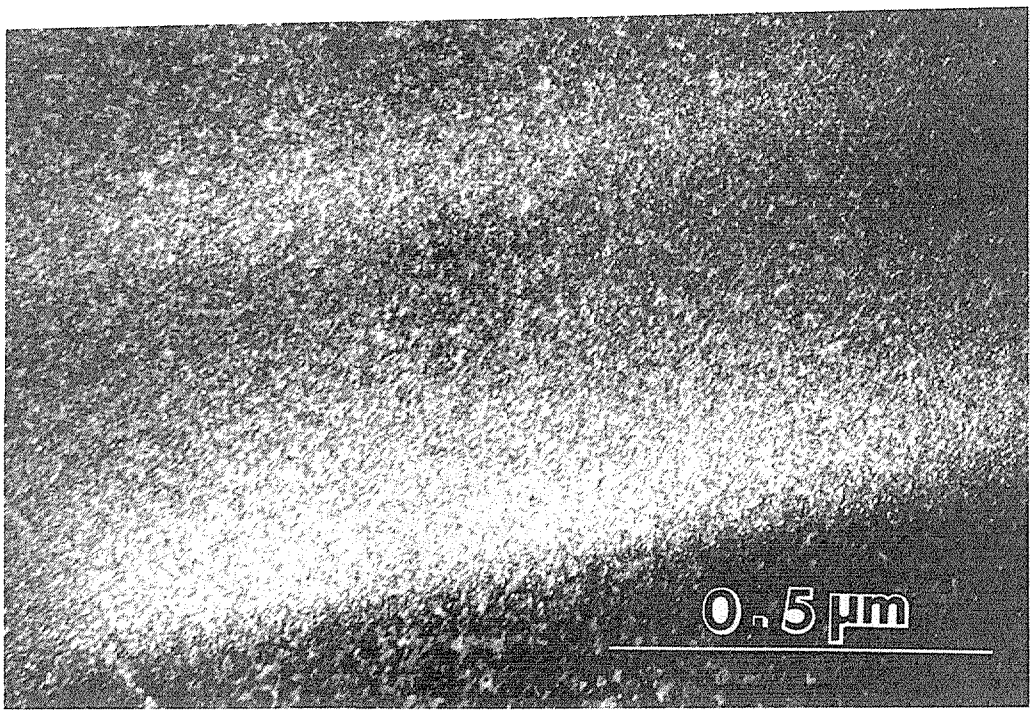

Figure 3 Dark-field micrograph of damaged region.

4.12 Microstructural and Microchemical Evolution in Vanadium Alloys under Ion Irradiation

N. Sekimura[1], T. Iwai[2], Y. Arai[1], S. Yonamine[1], H. Kakiuchi[1],
S. Nakamura[1], S. Hamada[3] and Y. Miwa[3]
Department of Quantum Engineering and Systems Science, Univ. of Tokyo[1]
Research Center for Nuclear Science and Technology, Univ. of Tokyo[2]
Materials Research Division, JAERI/Tokai[3]

1. Introduction

Vanadium alloys are attractive candidates for fusion blanket structural materials because of their high temperature mechanical properties and low induced radioactivities after neutron irradiation. However, it was recently shown that moderate additions of undersized solutes such as Fe, Cr and Si can induce swelling rates that are much higher than those observed in fcc alloys [1-3]. Fe additions in particular appear to induce large swelling without any indication of saturation occurring. The origin of this behavior and its relationship to other fusion-relevant irradiation variables are not yet known in detail.

In this study, microstructural and microchemical changes in V-5Cr-5Ti, V-5Cr and V-5Fe alloys under ion irradiation were examined focusing mainly on the effect of He generation on swelling and microstructural evolution.

2. Experimental

Three kinds of vanadium alloys were prepared by arc-melting in an inert gas atmosphere and annealing at 1273 K for 3.6 ks in high vacuum, followed by rapid cooling. They were irradiated with Ni^{3+} ions to 30 dpa at the damage peak depth with simultaneous implantation of helium by He^{+} ions at He(appm)/dpa ratio of 5 in the TIARA facility. Irradiation temperatures were 793 and 873K.

Irradiated surface of the specimens were removed by electropolishing and back-thinned to perforation to observed damage peak depth region by TEM (Transmission Electron Microscope). Microchemical distributions of irradiated specimens were also measured by EDS (Energy Dispersive X-ray Spectroscopy).

3. Results and discussion

Cavities were formed in irradiated V-5Fe at all the irradiation conditions. Cavities grow larger at 873K. Co-implanted helium was found to affect distributions of cavities in this alloy. Cavities were uniformly distributed in the matrix in the dual beam irradiated specimens, whereas single beam irradiation produces high density of cavities near the grain boundaries.

No cavity formation was detected in V-5Cr-5Ti irradiated only with Ni ions at 793 and 873K. At 873K, high density of V_2C precipitates were observed in the matrix of V-5Cr-5Ti and defect free zone was observed near the grain boundaries. Fig. 1 shows measured microchemical evolution in V-5Cr-5Ti irradiated with Ni ions at 873K. Ti atoms has their peaks at 50-100nm from the grain boundaries. These are considered to come

from the binding of Ti atoms with O (oxygen) atoms which are the major interstitial impurities in vanadium alloys. No segregation of Cr atoms were observed whereas Cr is undersized solute in vanadium alloys. At 520 Åé, no distinct segregation of solute atoms were detected.

Helium atoms produced by transmutation reactions in vanadium alloys under fusion conditions can enhance swelling as studied by tritium-trick method and DHCE (Dynamic Helium Charging Experiments). In this study, helium is also found to increase dislocation density of irradiated V-5Cr-5Ti alloys. Table 1 compares measured dislocation density in V-5Cr-5Ti irradiated with dual ions and single ions at 793 and 873K to 30 dpa. It was also found that Ti addition to V-5Cr reduces dislocation evolution.

References

1. H. Matsui, D. S. Gelles and Y. Kohno, Proceedings 15th ASTM International Conference on Effects of Radiation in Materials, ASTM STP 1125 (1992) 928.
2. H. Nakajima, S. Yoshida, Y. Kohno and H. Matsui, J. Nucl. Mater. 191-194 (1992) 952.
3. F. A. Garner, D. S. Gelles, H. Takahashi, S. Ohnuki, H. Kinoshita and B. A. Loomis, J. Nucl. Mater. 191-194 (1992) 948.

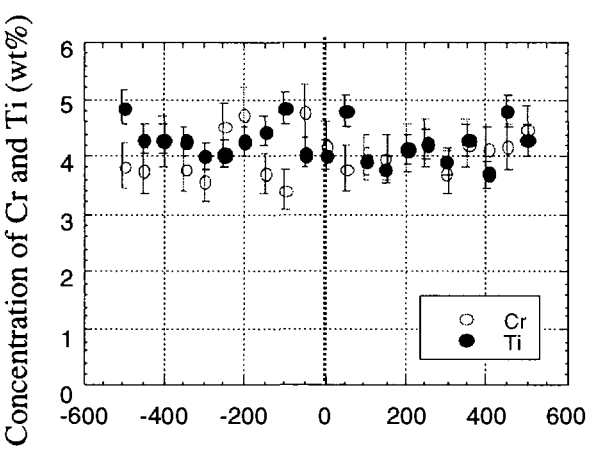

Fig. 1 Solute Distributions in V-5Cr-5Ti irradiated with Ni ions at 873K to 30 dpa.

Table 1 Dislocation Density in V alloys irradiated with Heavy Ions to 30 dpa (m^{-2}).

Irradiation Temp.	520℃	600℃
V-5Cr-5Ti single beam	1.8×10^{15}	1.7×10^{15}
V-5Cr-5Ti dual beam	2.1×10^{15}	2.0×10^{15}
V-5Cr dual beam		2.4×10^{15}

4.13 Void Formation in Heavy-ion irradiated Metals

Y. Shimomura, I. Mukouda, T. Iiyama, K. Noda*, Y. Katano*, T. Nakazawa* and D. Yamaki*
Applied Physics and Chemistry, Faculty of Engineering, Hiroshima University
*Material Innovation Laboratory, Department of Materials Science and Engineering, JAERI/Tokai

1. Introduction

When a metallic ions of high energy are injected from surface into metals, ions stop at the position corresponding to their range distance where a large number of point defect are generated.For heavy metal ions whose energy is 1 MeV, the range distance is almost 1μm. In many ion-irradiation experiments, damage structure is examined by transmission electron microscopy (TEM) with sample back-thinned from the backward side of ion entrance surface [1]. Another novel technique to observe a depth distribution of damage structure in ion irradiate specimens is to adherent on irradiated surface the same kind of metal by electro-plating [2]. Thin foil is prepared from metal foils having surface normal to the original surface. This method is not so easy for the observation of damage distribution along ion injected direction. We apply the FIB (Focused Ion Beam) technique to prepare the TEM specimen of irradiated specimens. The formation of voids in ion-irradiated Fe-Cr-Ni was successfully observed in the present work. Moreover FIB thinning technique can be utilized for TEM specimen preparation of all kinds of materials.

2. TEM Foil Preparation Technique

When we applied the thinning technique with Focussed Ion Beam (FIB) device at the first time at the room temperature, it was found that serious FIB damage is formed throughout specimens [3]. A specimen is a half circle platelet as shown in Fig. 1(a). Ion irradiation was carried out along the direction shown by arrow. After ion irradiation specimen was cut with FIB as shown in Fig. 1(b) for the TEM observation. To ensure the perfect beam exposure on specimen especially on dual beam irradiation, the specimen arrangement on the irradiation holder was carefully made as shown in Figs. 2(a) and 2(b). The detail of specimen holder was reported in the previous annual report by the present authors[3]. The FIB technique makes possible to prepare TEM specimens to an extended area such as 20μm(in width) x 5μm(in depth) x 0.1μm(in thickness). A high concentration of interstitials are generated during FIB thinning and aggregates to their clusters. These interstitial clusters due to FIB damage are the almost same size with those formed by high energy ion irradiation. To observe point defect clusters formed by ion irradiation, the formation of observable size of FIB damage have to be suppressed. We have developed "Cryotransfer FIB" technique in which an ion irradiated specimens at high temperature is thinned by FIB at 100 K and then transferred to the electron microscope without a serious contamination on surface and warming up of specimens. Figs. 3(a) and (b) show the cryotransfer FIB device which is mounted on the FIB of Seiko Instrument Inc. type SMI9200 and a cryotransfer specimens holder. The Cryo-FIB makes possible to observe ion damage formation which depend on the depth of specimens. This is due to the suppression of interstitial clustering which are formed by FIB thinning.

3. Experimental Results and Discussion

Fig. 4 shows voids in Fe-15Cr-20Ni alloy which was irradiated with (a) 5MeV Ni^{2+} ions and (b) dual beam of 5MeV Ni^{2+} ions and 0.6MeV He^{+} ions. Irradiation was carried

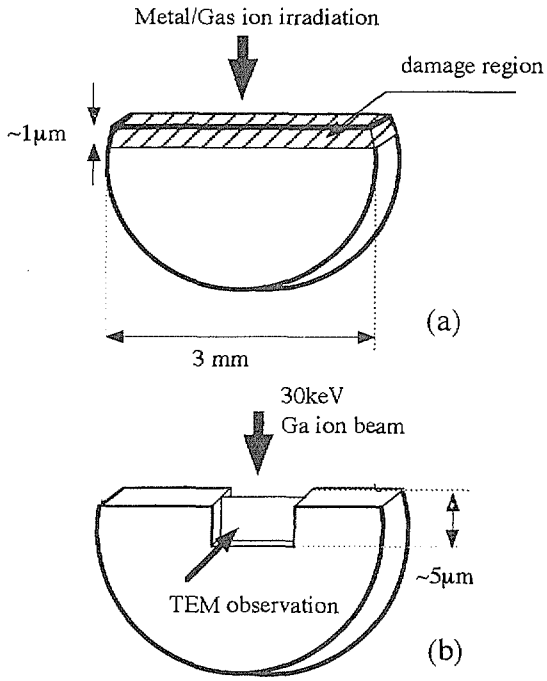

Fig. 1 The specimen configration of irradiation and FIB thinning.

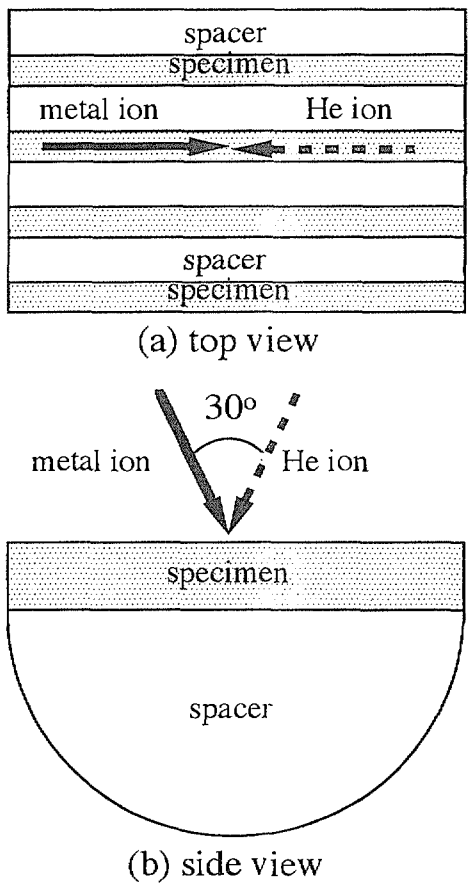

Fig. 2 The specimens arrangement on the irradiation holder.

out as-received specimens and residual-gas-free one at the same time. Residual-gas-free specimens were prepared by melting in highly evacuated vacuum as 10^{-5} Pa. The number density of voids in specimens irradiated with dual beam is larger than that of single beam. Experimental results can be summarized as follows: (1) Voids are observed in irradiated Fe-Cr-Ni with both dual beam and Ni ion only. (2) The number density of voids was much higher in specimens with dual beam irradiation. This indicates that helium atoms make important contribution on the formation of voids. (3) With single beam irradiation of Ni ion, the number density of voids in residual gas free specimen is smaller than that of as-received specimen. A complete suppression of void formation was not observed for residual gas free specimen irradiated with Ni ions only. (4) There was three significant depth zone at which voids form remarkably. One is the near entrance surface. Second one is the most significant that a large number of voids forms. Third one is the deepest isolated zone of void formation.

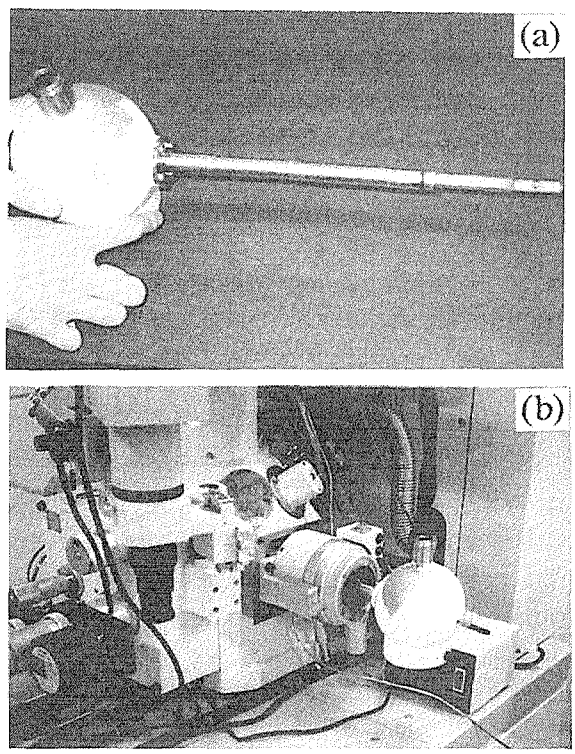

Fig. 3 Cryotransfer FIB device which is mounted on SMI9200.

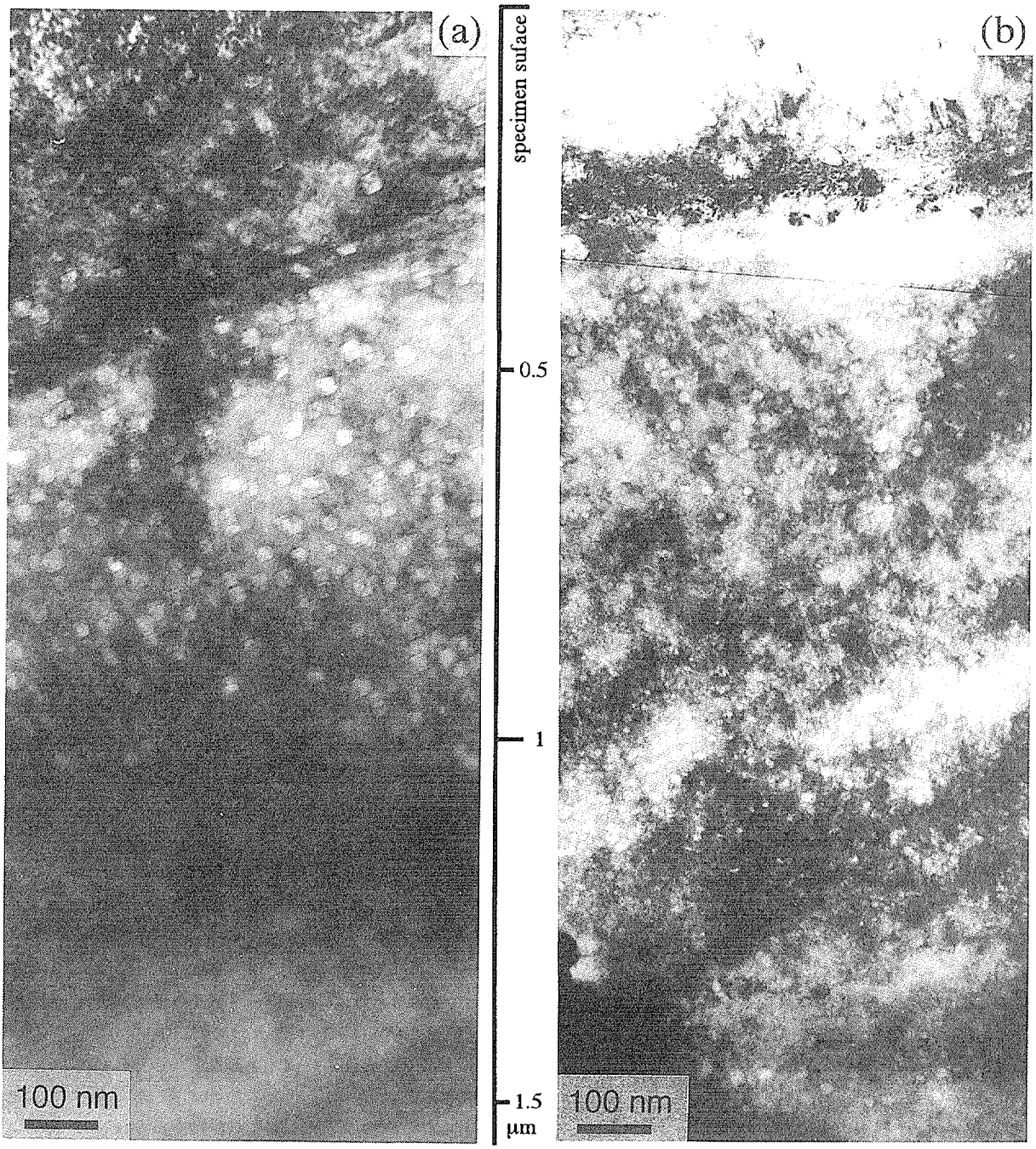

Fig. 4 Voids in Fe-15Cr-20Ni alloy which was irradiated with (a) 5MeV Ni^{2+} ions (b) 5MeV Ni^{2+} and 0.6MeV He^{+} ions simultaneously.

The second one is due to the damage formation of Ni ion irradiation. The third one may be void formation related to the helium ion stopping.

The present results show that a helium atom accelerate void formation and even in high evacuated residual gas free voids were observed in Ni ion irradiated Fe-Cr-Ni.

4. References

[1] K. Farrell: Radiation Effects 53 (1980) 175.

[2] S. J. Zinkle and R. L. Sindelar: Nucl. Inst. Meth. in Phys. Res. B16 (1986) 154.

[3] Y. Shimomura, I. Mukouda, K. Noda, D. Yamaki and S. Hamada: JAERI TIARA Ann. Rep. 5 (1996) 113.

4.14 The structural analysis of the surface of Nb^+-implanted TiO_2 crystal by means of RBS/Channeling method

Yasushi Aoki, Shunya Yamamoto, Kazumasa Narumi
and Hiroshi Naramoto
Dept. of Materials Development, JAERI-Takasaki

I. Introduction

Recently, ion implantation of insulators aiming at fabrication of optical devices has been attracting much interest. It is based on formation of compounds and fine particles in the surface layers of insulators. These phenomena are strongly dependent on the nature of substrates. TiO_2 is known as an oxide semiconductor and has excellent properties for a photo-catalyst, a gas sensor, etc. Though the ion implantation has been examined as a tool for improving the semi-conducting properties, the fundamentals of this technique which depends largely on the nature of TiO_2 substrate, such as annealing behaviors after implantation, are not clearly understood yet.

We have reported the last year[1] on the difference of defect formation between different implantation temperatures and of the annealing behaviors and on the location of implanted species for Nb implantation to the dose of ca. 1×10^{16} /cm^2. In this report, the damage accumulation to amorphization and the annealing behaviors for Nb-implanted TiO_2 with the higher dose of about 1×10^{17} /cm^2 are discussed below.

II. Experimental

Single crystalline TiO_2 synthesized by the Verneuil method (Nakazumi Crystal Lab.) was used as a implantation substrate. The main planes were normal to the <001> crystallographic axis and polished in optical grade. All samples were annealed at 600°C in air for 4 hours prior to implantation. Nb ion implantation was done at room temperature and at 130K with a 400 kV ion implanter of TIARA facility. The implanted samples were annealed isochronally for 1 hour in a aluminum furnace open to the air with increasing temperature from 300°C to 1200°C. At each annealing step, the atomic structure of the implanted layer was analyzed by 2MeV He^+ RBS/Channeling with using a 3MV single-ended accelerator of TIARA.

III. Results and Discussion

Fig. 1 shows the RBS/Channeling spectra for TiO_2 (001) crystal implanted at room temperature with 300keV Nb at the incident angle of 40°. The maximum dose (4×10^{16}/cm^2) is roughly the threshold for amorphization of TiO_2 crystal under ion implantation of Nb^+, while the threshold of 65K implantation was $1 - 5 \times 10^{15}$ /cm^2 in a similar experiment.

When 400keV Nb^+ ions were implanted into TiO_2 single crystal to the dose of 1.5×10^{17} /cm^2, the implanted surface layer became amorphous. In the sample suffered from isochronal annealing in air, at 500°C Nb had begun to react with oxygen to form oxides and the oxidation completed at 600°C. The diffusion of Nb over a long range occurred to the surface at 800°C and at 1000°C the diffusion into the bulk was also seen.

Finally, after 1200°C annealing, Nb atoms were homogeneously distributed in the surface layer at least 2000Å thick. The concentration of Nb atoms were about 1 % as an atomic ratio of Nb/Ti, as seen in Fig. 2. Almost all of Nb atoms were found to occupy the Ti sublattice sites by comparing the RBS yields obtained in <001> aligned and random geometries. Furthermore, the angular scan

measurements around <001> and <111> axes gave the same critical angles for both RBS yields of Ti and Nb. The ionic radii of Ti^{4+} and Nb^{4+} in rutile structure are 0.74Å and 0.72Å, respectively[2]. Therefore, NbO_2-TiO_2 type mixed oxide can be considered to form. It is supported by the fact that the XPS spectrum of the sample gave the chemical shift of Nb $3d_{5/2}$ peak corresponding to that of Nb^{4+}. The same behaviors were also observed for a TiO_2 crystal implanted at 130K. It indicated that the amorphous states formed by room temperature implantation and by low temperature implantation can not be distinguished as far as observing the thermal annealing behaviors.

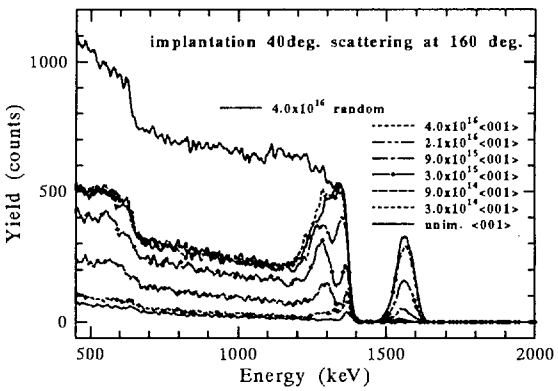

Fig. 1 The 2MeV $^4He^+$ RBS/Channeling spectra of TiO2(001) single crystal implanted with 300keV Nb^+ at the incident angle of 40°.

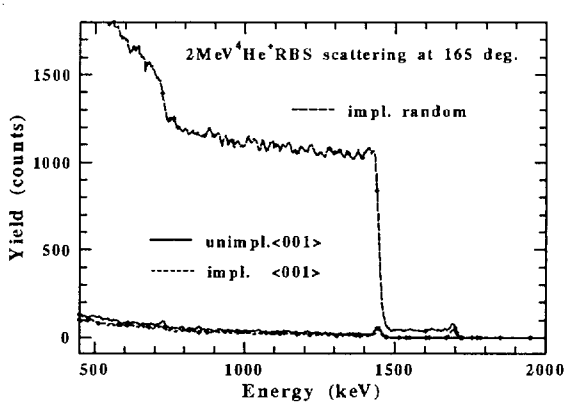

Fig. 2 The RBS spectra of TiO_2(001) single crystal implanted with 400keV Nb^+ to the dose of 1.5 x 10^{17} ions/cm^2 and annealed in air at 1200°C.

References

1) Y.Aoki, S.Yamamoto, H.Takeshita and H.Naramoto, Jaeri-Tiara Annual Report 1995(Vol.5) pp.116-117 (1996).
2) F.Gervais and W.Kress, Phys. Rev. B31, pp.4809-4814 (1985).

4.15 Amorphization in Sapphire Induced by Ion Irradiation

Hiroaki Abe, Hiroshi Naramoto and Shunya Yamamoto

Department of Materials Development, JAERI, Takasaki, Gunma 370-12, Japan

1. Introduction

Many of crystalline materials can be amorphized under irradiation with ions [1]. Early observations of amorphization in sapphire were done under irradiation with heavy ions, such as Cr, Nb and Kr with energy from 40 to 475 keV, in which effects of displacements and that of implanted ions are inseparable. Therefore, for the purpose of clarifying the damage effects on the irradiation-induced amorphization, we take irradiation with relatively high energy ions in thin films in this work, so that most of ions penetrate the target. One of objective of this work is to get insights into the effects of radiation damage on the irradiation-induced amorphization in sapphire. The effects of cascades, bunches of atomic displacements, will be discussed. The other is to clarify defect kinetics. Recrystallization is enhanced due to thermally-activated vacancy-interstitial recombination or irradiation-induced diffusion, both of which result in increase in dose-to-amorphization.

2. Experimental Methods

High-purity [0001] and [11$\bar{2}$0] oriented sapphire single crystals with an optical grade polish were cut into disks with 3 mm in diameter. They were ground to 50 μm in thickness, and dimpled to 10~20 μm in thickness. The dimpled surface was finally polished with 1 μm diamond paste to optical grade. The disks were, then, ion milled with 7 keV argon ions until a hole could barely be seen, followed by milling with 4 keV argon ions to remove damaged regions. The thin regions (less than 100 nm) of sapphire were taken in the experiments so that most of ions penetrate the specimen.

The TEM-Accelerators Facility at JAERI-Takasaki [2] was used in this work. Irradiation with O^+, Ar^{2+}, Kr^{2+} and Xe^{3+} was performed with accelerating voltage of 300 kV with ion fluxes of 10^{17}~10^{18} ions/m^{2}s at temperature from 90 to 300 K. Angles between the ions and the foil normal were about 30 degrees. To avoid the effects of simultaneous irradiation with ions and electrons, the electron beam was out of sample during ion irradiation. The amorphization fluence is defined as the minimum fluence at which only halo rings observable on the electron diffraction pattern from the selected area of 0.2 μm in diameter on a specimen.

TRIM-95 [3] calculations were performed for all ions and energies to estimate dose-to-amorphization in dpa (displacements per atom). Sample thickness of 100 nm and the displacement threshold energies (E_d) of 40 eV for both oxygen and aluminum were used. The rate of residual ions within the thickness are 1.3 and 2.7 % for 900 keV Xe and 600 keV Kr ions, respectively.

3. Results and Discussion

Selected area electron diffraction technique was taken to confirm the crystalline-to-amorphous transformation. In sapphire irradiated with 600 keV Kr^{2+} and 900 keV Xe^{3+} ions, diffuse halo rings, associated with the presence of amorphous regions, were observed, while the intensity of the diffraction spots from the remaining crystalline regions decreased with irradiation time and eventually disappeared. In case of irradiation with argon and oxygen ions, no amorphization was detected at 90 K up to dose of 50 dpa, while

onset of amorphization, defined as both spots and faint halo rings observable, was detected. When [11$\bar{2}$0] sapphire was irradiated with 600 keV Ar^{2+} ions at 130 K, planar defects on (10$\bar{1}$0) planes were formed.

Dose-to-amorphization in displacement per atoms (dpa) is defined as the dose at which the diffraction spots disappear and only the halo rings are observed. Figure 1 shows temperature dependence of the dose-to-amorphization in sapphire irradiated with 900 keV Xe^{3+} and 600 keV Kr^{2+} ions. Sapphire was amorphized by Xe and Kr irradiation to dose of about 3 and 4 dpa, respectively, at temperature from 90 to 160 K. The dose-to-amorphization, then, increased to 8 dpa, followed by exponential increase at temperature higher than 200 K. The apparent threshold temperature depends on ion flux and mass of projectile, whilst dose rate dependence was not observed at temperature from 90 to 200 K.

Table 1 is a summary of the experimental results together with range, stopping powers and energy densities of cascades. The range and the stopping powers were taken from tables [3]. The electronic and the nuclear stopping powers increase as increasing mass of projectiles, while the electronic stopping powers of Xe and Kr are identical. Because of large difference between Xe and Kr in the dose-to-amorphization even at 90 K as shown in figure 1, it is presumed that atomic recoils, nor electronic excitation, induces amorphization. Irradiation with light particles could not amorphize the sample, therefore cascades are predominant for the irradiation-induced amorphization. Energy density of cascades is one of the parameters describing nature of cascades [6]. Values of the energy density were estimated by computer simulation using TRIM. Energy density of 50-keV-Al cascades in sapphire is taken into account as an example. The generation rates of cascades with energies from 30 to 50 keV are about 0.008 and 0.002 for 900keV Xe and 600 Ar, respectively. The estimated energy density is 8.4×10^{-1} eV/atom, being high enough that the energy spikes are expected to be significant [6].

The stability of the amorphous regions is strongly influenced by kinetics of point defects. Unfortunately, defect kinetics below room temperature is poorly studied [7]. Decrease in zeroth moment of 379 nm emission band, assigned as oxygen di-vacancy, was observed at temperature from 100 to 250 K in [10$\bar{1}$0]-type proton-irradiated sapphire. The decrease is a non-radiative decay process with an activation energy of 0.057 eV. Di-vacancies are unstable at the temperature and they decompose to vacancies or recombine with close interstitials. When electrons were simultaneously exposed during ion irradiation, the area retained crystallinity. Subsequent irradiation with electrons at 90 K results in annealing of the damaged regions. The results indicate that defect annealing is assisted by electronic excitation and/or momentum transfer below the displacement threshold.

Table 1. Summary of results and calculated data. S_n, S_e denote electronic and nuclear stopping powers in units of eV/nm, respectively.

foil normal	projectile	results	range [nm]	S_e	S_n
[0001], [11$\bar{2}$0]	900keV Xe	amorphous	197	1.3×10^2	3.0×10^2
[0001], [11$\bar{2}$0]	600keV Kr	amorphous	191	1.2×10^2	1.7×10^2
[11$\bar{2}$0]	600keV Ar	planar defects	776	5.7×10^1	1.9×10^1
[11$\bar{2}$0]	300keV O	planar defects	374	8.6×10^1	7.8×10^0

4. Conclusions

At least four stages in ion-induced amorphization were observed below 300 K: (1) accumulation of heavily damaged regions (cascades) induces amorphization at temperature from 90 to 160 K, (2) annealing of close Frenkel pair within cascades may occur at temperature from 160 to 200 K, resulting in increase of dose-to-amorphization; (3) annealing of point defects frequently occur at temperature higher than 200 K attributable for the exponential increase in the dose-to-amorphization and for the ion-flux dependence of the apparent threshold temperature, and (4) sapphire retains its crystallinity at temperature higher than 250~300 K. Since the early observation reports amorphization even at room temperature, at which no amorphization was detected in this work. Therefore, effect of implanted ions is non-trivial for the amorphization at relatively high temperature in sapphire.

References

[1] H. M. Naguib and R. Kelly, Rad. Eff. 25 (1975) 1.

[2] H. Abe, H. Naramoto, K. Hojou, S. Furuno, JAERI-Research 96-047.

[3] J. F. Ziegler, J. P. Biersack and U. Littmark, 'The stopping and Range of Ions in Solids' (Pergamon, 1985).

[6] L. M. Howe and M. H. Rainville, Nucl. Instrum. Methods B19/20 (1987) 61.

[7] L. S. Welch, A. E. Hughes and G. P. Pells, J. Phys. C13 (1980) 1805.

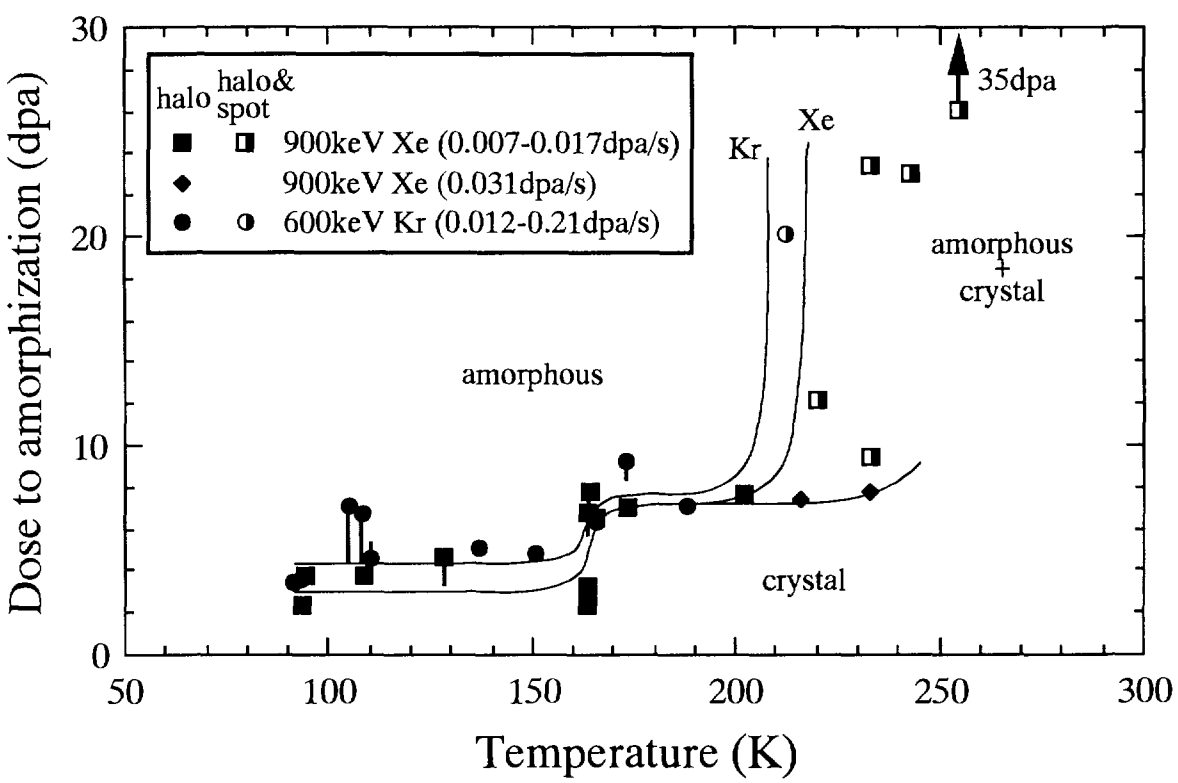

Figure 1. Temperature dependence of the dose-to-amorphization in c-plane sapphire irradiated with 600 keV Kr^{2+} and 900 keV Xe^{3+} ions. Note that no amorphization was detected under irradiation with 600 keV Ar^{2+} nor 300 keV O^{+} ions.

4.16 MICROSTRUCTURE EVOLUTION OF OXIDE CERAMICS UNDER CONCURRENT IRRADIATION WITH IONS AND ELECTRONS

K. Yasuda, R. Morisaki, M. Ohmura, C. Kinoshita, H. Abe* and H. Naramoto*

Department of Nuclear Engineering, Kyushu University
Hakozaki, Fukuoka 812-81, Japan
* Department of Materials Development, Japan Atomic Energy Research Institute,
Takasaki, Gunma 370-12, Japan

Introduction

Radiation with neutrons, ions, electrons and γ-rays in fusion reactors introduces primary knock-on atoms (PKAs) with a wide variety of energies and also ionization in materials. Synergistic irradiation effects with such particles are of importance to understand the fundamentals of point defect kinetics in fusion materials. We have investigated the role of irradiation spectrum on the nucleation and growth process of defect clusters in some oxide ceramics [1-3], which have potential uses as RF windows, insulators and magnetic coils in fusion reactors. Concurrent irradiation with ions and electrons in transmission electron microscopes interfaced with ion accelerators could be a powerful method to investigate the irradiation spectrum effects. They give us a wide variety of irradiation spectra, such as ratios of displacement damage and ionization, displacement cascades and isolated Frenkel defects, and enable us in situ observations. In this report, we present our recent progress of the concurrent irradiation study in TEM-accelerator facilities on stoichiometric and nonstoichiometric magnesium aluminate spinel and alumina.

Experimental

Single crystals of stoichiometric and nonstoichiometric magnesium aluminate spinel ($MgO \cdot nAl_2O_3$) and α-alumina (Al_2O_3) were thinned by ion milling and annealed at 1670 K for 2 hours in air. These samples were irradiated concurrently with 200 keV electrons and 300 keV ions (He^+, O^+, Mg^+, Ar^+) at 870 K in a TEM-accelerator facility in TIARA (Takasaki Ion Accelerators for Advanced Radiation Application) at JAERI (Japan Atomic Energy Research Institute) [4]. Microstructure evolution was recorded on films under irradiation.

Results and Discussion

Table 1 summarizes the defect clusters and microstructural features developed in stoichiometric spinel ($MgAl_2O_4$) under concurrent irradiation with 300 keV ions and 200 keV electrons at 870 K. Results under concurrent irradiation with 30 keV ions and 1000 keV electrons [1] are also shown in table 1 for a comparison. The preferential formation of bubbles is observed under concurrent irradiation with 300 keV He^+ ions and 200 keV electrons, though concurrent irradiation with 300 keV O^+ or Mg^+ ions and 200 keV electrons retards the formation of the interstitial loops inside the focused electron beam and promote the growth of loops at the periphery of the electron beam. A typical example of bright field images in spinel at 870 K is shown in fig. 1 irradiated concurrently with 300 keV O^+ ions and 200 keV electrons at relatively thin region (about 50 nm in thickness). Dislocation loops are seen only at the periphery of the focused electron beam, though no dislocation loops are nucleated at such a thin region solely with O^+ ion irradiation. This is suggesting us that interstitials introduced with O^+ ion irradiation are transported from the center toward the outside of the electron beam under 200 keV electron irradiation, enriching interstitials at the periphery of the electron beam. Possible mechanisms for the interstitial (cation) diffusion are not through displacement damage but are due to ionization enhanced diffusion [5] and/or radiation induced diffusion, because 200 keV electrons hardly produce displacement damage in spinel. No significant differences in microstructure under concurrent irradiation

with 30 keV ions and 1000 keV electrons in table 1 support the important role of soft irradiation spectrum for the concurrent irradiation effects.

In the nonstoichiometric spinel ($MgO \cdot 2.4Al_2O_3$) and alumina, no significant deference is seen in microstructure both inside and outside the focused electron beam: a high density of loops is observed under concurrent irradiation with 300 keV O^+ ions and 200 keV electrons at 870 K. Further experiments are now in progress for understanding the different phenomena in various oxides in terms of the production rate and the stability of the nuclei of dislocation loops under concurrent irradiation.

Table 1 A summary of the microstructure in $MgAl_2O_4$ at 870 K under concurrent irradiation with ions and electrons.

ions	electrons	inside the electron beam	outside the electron beam	featuters
300 keV He^+	200 keV e^-	bubbles (voids)	bubbles (voids)	high density of large defects inside the e-beam
300 keV O^+	200 keV e^-	suppression of loops	dislocation loops	thick region
300 keV O^+	200 keV e^-	dislocation loops	no defect clusters	thin region: loops only at the periphery of e-beam
300 keV Mg^+	200 keV e^-	suppression of loops	dislocation loops	large loops at the periphery of e-beam
30 keV He^+	1000 keV e^-	dislocation loops	dislocation loops	high density of loops inside the e-beam
30 keV Ar^+	1000 keV e^-	dislocation loops	dislocation loops	
30 keV Xe^+	1000 keV e^-	dislocation loops	dislocation loops	

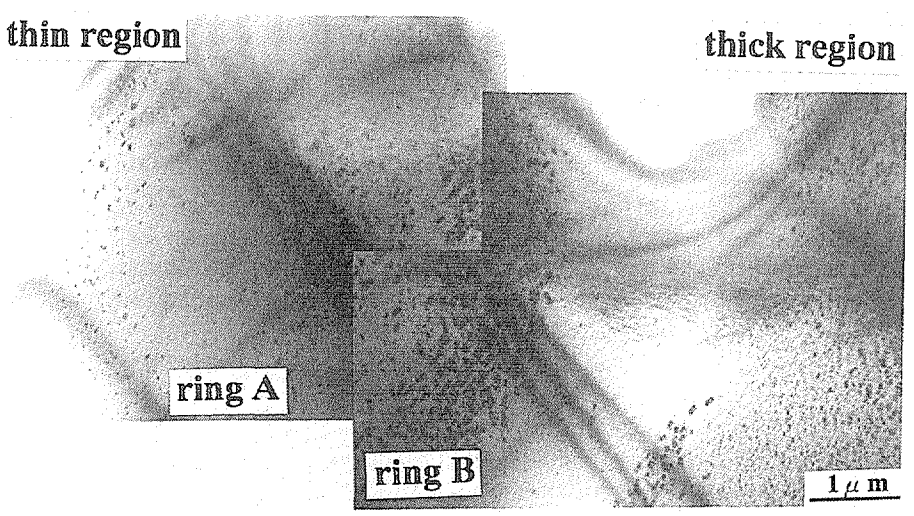

Fig.1 A bright field image in $MgAl_2O_4$ under concurrent irradiation with 300 keV O^+ ions and 200 keV electrons. The ring A and ring B correspond to the radius of the focused electron beam under concurrent irradiation condition and that for recording the microstructure on films. O^+ ion fluence was $1x10^{19}$ions/m^2.

References

[1] C. Kinoshita, H. Abe, S. Maeda and K. Fukumoto, *J. Nucl. Mater.*, **219**, 1995, 152.
[2] K. Yasuda, Y. Watanuki, C. Kinoshita and H. Abe, Annual Report, HVEM Lab., Kyushu University, **19**, 1995, 11.
[3] K. Yasuda, R. Morisaki, C. Kinoshita, H. Abe and H. Naramoto, Proc. of 7th int. symp. on Advanced Nuclear Energy Research, Takasaki, Japan, 1997, 384.
[4] H. Abe and H. Naramoto, K. Hojou, S. Furuno and T. Tsukamoto, Proc. of 7th int. symp. on Advanced Nuclear Energy Research, Takasaki, Japan, 1997, 365.
[5] S.J. Zinkle, *J. Nucl. Mater.*, **219**, 1995, 113.

4.17 Effect of temperature and stress on radiation-induced amorphozation in poly-Silicon

S.Ohnuki, T.Suda, N.Kawakami, M.Takeda,
H.Abe* and H.Naramoto*
Fuculty of Engineering, Hokkaido University
*Department of Materials Development, JAERI

1. Introduction

Irradiation and implantation of high energy ions are useful techniques for surface modification of advanced materials. During these process ion beams can produce nonequiliblium phases include amorphous phases, as well as irradiation-induced point defects and impurities with high concentration. In the case of Si ion implantation easily produces amorphous phase around ambient temperature, where its details of the formation mechanism and the thermal stability have been still unknown. On this point of view it can be expected that the formation is strongly depended on temperature, stress, impurities and internal defects such as grain boundaries. In this study, poly-Si was irradiated by inert gas ions at several conditions, and the major factors for irradiation-induced amorphization were studied.

2. Experimental

Poly-Si was deposited on (100) Si wafer with the thickness of 150 nm by CVD method. For controlling grain size, the pieces encapsuled in vacuum were annealed for 72, 168 and 336 hrs at 1173 K. After coating on the poly-Si surface by anti-acid racker, oxyside film was resolved on the Si wafer. Poly-Si film was scooped on Cu or Mo grid. For evaluating critical dose the irradiation of 300 keV Ar^+ was performed in TIARA facility, and 1.5 MeV Xe^+ was used for the in-situ observation in ANL Tandem/HVEM facility. For stress experiment, a tensile heating specimen holder was used in microscope. Table 1 shows experimental details, in which All of the experiments were performed in electron microscope under in-situ condition.

3. Result and Discussion

The critical dose of poly-Si irradiated by 300 keV Ar^+ was showed in Fig. 1 as the function of irradiation temperature and grain size, where the critical dose was defined by the disappearing lying patterns from crystalline in electron diffraction. The dose increased exponentially with temperature. At low temperatures (room temperature - 373 K), grain size had no effect on the dose. At high temperatures (373 - 473 K), the dose increased with increasing of grain size, where it was confirmed the preferential amorphization occurred from grain boundaries.

The preferential amorphization near grain boundary should be occurred by following factors: (1) imbalance of point defect concentration at local area [1]; faster mobile defect can sink to grain boundary which causes the increasing in concentration of other type defect. (2) local stress; on and near grain boundary, atomic bonding should distorted, which assists amorphization. (3) impurity segregation [2]; on grain boundaries, many impurities can segregate, which cause lattice distortion and local amorphization. Based on those possible reason, the experimental

result that the critical dose increased with increasing of grain size will be explained as follows: the total strain energy and/or amount of impurities will decrease with increasing of grain size, because the fraction of grain boundary area in unit volume decrease with increasing of the size.

Fig. 2 shows the time dependence of the width of the preferential amorphization near grain boundaries during Xe^+ ion irradiation at 423 K. The growth speed of the amorphous layer was similarly proportional to square root of irradiation time, which suggest the process depends on the diffusion process. In the case of stress condition, the growth speed increased obviously. In the case of stressed condition, the width of the amorphous zone was larger comparing with unstressed condition.

4. Summary

The preferential amorphous formation was observed at 423-475 K. By the way the critical dose increased with increasing of grain size. These results imply that amorphous formation in poly-Si is strongly depend on the internal stress and/or impurity segregation on grain boundary.

[1] H.A.Atwater and W.L.Brown: Appl. Phys. Letter, 56(1990)30.
[2] H.Ozaki et. al.: New Materials Handbook, (1988)317.

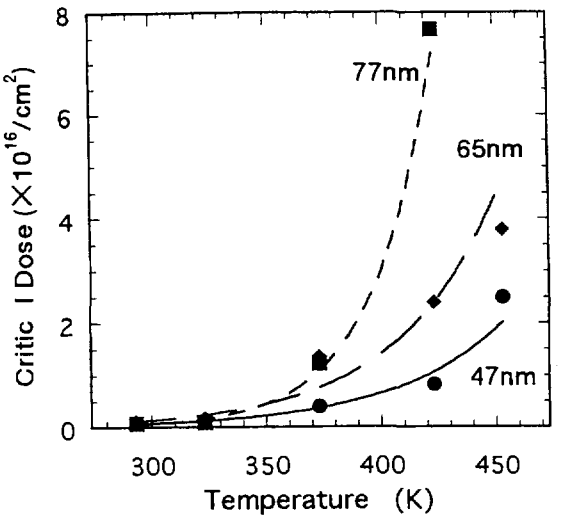

Fig.1. Temperature dependence of the critical dose for amorhozation with different grain size (300 keVAr$^+$)

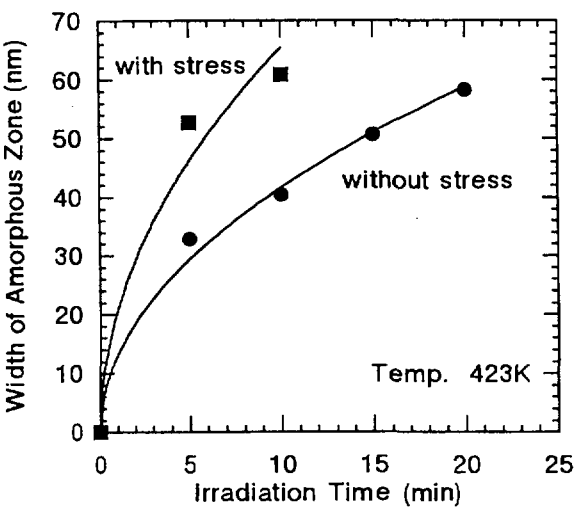

Fig.2. Effect of stress on the radiation-induced amorphization near grain boundary (1.5MeV Xe$^+$)

Table 1. Experimental conditions

Temp.	R.T.	323K	373K	423K	453K
without stress	○	○	○	○	○
with stress	—	—	—	○	—

4.18 Void Formation Behavior of Molybdenum Irradiated by Carbon Ion and Helium Ion.

A.Hasegawa[1], Y.Nemoto[2],M..Satou[1], K.Abe[1], S.Hamada[3] and Y.Miwa[3]

1) Quantum Science and Energy Engineering, Faculty of Engineering, Tohoku University

2) Graduate student, Tohoku University

3) JAERI/ Tokai

I. Introduction

Helium preimplantation effects on void formation behavior of molybdenum by carbon ion irradiation at 800 and 1000C was reported in the previous work to study helium effects on void lattice formation under ion irradiation conditions[1]. Void lattice is a three-dimensional damage structure of void which was observed in some irradiated metals such as molybdenum and niobium[2,3]. It have been studying by many researchers but the mechanism of lattice formation have not been clarified yet. In order to apply the void lattice structure as functional materials, we tried to form void lattice structure using ion irradiation.

In the previous work[1], void nucleation was enhanced by helium pre-implantation at 800C and 1000C, but void lattice was not observed under the irradiation conditions. Simultaneous implantation of helium generally enhanced void nucleation and swelling. This work will report result of simultaneous helium implantation of molybdenum using dual beam irradiation at 800C to study helium effects on void lattice formation.

II. Experimental

Powder metallurgical Mo was used for the irradiation specimens. Chemical composition of sample is shown in table 1. The specimen was punched out to 3mm ϕ disks from a Mo sheet and electro-polished and annealed at 1200℃ for 1hr for recrystallization. The specimen thickness is 0.25mmt and its grain size is 20 μ m.

Irradiation temperature was 800C because helium pre-implantation effect at 800C was relatively lower than that of irradiation at 1000C and simultaneous He implantation tended to enhance swelling at lower temperature region. Dual beam irradiation was carried out using a single-end accelerator and a tandem accelerator of TIARA. Accelerating energy of He^+ ion was 1.5MeV. Range of the He ion in molybdenum was 2.3 μ m. The total amounts of helium during simultaneous implantation were 165appm and 288appm and displacement damage by the helium implantation were 0.008 and 0.011 dpa respectively. Carbon ion bombardment was performed by 12MeV C^{3+} ion.. The depth distribution of damage by Carbon ion was already presented[1]. The combinations of displacement damage and implanted helium concentration were 0.76dpa/165appm and 0.28dpa/288appm respectively. In the case of 0.76dpa irradiation, helium pre-implantation of 100appm was also carried out at room temperature by a dynamitron accelerator of Tohoku University After implantation, 0.76dpa irradiated specimens were annealed at 1090℃ for 5min by a trouble of a heating controller.

In order to observe irradiation microstructure, sectioning and back thinning were carried out with a single jet electro-polishing machine. Layer of 2.3 μ m thickness from irradiated surface was removed by the sectioning process before back thinning. The thickness was correspond to the range of simultaneous implanted He ions. Microstructural observation was carried out by a transmission

electron microscope (TEM) at 200keV.

III. Results and discussion

Figure 1 shows typical micrographs of irradiated specimens in this work. Void was observed in all the irradiated specimen but void lattice structure was not observed in this experimental conditions. Void size histograms were single modal size distribution. Data of void size and number density compared to the data of the previous work are shown in fig. 2. In the case of 0.28dpa/288appm irradiation, cavity size became smaller than that of pre-implanted conditions. It may be attributed to lower level of displacement damage compared to that of the previous experiments. Void will be larger after higher level of irradiation. Larger void were observed in 0.76dpa irradiated specimens but the large void may be attributed to void growth during the post-irradiation annealing at 1090C.

Simultaneous implantation effect on void formation behavior was not clear in this experimental conditions. On the other hand, void distribution parameter such as size and number density of 1000℃ irradiated specimens are in the range of the parameter of void lattice formed molybdenum[4], therefore, further irradiation with low concentration of helium (about 100appm) may form void lattice structure in molybdenum.

Acknowledgment

Authors are grateful to staffs of TIARA for accelerator operation and to Prof. H.Matsui in IMR Tohoku University who kindly enabled us to use the microscope.

References

[1] K.Abe et al. TIARA Annual Report 1995, vol.5 (1996) pp.132-134
[2]J.H.Evans, Nature, 229 (1971) p.403
[3]K.Kurishan, Rad.Effects, 66 (1982) p.212
[4]K.Abe et al., Trans JIM, 34 (1993) p.1137

Table 1 Chemical Composition of Specimen (wt.ppm)

C	N	O	Ti	Al	Ca	Fe	Mo
30	10	5	10	20	20	10	bal.

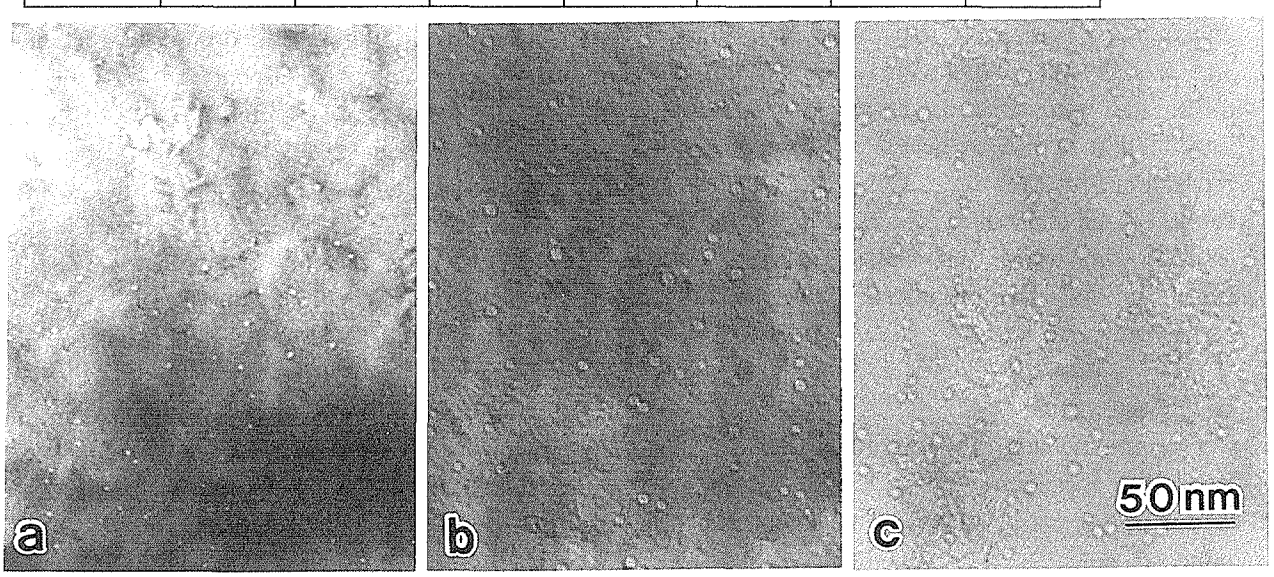

Figure 1. TEM micrographs of C^{3+} ion bombarded Molybdenum at 800℃.
(a) Dual beam irradiation (0.28dpa/288appmHe)
(b) Dual beam irradiation (0.76dpa/165appmHe) and 1090℃ annealing
(c) 100appm He pre-implantation, dual beam irradiation(0.76dpa/165appmHe) and 1090℃ annealing

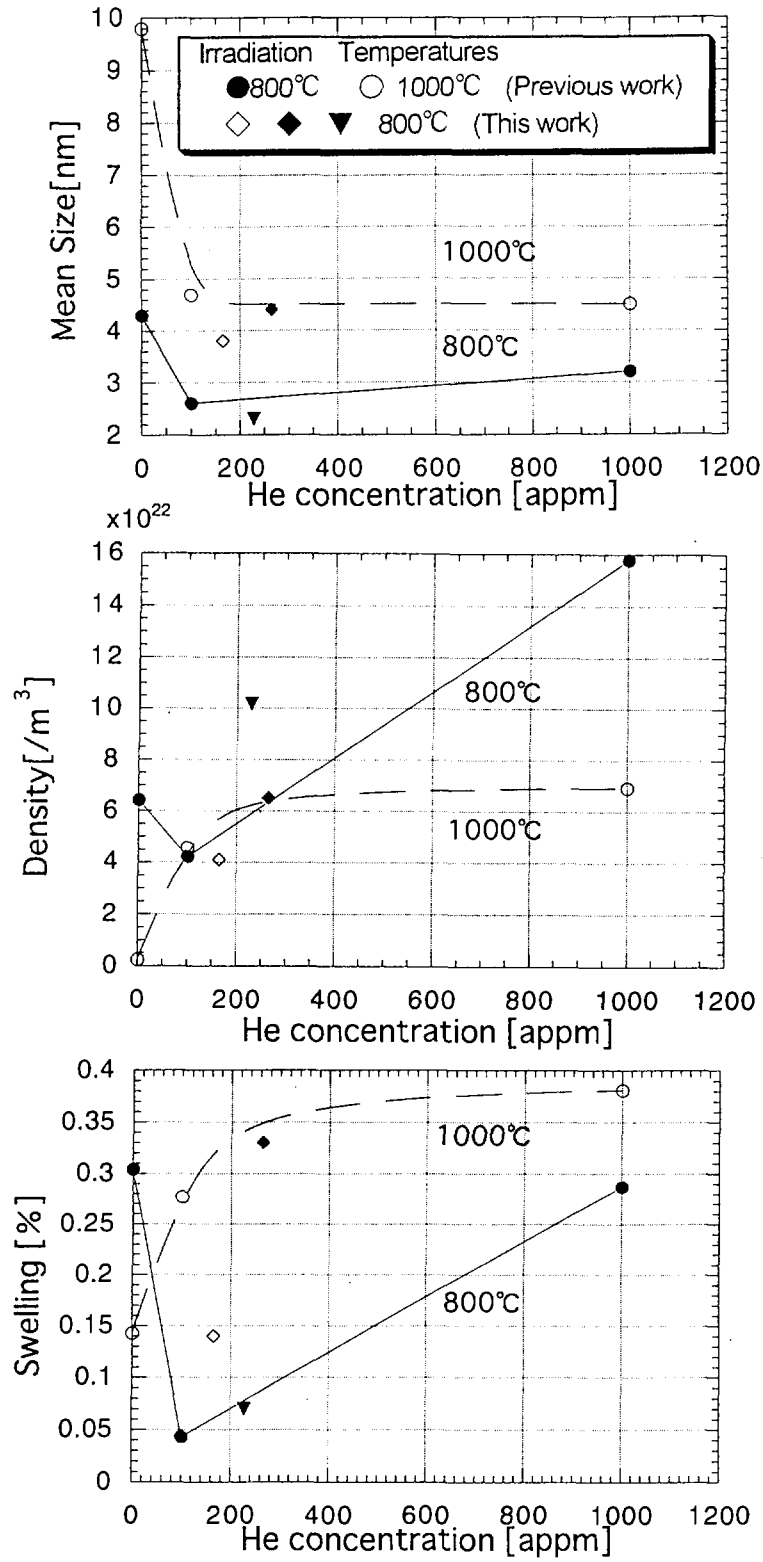

Figure 2. Summary of void parameter.

● Pre-implantation + 0.79dpa , ○ Pre-implantation + 1.0dpa

◇ Dual beam irradiation (0.76dpa/165appmHe) and 1090℃ annealing

◆ 100appm He pre-implanted, dual beam irradiation(0.76dpa/165appmHe) and 1090℃ annealing

▼ Dual beam irradiation (0.28dpa/288appmHe)

4.19 Anode performance of ion irradiated mesocarbon microbeads in secondary lithium ion batteries

S.Ishiyama and M.Asano

Japan Atomic Energy research Institute(JAERI), Tokai Establishment, Department of Advanced Nuclear Heat Technology, Tokai-mura, Naka-gun, Ibaraki-ken 319-11 Japan.
JAERI, Takasaki establishment, Department of Material development, Watanuki-machi 1233 Takasaki-city, Gunma-ken 370-12 Japan

1. Introduction

Recent R&D of new secondary battery of high energy density as a light and miniaturized energy source for portable equipments are pronounced in the world. Especially, technical advances of secondary lithium ion battery with the combination of carbon negative electrode and lithium positive electrode are manifest, and a lot of noticeable works[1-11] are reported.

However, higher performance have been demanding in these types of batteries, and inventions of higher capacity and lower cost materials of electrode materials are expected. One of candidate high performance electrode materials expected its practical use is Mesocarbon microbeads(MCMB) and some of those materials are utilized as domestic services now.

Recently, German and et al.[1] demonstrated good performance of lithium doped negative electrode for lithium battery, however, precise performance dependency on irradiation techniques and condition is not clear, and reported no information about another dorpants contributed for improvement of electrode performance.

Main purpose of present study is to enhance energy density and long cycling life of MCMB negative electrodes by irradiation techniques with electron beam accelerated by tandem type accelerator, and it has been found that the anode performance of MCMBs are improved by electron-beam irradiation.

2. Experimental

2.1. Materials and specimens

Two types of Mesocarbon Microbeads powders(MCMB, Osaka Gas Co. LTD., grain size >20μm), MCMB1(Annealing temperature ;1273K) and MCMB2(3073K), were prepared[10-11]. MCMB powders with PTFE binder were adhered on the surface(7.5mm x 5mm x 0.03mm^t) of nickel mesh(200 mesh; 50 mm x 50mm x with 0.5t) by compressed load. Those electrodes were dried in vacuum at 200°C for 6 hours prior to irradiation experiments. Active mass of MCMBs on a electrode was ca. 1.3g.

2.2. Irradiation experiments

Irradiation experiments of those electrodes were performed using electrostatic accelerator, TIARA in Japan Atomic Research Institute (JAERI). With this apparatus, electrons, H^+, B^+,F^{+2},Au^{+2} and Au^{+2} were accelerated up to 1.5 MeV and irradiated on the surface of the electrode targets. Electron beam current was measured by Faraday's cup measuring system located in vacuum chamber, which has four stages for irradiation samples and was evacuated up to 10^{-8} torr. During experiments, electron beam can be cut to control ion beam current density doped into the targets by shutter operation. Table 1 shows irradiation conditions for this experiments.

2.3. Charge-discharge capacity measurement

MCMB electrodes were tested by a galvanostatic charge-discharge examination(HJ-201B, HOKUTO DENKO Corp.). MCMB electrodes were placed in a two-electrode cell with 1 mol/l solution of $LiPF_6$ in a 1:1(by volume) of ethylene carbonate(EC) and di-ethylen carbonate(DEC). Lithium metal with three times larger than that of the WE was used as the counter electrode. This system were enclosed under argon atmosphere in globe box in order to avoid oxidation degradation of lithium counter electrode. In charge and discharge measurements, those electrodes were cycled at currents in the range of 0.1-0.5mA(=0.2-1.0 mA/cm^2) between cut-off voltages of 0-2V. The battery performance can be evaluated with the charge-discharge capacity obtained in present study.

3. Results and Discussion

Fig.1 shows electron exposure time dependency of discharge capacity of MCMB2 with a parameter of irradiation energy. It is very interesting that discharge capacity decreased at the beginning of irradiation, however, the capacity recovery was observed after 100 sec irradiation. These degradation

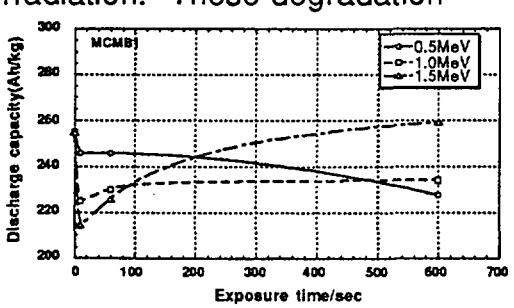

Fig. 1 Discharge capacity of irradiated MCMB1 by 0.1-1.5MeV electron beam.

behavior of discharge capacity of both materials exhibit strong energy dependency between 0 to 1.5 MeV. These changes can be explained that at the beginning of irradiation, electrons bombered into MCMB structure yields hole defects with tracks, which deteriorate electrical properties of MCMBs, then after 100sec irradiation, structural change in MCMB, such as recrystalization or nucleation of carbon new structure, may be occurred, these change is considered to be contribute to the improvement of MCMBs electrical performance.

Fig. 2 shows cyclic charge capacity of irradiated MCMB1 for 60 sec with charge-discharge cycle. Charge capacity of the irradiated samples decrease with cycle number and come down to the same of

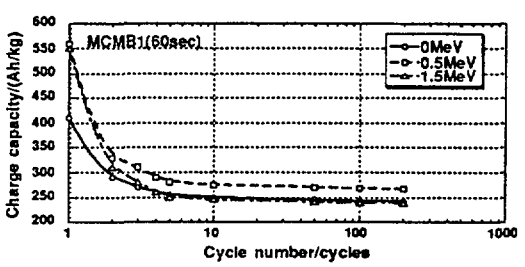

Fig.2 Cyclic charge capacity of irradiated MCMB1 after 60 sec irradiation.

unirradiated one within few cycles, except 0.5MeV irradiate sample . These degradation rate of MCMB1 is larger than that of MCMB2. MCMBs exhibits drastic degradation of charge capacity after first cycle, then moderately decrease after second cycle. These performance change is considered to be due to recrystalization or nucleation of carbon new structure, above mentioned.

4.References

[1]K.A.H.German,C.B.Weare,P.R.Vare kamp et al., Phys. Rev. Lett.,Vol.70(22),(1993)

3510-3513.
[2]S.Yawaguchi, T.Uchida and M.Wakhara, J. Electrochem. Soc. Vol.133(3)(1991)
677-687.
[3] L.W.Shacklette,T.R.Jow,Symp. on Materials and Processes for Lithium Batteries,
9-14 Oct. 1988,Conf-8810205, 408(1989)33-41.
[4] K.Inada,D.Ikeda, Y.Sato et al., *Primary and secondary ambient* temperature
Li batteries,Hololulu,Hawaii,18-23,Oct. 1987,530-539.
[5] K.M.Abraham, D.M.Pasquariello and G.F.Mcanprews, J. Electrochem. Soc. Vol.134
(11) (1987)2661-2676.
[6] J.R.Dahn,A.K.Sleigh,H.Shi et al., *in Lithium batteries* , New Materials, Developments
and Perspective, G. Pisyoia, p.1,Elsevier, Amsterdam(1994).
[7] K.Tatsumi, N.Iwashita, H.Sakaebe et al., J. Electrochem, Soc., **142**, 716(1995).
[8] A.Mabuchi, K.Tokumitsu, H.Fujimoto and T.Kasuh, ibid., **142**,1041(1995).
[9] T.Zheng and J.R.Dahn, Symth. Met., **73**,(1995)1-12.
[10] R.Fong et al., J. of Electrochem. Soc. 137(1990)2009-2015.
[11] K.Tatsumi et al., ibid., 142(2995)1090-1097.

4.20 Changes in microstructure and surface properties of metals by ion implantation

K. Hayashi, J. Saito, S. Kano, N. Kasai*, H. Kudo* and T. Seguchi*
Frontier Technology Sec., Oarai Engineering Center, PNC. *Advanced Materials Lab, JAERI/Takasaki.

1. Introduction.

It is necessary to develop high performance materials applied in severe environment in which radiation and corrosive, such as sodium exists. As the surface properties of materials are important in terms of corrosion resistance and wear resistance, surface modification by ion implantation is one of beneficial methods to create new materials with high reliability. In this study, SUS316FR, Mod.9Cr-1Mo steel and Nb-1Zr were implanted with nitrogen and magnesium ions and the surface properties were investigated. The purpose of N implantation was to form nitride phase on the metal surfaces, and the aim of Mg implantation is to form stable magnesium oxide film on the surface.

2.Experimental method.

Specimens used were mechanically mirror polished SUS316FR, Mod. 9Cr-1Mo steel and Nb-1Zr with the sizes of 20 X 6 X 2 mm. Those were clumped on a Cu holder and the implantation of N or Mg was conducted at room temperature under vacuum of $<10^{-5}$ Pa. For the specimens implanted with N ions, surface hardness measurement, structural analyses by the X-ray diffraction(XRD) and depth profiling by glow discharge spectroscopy(GDS) were carried out. Then they were immersed in liquid sodium at 923K for 1000 hr. to examine the compatibility with Na. After the Na corrosion test, depth profiles of N and Na were measured by GDS. For Mg implanted specimens, structural analyses and heat treatment for oxide film formation were carried out. The specimens were analyzed by XRD and Fourier transfer infra-red absorption(FT-IR).

3. Results and discussion.

3-1. Nitrogen implanted specimens.

Summary of the hardness change, structural analyses and depth profiling in the N implanted specimens is as follows.[1]

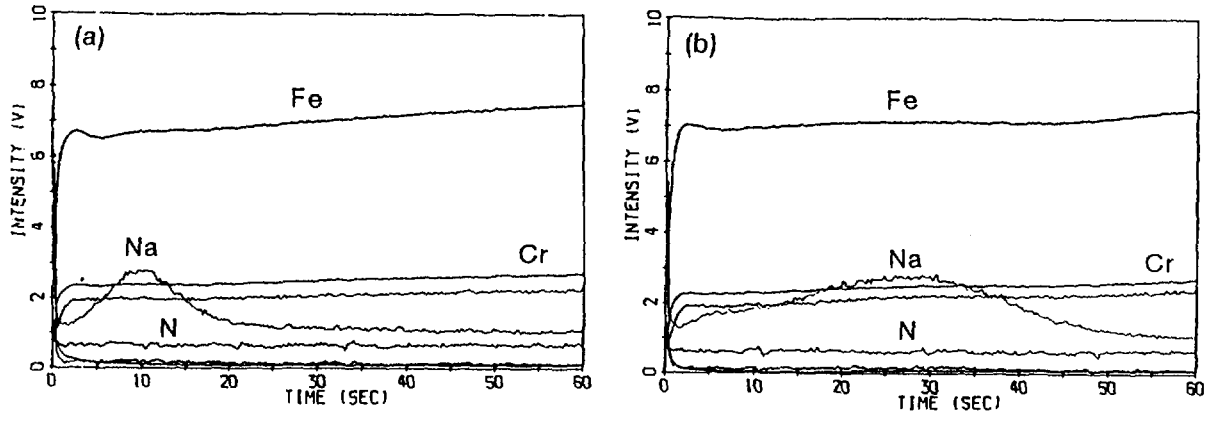

Fig.1. GDS depth profiles of Mod. 9Cr-1Mo steel after Na corrosion test.
(a) unimplanted, (b) implanted with $6X10^{17}$ N/cm^2 at 300 keV.

1. Surface hardness of the N implanted specimens increased with increasing the nitrogen dose and the ion energy.
2. At lower doses, N atoms exist at the interstitial position of the host lattice. At higher doses, nitride phase formation was detected.

GDS depth profiles of the unimplanted and $6X10^{17}$ N/cm^2 (6E17 N)implanted Mod. 9Cr-1Mo steel after the corrosion test are shown in Fig.1. In both specimens, Na penetration was observed and the depth of Na penetration in the implanted specimen was deeper than that in the unimplanted specimen. As nitrogen was not detected after the Na corrosion test, nitrogen is considered to dissolve into liquid Na during the test.

By the microscopical observation, the surface of the implanted specimen showed preferential etching of grain boundaries caused by the N implantation. The deep Na penetration in the implanted specimen is considered to be the result of Na invasion through the grain boundaries. In the case of N implanted SUS316FR and Nb-1Zr, no changes in corroded surface were observed in the corrosion behavior by liquid sodium in comparison with the unimplanted specimen.

3-2. Magnesium implanted specimens.

Magnesium oxide was reported to have high corrosion resistance in liquid sodium[2]. As Mg is immiscible element in Fe[3], implanted Mg is expected to segregate at surface by redistribution after the implantation as the case of yttrium implantation in steel[4].

In Fig.2, XRD spectra of the SUS316FR implanted with 3E17 Mg and 6E17 Mg are shown. For the specimen implanted with 3E17 Mg, there are large peaks originated from γFe . On the contrary, for the specimen implanted with 6E17 Mg, there are a few extra peaks in addition to the strong peaks of γFe. These new peaks are considered to be originated from magnesium oxide[5].

FT-IR spectra of the unimplanted, as-implanted 3E17 Mg and 3E17 Mg implanted and heat treated SUS316FR are shown in Fig. 3. The heat treatment was carried out at 673 K for 2 hrs. in air. As seen in the figure, a broad absorption peak from 600 to 800 cm^{-1} is observed in the

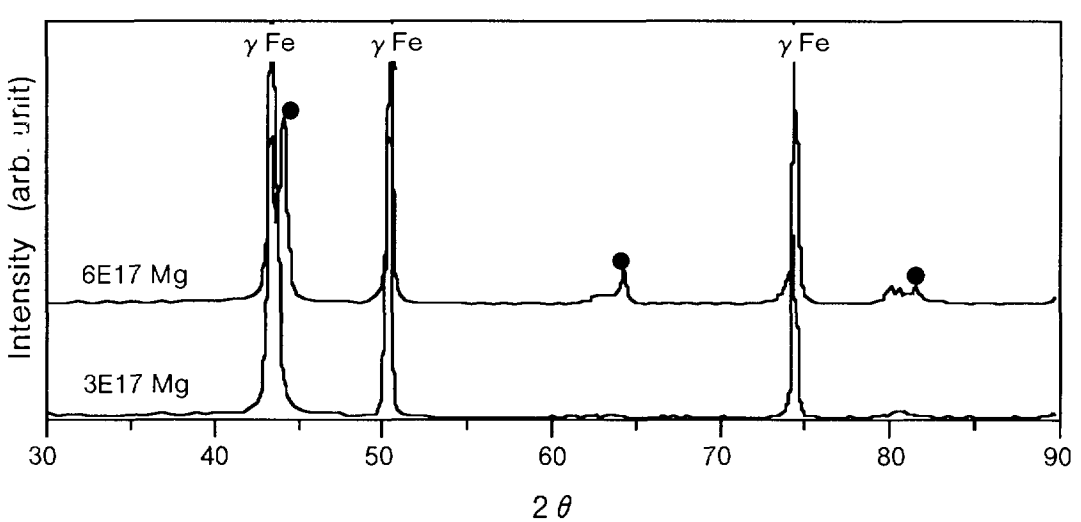

Fig.2. XRD spectra of 300 keV Mg implanted SUS316FR.
Diffraction peaks marked ● are considered to be MgO.

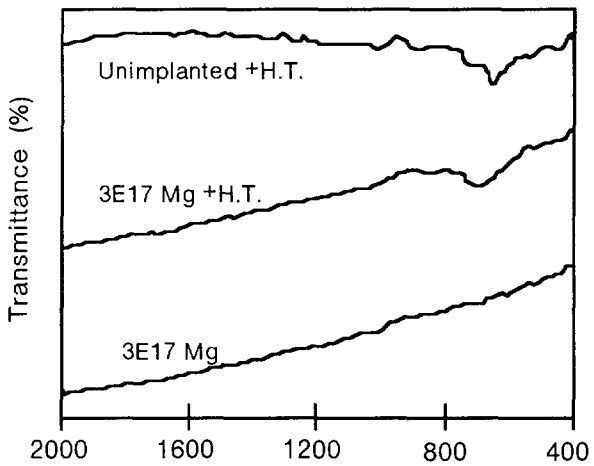

Fig.3. FT-IR spectra of unimplanted, 3E17 Mg implanted and 3E17 Mg implanted and heat-treated SUS316FR. (heat treatment : 673K, 2 hrs., in air)

heat treated specimens. On the contrary, no absorption peaks are observed in the as-implanted specimens. So, the broad absorption peak is attributed to surface oxide formed by the heat treatment. Comparing the absorption peaks in the unimplanted and 3E17 Mg implanted specimens, the peak of the implanted specimen shifts toward higher wave numbers. This shift means the existence of magnesium oxide.

From the XRD analyses, magnesium oxide is considered to exist at the steel surface even in as-implanted condition by high dose Mg implantation. For the specimen implanted with low dose Mg ions, in which magnesium oxide was not detected by XRD in as-implanted condition, the oxide layer was formed by heat treatment in air.

Acknowlegdement.

Authors gratefully acknowledge Mr. Y. Hirakawa and Mr. E. Yoshida of PNC for Na corrosion test.

References

1. J. Saito et.al. : JAERI TIARA Ann. Rep. vol.5 1995, p138.
2. Y.Tachi : Ceramics 30 (1995) 989.
3. Binary Alloy Phase Diagrams, 2nd Edition : ed. Massalski (ASM international) 1990.
4. K.Hayashi et.al. : Nucl. Instrum. Methods, in press.
5. JCPDS 30-0794

4.21 Diffuse x-ray scattering from defect clusters in FCC metals irradiated with electrons

Hideki Yuya*, Hiroshi Maeta**, Hideo Ohtsuka**, ,
Norimasa Matsumoto**, Hiroyuki Sugai**,
Kohji Yamakawa***, Akihiro Iwase**, Tsuneo Matsui*

*Department of Quantum Engineering, Graduate School of Engineering,
Nagoya University, Furo-cho, Chikusa-ku, Nagoya 464-01, Japan
**Department of Materials Science and Engineering,
JAERI Tokai, Ibaraki 319-11, Japan
***Faculty of Engineering, Hiroshima University,
Kagamiyama, Higashi-hiroshima 724, Japan

1.Introduction

In alloys, it is important to understand the radiation process which is interaction between defects and solute atoms. Transmission electron microscope (TEM) have been applied to investigate radiation processes in many cases. However, size of defect clusters ranges from an atom to relatively large dislocation loops, some of which well below the visibility limit of TEM. The determination of the structural properties of such small clusters (<2-3nm) has, therefore become a unique application field of the Diffuse x-ray Scattering (DXS) technique.

We investigated the structures of defect clusters in pure Ni and dilute Ni alloys with the DXS technique. Although nickel is of great importance in many base alloys for nuclear reactors, structure of the small defect clusters has poorly investigated.

2.Experimental

(i)Samples and electron irradiation

High purity single-crystal samples of Pure Ni and Ni alloys (Ni-0.04at.%Cu, Ni-0.05at.%Fe) were spark-cut into $4\times4\times1$ mm^3 from a large single crystal grown by the Czochoralski method. After removing the surface layer by electropolishing, the samples were annealed in vacuum at 900K for 5 hours.

The samples were irradiated with 2MeV electrons up to $1\times10^{18}e^-/cm^2$ near liquid-nitrogen temperature.

(ii)X-ray measurements

The DXS experiments on electron irradiated samples were performed with four circle diffractometer at room temperature installed at BL-27B at Photon Factory of National Laboratory for High Energy Physics in Tsukuba. Diffuse scattering was always measured near 111 reflection. Some additional measurements to confirm avoiding 'streak' that is very high background intensity from the samples.

The diffuse scattering intensities were determined by subtracting the background scattering from the sample in which all of defects were annealed out due annealing at 900K for 1 hour. The measured intensity after annealing was almost identical to the

one before electron irradiation. Background from temperature effects and Compton scattering effects can be removed by taking a difference between irradiated samples and ones. The high flux photon beam enables us to isolate diffuse scattering clearly.

3.Results and Discussion

(i)Size of the interstitial and vacancy clusters

The results of measurements of the diffuse scattering, as obtained after subtraction of background, are shown in Fig.1 to 2 for Ni, Ni-Cu, and Ni-Fe samples. The intensity of the measurements is shown in a double logarithmic plot as a function of q that is the distance from the reciprocal lattice point. Figure 1 shows the diffuse scattering intensity as a function of positive q relative to the reciprocal lattice vector. This plot allows to obtain information about the interstitial-type clusters. Figure 2 shows the intensity as a function of negative q corresponding to information about the vacancy-type clusters.

Close to the Bragg reflection the diffuse scattering from a statistical distribution of point defects is dominated by Huang diffuse scattering. The theory of DXS from defect clusters has been extensively reviewed[2] gives the expression of Huang diffuse scattering for $q \parallel h$:

$$\frac{d\sigma}{d\omega} \propto (r_e f(K))^2 \left\{ \frac{Kb\pi R^2}{q} \right\}^2 \quad q << 1/R \quad (1)$$

where K is the scattering vector, h the reciprocal lattice vector, r_e the classical electron radius, f the atomic scattering factor, b the burgers vector and R the radius of a cluster.

For agglomerated defects, Huang region is the limited to $q < q_o = 1/R_{cl}$, where R_{cl} is the cluster radius. For $q > 1/R_{cl}$, there is the Stokes-Wilson scattering which is given by

$$\frac{d\sigma}{d\omega} \propto (r_e f(K))^2 \left\{ \frac{Kb\pi R^2}{q^4} \right\} \quad q > 1/R \quad (2)$$

From the measurements, one gets a rough estimation of the cluster radius R_{cl} according to the relation $q_o R_{cl} = 1$[3], q_o is the value at which the $1/q^4$ law (Stokes-Wilson scattering region) changes to the $1/q^2$ law (Huang diffuse scattering region).

Some curves in Fig 1 and 2 shows a Huang region for small q value. At large q, the $1/q^4$ law indicates the presence of the defect clusters. The results are reported in table 1. The estimation of either interstitial or vacancy number N in cluster have been carried out by assuming that these loops are in the {111} plane with Burgers vector $b=a/3[111]$. Using $N=\pi bR^2/V_a$[3], where V_a is atomic volume, we obtained the results as shown in table 1. We get R_{cl}~1 to 2 nm.

(ii)Defects concentration

Eq.(1) and (2) that give diffuse scattering cross section per cluster allow us to deduce the defect concentration. Fig.1 and 2 showed that the concentration of defect agglomerates was affected by addition of solute Cu and Fe atoms. For either interstitial-type or vacancy-type case, the $1/q^4$ region (Stokes-Wilson scattering region) shows that diffuse scattering intensity are almost identical. For the $1/q^2$ region (Huang scattering region), on the

contrary, diffuse scattering intensity of Ni alloy was higher than that of pure Ni. This indicates that the formation of small defect clusters are influenced by solute atoms. The more over-size solute atoms Ni alloy contains, the more small defect clusters are nucleated.

4.References

1)P.Ehrhart.,J.Nucl.Mater.216:170-198(1994)

2)H.Maeta, B.C.Larson, T.P.Sjoreen, K.Thomas, O.S.Oen,and J.B.Lewis.,Mat.Res.Soc. Symp.Proc.138:81-86(1989).

3)P.Erhart and U.Schlagheck.,J.Phys.F:Metal Phys.4:1589-1598(1974)

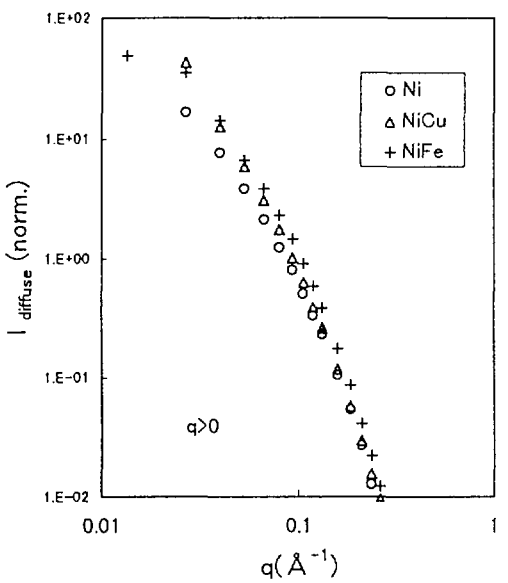

Fig.1. Diffuse scattering intensity as a of positive q

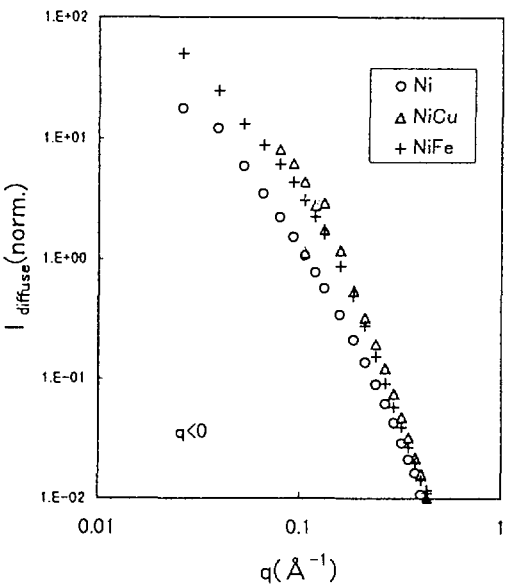

Fig.2. Diffuse scattering intensity as a of negative q

Table 1 Rough estimation of the dislocation loop radius R_{cl} and number of interstitial atom or vacancy in a dislocation loop.

material	Ni		NiCu		NiFe	
type	Interstitial	Vacancy	Interstitial	Vacancy	Interstitial	Vacancy
R_{cl}(nm)	1.5	0.6	1.5	1.6	1.0	1.1
N	126	24	126	153	54	68

5. Materials Analysis

(continued to the next page)

5．1 Application of ERD method to study hydrogen and helium behaviors in Ti, Zr and Nb membranes

S. Nagata, K. Takahiro, S. Yamaguchi, S. Yamamoto*, B. Tsuchiya*,
Y. Aoki* and H. Naramoto*
Institute for Materials Research, Tohoku University
*Department of Materials Development, JAERI

1. Introduction

It is well known that the radiation induced defects act as trapping sites for hydrogen atoms. Particularly, helium ion implantation effectively produces hydrogen traps in some transition metals [1,2] . In fusion device, both hydrogen isotopes and helium are implanted simultaneously into the plasma facing materials. Interactions between the hydrogen and the helium is of importance, because the interaction will modify substantially the transport behavior of hydrogen in materials. However, a few number of quantitative studies on the hydrogen - helium interactions has been reported so far.

In the present work, the retention of helium and the enrichment of hydrogen in the membranes containing about 0.1 at.% H during ^{4}He implantation was measured as a function of the incident He dose at temperatures between 300 and 650 K. Subsequent annealing experiments have been performed to examine the association between hydrogen and defects introduced by He implantation in the Ti, Zr and Nb membranes.

2. Experimental

Specimens used were polycrystalline Ti, Zr and Nb membranes with thickness of 3 - 5 μ m containing 0.1 - 0.2 at. H. Prior to the measurement, the specimen was annealed at 900 K for one hour. The ^{4}He implantation were carried out with a 400 kV ion implantor or a 10 kV ion gun with velocity filter. During and after the implantation, the concentration profiles of H and He atoms in the membranes were simultaneously measured by the ERD method of trans mission geometry using 4 - 13 MeV C or O ion beams.

In order to examine the association between hydrogen and defects or He bubbles created by He implantation, annealing and ageing experiments were performed. After ^{4}He implantation to a dose of 2×10^{20} He/m^2 at room temperature, the H and He profiles in the membranes were measured simultaneously during subsequent heating and cooling between 650 and 350 K.

3. Results and discussion

Figure 1(a) and (b) show the recoil particle energy spectra (ERD spectra) from $NbH_{0.01}$ after the ^{4}He implantation to a dose of 1×10^{21} He/m^2 with 100 keV and 10 keV ions, respectively. A broad peak at higher energy was originated from the He recoil particles which were retained at the depth corresponding to the projected range of implant He ions. As for the energy spectrum from the H atoms, a small pronounced peak is appeared after the ^{4}He implantation as seen in fig. 1(a). The position of the small peak nearly corresponds to the depth of 0.5 μ m, which is close

to the mean projected range for 200 keV ^{4}He on Nb. On the other hand, hydrogen concentration at the depth deeper than 0.5 μm is decreased, and the amount of hydrogen observed at surface is not changed during the ^{4}He implantation. The diffusion of hydrogen in Nb is known to be very fast even at room temperature. Therefore, these results indicate that H atoms are trapped the near-by defects created by the ^{4}He implantation, and the supply of the hydrogen from the unimplanted region would occur simul-taneously. The ERD spectra during the implantation with 10 keV ^{4}He is shown in fig. 1(b), where the enrichment of the H atoms was also occured near the range of the incident ^{4}He ions, and the decrease of hydrogen concentration was recognized in the unimplanted region. Similar enrich-ment and loss behavior of the hydrogen atoms were also observed for the Ti and Zr membranes.

The amount of He and H atoms retained at the near surface region during 10 keV ^{4}He implantation on Ti, Nb and Zr are shown in fig. 2 (a), (b) and (c), respectively. A linear increase of the number of the retained helium was observed for all membranes up to the ^{4}He dose less than 2 x

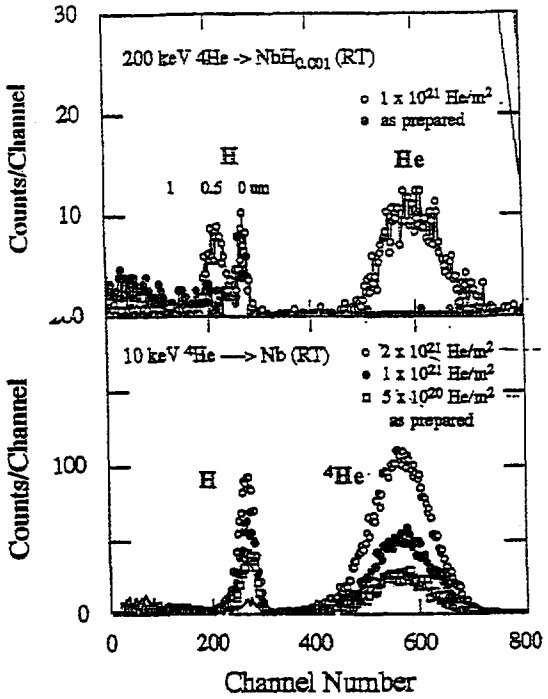

Fig. 1 Energy spectra of H and He from $NbH_{0.001}$ specimen. (a) 100 keV, (b) keV.

10^{21} He/m^2. These results indicate that almost all implanted ^{4}He ions were trapped in Ti, Nb and Zr at the biginning of the implantation. In contrast to the initial linear increase and the subsequent obivious saturation behavior of ^{4}He trapping, H atoms accumulated slowly near the implanted region and gradually tend to saturate. The dose dependence of the hydrogen enrichment shown in fig. 2 may be

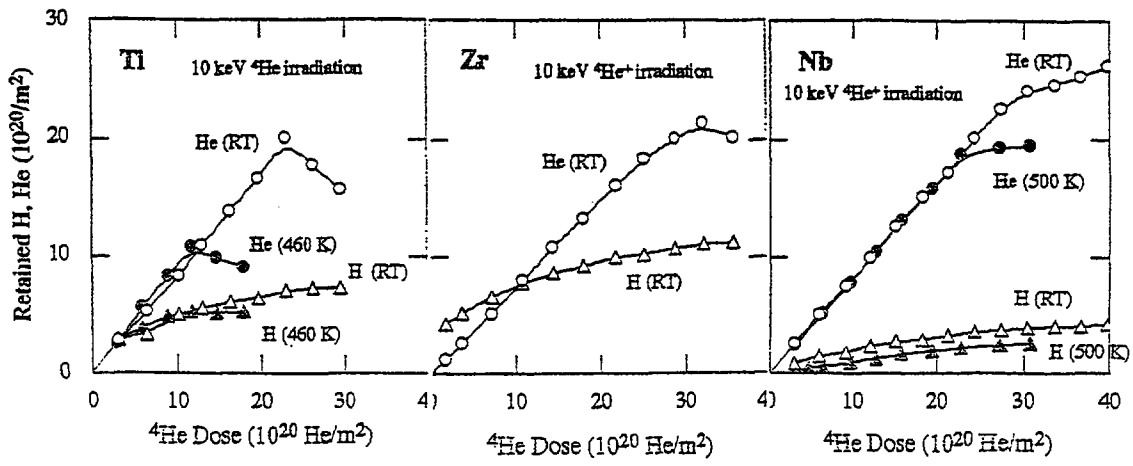

Fig. 2 He retention and H enrichment for Ti(a), Zr(b) and Nb(c) against He dose.

explained by the number of the defects produced by the ^{4}He implantation, if the enriched H atoms were trapped by the defects including the He bubbles. It can be reasonably assumed, therefore, that the enriched H atoms will be the same depth profile as the defect profile. From the ratio of the enriched H atoms to the retained He atoms, the number of the H atoms trapped by the single He atom were estimated to be 0.44, 0.55 and 0.16 for Ti, Zr and Nb, respectively.

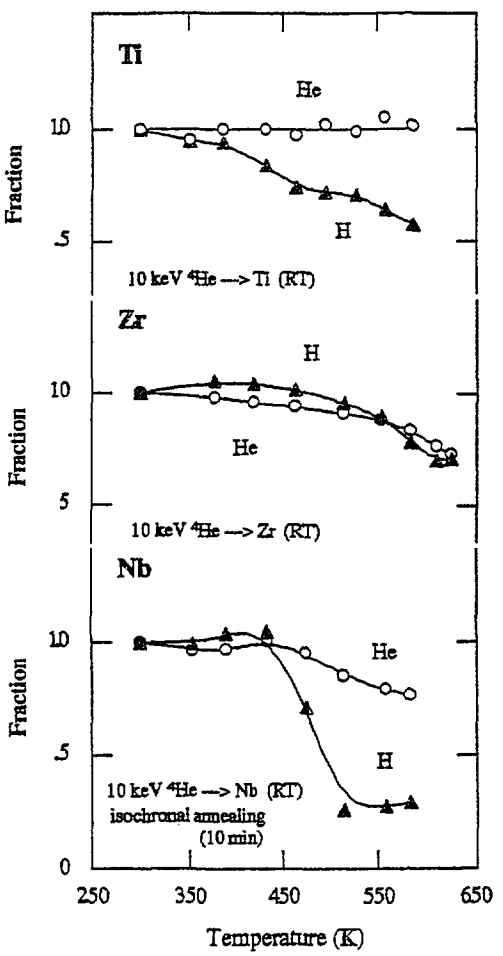

Fig. 3 Temperature dependence of the retained He and the enriched H.

The temperature dependence of the retained helium as well as the enriched hydrogen for each metals was shown in fig. 3, where the normalized yields for the near surface region were plotted against the annealing temperatures. No release of the retained He was observed on Ti during the isochronal annealing, while the enriched H atoms decreased with increasing temperature, and about half of the initial concentration remained at 600 K. On the other hand, in Zr the temperature dependence of the H retention is nearly coinside with that of the He retention, and the both curves decreased slowly with increasing temperature. The H trapping in Zr should be closely related to He atom in comparison with Ti. In the case of the Nb membrane, the decreasing of both H and He retention began at 450 K, then the H retention adruptly decreased at 500 K. The experimental results described above may suggest that defects created by the ^{4}He implantation are responsible to the enrichment of the H atom. The trapping mechanism of the H atoms by the defects created by the ^{4}He implantation, however, is complicated by the existence of the He atoms. Further investigation is required to examine the mechanism involved in the trapping of H and He atoms, and to characterize the defects formed by the ^{4}He implantation.

4. Reference

1) J. Bottiger, S.T.Picraux, N.Rud and T. Laursen, J. Appl. Phys., 48 (1977) 920.

2) F. Besenbacher, J. Bottiger and S.. M. Myers, J. Appl. Phys., 53 (1982) 3547.

5．2 Studies on the Processes of Atomic Adsorption and Desorption at the Solid-Liquid Interface by In-situ RBS Technique

K.Morita[1], J.Yuhara[1], R.Ishigami[1], B.Tsuchiya[1], K.Soda[1], S.Yamamoto[2]
Y.Aoki[2], K.Narumi[2], H.Naramoto[2], T.Ohnuki[3], and K.Saitoh[4]
Dept.Cryst.Sci., Nagoya University[1], Takasaki Establishment, JAERI[2],
Tokai Establisment, JAERI[3], National Indust. Res. Institute, Nagoya[4].

I. Introduction

Understanding of adsorption and desorption processes of atomic and molecular species at the liquid-solid interface is of essential interest in point of views of fundamentals and applications. In the technology for geologic radioactive waste disposal, adequate containment is estimated to result principal from low solubility-limited release rates of the radioactive reactor products, even if low-velocity flowing ground water is present. The partition coefficients of various radioactive nuclides between the surface of mineral stones and the modeled ground water have been obtained using the radioactivity measurement of nuclear reactor products [1,2]. For estimation of a period of time for radioactive material to reach the biosphere, reliable data on the rate constants for the adsorption and desorption at the liquid-solid interface are primarily required.

The in-situ RBS system has been developed in order to measure the depth distribution of stable heavy nuclides adsorbed at the inner surface of a thin film window of a liquid container [3], which is irradiated with a probing MeV ion beam and to determine the rate constants of sorption and dissolution of various nuclides at the liquid-solid interface.

In this paper, we report the experimental results on dissolution of a lead layer adsorbed physically at the SiO_2 surface into water at different pH which has been measured using the in-situ RBS system.

II Experimental

The thin window of the silicon specimen was fabricated using preferentially slow etching of heavily B-implanted silicon. The thinning process was almost similar to the work of Cheung [4]. The details were described elsewhere [5].

Deposition of the Pb layer onto the silicon widow and measurement of the Pb thickness were done in the other chamber [6]. The thickness of the Pb layer measured by means of the RBS technique was 24ML/Si(100).

The silicon disk with a thinner window of 3mm in diameter was used for the wall of the sample assembly, which is installed in the small vacuum chamber of the experimental apparatus shown schematically in Fig.1. The sample assembly was made of stainless steel and quartz glass, and sealed with O-rings. The vacuum chamber was connected to a beam line of 3 MeV Tandem accelerator. The sample was irradiated with 9 MeV He^{++} ion beam through a carbon slit with a hole of 2mm in diameter in order to reduce the background scattering. The backscattered ions were measured with an annular-type SSB detector.

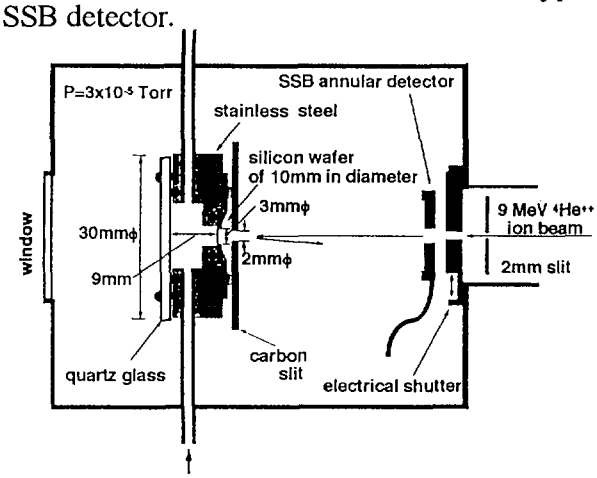

Fig.1 Experimental arrangement of an in-situ RBS system for measuring nuclides adsorbed at the liquid-solid interface.

III Results and Discussion

Fig.2 shows a typical RBS spectrum of 9 MeV He^{++} ion beam from the silicon window with the Pb layer as-deposited on the back-surface in the sample assembly, of which air was included in the inner chamber. It is seen from Fig.2 that the weak peak from the Pb layer appears around the channel number of 600 marked by the arrow (Pb_B). The thickness (coverage) of the Pb layer was

measured as a function of time elapsing after injection of water with different pH into the inner chamber.

Fig.3 shows the Pb coverage as a function of time elapsing after injection of deionized water into the inner chamber. It is seen from Fig.3 that the Pb coverage does not change at all. Namely, Pb on the SiO_2 surface does not dissolute into deionized water.

Fig.4 also shows the Pb coverage as a function of time elapsing after injection of water at pH higher than pH9 which includes dilute NH_3. It is also seen from Fig.4 that Pb does not dissolute into alkaline water.

Fig.5 shows the Pb coverage as a function of time after injection of water at pH5 which includes dilute HNO_3. It is clearly seen from Fig.5 that Pb coverage decreases linearly with elapse time from 24ML to 3ML. This fact indicates that the dissolution of Pb is the zero-th order reaction kinetics. The rate constant of dissolution was obtained to be 0.065 s^{-1} when the surface density was assumed to be 1.03×10^{15} atoms/ cm^2.

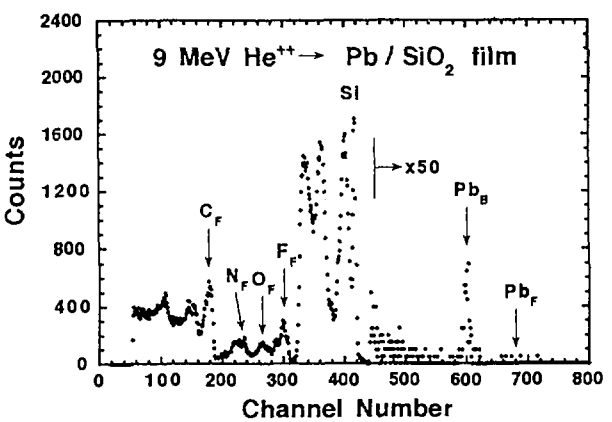

Fig.2 RBS spectra of 9MeV He^{++} ion beam from the silicon window of the sample assembly with a Pb layer as-deposited on the back-surface

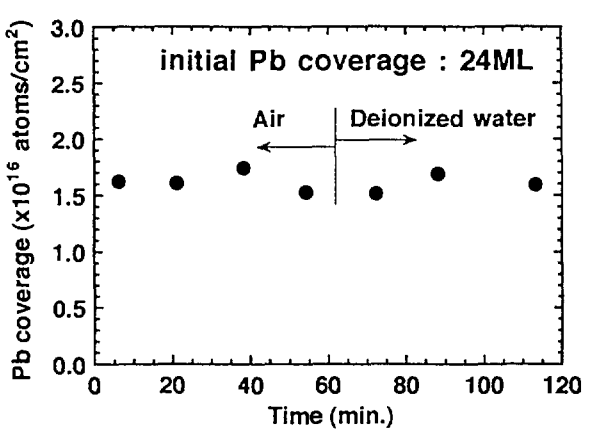

Fig.3 Pb coverage as a function of time elapsing after injection of deionized water.

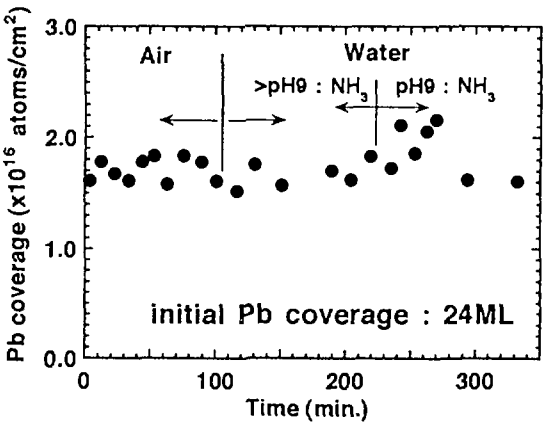

Fig.4 Pb coverage as a function of time elapsing after injection of alkaline water.

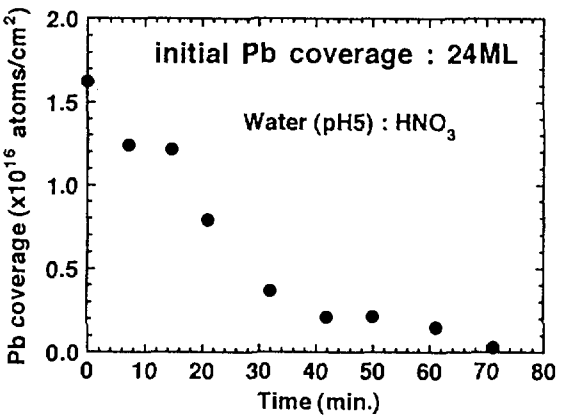

Fig.5 Pb coverage as a function of time elapsing after injection of acid water.

IV Summary

The dissolution of Pb layers deposited physically on the SiO_2 surface to water at different pH has been measured by means of in-situ RBS measurement. It is found that Pb does not dissolute in alkaline water but acid water, and that the dissolution in the latter case is the zero-th order reaction kinetics and the rate constant is 0.065 s^{-1}.

Reference

[1] S. Sato, H. Furuya *et al.*, Proc. 5th Int. Symp. on Water-Rock Interaction, ed. by H. Aromannsson *et al.*, Reyjavik, 1986.

[2] S. Sato, H. Furuya *et al.*, Sci. Basis for Nucl. Waste Management IX, ed. by L. Werme, Materials Research Society, Pittsburgh, 1986, p.763.

[3] K. Morita, J. Yuhara *et al.*, Radiation Physics and Chemistry, 49 (1980) 603.

[4] N. W. Cheung, Rev. Sci. Instrum. 51 (1997) 1212.

[5] K. Saitoh *et al.*, Proc. 10th Int. Conf. on Ion Implantation Technology, ed. by S. Coffa *et al.*, 1995, pp.998-1001.

[6] J. Yuhara, R. Ishigami, and K. Morita, Surf. Sci. 326 (1995) 133.

5.3 Ion-induced electrons from crystal targets bombarded with MeV ions: Isotropic emission

Hiroshi Kudo, Shunya Yamamoto*, Kazumasa Narumi*,
Yasushi Aoki*, and Hiroshi Naramoto*
Institute of Applied Physics, University of Tsukuba
*Department of Materials Development, JAERI

1. Introduction

When fast ions are incident on a solid target, the ion-induced electron emission from the surface mainly results from kinetic processes, i.e., recoil of target electrons. The recoiled electrons contribute to the whole energy range of the observed continuum spectrum, after undergoing elastic and inelastic scatterings by the target atoms.

In the past, energy spectra of ion-induced electrons from single crystal targets bombarded with MeV/u ions have been reported in a number of papers.[1] The spectrum yield at keV energies is decreased under channeling incidence conditions since the target atoms in the subsurface layer are effectively shadowed. For precise analysis of the experimental results, however, it must be investigated whether the spectrum yield discernibly or hardly depends on the crystallographic direction of the outgoing path (towards the spectrometer). Recently, for example, Alkemade and coworkers have discussed a possibility of enhanced electron yields in axial directions of crystal targets.[2]

In angle-resolved spectroscopy of x-ray photoelectrons and Auger electrons for single crystals, in which electrons of several hundred electron-volts are measured, enhancement of the electron yield has been observed over an angular range of ten degrees in an axial direction of the target crystal.[3] This effect has been explained by forward-direction focusing of the emitted electrons by the attractive potential of the overlying atoms. A similar effect at the same or a higher energy range is of essential interest in consideration of the ion-induced electron emission.

In a classical picture, the forward-direction focusing effect mentioned above can be regarded as a low-energy limit of electron channeling.[4] Indeed, the spiral trajectory of channeled electrons along the crystal axis should correspond to the focusing trajectory at low energies. Recently, channeling of conversion electrons of hundred kilo-electron-volts emitted from implanted radioactive isotopes has been studied.[5] In this case, the angular width of the enhanced yield is typically in the range 1-5°.

It is anticipated that the angular width of the enhanced electron yield due to the forward-direction focusing effect should decrease with increasing the electron energy, according to calculations by Poon and Tong.[6] Of course, this behavior is consistent with the energy dependence of electron channeling. Accordingly, if the forward-direction focusing effect appears in the ion-induced electron emission, the enhanced electron yield at keV energies might have an angular width lying in the range 1-10°. In the present work, emission-angle dependence of the ion-induced keV electrons near axial directions of the crystals has been measured to investigate an influence of the crystal structure on the outgoing process of the electrons.

2. Experiment

The ion-induced electrons from single crystal targets were energy-analyzed using a 45° parallel-plate electrostatic spectrometer of the double-deflection type. The spectrometer was placed at an angle of 150° with respect to the beam direction. The angular acceptance of the spectrometer was approximately 2.3° × 2.3° (a solid angle of 1.6×10^{-3} sr).

First, the axial direction perpendicular to the crystal surface was aligned with the ion beam direction by measuring the channeling dips of the ion backscattering yield using a

particle detector located at a backward direction. Next, the axial direction was aligned with the entrance axis of the spectrometer by rotating the crystal by 30° with respect to a θ rotation axis perpendicular to the beam direction.

The wide energy acceptance of the spectrometer $\Delta E/E$=0.27 was chosen to obtain sufficient count rate for mapping of the electron yield as a function of the rotation angles θ and ϕ (tilt angle). For chemically etched Si(100) and Ge(111) samples, the electron yield over a fixed energy range (E-$\Delta E/2$ to E+$\Delta E/2$) has been measured as a function of θ and ϕ. The target temperature was ~295K and the pressure in the chamber was in the range of 10^{-5} Pa. The measurements were carried out using the ion beams from the 3-MV single-ended accelerator and the 400-kV ion implanter at JAERI-Takasaki. The beam current on target was 10-20 nA for a beam spot size of approximately 1×1 mm^2.

3. Results and discussion

The electron-energy spectra observed in the present experiments are similar to those reported previously. The spectrum shape of the continuum yield at keV energies is predominantly characterized by the ion velocity irrespective of ion species, and the yield becomes lower for higher electron energy.

Typical angular dependence obtained is shown in Fig. 1 for 2.5 MeV H$^+$ incident on a Ge(111) crystal. While the vertical axis in Fig. 1(a) is taken in the upward direction for easy finding of an enhanced electron yield, that in Fig. 1(b) is taken in the downward direction for a clear presentation of the shadowing pattern. The measured energy range of the electrons was 2.0-2.6 keV. For Ge, the L-shell Auger yield at ~1.2 keV is superimposed on the continuum spectrum yield. Therefore, the angular dependence of the continuum yield for Ge has been measured at electron energies higher than 2 keV.

In Fig. 1(a), $\theta=\phi=0$ is taken to be the rotation angles at which the Ge<111> axis is aligned with the entrance axis of the spectrometer. In this case, the crystal was mounted on the 3-axis goniometer so that neither axial nor planar channeling of incident ions occur within the 12°× 12° range of θ and ϕ. The angular step of 0.6° for θ and ϕ, which is 26% of the spectrometer's acceptance angle (2.3°), has been chosen to search for an enhanced yield having an angular width in the range 1- 10°. For each angular step, the electron yield was measured for a fixed beam dose of 3.1×10^{12} H$^+$/cm^2. Figure 1(a) shows no crystallographic symmetry associated with Ge<111> within a statistical error of ~3%.

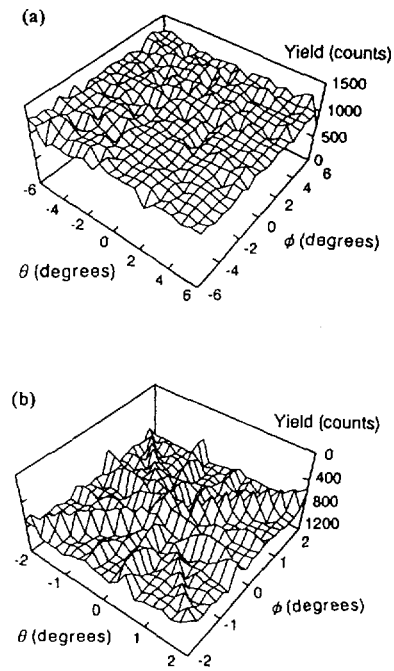

Fig. 1. Angular dependence of the electron yield integrated over an energy range 2.0-2.6 keV, emitted from a Ge(111) surface bombarded with 2.5 MeV H+, shown as a function of the rotation angles θ and ϕ. (a): Ge<111> aligned with the entrance axis of the spectrometer at $\theta=\phi=0$, (b): Ge<111> aligned with the ion beam direction. Note that in Fig. 1(b) $\theta=\phi=0$ is taken for the Ge<111> channeling incidence, and that the vertical axis is directed downwards.

Figure 1(b) shows a similar mapping obtained when Ge<111> is aligned with the ion beam direction (channeling incidence condition). It is notable that in this mapping no major axial nor planar direction of the crystal coincided with that of the entrance axis of the spectrometer. In this case, we obtain a clear shadowing pattern for Ge<111> with prominent ridges due to (110) planar shadowing. The Ge<111> yield is reduced by a factor of 0.5 compared to the

nonchanneling case. This pattern is essentially the same as those observed previously at an observation angle of 180°. It should be noted that in the mapping shown in Fig. 1(b) the accumulated beam dose on the crystal surface ranges from 3.1×10^{12} (at $\theta = \phi = -2°$) to 1.4×10^{15} H^+/cm^2 (at $\theta = \phi = 2°$). Therefore, the clear shadowing pattern obtained indicates absence of a radiation-induced effect that influences the electron emission from the crystal surface.

In a similar manner, the angular dependence of the electron yield has been investigated for Ge<111> at higher electron energies (3.3-4.3 and 4.6-6.0 keV), and also for Si<100> for 1.3-1.7, 2.6-3.4 and 3.3-4.3 keV electrons induced by 2.0 MeV H^+, for 0.86-1.1 and 1.5-2.0 keV electrons induced by 1.5 MeV He^+, and for 0.45-0.59 keV electrons induced by 0.37 MeV He^+. For the measurements with 0.37 and 1.5 MeV He^+, the inner-shell electrons of Si predominantly contribute to the electron yield since the measured energy ranges are well above the corresponding values of the binary-encounter peak energy (the maximum energy transferred to a free electron at rest) 0.82 and 0.20 keV for 1.5 and 0.37 MeV He^+, respectively. For Si, the electron yield at energies lower than ~1.6 keV includes energy-degraded Si K-shell Auger yield. In any case, however, we have observed no discernible increase nor decrease in the electron yield, typically within a statistical error of ~3%, that reflects the crystallographic symmetry with respect to the direction of the entrance axis of the electron spectrometer.

An approach from the forward-direction focusing effect and the electron channeling, mentioned earlier, is useful to account for the observed isotropic behavior of the outgoing electrons. According to Egelhoff,[3] the forward-direction focusing effect of 0.917-keV Auger electrons from Cu disappears after passing through 10 monolayers of Ni (~20 Å thick) because of multiple scattering. This indicates the existence of an attenuation length L for the forward-direction focusing effect. The value of L should be greater for higher-energy electrons, although detailed dependence of L on the electron energy is not well known. When the electron energy is increased to several hundred keV, L should correspond to the dechanneling length for electron channeling. For example, the measured dechanneling length is ~200 Å for 219 keV electrons in Cu<100>.

Accordingly, we may roughly assume that the values of L for the keV electrons in the present case lie in the range ten to hundred Å. For clear observation of the enhanced yield, the number of focused electrons started near the lattice sites (by scattering events) in the surface layer of thickness L must be at least comparable to the number of the defocused (multiply scattered) electrons contributing from behind the surface layer. It is important to note that such conditions were essentially satisfied in the observations of the forward-direction focusing effect and the electron channeling effect, referred above. Actually, in those cases the atoms that emit the electrons of characteristic energy were embedded in a surface layer thinner than the corresponding value of L. In contrast, the ion-induced electron yield should inherently include contribution from the electrons escaped through a surface layer thicker than the value of L. Probably, the isotropic emission character, independent of the crystallographic direction of the outgoing path, is one of fundamental aspects of the ion-induced electron emission from a single crystal target.

References

1) H. Kudo, A. Tanabe, T. Ishihara, S. Seki, Y. Aoki, S. Yamamoto, P. Goppelt-Langer, H. Takeshita, and H. Naramoto, Nucl. Instr. and Meth, B115 (1996) 125, and references therein.
2) P. F. A. Alkemade, L. Flinn, W. N. Lennard, and I. V. Mitchell, Phys. Rev. A53 (1996) 886.
3) W. F. Egelhoff, Jr., Phys. Rev. Lett. 59 (1987) 559.
4) H. Hofsäss and G. Linder, Physics Reports 201 (1991) 121.
5) G. Linder, K. Bendel, M. Minde, E. Recknagel, and Th. Wichert, Nucl. Instr. and Meth, 194 (1982) 193.
6) H. C. Poon and S. Y. Tong, Phys. Rev. B30 (1984) 6211.

5．4 Fine Structure of Copper L X-Ray Spectra (II)

K. Kawatsura, T. Inoue, T. Adachi, T. Igarashi, N. Terazawa, S. Arai,
Y. Aoki*, S. Yamamoto*, K. Narumi* and H. Naramoto*
Faculty of Engineering and Design, Kyoto Institute of Technology,
*Department of Materials Development, JAERI.

1. Introduction

The fine structure of the K X-ray diagram lines of the 3d transition elements has been the subject of numerous experimental and theoretical studies[1,2]. This was motivated by their asymmetric shapes, indicating large contributions from processes other than the main single electron bound-bound diagram transitions which dominate the corresponding symmetric emission lines of high Z atoms. Recently, we have reported[3] that broad satellite peaks are observed on the high-energy side of the L X-ray diagram lines in 3d transition metals (Cr, Mn, Fe and Co) by 0.08 MeV/u N and 0.04 MeV/u Ne ion impacts and the $L\alpha_{1,2}$ lines are shifted to lower energy.

We report the high resolution measurement of L X-ray spectra from a thick copper target produced by 1.0 MeV/u H, 0.64 and 0.073 MeV/u Si ion impacts[4-6].

2. Experiment

The experiments were performed at the TIARA accelerator facility of the JAERI of Takasaki using a 3 MV single-ended, and a 3 MV tandem electrostatic accelerator. The X-ray crystal spectrometer with a flat crystal and the block diagram of the X-ray detector electronics are similar to those described in detail previously[3,4]. The base pressure in target chamber was 1.0×10^{-4} Pa during this experiment. The ion beam (5×5 mm^2) was incident on a thick Cu target normal or 45° to the surface. The X rays emitted at a take-off angle of 45° were detected by a proportional counter with a thin polyester window of 1.0 μm thickness (Yunitika Co. Ltd.). This counter was operated at +1600 V in a flow mode of 50 ml/min utilizing PR gas (Ar 90 % + CH_4 10 %) at atmospheric pressure. The Cu L X-ray spectra were analyzed with a flat single crystal of rubidium acid phthalate (RbAP(100), 2d = 2.612 nm).

3. Results and discussion

The experimental results for 1.0 MeV/u H ion impact on a thick Cu target are 810.9 eV for Lι, 831.2 eV for Lη, 929.7 eV for $L\alpha_{1,2}$, 950.0 eV for $L\beta_1$, and 1022.0 eV for $L\beta_{3,4}$ X-ray emission lines, respectively[4]. These values are in good agreement with those of 811.1, 832, 929.7, 949.8 and 1022.8 eV given by Bearden[7].

Fig. 1 shows high resolution L X-ray emission spectra of Cu produced by 1.0 MeV/u H^+, 0.64 MeV/u Si^{5+}, and 0.075 MeV/u Si^{2+} ion impacts. For heavy ion impact, very complicated and intense structures are found at the high energy side of $L\alpha_{1,2}$ and $L\beta_1$ lines. They are considered to be the satellite and hypersatellite lines due to multiple L- and M-shell excitation and ionization[4-6]. In the case of low energy Si ion impact, it seems to be due to excitation and ionization processes other than pure Coulomb interaction, i.e. due to the electron promotion via molecular orbital formation between 2s and 2p levels of Si and 3s and 3p levels of Cu.

The figure also shows broad and intense bands at the energy region of 850 eV and 1055 eV and a broadening of the $L\alpha_{1,2}$ line to the lower energy. The broad and intense bands are attributed to the satellites and hypersatellites of the Lι and Lη lines and the $L\beta_{3,4}$ line, though in the latter case, the

energy shift to the higher energy are so large.

4. References

1. L.G.Parratt, Rev. Mod. Phys., **31** (1959) 616.
2. M.Deutsch, G.Holzer, J.Hartwig, J.Wolf, M.Fritsch, and E.Forster, Phys. Rev., **A51** (1995) 283.
3. K.Kawatsura, K.Ozawa, M.Terasawa, K.Komaki, and F.Fujimoto, Nucl. Instrum. Methods Phys. Res., **B75** (1993) 28.
4. H.Kageyama et al., Int. J. PIXE, **5** (1995) 203.
5. H.Kageyama et al., Nucl Instrum. Methods Phys. Res., **B107** (1996) 47.
6. K.Kawatsura et al., Radiat. Phys, Chem, **49** (1997) 617.
7. J.A.Bearden, Rev. Mod. Phys., **39** (1967) 78.

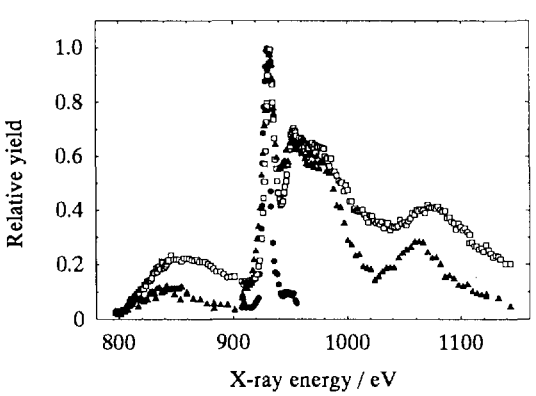

Fig. 1 LX-ray emission spectra of Cu produced by(●), 1.0 MeV/u H^+; (□), 0.64 MeV/u Si^{5+}; (▲), 0.075 MeV/u Si^{2+} ion impacts.

5．5 Ion Irradiation Effect on Single-crystalline Cu/Nb/α-Al_2O_3

B. Tsuchiya*, S. Yamamoto, K. Narumi, Y. Aoki, H. Naramoto
and K. Morita*
Dept. of Mater. Develop., JAERI/Takasaki/*School of Eng., Nagoya Univ.

1. Introduction

Ion beam mixing studies have been made to prepare quasi-stable materials, and the detailed overviews can be seen in references[1]. But there remain the problems to be studied about the fundamental nature of the atomic mass-transport. Recently, P. J. Partyka et al. have performed the ion beam mixing study in Cu/Nb immiscible system with 2.0 MeV Kr^+ ions[2], however, the change of crystal quality at the interface has not been studied. It is of essential importance to analyze the micro-structural change during irradiation in order to understand the kinetic process of the mixing in more detail.

In the present report, the microstructural change in Cu(111)/Nb(110)/sapphire$(11\bar{2}0)$ substrate is analysed at low temperatures and RT by using RBS/channeling technique at dual beam analysis system of TIARA.

2. Experimentals

Various kinds of single-crystalline films were grown hetero-epitaxially on sapphire $(11\bar{2}0)$ substrate under the conditions established by S. Yamamoto et al.[3]. The thickness of Cu and Nb layers were determined to be 50 and 71 nm, respectively, with RBS technique. The orientation relationship was determined with RBS/ channeling and diffraction techniques.

Ion beam irradiation was performed using a dual beam analysis system with 3 MV single-stage accelerator and 400 kV implantor, developed at TIARA[6]. The samples were irradiated with 260 keV Ar^+ ions at 56 K and room temperature. One of those specimens were cooled down with helium cryogenic system. At several fluences, the microstructures of multi-layer samples were characterized with 2.7 MeV He^+ RBS/channeling technique so that each contribution from Cu, Nb and Al of sapphire can be separated. The range of Ar^+ ions incident 40 degrees off to the surface normal is far beyond the Cu/Nb layers according to the TRIM code calculation. After the irradiation at several fluences, the surface topographs were characterized with scanning electron microscopy(SEM).

3. Results

Fig. 1 shows RBS spectra under the random and aligned conditions before and after irradiation at 6.2×10^{14} ions/cm^2 and 4.6×10^{16} ions/cm^2 at 56 K. The two solid lines represent the random and aligned spectra before ion irradiation. Typical change after the irradiation on Cu/Nb system can be seen in the energy region of 1.9 MeV-2.2 MeV. The leading edges from Nb layer shift to the high energy side. This can be attributed to the sputtering localized only in the Cu layer. In accordance with this sputtering, the backscattered intensities of 2.7 MeV $^4He^+$ ions from the Cu layer in the random and the aligned spectra become coincided with each other, which implies the reordering of implanted atoms in single-crystalline layer is caused. But the possibility of amorphization

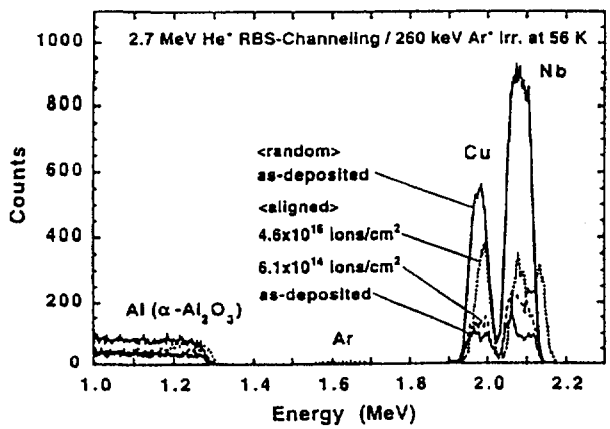

Fig. 1: RBS aligned spectra obtained from 50nm Cu(111)/71nmNb(110)/sapphire$(1\bar{1}20)$ sample, which was as-deposited and irradiated at the fluences of 6.2×10^{14}/cm^2 and 4.6×10^{16}/cm^2 with 2.7 MeV $^4He^+$ RBS/channeling technique.

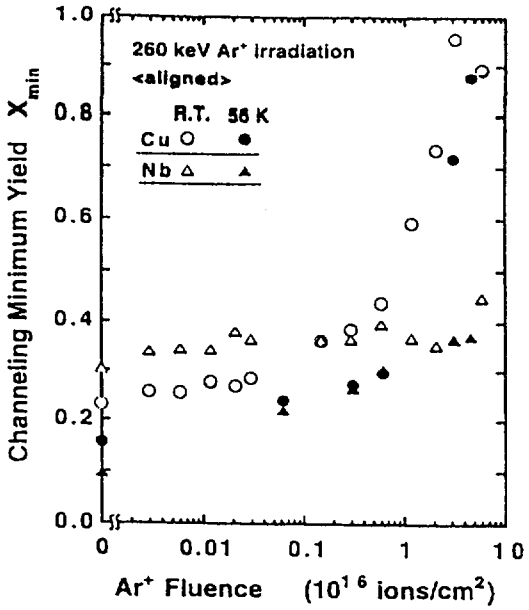

Fig. 2: Crystal quality change in Cu and Nb layers as a function of 260keV Ar+ ion fluence at 56 K and RT.

can be excluded because there is no any evidence of mixing with Nb layer and the introduction of highly distorted imperfections in the aligned spectrum from Nb layer. Under the present condition, the maximum defect production is caused in the sapphire substrate, and the uniform ion-beam mixing along the depth can be expected in Cu and Nb layers. The bump in the region of 1.2 MeV-1.3 MeV after irradiation is formed through the defect generation by in the sapphire crystal lattice.

In Fig. 2, the minimum yields χ_m for Cu and Nb layers are plotted as a function of Ar^+ ion fluence at 56 K and RT. The data at low temperature are systematically lower because of low vibrational amplitude, however, the considerable change can be observed in the Cu layer. Irrelevant to the implantation temperature, the lattice disorder in Cu layer is induced at the slow rate at the beginning followed by the high rate stage starting from $\sim1\times10^{16}$ /cm^2. In the whole range of the irradiation, the sputtering rate in the Cu layer is constant (3.1 and 7.0 atoms/ion at 56 K and RT, respectively) even if the inhomogeneous erosion is caused as observed with SEM. The sputtering rate obtained at 56 K seems to be reasonable[5-7], and the reported data at RT might contain the thermal effect. The irregular erosion on Cu surface could be explained by the atomistic diffusion kinetics judging from the result in Fig. 2.

References

1) For example: M. Nastasi, J. W. Mayer, Mat. Sci. Eng. **R12**(1994)1.
2) P. J. Partyka, R. S. Averback, I. K. Robinson, Y. S. Lee, C. P. Flynn and P. Bellon, Mat. Res. Soc. Symp. Proc. **396**(1996)107.
3) S.Yamamoto, H. Naramoto, K. Narumi and Y. Aoki, private communication.
4) H. Naramoto, Y. Aoki, S. Yamamoto and H. Abe, Nucl. Instr. Meth. **B127/128** (1997)599.
5) N. Matsunami et al., Atomic data and nuclear data tables **31**(1984)1.
6) G. Dupp and A. Scharmann, Z. Physik **192**(1966)284.
7) P. Sigmund, Phys. Rev., **184**(1969)383.

5．6 Channeling Analysis of Single-crystalline Nb Film on α-Al_2O_3 Implanted with Cu Ions

H. Naramoto, S. Yamamoto, K. Narumi, B. Tsuchiya* and Y. Aoki

Dept. of Mater. Develop., JAERI/Takasaki; *JAERI Research Student(1996FY)

1. Introduction

Materials processings using energetic beams like ion implantation, ion beam mixing and pulse laser annealing have been employed to realize new materials with different phases[1-3]. These techniques are commonly based on atomic rearrangement under the non-equilibrium condition but the kinetics for the atomic rearrangement are not well known. For example, the implanted different atoms themselves have chemical potentials to be transferred from the situated sites, however, it is not well sure whether it is caused non-diffusively (explosively) or diffusively (gradually). Under the just-processed condition, it is needed to study how to control the nucleation process of new phases from the unstable state for the development of new functional materials.

In the present study, the ion implantation and the on-site analysis are made at low temperatures using a dual beam analysis system[4]. $^{63}Cu^+$ ion implantation into Nb single-crystalline film on sapphire is chosen as one of the combinations in immiscible systems.

2. Experimentals

Single-crystalline Nb films with three major orientations were grown at 700 ℃ on sapphire substrates with three different orientations under the ultra high vacuum with MBE technique: Nb(100)//α-$Al_2O_3(10\bar{1}2)$, Nb(110)//α-$Al_2O_3(11\bar{2}0)$, Nb(111)//α-Al_2O_3 (0001). In this experiment, three kinds of experimental parameters like the Nb layer thickness, the implantation energy of $^{63}Cu^+$ ions and the incident energy of probing $^4He^+$ ions were chosen so that the contributions from Nb layer and implanted Cu atoms can be separated properly in RBS spectra. Typical combination is analysing 2.7 MeV $^4He^+$ ions, implanting 160 keV $^{63}Cu^+$ ions and 100nm Nb thickness.

In the dual beam experiment, ion beam for implantation was scanned and incident 40 degrees off the surface normal. The analyzing $^4He^+$ ion beam is incident almost parallel to the surface normal. In the entire course of the implantation, samples were kept at low temperature to avoid thermal effects, and also special attentions were paid not to induce the accidental misorientations.

After the Cu implantation up to 2×10^{16} /cm^2, the angular scans were made around <100>, <110> and <111> axes of Nb with the corresponding scans on Cu.

3. Results

Fig. 1 shows 2.7 MeV $^4He^+$ RBS/channeling spectra from the Nb layer implanted with 160 keV ^{63}Cu ions as a function of implantation dose. Implantation and analysis were performed at 60 K. Two spectra with higher yield are taken under the random condition before (wider one) and after (narrower one)

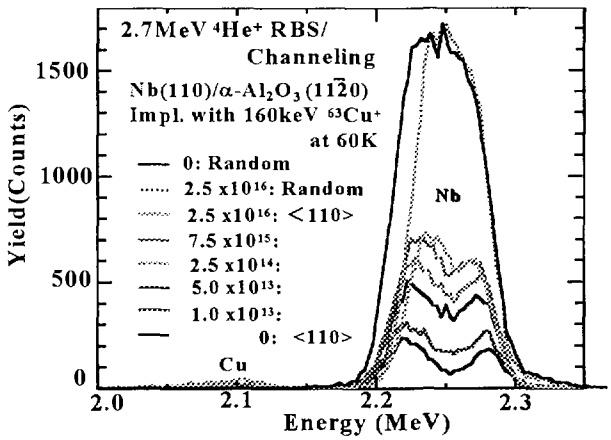

Fig. 1: 2.7 MeV $^4He^+$ RBS/channeling spectra from Nb(110)/sapphire substrate as a function of implantation dose of 160 keV $^{63}Cu^+$ ions. Implantation and analysis were made at 60K. The contribution from sapphire substrate is not included.

the implantation. The others are taken under <110> aligned condition as a function of implantation dose. The estimated projected range of Cu is far beyond the Nb layer, and the uniform defect production along the depth is expected. At the initial stage of implantation, the damage is accumulated linearly even in hard bcc lattice of Nb. In the dose region higher than 1×10^{16} ions/cm^2, the damage level is almost saturated and the loss of Nb becomes prominent through sputtering evidenced as narrowing in random spectrum from Nb layer. The leading edges of Nb before and after the implantation of 2.5×10^{16} ions/cm^2 are the same in their feature and any roughening after heavy implantation is not observed which is different from Nb implantation into soft fcc Cu. On the contrary, there appears some difference between random and aligned spectra from implanted Cu, which implies the substitution of Nb lattice by Cu or coherent precipitation of Cu in immiscible Nb lattice.

In order to identify the coherency of implanted Cu atoms, the angular scans were made around Nb<110> axis by setting windows for Nb and Cu. The same kinds of experiments were also employed on Nb(100) and Nb(111) samples. Fig. 2 shows the result of angular scans around Nb<110> axis with the result of implanted Cu. The widths at the half-maximum for Nb and Cu are 1.70 and 1.48 degrees, respectively and the results around Nb<100> and Nb<111> are almost the same for Nb and Cu. The present results are consistent with the crystal growth of Cu coherent with the Nb lattice at low temperature under the compulsorily mixed state between Nb and Cu.

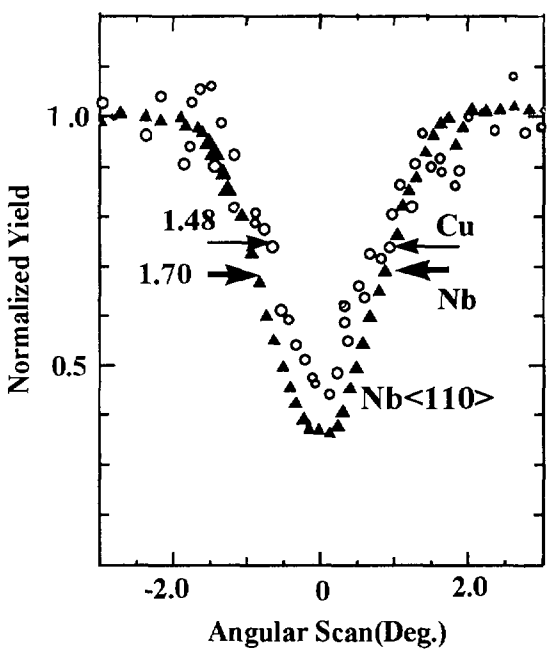

Fig.2: Angular scan of RBS signal from Nb and implanted Cu around Nb<110> axis.

References

1) C. W. White, C. J. McHargue, P. S. Sklad, L. A. Boatner and G. C. Farlow, Materials Science Reports **4**(1989)41.

2) M. Nastasi, J. W. Mayer, Mat. Sci. Eng. **R12**(1994)1.

3) J. Khan, Sym. Proc. vol. **201** ed. H. A. Atwater, F. A. Houle and D. H. Lowndes(Materials Research Soc.)pp465.

4) H. Naramoto, Y. Aoki, S. Yamamoto and H. Abe, Nucl. Instr. Meth. **B127/128** (1997)599.

5．7 Characterization of single-crystalline Cu/Nb films by ion beam analysis

S. Yamamoto, B. Tsuchiya, K. Narumi, Y. Aoki and H. Naramoto
Dept. of Materials Development, JAERI

Ⅰ. Introduction

Successful growth of single-crystalline Cu/Nb films on sapphire substrates with different orientations is reported based on the crystal symmetry characterization using the planar channeling technique. The difference in lattice structure and the big lattice mismatching was overcome by adjusting the substrate temperatures. The layered structure was prepared by using electron-beam evaporation under UHV condition. In this context, Nb/Cu system which are immiscible even at higher temperature[1], is suitable for exploring a condition of multilayered structure growth with the sharp interface but might not be so for single crystal growth. It is demonstrated that the single-crystalline Cu/Nb layers on α-Al_2O_3 is formed with the excellent crystal quality by controlling the substrate temperatures. The growth habit depends on the substrate orientations: Cu(111)/Nb(110) on sapphire$(11\bar{2}0)$ and Cu (100)/Nb (100) on sapphire$(1\bar{1}02)$.

Ⅱ. Experimental

Nb and Nb/Cu films were deposited on four kinds of major crystallographic planes, $(11\bar{2}0)$, (0001), $(1\bar{1}02)$ and $(10\bar{1}0)$ sapphire (α-Al_2O_3) substrates using the electron beam evaporation technique under UHV condition. All of sapphire substrates were pre-heated at 1450°C for 12 hours in air to eliminate the induced strain during polishing. During evaporation, the vacuum in a growth chamber was maintained around 5 x 10^{-8} torr after a long term evaporation to trap the residual gases with deposited Nb on the chamber wall. The thickness of each layer was monitored with quartz oscillators which were calibrated with Rutherford backscattering spectroscopy (RBS) measurements. The Nb and Cu films were deposited at the rate of about 0.2 nm/s onto the sapphire substrate kept at 750°C for Nb and less than 600°C for Cu. The typical thicknesses of Cu and Nb layers were in the range of 50 nm to 250 nm, respectively. At each step of evaporation, the surface structure was examined with low energy electron diffraction (LEED) technique. The surface structure of the top Cu layer was observed by SEM to check a possibility of columnar growth.

The layered samples were analyzed with RBS/channeling method using 3 MV single stage accelerator at TIARA, JAERI/Takasaki. The analyzing beams of ^{4}He ions with energy of 1.5 to 2.7 MeV were incident on samples. Backscattered particles were detected by standard surface barrier detectors at 165° to the incident beam.

Ⅲ. Results and discussion

Fig. 1 illustrates the <110> axial channeling results of 2.0 MeV ^{4}He ions in single crystal Nb(110) layer with 100 nm thickness on $(11\bar{2}0)$ sapphire substrate. χ_{min}, the ratio between the random and the aligned yield at the fixed thin layer is an important parameter to characterize the crystal perfection. Judging from χ_{min}

specified at the depth (~10 nm) just behind the surface peak at Nb layer, the crystal quality is almost the same as in a bulky Nb crystal at the corresponding depth. A comparison among the channeling data from Nb layers prepared under several different conditions shows that the quality of single crystal Nb films is dependent on the substrate temperature during evaporation. For the growth of high quality Nb single crystal layer it is needed to employ the high temperature condition. In this figure it is recognized that some amounts of disorder exist around the interface region between Nb layer and sapphire substrate, however, the interface is not mixed with each other under the present condition. The crystallographic analysis was examined by setting the energy windows of RBS spectra at Nb and Al component of sapphire. The orientation relationships obtained from planer channeling measurements were as follows:

Nb($1\bar{1}0$)/sapphire($1\,1\bar{2}0$), [111] || [0001]

Nb(111)/sapphire(0001), [$1\bar{1}0$] || [$1\,1\bar{2}0$]

Nb(001)/sapphire($1\bar{1}02$), [$1\bar{1}0$] || [$1\,1\bar{2}0$]

Nb($1\bar{2}1$)/sapphire($10\bar{1}0$), [111] || [0001].

The same crystallographic relationship was observed based on TEM analysis in small area[1] but this is the first time to examine the whole area of grown layer under the channeling condition. On the other hand, Cu deposition on sapphire with the thickness of 100 nm, the epitaxial growth was not realized at the substrate temperature ranging from 200°C to 700°C. The structure of Cu layer tends to be highly textured perpendicular to the substrate with the increase of substrate temperature.

An additional deposition of Cu on Nb layer has spent so much time to find out a suitable condition for the single crystal growth of Cu. The substrate temperature was changed from RT to 600 °C. Different from simple imagination, the best condition for single crystal growth with the smooth surface was around 200 °C. The SEM photographs show that the higher substrate temperature induces the island growth, however, each island is connected coherently judging from the studies of channeling and LEED analyses.

Fig. 2 illustrates RBS/channeling results of the Nb and Cu layers were deposited with the same thickness of 50 nm on sapphir($1\,1\bar{2}0$) substrate. By employing rather higher energy 2.7 MeV $^4He^+$ ions, the mass-resolution in the spectra has become good enough to judge the interface sharpness. The peak at the 2.2 MeV corresponds to the Nb layer, and the peak at 2.1 MeV to the top surface Cu layer. The orientation relationship between Cu layer and Nb layer was determined through the angular mapping of planer channeling. The results shows that the Cu(111) layer grow on Nb(110) layer. The crystallographic relationship between Cu and Nb layers can be explained by stacking the closest-packed planes of bcc Nb and fcc Cu. The single crystal growth of Cu on Nb(100)/sapphire($1\bar{1}02$) was also successful around 200 °C but at higher temperatures the columnar structure appeared.

References

1. Ed. By T. B. Massalski(chief), H. Okamoto, P. R. Subramanian and L. Kacprzak, Binary Alloy Phase Diagrams 2nd edition vol. 2(ASM International, 1990).
2. D. M. Tricker and W. M. Stobbs, Phil. Mag. 71, 1037(1995). and Phil. Mag. 71,1051(1995).

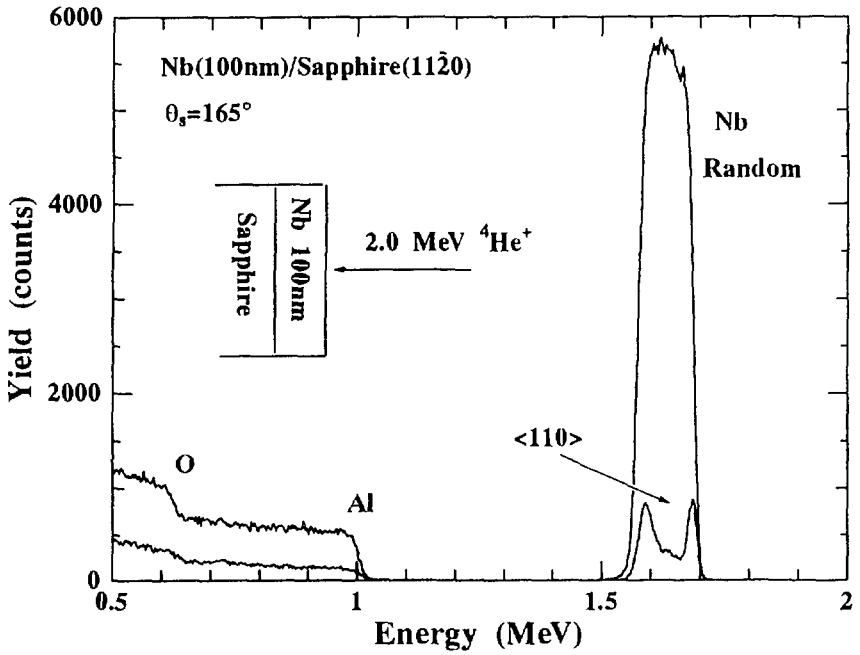

Fig. 1. 2.0 MeV ^{4}He RBS/channeling spectra from Nb(110) single-crystalline film on (11$\bar{2}$0) sapphire substrate. Thickness of Nb film is about 100 nm.

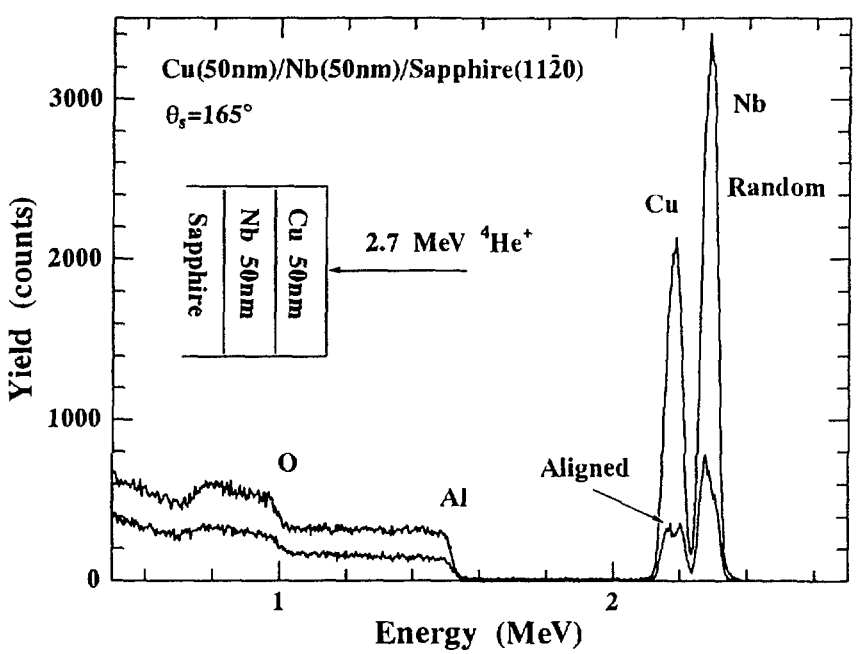

Fig. 2. 2.7 MeV ^{4}He RBS/channeling spectra from Cu(111)/Nb(110) single-crystalline film on (11$\bar{2}$0) sapphire substrate. Thickness of Cu and Nb layers are 50 nm each.

5．8 Surface alloying of immiscible metals: Ni(111)-($\sqrt{3}\times\sqrt{3}$) R30°-Pb

K. Umezawa, S. Nakanishi and T. Yumura, S. Yamamoto*,
Y. Aoki* and H. Naramoto*
Dept. of Physics, University of Osaka Prefecture,
*Dept. of Materials Development, JAERI/Takasaki

1. Introduction

The investigation of metal on metal overlayer systems is an interesting and important subject for understanding surface related phenomena such as catalytic reactions and surface specific compound formation. The Stranski-Krastanov growth mode is common for metal on metal systems when deposition occurs at low temperature or when the components exhibit little tendency for alloy formation. However in many systems it is of interest to consider the possibility of bulk or surface alloy formation. In recent studies, elements which are immiscible in the bulk have been found to form stable two-dimensional mixtures at the surface [1-3]. These studies include Alkali-metal adsorbates on Al(111) and (001), Au on Ni(110) and Ag on Pt(111), respectively. Related theoretical work was proposed by Tersoff as well [4].

In a continuation of previous work [5], we found that upon annealing the Pb-Ni(111) system to 600°C, the surface tends to equilibrate at a ($\sqrt{3}\times\sqrt{3}$) R30° structure if sufficient Pb is present. This paper reports results of our studies of a Ni(111)-($\sqrt{3}\times\sqrt{3}$) R30°-Pb structure by low energy impact collision ion scattering spectroscopy (ICISS) combined with low energy electron diffraction (LEED) and MeV ion scattering. We conclude that this ($\sqrt{3}\times\sqrt{3}$) R30° structure shows surface-confined alloy formation in immiscible systems. We used the ion scattering analysis programs for comparison with experimental data: the calculations for the three-dimensional cross section for ions that scatter sequentially and classically from two atoms, and are computationally very fast.

2. Experimental procedures

The experimental procedures described here were performed in an ultra-high vacuum systems with LEED, AES and ICISS facilities. The base pressure during the experiment was maintained below 5×10^{-8} Pa. After a Ni(111) substrate (ϕ12mm×0.5mm thickness) was mounted on a standard UHV-XYZ manipulator, it was extensively cleaned in situ by repeated cycles of 500 eV-Ar^+ bombardment and subsequent annealing at 500 °C to remove the surface damage. Lead was evaporated at a rate of about 0.03 ML/min. onto the Ni(111) crystal to a coverage of 0.45 ML at room temperature, then annealed at a substrate temperature of 600 °C. The Ni(111)-($\sqrt{3}\times\sqrt{3}$) R30°-Pb LEED patterns were finally observed after cooling of the substrate to room temperature.

The ICISS spectra were taken by chopping the primary 3 keV-Ne^+ beam and detecting 180° backward scattered particles after free flight through a drift tube of 60 cm by a micro channel plate (MCP) detector which was coaxially

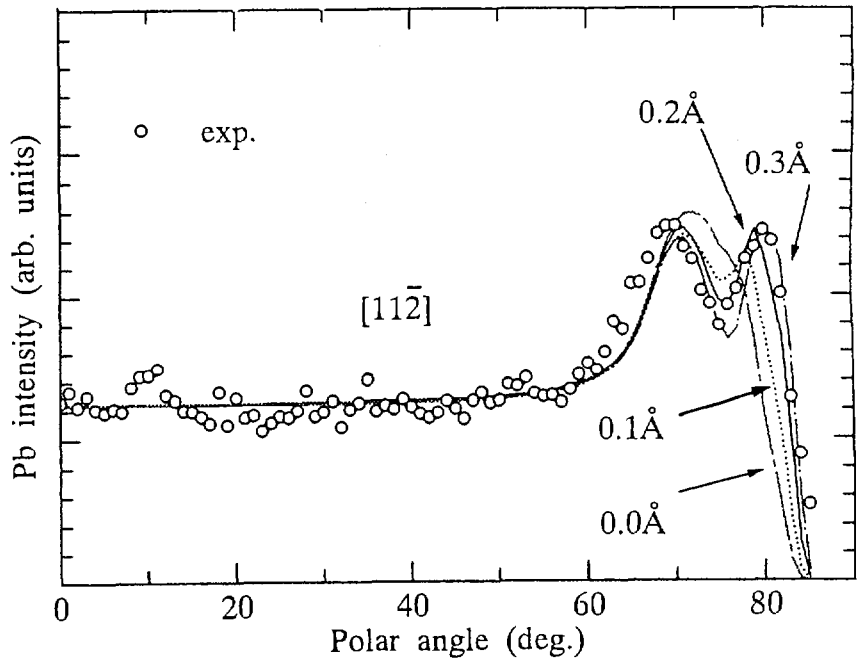

Fig. 1 A series of ICISS polar angle scans and computer simulations for 3 keV-Ne^+ ions backscattered from Pb atoms along the [1$\bar{1}$2] azimuths. Circles and the broken curves show the experimental data and computer simulations based on the model shown in fig. 2, respectively.

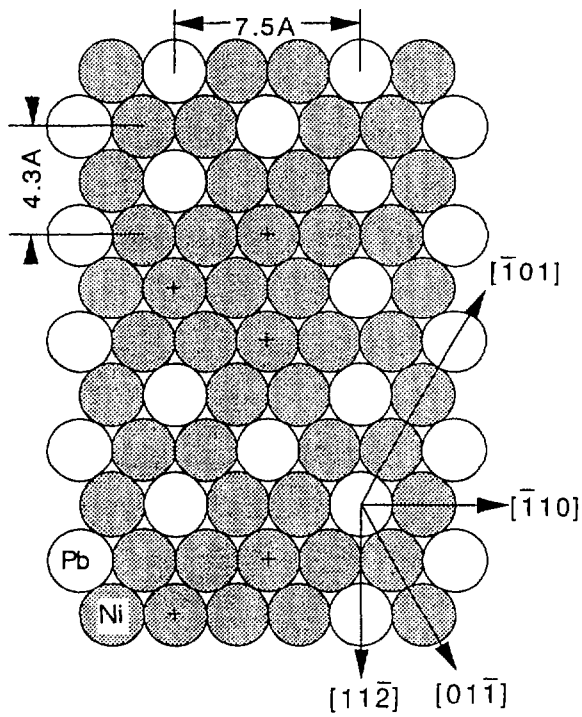

Fig. 2 Ball models showing partial of Pb incorporation with ($\sqrt{3}\times\sqrt{3}$) R30° ordering (1/3 of Pb atoms are missing to the ideal ($\sqrt{3}\times\sqrt{3}$) R30° structual model.). The "+" symbol represents the positions of Pb atoms in the ideal structure.

mounted along the primary tube. Polar angle scans were performed from -85° to +85° in 1° increments. Also, the Pb coverage at completion of the $(\sqrt{3}\times\sqrt{3})$ R30° structure was verified by RBS measurements using 2 MeV-He^+ ions.

3. Results and discussion

The intensity of ions scattered from Pb as a function of polar angle is shown in fig. 1. Along the $[1\bar{1}2]$ azimuth shown in fig. 1, two Pb signal peaks were observed at 72° and 81°. The presence of two peaks indicates that more than one Pb spacing exists along the $[1\bar{1}2]$ direction. A structure model was examined to explain experimental results as shown in fig 2. In this structure model 1/3 of Pb atoms corresponding to an ideal $\sqrt{3}\times\sqrt{3}$ structure are missing and the remaining Pb is incorporated into first Ni layer. The Pb spacings based on calculations of the nearest-neighbor distance of Ni (2.49Å) are 4.3 Å, 8.6 Å and 12.9 Å along the $[1\bar{1}2]$ azimuth, respectively. In fig. 2, lines represent the calculated Pb intensity depending on the Pb height from 0.0 to 0.3Å above the center of mass position of the first layer of Ni atoms. At the Pb height of 0.0Å which corresponds to the ideal incorporated case, the calculated curve is inconsistent with the experimental data. For this case the peak at around 70° on the calculated curve is due to focusing effects of the nearest neighbor Ni atoms since both Pb and Ni atoms have the same height. However, at a Pb displacement of 0.2Å with respect to the first Ni layer, calculated curves nicely fit the Pb polar scattering peak positions. Especially, double peaks are clearly observed in the $[1\bar{1}2]$ azimuth. The calculated critical angles for different Pb spacings, 4.3Å, 8.6Å and 12.9Å correspond to 72.7°, 80.7° and 81.9°, respectively. These calculations indicate that triple peaks are predicted over the polar angle of 70.0°. In practice, it is hard to distinguish the small angle difference between 80.7° and 81.9° using the present experimental system. This is the reason why experimental data show only double peaks along this direction. The model of fig. 2 is not an ideal structure model in order to explain the experimental data, but this model shows a defect of 33% of Pb atoms corresponding to an ideal $\sqrt{3}\times\sqrt{3}$ structure.

The physics behind this surface structure model is that a pair of elements, Pb and Ni, which are immiscible in the bulk form a mixture confined to a single atomic layer at the surface.

References

[1] J. Neugebauer and M. Scheffler, Phys. Rev. Lett. **71** (1993) 577.

[2] L. P. Nielsen, F. Besenbacher, I. Stensgaard, E. Lægsgaard, C. Engdahl, P. Stoltze, K. W. Jacobsen and J. K. Nørskov, Phys. Rev. Lett. **71**(1993) 754.

[3] H. Röder, R. Schuster, H. Brune and K. Kern, Phys. Rev. Lett. **71** (1993) 2086.

[4] J. Tersoff, Phys. Rev. Lett. **74** (1995) 434.

[5] K. Umezawa, A. Takahashi, T. Yumura, S. Nakanishi and W. M. Gibson, Surf. Sci. **365** (1996)118.

5．9 Positron Trapping Defects in Vitreous and Metamict SiO_2

M. Hasegawa, M. Saneyasu, A. Kawasuso*, Z. Tang and S. Okada*
Institute for Materials Research, Tohoku University
**Advanced Radiation Technology Center, JAERI*

1. Introduction

Silica glass (vitreous SiO_2 : v-SiO_2) has been widely used in electronics and communication technology, for example, in glass fiber wave guides, metal oxide semiconductor (MOS) devices and an optical lens for the lithography of large-scale integrated devices [1]. Thus it is of technological importance to study irradiation effects in silica glass because they are subjected to photon, particle irradiation or ion implantation in their device processing. Irradiation-induced defects have been extensively studied by ESR (electron spin resonance) and optical absorption. However, ESR technique is only applicable to paramagnetic defects, such as E'-centers, peroxy radicals (POR) and non-bridging oxygen hole centers (NBOHC), but not to diamagnetic defects. Positron annihilation will be applicable to paramagnetic and diamagnetic vacancy-type defects.

Several groups have studied positron annihilation on v-SiO_2 and crystalline alpha-quartz (c-SiO_2). However, there have been few efforts to clarify physical origin of positron trapping at irradiation-induced defects and positronium (Ps) formation. In this study, we have performed positron lifetime measurements on specimens irradiated in the same conditions. We have made the experiments on synthetic v-SiO_2 with high purity (total metallic impurities and OH are less than 1 at. ppm in their concentrations) and synthetic c-SiO_2 for comparison.

After higher dose irradiation, c-SiO_2 is subject to metamictization (crystalline-glass phase transition) [2]. Then it is very interesting to study positron annihilation in this metamict state (m-SiO_2).

In this project we try to employ an internal positron source method of ^{22}Na ($^{28}Si(p, ^{7}Be)^{22}Na$) in SiO_2 to obtain detailed and precise positron lifetime parameter analysis with taking advantage of no source component problem for the internal positron source. In this report we present the internal positron source method and formation of Ps in microvoids in v-SiO_2 and m-SiO_2.

2. Experiment

High purity synthetic v-SiO_2 specimens (Nippon Silica Glass ES; Shin-Etsu Quartz, Suprasil F300)($8 \times 8 \times 1$ mm^3) were stacked and attached to an aluminum holder cooled by running water. To introduce the internal source of ^{22}Na, the stacked samples were irradiated with 70MeV proton beam: the beam current was about 1 μA for 12 hours and the beam diameter was about 10mm. The irradiation temperature was estimated to be less than 400℃. These v-SiO_2 and c-SiO_2 samples were also fast-neutron irradiated in the Japan Materials Testing Reactor below 150° C. After irradiation, positron lifetime measurements were made at room temperature using a conventional fast-fast lifetime spectrometer with a time resolution of 200ps (FWHM).

3. Results and Discussion

Figure 1 shows positron lifetime spectra for the proton-irradiated samples (ES) with the internal positron source and for the

positron ^{22}NaCl source (about 0.5MBq) sandwiched with thin Myler films (5 μm). The spectrum for the unirradiated samples was found to include positron source components of about 9%: 0.340ns (7.8%) and 1.379 ns (1.3%). These source components come from positron annihilation in the ^{22}NaCl source and the Myler films. However the proton-irradiated samples containing the internal ^{22}Na source show no such source components. Then we can say that the internal source sample are well suited for detailed and precise analysis for positron lifetimes of 0.3 ~2ns. Furthermore the internal source method is also suitable for positron lifetime and Doppler broadening measurements at high temperatures where positron source supporting films, such as Myler films, are not stable. However, the proton-irradiation induced ^{22}Na activity was very low (0.05MBq for each plate of SiO_2). Then longer time irradiation or higher beam current irradiation is very necessary.

Next we mention Ps formation in microvoids in v-SiO_2 and m-SiO_2 [3]. In v-SiO_2, Ps is known to form in structural microvoids, which are closely correlated to higher membered-rings [4]. An average radius of microvoid of 0.3nm is estimated both from pick-off annihilation rate ($1/\tau_3$)[5] and Ps ACAR distributions [4,6]. As stated above, c-SiO_2 undergoes metamictization after higher dose irradiation than 1×10^{20}n/cm^2 [2]. In Fig.2, the densities of v-SiO_2 and c-SiO_2 are plotted against the irradiation dose. The density of c-SiO_2 shows a rapid and marked decrease after irradiation around 1.0×10^{20}n/cm^2. This decrease is associated with metamictization from c-SiO_2 to m-SiO_2. The density of v-SiO_2 shows a slight increase after irradiation: irradiation-induced compaction [2]. In Fig. 3, o-Ps pick-off annihilation lifetime of about 1.8ns is seen after metamictization and gives an average radius of about 0.3nm estimated by a free volume theory for Ps [5], which is very close to that of v-SiO_2. This demonstrates that the microvoids with the average radius of 0.3nm are associated with intrinsic structural open spaces in topologically disordered silica [7]: v-SiO_2 and m-SiO_2. The structural studies of these microvoids by Ps are expected to provide us with unique information about SiO_4 network arrangements in subnanometer scale.

4. References

[1] D.L. Griscom: J. Ceram. Soc. Japan: **99**, 923 (1991).

[2] F.W. Clinard, Jr. and L.W. Hobbs: "Physics of Radiation Effects in Crystals", Ed. by R.A. Johnson and A.N. Orlov, (Elsevier, Amsterdam 1986) p387.

[3] M. Saneyasu et al.: Mat. Sci. Forum (in press).

[4] M. Hasegawa et al.: Sci. Rep. RITU **A40**, 203, (1994) ; Mat. Sci. Forum **175-178,** 269 (1995) ; Nucl. Instr. Meth. **B116**, 347, (1996).

[5] H. Nakanishi and Y.C. Jean: "Positron and Positronium Chemistry", Ed. by D.M. Schrader and Y.C. Jean, (Elsevier, Amsterdam, 1988) p159.

[6] M. Tabata et al.: J. Nucl. Mat. **239**, 228 (1996).

[7] P.K. Gupta: J. Am. Ceram. Soc. **76** (1993) 1088.

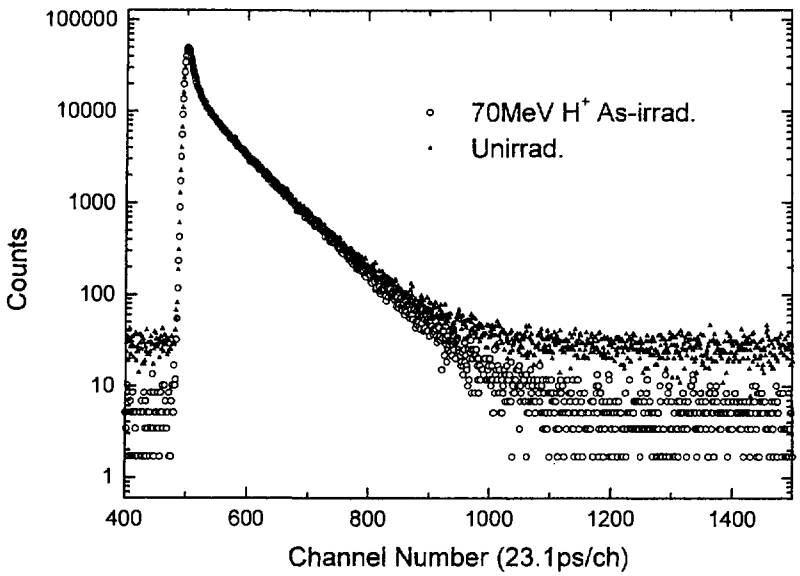

Fig.1. Positron lifetime spectra for v-SiO_2 irradiated with 70MeV proton beam and for unirradiated SiO_2. For the positron lifetime measurements a usual "external" $^{22}NaCl$ source was used.

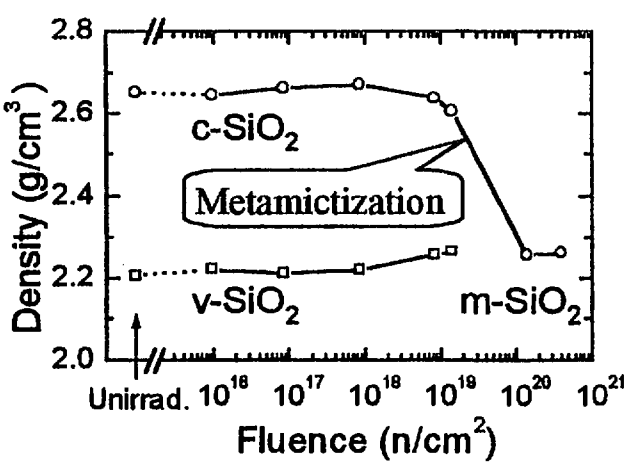

Fig. 2. Fast-neutron dose dependence of positron lifetime parametetrs of c-SiO_2.

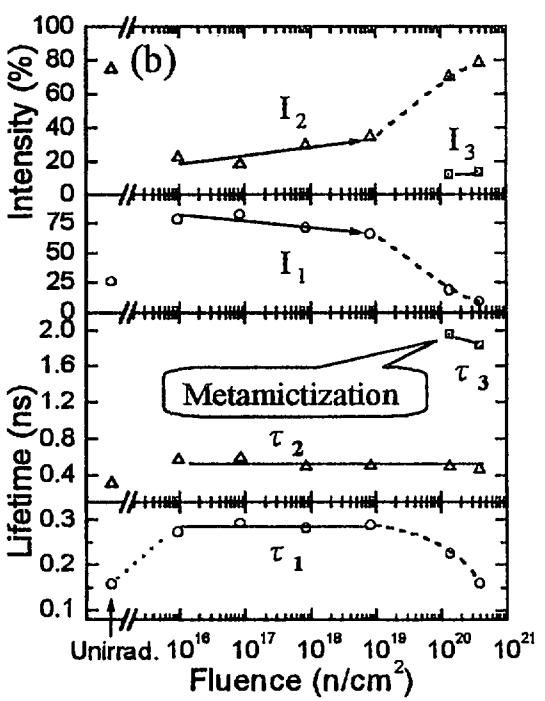

Fig.3. Fast-neutron dose dependence of densities of v-SiO_2 and c-SiO_2.

5.10 Vacancy-hydrogen interaction in proton-implanted Si studied by positron lifetime and infrared absorption measurements

A. Kawasuso, H. Arai and S. Okada
Japan Atomic Energy Research Institute, 1233 Watanuki,
Takasaki 370-12, JAPAN

1. Introduction

Hydrogen in Si has a high reactivity and hence interacts with various impurities and defects to modify their electrical property, e.g., the passivation of electrical active donors and acceptors, the termination of dangling bonds at vacancies, dislocations and surfaces [1]. Hydrogen also activates some electrical "inactive" impurities such as carbon and oxygen due to the formation of complexes. Recently, it has also been shown that hydrogen enhances the thermal donor formation [2]. Defects induced by proton implantation have been studied mainly with infrared (IR) absorption measurement. Many absorption lines related to local vibration of hydrogen atoms trapped at defects are observed after proton implantation. However, infrared absorption method hardly determine if the observed line is vacancy-related or interstitial-related. To elucidate this problem, we performed positron lifetime and infrared absorption measurements with isochronal annealing. We report that some absorption lines are assigned to vacancy-hydrogen complexes.

2. Experimental

Specimens used in this work were cut from a floating-zone grown Si single crystal doped with $1x10^{16}$ cm^{-3} phosphorus. The specimens were implanted with 6 MeV protons up to a dose of $5x10^{15}$ p/cm^2 at room temperature. As a reference, 3 MeV-electron-irradiated ($1x10^{18}$ e/cm^2) and 6 MeV-alpha-implanted ($5x10^{15}$ α/cm^2) specimens were also prepared. Isochronal annealing was carried out from 100 to 700℃ with a temperature step of 25℃ for 20 min in a dry argon atmosphere. Positron lifetime measurement was performed using a conventional spectrometer with a time resolution of 230 ps. Lifetime spectra were decomposed to two exponential terms (bulk and defects): $L(t)=(I_1/\tau_1)\exp(-t/\tau_1)+(I_2/\tau_2)\exp(-t/\tau_2)$. Positron trapping rate (κ) was determined based on the two-state trapping model. The bulk positron lifetime was determined to be 220 ps using unirradiated Si. Infrared absorption measurement was performed at 6 K using a JEOL FT-IR JIR-100 spectrophotometer.

3. Results

Figure 1 shows the annealing behavior of the second lifetime (τ_2) related to positron annihilation at vacancy-type defects. In the cases of electron irradiation and alpha implantation, the lifetime τ_2 increases with increasing annealing temperature. This clearly shows the evolution of vacancy-clusters after the annealing of small vacancies. On the contrary, the lifetime τ_2 for the proton-implanted Si first decreases at 100-200℃, increases at 300℃, decreases again at 400℃ and increases again at 600℃. This peculiar annealing behavior is probably caused by the interaction between hydrogen atoms and vacancies. The deviation of the

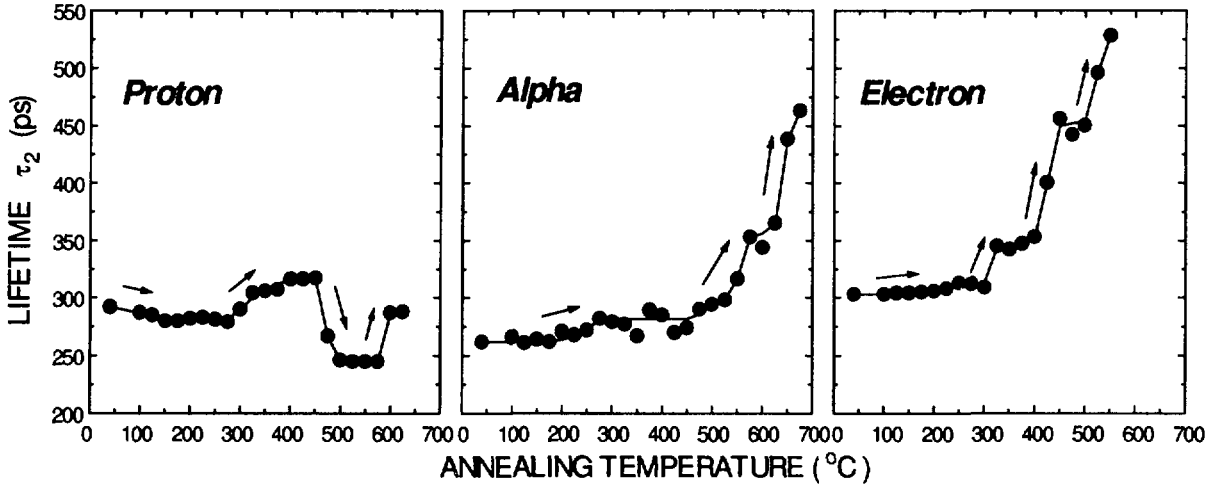

Fig.1 Annealing behavior of lifetime τ_2 for proton and alpha-implanted and electron-irradiated Si.

first lifetime (τ_1) from that expected in the two-state trapping model was observed for the proton-implanted Si suggesting the presence of another defect component which gives the lifetime close to the bulk lifetime.

Figure 2 shows the infrared absorption spectra obtained for the proton-implanted Si. In addition to the divacancy-related line (2768 cm^{-1}), many absorption lines are observed from 1900 cm^{-1} to 2250 cm^{-1}. These characteristic lines are originating from local vibration of hydrogen atoms. Thus, the presence of hydrogen-defect complexes is confirmed. It is proposed theoretically that the lines below and above 2000 cm^{-1} are associated with interstitial-hydrogen complexes and vacancy-hydrogen complexes, respectively [1].

Figures 3 and 4 show the annealing behaviors of the positron lifetime (τ_2), the trapping rates (κ_1, κ_2) and the IR absorbance (>2000cm^{-1}). At 100-200℃, the 2768 cm^{-1} absorbance decreases. Since divacancies in Si start to migrate above 250℃ [3], the decreases in the 2768 cm^{-1} absorbance is attributed to the capture of hydrogen atoms by divacancies. The trapping rate κ_2 decreases and the lifetime τ_2 shortens in the same temperature range. The shortening of the lifetime τ_2 is explained as the reduction of divacancy open volume due to the attachment of hydrogen atoms. At 300-350℃, the 2768 cm^{-1} absorbance and the trapping rate κ_2 decrease and the lifetime τ_2 prolongs towards 318 ps. These results suggest the formation of vacancy-clusters due to the migration of divacancies. At 450-500℃, the lifetime τ_2 suddenly decreases to

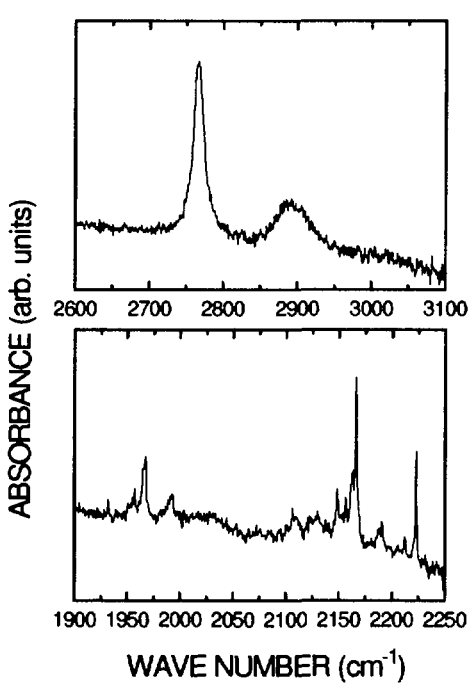

Fig. 2 IR spectra for proton-implanted Si.

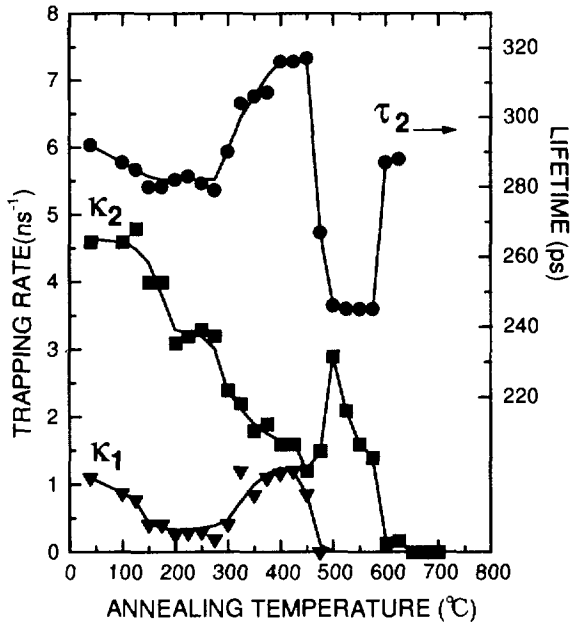

Fig. 3 Annealing behavior of positron lifetime and trapping rates for proton-implanted Si

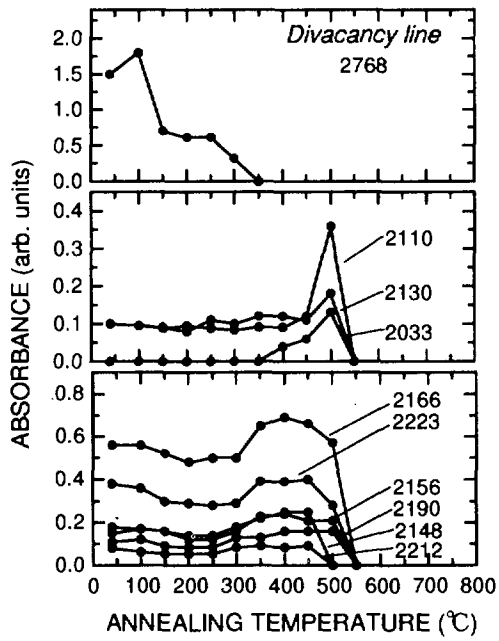

Fig. 4 Annealing behavior of absorbances (>2000 cm^{-1}) for proton-implanted Si

245 ps. It is worth to note that no vacancy-cluster formation proceed. This result suggests the break-up of vacancy-clusters and the formation of higher-order vacancy-hydrogen complexes, such as divacancy and multi-hydrogen complexes. The trapping rate κ_2 shows a peaked behavior at 500℃. The 2033, 2110 and 2130 cm^{-1} absorbances also show similar features. Accordingly, these lines can be correlated with the positron annihilation centers giving rise to the lifetime 245 ps. The trapping rate κ_1 in Fig.3 is arising from another vacancy component which contributes to the first lifetime (τ_1) as mentioned above. The positron lifetime responsible for the defects is expected to be close to the bulk lifetime. (Here, it is assumed to be 230 ps.) Probably, such defects are related to single-vacancy and mult-hydrogen complexes. The trapping rate κ_1 first decreases at 150℃, increases at 300-350℃ and finally diminishes at 500℃. The 2148-2223 cm^{-1} absorbances show the similar annealing behavior. Thus, these absorption lines can be correlated with the above positron annihilation centers. All the absorption lines diminish above 550 ℃. The trapping rates κ_1 and κ_2 also reach the detection limit up to 600℃. These results show that all hydrogen-vacancy complexes anneal out up to 600℃.

In this research, it is clearly shown that the annealing behavior of positron lifetime for the proton-irradiated Si is quite different from that for alpha or electron-irradiated Si. From the combination with IR measurement, it is clarified that the peculiar annealing behavior of the lifetime is caused by the vacancy-hydrogen interaction. The annealing behavior of the IR lines above 2000-2250 cm^{-1} is well correlated with that for positron lifetime and trapping rates.

4. References

[1]Hydrogen in Semiconductors, eds. J.I.Pankove and N.M.Johnson, Academic Press, 1991.

[2]H.J. Stein and S.K.Hahn, J. Appl. **75** (1994) 3477.

[3]G.D.Watkins and J.W.Corbett, Phys. Rev. **138** (1965) 543.

5.11 RBS and RNRA Studies on Sorption of Europium by Mineral

Toshihiko OHNUKI, Naofumi KOZAI, Hiroshi ISOBE, Takashi MURAKAMI[2], Shunya YAMAMOTO[3], Kazumasa NARUMI, Yasushi AOKI[3] and Hiroshi NARAMOTO[3]

Department of Environmental Safety Research, JAERI/Tokai,
Mineralogical Institute, The University of Tokyo[2],
Department of Materials Development, JAERI/Takasaki[3]

I. Introduction

In the high level radioactive waste (HLW) disposal, the various engineered and natural barriers avoid any contact of Trans Uranium (TRU) elements with the biosphere. The engineered barriers include the waste form, the canister, overpack and the backfill materials[1]. In most disposal concepts, borosilicate glass is produced and filled directly into canisters for disposal[2]. It should be noted that glass is not thermodynamically stable, but is in a metastable state.

The performance of the natural barriers depend on the geological, mineralogical and hydrological conditions of the waste repository. Since the geological conditions may change during geological time scale, the performance of the natural barriers may change. In order to prevent the dispersion of TRU elements, one of the concepts is that an additional barrier is loaded to backfill materials.

Apatite, $Ca_5(PO_4)_3(OH, F)$ is regarded as a possible additive to backfill materials. Because apatite absorbs many kinds of cations including UO_2^{2+} and Th^{4+} from aqueous solutions under normal conditions[3], and keeps a crystalline form more than 10 million years[4]. However, the sorption mechanism of TRU elements on apatite have not been known.

Rutherford Backscattering Spectroscopy (RBS) and Resonant Nuclear Reaction Analysis (RNRA) can give depth profiles of elements in materials from the surface. In the present study, the sorption mechanism of europium, an alternative of trivalent TRU, such as Am(III) and Cm(III), has been studied based on the depth profiles of elements obtained by RBS and RNRA.

II. Experimental

The single crystals of apatite were contacted with 10 ml Eu solution of 0.1 mM at pH 6.4 for 10 days at 40 and 75 ℃. After separation of apatite from the Eu solution, the depth profiles of elements of Eu, Ca, P and O in the apatite were measured by 2.4 MeV ^{4}He RBS. The hydrogen depth profiles were determined by RNRA of $^1H(^{15}N, \alpha\gamma)^{12}C$ at 6.385 MeV. The concentrations of Eu, Ca and P in the solutions were measured by inductively coupled plasma atomic emission spectroscopy (ICPAES). The depth profiles of elements in the fresh apatite which was not contacted with the Eu solution were obtained as reference case.

III. Results and discussion

The fresh apatite contains small amounts of the heavier elements than Ca (Fig. 1a). However, no peak of heavy element is observed. On the contrary, the peak of Eu in RBS spectrum is observed in Fig. 1b. The pHs of the solutions are 6.9 at 40 ℃ and 6.2 at 75℃.

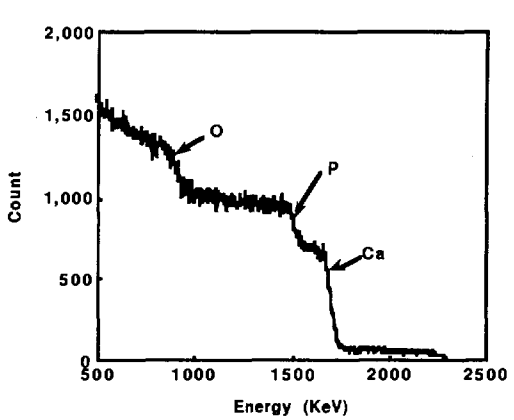

Fig. 1a RBS spectra of the fresh apatite.

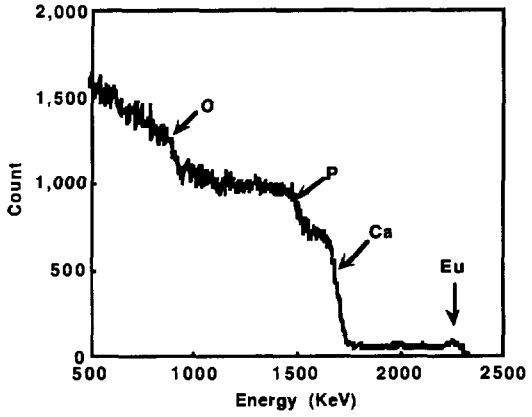

Fig. 1b RBS spectra of the apatite contacted with the Eu solution at 40℃.

An RBS spectrum obtained by subtracting fresh apatite one from an Eu-sorbed apatite one (hereinafter called subtract RBS spectra) at 40 ℃ is shown in Fig. 2. The positive peak for Eu and the negative peak for Ca are observed in Fig. 2. This indicates that Eu is sorbed on the apatite, and a fraction of Ca is released from the apatite.

The peak height for Eu in the RBS spectrum of the apatite obtained at 75 ℃ was higher than that of the apatite at 40 ℃ (Fig. 3). And the energy of the lower edge of the peak for Eu in the apatite obtained at 75℃ is lower than that in the apatite obtained at 40℃. This shows that Eu intrudes to deeper position at higher temperature. We assume that the chemical form of apatite is $Ca_5(PO_4)_3F$ and the density of apatite is 2.3 $g \cdot cm^{-3}$. The depths where Eu intruded into the apatite are then determined to be 290 and 350 nm at 40 and 75℃, respectively.

The depth profile of hydrogen in the fresh apatite and apatite on which Eu was sorbed at 40 and 75℃ are shown in Fig. 4. Small amounts of difference among three kinds of samples were detected by employing RNRA. The depth profile of hydrogen in the fresh apatite and the apatite on which Eu was sorbed was similar to that of the fresh apatite. This indicates that hydrogen does not intrude into the apatite during the sorption experiments. Thus, hydrogen does not contribute to the release of calcium from the apatite during the sorption experiment.

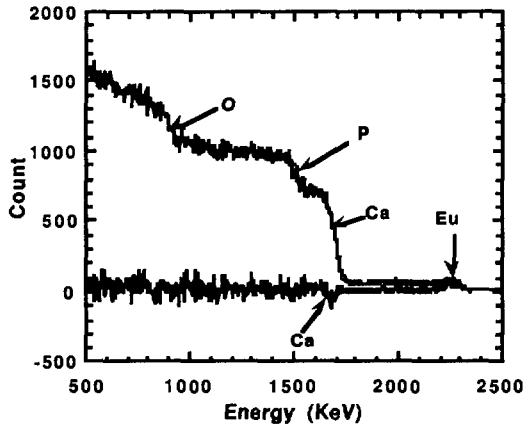

Fig. 2 The subtracted RBS spectra of the apatites on which Eu was sorbed at 40 ℃ from that of the fresh apatite.

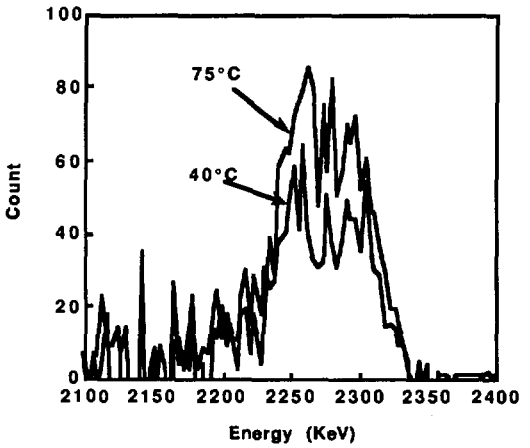

Fig. 3 RBS spectra of the apatite at the energy range from 2100 to 2400 KeV.

The concentrations of Ca, Eu and P in the solutions at 40 and 75℃ are shown in Fig. 5. The concentration of Eu sorbed on the apatite increased with temperature. And the concentration of Ca in the solution also increased with temperature. The exchange of Eu for Ca in apatite can be expressed by the equation.

$$1.5\text{Ca-Apatite} \rightleftarrows \text{Eu-Apatite}.$$

If all calcium released from the apatite is assumed to be exchanged for Eu, the relative

fraction of Eu exchanged for Ca are calculated to be 0.12 and 0.18 to the fractions of Eu sorbed at 40 and 75 ℃, respectively.

Europium exists as Eu^{3+} in the solution around pH 6.5. Since higher valence cation has higher selectivity of the sorption on minerals, trivalent europium is preferentially sorbed on apatite to sodium which is a counter cation in the solution. Eu aquo ions adsorb rapidly at the highly polar apatite surface[4]. Approximately 40% of equilibrium fraction of Eu are sorbed on hydroxyapatite[5]. However, approximately 0.3 of total Eu is sorbed on apatite for 10 days at 40℃ (Fig. 5). Specific surface area of apatite is 6.4×10^{-4} $m^2 \cdot g^{-1}$. This value is quite lower than those of kaolinite (26.4 $m^2 \cdot g^{-1}$) and sericite (2.2 $m^2 \cdot g^{-1}$). This is the reason of the slow sorption rate.

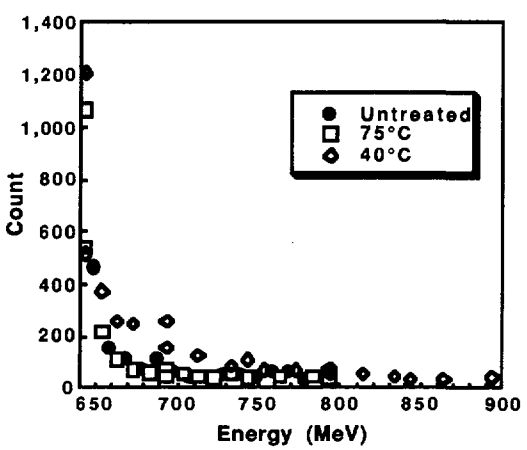

Fig. 4 Depth profile of hydrogen in the fresh apatite and apatite on which Eu was sorbed at 40 and 75℃.

Coordination numbers and ionic radii between Eu(III) and Ca(II) are similar. In a variety of biochemical molecules Eu has been used as replacement probe for Ca[6]. These facts support the replacement of Eu to Ca in the structure of apatite.

In the initial stage of the alteration of feldspar, hydrogen is exchanged for cations in the structure of feldspar. However, hydrogen does not intrude into the apatite during the sorption experiment. Thus, the release of Ca from the apatite is not caused by the exchange of hydrogen for calcium in the structure.

Therefore, a fraction of Eu is exchanged for Ca in the structure of apatite.

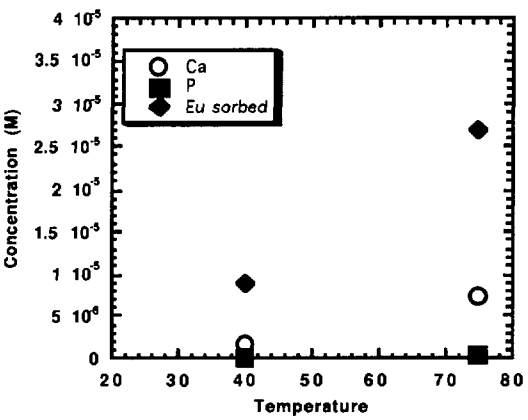

Fig.5 concentrations of Ca, Eu and P in the solutions at 40 and 75℃.

References

1 I. S. Roxburgh, Geology of High Level Waste Disposal, Chapman and Hall, New York(1987).
2 A. E. Ringwood, Fortshr. Mineral., 58, (1980) 149.
3 T. Banba, et al., JAEI-M 93-116(1993).
4 A. S. Posner, J. Biomed. Mat. Res., 19, (1985)241.
5 G. Bidoligo, P.N. Gibson, E. Haltier, N. Omenetto, Radiochem. Acta, 58/59, (1992)191.
6 W. Horrocks, W. De, Jr., M. Albin, in Progress in Inorganic hemistry, 31, John Wiley and Sons, New York, (1981) 1.

5．12 Energy Losses of MeV B Clusters Transmitted through Carbon Foils

K. Narumi*, K. Nakajima, K. Kimura, M. Mannami, S. Yamamoto*, Y. Aoki* and H. Naramoto*
Department of Engineering Physics and Mechanics, Kyoto University, *Department of Materials Development, JAERI

1. Introduction

The charge of an ion traveling through a solid induces the density fluctuation of valence electrons in the solid. This induces the dynamic oscillatory potential, which is called the wake potential.[1] The ion is decelerated by the wake potential induced by the ion itself. If another ion exists in the vicinity of the ion, for example, in the case of a molecular or cluster ion, the motion of each of the ions is affected by the wake induced by the other ions.[2] Thus the energy loss of such ions may be different from the sum of the energy losses of the constituents traveling through the solid at large distances from each other. This is called the vicinage effect.

The vicinage effect was first demonstrated by Brandt *et al.*, who measured the energy loss of ~100-keV/atom H_2^+ and H_3^+ ions transmitted through carbon and gold foils.[3] The energy-loss ratio, *i.e.*, the ratio of the energy loss per atom of the cluster to the energy loss of the isolated atomic ion, was larger than unity. The result was well explained by the wake concept. Similar experimental studies for diatomic molecular ions have been done by several groups.[4-7] The energy-loss ratio was larger than unity for fast light molecular ions and less than unity for slower ions.

Recently, the acceleration of large clusters has been possible[8, 9] and several groups measured the energy loss of large clusters transmitted through thin foils.[8, 10, 11] The Lyon group measured the energy loss of 10 to 120-keV/atom H_n^+ clusters ($n \leq 25$) penetrated through carbon.[8] Observed energy-loss ratio varies with the energy of the cluster, that is, it is less than unity at lower energies and larger than unity at higher energies. The groups of Orsay and Germany reported the energy loss of MeV C_n^+ clusters passing through foils, independently.[10, 11] Especially, Orsay group has investigated the interaction of the carbon cluster with matter[12] and reported the astonishing pulse height defect of a solid-state detector for a direct impact of a C_{60} molecule. Although such experimental results for the energy loss of large clusters in solids have been reported, the vicinage effect or cluster effect is not so obvious. In order to observe the vicinage effect in the cluster-solid interaction, we measured energy losses of 0.8-MeV/atom small B_n ($n \leq 4$) clusters transmitted through thin carbon foils and present obtained experimental results.

2. Experimental

Singly charged negative $^{11}B_n$ cluster ions (n = 2 to 4) were produced in a conventional Cs sputter ion source and injected into the 3-MV tandem accelerator of JAERI/Takasaki after the mass separation. They were accelerated with the terminal voltage and stripped into the positive cluster ions on the collisions with a N_2 gas at the terminal. Then singly charged positive $^{11}B_n^+$ cluster ions were accelerated at the second stage of the tandem accelerator and separated by a switching magnet. The ion beam was collimated by an XY-slit and an aperture to a diameter of 1 mm, and introduced in a scattering chamber where the vacuum was in the range of 10^{-8} Torr.

We used self-supporting carbon foils ranging from 2-17 $\mu g/cm^2$ as the target. The thicknesses of the foils were determined by comparing the energy loss of the transmitted 0.8-MeV B^+ ions with the stopping power value calculated by the TRIM code. The foils were mounted on a movable holder, which was capable of holding 10 foils, so that it was possible to measure the energy spectra of the ions with or without a carbon foil. The transmitted ions were detected by a solid-state detector (SSD) located about 1 cm downstream from the carbon foil. Thus it was possible to detect all the fragments after penetration of a B cluster through the foil and the accumulated energy of all the fragments were measured as one signal. The dead-layer thickness of the SSD was equivalent to about 500 Å in Si.

3. Results and Discussion

An example of observed energy spectra of the primary 3.2-MeV B_4^+ ions is shown in Fig. 1. In addition to the main peak due to the primary B_4^+ ions, there are three peaks at lower energies. They are due to the fragments, which result from collisions of the primary B_4^+ ions with a residual gas between the switching magnet and the chamber. Similar energy spectra were observed for 1.6-MeV B_2^+ and 2.4-MeV B_3^+ ions.

Figure 2 shows observed energy spectra of the primary 3.2-MeV B_4^+ ions and the B_4 clusters transmitted through the carbon foil whose thickness was 2.0 $\mu g/cm^2$. Although the transmitted B_4 clusters have lost certain amount of their kinetic energy by the penetration through the foil, the pulse height due to the transmitted B_4 clusters is obviously larger than that due to the primary B_4^+ ions. Such a pulse height defect was also observed for the primary B_2^+ and B_3^+ ions. When a heavy ion is impacted into the SSD, it produces a plasma column. Electron-hole pairs within the plasma column are shielded from the electric field created by the applied bias voltage and recombine with a high probability. Thus an incomplete charge collection leads to the loss of pulse amplitude. A similar situation occurs in the response of the SSD to the cluster ions; high energy deposition due to the dense atomic cluster produces a dense plasma. On the other hand, most of the primary cluster ions are dissociated by collisions with target atoms or electrons on impinging upon the target. The fragments repel each other by their mutual Coulomb force (the Coulomb explosion). When the fragments reach the detector, the internuclear distances are long enough that each fragment is detected as an isolated ion. The electronic stopping power of Si for the isolated B ion is less than 5 $keVcm^2/\mu g$, below which the recombination of electron-hole pairs is negligible.[13] Thus, no loss of the pulse height occurs for the isolated B ions, *i.e.*, the B fragments after the dissociation.

In order to determine the energy loss of the transmitted B_n clusters, it is necessary to know the pulse height of the primary B_n^+ cluster ions. However, the observed pulse height of the primary B_n^+ cluster ions is not true one because of the pulse height defect. As shown in Fig. 1, the incident ion beam includes the fragment B ions, which are produced by the collisions of the primary B_n^+ ions with the residual gas in the beam line. The energy transfer on the collisions must be negligible, and neglecting the effect of the Coulomb explosion, the energy of the fragment B ions is one-nth of that of the primary B_n^+ ions. Therefore, we regarded n times as much as the pulse height of the fragment B ions as that of the primary B_n^+ ions. The energy loss was determined by the difference between the mean energies of both the primary and the transmitted B_n clusters. In determining the energy loss, the energy loss in the dead layer was taken into account, which was calculated with the use of the stopping power of Si for B by the TRIM code. The energy loss by the elastic collisions in the SSD was neglected.

Figure 3 shows the foil-thickness dependence of the ratio of the energy loss per atom of B_n clusters to the energy loss of isolated B ions, $\Delta E(B_n)/n\,\Delta E(B)$, where $\Delta E(B_n)$ is the energy loss of B_n clusters transmitted through the carbon foils at the incidence of B_n^+ ions. For each foil thickness, we measured the energy loss several times, and the experimental errors were mainly due to the distribution of the observed energy loss. Energy-loss ratio is larger than unity at thinner foils and approaching unity with increasing foil thickness, which indicates the vicinage effect in the cluster-solid interaction. Considering the errors, no obvious dependence on the size of the primary cluster is recognized.

According to the theoretical studies, the stopping power for a small cluster ion depends on the velocity of the projectile, internuclear distance and the atomic arrangement relative to the

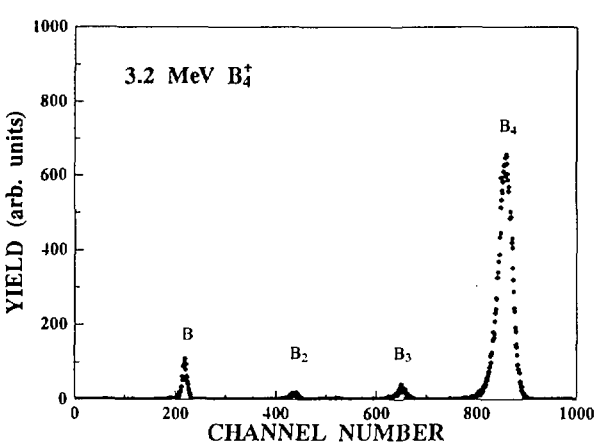

Fig. 1 Example of observed energy spectra of primary 3.2-MeV B_4^+ ions.

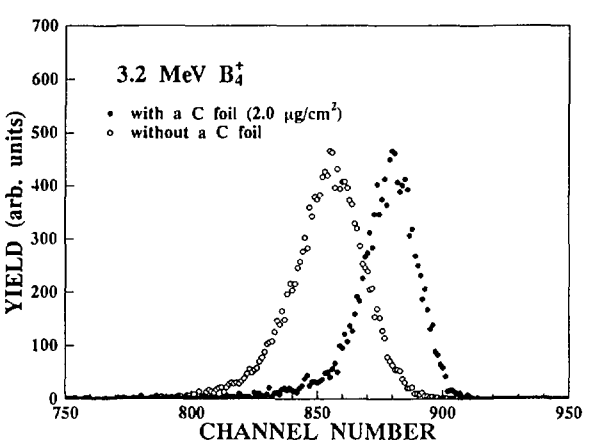

Fig. 2 Energy spectra of 3.2-MeV B_4^+ ions without a foil (full circles) and with a foil whose thickness was 2.0 $\mu g/cm^2$ (open circles).

direction of motion of the center-of-mass.[14, 15] When a cluster ion enters a solid, it is immediately dissociated by collisions with target atoms or electrons. The fragments of the cluster repel each other by the mutual Coulomb force and the internuclear distances are larger as the cluster travels through the target. Therefore, observed foil-thickness dependence of the energy loss of B_n clusters reflects the variation of the stopping power for the constituents in the cluster with increasing internuclear distance; the stopping power is enhanced immediately after the entry of the cluster into the target and approaching that for the isolated ion as the internuclear distance is getting large. Our experimental result that the energy-loss ratio for 0.8-MeV/atom small B_n clusters is larger than unity at thinner foils and approaching unity with increasing foil thickness is interpreted as described above. In order to have a further insight into the energy-loss process of the cluster ions in solids, however, theoretical consideration is indispensable.

Acknowledgements

The authors are grateful to the crew of 3-MV tandem accelerator of JAERI/Takasaki for their nice operation of the cluster ion beam.

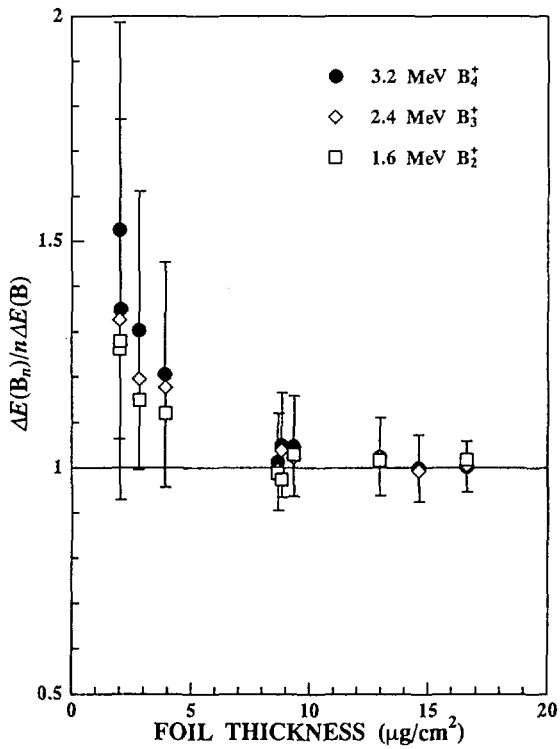

Fig. 3 Foil-thickness dependence of the ratio of the energy loss per atom of B_n clusters to the energy loss of isolated B ions. Only the errors for B_4 are shown.

References

1) J. Neufeld and R. H. Ritchie, Phys. Rev. **98** (1955) 1632.
2) D. S. Gemmell, J. Remillieux, J. -C. Poizat, M. J. Gaillard, R. E. Holland and Z. Vager, Phys. Rev. Lett. **34** (1975) 1420.
3) W. Brandt, A. Ratkowski and R. H. Ritchie, Phys. Rev. Lett. **33** (1974) 1325.
4) J. W. Tape, W. M. Gibson, J. Remillieux, R. Laubert and H. E. Wegner, Nucl. Instrum. Methods **132** (1976) 75.
5) J. C. Eckardt, G. Lantschner, N. R. Arista and R. A. Baragiola, J. Phys. C **11** (1978) L851.
6) R. Laubert, IEEE Trans. Nucl. Sci. **NS26** (1979) 1020.
7) M. F. Steuer, D. S. Gemmell, E. P. Kanter, E. A. Johnson and B. J. Zabransky, Nucl. Instrum. Methods **194** (1982) 277.
8) E. Ray, R. Kirsch, H. H. Mikkelsen, J. C. Poizat and J. Remillieux, Nucl. Instrum. Methods B **69** (1992) 133.
9) S. Della-Negra, A. Brunelle, Y. Le Beyec, J. M. Curaudeau, J. P. Mouffron, B. Waast, P. Håkansson, B. U. R. Sundqvist, E. Parilis, Nucl. Instrum. Methods B **74** (1993) 453.
10) K. Baudin, A. Brunelle, M. Chabot, S. Della-Negra, J. Depauw, D. Gardès, P. Håkansson, Y. Le Beyec, A. Billebaud, M. Fallavier, J. Remillieux, J. C. Poizat and J. P. Thomas, Nucl. Instrum. Methods B **94** (1994) 341.
11) Ch. Tomaschko, D. Brandl, R. Kügler, M. Schurr and H. Voit, Nucl. Instrum. Methods B **103** (1995) 407.
12) A. Brunelle, S. Della-Negra, J. Depauw, D. Jacquet, Y. Le Beyec, M. Pautrat, Ch. Schoppmann, Nucl. Instrum. Methods B **125** (1997) 207.
13) B. D. Wilkins, M. J. Fluss, S. B. Kaufman, C. E. Gross and E. P. Steinberg, Nucl. Instrum. Methods **92** (1971) 381.
14) N. R. Arista, Phys. Rev. B **18** (1978) 1.
15) C. D. Denton, I. Abril, J. Pérez-Pérez, R. Garcia-Molina and N. R. Arista, Radiat. Eff. in press.

6. Nuclear Chemistry and Radioisotope Production

6.1 PRODUCTION OF POSITRON EMITTERS AND APPLICATION OF THEIR LABELED COMPOUNDS TO STUDIES ON PLANTS

N. S. Ishioka, H. Matsuoka, S. Watanabe, A. Osa*, M. Koizumi* and T. Sekine*
Department of Radioisotopes, JAERI, * Department of Chemistry and Fuel Research, JAERI

1. Introduction

Positron emitting radionuclides such as ^{11}C, ^{13}N, ^{15}O and ^{18}F have been incorporated into a variety of radiopharmaceuticals for clinical diagnoses using positron emission tomography (PET). In plant physiology, however, these short-lived positron emitters have little been used; instead, long-lived β^- ray emitters have been used. This is partly because the positron emitters are too short-lived to be available in laboratories of biology.

Recently, the TIARA has provided new possibilities of studying dynamically the physiological function of plants *in vivo* with positron emitters: a positron-emitter two-dimensional imaging system [1] has been developed together with production methods of positron emitters. In the present paper, some experience on the production of positron emitters and their labeled compounds is described.

2. Production and application of positron emitters

Table1 shows the positron emitters produced so far. Being indispensable to life, water is a useful target material in the present study: ^{18}F can be produced in the $^{16}O(\alpha,pn)^{18}F$ and $^{18}O(p,n)^{18}F$ reactions, and ^{13}N in the $^{16}O(p,\alpha)^{13}N$ reaction. We have developed the irradiation system of water to keep the purity of the target for producing ^{13}N and ^{18}F in water. Figure 1 shows a Ti vial, which is able to contain 6 ml of liquid and have a Ti window for particle irradiation, and an Al holder, which houses the Ti vial, for irradiation of liquid. Instead of transporting through a long tube, 6 ml of water in a Ti vial, is transferred by a small truck between the irradiation port and the hot cell. In addition, using frozen water as a target, the increase of temperature of the target during irradiation was reduced.

Using the water target system we produced $^{18}F^-$ and $^{13}NO_2^-/^{13}NO_3^-$ in water. As the irradiated water target contained an impurity of ^{48}V from proton and α-particle activation of the Ti window, and, in the production of ^{13}N, an impurity of ^{18}F from proton activation of ^{18}O (0.2% natural isotopic abundance and 0.02% in depleted water), the impurities were separated together with $^{13}NH_4^+$ ion from the target by cation exchange and basic alumna chromatography.

Aqueous $^{18}F^-$ has been used for evaluating

Table 1 Production and application of positron emitters in TIARA

Nuclide	Half-life	Reaction	Target material	Tracer for experiments on plants
^{11}C	20 min	$^{14}N(p,\alpha)^{11}C$	N_2 gas	$^{11}CO_2$, ^{11}C-Methionine
^{13}N	10 min	$^{16}O(p,\alpha)^{13}N$	$H_2{}^{16}O$ ice, ^{18}O-depleted ice	$^{13}NO_2^-$, $^{13}NO_3^-$
^{18}F	110 min	$^{16}O(\alpha,pn)^{18}F$	$H_2{}^{16}O$ ice	
		$^{18}O(p,n)^{18}F$	$H_2{}^{18}O$ ice	Aqueous $^{18}F^-$, ^{18}F-FDG
^{48}V	16 day	$^{45}Sc(\alpha,p)^{48}V$	Sc foil	Aqueous ^{48}V

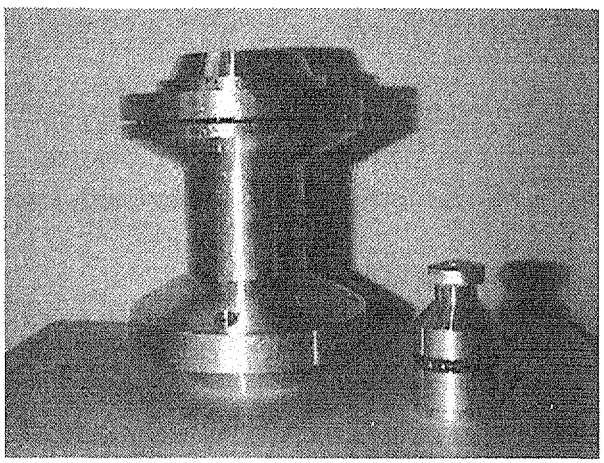

Fig.1 Ti vial and Al target holder, which houses the Ti vial, for liquid irradiation.

the uptake of water from the stems of plants. Deoxy-glucose labeled with ^{18}F is now available and will be used to see the behavior of glucose, which is produced by photosynthesis in plants. Furthermore, the behavior of $^{13}NO_2^-$ and $^{13}NO_3^-$ in plant is expected to give information on nitrogen metabolism.

Carbon-11 atoms are produced in the $^{14}N(p,\alpha)^{11}C$ reaction. The $^{11}CO_2$ produced from the ^{11}C atoms and the remaining oxygen in the target chamber were condensed by using liquid Ar and separated from the target gas. The $^{11}CO_2$ was applied to experiments on translocation of the glucose produced in a leaf by carbonic acid assimilation. Further, ^{11}C-labeled methionine synthesized from the $^{11}CO_2$ has been utilized for measurement of the translocation rate of the amino acid in Fe-deficient plants.

Vanadium-48 with a half-life of 16 day can be produced in the $^{45}Sc(\alpha,p)^{48}V$ reaction and be used to make clear the effect of its ions to the process of plant growth.

3. Results

Table 2 shows typical irradiations and the production yields of these positron emitters. We obtained a sufficient amount of radioactivity of these positron emitters for experiments on plants. This amounts are much smaller than in PET studies in medicine,

On the production of $^{13}NO_2^-$ and $^{13}NO_3^-$, the longer-lived $^{18}F^-$ can be reduced by using ^{18}O-depleted water in addition to the purification by chromatography as mentioned above. This enables us to measure the translocation of the positron emitter in the sample for a longer period of time.

References

[1] T. Kume, S. Matsuhashi, M. Shimazu, H. Ito, T. Fujimura, K. Adachi, H. Uchida, N. Shigeta, H. Matsuoka, A. Osa and T. Sekine, Appl. Radiat. Isot. (in press).

Table 2 Typical irradiations and production yields of positron emitters

Product	Beam	Primary energy	Incident energy on target	Beam current	Irradiation time	Yields (E.O.B.)
$^{11}CO_2$	proton	20 MeV	11 MeV	0.1 μA	10 min	37 MBq
^{11}C-methionine				1 μA	15 min	70 MBq
Aqueous $^{18}F^-$	α-particle	50 MeV	42 MeV	1 μA	40 min	70 MBq
^{18}F-FDG						38 MBq
Aqueous $^{18}F^-$	proton	20 MeV	16 MeV	1 μA	40 min	620 MBq
^{18}F-FDG						58 MBq
$^{13}NO_2^-$, $^{13}NO_3^-$	proton	20 MeV	16 MeV	1 μA	20 min	520 MBq

6. 2 Development of a Laser Ion Source for the TIARA-ISOL

M. Koizumi, A. Osa, T. Sekine, and M. Kubota*
Department of Chemistry and Fuel Research, JAERI
*Department of Physics, Faculty of Science, Toho University

1. Introduction

A laser ion source (LIS), which is based on a technique of resonance ionization of atoms [1], can be a universal method for element selection in on-line isotope separation. In this ion source, atoms are excited stepwise to the ionization state by two or three laser beams tuned to the transition energies specific to the element of interest. The combination of an LIS with a mass separator, therefore, has the capability of providing mono-isotopic radioactive beams [2-3]. For the isobar free isotope separation of nuclei produced through heavy-ion-induced reactions with the TIARA-ISOL, a hot-cavity-type LIS, named FLINT-IS, was constructed [4].

2. Off-line experiments with a stable Ba isotope

For on-line experiments, a high-repetition-rate laser is favorable for an LIS to ionize atoms efficiently. Instead of a 50-Hz repetition rate Nd:YAG laser (Continuum, Powerlight 6050: 70-mJ output power at 532 nm) used previously, therefore, an excimer laser (Lambda Physik, LPX 204 I; 200-mJ pulse energy at 308 nm with XeCl gas) with a maximum repetition rate of 400 Hz was introduced as a pump laser.

Since dye lasers have the limitation of their output power, the ionization scheme of atoms should be chosen to optimize the ionization efficiency. For the ionization of Ba atoms, we employed a two-color two-step ionization scheme as seen in Fig. 1. The laser beam from the excimer laser was divided into two, pumping two dye lasers (Lambda Physik, FL3001; and Lambda Physik, SCANmate 2E). The

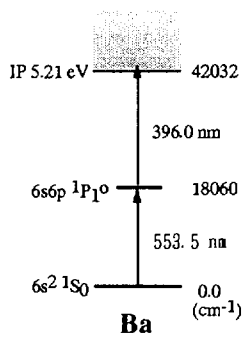

Fig. 1. Atomic energy levels relevant to the ionization of Ba atoms.

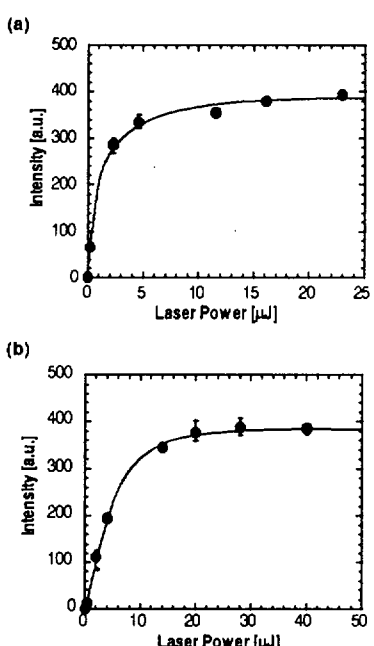

Fig. 2. Laser power dependence of the resonance ionization signal observed with a off-line resonance ionization test chamber. (a) First-step (553.5 nm). (b) Second-step (396.0 nm).

beams from the dye lasers were transported through a 30-m quartz optical fiber with a diameter of 0.4 mm from the control room to the target room; the total transport efficiency was about 30%. For the first- and second-laser, dyes of Coumarin-153 and P-BBO were used, respectively; the typical powers were 20 μJ and 40 μJ at the entrance window of the FLINT-IS.

Fig. 2 shows saturation curves of the transition measured with an off-line resonance ionization test system [5]. The diameters of the laser beams at the interaction zone with Ba atoms were about 1 cm. During the measurement, the laser power of one of two lasers was fixed at the maximum energy. From the measurement, we concluded that the laser powers are strong enough to saturate the ionization probability in the FLINT-IS.

Fig. 3 shows the laser frequency dependence of the mass-separated ^{138}Ba photoion yield from the FLINT-IS. The yield increases almost linearly with laser frequency. Even with the 400-Hz repetition rate, the yield is not saturated yet. Fig. 4 indicates the temperature dependence of the ratio of the photoion current to the background ion current; the photoion current was deduced from the ion current difference when the lasers were on and off. The temperature was measured at the oven of the FLINT-IS with a radiation thermometer (Minolta, TR-630A). As the temperature increased, the ratio decreased due to the increased current of ions formed in surface ionization. The ratio can be improved by introducing an electric deflector which gates the continuous ion beam formed in surface ionization.

3. ^{128}Ba radioisotope separation with the FLINT-IS

To measure the efficiency of radioisotope separation with the FLINT-IS, we performed on-line experiments. The nuclear reaction employed was ^{nat}Mo (^{36}Ar, xp yn) ^{128}Ba ($T_{1/2}$ = 2.43d). The target thickness was about 3 mg/cm^2; the energy of the Ar^{8+} beam was 195 MeV, and its averaged current was about 1.5 eμA. The mass-separated $^{128}Ba^+$ ions with the TIARA-ISOL were detected with a particle detector (Murata, Ceratron EMT-6081B) at the end of the beam line. The particle signals were counted with a multi-channel scaler (MCS), the start signal of which was given by the

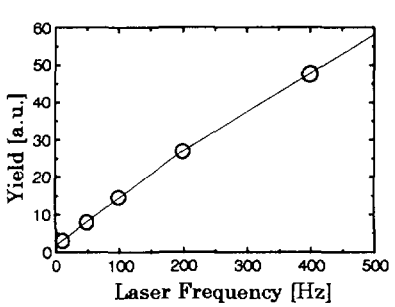

Fig. 3. The laser frequency dependence of the ion yield from the FLINT-IS. The line is drawn to guide the eye.

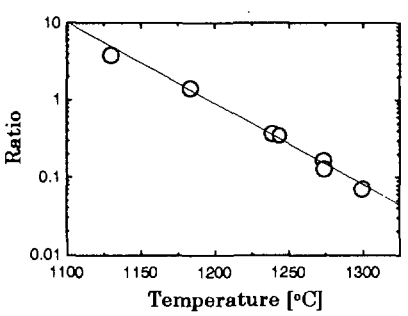

Fig. 4. The temperature dependence of the ratio of the photoion current to the ion current formed in surface ionization.

laser shot. Fig. 5 is a MCS spectrum accumulated for 10^5 laser shots. The spectrum obviously shows that the photoions were produced as a bunched beam coincident with the laser shot.

To assure ourselves that the peak was due to ^{128}Ba photoions, we detuned the first-step laser frequency: then, the peak vanished. Since no peak was observed at the mass M = 128.5 a.m.u., and at the resonant conditions, the peak contained no stable-isotope Ba ions. Finally, we concluded that the peak was produced by resonantly photo-ionized Ba atoms with a mass of 128 a.m.u. produced in the nuclear reaction.

Assuming the nuclear reaction cross section to be about 100 mb, the production rate of ^{128}Ba is about 2×10^6 s^{-1}. From the peak of the MCS spectrum, the yield of the ^{128}Ba photoions summed within 30 μs is about 100 s^{-1}. The efficiency of the radioisotope separation with the FLINT-IS is, therefore, 0.5×10^{-4}, which is much less than the predicted value[4].

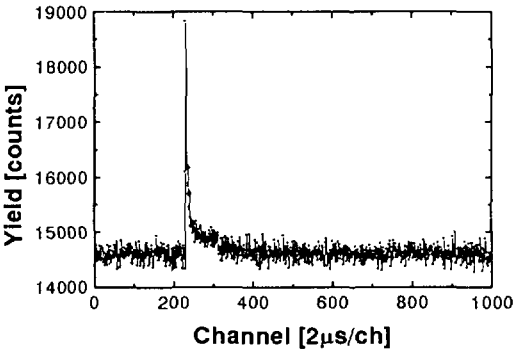

Fig. 5. An MCS spectrum of mass separated ion beam at M = 128.

4. Summary

For element-selective on-line isotope separation, a hot-cavity-type LIS has been constructed. Its performance was tested in off-line and on-line experiments with stable Ba isotopes.

In off-line experiments, we observed that the high frequency laser enhances the yield of the photoion current. For practical use, the temperature of the hot cavity must be elevated from that in the present off-line experiments; the ions produced continuously in surface ionization will prevail over the photoions as seen in Fig. 4. An electric deflector will be introduced to gate the ions produced in surface ionization. Also, use of a material with a low work-function, such as TaC [2], should be considered in the construction of a hot-cavity.

In on-line experiments, we observed mass-separated ^{128}Ba radioisotope photoions from the ISOL equipped with the FLINT-IS. The reason of the low efficiency of the FLINT-IS should be studied.

References

[1] V.S. Letokhov, Laser Photoionization Spectroscopy (Academic Press. 1987).

[2] V.I. Mishin, V.N. Fedoseyev, H.-J. Kluge, V.S. Letokhov, H.L. Ravn, F. Scheerer, Y. Shirakabe, S. Sundell, O. Tengblad and the ISOLDE Collaboration, Nucl. Instr. Meth. B73 (1993) 550.

[3] V.N. Fedoseyev, Y. Jading, O.C. Jonsson, R. Kirchner, K.-L. Kratz, M. Krieg, E. Kugler, J. Lettry, T. Mehren, V.I. Mishin, H.L. Ravn, T. Rauscher, H.L. Ravn, F. Scheerer, O. Tengblad, P. Van Duppen, A. Wöhr, and The ISOLDE Collaboration, Z. Phys. A353 (1995) 9.

[4] M. Koizumi, A. Osa, T. Sekine, and M. Kubota, Nucl. Instr. and Meth. B, in printing.

[5] M. Koizumi, A. Osa, T. Sekine, T. Horiguchi, and M. Asai, JAERI TIARA Ann. Rep. 4 (1994) 178.

6.3 DEVELOPMENT OF AN ^{42}Ar-^{42}K GENERATOR BY MEANS OF THE ^{40}Ar(α,2p) REACTION

N. S. Ishioka, A. Osa*, S. Watanabe, T. Sekine* and Y. Shida**
Department of Radioisotopes, JAERI, * Department of Chemistry and Fuel Research, JAERI and **Institute for Nuclear Study, The University of Tokyo

1. Introduction

Potassium is abundant in nature, and is an important element to make our body. There is potential interest in using a carrier-free radiotracer of K for physiological and pharmacokinetic studies of K in human body. Being highly useful radiotracers, carrier-free ^{42}K and ^{43}K can be produced by the ^{41}K(n,α)^{42}K, ^{42}Ca(n,p)^{42}K and ^{45}Sc(n,γ)^{42}K reactions using a reactor or by the ^{40}Ar(α,pn)^{42}K and ^{40}Ar(α,p)^{43}K reactions using an accelerator. Further, ^{42}K can be obtained with an ^{42}Ar-^{42}K generator system produced by the ^{40}Ar(t,p)^{42}Ar and ^{40}Ar(α,2p)^{42}Ar reactions. As seen from the physical characteristics of ^{42}K and ^{43}K summarized in Table 1, they are usually of limited accessibility because their half-life is about a half or one day. In contrast, with an ^{42}Ar-^{42}K generator, ^{42}K can be obtained daily in carrier- and salt-free state.

Until recently ^{42}Ar-^{42}K generators were produced by the ^{40}Ar(t,p)^{42}Ar reaction in Munich.[1] However, the triton beam in Munich is not available now. So we are interested to explore the feasibility of cyclotron production of an ^{42}Ar-^{42}K generator using the ^{40}Ar(α,2p)^{42}Ar reaction. In the present work, an ^{42}Ar-^{42}K generator has been developed using high energy α-particles from the TIARA AVF cyclotron.

2. Experimental

The gas-target chamber for α-beam irradiation consists of an aluminium body, 43 cm long, 18 mm in diameter. The double window in front of the target consists of a 100 μm thick Ti foil to close the target and a 100 μm thick Ti foil to separate the cyclotron vacuum. A cooled helium gas at 0℃ flows through the two foils and cools the windows. The target body is cooled by flowing water. The target chamber was filled with Ar gas to a pressure of 2.5 kg/cm^2. The Ar gas was irradiated for 30 min with α-particles at a beam current of 1.2 μA; the incident energy on target was about 40 MeV. After the irradiation, the ^{42}Ar was led from the target chamber to a hot-cell in a stainless steel tubing, 1/16 inches in diameter. Part of the ^{42}Ar was collected in a metal cylinder (about 6 cm diameter, 15 cm height) which was described in detail by H. Homareda.[2] Gamma-ray spectra of the cylinder were measured several times using a Ge detector.

Table 1 Nuclear properties and production reactions of ^{42}Ar, ^{42}K and ^{43}K

Nuclide	Half-life	β-Energy MeV (%)	γ-energy MeV (%)	Specific activity GBq/g*	Formation
^{42}Ar	33.0 y	0.56 (100)	no	9.6×10^3	^{40}Ar(t,p)^{42}Ar ^{40}Ar(α,2p)^{42}Ar
^{42}K	12.36 h	1.97 (18) 3.52(81)	1.525 (18)	2.2×10^8	^{42}Ar→^{42}K ^{41}K(n,)^{42}K ^{40}Ar(α,pn)^{42}K
^{43}K	22.3 h	0.827 (87)	0.373 (70) 0.618 (80)	1.2×10^8	^{40}Ar(α,p)^{43}K

* In carrier-free state

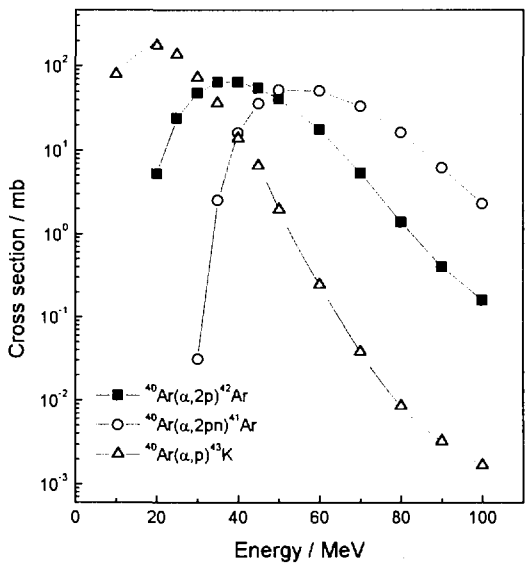

Fig.1 ALICE code calcuration of the excitation functions of the ^{40}Ar(α,2p)^{42}Ar, ^{40}Ar(α,2pn)^{41}Ar and ^{40}Ar(α,p)^{43}K nuclear reactions.

3. Results and discuttion

The theoretical ^{40}Ar(α,2p)^{42}Ar, ^{40}Ar(α,2pn)^{41}Ar and ^{40}Ar(α,p)^{43}K excitation functions are shown in Fig.1, which were calculated by the ALICE code. [3] The calculation predicts that a maximum cross section of the ^{40}Ar(α,pn)^{42}Ar nuclear reaction is ~70 mb for 35-40 MeV α-particles and can be produced in α energies more than 20 MeV. One can note that ^{41}Ar with a half-life of 1.8 hr is produced by α energies more than 40 MeV and ^{43}K is produced by α energies more than 8 MeV.

Fig.2 shows a γ-ray spectrum of the cylinder containing the irradiated Ar gas after the ^{41}Ar had decayed. As the impurity of ^{43}K was adsorbed by the inner wall of the target chamber, we were not able to find its γ-rays in the spectrum. The 1.5 MeV γ-ray of ^{42}K, however, was seen as the daughter nuclide from the gaseous cow, as shown in Fig.2.

The experimental yield of the ^{42}Ar-^{42}K generator is in reasonable agreement with the thick target yield calculated from the excitation function in Fig.1.

References

[1] H. Wegmann, E. Hunges, H. Muthig and H. Morinaga, Nucl. Inst. and Meth., 179, 217 (1981).
[2] H. Homareda and H. Matsui, Radioisotopes, 35, 33-36 (1986).
[3] M. Blann and J. Bisplinghoff, Lawrence Livermore National Laboratory Report COO-3494 27 (1975).

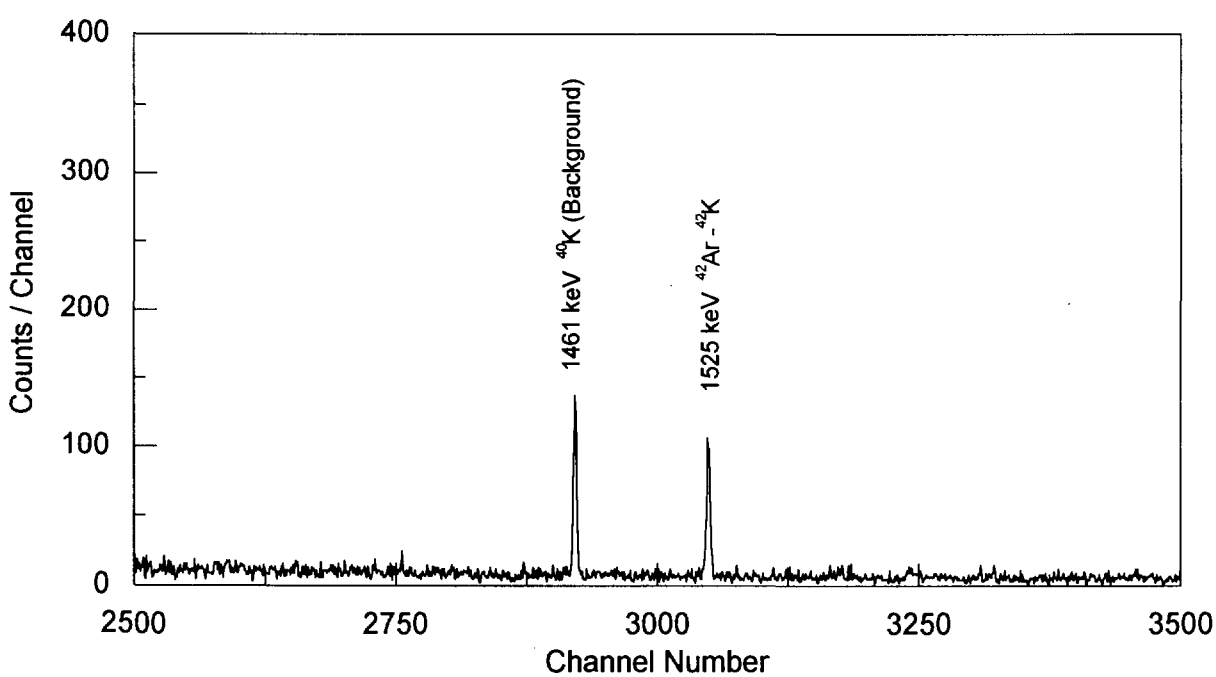

Fig.2 A γ-ray spectrum of the Ar gas 16 days after irradiation with a 42-MeV α-beam

6. 4 Measurement of the Atomic Masses of $^{126-128}$La Isotopes

Y. Kojima, M. Asai, A. Osa*, M. Koizumi*, T. Sekine*, M. Shibata, H. Yamamoto and K. Kawade
School of Engineering, Nagoya University, * Department of Chemistry and Fuel Research, JAERI

1. Introduction

Atomic masses are one of the most fundamental quantities because they manifest all interactions contributing to nuclear binding. From extensive studies of atomic masses, nuclear shell structure and shape dependent properties have been identified. Precise experimental values on atomic masses of unstable nuclei provide an essential input to theoretical efforts to refine and develop nuclear models.

The measurement of Q_β-values with a small HPGe detector is convenient to determine atomic masses, especially for short-lived nuclei.[1,2] In the present work, this method was applied to measurements of β^+-ray maximum energies of $^{126-128}$La at the TIARA isotope separator on-line (TIARA-ISOL). The atomic masses derived from the Q_{EC}-values were compared with theoretical predictions.

2. Experiment

The $^{126-128}$La activities were produced by heavy-ion fusion-evaporation reactions at the TIARA-ISOL connected with the AVF cyclotron.[3] The 195-MeV $^{36}Ar^{8+}$ beam with an intensity of about 0.12 particle μA was delivered to a 3 mg/cm^2 ^{nat}Mo target for producing ^{127,128}La, and a 3 mg/cm^2 isotopically enriched ^{94}Mo target for ^{126}La. Reaction products were ionized in a thermal ion source and mass-separated as monoxide ions. The mass-separated ions were implanted into an aluminum-coated Mylar tape in a tape-transport system. During this period of collecting the radioactivities, β-ray measurement was carried out, as described later. The source was periodically transported to a detector station for $\gamma - \gamma$ angular correlation measurement[4] at time intervals of 100 s, 300 s and 324 s for ^{126}La, ^{127}La and ^{128}La, respectively.

Beta-ray singles and $\beta - \gamma$ coincidence measurements were performed with a planar-type HPGe detector (crystal size of 25 mm$^\phi \times$ 13 mm^t) for β-rays and a 28.4% n-type HPGe detector for γ-rays. Beta-ray spectra were measured through a 50 μm^t Mylar window.

In the β^+-ray measurements, the main amplifier was operated in a short shaping time constant of 0.5 μs, and the counting rate of the singles spectrum measurement was kept below 3000 cps to reduce a pulse-pileup effect.

Coincidence data were recorded on a magnet-optical disk in event by event mode. About 7.2 $\times$ 10^7, 5.3 $\times$ 10^7 and 5.2 $\times$ 10^7 events were accumulated during a measuring period of 57, 58 and 61 h for A = 126, 127 and 128, respectively.

Energy calibration of the β^+-ray detector was made up to 8.6 MeV using a standard γ-ray source of ^{56}Co and prompt γ-rays in the thermal neutron capture of ^{35}Cl. The thermal neutrons were generated by a ^{252}Cf neutron source of 950 kBq.

3. Results and discussion

After each of the β^+-ray spectra obtained was unfolded with experimental response functions for monoenergetic positrons,[5,6] the Fermi-Kurie plot was produced. The endpoint energy of the β^+-rays was derived from the fit of a straight line using the maximum likelihood method for Poisson distribution. The energy losses of positrons were estimated for the collection tape, the Mylar window, the air and the beryllium window of the detector from the energy loss table by Pages *et al.*[7] The detailed analysis pro-

cedure of a β^+-ray spectrum was described in ref. 5.

^{126}La. In an earlier work, the isomerism in ^{126}La was reported by Genevey *et al.*[8] From $\gamma-\gamma$ coincidence measurements, we constructed the detailed decay scheme of ^{126}La involving more than 100 new γ-rays. The part of the decay scheme to be used in the present analysis is consistent with the results by Genevey.

Relatively strong β-feedings to the levels of 710.9 keV (4^+) and 1938.7 keV (5^-) were observed in the decay of the high-spin isomer. From the $\beta-\gamma$ coincidence data, endpoint energies were obtained and the Q_{EC}-value was determined for the first time to be 7710(100) keV.

In order to derive the Q_{EC}-value of the low-spin isomer of ^{126}La, the spectrum of β^+-rays feeding to the 2029.7 keV 0^+ level was analyzed. The Q_{EC}-value was deduced to be 7910(400) keV.

The present results suggest that the high-spin isomer is the ground state of ^{126}La.

^{127}La. Fermi-Kurie plots of the unfolded spectra of β^+-rays feeding to the levels of 293.5 and 1671.1 keV are shown in Fig. 1. The resulting Q_{EC}-value of 5010 keV is 310 keV higher than the evaluated value by Audi *et al.*[9]

^{128}La. The 2425.5 keV level is known to be strongly populated in the decay of the high-spin isomer of ^{128}La. The Q_{EC}-value of 6820(100) keV was derived from the spectra of β^+-rays coincident with the γ-rays of 626.0, 1053.1 and 1100.9 keV. The present value is in reasonable agreement with the previous result of 6650(400) keV,[10] but the precision has been much improved.

The experimental Q_{EC}-values obtained are summarized in Table 1 together with the results by other authors and the evaluated values. The present results show that these nuclides are somewhat more unstable than evaluated previously.

With the present Q_{EC}-values and the well-evaluated mass excesses of Ba isotopes,[9] the mass excesses of $^{126-128}$La were obtained, assuming the high-spin isomeric state to be the ground state of ^{126,128}La. In order to check the predictability of mass formulas, the deviations of the experimental masses and the theoretical ones from the evaluated values are presented in Fig. 2. This figure indicates that the formula of Möller and Nix[12] is in the best agreement with the experimental values.

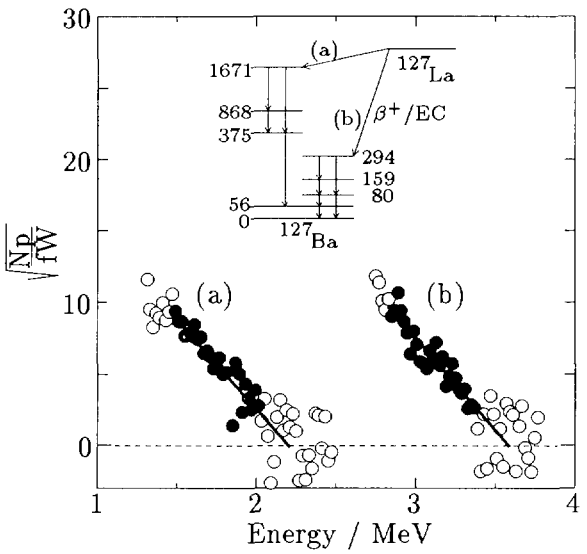

Fig. 1: Fermi-Kurie plots of the unfolded spectra of ^{127}La for β^+-rays feeding to the levels of (a) 1671 keV and (b) 294 keV. Fitting regions are indicated by closed circles. A partial decay scheme is shown in the inset.

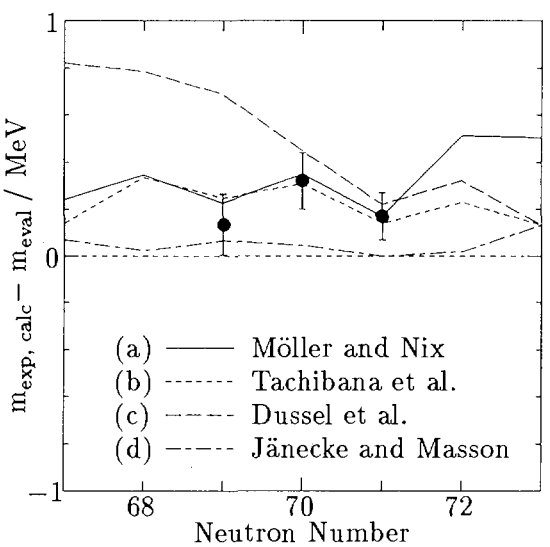

Fig. 2: Deviations of the experimental atomic masses, m_{exp}, and the calculated ones,[11] m_{calc}, from the evaluated values of La isotopes, m_{eval}, by Audi *et al.* (a) unified macroscopic-microscopic model of Möller and Nix, (b) empirical formula of Tachibana *et al.*, (c) α-line systematics of Dussel *et al.* and (d) Garvey-Kelson mass relations of Jänecke and Masson.

4. Conclusion

From $\beta - \gamma$ coincidence measurements with HPGe detectors, Q_{EC}-values of ^{126,127}La were determined for the first time and ^{128}La with an improved accuracy.

With our experimental method, systematic Q_{EC} measurements for neighboring La isotopes are in progress.

References

[1] R.C. Greenwood and M.H. Putnam, *Nucl. Instr. and Meth.* **A337**(1993)106.

[2] A. Osa, T. Ikuta, K. Kawade, H. Yamamoto and S. Ichikawa, *J. Phys. Soc. Jpn.* **65**(1996)928.

[3] T. Sekine, A. Osa, M. Koizumi, S. Ichikawa, M. Asai, H. Yamamoto and K. Kawade, *Z. Phys.* **A349**(1994)143.

[4] M. Asai, K. Kawade, H. Yamamoto, A. Osa, M. Koizumi and T. Sekine, *Nucl. Instr. and Meth. A,* in press.

[5] A. Osa, T. Ikuta, M. Shibata, M. Miyachi, H. Yamamoto, K. Kawade, Y. Kawase and S. Ichikawa, *Nucl. Instr. and Meth.* **A332**(1993)169.

[6] Y. Kojima, T. Ikuta, M. Asai, A. Taniguchi, M. Shibata, H. Yamamoto and K. Kawade, *Nucl. Instr. and Meth.* **B126**(1997)419.

[7] L. Pages, E. Bertel, H. Joffre and L. Sklavenitis, *Atomic Data* **4**(1978)1.

[8] J. Genevey, A. Gizon, N. Idrissi, B. Weiss, R. Béraud, A. Charvet, R. Duffait, A. Emsallem, M. Meyer, T. Ollivier and N. Redon, *Proc. of the 5th Int. Conf. on Nuclei far from Stability,* Rosseau Lake, Canada, (1987) p.419.

[9] G. Audi and A.H. Wapstra, *Nucl. Phys.* **A595**(1995)409.

[10] A.C. Li, I.L. Preiss, P.M. Strudler and D.A. Bromley, *Phys. Rev.* **141**(1966) 1089.

[11] P.E. Haustein (editor), *Atomic Data and Nucl. Data Tables* **39**(1988)185.

[12] P. Möller and J.R. Nix, *Atomic Data and Nucl. Data Tables* **39**(1988)213.

Table 1: Q_{EC}-values deduced from β^+-ray maximum energy measurements.

Nuclide	Level (keV)	Endpoint energy (keV)	Q_{EC} present (keV)	Q_{EC} other (keV)	Q_{EC} evaluated[a] (keV)
^{126}La(H.I.)[b]	710.9	5900(150)	7710(100)		7570(300)#
	1938.7	4780(120)			
^{126}La(L.I.)[b]	2029.7	4860(400)	7910(400)		
^{127}La	293.5	3580(100)	5010(70)		4700(250)#
	1671.1	2320(90)			
^{128}La(H.I.)[b]	2425.5	3370(100)	6820(100)	6650(400)[c]	6650(400)

a) Audi and Wapstra.[9]

b) H.I. and L.I. indicate a high- and a low-spin isomer, respectively.

c) Li *et al.*[10]

values estimated from systematic trends.

6．5 Diffusion Studies in Titanium and Titanium-Base Intermetallic Compounds

H. Nakajima, W. Sprengel, K. Nonaka[+], A. Yamaguchi[+], T. Sekine[++]
N. Shigeta[++], M. Koizumi[++], A. Osa[++]
Institute of Scientific and Industrial Research, Osaka University; Faculty of Engineering, Iwate University[+]; Department of Radioisotopes, JAERI Takasaki[++]

1.Introduction

Titanium and Titanium-base intermetallic compounds are promising materials for aerospace applications etc. because of their low density and high temperature strength. For improvement and development of these materials knowledge of their atomic transport mechanism is essential. The aim of this research project is to investigate the diffusion behavior of Ti in titanium and intermetallic compounds of the Ti-Al and Co-Ti system. In this project interdiffusion experiments in combination with self-diffusion measurements are carried out to elucidate the diffusion mechanism. For self-diffusion studies the radioactive tracer method is used which is the only possible method to measure self-diffusivities. In the case of Ti self-diffusion the suitable isotope ^{44}Ti is commercially not available. Therefore, ^{44}Ti was produced using the facilities of JAERI/Takasaki.

2. Experimental

For the interdiffusion experiments single-phase interdiffusion couples were prepared for TiAl and CoTi from polycrystalline $Ti_{50}Al_{50}$ and $Ti_{46}Al_{54}$, and $Co_{50}Ti_{50}$, and $Co_{54}Ti_{46}$ alloys, respectively. The diffusion couples were annealed in vacuum in an electric resistivity furnace for various times in the temperature range from 1116 to 1583 K. After annealing the concentration distribution in the diffusion zone was analyzed perpendicular to the bonding interface with an electron probe microanalyzer (EPMA) in wavelength dispersive mode.

For the Ti self-diffusion experiments ^{44}Ti was produced using the AVF cyclotron at JAERI/Takasaki. A ^{45}Sc-target (purity 99.9%) was irradiated with a proton beam according to the following reaction: ^{45}Sc(p, 2n)^{44}Ti. Details of the process including separation of ^{44}Ti and purification are given elsewhere [1]. Figure 1 shows a γ -spectrum of the final ^{44}Ti solution.

3. Results and Discussion

The data of the measured concentration profiles from the interdiffusion experiments were fitted to the complementary error function, which is the solution of Fick's Second Law of diffusion for the diffusion geometry used [2]. The obtained interdiffusion coefficients D as function of the reciprocal temperature T are shown in Figure 2. In both cases, γ -TiAl and CoTi, the temperature dependence of the interdiffusion coefficient is described by Arrhenius laws: The results obtained for γ -TiAl are

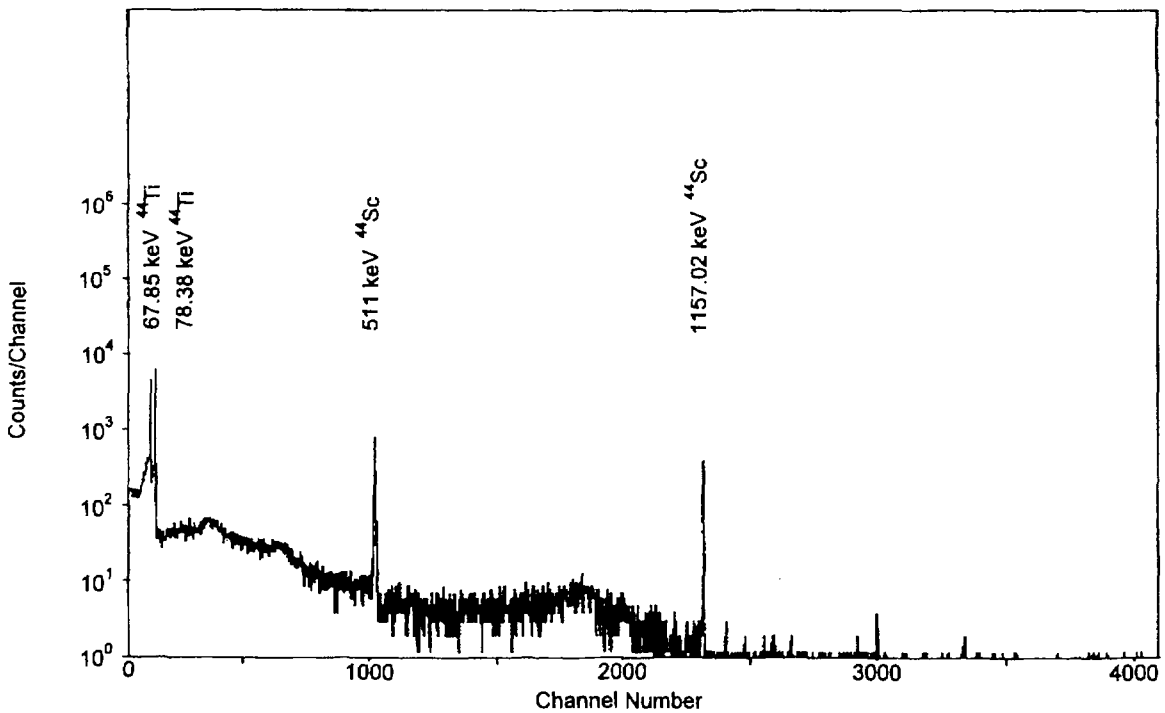

Figure 1: γ -spectrum of the purified ^{44}Ti solution.

$$D(T) = 2.8 \cdot 10^{-4} \exp\left(\frac{-(295 \pm 10)\text{kJ/mol}}{RT}\right)\frac{\text{m}^2}{\text{s}}$$

and for CoTi

$$D(T) = 5.4 \cdot 10^{-5} \exp\left(\frac{-(265 \pm 11)\text{kJ/mol}}{RT}\right)\frac{\text{m}^2}{\text{s}}$$

Interdiffusion experiments and production of ^{44}Ti were successfully carried out. As a next step self-diffusion experiments on γ -TiAl and CoTi single crystals are in progress using the ^{44}Ti isotope.

4. References

1) Present authors, JAERI TIARA Annual Report **5** (1995) 191.

2) J. Philibert, *Atom Movements-Diffusion and Mass Transport in Solids*, Les Editions de Physique, Les Ulis, France, 1991.

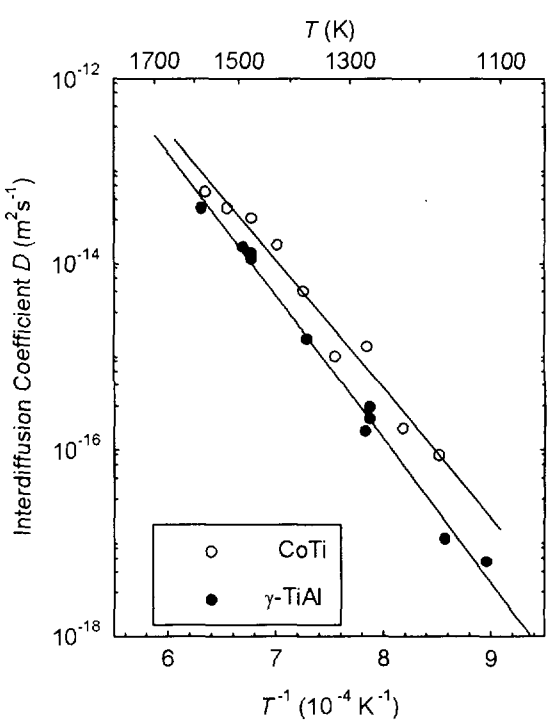

Figure 2: Temperature dependence of inter-diffusion coefficients D for γ -TiAl and CoTi.

6.6 Production of polarized unstable nuclear beam by grazing ion - surface scattering

T. Ohtsubo, S. Ohya, H. Kimura*, K. Hori*, S. Yachida*, S. Muto**, T. Sekine***, M. Koizumi*** and A. Osa***

Department of Physics, Niigata University, *Graduate School of Science and Technology, Niigata University, **KEK, ***Department of Radioisotopes, JAERI

The polarized unstable nuclear beams are very useful for not only nuclear physics but also material sciences[1]. The nuclear magnetic resonance (NMR) of the polarized nuclei can be detected by observing the change of the angular distribution of the radiation. The high sensitivity of the NMR with radiation detection allows the study of extremely dilute samples in condensed-matter physics or the determination of nuclear moments with high precision.

In order to obtain the polarized unstable nuclear beam, we investigate a grazing ion - surface scattering method. In this method, the fast atomic beam hits the clean surface of the crystal at the grazing incidence. Because the atomic collision at the surface is anisotropic, then the scattered atom obtained the orbital angular momentum, i.e., is polarized. Detailed investigations of this method have been reported by using the stable isotope nuclei[2,3]. However, no direct measurement of the nuclear polarization by detecting the radiation has been performed. The aim of the present study is to observe the nuclear polarization by grazing ions - surface scattering.

The experiments have been performed using the on-line isotope separator (ISOL) at Japan Atomic Energy Research Institute, Takasaki. The Ba activities were produced using Zr(^{36}Ar,xnyp) reactions at 195 MeV. They were ionized in a surface-ionization ion source of the mass-separator. Figure 1 shows the side view of the scattering chamber. The separated ^{123}Ba (I^{π} = 3/2$^-$, $T_{1/2}$ = 2.7 m) nuclei was bent onto the target of Si single crystal by a pair of electric field plates. The typical electric field was 280 V/cm, and the grazing angle of incidence was Φ_{in} ~ 2°. The surface of Si was polished by chemical etching. The scattered atom flights in vacuum, and the atomic polarization is transferred to the nuclear polarization through the hyperfine interaction during the flight. Then the scattered atom was implanted in a barium fluoride (BaF_2) single crystal stopper. Implanted ^{123}Ba nuclei are sit on the substitutional sites of Ba and their polarization may be preserved because there is no paramagnetic interaction at the substitutional site. The strong magnetic field parallel to the polarization axis was applied at the crystal in order to decouple the hyperfine interaction and preserve the nuclear polarization during the implantation process. Two Si detectors of 50 mm^2 area and 0.5 mm thickness were mounted in the vacuum chamber at the 0° and 180° with respect to the polarization axis for beta ray detection, . The gamma rays were observed by the pure Ge detectors placed at 0°, 90° and 180° with respect to the orientation axis. For the NMR, the radio-frequency (rf) oscillating field was applied to the stopper perpendicular to the external magnetic field.

Test experiments were performed. However, we could not observe the polarization of ^{123}Ba owing to some problems (fluctuation of beams, nose by rf field, intensity of beam)

For the next step, we are now improving on the NMR system, beta ray counting system and the beam collimating system. For the high efficiency on the NMR we are constructing the high power rf system. A plastic scintillation counter system is adopted for the beta ray detection because Si detectors may suffer the high power rf noise. In order to avoid the influence from the difference of each beam spot, the incident

beam is collimated at the front of the electric deflector.

Reference

[1] H. Ackermann et al., *Hyperfine Interactions of Radioactive Nuclei*, edited by J. Christiansen (Springer Verlag Berlin 1983) Chapter 6.
[2] A. Schirmacher and H. Winter, *Phys. Rev.* A47: 4891-4907 (1993)
[3] H. Winter and R. Zimmy, *Hyperfine Interactions* 22: 237-250 (1985)

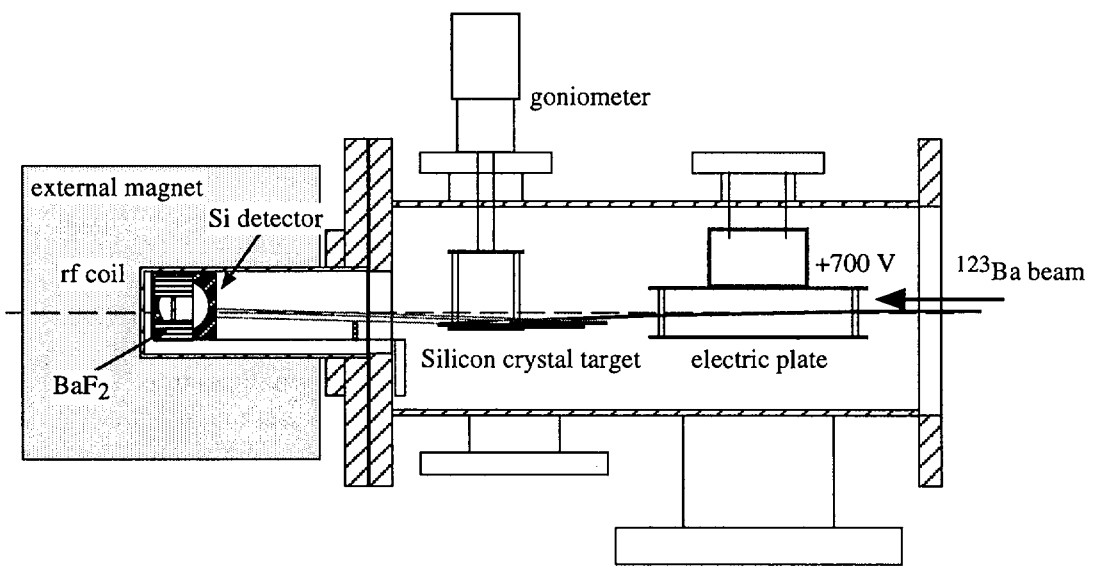

Fig. 1. Side view of the scattering and NMR chamber.

6．7 Change of the Nuclear Charge Radius in the Mössbauer Transition of ^{133}Cs

H. Muramatsu[1], E. Tanaka[1], H. Ishii[1], T. Miura[2], Y. Fujita[2], M. Koizumi[3], A. Osa[3], T. Sekine[3], M. Yanaga[4], K. Endo[5], H. Nakahara[6], and M. Fujioka[7]
[1]*Faculty of Education, Shinshu University*, [2]*High Energy Accelerator Research Organization*, [3]*Department of Chemistry and Fuel Research, JAERI*, [4]*Faculty of Science, Shizuoka University*, [5]*Showa College of Pharmaceutical Sciences*, [6]*Faculty of Science, Tokyo Metropolitan University*, [7]*CYRIC, Tohoku University*

1. Introduction

The Mössbauer isomer shift arises due to the Coulomb interaction between the nuclear and electronic charge distributions. If it is assumed that a nucleus is a sphere of charge with a radius of R in the ground state, and the electron density over the nuclear volume is constant($\rho(0)$), the isomer shift(δ) can be written as

$$\delta = (4/5)\pi Ze^2R^2(\Delta R/R)\Delta\rho(0), \qquad (1)$$

where Z is the nuclear charge, e the electronic charge, $\Delta R/R$ the relative difference of the nuclear charge radius between the excited and ground states, $\Delta\rho(0)$ the difference in the total electron density at the nucleus between the absorber and the source materials, respectively. Thus an exact knowledge of $\Delta R/R$ is essential for a quantitative interpretation of the isomer-shift data in terms of a change in the electron density. If one can exactly determine the $\Delta R/R$ values for respective Mössbauer nuclei, it would be possible not only to quantitatively discuss the isomer-shift data for each element, but also to directly compare isoelectronic compounds of different Mössbauer elements.

The value of $\Delta R/R$ for the 81 keV transition of ^{133}Cs has been proposed by several authors in theoretical or Mössbauer-measurement approaches[1)-4)]. Although the sign of $\Delta R/R$ is considered to be positive, its magnitude is still controversial; the proposed value of $\Delta R/R$ ranges from 0.15×10^{-4} to 2×10^{-4}. These determinations, except for the nuclear-theory calculation[1)], however, are based mainly on Mössbauer measurements and the hypothetically defined electron configurations of cesium. Thus, in this report, the determination of $\Delta R/R$ in the 81 keV($M1$+2.8%$E2$) transition of ^{133}Cs by using the conversion method, which is one of the so-called direct methods, is described.

2. Experimental

The source sample in this work was prepared by the implantation of ^{133}Xe ($T_{1/2}$=5.25d), which decays to the Mössbauer level of ^{133}Cs. Ion-implantation of ^{133}Xe was carried out at a terminal voltage of 20 kV at room temperature by means of an electromagnetic isotope separator of the JAERI TIARA. As host materials, high purity metallic foils of Al, Cr, V, Mo and Rh were chosen for the ion-implantation of ^{133}Xe. The ^{133}Cs Mössbauer spectra were measured using a single-line absorber of CsCl with 360 mg/cm^2 Cs thickness while keeping both the source and absorber at 4.2 K. The 81 keV γ-rays of ^{133}Cs from the implanted source were detected with a thin NaI(Tl) scintillation detector.

The internal-conversion electron spectra of the same samples that were used in Mössbauer measurement were measured using the $\pi\sqrt{2}$ iron-free β-ray spectrometer having ρ =75 cm at the Institute for Nuclear Study, the University of Tokyo. For measurements of the internal-conversion electrons, a single-wire proportional counter (SWPC) with a multislit (49 slits, 0.5 mm slit-width) was used as a focal-plane detector. More detail experimental procedures are given in the previous report[5].

3. Results

Fig.1 shows the Mössbauer spectra for the Al, Cr, V, Mo and Rh samples. The Mössbauer absorption spectra were analyzed by a least-squares method. When the spectrum indicated more than one absorption peak; the radioactive atoms were introduced by implantation into more than one site, the averaged isomer shift($\bar{\delta}$) of the source sample was estimated by using the site-population of the implanted atoms deduced from recoilless fractions for different sites, referring to the previous data[6] as well as the results for temperature dependence of

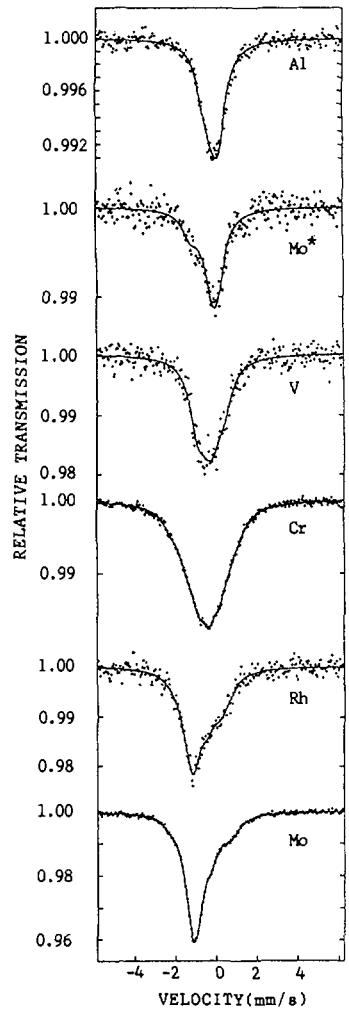

Fig.1. Mössbauer spectra taken for the sources of ^{133}Xe implanted into Al, Cr, V, Rh and Mo with a CsCl absorber. The spectra were measured at liquid-helium temperature.

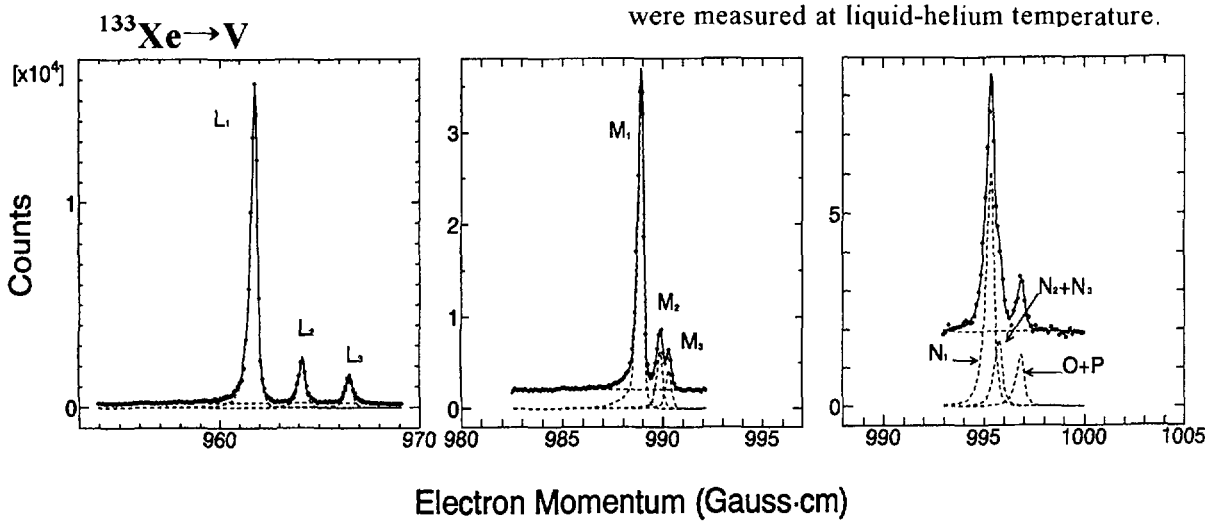

Fig.2. The *L*-, *M*- and *N,O+P*-conversion lines of the 81 keV transition in ^{133}Cs into V. The solid curves indicate the result of least-squares fittings using the conversion line shapes shown by the broken curves.

the spectrum; this quantity should correspond to the measured internal-conversion intensity, which is indeed the population-average of the conversion intensities from different sites. Fig.2 shows typical conversion-electron spectra in the region of the L-lines, M-lines and N-, O+P-lines of the 81 keV transition in ^{133}Cs. The momentum resolution was about 0.05%, though the spectrometer resolution was set at 0.03%. The conversion spectra were analyzed by a least-squares fitting using the computer code ACSEMP[7]. The L-conversion lines were completely resolved into three subshells, but not in the M, N ,O and P shells. The O- and P-lines could not be resolved at all due to a limit of the experimental momentum resolution. The O-lines including a small contribution of P-lines(O+P lines) were assumed to have the same shape as that of the N_I-line.

In spite of the situation that the valence-shell conversion, which is normally considered to be the most sensitive to the change in the chemical environments, cannot be separately measured, the derivation of $\Delta R/R$ is considered to still be possible; using the proportionality of the conversion coefficient to the electron density[8], the chemical effect on the ratio of the outer-shell electron density, $\rho_{o.s.}(0)=\rho_{5s}(0)+\rho_{5p}(0)+\rho_{6s}(0)$, to the inner-shell electron density, $\rho_{4s}(0)$, is examined. Details were discussed in the previous report[5].

The general equation for the isomer shift[Eq.(1)] then can be rewritten with the correlation between the averaged isomer shift ($\bar{\delta}$) and the change in $(\alpha_O+\alpha_P)/\alpha_{NI}$ as

$$\bar{\delta} = (4/5)\pi Z e^2 R^2 (\Delta R/R)\rho_{4s}(0)_{theor.} \times \Delta[(\alpha_O + \alpha_P)/\alpha_{N_1}] + const. \quad (2)$$

where α is the internal conversion coefficient, and $\Delta[(\alpha_O+\alpha_P)/\alpha_{NI}]$ is equated with $\Delta[\rho_{o.s.}(0)/\rho_{4s}(0)]$. As is easily seen from Eq.(2), the ratios $\rho_{o.s.}(0)/\rho_{4s}(0)$ obtained from conversion measurements linearly correlate to the average isomer shifts $\bar{\delta}$ determined by Mössbauer experiments. The data of the present work were fitted to a straight line by a weighted least-squares analysis. The slope of this straight line includes the information of $\Delta R/R$. Although the analysis is in progress, as according to Eq.(2) and using a relativistic value of $\rho_{4s}(0)_{theor.}$=1344.7 a.u. calculated by Band *et al.*[9] for an isolated neutral Cs atom, we obtain the following tentative value for the change of nuclear charge radius: $\Delta R/R = +(1.5 \pm 0.6) \times 10^{-4}$, where $R=1.2 \times A^{1/3}$ fm was used. This means that the charge radius of the first excited state is 0.015% larger than that of the ground state.

References

1)R.A.Uher and R.A.Sorensen, Nucl. Phys. **86**, 1 (1966).

2) G.J.Perlow, A.J.F.Boyle, J.H.Mershall and S.L.Ruby, Phys. Lett. **17**, 219 (1965).

3) A.J.F.Boyle and G.J.Perlow, Phys. Rev.**149**, 165 (1966).

4)W.Henning, D.Q.Quitmann, E.Steichele, S.Hüfner and P.Kienle, Z. Physik,**209**, 33 (1968).

5)H.Muramatsu, E.Tanaka, H.Ishii, T.Miura, Y.Fujita, M.Koizumi, A.Osa, T.Sekine, M.Yanaga, K. Endo, H.Nakahara, and M.Fujioka, JAERI TIARA Annual Report No.5, 193(1995)

6) H.Pattyn, P.Hendrickx, K.Milants, J.de Wacher and S.Bukshpan, Hyp. Int. **79**, 807 (1993); E. Verbiest, Ph.D. thesis, Katholiek Universiteit Leuven, 1983.

7) M.Fujioka and M.Takashima, J.Phys.**40**, C2, 32(1979).

8)I.M.Band, L.A.Sliv and M.B.Trzhakovskaya, Nucl. Phys. **A156**,170(1970).

9) I.M.Band and V.I.Fomichev, Atom. Data and Nucl. Data Tables, **23**,295(1979).

7. Radiation Shielding for Accelerator Facilities

7．1 Radiation Streaming Measurement in a Labyrinth of Light Ion Room 2 at TIARA (II)

Su. Tanaka, Y. Nakane[2], Y. Sakamoto[2], S. Meigo[2], H. Nakashima[2], M. Nakao[3], T. Kurosawa[3] and T. Nakamura[3]
Advanced Radiation Technology Center, JAERI, Accelerator Radiation Lab. Center of Neutron Science, JAERI [2], Cyclo. R.I. Center, Tohoku Univ.[3]

I. Introduction

It is important to estimate radiation streaming through a labyrinth as well as radiation transmission through a bulk shield for shielding design of high-energy accelerator facilities. Benchmark data of the radiation streaming are required to confirm the applicability of empirical formulas and Monte Carlo transport codes which are generally used for the shielding design. Hence, we had been carried out a streaming experiment in a labyrinth of Light Ion Room 2 (LIR2) and Heavy Ion Room 1 (HIR1) at TIARA[1), 2)], using a p-Cu white neutron and photon source generated by protons of 68 MeV.

Here in this study, we further measured the photon streaming in the labyrinth of LIR2 using the same white neutron and photon source as in the previous experiment[1)].

The benchmark data measured in this experiment are divided into two categories: radiation distribution in the target room, and radiation distribution along the labyrinth. The measured quantities are thermal neutron flux and dose equivalent for photon.

II. Experimental

A plan view of the experimental geometry of LIR2 is presented with the location of neutron and photon source, and the measurement points in Fig.1. The labyrinth has three legs of which the cross sections are 1.5 m width and 3.5 m height for the first and second legs, 3.0 m height for the third leg. A door made of 4.6 mm-thick steel is placed at the end of the third leg. The dimension of the target room is 8.5 m x 7.5 m in floor area and 4.8 m in height. In this experiment, protons of 68 MeV accelerated by the AVF cyclotron were vertically transported along the beam transport line from the Light Ion Room 1, and stopped fully by a Faraday cup of thick-Cu target placed 108 cm above the floor to produce white neutrons and photons.

During the experiment, the source intensity was monitored with proton beam currents at the Farady cup, and counts of rem counters (Studsvik 2202D) placed at the points 4 and 11 in the labyrinth. Distributions of thermal neutron flux and photon dose equivalent in the room were measured using a TLDs (Harshaw TLD100, TLD700). Besides, photon dose equivalent along the labyrinth were measured with TLD (TLD-700) and ionization chamber (ALOKA ICS-151).

III. Results and discussion

The photons in the room consist of direct photons emitted from the target, and secondary photons due to Compton scattering of direct photons, inelastic scattering of fast neutrons and capture of thermal neutrons from the concrete walls. The distribution of photon dose equivalent in the room was measured with TLDs placed at the points of RSn, RMn and RNn (n=1,2,3), and 0.5, 1.08 and 2.54 m in height from the floor, respectively. Figure 2 shows the measured photon dose equivalent rate as a function of distance from the source. The dose equivalents become larger than a solid line of inverse-square law with the distance, and the ratio of secondary to direct photon dose equivalents is 100% at 4 m from the target.

Photon dose equivalent rates along the labyrinth measured with the TLD and ion chamber are shown in Fig.3, comparing with the neutron dose equivalent rates measured with a rem counter and Bonner ball detector in our previous experiment[1)]. The two values measured by the TLD and ion chamber are in reasonable agreement each other within the errors of measurements. The ratio of photon to neutron dose equivalents is 10% at the first corner, 20% at the second corner and 100% in the third leg. It must be pointed out that estimation of photon streaming is important in the design of long labyrinth for high-energy accelerator facilities.

References

1. Su. Tanaka et al., JAERI TIARA Annual Report 1994(Vol.4), pp.195-197 (1995)
2. Su. Tanaka et al., JAERI TIARA Annual Report 1995(Vol.5), pp.199-201 (1996)

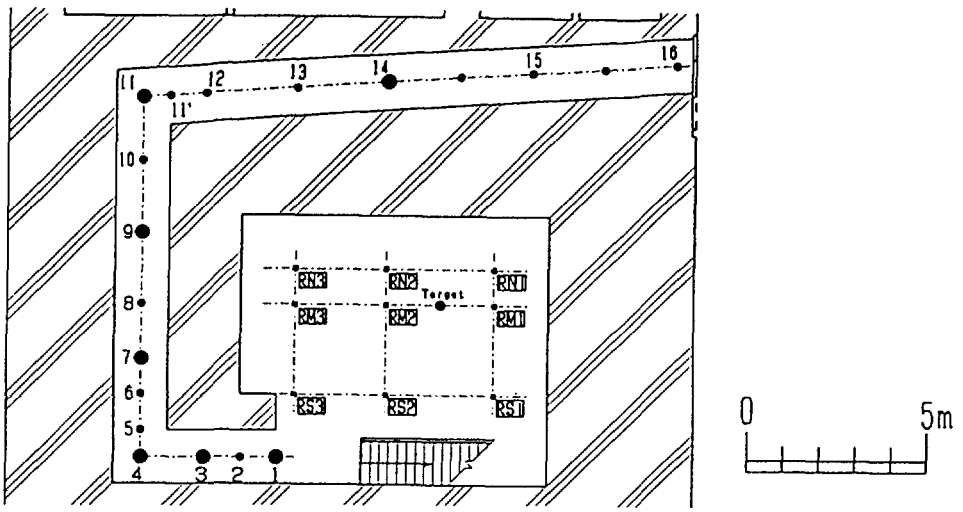

Fig.1 Plane view of an experimental room for radiation streaming experiment

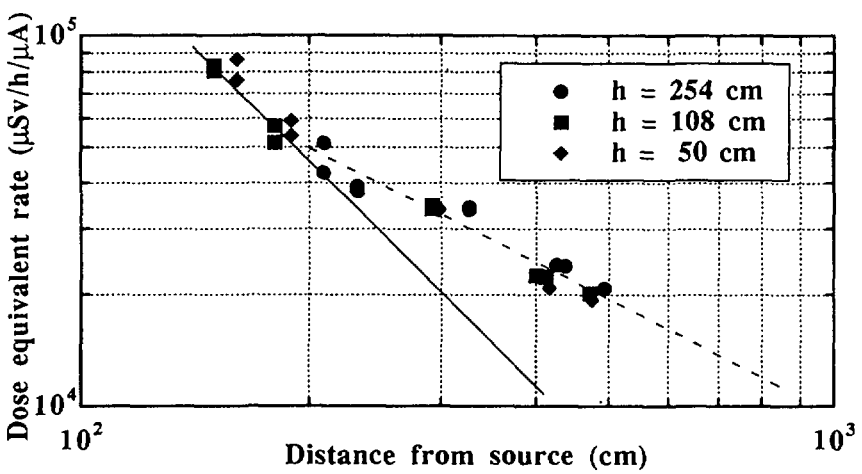

Fig.2 Measured photon dose equivalent rate as a function of the distance from the source

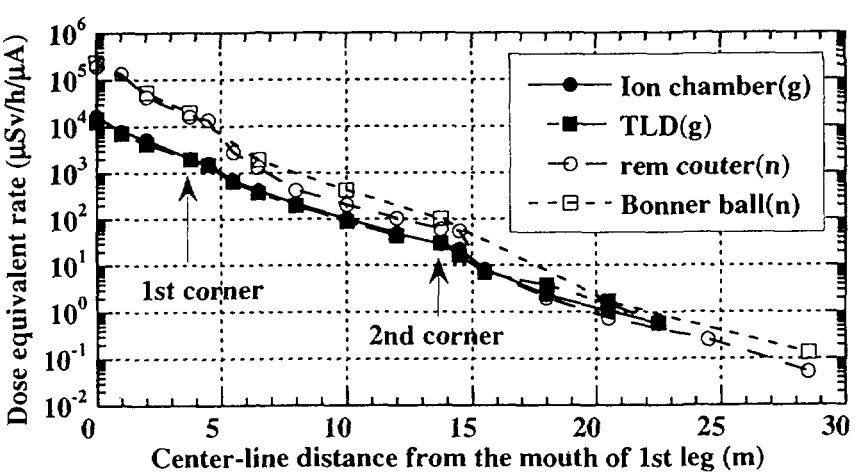

Fig.3 Photon dose equivalent rates along the labyrinth measured with the TLD and ion chamber, and neutron dose equivalent rates measured with rem counter and Bonner ball detector

7．2 Thick Target Double Differential Yields of Neutrons And Gamma Rays for Charged Particles

K. Shin, S. Ono, S. Meigo[1], H. Takada[1], N. Sasa[1], H. Nakashima[1], S. Tanaka[2]

Department of Nuclear Engineering, Kyoto University,

[1] Japan Atomic Energy Research Institute, Tokai Establishment

[2] Japan Atomic Energy Research Institute, Takasaki Establishment

1. Introduction

Double differential thick target neutron yields data are inevitable for accelerator shielding design as source term data Unfortunately, there are very small number of thick target neutron double differential yields data. For gamma rays, almost no data exists . One of the objectives of the measurements is to systematically store such data for various ions with different combinations of targets.

Recently, simulation methods[1)] for proton induced nucleon productions based on the intra-nuclear cascade model have been improved, also QMD[2)] becomes available for the estimation of double differential cross sections of neutron production from heavy ion reactions. There are still some problems in the accuracy of the prediction of neutron spectra for the 2. Experimental Method

2. Experimental Method

The experiment was performed at the AVF cyclotron TIARA. Accelerated ion beams of 68-MeV protons, 100-MeV alphas, 220-MeV $^{12}C^{5+}$ and 460-MeV $^{40}Ar^{13+}$ from the cyclotron, which were chopped to pulses, hit the thick targets set in a chamber. The experimental arrangement is shown in Fig. 1. Combinations of the incident ions and the targets for which measurements were made, are in Table I. The contribution of the background radiation was measured at every angle, using an iron shadow block of $20 \times 20 \times 80$ cm^3.

Secondary neutrons emitted at angles of 0° , 15° , 30° , 45° , 60° , 90° and 120° to the beam direction were measured by the TOF method, using a 12.7 cm in diameter by 12.7 cm in thickness BC501A scintillator. The secondary gamma rays were measured simultaneously with neutrons by the same detector. The obtained pulse-height spectra were unfolded to gamma-ray energy fluences by the FERDO-U code[3)]. The number of particles incident on the target was measured by the current integrator connected to the target.

3. Calculation Method

Calculations of the inclusive differential neutron production cross sections were made by the QMD code and the statistical decay model (SDM) calculation. Since the experiments were carried out with the thick target, calculations of the differential neutron cross sections were made at several energy points, and the data were integrated with the ion range to obtain thick target yields.

For protons, calculations by the revised NMTC/JAERI was also used. The modifications[4] in the intra-nuclear cascade calculation with the pre-equilibrium process (NMTC-3STEP), or inclusion of nuclear medium effects in terms of the reflection and refraction with the in-medium nucleon-nucleon cross sections (NMTC-ISOBAR).

4. Results of the Analysis

An example of the neutron spectra of the 68-MeV proton incidence are showed in Fig. 2 for the Au target. The NMTC-3STEP tends to give overestimation of the neutron spectra at the forward angles, but gave a good agreements at the backward angles. The similar trend is seen for other targets. The NMTC-ISOBAR gave satisfactory agreement with the experiment at all angles.

The QMD+SDM calculation generally gave an underestimation to measured neutron spectra for the 100 MeV alpha incidence, especially at forward angles. On the other hand, it gave overestimation of the neutron spectra for heavier ions. The comparison of the QMD calculation with present experimental data are demonstrated in Figs. 3 for the 220-MeV C ions incident on the C target. When the target becomes heavier, the agreement becomes better at forward angles, while the neutron fluences at large angles are still overestimated.

Gamma-ray spectra of the 68-MeV proton incidence on the C target showed strong discrete gamma rays from the 1st and 2nd excited levels of carbon. The similar spectra were seen for gamma rays of 100-MeV alpha particles on the C target. These discrete gamma rays becomes obscure when the incident ion becomes heavier. The gamma-ray yields are almost isotropic for all cases.

References

1)Secondary Specialists' Meeting on Shielding Aspects of Accelerators, Targets and Irradiation Facilities (SATIF2), 12-13 Oct. 1995, CERN, Geneva, OECD/NEA.

2)K. Niita et al., Phys. Rev. C52, 2620 (1995).

3)K. Shin, et al., Nucl. Technol., 53, 78 (1981).

4)H. Takada, J. Nucl. Sci. Technol., 33, 25 (1996).

Table I Combinations of Ion and Targets

Ion	Energy(MeV)	Targets
P	68	Be, C, Al, Cu, Nb, Au, Pb
He	100	C, Fe, Au
C	220	C, Fe, Zr
Ar	460	C, Fe, Zr

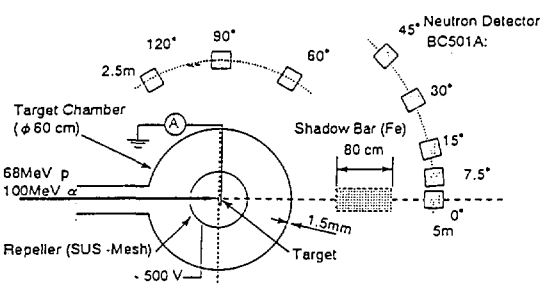

Fig1. Experimental arrangement

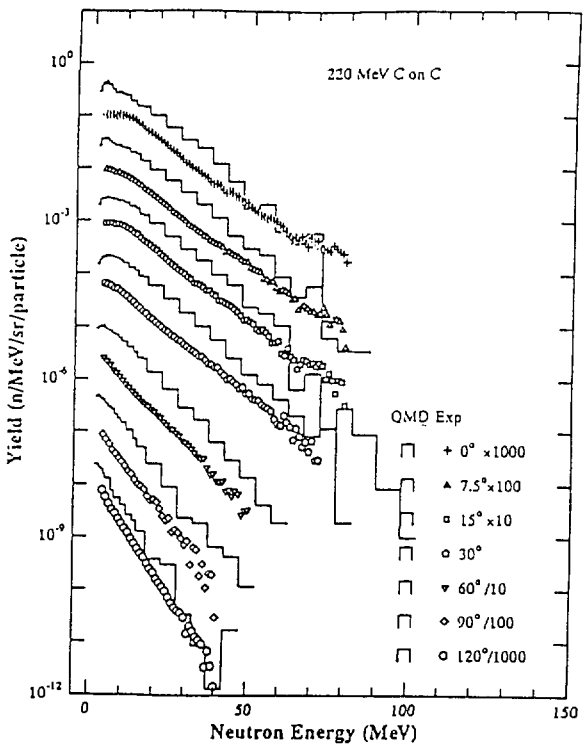

Fig.3 Neutron spectra from C+C

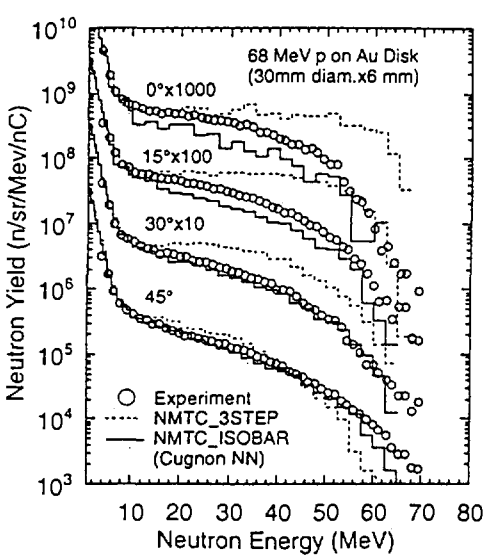

Fig.2 Neutron spectra fron p+Au

7．3 Measurements of charged particle emission data for Ten's MeV neutrons and the characterization of ^{7}Li(p,n) neutron sources

Y. Nauchi, M. Baba, T. Iwasaki, T. Sanami, T. Suzuki, T. Nakamura[1], S. Tanaka[2], S. Meigo[3], H. Nakashima[3], H. Takada[3], N. Nakao[4], Y. Watanabe[5], M. Harada[5]

Department of Quantum Science and Energy Engineering, Tohoku University, [1]Cyclotron Radio Isotope Center, Tohoku University, [2]Advanced Radiation Technology Center, JAERI, [3]Center for Neutron Science, JAERI, [4] Tanashi Branch, High Energy Accelerator Research Organization, Tanashi, [5]Department of Energy Conversion Engineering, Kyushu University

1. Introduction

We are conducting the studies of double differential cross sections (DDXs)[1] for charged particles emission reactions using the ^{7}Li(p,n) source at TIARA. During the last year, new measurements were carried out for (n,xp), (n,xd) reactions of aluminum and carbon for 75 and 65 MeV neutrons. These data are essential for the studies of fast neutron therapy, radiation damage, accelerator-driven reactors and neutron detectors.

We also extended the measurements of the the ^{7}Li(p,n) neutron spectra to Ep=65 and 80MeV to provide basic data for experiments using the source.

2. (n,xp), (n,xd) DDX measurement

2.1 Experiment and Data Processing

We performed the experiments at LC course in TIARA. Figure 1 shows the geometry for angles larger than 20° (inclined geometry). Disk shape samples 7 cm in diameter were placed 5.5m from the target and irradiated by neutron flux of $\sim 10^{4}$n/cm^{2}/s in the air environment. The samples of carbon (110mg/cm^{2} thick) and aluminum (160mg/cm^{2} thick) were viewed simultaneously by two counter telescopes located 14.5～20cm from the samples. Each telescope consists of a transmission type Si-SSD detector (150 μ m thick) and a NaI(Tl) scintillatior (3cm thick). Measurements were done at 25, 40, 55 and 70° in this geometry. The measurements at 12 and 17° were done using an "annular geometry" as described elsewhere[2].

Pulse heights data of the SSD and NaI were accumulated event by event together with time-of-flight (TOF) data between the NaI detector and the RF signal of the cyclotron. Particle identification was done by the ΔE-E method). Then the neutron energy for the event was determined by the TOF information. The pulse heights spectra were converted into the energy spectra using a linear response of NaI and the recoil proton spectrum by the peak neutrons in ^{7}Li(p,n) source. Then the spectra were corrected for the energy loss in the sample, air, SSD and aluminum windows in the front of detectors. Finally, the DDXs were deduced by correcting the spectra for neutron flux, the number of sample atoms and solid angles.

2.2 Results

The C(n,xp) DDX data (dot) are shown in fig. 2 with the data of U. C. Louvain[3] (square) for 62.7MeV neutrons. These data show agreement both in spectral shape and in magnitude. The C(n,xp) spectra consists of isolated peaks in high energy region that show

strong forward peaking and of continuum structures in low energy region.

Figure 3 shows the Al(n,xp) DDX data (dot) with calculations by ISOBAR code (solid line) which is a cascade model code updated by considering in-medium effects on nucleon-nucleon cross sections, and of FKK-GNASH code (dashed line)[4]. Both code reproduced the continuum spectra of experimental data. It is expected to extend the measurement to lower energy region where two codes show differences.

In contrast to the (n,p) case, the results of FKK-GNASH differ markedly from the experiment of Al(n,xd) spectra as shown in fig. 4. More experimental data are needed to improve the model calculations.

3. Characterization of ^{7}Li(p,n) neutron sources

The ^{7}Li(p,n) neutron fluxes have been measured by a proton recoil counter telescope (PRT) which was used in the DDXs measurements mentioned above. The neutron spectra has been measured by the TOF method using a BC501 scintillator. New neutron spectra for Ep=65MeV and 80MeV are shown in fig. 4. Similarly with the spectra in other energies, they consists of high energy peak by the ^{7}Li(p,$n_{0,1}$) reactions and a low energy continuum part. Solid lines in fig. 4 show 3-body phase space distribution for the ^{7}Li(p,n ^{3}H) α reaction. The calculation reproduce the spectral shape in the low energy region as well as other proton energy points[2].

Until now, the measurements of the neutron spectra have been completed at 8 energy points between 40MeV and 90MeV. The numerical data of the new measurements are shown in table 1 with previous measurements. Most values of ^{7}Li(p,$n_{0,1}$) cross section are in the range of 33～36mb/sr, then we can estimate the neutron flux from the thickness of the Li target and the beam current.

Table 1. neutron flux of LC course

Ep (MeV)	En (MeV)	FWHM (MeV)	Φ 10^{6}n/sr/ μC	Li(p.n) σ mb/sr	Error (%)
45	40.5	2.3	3.46	35.0	3.3
50	45.4	2.4	2.70	29.8	3.24
55	50.9	5.1	3.82	33.4	4.6
60	55.3	2.9	4.45	34.6	3.5
65	60.6	2.6	4.17	33.8	3.42
70	65.2	2.5	4.82	33.9	3.9
80	75.0	3.4	5.34	35.5	4.4
90	84.6	5.75	6.35	35.1	6.2

There are several ^{7}Li(p.n) neutron source facilities in the world, but detailed data on the neutron spectra are scarce. The experimental data for the intensity and spectra were provided to the facilities.

Acknowledgement

The authors would like to thank to Dr.. Chadwick for providing us the calculation by FKK-GNASH.

References

1) M. Baba et. al., Proc. of Int. Conf. On Nucl. Data for Sci. and Technol., (Gatlinburg, 1994), p. 90
2) M. Baba et. al.., JAERI TIARA Annual Report 1995 Vol. 5 p. 205
3) I. Slypen et. al., Phys. Rev. C Vol. 51 1303 (1995)
4) M. B. Chadwick et. al., Nucl. Sci. and Eng. 123, 1 (1996) and private comunications

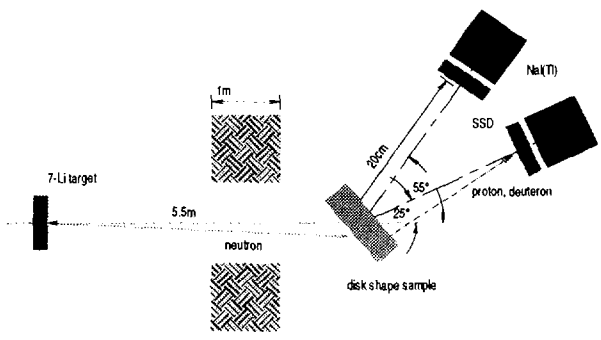

Fig. 1 experimental set up

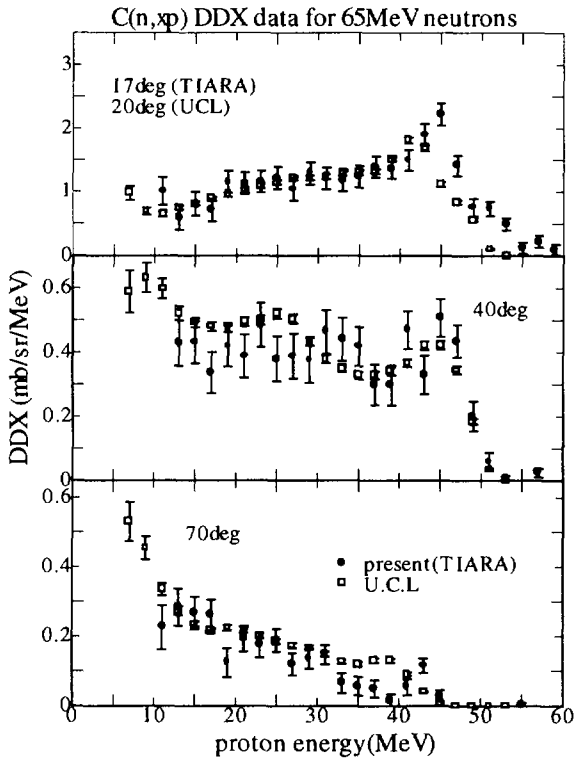

Fig.2 C(n,xp) DDX data at En=65MeV

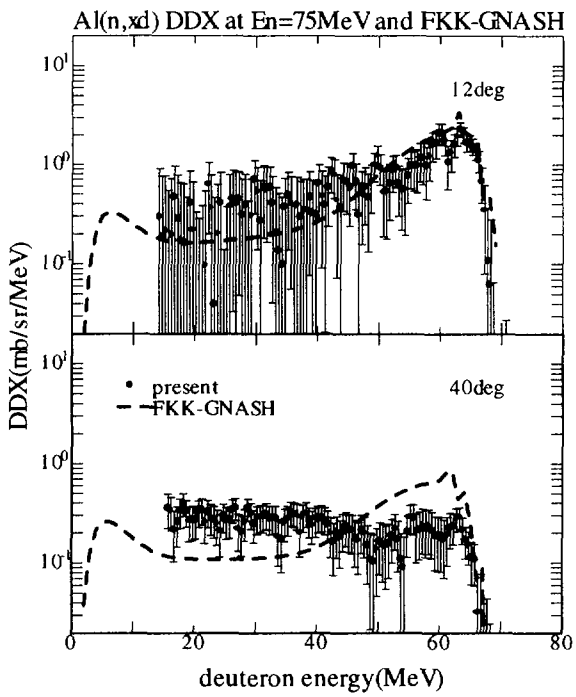

Fig. 4 Al(n,xd) DDX data at En=75MeV

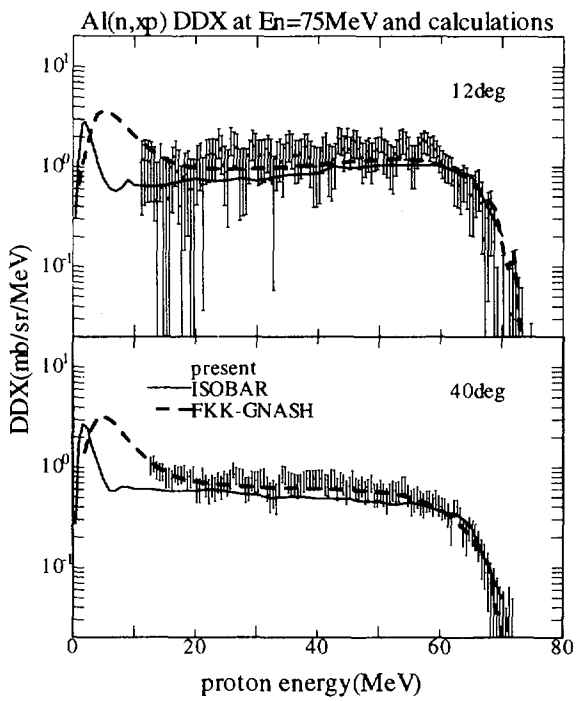

Fig. 3 Al(n,xp) DDX data at En=75MeV

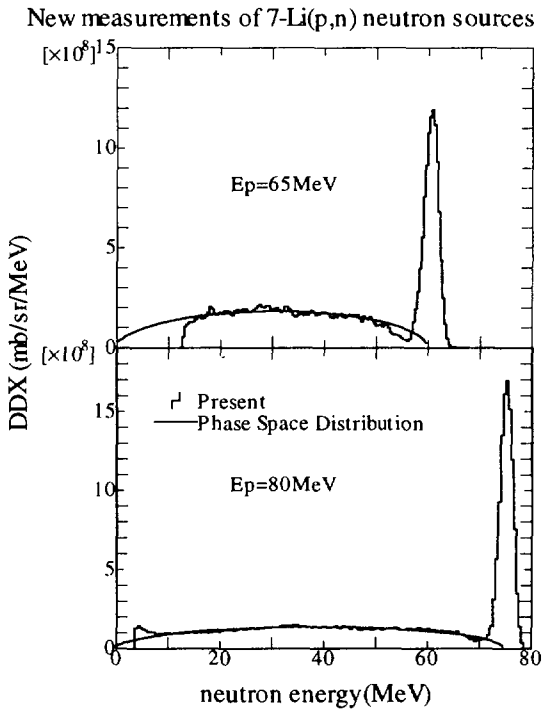

Fig. 5 New measurements of 7Li(p,n) sources

7．4 Measurements of Neutron Activation Cross Sections

E. Kim,[1] T. Nakamura,[1] A. Konno,[1,5] Y. Uwamino,[2] M. Imamura,[3,6] N. Nakao,[3,7] S. Shibata,[3,8] and Su. Tanaka[4]

[1]Cyclotron and Radioisotope Center, Tohoku University, [2]Institute of Physical and Chemical Research, [3]Institute for Nuclear Study, University of Tokyo, [4]Takasaki Research Establishment, Japan Atomic Energy Research Institute, [5]Onagawa Nuclear Power Station, Tohoku Electric Power Co., Inc., [6]National Meseum of Japanese History, [7]The organization has changed on April 1, 1997 into High Energy Accelerator Research Organization, [8] Research Reactor Institute, Kyoto University

1. Introduction

The high-energy and high-intensity accelerators have increasingly being used in nuclear physics, radiotherapy, material damage study and so on. This increases the demand for neutron cross sections in the high energy region. The estimation of induced radioactivaties for radiation safety design requires neutron activation cross sections. Nevertheless, neutron activation cross section data in the energy range above 20 MeV are very poor and no evaluated data file exists. In this study, we measured the neutron activation cross sections using quasi-monoenergetic neutrons in the energy range above 20MeV.

2.Experimental

Irradiation experiments from 40 to 90MeV neutron energies were performed in the quasi-monoenergetic neutron fields produced by the ^{7}Li(p,n)^{7}Be reaction at the LC beam line of LIGHT ION ROOM 3 at TIARA. The Li-targets (99.98% ^{7}Li enriched) of 3.6 to 6.75mm thickness were bombarded by proton beams of 43, 48, 58 and 88MeV energies. The neutron produced in the forward direction from the target were transported through the collimator (10.9cm diam by 220cm long) for sample irradiation and the proton beams passed through the target were swept out by the magnet to the beam dump. In the irradiation experiments, the neutron spectra were measured with the TOF method using a BC501A organic liquid scintillator. The absolute neutron flux of source neutrons in the monoenergetic peak per proton beam charge was obtained from a Proton Recoil counter Telescope (PRT) measurement. Two fission chambers of ^{238}U and ^{232}Th were placed near the target for neutron monitoring during irradiation and were calibrated to the proton beam current. The irradiation experiment was performed at 400cm behind the lithium target by placing the samples at the collimator exit.

The irradiated samples are ^{12}C, ^{27}Al, ^{nat}Cu, ^{59}Co and ^{209}Bi. Irradiation consisted of short irradiation time (30min to 2 hours) and long irradiation time (about 20hours) by considering the half life of produced nuclei. The gamma rays emitted from irradiated samples were measured with a high purity Ge detector.

3.Analysis

The reaction rates of radioisotopes identified from the gamma-ray spectra were estimated after corrected for the peak efficiency of Ge detector, the coincidence-summing effect, the self-absorption effect in thick samples, and also for the beam current fluctuation during sample irradiation. The peak efficiency of the HP-Ge detector was determined by using the standard mixed gamma-ray source and the correction factor for self absorption of gamma rays in the samples were

calculated by the Monte Carlo code, PEAK[1]. The coincidence-summing effect caused by the coincidence detection of two or more gamma rays in the gamma ray spectrum was corrected by using the SUMECC code[2]. Fluctuation of the neutron flux during the irradiation was treated by using the proton beam current monitor data recorded by the MCS.

The reaction rate per beam current, R, corrected for beam current fluctuation becomes

$$R = \frac{\lambda \cdot C}{N \cdot \varepsilon \cdot \gamma \cdot e^{-\lambda \cdot T_c} \cdot (1 - e^{-\lambda \cdot Tm}) \cdot \sum_i \{Q_i \cdot e^{-\lambda \cdot (n-i) \cdot \Delta t}\}}$$

where λ is decay constant (sec^{-1}), C total counts of gamma-ray peak area, N number of atoms in the target (atom), ε peak efficiency, γ branching ratio of gamma rays, T_c cooling time (sec), T_m counting time(sec) and Q_i beam current (Coulomb) for irradiation time interval Δt (sec).

The cross section at the peak neutron energy $\sigma(E_{peak})$ can be obtained as follows,

$$\sigma(E_{peak}) = \frac{R \cdot f}{\phi(E_{peak})}$$

where $\phi(E_{peak})$ is the peak neutron fluence given by PRT. The f value is the ratio of peak reaction rate from E_{min} (minimum energy of the monoenergy peak) to E_{max} (maximum energy of the monoenergy peak) and total reaction rate from E_{th} (threshold energy) to E_{max}, the peak-to-total ratio of reaction rate, which is expressed as,

$$f = \frac{\int_{E_{min}}^{E_{max}} \sigma(E) \cdot \phi(E) \cdot dE}{\int_{E_{th}}^{E_{max}} \sigma(E) \cdot \phi(E) \cdot dE}.$$

The f value is at first estimated from the lowest peak neutron energy by using the measured neutron flux, $\phi(E)$ and the cross section, $\sigma(E)$, of the evaluated high energy data files, ENDF/B-VI or experimental data complied by McLane et al.[3].

The errors of cross section data were obtained as the statistical errors (0.5%~30%) of the reaction rates, the errors (between 4% ~ 15%) of peak neutron fluences, the error (5%~40%) of the f value which is the peak-to-total ratio of reaction rate for the correction of the contribution to the reaction rate due to the low-energy neutron tail. For the coincidence-summing effect, since the branching ratios of ^{202}Bi to ^{198}Bi isotopes produced by ^{209}Bi(n,8n) to ^{209}Bi(n,12n) reactions are not definitely given, we assumed an additional 10% errors by neglecting the correction of the coincidence-summing effect.

4. Results and Discussion

In this study, we obtained the neutron activation cross sections of ^{12}C(n,2n)^{11}C, ^{27}Al(n,2nα)^{22}Na, ^{59}Co(n,2n)^{58}Co to ^{59}Co(n,4n)^{56}Co, ^{nat}Cu(n,sp)^{56}Mn, ^{nat}Cu(n,sp)^{58}Co, ^{nat}Cu(n,xn)^{60}Cu, ^{nat}Cu(n,xn)^{61}Cu, ^{nat}Cu(n,sp)^{65}Ni and ^{209}Bi(n,3n)^{207}Bi to ^{209}Bi(n,12n)^{198}Bi reactions. Our experimental results for ^{12}C(n,2n)^{11}C and ^{209}Bi(n,3n)^{207}Bi to ^{209}Bi(n,12n)^{198}Bi reactions are the first experimental data. As examples, Figs.1 to 4 give the obtained neutron activation cross section data. Our experimental data were compared with other experimental data, calculated cross section data by Odano[4] (^{59}Co) and ENDF/B-VI[5] high energy file data calculated with the ALICE code[6].

We found that the ^{12}C(n,2n)^{11}C cross section has a constant value of about 20mb in the energy range above 40MeV. The obtained cross section data of ^{59}Co(n,xn) reactions, ^{nat}Cu(n,x)reactions and ^{209}Bi

(n,xn) reactions showed very good agreement with the calculated cross sections and ENDF/B-VI high energy file data.

5.Reference

1) T.Nakamura and T.Suzuki, Monte Carlo Calculation of Peak Efficiencies of Ge(Li) and pure Ge Detector to Voluminal Sources and Comparison with environmental Radioactivity Measurement . Nucl. Inst. and Meth. 205,211 (1983)

2) A.Torii, Y.Uwamino, and T.Nakamura, INS-T-468, Institute for Nuclear Study, University of Tokyo(1987)

3) V.MaLane, C.L.Dunford and P.F.Rose, Vol.2, Neutron Cross Section Curves, Academic press., New York (1988)

4) N.Odano and S.Iwasaki, JAERI-M 94-019, p310-319, Proceedings of 1993 symposium on Nuclear Data(1994)

5) National Nuclear data Center,Brookhaven National Laboratory, "Evaluated Nuclear data file" ENDF/B-VI(1990)

6) M.Blamm, CODE ALICE/89, private communi-cation (1989)

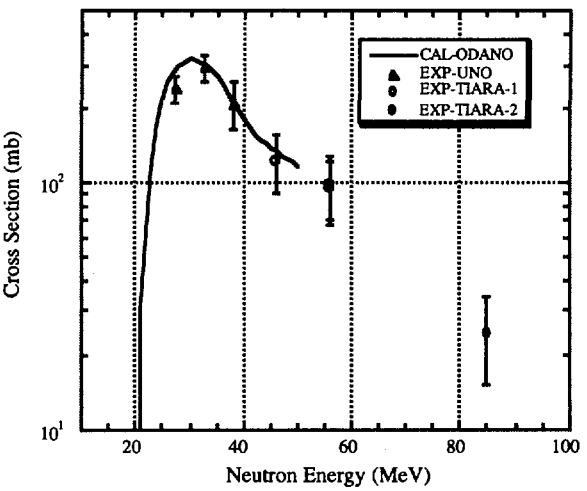

Fig.2 ^{59}Co(n,3n) ^{57}Co Reaction Cross Section

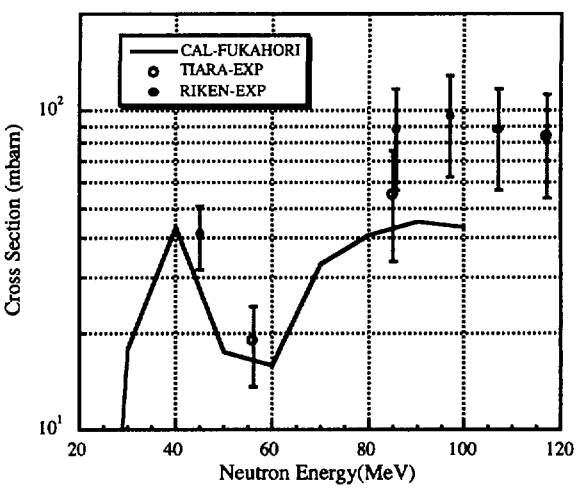

Fig.3 ^{nat}Cu(n,sp)^{58}Co Reaction Cross Section

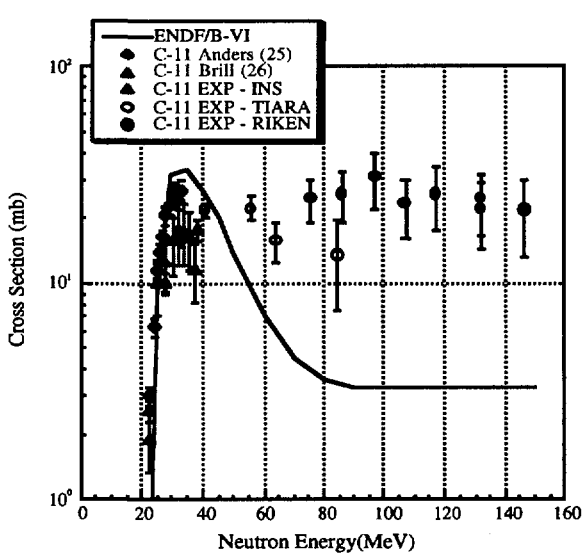

Fig.1 ^{12}C(n,2n)^{11}C Reaction Cross Section

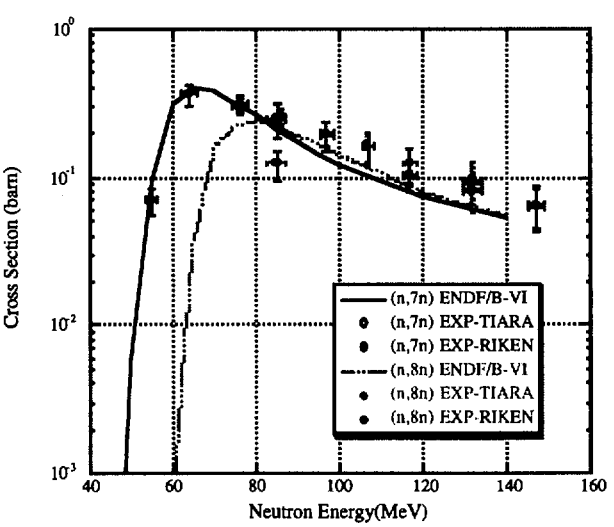

Fig.4 ^{209}Bi(n,7n)^{203}Bi and ^{209}Bi(n,8n)^{202}Bi Reaction Cross Sections

7．5 Measurement of Fission Reaction Rate of ^{237}Np and ^{238}U in Polyethylene by 65 MeV Quasi-Monoenergetic Neutron Source

Tomohiko Iwasaki, Yoshimasa Sakuya, Takashi Tabei, Naohiro Hirakawa
Yukio Sakamoto[1], Hiroshi Nakashima[1], Susumu Tanaka[2]
Department of Quantum Science and Energy Engineering Tohoku University
[1]Center for Neutron Science, JAERI [2]Advanced Radiation Technology Center, JAERI

1. Introduction

Recently, an accelerator-driven system has been proposed for transmuting minor actinides (MA) and long-lived fission products (LLFP) in high level waste (HLW). In the system, protons are accelerated up to about 1 GeV and are injected a heavy element target such as lead. Then many neutrons are generated via spallation reaction.

The energy of spallation neutrons extends to several hundreds MeV. Thus, it is necessary to prepare a code that is sufficient to simulate the transport of particles in the high-energy region from a few GeV to several tens MeV. Some codes have been developed. The NMTC is one of the codes. The NMTC/JAERI[1)] is an improved version of the NMTC by Japan Atomic Energy Research Institute (JAERI). The NMTC/JAERI is based on the intra-nuclear cascade model[2)] and the evaporation model[3)] and is competent for simulating nuclear reaction and transport particles above a few hundreds. However, it is not considered that the NMTC/JAERI is sufficient to analyze in light elements systems and/or in low particle energies below 100 MeV[4)]. This situation is serious for designing molten salt- or sodium-cooled reactor, carbon-moderated core or water-cooled target[5)], because light elements such as H, Li, Be, C and Na are used as the primary element in those system. Thus, it is necessary to see the applicability of the NMTC/JAERI for such light elements and particle energies below 100 MeV. We measured fission reaction rates of ^{237}Np and ^{238}U in the polyethylene system irradiated by 65 MeV mono-energetic neutrons at the TIARA facility of the JAERI. By comparing the experimental values with the calculated values by the NMTC/JAERI, we examined the applicability of the code.

2. Experiment

A). Experimental Facility

The present experiment was carried out at the TAKASAKI Ion Accelerator for Advanced Radiation Application (TIARA) facility[6)] of the JAERI. A 90 MeV AVF cyclotron of this facility was employed in this study.

B) Experimental setup

The experimental setup is shown in Fig.1. An iron collimator and five polyethylene blocks were employed. The iron collimator was 118.0cm × 118.5cm × 85.5cm and had a hole of 10.9 cm in diameter. The polyethylene blocks were 118.0cm × 118.5cm in surface area. Four of the five polyethylene blocks had the thickness of 30.7cm and the other had the thickness of 10.4cm.

The polyethylene blocks were lined up behind the collimator as shown in Fig.1, keeping a gap of about 3cm between the blocks in order to insert detectors. The measurement of fission reaction rates of ^{237}Np and ^{238}U in polyethylene was carried out. The measurement points were 0.8cm, 34.2cm, 47.4cm and 81.3cm distant from the iron collimator. These points are 0.0cm, 30.7cm, 41.1cm, and 71.8cm of polyethylene thickness, respectively. Then detectors were placed along the axis of neutron beam.

C) Detector

Fission chambers of ^{237}Np and ^{238}U were employed in this experiment. The fission rate distribution of ^{237}Np is useful for a transmutation study as the experimental benchmark data. The ^{238}U data is suitable for validating such a code as the NMTC/JAERI since the fission cross section of ^{238}U is well known. The specification of the detectors is shown in Table Ⅰ.

D) Neutron Source

The quasi mono-energetic neutrons of 65 MeV were used in this experiment. The neutron was produced from ^{7}Li (p, n) reaction by injecting protons of 68 MeV into a lithium target. The neutron energy spectrum is shown in Fig. 2.

Table I Detector specification of ^{237}Np and ^{238}U fission chambers

Detector	Active Length	Diameter (cm)	Coated Thicknes
Np237 FC	2.48	0.64	300
U238 FC	2.48	0.64	1000

3. Result and Discussion

The present experiment results and the calculated values by the NMTC/JAERI are shown in Fig.3. The calculated values were normalized to the experimental one at 0.0 cm of polyethylene thickness. The fission rates and C/E values are shown in Table Ⅱ. As shown in Table Ⅱ, the calculated values are larger than the experiment values at every points for both chambers. This overestimation becomes larger when polyethylene becomes thicker. When the polyethylene thickness is 71.8 cm, it is found that the C/E value reaches to about 2.0 for both ^{237}Np and ^{238}U fission rates. To investigate the reason of this overestimation, we examine the measured fission reaction rates by comparing these with two other experiments[7), 8)]. In the experiments, the same neutron source with the same peak neutron energy was used for the system of light element materials. The results are shown in Fig.4. The measured fission rates agree well with two other experiments. From this result, it is confirmed that the present experiment is reliable. Therefore, we suppose that the overestimation of the fission rates comes from some problems in the analysis.

Table II Experimental and calculated fission rates of ^{237}Np and ^{238}U

Poly Thick Ness (cm)	Fission Rate (Np237 FC)			Fission Rate (U238 FC)		
	Exp.	Cal. Norm*	C/E	Exp.	Cal. Norm*	C/E
0.0	4.76E-8	4.76E-8	1.00	1.14E-7	1.14E-7	1.00
30.7	1.10E-8	1.61E-8	1.46	2.91E-8	4.14E-8	1.42
41.1	6.50E-8	9.64E-9	1.48	1.65E-8	2.51E-8	1.52
71.8	1.45E-9	2.88E-9	1.98	3.90E-9	7.49E-9	1.92

***The calculated values are normalized to the experimental one at 0.0cm of polyethylene thickness.**

4. Conclusion

To investigate the applicability of a computing code for designing an accelerator-driven transmutation system, we measured fission reaction rates of ^{237}Np and ^{238}U in a polyethylene system irradiated by 65 MeV quasi mono-energetic neutrons. The present experiment was carried out at the TIARA facility in the JAERI. The experiment was analyzed by the NMTC/JAERI together with the MCNP/4A. Then, it is found that the NMTC/JAERI overestimates both fission rates of ^{237}Np and ^{238}U in polyethylene. The C/E values by the NMTC/JAERI are about 2.0 at 72 cm of polyethylene thickness.

Reference

1) Y.NAKAHARA, T.TSUTSUI: JAERI-M 82-198 (1982) [in Japanese]

2) H.W.BERTINI: Phys. Rev. 188, p1711 (1969)

3) L.W.DRESNER: ORNL-TM-196 (1962)

4) H.TAKADA: J. Nucl. Sci. Technol. 33, p275-282 (1996)

5) H.KATSUTA et al: Proc. of Seventh International Conference on Emerging Nuclear energy Systems, Chiba, Japan, Sep.20-24, p.424 (1993)

6) S.SATO: Proc. of International Conference on Evolution in Beam Applications, Takasaki, Japan, Nov.5-8, 1991, p239 (1991)

7) N.NAKAO et al: J. Nucl. Sci. Technol., 34, p.348-359 (1997)

8) Y.NAKANE et al: Proc. of the 18th International Conference on Nuclear Tracks in Solids, September 1-5, 1996, Cairo, Egypt (1996)

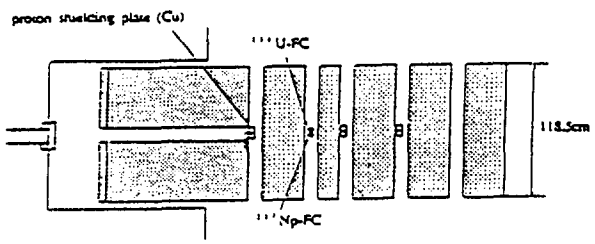

Fig.1 Setup of experimental apparatus used in this study

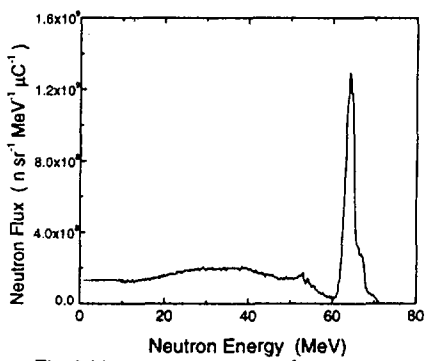

Fig.2 Neutron spectrum of source neutrons

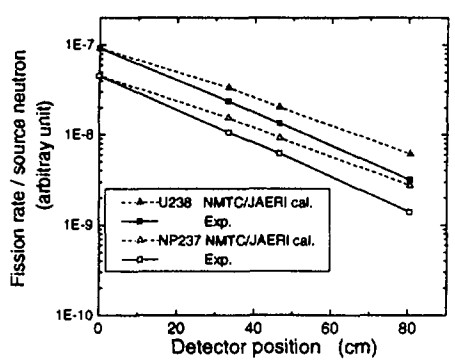

Fig.3 Measured and calculated results

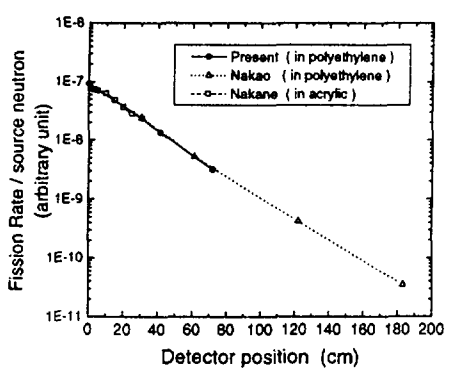

Fig.4 Comparison with two other experiments

8. Accelerator Technology

(continued to the next page)

8. 1 Development of Visual Beam Adjustment Method for the Beam Transport

Takashi AGEMATSU and Kazuo ARAKAWA
Advanced Radiation Technology Center, JAERI

1. Introduction

We have developed a computer-based visual beam adjustment system[1] for JAERI AVF cyclotron operation. This system provides CRT display of the cyclotron beam trajectories, feasible setting regions, and search traces which were designed to improve beam parameter adjustment.

A new computer-based operation system which assists inexperienced operators has been implemented for the beam transport system at the JAERI AVF cyclotron. This new system provides CRT display of the beam trajectories and beam envelope at real-time. To examine the reliability of this system, the simulation result was compared with that of the actual operations.

2. Visual interfaces

Ion beams extracted from the cyclotron are transported to a target point without any beam loss in the beam ducts. The beam transport system consists of bending and focusing magnets, beam monitors, beam shutters, etc. There are 9 bending magnets, 85 quadrupole magnets and 10 beam steering magnets in 10 horizontal and 4 vertical beam course which transport ion beam to 17 target ports on the ways or at the ends of the beam courses located in 8 ion rooms. An achromatic and telescopic beam transport system was designed for high transmission efficiency of ion beams and good adjustability of the magnet parameters using the beam optics calculation program TRANSPORT[2].

The ion beams extracted from an AVF cyclotron have large emittance and energy variations. Beam transport system start-up operations require dozens of adjustable parameters to be finely tuned to maximize beam transmission efficiency. Generally, the transportation of accelerated ion beam is efficiently realized by setting quadrupole magnets at parameter for a magnetic field gradient designed by TRANSPORT-code. However inexperienced operators have a difficult time because operator consoles displaying measured beam parameters, alarm information, component status, etc. do not provide enough information to guide these new operators. There are two ways of describing the ion transfer properties. One is the ray tracing that is used to study the behavior of individual ion trajectories. The other is the phase space ellipsoid method that treats the beam envelopes characterized by the boundaries of the phase space volume.

The new computer-based operation system provides two kinds of visual human interfaces to support the beam adjustment of the beam transport system as follow: i) beam envelope and trajectory are rapidly simulated and graphically displayed them on a CRT whenever the operators change the excitation current of the magnet, ii) historical displays of simulating beam envelope and trajectory are superimposed on CRT. For simulation the beam envelopes/trajectories, these interface have special four functions as follow; i) the excitation current can be set to a discretionary quadrupole magnet, ii) initial setting parameters (energy ,ellipse, etc.) for calculating the beam envelope and trajectory can change free, iii) the all narrow channels which are an obstacle to pass through the beam in the beam transport line, iv) the beam ellipse can be display whenever the operator changes the adjustable parameter of the magnets.

In order to speed up the simulation time of the beam envelop, beam and transfer matrix is calculated by using simple matrix methods. The beam envelope calculation is performed on the basis of the phase space

ellipse. The beam trajectories are calculated at five positions on the ellipse including a center point as shown in Fig. 1. The excitation current and/or field of the magnet is calculated by considering the effect of the field saturation.

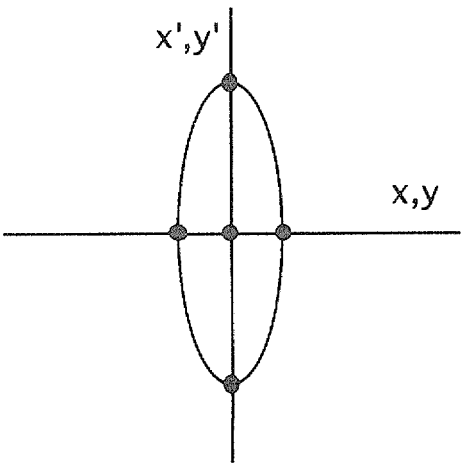

Fig. 1 The elliptical phase space and the representative five ion particles at the first waist point of the cyclotron exit.

3. Examination of the system

In case of the ion do not move close to the beam axis, namely, the ion beam is not paraxial, the beam trajectories were simulated. We examined the beam trajectories by the real beam operations of 45MeV H^+. In real beam operation, the beam axis was changed by changing the field of steering magnet which is located at the cyclotron exit. The beam changes not only the position but also the profile on the target as shown in Fig. 2. The typical simulated beam trajectories for 45MeV H^+ are shown in Fig. 3. Fig. 3 (a) shows the simulated beam trajectories in case of the ion move close to the beam axis. Fig. 3 (b) shows the simulated beam trajectories by setting excitation current to +10A of a CSTE (horizontal steering magnet).

4. Conclusion

The beam adjustment interface calculates the beam trajectories/envelopes using actual parameters and displays them on a CRT. This display shows a historic summary of simulated beam trajectories/envelopes after any parameter "setting" adjustment by an operator. Operators can refer to either display, correct the differences between them, and search for the optimum set point which provides desirable beam envelope/trajectories.

Since, operators are able to quickly gain valuable operation experience which ultimately leads to a reduction of the time to reach the planned beam transport condition.

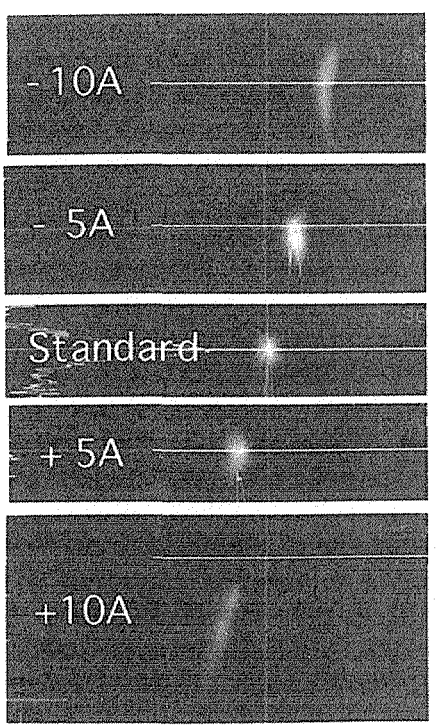

Fig. 2 The change of beam profile on the almina monitor at the target point LB2.

In actual operation, by changing field strength of horizontal steering magnet located at the cyclotron, the change of profiles is measured with 45MeV H^+.

5. References

1) T.Agematsu, K.Arakawa, and S.Okumura, *Proc. 14th Int. Conf. on Cyclotron and Their Applications, Cape Town, South Africa*, pp.284-287(1995).
2) K.L.Brown et al. , *SLAC Report*, No.91(1974).

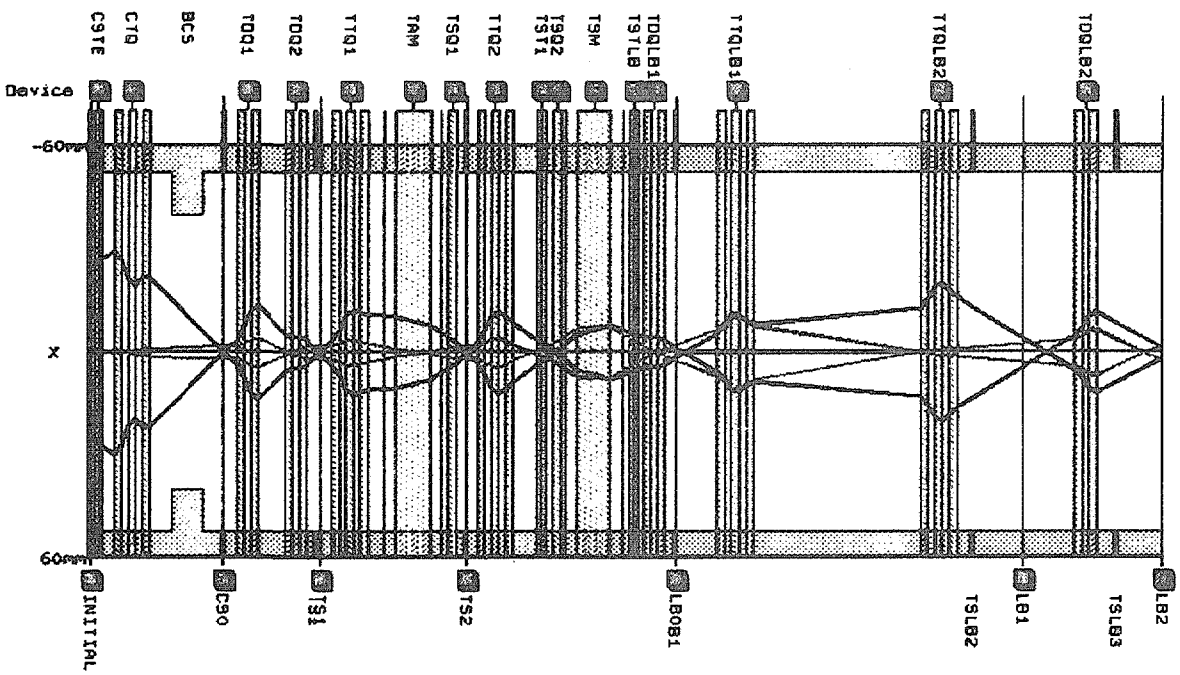

(a) Beam trajectories by standard condition, namely the ion beam move close to the beam axis.

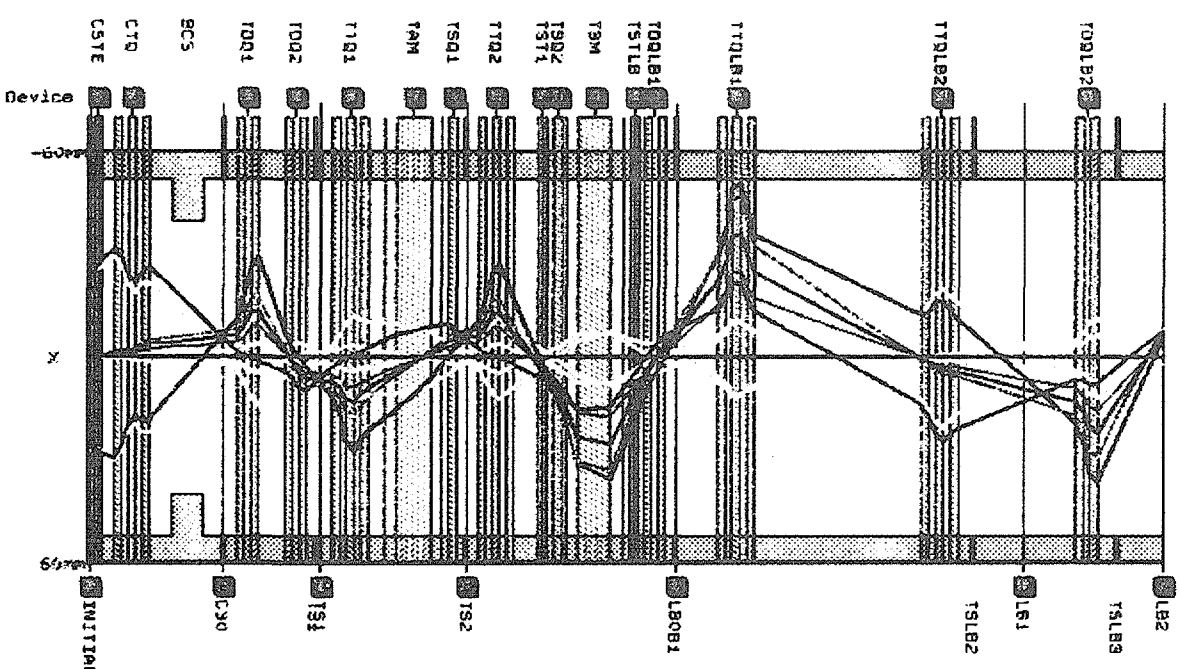

(b) Beam trajectories by setting excitation current to +10A of CSTE (the ion beam is not paraxial).

Fig. 3 Beam trajectory simulation for 45MeV H^+ in the beam transport system of the cyclotron.

8. 2 Development of Beam Instruments for a Cyclotron

S.Okumura, M.Fukuda, I.Ishibori, T.Agematsu, A.Matsumura and K.Arakawa
Advanced Radiation Technology Center, JAERI

1. Introduction

Ions extracted from the cyclotron have many properties, such as energy, beam intensity, etc.. It is important to evaluate these quantities precisely for irradiation experiments and adjustment of the cyclotron.

A cyclotron beam has time properties of beam pulse width and a frequency that are significant quantities for a TOF experiments. A beam phase monitor has been developed to measure the quantities precisely for optimizing cyclotron parameters and for offering users the time properties.

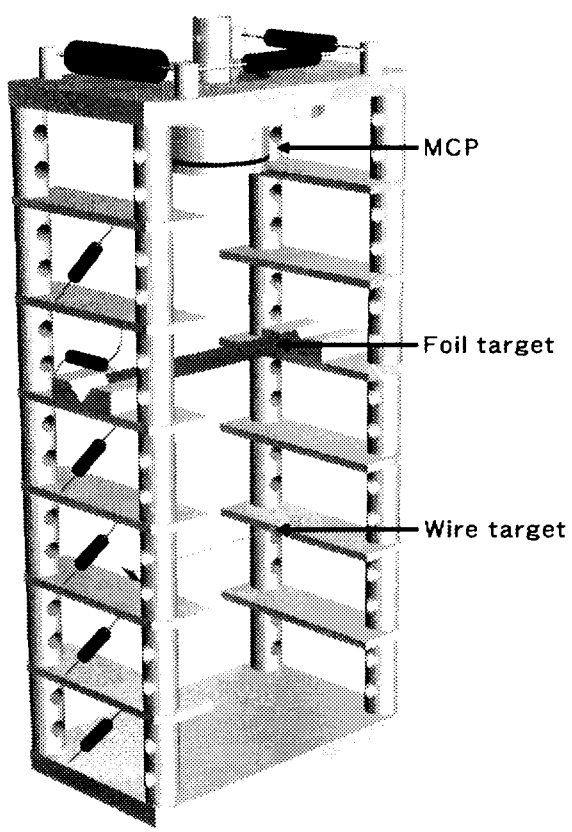

Fig. 1
A general view of the beam phase monitor.

2. Beam Phase monitor

Figure 1 shows a general view of the beam phase monitor. The beam phase monitor is a fast timing detector with a micro-channel plate (MCP) which is multiplying secondary electrons coming from a thin target foil, a 3 micron thick aluminum-strip, when ions pass through it[1]. The foil target is mounted at a distance of 50 mm from the MCP, and alternatively a wire target can be also mounted. The secondary electrons are collected to the MCP with an electrostatic field produced with seven sets of electrodes. Time resolution measurement of the beam phase monitor has been performed with the foil target.

3. Measurement of time resolution

Overall time resolution including the contribution of the beam phase monitor was evaluated by a time-of-flight (TOF) measurement. Figure 2 shows a schematic drawing of the setup. After passing through the beam phase monitor, ions are extracted from a vacuum chamber and detected by the plastic scintillation counter in air. A flight time of an ion is determined using the beam phase monitor as a start counter and a plastic scintillation counter as a stop counter. Fast timing signals from the start and the stop counters are fed into constant-fraction discriminators. The fast logic signals derived from the discriminators are used for the determination of coincidences between the events detected at the start and the stop counters and for the measurement of the time difference between the coincident events with a time-to-amplitude converter. TOF measurements have been carried out for 225 MeV $^{16}O^{7+}$ and 220 MeV $^{12}C^{5+}$ beams. The time resolutions are dependent on the electrostatic field for collecting secondary-electrons. The best time resolutions are 190 ps FWHM for 225 MeV $^{16}O^{7+}$ at the electrode voltages of -0.5kV and 230 ps FWHM for 220 MeV $^{12}C^{5+}$ at -0.8kV. Figures 3 and 4 show the TOF spectra obtained for these cases.

4. Conclusion

The time resolutions show good performance of the beam phase monitor. The intrinsic time resolutions of the beam phase monitor are better than the measured values,

since the overall time resolutions include the resolutions of the plastic scintillation counter and the signal processing circuits. We will install the beam phase monitor in the beam line near the exit of the cyclotron for ordinary monitoring of the beam phase.

5. References

1) S. Okumura et al., JAERI TIARA Annual Report 5: 220-221 (1995)

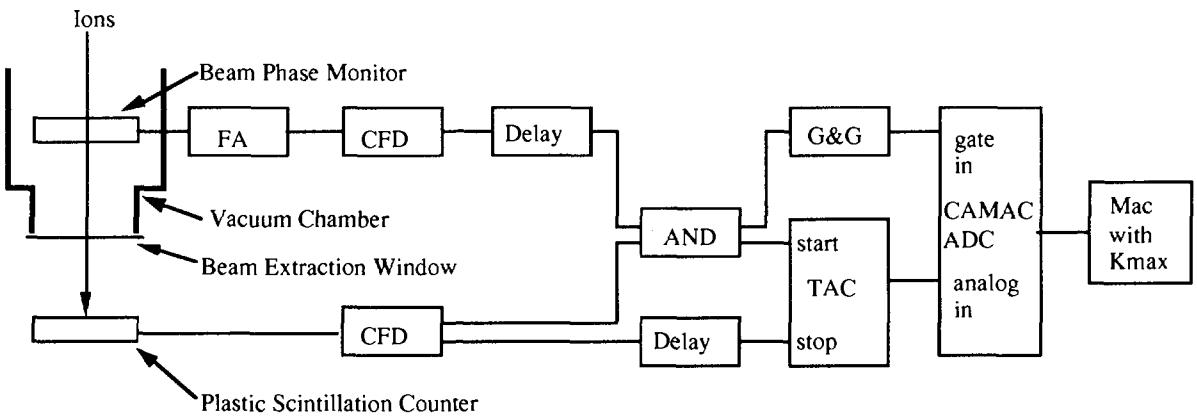

FA:Fast-Timing Preamplifier VT120A(ORTEC)
CFD:Quad 200-MHz Constant-Fraction Discriminator 935(ORTEC)
Delay:Nanosecond Delay 425A(ORTEC)
AND:TRIPLE 4-FOLD 1-VETO COINCIDENCE MODULE 470(KAIZU)
G&G:DUAL GATE GENERATOR 1500(KAIZU)
TAC:Biased Time-to-Amplitude Converter 457(ORTEC)
CAMAC ADC:ANALOG-TO-DIGITAL CONVERTER 2259B(LeCroy)
Mac:Macintosh computer
Kmax:Data acquisition system(Sparrow)

Fig. 2 A schematic drawing of the setup.

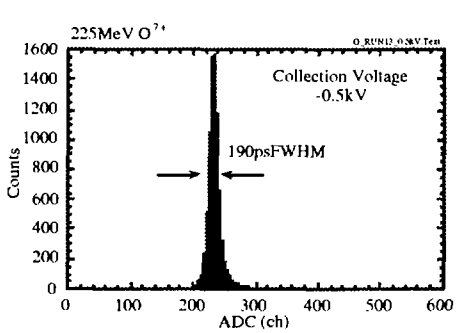

Fig. 3
A TOF spectrum for 225 MeV $^{16}O^{7+}$.

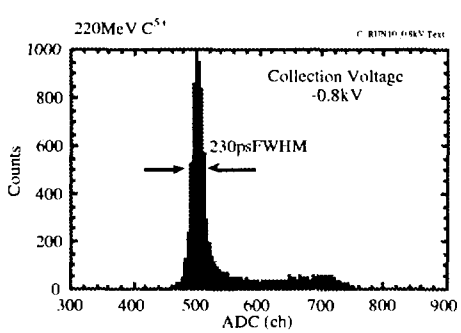

Fig. 4
A TOF spectrum for 220 MeV $^{12}C^{5+}$.

8．3 Present Status and Beam Acceleration Tests on Cyclotron

Kazuo ARAKAWA, Yoshiteru NAKAMURA, Mitsuhiro FUKUDA, Takayuki NARA, Takashi AGEMATSU, Susumu OKUMURA , Watalu YOKOTA, Ikuo ISHIBORI and Hiroyuki TAMURA.
Advanced Radiation Technology Center, JAERI

1. Introduction

The operation of the AVF cyclotron for experiment was started from January 1992 in daily operation mode on a trial base. The weekly continuous operation was started from September 16 1992. The total operation times attained to 16749 hours in March 1997. There are two major reasons driving the need for fast energy/ion switching. The first is the requirement of material science research (for example single event upset studies) for beams of a wide range of energies and ion species. The second is the need for economic and efficient operation of the accelerator. To meet the requirement, we have been developed of a cocktail beam acceleration technique at the JAERI-AVF cyclotron.

2. Present status

(1)AVF cyclotron

The AVF cyclotron was smoothly operated for experimental utilization in FY 1996. The beam time for experiments was 3132 hours in FY 1996. The AVF cyclotron provides a wide range of ions, energies, and intensities in support of the experimental program. Thirty-eight kinds of ion species were provided for experiments.

The accumulation of induced radioactivity in the acceleration chamber is making it more difficult to conduct maintenance work inside the cyclotron. The strong sources of radiation are the electrostatic deflector (100 mSv/h) and magnetic channel (160 mSv/h) as shown in Fig.1.

For the protection against radiation hazards, now it will be necessary to replace some of the strongly activated parts, such as main probe-head, magnetic channel, and magnetic channel probe-head.

We had the following machine troubles; (1) breakdown of a high voltage of an ECR ion source by increasing a humidity in the room , (2) an inflector stem (about 150 kg weight) crashed on a cyclotron upper yoke from a stem carrier.

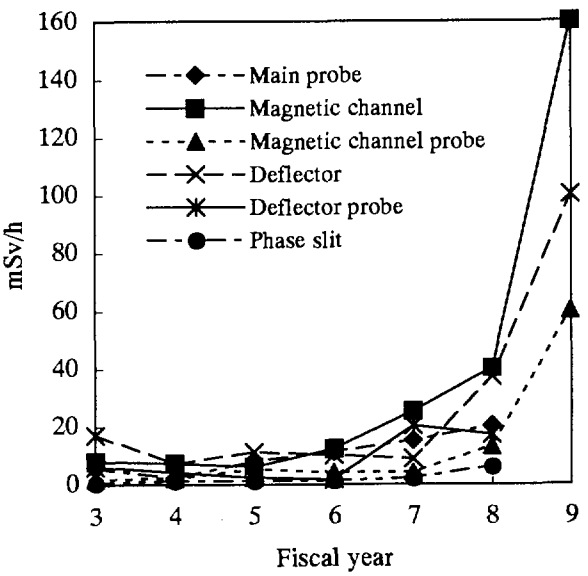

Fig.1 Accumulation of induced radioactivity in the acceleration chamber of the cyclotron.

(2) Ion source

ECR ion beams are presently used for two purposes; (1) injection of highly charged ion beam into the AVF cyclotron, (2) study and development of the ECR for high charged ion beams of gaseous. Total operation time for the ECR ion source was 2498 hours, and monthly operation times are shown in Fig.2. The breakdown of the high voltage occurred frequently by a discharge in the ECR ion source because the humidity is not good condition in the room.

Total operation time for multi-cusp ion source was 854 hours, and monthly operation times are shown in Fig. 2. The multi-cusp ion source was smoothly operated without any trouble.

3. Beam development

(1) Cocktail beam acceleration

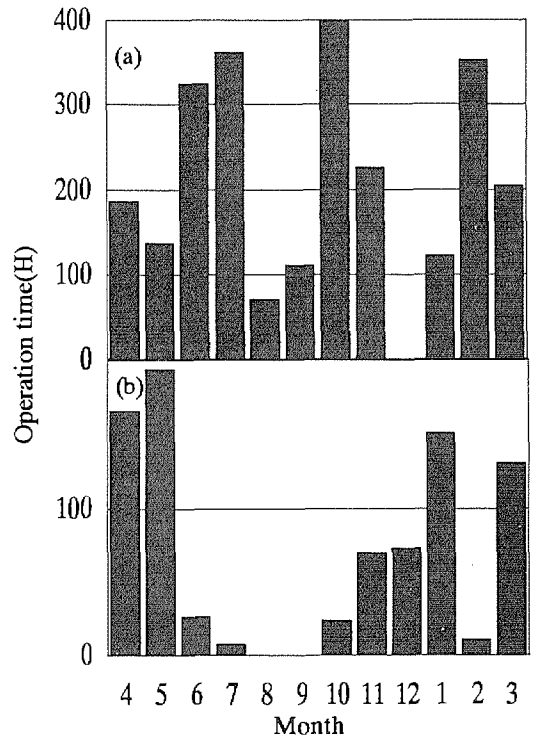

Fig.2 Monthly operation times in FY 1996. (a) ECR ion source, (b) multi-cusp ion source.

Cocktail beam acceleration[1] is one of the most time-saving methods for changing the ion species and/or the energy. Ion"cocktail", which are composed of ions with the same or very close mass to charge ratio (M/Q), are produced in an ECR ion source, injected into the cyclotron, accelerated at the same time and extracted separately by a fine tuning of the magnetic field or a slight changing of the RF frequency.

Particle identification was carried out by measuring a pulse height from an SSD. The results of the cocktail beam acceleration test are summarized in Table 1. The extracted beam current for 56 MeV $^{15}N^{3+}$, 75 MeV $^{20}Ne^{4+}$, 150 MeV $^{40}Ar^{8+}$ and 322 MeV $^{84}Kr^{17+}$ ions are 0.7, 1.0, 2.0 μA and 0.08 μA (electrical ampere) respectively. The time required for changing the ion species and/or energy is only one minute for the cocktail beam acceleration.

(2) Other new beam acceleration

The beam acceleration tests have been conducted for 65 and 80 MeV H^+, and 30 MeV $^4He^{2+}$, Protons is generated by the multi-cusp ion source, and He ions by the ECR ion source. The results of the beam acceleration test are summarized in Table 1. The 65 and 80 MeV H^+ beam currents are limited within 3.0 μA for the present to avoid unnecessary induced radioactivity of the machine parts.

(3) Extraction current and transmission

Particles accelerated and extracted so far are listed in Table 2. The extraction efficiency is defined by the ratio of the beam current measured with the main probe at r=900 mm to that with the Faraday cup (FC) just after cyclotron. The average extraction efficiencies for harmonic 1, 2 and 3 are 56 %, 63% and 56 %, respectively.

The overall transmission efficiency is defined by the ratio of the beam current with the FC just after analyzing magnet at the injection line to that with FC just after cyclotron. The average transmission efficiencies for harmonic 1, 2 and 3 are 13 %, 16% and 11% , respectively.

4. Reference

1)M. A. McMahan, et al., "Using a Cyclotron Plus ECR Source for Detector Evaluation and Calibration," Nucl. Instr. and Meth. A253(1986)1.

Table 1 Results of a cocktail beam acceleration tests.

Ion	Energy (MeV)	Harmonic No.	Frequency (MHz)	Extracted Intensity	Extraction Efficiency (%)	Overall Transmission (%)
$^{15}N^{3+}$	56	3	13.867	0.7	21	5.0
$^{20}Ne^{4+}$	75	3	13.873	1.2	26	5.4
$^{40}Ar^{8+}$	150	3	13.881	2.3	26	6.2
$^{84}Kr^{17+}$	322	3	14.048	0.08	20	5.0

Table 2. Results of Extracted Intensity and Transmission

Particle	Energy (MeV)	Harmonic No.	Frequency (MHz)	Extracted Intensity (eμA)	Extraction Efficiency (%)	Transmission (%)
H^+	10	2	14.97	12	80	27
	20	2	21.03	5.0	77	21
	30	1	12.77	5.0	67	22
	45	1	15.46	30	79	14
	50	1	16.23	5.0	44	14
	55	1	16.9	5.0	63	14
	60	1	17.65	5.0	57	22
	65	1	18.30	3.0	-	12
	70	1	18.92	5.0	42	12
	80	1	20.08	3.0	47	13
	90	1	21.14	10	48	7.7
D^+	10	2	10.63	11	29	3.7
	35	2	19.70	40	59	4.6
	50	1	11.76	20	49	7.2
$^4He^{2+}$	20	2	10.67	5.5	69	11
	30	2	13.11	1.4	42	10
	50	2	16.77	20	62	17
	100	1	11.81	10	32	10
$^{12}C^{5+}$	220	2	20.42	0.25	77	22
$^{16}O^{5+}$	100	3	17.98	1.7	34	8.1
$^{16}O^{6+}$	160	2	15.11	1.9	58	21
$^{16}O^{7+}$	225	2	17.87	0.2	54	10
$^{16}O^{7+}$	335	2	21.68	0.05	29	4.2
$^{20}Ne^{6+}$	120	3	17.70	1.6	53	18
$^{20}Ne^{7+}$	260	2	17.48	0.33	70	19
$^{20}Ne^{8+}$	350	2	19.88	1.5	63	23
$^{36}Ar^{8+}$	195	3	16.82	2.5	63	13
$^{36}Ar^{10+}$	195	3	16.83	0.10	43	1.2
$^{40}Ar^{8+}$	175	3	15.14	3.0	73	15
$^{40}Ar^{11+}$	330	2	13.68	0.6	86	20
$^{40}Ar^{13+}$	460	2	16.24	0.03	63	24
$^{84}Kr^{20+}$	520	2	11.98	0.05	72	20
$^{129}Xe^{23+}$	450	3	13.46	0.2	72	11

8．4 Developement of ECR Ion Source in TIARA

W. Yokota, Y. Saitoh, T.Nara, Y.Ishii, K. Arakawa
Advanced Radiation Technology Center, JAERI

I . Introduction

Two types of ECR ion sources have been developed to expand the energy region and increase the ion species provided by the accelerators in the TIARA facility. One is the ECR-18 for production of highly charged metal ions under development for the AVF cyclotron. The other is the MINI-ECR for production of medium charged ions, which is placed in the high voltage deck of the 400 kV ion implanter.

II ECR-18

1. Performance of ECR-18

For further improvement of the ECR-18 basic performance, we modified the microwave feeding into the plasma. The waveguide was elongated to position its end at a rear peak of the mirror field distribution. A shielding plate having many holes of 5 mm diameter was also set at the position so that microwave could be absorbed by the plasma without propagating backward of the plasma chamber. Furthermore, an aluminum plate of 0.2 mm thick was attached to cover all inner surface of the plasma chamber to increase secondary electron emission efficiency. We observed Ar^{14+} ions as a result of these modification. It is considered, from the mass vs. charge spectrum, that Ar^{15+} ions should be generated although they could not be distinguished from O^{6+} because of the same mass to charge ratios.

2. Metal Ion production

Nickel ion generation from a ceramic rod was carried out by using direct insertion of a ceramic rod. A rod of nickel oxide (NiO) was inserted into the plasma from the rear end of the plasma chamber. As the rod moving deeper into the chamber, decrease of high charge state oxygen ions was observed. This is considered to be attributed to a conductive support for the rod which might cause thinning plasma density or disturbing microwave absorption. Nevertheless, we observed Ni ions with

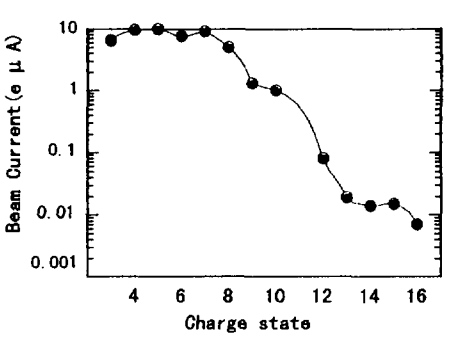

Fig. 1 Charge state distribution of Ni ion extracted from ECR-18 with ceramic rod.

charge state up to $^{16+}$ as shown in Fig. 1. Use of non-conductive material for the rod support and improvement of the way to support will be necessary to obtain higher charge state ions.

Ⅲ. MINI-ECR

1. Performance of MINI-ECR

To increase beam intensity from the MINI-ECR, configurations of a puller electrode and an extraction hole of the plasma chamber are modified. In general, a diameter of the extraction hole is equal to or smaller than that of the puller erectrode. However strong convergence effect is expected by using an electrode with a smaller diameter hole. That should improve the beam emittance extracted from the ion source and tranportation efficiency. We made a test to confirm it with Ar beam by using the 8 mm diameter extraction hole and 6 mm diameter puller extrude. In the result, increment of beam current was observed for $Ar^{1+\sim4+}$ (ex. Ar^{3+}:15 μ A→18 μ A). The increment of beam current is also obtained for N_2, O_2, Xe, respectively.

2. ECR plasma Analysis

We investigated the relationship between support gas pressure and plasma potential in the MINI-ECR to explain the mechanism of the support gas method. It is well known that intensity of highly charged ion beam extracted from an ECRIS is enhanced by mixing a light support gas with a gas of interest. However, the details of the mechanism is not obvious. Plasma potential was obtained by measuring both the magnetic field in the analyzing magnet and the extraction voltage precisely. The experiment was carried out by using Ar main gas with O_2 support gas. In the result, we observed that the Ar plasma potential of 29 V was reduced to 23 V by mixing the O_2 gas. The reduction of the plasma potential was reported for the high power ECR ion source[1]. These results strongly suggest that the role of the gas mixing is to reduce the plasma potential and this lead to production of higher charge state ions.

Reference

1) Z. Q. Xie, C. M. Lyneis, Rev. Sci. Instrum. 65 (9) 2947 (1994)

8.5 Estimation of Charge Exchange Cross Section for Multiply Charged Ions Accelerated in JAERI AVF Cyclotron (II)

Y. Nakamura
Advanced Radiation Technology Center, JAERI

1. Introduction

The charge exchange cross section (CECS) for heavy ions is one of the important data to design the vacuum requirement for the accelerator as an AVF cyclotron especially. So far, we have already obtained several fundamental data[1),2)] for the vacuum environment and the preliminary result[3)] about the CECS.

Furthermore, in order to improve the reliability of the CECS value, we examined the method of data treatment for the estimation of CECS.

2. Investigation for data treatment method

Generally, the numerical value for the CECS which is estimated based on the current distribution on a radial main probe has a little larger deviations because heavy ions extracted from ECR ion source usually show large fluctuation for a short time and slight drifting during relatively long one. Therefore, suitable data treatment method has to be found out carefully for getting reliable CECS. We considered below two items.

(i) Calculation method for average CECS

An average CECS is calculated using the main probe currents I_1, I_2 ----- I_M corresponding to the pressure levels of M steps. Two CECS's of σ_a and σ_b can be expressed in following two equations which are shown as a function of the probe current ratio, respectively.

$$\sigma_a = \frac{k \cdot \sum_{m=1}^{M-1} f\left(\frac{I_1}{I_{m+1}}\right)}{M-1} \quad (1)$$

$$\sigma_b = \frac{k \cdot \sum_{m=1}^{M-1} f\left(\frac{I_m}{I_{m+1}}\right)}{M-1} \quad (2)$$

Where k is a constant. The value of σ_b is calculated on the basis of standard probe current (I_1) at the lowest pressure when feeding gas is not supplied at all into the cyclotron vacuum chamber. On the other hand, the σ_a is obtained by the sequential ratios of the probe current.

An example of estimated results is shown in Fig. 1 in case of $^{36}Ar^{8+}$, 195 MeV ions. This figure shows the change of the enlarged CECS between 0.05 and 0.1 of the velocity ratio to light speed (beta). The σ_a gives excellent result since it has smaller sinusoidal component than that of σ_b. A main reason induced this result is supposed that the calculating reliability is improved if the probe current I_1 is measured under steady state, because the ratio of two currents in equation (1) always has greater value than equation (2).

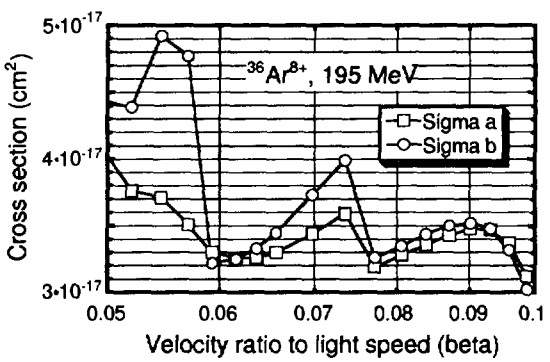

Fig. 1 A comparison of σ_a and σ_b for $^{36}Ar^{8+}$, 195 MeV ions.

(ii) Calculating condition for individual CECS value

The main probe current is lowered gradually with the increase of cyclotron radius as the beam attenuation by charge exchange reaction is promoted in case of the increase of internal pressure by gas feeding. For this phenomenon, the CECS obtained over the range of small probe current shows large fluctuation particularly at the range around 0.1 of beta or more. Therefore, we put an assumption that the individual CECS smoothly reduces as shown in below equation as the number of turns of the ion (n) becomes to be large.

$$\sigma_n \geq \sigma_{n+1} \quad (3)$$

Table 1 The kind of measured ion beams and those parameters associated with the estimation of the charge exchange cross section.

Accelerated ion	Energy (MeV/u)	Charge state	Harmonic number	Radio frequency (MHz)	Dee voltage Vdee1 & Vdee2 (kV)		Extraction voltage of ion source (kV)	Beta (velocity ratio to light speed)
H^{+}, 10 MeV	10.0	1	2	14.970	11.73	10.92	3.14	0.146
$^{12}C^{5+}$, 220 MeV	18.3	5	2	20.417	42.79	41.05	12.80	0.198
$^{20}Ne^{7+}$, 260 MeV	13.0	7	2	17.475	34.91	36.44	11.70	0.167
$^{20}Ne^{8+}$, 350 MeV	17.5	8	2	19.877	38.88	40.79	13.74	0.194
$^{36}Ar^{8+}$, 195 MeV	5.4	8	3	16.824	36.21	37.86	10.55	0.108
$^{40}Ar^{8+}$, 175 MeV	4.4	8	3	15.067	34.14	38.31	9.47	0.0969
$^{84}Kr^{20+}$, 520 MeV	6.2	20	2	11.980	25.76	26.16	8.81	0.115
$^{4}He^{2+}$, 50 MeV	12.5	2	2	16.770	27.22	28.25	8.52	0.164
$^{40}Ar^{13+}$, 460 MeV	11.5	13	2	16.240	33.39	34.05	10.97	0.157
$^{4}He^{2+}$, 20 MeV	5.0	2	2	10.670	11.16	10.08	3.15	0.104
$^{16}O^{4+}$, 100 MeV	6.3	4	2	11.919	22.50	22.51	7.44	0.116
$^{4}He^{2+}$, 30 MeV	7.5	2	2	13.110	14.57	15.24	4.71	0.127
$^{20}Ne^{6+}$, 120 MeV	6.0	6	3	17.695	29.36	32.43	9.10	0.113

Figure 2 shows a typical example in case of the adding on the restriction of equation (3). A lot of corrected CECS's seem to rather approach along the straight line of approximation formula.

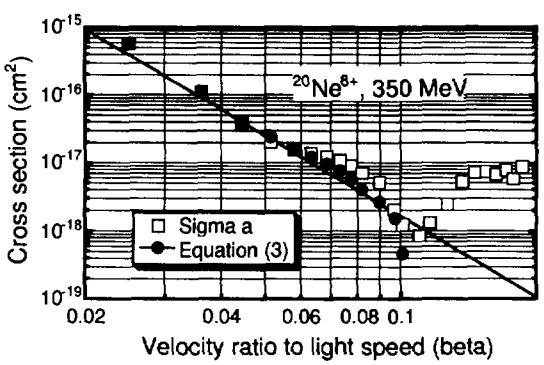

Fig. 2 An example of cross section data corrected by equation (3) for $^{20}Ne^{8+}$, 350 MeV ions.

3. A kind of measured ion beams for the estimation of CECS

Table 1 summarizes the kind of ion beams and those parameters associated with the estimation of CECS. Although a principal object for the experiment was multiply charged heavy ions, the measurement was also carried out some light ions having relatively low energy for future reference.

4. Future plan

At the present time, while we use a BA gauge as our temporary standard, an absolute calibration for the actual pressure into the cyclotron will be performed using a spinning rotor gauge which has been scheduled to purchase. Furthermore, we would like to get finally the reliable empirical formulae which consist of the function including the charge state and velocity of the ion, by our effort for the reinforcement the kind of ions which should be examined.

5. References

1) Y. Nakamura, I Ishibori, *et al.*, TIARA Annual Report, vol. 3, p213 (1993)
2) Y. Nakamura, I. Ishibori, *et al.*, Proc. 14th Int. Conf. on Cycl. and their Applic., Cape Town, South Africa, p276 (1995)
3) Y. Nakamura, I Ishibori, *et al.*, TIARA Annual Report, vol. 5, p227 (1995)

8. 6 Acceleration of Cocktail Ions with M/Q ≈ 4 and 5

M. Fukuda, K. Arakawa, S. Okumura, Y. Nakamura, T. Nara,
T. Agematsu, I. Ishibori, H. Tamura and W. Yokota
Advanced Radiation Technology Center, JAERI

1. Introduction

For research in materials science and biotechnology, linear energy transfer(LET) is one of essential parameters that determines radiation effects in a material. Different LET can be brought about in a target material by changing ion species and/or energy of an incident particle. For a cyclotron beam, more than an hour is required for changing an acceleration condition. Because a cyclotron magnet needs to be re-excited by a cycling excitation method to keep accurate reproduction of an isochronous field. And because all of cyclotron parameters are replaced by other ones, and all of the cyclotron system must be restarted.

In order to meet a request of users to use plural ion species and/or energy in the same beam time without great loss of time, cocktail beams for mass to charge ratio(M/Q) of 4 and 5 have been developed. Cocktail acceleration[1,2] is an epoch-making method to save the time for changing the ion species and energy. In the cocktail acceleration, only one or two parameters are adjusted to change the ion species and energy. Thus the time-consuming magnet re-excitation process can be excluded, and the change of the acceleration condition is completed within a few minutes.

Cocktail ions produced by an ECR ion source consist of different kinds of ions with almost the same M/Q. The cocktail ions cannot be separated by an analyzing magnet in an injection system because of very close M/Q. The cocktail ions are injected into the cyclotron and accelerated simultaneously. All of the cyclotron parameters are optimized for one of the cocktail ions. A set of the parameters are regarded as a standard condition. Small difference of the M/Q from the standard ion gives rise to a drift of a beam phase. A small lag of revolution period for other cocktail ions amounts to deceleration of the ions before extraction. Finally, only the standard ion is extracted from the cyclotron. Other cocktail ions can be also fully accelerated by slightly changing the magnetic field and/or an acceleration frequency(RF frequency) relative to the difference of the M/Q.

Parameters of the cocktail ions are listed in Table 1. The cocktail ions with M/Q ≈ 5, 56 MeV $^{15}N^{3+}$, 75 MeV $^{20}Ne^{4+}$, 150 MeV $^{40}Ar^{8+}$ and 323 MeV $^{84}Kr^{17+}$, have been offered users tentatively. Some of the M/Q ≈ 4 cocktail ions have very close M/Q. For example, the difference of the M/Q between $^{16}O^{4+}$ and $^{20}Ne^{5+}$ is of the order of 6×10^{-5}. The difficulty of the M/Q ≈ 4 cocktail beam lies in the fact that the ions with the very close M/Q are extracted from the cyclotron simultaneously.

2. Cocktail Ions with M/Q ≈ 5

First an argon gas was fed to the ECR ion source together with a oxygen gas as support. Only the $^{40}Ar^{8+}$ was injected into the cyclotron, and all of the cyclotron parameters were optimized for the 150 MeV $^{40}Ar^{8+}$ to produce a standard acceleration condition.

Next, the argon gas was replaced by a mixture gas of argon, neon and krypton to generate the cocktail ions. An enriched

Table 1: Parameters of the cocktail ions with $M/Q \approx 5$ and 4.

Ion	Mass Number M	Atomic Number Z	Charge State Q	M/Q	Δ(M/Q)/(M/Q)	Energy (MeV)	RF Frequency (MHz)	Stopping Power in Silicon (MeV/(mg/cm^2))
N	15	7	3	4.9995	+9.4 x 10^{-4}	56	13.867	3.3
Ne	20	10	4	4.9976	+5.6 x 10^{-4}	75	13.873	6.1
Ar	40	18	8	4.9948	0	150	13.881	15
Kr	84	36	17	4.9354	-118.9 x 10^{-4}	323	14.047	40
He	4	2	1	4.0021	+9.8 x 10^{-4}	25	11.908	0.2
C	12	6	3	3.9995	+3.2 x 10^{-4}	75	11.916	1.8
O	16	8	4	3.9982	0	100	11.919	3
Ne	20	10	5	3.9979	-0.6 x 10^{-4}	125	11.920	4.6
Ar	40	18	10	3.9957	-6.2 x 10^{-4}	250	11.926	13
Kr	84	36	21	3.9952	-7.3 x 10^{-4}	525	11.928	36

nitrogen-15 gas was also fed to the ECR ion source by another gas supply pipeline. The four kinds of ions, $^{15}N^{3+}$, $^{20}Ne^{4+}$, $^{40}Ar^{8+}$ and $^{84}Kr^{17+}$ were injected into the cyclotron simultaneously. By changing the RF frequency to the optimum value for each ion species, one of the cocktail ions was fully accelerated and extracted from the cyclotron. The other cocktail ions entered a deceleration phase region before extraction. Dependence of beam intensity on the RF frequency is shown in Fig. 1. The ion species was identified by a pulse height obtained with an SSD, where the energy of the cocktail ions is approximately proportional to a mass number. No intermixture of different ion species was found in each cocktail ion beam.

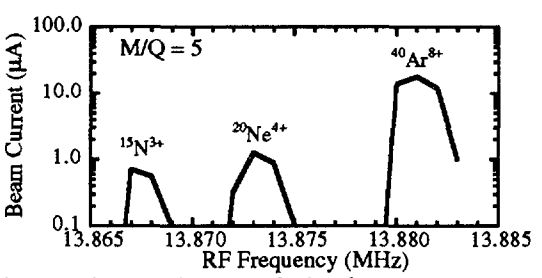

Fig. 1 Dependence of the beam intensity on the RF frequency. The optimum RF frequency for the cocktail ions are 13.867 MHz for the 56 MeV $^{15}N^{3+}$, 13.873 MHz for the 75 MeV $^{20}Ne^{4+}$ and 13.881 MHz for the 150 MeV $^{40}Ar^{8+}$.

Intensity of the cocktail beams depends mainly on charge state of the ions, a mixing ratio of the cocktail gas and the ECR parameters. Beam intensity of more than a hundred nA was obtained for the 56 MeV $^{15}N^{3+}$, 75 MeV $^{20}Ne^{4+}$ and 150 MeV $^{40}Ar^{8+}$ beams as shown in Fig. 1. The 323 MeV $^{84}Kr^{17+}$ beam , by contrast, had relatively low intensity of 1 nA at most. In order to obtain an intense $^{84}Kr^{17+}$ beam, the cocktail gas was replaced by a pure krypton gas, and a single $^{84}Kr^{17+}$ ion was injected into the cyclotron. At least 10 nA $^{84}Kr^{17+}$ beam was obtained by the single ion acceleration. However, half an hour's changing time was required for replacing the gas in the present gas supply system of the ECR ion source.

3. Cocktail Ions with M/Q ≈ 4

The oxygen gas and the mixture gas of argon, neon and krypton were used to generate the cocktail ions with M/Q ≈ 4. All of the cyclotron parameters for accelerating the M/Q ≈ 4 cocktail ions were opti-

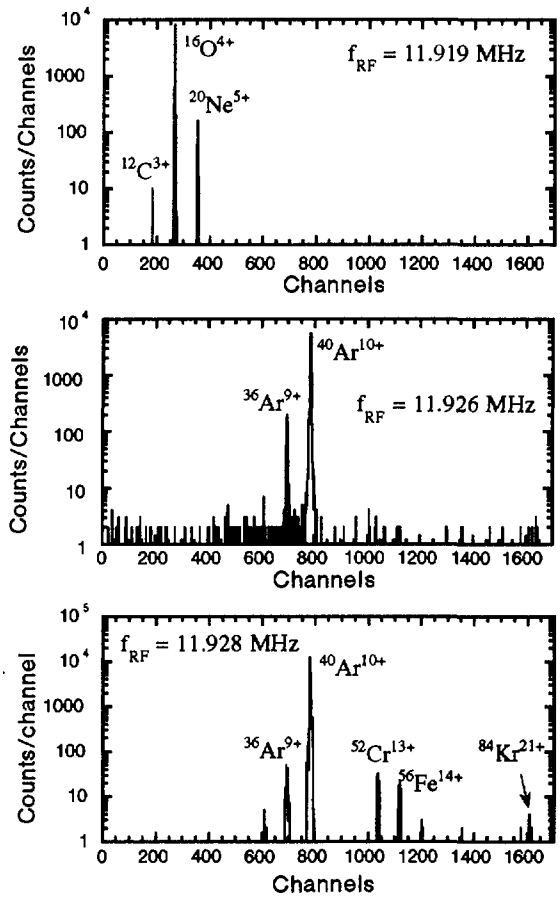

Fig. 2 Pulse height spectra of the M/Q $\approx$ 4 cocktail ions measured with a SSD. The spectra were obtained at three RF frequencies: f_{RF} = 11.919 MHz, 11.926 MHz and 11.928 MHz.

mized for 100 MeV $^{16}O^{4+}$. Pulse height spectra of the cocktail ions obtained at three different RF frequencies were shown in Fig. 2. Parameters except for the RF frequency were the same as the 100 MeV $^{16}O^{4+}$. Plural ion species were observed in the pulse height spectra. The insufficient separation of the cocktail ions was due to large phase acceptance of the JAERI AVF cyclotron. Before entering the deceleration phase region, undesirable cocktail ions were extracted from the cyclotron. In order to exclude the undesirable cocktail ions, an acceleration voltage was lowered by 28 % so that a revolution number could be increased to encourage the phase drift. A mixture rate of the $^{12}C^{3+}$ and $^{20}Ne^{5+}$ in the 100 MeV $^{16}O^{4+}$ beam was reduced to less than 1×10^{-3}. A more effective method for completely excluding the undesirable ions is now being developed.

4. References

1) M.A. McMahan, et al., *Nucl. Instr. and Meth.* A253:1-9 (1986)
2) M. Fukuda, et al., *JAERI TIARA Annual Report* 5:229-231(1995)

8．7 Examination of Vacuum Characteristics for Some Rotary Shutters

Y. Nakamura
Advanced Radiation Technology Center, JAERI

1. Introduction

In cyclotron facility, nine rotary shutters have been installed into the shielding walls so that leakage radiation as neutrons and gamma rays shall not penetrate the other ion rooms without the objective one. These shutters have mechanical driving system to rotate their shielding materials, vacuum system consisted of beam duct and evacuation pumps, and so on. The mechanism in connection with vacuum is adopted a cap-seal structure which has double O-rings around the shaft because of the rotation of shielding materials. The maximum number of opening-closing operation for these shutters reached up to 1870 in Aug. 1996 since the installation in 1991, contrary to what we expect, it exceeds much more than around a few hundred times of initial prediction for a year. We attempted to make sure the reliability and durability for some representative rotary shutters.

2. Structure of rotary shutter related to vacuum performance

A detail structure at the part of the driving shaft penetration of the rotary shutter is shown in Fig. 1. The regions connected to vacuum condition are separated into three parts. One is high vacuum region, the other is medium one and another is of course atmospheric one. High vacuum region is usually pumped up by a TMP and two ion sputter pumps. Medium vacuum region between two cap-seal "A" and "B" is evacuated by a small rotary pump. The cap-seal "A" which has two O-rings is completely the same structure as the cap-seal "B". However, two O-rings of each seal are made of different material.

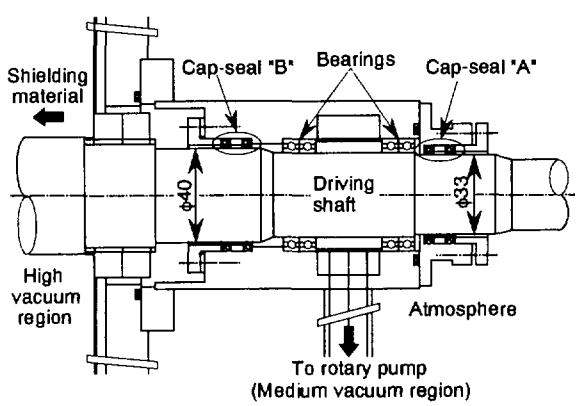

Fig. 1 A detail structure of a rotary shutter with the driving shaft penetration.

3. Condition of vacuum system on measurement

A typical constitution of vacuum section including the rotary shutter is illustrated in Fig. 2. Actually, only two ion pumps equipped with beam line at both sides of the shielding wall were stopped prior to measurement because the increase of vacuum pressure in the beam line might be induced for rotary shutter operations. Furthermore, both valves positioned at the boundary of the vacuum section were closed owing to the prevention against the contribution from the adjoining sections. A cold cathode and a Pirani gauge monitoring to the pressure in the beam line have been fixed up directly at its duct downstream the rotary shutter. An additional Pirani gauge was mounted newly in the evacuation line from the rotary pump for narrow space of the cap-seal.

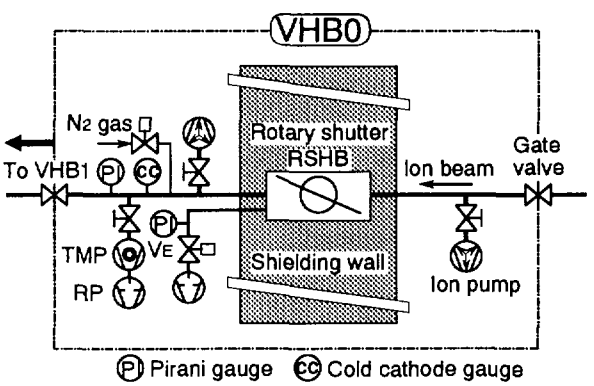

Fig. 2 The constitution of vacuum section "VHB0" including the rotary shutter "RSHB".

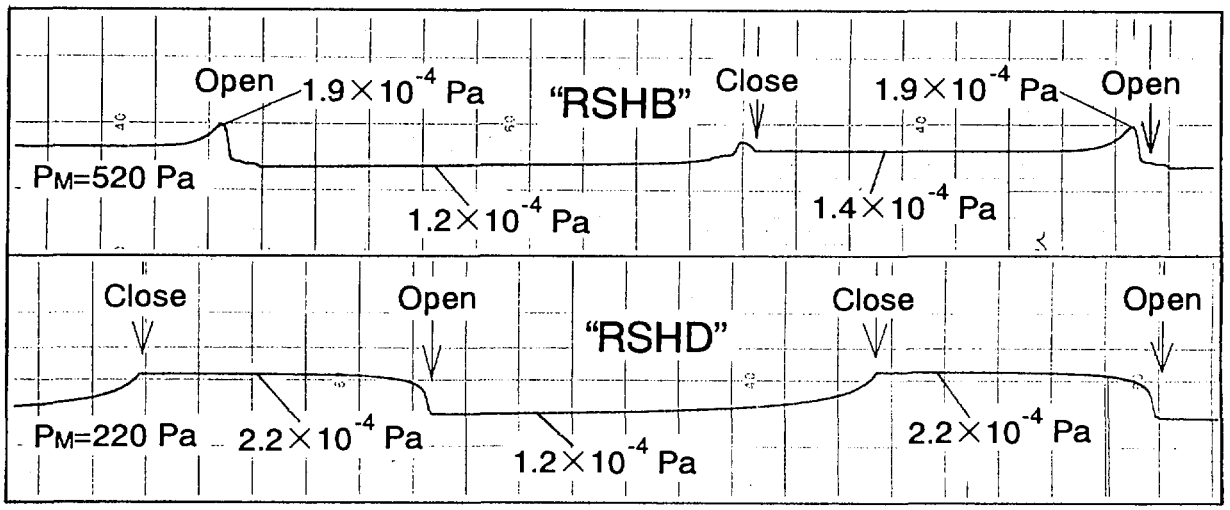

Fig. 3 Pressure changes in high vacuum regions under opening and closing operations.

4. The result of vacuum pressure measurement

The pressure changes at medium and high vacuum region for three rotary shutters were measured. So far, the rotary shutter "RSHB" in the HB beam course has been operated the busiest among nine shutters, the number of operations attained to 1870 at the time of Aug. 1996 as mentioned before. The other "RSHC" is medium degree with the operational numbers of 1290. For another "RSHD", the number of operations which is accounted at 570 is smaller relatively.

We measured the pressure changes for rotary shutter operations under two conditions, relatively low and high pressures at medium vacuum region, using a couple of cold cathode and Pirani gauge. Figure 3 shows that the pressure change in high vacuum region of the "RSHB" appears slightly during the rotation when the medium vacuum region has been kept at relatively high pressure such as 520 Pa.

However, any pressure increments at static condition were not observed at both region originating in cap-seal structure although the pressure in medium region changes about a few ten percent by opening and closing operations. And, the pressure in high vacuum region also deviates because of the large change of vacuum conductance in the beam line duct.

Contrarily, in cases of "RSHC" and "RSHD", the pressure increments by the cause of cap-seal structure during movement didn't occur at all under same operational conditions.

5. An estimation of leakage rate

In general, the pressure change in a vessel is expressed by

$$P(t) = \frac{Q_L}{V} \cdot t + P_0(t). \qquad (1)$$

Where, P(t) is the pressure at t(h) after the cessation of evacuation, $P_0(t)$ the pressure caused by outgassing, Q_L leakage rate and V volume. It has been known that $P_0(t)$ saturates to constant value after long time past though it increases with time in the range of short time. The pressure increment in the medium vacuum region is shown in Fig. 4.

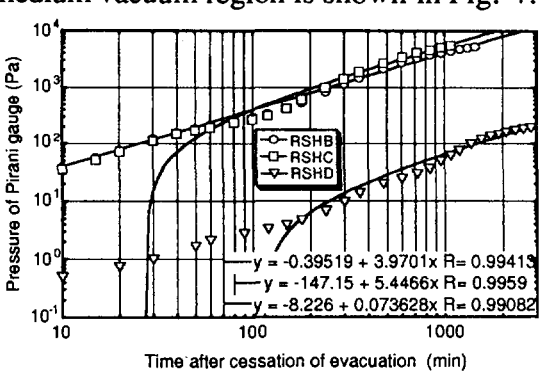

Fig. 4 Pressure changes in medium vacuum region after the stopping of evacuation.

The pressure change becomes to be proportional to the time more than around 100 min. The leakage rates for "RSHB" and "RSHC" calculated from their inclinations are almost same, but one for "RSHD" is estimated at 1/60 of the former value. Since the volume in medium region can be assumed at about 5 L, leakage rates for "RSHB" and

"RSHC" are evaluated at about 4.0×10^{-4} Pa/m^{3}s.

6. Analysis and investigation for leakage rate

An analysis model in order to estimate the equilibrium pressure in the rotary shutter is shown in Fig. 5. The vacuum can be maintained surely by two cap-seal structures around the driving shaft penetrating medium and high vacuum regions.

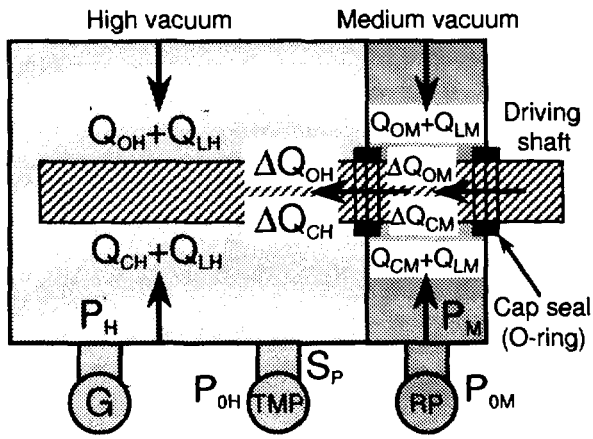

Fig. 5 An analysis model to estimate the equilibrium pressure.

For example, the equilibrium pressure in high vacuum region is expressed in below equation with static condition at full-opening situation.

$$P_{H1}=\frac{Q_{OH}+Q_{LH}}{S_P}+P_{OH} \qquad (2)$$

Where, P_{H1} is equilibrium pressure in high vacuum region, Q_{OH} outgassing rate, Q_{LH} leakage rate, P_{OH} ultimate pressure and S_P effective pumping speed of the TMP. And, the pressure when the rotary shutter is just opened, P_{H2}, is also given by

$$P_{H2}=\frac{Q_{CH}+Q_{LH}+\Delta Q_{OH}}{S_P}. \qquad (3)$$

In a similar way of expression, Q_{CH} is outgassing in high vacuum region with static condition at closing position, ΔQ_{OH} the increment of leakage rate at opening operation. The outgassing and leakage rates in medium and high vacuum region are estimated based on the result of pressure measurement. The result is summarized in Table 1.

The outgassing and leakage rates for three rotary shutters were obtained almost same values with the static condition. However, for the rotary shutter "RSHB", a little large leakage rates such as 1×10^{-5} Pa/m^3/s under rotating movement in high vacuum region and 1×10^{-4} Pa/m^3/s at closing operation in the medium one were observed only for 15 seconds during the operational condition, respectively.

Table 1 Outgassing and leak rates in medium and high vacuum regions.

	RS Name	RSHB		RSHC		RSHD	
High vacuum region	Medium vac. region (Pa)	520	0.6-1.0	320	0.3-0.6	220	0.22
	$Q_{CH}+Q_{LH}$	2.4	2.6	5.0	5.0	2.4	2.0
	$Q_{OH}+Q_{LH}$	2.8	4.4	7.6	8.8	4.4	2.8
	ΔQ_{OH}	1.4					
	ΔQ_{CH}	0.6					
Medium vacuum region	$Q_{CM}+Q_{LM}$		98		70		31
	$Q_{OM}+Q_{LM}$		160		42		31
	ΔQ_{OM}						
	ΔQ_{CM}		9.6				

All of these values without medium vac. region are given in unit of 10^{-5} Pa/m^3/s.

7. Summary

Three rotary shutters "RSHB", "RSHC" and "RSHD" are so still sound that the pressure in high vacuum region is not affected by repeating movements of opening and closing operations. However, the cap-seal of the "RSHB" may suffer to slight frictional damage by mechanical stress since the pressure in high vacuum region increases simultaneously during the rotating movement. It seems that the rotary shutter "RSHD" among three is kept at the best condition because the pressure increment at build-up state is very small and the pressure deviation in medium vacuum region is not also observed during rotating movement.

At the present time, in conclusion, it is thought that three is no problem especially in the functional part related to vacuum performance from the viewpoint of practical use for all of nine rotary shutters.

8. References

1) S. Tanaka, Y. Nakamura, *et al.*, Proc. of Annual Meeting in Autumn, 1991, Atomic Energy Society of Japan, M55, p807 (1991)
2) Y. Nakamura, I. Ishibori, *et al.*, TIARA Annual Report, vol. 2, p200 (1992)

8.8 Development of microbeam application techniques

Takuro SAKAI, Yutaka NAITOH, Tsuyoshi HAMANO*, Toshio HIRAO* and Tomihiro KAMIYA

Advanced Radiation Technology Center, JAERI
*Department of Materials Development, JAERI

1. Introduction

Light and heavy ion microbeam systems have been completed in TIARA. One is connected to the 3 MV single-ended accelerator for light ions, and the other is installed in the 3 MV tandem accelerator for heavy ions. The former system is designed to achieve a sub-micron spatial resolution with a high beam current (>100 pA) for high spatial resolution local area analyses such as PIXE, RBS and NRA. The latter system is used mainly for the studies on transient phenomena at specified positions in pn diodes which are induced by high energy single heavy ion injection with high positioning accuracy .

In order to perform elemental mappings and imagings using these scanning microbeam systems, a multi-parameter data acquisition system is necessary to develop. On the other hand, the technique, which controls the position and the timing of an incident ion to the sample exactly is useful for the studies on analyzing single event phenomena in semiconductor devices.

These systems have been developed and described below.

2. Data acquisition system

While CAMAC based multi-parameter acquisition systems have been widely used for two dimensional microbeam analyses [1], a commercially available PC based system becomes to provide faster data handling with lower cost by recent rapid progress of computer technology [2, 3]. We have developed a real time data acquisition and processing system. Figure 1 shows the schematic diagram of the beam scanning and the data acquisition systems. The beam scanning system generates control signals of high voltage being applied to beam deflector electrodes, and also takes magnitude signals of secondary electron currents to display a secondary electron image of samples [4]. The PC is equipped with a recent fast processor, a large volume memory and a general multi-channel Analogue to Digital Converter (ADC)

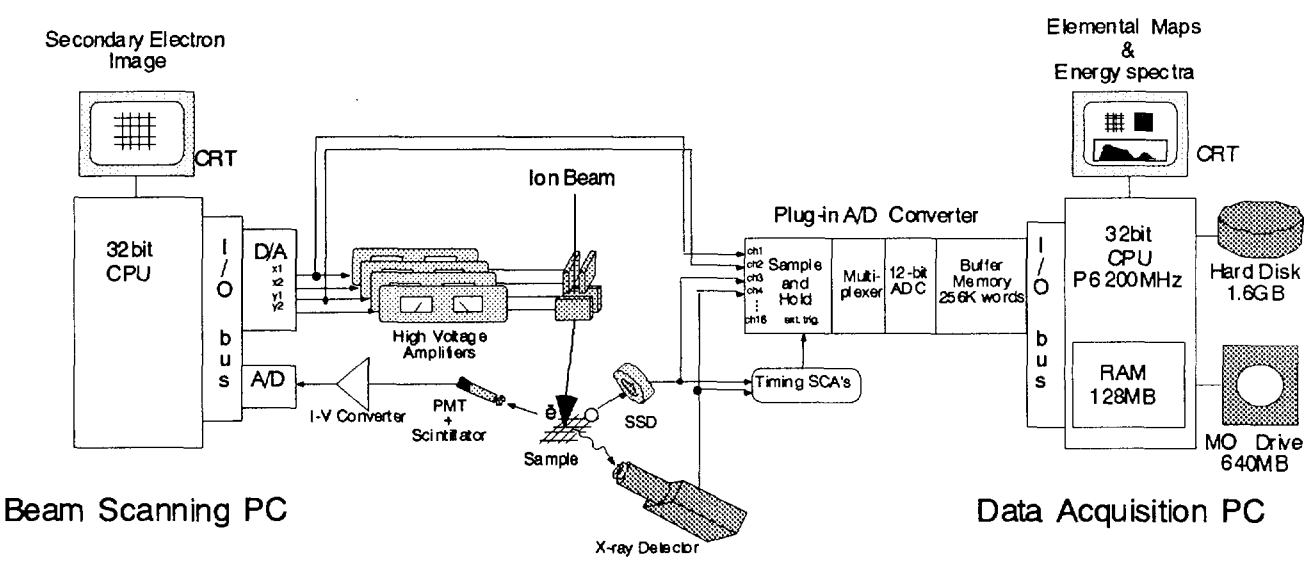

Fig. 1 Schematic of the beam scanning and the data acquisition systems in TIARA

interface board. When a signal from a x-ray detector (PIXE), from a particle detector (RBS) or from others triggers this ADC for data acquisition, X-Y beam scanning control signals which indicate the beam position are also digitized in the same time. These data are addressed in the 3D matrices in the memory space, that consists of 1024 channels for energy spectrum and 150x150 pixels for the corresponding beam scan area. Real time data processing can be done in addition to this data acquisition by the fast processor with the large memory.

Simultaneous PIXE and RBS elemental mapping and ion beam induced current (IBIC) imaging on fine structure diodes have been demonstrated with this system [5].

3. Single ion hit technique

Single ion detection and control of beam injection to a sample are essentially required for this system. Because a detection loss of single ion injection, miscountings due to a noise or following ions hitting to the sample causes the number of injected ion to be uncertain. The pulsed beam, limiting the active time of ion injection to the sample and the gated single ion detection within the pulsed periods were adopted to reduce the noise counting and the beam injection control.

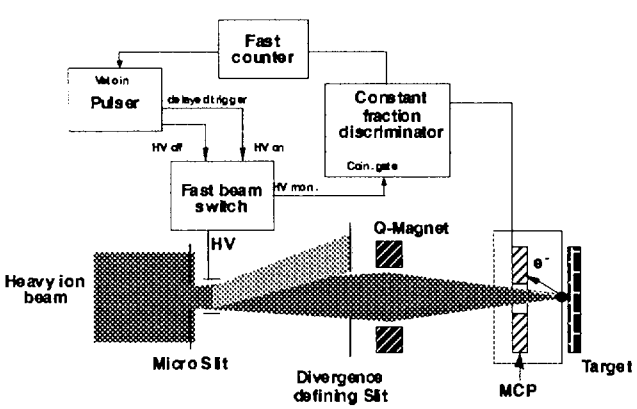

Fig. 2 Schematic of the single ion hit system

The pulsed beam is formed by a fast beam switch and a divergence defining slit. Figure 2 illustrates the schematic diagram of the single ion hit system. Normally the high voltage of the fast beam switch is applied to a deflector electrode (beam off). When a beam injection requirement trigger is formed by the research pulser (STANFORD RESEARCH SYSTEMS, DG535), the high voltage falls down to 0 V and ions can go through the collimation slit (beam on). A delayed trigger is formed by the pulser after the preset time passed, since the formation of the requirement trigger and then the voltage of the beam switch rises up to 500 V again (beam off). The pulse repetition rate can be changed from 0.001 Hz to 100 kHz. The initial ion beam current was reduced to about 0.01 ions/pulse by a mesh beam attenuator located between an ion source and the accelerator in order to minimize the probability that one pulse includes plural ions.

The single ion hit was accomplished by combining the beam pulsing system with the single ion detection system. An annular type MCP (HAMAMATSU, F1094-21SH) and a constant fraction discriminator, which is gated in the same period of beam pulse, are used as the single ion detection system. The continuous beam injection requirement trigger is formed in a preset repetition rate until a counted number of detection signals will reach a preset value of the fast counter.

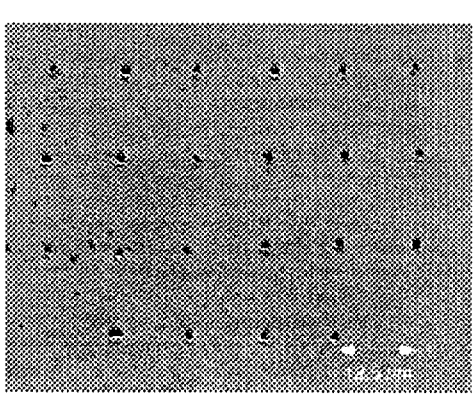

Fig. 3 The array of etch pits on the CR-39 which were produced by 15 MeV Si single ion hitting.

It is necessary to verify whether a single ion makes a hit within the aimed local area or not. A nuclear track detector, CR-39 on which a single ion hit remains as a latent track was employed for the verification. The tracks can be observed as etch pits after chemical etching process. Figure 3 shows the microscopic photograph of an array of single ion etch pits on the CR-39 for 15 MeV silicon ions. The widths of beam pulse and the gate for the detection system were set to be 10 μsec. The hit array demonstrates a success for the single ion manipulation [6].

4. Summary

Multi-parameter data acquisition system for 2 dimensional analyses and single ion hit system for studies on single event phenomena have been developed. The acquisition system enabled elemental analysis in a microscopic area and the evaluation of collected charge distribution in fine diodes. Single ion manipulation has been achieved by combining a beam pulsing system with a gated detection system. This system can be applied to single event upset (SEU) mapping on random access memory devices for the precise evaluation of the SEU cross section in a microscopic sensitive area.

Reference

[1] for example, see G. W. Grime et. al., Nucl. Instr. and Meth. B54 (1991) 52.

[2] M. Bogovac, I. Bogdanovi´c, F. Fazini´c, M. Jaksi´c, L. Kukec and W. Wilhelm, Nucl. Instr. and Meth. B89 (1994) 219.

[3] G. W. Grime and M. Dawson, Nucl. Instr. and Meth. B104 (1995) 107.

[4] T. Kamiya, T. Sakai, T. Hamano, T. Suda and T. Hirao, to be published in Nucl. Instr. and Meth. B.

[5] T. Sakai, T. Hamano, T. Hirao, T. Kamiya, K. Murozono, J. Inoue, S. Matsuyama, S. Iwasaki and K. Ishii, submitted to Nucl. Instr. and Meth. B.

[6] Takuro Sakai, Tsuyoshi Hamano, Tamotsu Suda, Toshio Hirao and Tomihiro Kamiya, to be published in Nucl. Instr. and Meth. B.

8.9 Development of the ion generation methods for the ion implanter

K.Ohkoshi, T.Orimo*, Y.Saitoh and S.Tajima
Advanced Radiation Technology Center, JAERI
*Beam Operation Co. Ltd.

1. Introduction

A 400kV ion implanter in TIARA has been provided a wide variety of ions from proton to bismuth for various experiments. In order to produce many ion species, we have developed two new generation methods, which were a disk and a filament method.

2. Ion source

A Freeman type ion source is used to generate the ions. The structure of the ion source is illustrated in fig.1. The material gas or vapor is fed into an arc chamber to make the arc plasma. The electrons from the tungsten filament are accelerated toward the arc chamber wall with 100V potential. The constant magnetic field of about 150Gauss is applied in parallel with the filament to lengthen electron trajectory. The positive ions are extracted from the arc plasma in the chamber and are accelerated after mass analyzing.

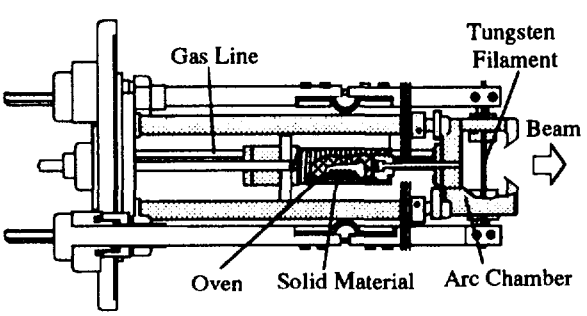

fig.1 Freeman Ion Source

3. Ion generation methods

The Gas and oven methods are generally used to produce the ions with using Freeman ion source. In the case where the gas contained objective element is obtained, the gas method is available. If it can not obtain the suitable gas, the oven method is used. To produce the vapor of the solid material, pure or compound containing objective element, is inserted into the oven. But the oven method is impossible to produce the vapor of element having high melting point. Consequently, we were developed disk method and a filament method.

The disk made of objective material put into the arc chamber as shown in fig.2. The temperature of the disk surface becomes about 1500℃ with heating of plasma, so that the vapor of the element is produced.

The filament method is used for refractory metal such as niobium and molybdenum. In the filament method, the tungsten filament is replaced with another one made of objective material as shown in fig 3. The objective ions are ionized directly in the argon plasma.

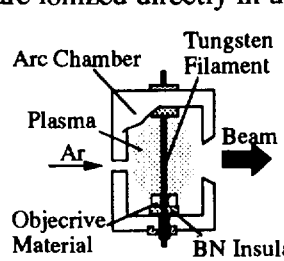

fig.2 Disk Method

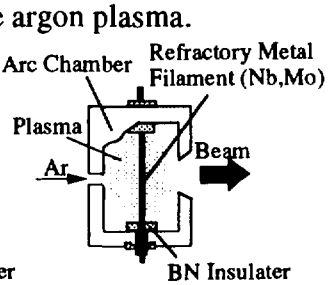

fig.3 Filament Method

4. Summary

The TIARA ion implanter has been generated and accelerated thirty three kinds of ions with using four generation methods. The details of each ion, method, material and maximum beam intensity are listed in table.1.

5. Reference

1)S.Tajima et al., JAERI-tech 96-029(1996)
2)J.H.Freeman, Nucl. instrum. and methods, 22,306 (1963)

table.1 Available Ion Species for the Ion Implanter

Ion	Ion Generation Method	Ion Material	Beam Current of Max(μA)
^{1}H	Gas	H_2+Ar	8
^{4}He	Gas	He+Ar	13
^{12}C	Gas	CO_2	10
^{14}N	Gas	N_2	25
^{16}O	Gas	CO_2	10
^{19}F	Gas	SF_6	5.6
^{20}Ne	Gas	Ne	30
^{24}Mg	Oven	Mg	60
^{27}Al	Oven	AlF_3	4
^{31}P	Oven	P	100
^{32}S	Gas	SF_6	22
^{35}Cl	Oven	AgCl	5.7
^{40}Ar	Gas	Ar	100
^{41}K	Oven	KCl	20
^{48}Ti	Disk	Ti	3.4
^{51}V	Disk	V	2.7
^{52}Cr	Oven	$CrCl_3$	40
^{55}Mn	Oven	$MnCl_2$	12
^{56}Fe	Oven	$FeCl_2$	20
^{58}Ni	Oven	NiCl	15
^{63}Cu	Oven	CuCl	15
^{75}As	Oven	As	100
^{80}Kr	Gas	Kr	100
^{93}Nb	Filament	Nb	6.4
^{98}Mo	Filament	Mo	3.5
^{107}Ag	Oven	AgCl	30
^{132}Xe	Gas	Xe	20
^{138}Ba	Oven	Ba	2
^{139}La	Oven	LaCl	2
^{153}Eu	Oven	Eu	30
^{166}Er	Disk	Er	1
^{184}W	Filament	W	2
^{209}Bi	Oven	Bi	30

8．10 Acceleration of Cluster Ions by 3 MV Tandem (Ⅲ)

Y.Saitoh, K.Mizuhashi, and S.Tajima
Advanced Radiation Technology Center, JAERI

1. Introduction

Irradiation of molecular or small cluster ions in materials has attracted attention in points of surface modification of materials and study of nonlinear effects in the energy deposition process. Different kinds of ions can be implanted simultaneously in a same spot of a target by using molecular ions which consist of different atoms. MeV clusters transfer the large energy density in materials, so that deferent phenomena from those induced by irradiating elemental ions should be expected. Expanding the species of small clusters assists the investigation of the phenomena. In the TIARA facility, the ion cluster or molecular beam of $C_{2\sim8}$, $Si_{2\sim4}$, $B_{2\sim4}$, LiF and O_2 have been available. In addition to these ions, the ion beam of $Cu_{2,3}$, $Al_{2\sim4}$ and AlO were obtained in the energy of 6 MeV. Especially, the double charged positive ion beam in the energy of 9 MeV was obtained for AlO.

2. Negative beam of Cu_n, Al_n and AlO

Singly charged negative Cu_n and Al_n cluster and AlO molecular ions are produced in a conventional Cs sputter ion source[1] and injected into the 3 MV tandem machine. In the ion source, various mass ions consisting of elemental, molecular, and cluster form, are extracted from the surface of the cathode by positive Cs ions sputtering. The cathodes made of pure copper and aluminum metals were prepared for generating Cu and Al cluster ions, respectively. And aluminum oxide (Al_2O_3) powder pressed into a cathode holder was prepared for generating AlO molecular ions.

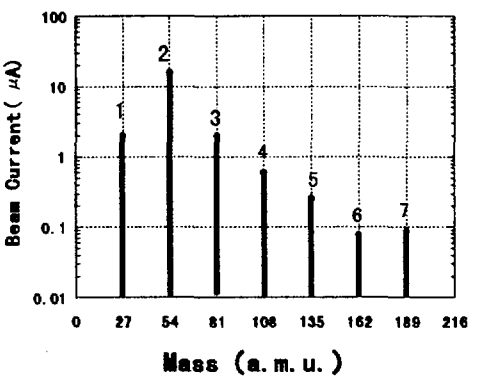

Fig. 1. Aluminum cluster mass spectrum extracted from the ion source.

Al clusters of up to seven atoms/ion are obtained in beam current of some hundreds nA from the source. The mass spectrum of Aluminum clusters is shown in fig. 1.

3. Acceleration of cluster ions

Ions injected to the tandem machine are accelerated toward the high-voltage terminal positioned in the middle of the accelerator vessel. Most of cluster or molecular ions are dissolved into the elements by collisions with the stripper gas (N_2) at the terminal. However, small amount of cluster ions are survived and stripped to singly charged positive ions, and accelerated toward the ground level. The survival probability of a cluster ion depends on the pressure of stripper gas. Fig. 2 shows the beam intensity of Al_n (n=2～4) in the energy of 6 MeV with respect to the stripper gas pressure. The beam current of 2 nA for Al_4 was obtained at the pressure of 2.1×10^{-8} Torr measured at the beam line just before the accelerator tank.

The available cluster and molecular

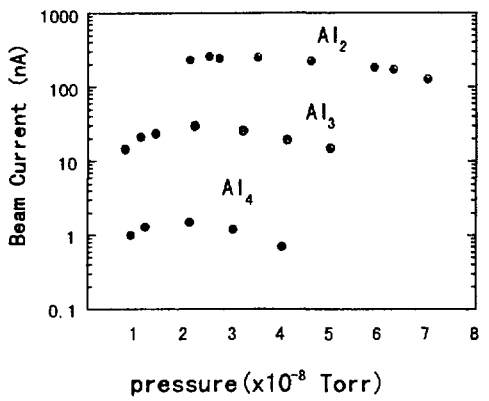

Fig. 2 Beam intensity of Aluminum cluster in the energy of 6 MeV with respect to the gas pressure.

beam by the 3 MV tandem accelerator were summarized at table 1. We will perform the acceleration of metallic cluster ions.

Reference

1. Y.Saitoh, S.Tajima, I.Takada, K. Mizuhasi, S. Uno, Y. Nakajima, and Y.Ishii, JAERI Annual Report 1994 (Vol. 4) 234-235

Table 1. Avaiable high energy cluster and molecular beams (nA) by the 3MV tandem accelerator.

atoms/cluster Spesies	2	3	4	5	6	7	8
Carbon	900	34	42	3	10	1	2
silicon	190	9	1	----------	----------	----------	----------
Boron	64	4	3	----------	----------	----------	----------
Oxygen	4	----------	----------	----------	----------	----------	----------
LiF	1	----------	----------	----------	----------	----------	----------
Cu	7	1	----------	----------	----------	----------	----------
Al	250	30	2	----------	----------	----------	----------
AlO	1	----------	----------	----------	----------	----------	----------

8．11 Study on the Stability of Beam Energy at the TIARA Single-ended Accelerator

Y. Ishii, S. Tajima, I. Takada, K. Mizuhashi, Y. Saitoh, S. Uno, K. Okoshi, Y. Nakajima.

Beam Engineering Division, Advanced Radiation Technology Center, JAERI

1.Introduction

The measurement techniques of the energy stability have been developed for 0.4-3.0MeV proton beams produced by the 3MV single-ended accelerator by using the resonances of the reaction $^{27}Al(p, \gamma)^{28}Si$. These previous studies[1,2] suggested that the promising resolution of the stability measurements be within about $\pm 1 \times 10^{-4}$ when using the resonance at 0.992MeV.

In the present paper, the energy stability was studied by two different methods on the basis of this resonance reaction and energy analysis using the 90° analyzing magnet, as a cross-check.

2.Experiments

The experiment based on the resonance was carried out using an about 1000Å thick Al target, a NaI scintillator for γ-ray measurement and a silicon semiconductor detector (SSD) as the beam current monitor, which are equipped in the target chamber. The total yield of γ-rays induced by the resonance was normalized to that per unit current.

The 90° analyzing magnet used in another experiment was connected with the beam line of the accelerator. The both gaps of the slits placed up- and down-stream of the magnet were adjusted to achieve the resolution of about $\pm 2 \times 10^{-4}$. The beam current was measured by a Faraday cup as the function of the magnetic field.

3.Result and Discussion

The experimental results for two methods, based on the resonance and the 90° analyzing magnet, are shown in Fig.1 and Fig.2, respectively. In Fig.1, total yield of γ-rays is plotted as the function of beam energy with the solid line, and its differential value is fitted by a Gaussian function by using broken line. Figure 2 shows the relation of beam current and the intensity of the magnetic field which proportional to beam energy as indicated upper abscissa. From both figures, the full widths at half maximum (FWHMs) of energy spread were estimated, which is defined as energy resolution (ΔE). The widths and the stability of the beam energy (ΔE/E) (E: mean beam energy, 0.9918MeV) are listed in the Table 1. The stability values independently estimated from two different methods are in good agreement at $\sim 3 \times 10^{-4}$.

Combination of two different methods demonstrates its usefulness at beam energy of ~ 1.0MeV, and leads us to extend its application to beam energies higher than 1MeV.

Reference

1) Y. Ishii et al. TIAEA annual report Vol.3
JAERI-Review 95-019 p.227(1995)

2) Y. Ishii et al. TIARA annual report Vol.4
JAERI-Review 96-017 p.236(1996)

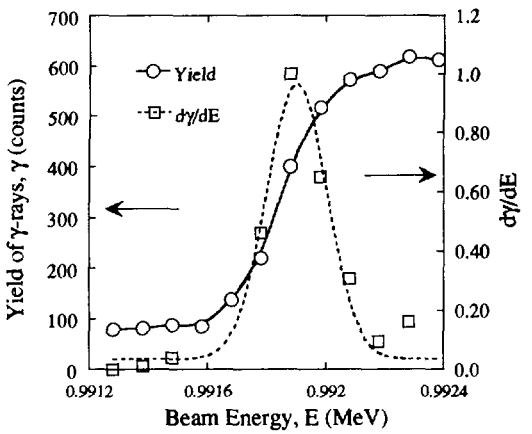

Fig.1 The yield of γ-rays(γ) induced by the resonance of the reaction $^{27}Al(p,\gamma)\ ^{28}Si$ (left ordinate) and its differential value (dγ/dE) (right ordinate) as the function of beam energy. The broken line is the fitting by a Gaussian function.

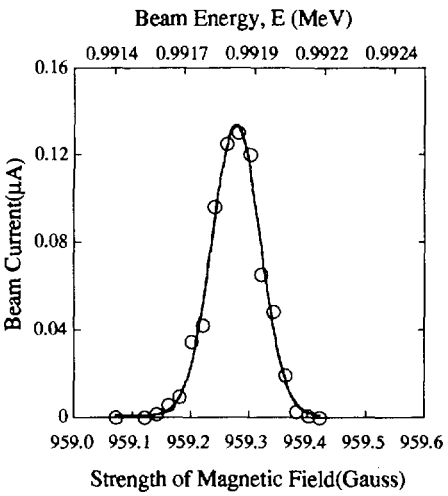

Fig.2 The beam current and the intensity of the magnetic field of the 90° analyzing magnet (bottom abscissa) which is proportional to beam energy (upper abscissa). The curve is a Gaussian fitting.

Table 1

Beam stability estimated by using two methods based on the $^{27}Al(p, \gamma)^{28}Si$ resonance at 0.992MeV and the 90° analyzing magnet.

	Resonance Reaction	Magnetic Analysis
FWHM(ΔE)* (eV)	337	288
Stability (ΔE/E)	3.4×10^{-4}	2.9×10^{-4}

*FWHM(ΔE): full width at half maximum of energy spread. (resolution)

E: mean beam energy estimated at 0.9918MeV.

8.12 Development of an Ultra-fine Ion-beam Apparatus

Yasuyuki Ishii, Akira Isoya and Ryuichi Tanaka
Advanced Radiation Technology Center, JAERI

1.Introduction

The production technique of ultra-fine ion beams with the size of much less than 0.1μm in diameter has been developed by using two types of single aperture lens having the beam focusing and acceleration functions[1,2] and the modified duoplasmatron ion source[3]. On the basis of the preliminary study on the lens system and the prototype ion source[3], we fabricated the ultra-fine ion beam apparatus and studied characteristics of the ion source. A simple knife edge device was also developed for measurement the beam size of less than 0.1μm with the sufficient spatial resolution.

2.Ion source and its characteristics study

The modified duoplasmatron ion source, as shown in Fig.1, was designed to produce beams with the narrow energy width and relatively high intensity as the following two steps:

1) Plasma is leaded into the vacuum(10^{-4}Pa) region through the non-magnetic anode electrode(Cu) with 0.2mm diameter aperture hole keeping its plasma state. The applied voltage to the anode, V_{anode}, is 58.8V.

2) Ions produced from the plasma are accelerated during traversing through a flat plasma sheath to the extraction electrode(Fe).

The energy width was preliminarily evaluated as described in the previous paper[3]. In the present study, the overall beam current(Iext) and the beam current after passing through the 0.2mm diameter hole of the extraction electrode(Ic) were respectively measured at the extraction electrode and the Faraday cup (suppression voltage: ~ 30V). Relations between the extraction voltage and the ion beam currents measured at two locations are shown in Fig.2. The currents, Iext and Ic, increases with the voltage up to reach plateau part. Iext and Ic are respectively higher than 40μA and 0.1μA in the range over 40V, when the applied voltage about 60V is almost equivalent to that at the anode electrode. The contamination of electrons in ion beams observed as minus current may be negligible under this condition. The brightness(B_n) estimated for 0.2mm diameter beam of 0.1μA was about $1\times10^{6}Am^{-2}rad^{-2}eV^{-1}$, assuming diver-gence angle of 1×10^{-3}rad at the aperture of the anode electrode.

The beam with currents over 0.1μA and the brightness of $10^{6}Am^{-2}rad^{-2}eV^{-1}$

order, which is regarded as the beam at the first acceleration lens, suggests that the developed ion source should have sufficient functions to produce the ultra-fine ion beam ultimately with 100pA order.

3. Measuring device of the beam size

The knife edge device using the sharpened razor's blade and the piezo-actuator for its position control is illustrated in Fig.3. The beams size can be evaluated by measuring current change when the knife edge is moving across the beam path. The knife blade with the straightness of less than 0.1μm was obtained so far by using a tool for sliding the knife edge on the rapping sheets containing ultra-fine powder (~0.1μm). It is sufficient to use for beam size measurement combining with the actuator.

The fabrication of the ultra-fine ion beam apparatus was almost completed. It leads us to study characteristics of the produced ion beams using the knife edge device under development.

Reference

1)A. Isoya, Proc. Int. Conf. on *Application of Nuclear Techniques.* Creta, Greece, (1990) P.334

2)A. Isoya, Proc. Int. Conf. on *Evaluation in Beam Applications.* Takasaki, Japan, (1991) P.397

3)Y. Ishii, R. Tanaka and A. Isoya, Nucl. Instr. and Meth., B113(1996)75

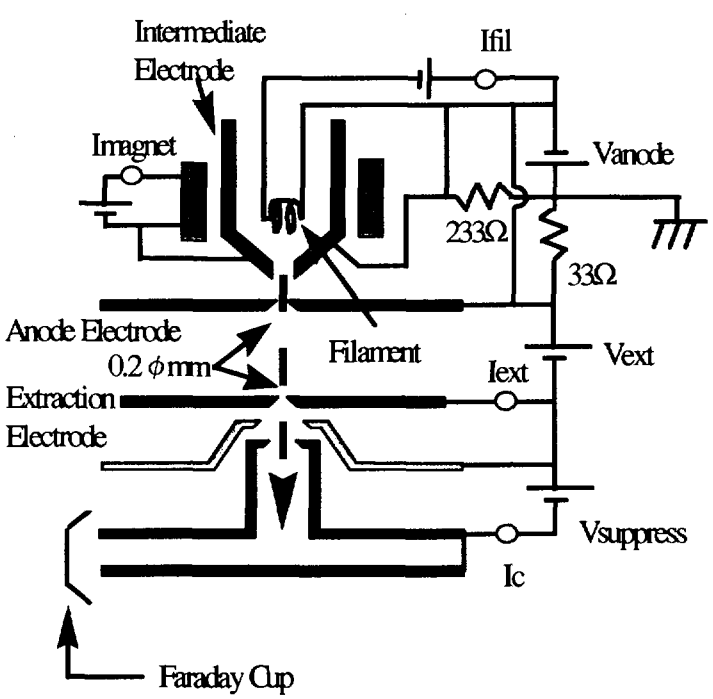

Fig.1 Schematic diagram of the ion source.

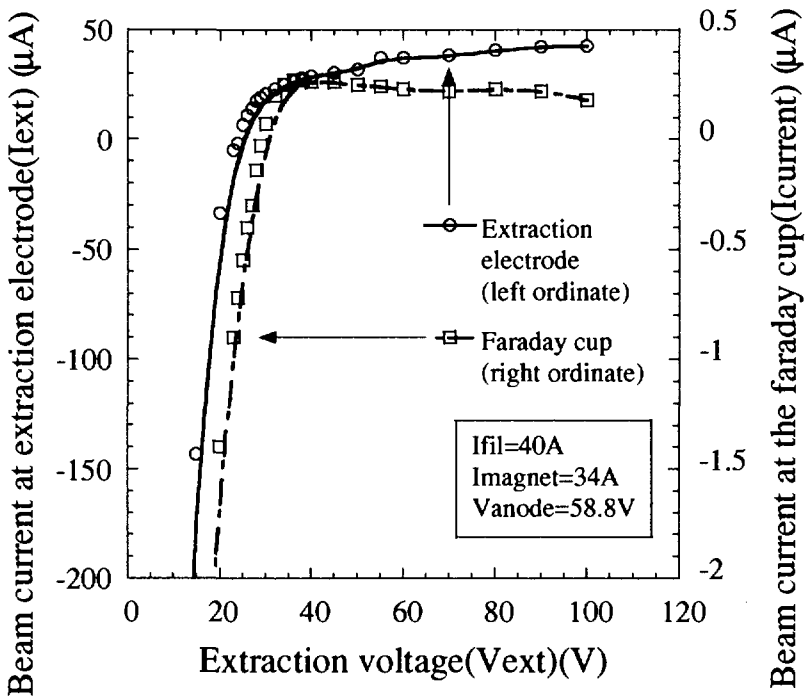

Fig.2 Relation between the extraction voltage and the beam current, at Vext, Iext and Ic in Fig.1.

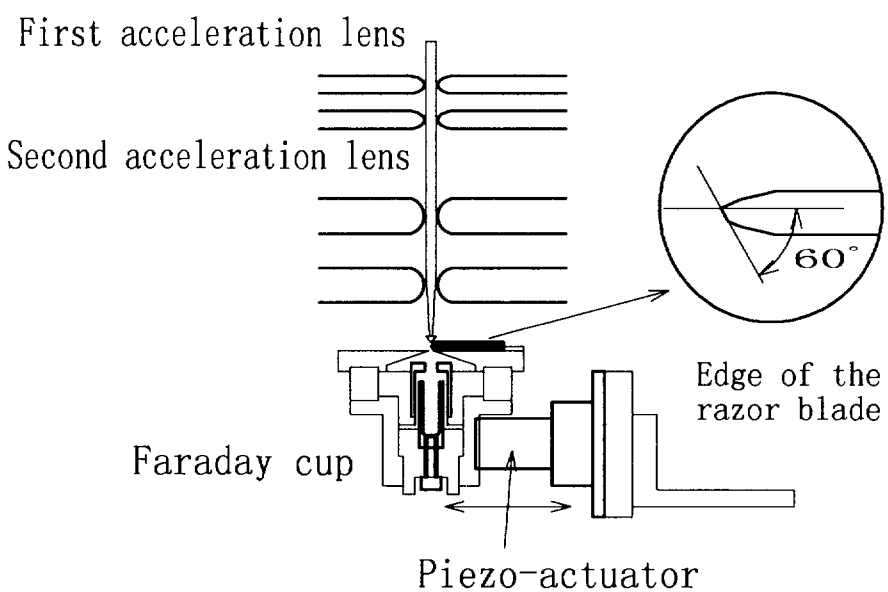

Fig.3 The knife edge device using the sharpened razor's blade and the piezo-actuator.

8. 13 Development of a High-precision Beam Profile Monitor (III)

T. Kurihara, H. Kobayashi*, T. Urano*, T. Suwada*,
Y. Aoki**, S. Okada**, and A. Kawasuso**
Institute of Materials Structure Science, KEK
*Accelerator Research Laboratory, KEK
**Japan Atomic Energy Research Institute, Takasaki

Abstract

The Photon Factory 2.5 GeV electron linac is now being upgraded for the KEKB[1] project. We have developed and installed several types of monitors since 1993. A high-precision beam profile monitor is one candidate for this purpose. Alumina screen (Desmarquest AF995R, chromium-activated alumina ceramics), is often used as a beam profile monitor for diagnosis of a linac beam. Typical thickness of alumina phosphor screen is about 1mm. Especially for the low energy beam part of the linac, scattered electrons in such a thick screen produce enlarged beam profiles. A thin film phosphor screen with rare earth ion implanted alumina layer on aluminum plate has been designed and manufactured to produce a high-precision beam profile monitor.

Introduction

The KEKB, an asymmetric, double-ring electron-positron collider, requires an upgrade of the injector linac in order to increase the energy of the electron and positron beams to 8 and 3.5 GeV, respectively. Formerly it was 2.5 GeV. It is very important to get a real image of the beam from the injector linac. Therefore, it is desirable to monitor the beam position and beam profile as well as the beam current in the linac. An elaborate beam-monitoring system is indispensable in order to realize stable operation of the linac with high current beams for KEKB. In this connection, we have developed and installed several types of monitors since 1993. The bunch and profile monitor utilizing optical transition radiation (OTR), a stripline-type beam-position monitor (BPM), a wire scanner, and a beam profile monitor. The demand of a low-emittance electron linac has increased in these years, for applications such as the free-electron laser, coherent synchrotron radiation, and others. It is very important to transport and accelerate the beam emitted from the cathode with negligible emittance growth. There is some attempt to build up an emittance measurement system for a low emittance beam[2]. At that time, a plastic scintillator which was 10 μm thin and had a fast scintillation characteristic had been adopted to measure the beamlets' image with a high temporal and spatial resolution. An inorganic scintillator with thin thickness is necessary for the injector linac for permanent use. We try to make a oxide layer on aluminum surface. With ion implantation technique, we could get a luminescent layer in oxide layer on aluminum surface. We tried to make nearly 10 μm thin oxide layer on aluminum and to make luminescent layer on alumina with rare earth[3,4,5] ion implantation technique.

Experimental

Aluminum plate with nearly 10 μm oxide layer of thickness 1 mm was prepared as a starting material. Purity of aluminum was 99.999%. After fabricating oxide layer on surface with anodization technique, specimens were implanted at room temperature with 350 keV Er or Eu to fluences in the range 1×10^{12} /cm^2 - 1×10^{17} /cm^2. Eu ion implantation profiles have been generated for alumina using the simulation code TRIM. Ion Implanter was used for this implantation experiment.

After implantation, specimens were mounted on the specimen holder of the beam profile monitor test bench in KEK. These specimens were irradiated with 150 keV electron beam from the linac. The intensity of the linac beam was measured using the current monitor. The charge of the electron beam was 2 nC for the 2 ns width electron beam and 30 nC for the 10 ns width electron beam. The repetition rate of the beam was 25 Hz. Optical emission from the specimen was taken by CCD camera.

Beam monitoring is the conventional one which used in 2.5 GeV electron linac.

Light emissions induced by 150 keV electron beam were observed from Eu implanted specimen. (Fig. 1) The charge of the electron beam of this observation was 30 nC. During the Eu ion implantation, light emissions with Eu ion was observed. The range of the fluences was from 1.2×10^{15} /cm^2 to 2.8×10^{16} /cm^2. The specimens for electron irradiation were selected from those fluence range.

Conclusion

With 30 nC electron beam of the energy of 150 keV, optical luminescence was observed with specimens as Eu implanted to fluences in the range 1.2×10^{15} /cm^2 - 2.8×10^{16} /cm^2. There is no luminescence from the Er implanted specimen owing to the low fluence of 1×10^{14} /cm^2.

References

1) S. Kurokawa, BUTSURI Vol. 49, No. 9 (1994) 720

2) Y. Yamazaki, T. Kurihara, H. Kobayashi, I. Sato and A. Asami, Nucl. Instrum. & Methods in Phys. Res. A322 (1992) 139

3) I. Mizuki, N. Baba and S. Tajima: Jpn. J. Appl. Phys. 16 (1977) 971.

4) W. P. Ganley, P. M. Mooney and D. Huminik: Thin Solid Films 3 (1969) 377.

5) M. Katsuno, S. Morisaki, N. Baba, M. Iwaki and K. Takahashi: Jpn. J. Appl. Phys. 25 (1986) 1262.

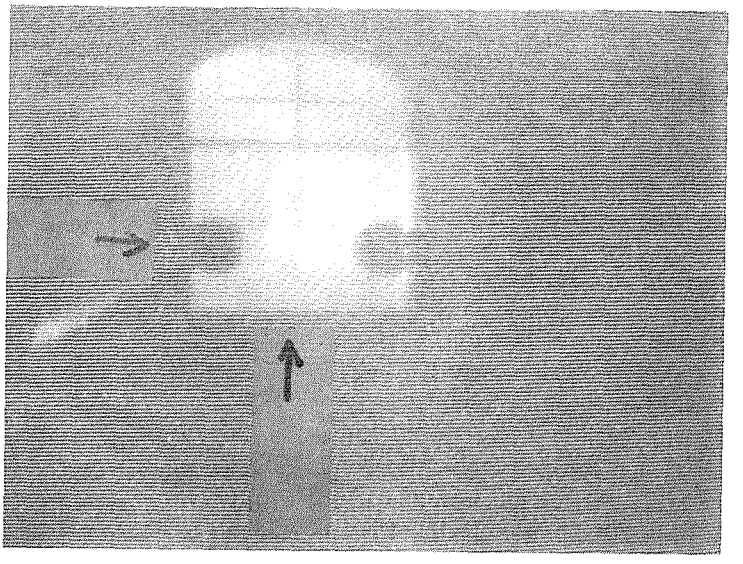

Figure 1 Light emission from Eu implanted Alumina oxide layer on Aluminum.

8.14 Development of a micro-PIXE camera

S.Matsuyama, K.Ishii, H.Yamazaki, S.Iwasaki, K.Murozono,
J.Inoue, T.Hamano, T.Sakai*, T.Kamiya* and R.Tanaka*
Department of Quantum Science and Energy Engineering, Tohoku University
*Takasaki Radiation Chemistry Research Establishment, JAERI

1. Introduction

High-energy microbeam is a powerful means for study of microscopic irradiation[1]. We combine the microbeam technique with particle-induced X-ray emission (PIXE) analysis, which is known to be a novel technique for trace elemental analysis, and develop a micro-PIXE system to measure spatial distribution of elements in a microscopic region, which provides complimentary information in medical, biological, and archaeological fields. We call this system a micro-PIXE camera.

2. Micro-PIXE Camera

A Light-ion microbeam apparatus connected to a 3 MV single-ended accelerator in TIARA, JAERI was used in this study. A beam spot size of 0.3 μm with a beam current of 11 pA was obtained with this system[2,3]. Figure 1 shows a schematic diagram of beam scanning system and data acquisition system for elemental mapping. Proton beams are scanned across the surface of a specimen by two sets of deflection plates which carry sawtooth voltages. The X-rays emitted from the specimen were measured by a Si(Li) detector. In the micro-PIXE camera, X-ray energy and beam position must be measured at the same time in order to get spatial distributions of elements. For this purpose, we used a beam scanning system of TIARA light-ion microbeam apparatus and newly developed a data acquisition system for X-ray energy and beam position. Scanning voltages were given by amplifying two sets of sawtooth signals generated by a computer and digital-to-analog converters (DAC). The scanning speed at its maximum is six seconds per one scan. The beam position is directly proportional to the scanning voltage.

Figure 2 shows a block diagram of the data acquisition system. The system consists of a multi-parameter data acquisition system and ADCs for detector pulse signals and for scanning voltage signals. The multi-parameter data acquisition system is manufactured by Laboratory equipment Co. Ltd. Data format of the ADC for scanning voltage signals is compatible with that of ADC for detector pulse signal. A timing chart of this system is shown in figure 3. When an X-ray signal is detected with one of the ADCs for detector pulse signals, it triggers a data acquisition cycle. After one μ second, the ADCs for scanning voltage signals start conversion. The conversion time is nine μ seconds for any voltage. After the detector pulse and a scanning voltage are converted to digital formats, digital data are saved in a list file. It takes twenty μ seconds for one data acquisition cycle. This system can sort the data for selected element/energy region and generate an elemental map while the data are being collected. Though the memory size of the collected list data tends to be large, it is not disadvantageous since we can have a large capacity removable media now. This system can also get secondary electron images. It is interesting to compare the elemental map with the secondary electron image which shows a shape of specimen.

3. Results

Performance of the data acquisition system was tested by measuring an elemental map of a Cu mesh (1000 mesh/inch). Figure 4 shows a secondary electron image and an elemental map of Cu from Cu mesh using 2 MeV protons focused down to 0.8 μm. The elemental map shows that Cu element is homogeneously distributed. On the other hand, the intensity of secondary electrons increases at the edges of the mesh.

As an example of application to medical and biological fields, we measured the elemental maps of blood cells and a pollen. Figure 5 shows an elemental map of K from red blood cells. It takes seven and a half hours to get one image under the beam current of 100 pA. The elemental image of the red blood cells is not focused than that of Cu mesh. It was caused by drift of a sample stage or chamber. The reason of drift is now investigation in our laboratory. Figure 6 shows the secondary electron image and elemental image of K from a pollen of chrysanthemum taken with a 10 μm 2 MeV

proton beam. While the intensity of secondary electrons is large at the circumference of the pollen, potassium is uniformly distributed.

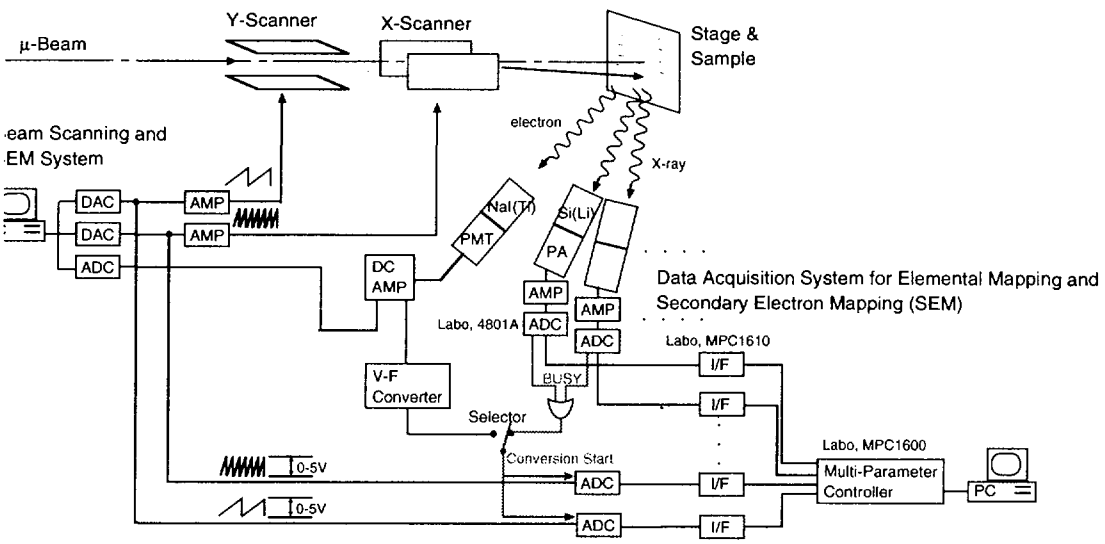

Fig.1 Schematic diagram of beam scanning and data acquisition system for elemental Mapping.

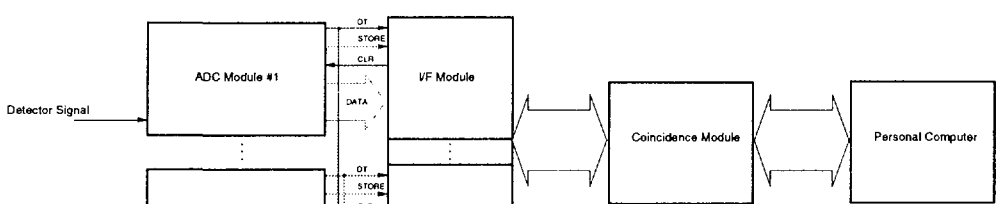

Fig.2 Block diagram of data acquisition system.

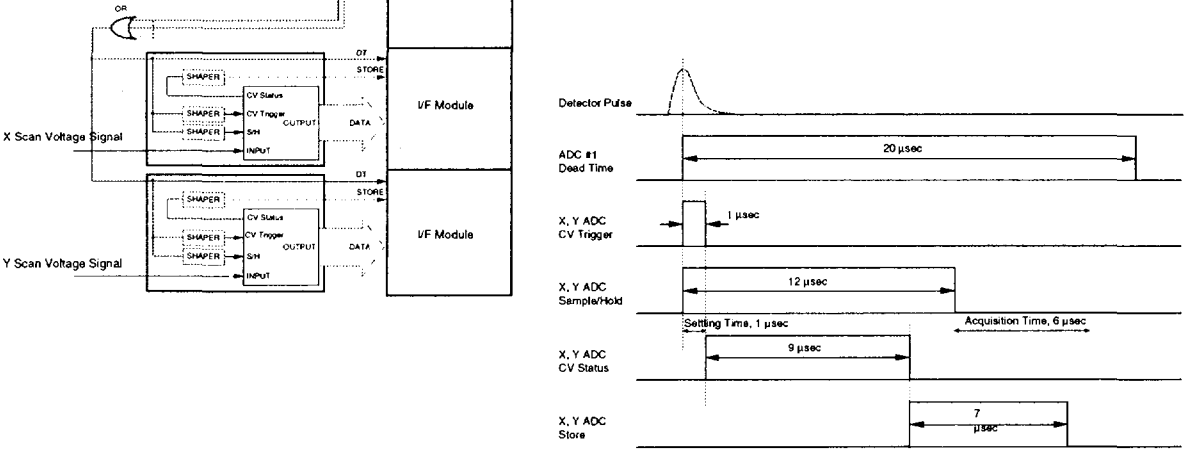

Fig.3 Timing chart of data acquisition system.

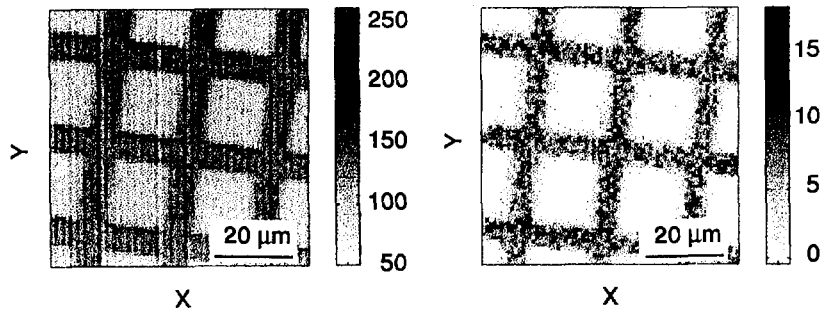

Fig.4 Secondary electron image and elemental map of Cu from Cu mesh (1000 mesh/inch).

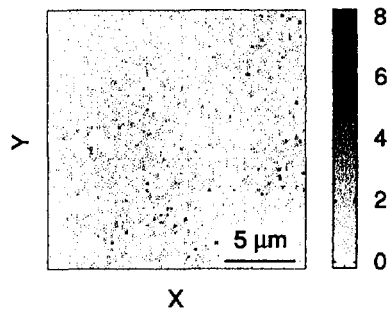

Fig.5 Elemental map of K from red blood cells.

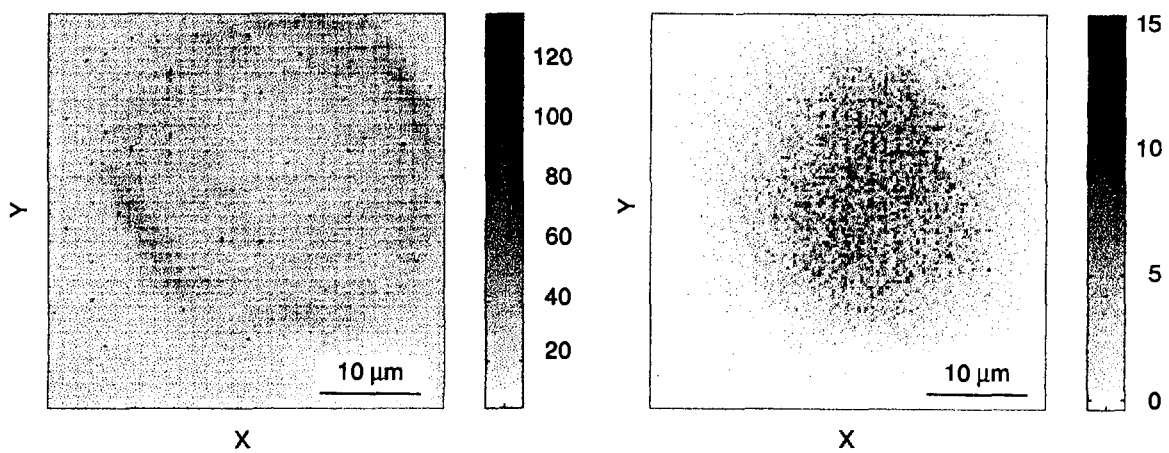

Fig.6 Secondary electron image and elemental image of K from a pollen of chrysanthemum.

4.Summary

The data acquisition system for PIXE camera was developed. This system is applicable to μ-RBS, STIM and local element analysis combined with the methods mentioned above. As an example of application to the biological and medical fields, we measured the elemental maps of red blood cells and a pollen of chrysanthemum. Because of drift of the target, the elemental image was not so focused. Target drift should be removed for the practical use of this system. It took a long hour to get one elemental image. We are now planning to develop a multi-detectors system to increase the detection efficiency. It will lead to a high-speed elemental mapping. Our present data acquisition system is applicable to the multi-detectors system without any modification. Furthermore, we are planning to develop an in-air micro PIXE camera to analyze specimens without any difficulties in sample preparation. This camera becomes a powerful means for the elemental study of cells in vivo.

5. References

1) F.Watt and G.W.Grime, Principles and Applications of Highenergy Ion Microbeams (Adam Hilger, Bristol, 1987)
2) T.Kamiya et al., Nucl. Instr. And Meth. B104 (1995) 43
3) T.Kamiya et al., Nucl. Instr. And Meth. B118 (1996) 447

9. Status of TIARA 1996

9. 1 UTILIZATION OF TIARA FACILITIES

Utilization and Coordination Division,

Advanced Radiation Technology Center, JAERI

1. Introduction

TIARA is a center of ion accelerator facilities composed of four ion accelerators, an AVF cyclotron, a 3MV tandem accelerator, a 3MV single-ended accelerator, and a 400kV ion implanter. These accelerators have been fully served for ion beam applications since January 1994.

2. Utilization System

TIARA is opened for public use: it receives applications of the experimental subjects in wide areas once a year from outside users as well as JAERI staffs. The subjects are approved after the official investigation by TIARA General Program Committee(GPC). To attain an effective outcome of the research program, the utilization time of each accelerator is fairly allotted to the subjects three times per year by the Program Advisory Committee (PAC) under the GPC, which are both publicly organized.

Charges for the utilization are remitted in the case that a contract of the joint research between JAERI and a university or a company or that of the projective joint research between JAERI and universities is made. The results of research have to be published at the TIARA Research Review Meeting and in the JAERI TIARA Annual Report. There is another system of visitor use with charges but without the publication duty.

3. Experimental subject approved

The number of subjects using cyclotron approved in FY 1996 for the experiment was 45 while the total number using three electrostatic accelerators was 46 as shown in Table 1. Table 2. Shows the number allotted to users under various contracts.

Table 1. Number of experimental subjects at various research fields.

Fields of Research	Number of subjects	
	cyclotron	electrostatic accelerators
Materials for space	5	4
Materials for fusion	1	15
Biotechnology	12	3
Functional materials	5	17
RI & nuclear chemistry	6	0
Radiation chemistry	7	0
Basic technology	9	7
Others	0	0
Total	45	46

Table 2. Number of experimental subjects at various relations with users.

Relations with visitors		Number of subjects	
		cyclotron	electrostatic accelerators
JAERI staff	Takasaki Establishment	12	13
	Others	4	11
Universities under Cooperative research		10	13
Universities under Projective joint research		12	3
Private companies or Governmental institutes under joint research		5	6
Others under Cooperative & Joint Research		2	0
Total		45	46

4. Allotted time to users

The cyclotron has been continuously operated from Monday to Friday. The utilization time for the cyclotron is allotted by the hour. In the case of electrostatic accelerators, on the other hand the utilization time is allotted by the day from 9 a.m. to 6 p.m.: (A mode), or from 9 a.m. to 10 p.m.: (B mode).

As shown in Table 3, the cyclotron was used in various research fields, until the electrostatic accelerators were mainly used in the field of functional materials. The ratios of allotted time to JAERI staff were ca.35% in the cyclotron utilization and ca. 65% in the utilization of other electrostatic accelerators as shown in Table 4.

Table 3. Utilization of accelerators in FY 1996 at various research fields.

Fields of Research	utilization time at each period															
	cyclotron [h]				tandem accelerator [d]				single-ended accelerator [d]				ion implanter [d]			
	8-1	8-2	8-3	total	8-1	8-2	8-3	total	8-1	8-2	8-3	total	8-1	8-2	8-3	total
Material for space	182	140	117	439	12	11	6	29	-	-	1	1	3	2	2	7
Material for fusion	13	0	13	26	13	11	10	34	14	9	13	36	11	8	6	25
Biotechnology	155	107	127	389	4	5	2	11	-	-	-	-	-	-	-	-
Functional materials	47	23	20	90	9	14	14	37	21	30	19	70	32	35	33	100
RI & nuclear chemistry	155	68	108	331	-	-	-	-	-	-	-	-	-	-	-	-
Radiation chemistry	159	130	98	387	-	-	-	-	-	-	-	-	-	-	-	-
Basic technology	410	198	228	836	13	13	12	38	10	17	11	38	-	5	1	6
Total	1121	666	711	2498	51	54	43	148	45	56	44	145	46	50	42	138

Table 4. Utilization of the accelerators in FY 1996 at various relations with users.

Relation with visitors		utilization time at each period															
		cyclotron [h]				tandem accelerator [d]				single-ended acceler. [d]				ion implanter [d]			
		8-1	8-2	8-3	total	8-1	8-2	8-3	total	8-1	8-2	8-3	total	8-1	8-2	8-3	total
JAERI staff	Takasaki Establishment	367	219	235	821	27	29	23	79	20	37	17	74	20	28	23	71
	others	79	29	49	157	7	6	6	19	14	10	13	37	8	2	4	14
Universities under Cooperative research		128	62	102	292	9	12	7	28	4	9	8	21	3	5	4	12
Universities under Projective joint research		375	229	205	809	6	6	6	18	7	-	6	13	10	11	10	31
Private companies or Governmental institutes under joint research		157	113	102	372	2	1	-	3	-	-	-	-	5	4	1	10
Others under Cooperative & Joint Researches		15	14	17	46	-	-	-	-	-	-	-	-	-	-	-	-
Visitors use with charges		48	105	106	259	3	5	4	12	-	-	-	-	3	2	-	5
Total		1169	771	816	2756	56	59	46	161	45	56	44	145	49	52	42	143

9. 2 Operation of AVF Cyclotron

Kazuo ARAKAWA, Yoshiteru NAKAMURA, Watalu YOKOTA,
Mitsuhiro FUKUDA, Takayuki NARA, Takashi AGEMATSU,
Susumu OKUMURA, Ikuo ISHIBORI and Hiroyuki TAMURA
Advanced Radiation Technology Center, JAERI

The JAERI AVF cyclotron was smoothly operated according to a beam-time allotment approved in program advisory committee.

The total operation time in the FY 1996 was 3132 hours, and monthly operation times are shown in Fig. 1. The beam time for experiments was 2800 hours in FY 1996. The percentage of time used for experiments including visitors use with charge, beam developments, and tunings were 89.0%, 4.6% and 6.4%, respectively. Thirty-eight kinds of ion species including cocktail beam M/Q≒5 ions, $^{15}N^{+3}$ (56 MeV), $^{20}Ne^{4+}$ (75 MeV) $^{40}Ar^{8+}$ (150 MeV) and $^{84}Kr^{17+}$ (322 MeV), were provided for experiments. The accelerated particles and their beam times are also shown in Fig. 2. The beam time for heavy ions was 67% of all as shown in Fig. 2. Regular yearly over-haul was carried out for 5 weeks in the summer.

We had the following machine troubles; (1) break down of a high voltage of an ECR ion source by increasing a leak current, and (2) an inflector stem (about 150 kg weight) crashed on a cyclotron upper yoke from a stem carrier. About 250 hours of time lost was due to these troubles and we had to cancel or reschedule the beam time for repair.

In order to meet the requests from many groups of researchers, the accelerated particles, their energies and the beam course are changed as shown in Table 1.

Table 1 Frequencies of particle, energy and beam course change in FYs.

FY	Particle	Energy	Beam Course
1994	70	74	145
1995	61	89	186
1996	81	97	188

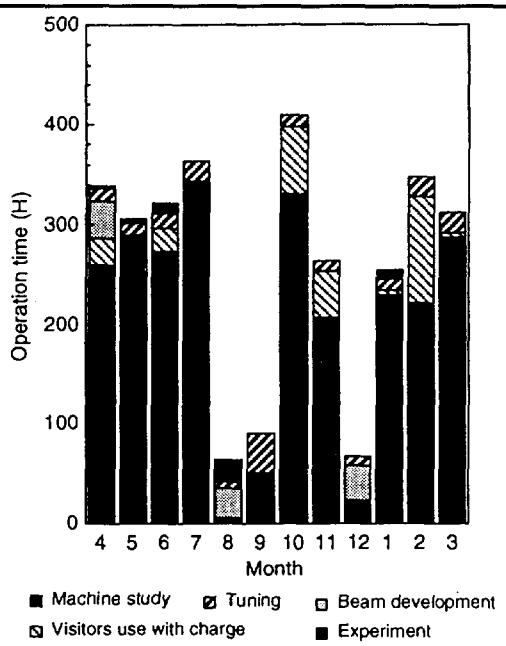

Fig1. Monthly operation times in FY1996.

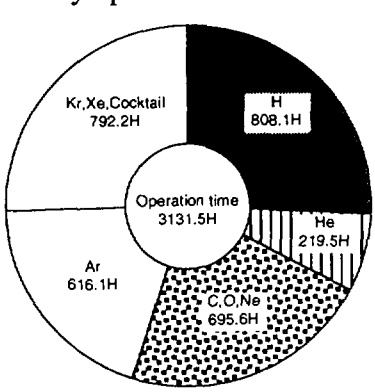

Fig.2 Beam times of accelerated ions in FY1996.

9. 3 Operation of the Electrostatic Accelerators

S. Tajima, I. Takada, K. Mizuhashi, S. Uno, K. Okoshi, Y. Nakajima,
Y. Saito, Y. Ishii, T. Sakai

Ion Accelerator Operation Division
Advanced Radiation Technology Center, JAERI

The three electrostatic accelerators were operated smoothly for various experiments in FY 1996. To make sure effective utilization for the experiments, the maximum operation time of the accelerators a day was extended until 11 p.m. o'clock from second machine time when started in end of August. Total operation time for each accelerator in this fiscal year were 1582 hours for the 3MV tandem accelerator , 1860 hours for the 3MV single-ended accelerator and 1809 hours for the 400kV ion implanter. In the case of the tandem, operation time in this year increased about thirty percents as compared with it in last year. Yearly operation time for each machine within last six years is shown in Fig.1.

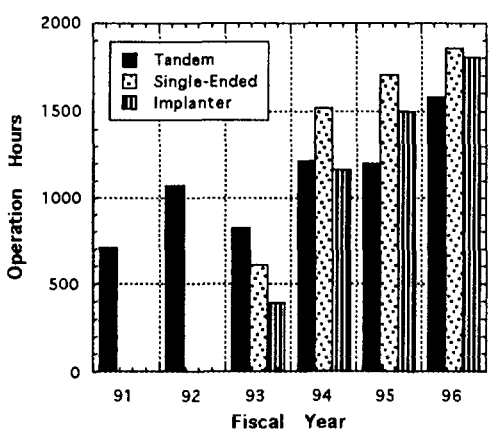

Fig. 1 Yearly Operation Time for Each Electrostatic Accelerator within Last Six Years.

The three accelerators were used with different kinds of operation mode, single beam, multiple beams such as triple and dual beams, micro-beams and electron beam. Fig.2 shows the percentage of the operation mode for each machine. The percentage of the multiple beam utilization for the tandem, single-ended and implanter were 14%, 23% and 28% respectively.

Two cluster ion species, Al and Cu, for the tandem accelerator and four new ions, Ba, Cu, Eu and Al for the ion implanter were developed in this year.

The regular maintenance of the accelerators were carried out in April, August and December. During this term many improvements and renewals for each machine were performed as follows; 1) A damaged high voltage cable which was used for stabilizing the terminal voltage of the tandem, was replaced with new one. 2) In order to improve the setting position of the shield electrodes of the single-ended, all the electrode supports were replaced with modified ones which were made of cast aluminum and also have large mechanical strength to keep its position. 3) The connecting bolts made of brass on the balance circuit of Schenkel high-voltage generator of the single-ended were changed for ones made of copper, because the brass bolts were strongly heated by the high frequency current. 4) To stop the corona discharge, a failed utility duct of the implanter was changed for modified one.

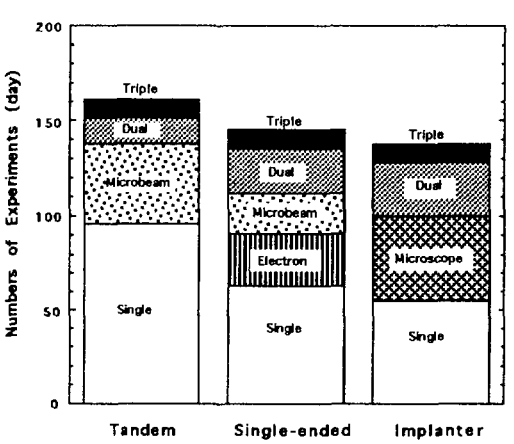

Fig. 2 Percentages of Operation Mode for Each Electrostatic Accelerators in FY 1996.

9.4 Radiation Control & Radioactive Waste Management in TIARA

Safety Division & Utilities and Maintenance Division,
Department of Administrative Services, TRCRE, JAERI

1. Radiation Control

1.1 Individual monitoring

(1) Individual monitoring for the radiation workers

Table 1 shows a distribution on effective dose equivalent of the radiation workers in fiscal 1996. The effective dose equivalent values of almost workers were less than 0.2 mSv (minimum detectable dose equivalent). Maximum dose equivalent was 2.0 mSv/y due to the overhauling of the cyclotron.

(2) Individual monitoring for the visitors and others.

Table 2 shows number of persons who have been temporally entered the radiation controlled areas. the effective dose equivalent of all persons were less than 0.2 mSv.

Table 1. Distributions on the effective dose equivalent in fiscal 1996.

Items \ Persons / Periods		Number of persons: 1st quarter	2nd quarter	3rd quarter	4th quarter
Distribution range on effective dose equivalent HE: Effective dose equivalent*1 (mSv)	HE ≦ 0.2	288	338	349	369
	0.2 < HE ≦ 1.0	5*2	6	0	0
	1.0 < HE ≦ 5.0	0	1*2	0	0
	5.0 < HE ≦ 50.0	0	0	0	0
	50.0 < HE	0	0	0	0
Persons for radiation control (A)		293	345	349	369
Exposure above 1 mSv	Persons (B)	0	1	0	0
	(B)/(A) ×100 (%)	0	0.29	0	0
Mass effective dose equivalent (man mSv)		1.6	3.6	0	0
Mean dose equivalent (mSv)		0.01	0.01	0	0
Maximum dose equivalent (mSv)		0.5	1.5	0	0

*1 Not detected according to internal exposure.

*2 The same worker was exposed during 1st and 2nd quarter.

Table 2. Number of temporary entrance persons to radiation controlled areas in fiscal 1996.

Temporary entrance persons \ Persons / Periods	Number of persons: 1st quarter	2nd quarter	3rd quarter	4th quarter	total
Visitors and others	493	463	476	352	1784

1.2 Monitoring of radioactive gases

Table 3 shows the maximum radioactive concentrations and total activities for radioactive gases released from TIARA's stack, during each quarter of fiscal 1996. The least amount of ^{41}Ar, ^{13}N and ^{11}C were detected for some time on operation of the cyclotron, but the pulverized substances (^{65}Zn, etc.) were not detected.

Table 3. Monitoring results of released gaseous radioactivities in fiscal 1996.

Nuclide	Items \ Periods	1st quarter	2nd quarter	3rd quarter	4th quarter	total
^{41}Ar	Maximum concentration (Bq/cm^3)	3.2×10^{-4}	$<1.5\times10^{-4}$	$<1.5\times10^{-4}$	$<4.5\times10^{-5}$	3.2×10^{-4}
	Total activity (Bq)	1.6×10^{9}	0	1.0×10^{8}	2.0×10^{8}	1.9×10^{9}
^{13}N	Maximum concentration (Bq/cm^3)	$<1.5\times10^{-4}$	–	–	–	$<1.5\times10^{-4}$
	Total activity (Bq)	2.3×10^{7}	–	–	–	2.3×10^{7}
^{11}C	Maximum concentration (Bq/cm^3)	–	$<1.5\times10^{-4}$	$<1.5\times10^{-4}$	$<4.5\times10^{-5}$	$<1.5\times10^{-4}$
	Total activity (Bq)	–	4.1×10^{8}	8.5×10^{7}	1.5×10^{7}	2.4×10^{8}
^{65}Zn	Maximum concentration (Bq/cm^3)	$<9.8\times10^{-11}$	$<6.5\times10^{-10}$	$<5.6\times10^{-10}$	$<5.6\times10^{-10}$	$<6.5\times10^{-10}$
	Total activity (Bq)	0	0	0	0	0

1.3 Monitoring for external radiation and surface contamination

External radiation monitoring was routinely carried out in/around the radiation controlled areas and surface contamination monitoring was also carried out. No unusual value of dose equivalent rate or contamination was detected.

Figure 1 displays a distribution of the dose equivalent rate at the radiation controlled area in the cyclotron building as an example.

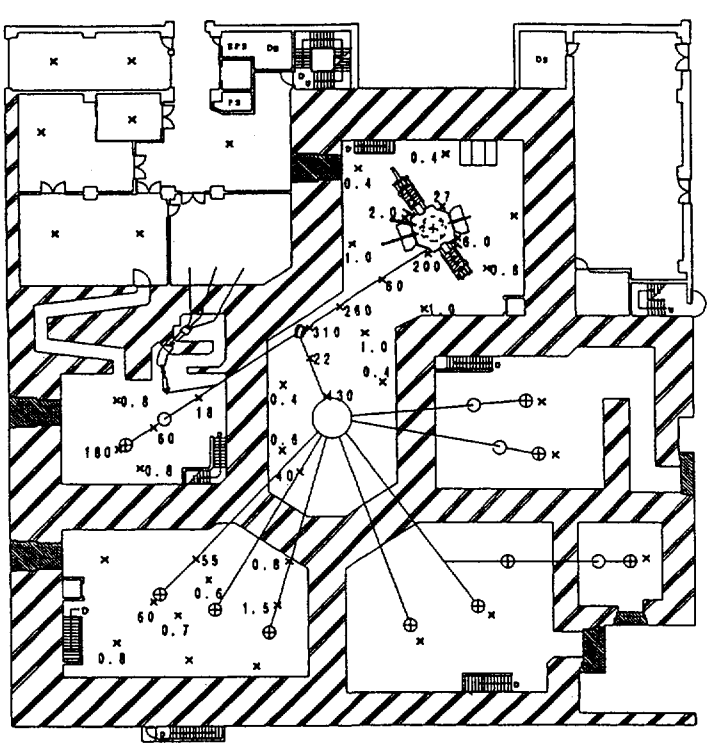

Fig. 1
Dose rate distribution at the radiation controlled area in the cyclotron building.

Date measured :
March 18, 1997
Measuring position :
Indicated with × above 1 m from floor
Unit : μ Sv/h
(numerics less than 0.2 μ Sv/h are not indicated)

1.4 Authorized radioisotopes

Table 4(a) shows a list of sealed radioisotopes authorized at the end of fiscal 1996. These isotopes are used in TIARA as checking sources for several kinds of radiation detectors.

Table 4(b) shows a list of unsealed radioisotopes authorized at the end of fiscal 1996. These are used mainly for research and development on radiation resistant materials in severe environment, biotechnology, new functional materials and radioisotopes.

Table 4. List of radioisotopes authorized at the end of fiscal 1996 in TIARA.

(a) Sealed radioisotopes

Authorization No. and Date	Nuclides and Amounts	Places Used	Places of Strage
No.6415 Jan. 30, 1995	^{241}Am 3.7 GBq ×1	Cyclotron Building Light Ion Room 1 to 3 Heavy Ion Room 1 to 3 Cyclotron Vault Light Ion Preparation Room Heavy Ion Preparation Room Heavy Ion Measuring Room Multiple Beam Building Target Room 1 Tandem Accelerator Room	Cyclotron Building
	^{22}Na 370 MBq ×1 3.7 GBq ×1	Ion Beam Research Building Hot Sample Testing Room Electron Accelerator-1 Building Vertical Beam Experimental Room	Electron Accelerator-1 Building RI storage box in Vert.B.Exper.Room
	^{57}Co 370 MBq ×4 ^{119m}Sn 370 MBq ×4	Cyclotron Building ISOL Room Ion Beam Research Building Hot Physics Laboratory	Cyclotron Building RI storage box in ISOL Room

(b) Unsealed radioisotopes

Authorization No. and Date	Places Used	Nuclides and Amounts of annual use		Nuclides and Amounts of annual use	
No.728 April 12, 1995	Cyclotron Building	^{22}Na	4.680 GBq	^{68}Ge	2992.800 MBq
		^{26}Al	72.000 MBq	^{73}As	10736.800 MBq
		^{37}Ar	8914.400 MBq	^{75}Se	9392.800 MBq
	Ion Beam Research Building	^{42}Ar	440.000 MBq	^{85}Sr	9.296 GBq
		^{44}Ti	440.000 MBq	^{88}Y	1.312 GBq
		^{46}Sc	1322.960 MBq	^{89}Sr	9.296 GBq
		^{49}V	8537.800 MBq	^{95m}Tc	9.296 GBq
		^{54}Mn	2.622 GBq	^{99}Tc	2.096 GBq
		^{56}Co	4.378 GBq	^{101}Rh	2.126 GBq
		^{57}Co	14.320 GBq	^{105}Ag	2098.960 MBq
		^{58}Co	16.504 GBq	^{109}Cd	2.296 GBq
		^{59}Ni	1.880 MBq	^{113}Sn	9354.400 MBq
		^{60}Co	90.800 MBq	^{119m}Sn	8.912 GBq
		^{63}Ni	9314.800 MBq	^{125m}Te	13.712 GBq
		^{65}Zn	5.704 GBq	^{125}I	888.000 MBq

(continued to the next page)

(Table 4(b) continued from the preceding page)

Nuclides and Amounts of annual use		Nuclides and Amounts of annual use		Nuclides and Amounts of annual use	
^{127m}Te	13.712 GBq	^{61}Cu	10577.680 MBq	^{123}I	17.776 GBq
^{127}Xe	13.712 GBq	^{62}Cu	10751.200 MBq	^{123}Xe	2.576 GBq
^{129m}Te	12.912 GBq	^{62}Zn	10751.200 MBq	^{124}I	680.000 MBq
^{139}Ce	9.528 GBq	^{63}Zn	9137.680 MBq	^{125}Xe	2.576 GBq
^{141}Ce	9.528 GBq	^{64}Cu	10.560 GBq	^{125}Pr	8.800 MBq
^{144}Ce	8.432 GBq	^{65}Ni	5087.280 MBq	^{127}Te	9.776 GBq
^{146}Gd	2.312 GBq	^{66}Ni	9087.280 MBq	^{127}Cs	2.576 GBq
^{148}Eu	2.312 GBq	^{66}Ga	6452.880 MBq	^{127}Pr	8.800 MBq
^{149}Eu	2.328 GBq	^{66}Ge	11528.080 MBq	^{128}Ba	9.776 GBq
^{150}Eu	1.096 GBq	^{67}Cu	10596.880 MBq	^{129}Te	12.680 GBq
^{151}Gd	13.712 GBq	^{67}Ga	12080.080 MBq	^{129m}Xe	12.680 GBq
^{153}Gd	9.528 GBq	^{68}Ga	9636.880 MBq	^{129}Cs	12.680 GBq
^{181}Hf	3112.800 MBq	^{69}Zn	9377.680 MBq	^{129}Ba	5.760 MBq
^{182}Ta	1.336 GBq	^{69m}Zn	9.320 GBq	^{130}Ce	2.240 MBq
^{183}Re	9.296 GBq	^{69}Ge	9496.080 MBq	^{131}I	180.000 MBq
^{184}Re	9.296 GBq	^{70}Ga	9.320 GBq	^{131}Cs	9.776 GBq
^{184m}Re	9.296 GBq	^{71}As	9392.080 MBq	^{131}Ba	9.776 GBq
^{207}Bi	2.312 GBq	^{72}Ga	2.920 GBq	^{131}La	3.376 GBq
^{11}C	402218.400 MBq	^{72}As	16088.080 MBq	^{132}La	3.360 GBq
^{13}N	114.160 GBq	^{72}Se	3416.080 MBq	^{133}Xe	9.776 GBq
^{15}O	114.160 GBq	^{73}Ga	5406.480 MBq	^{133}La	5.760 MBq
^{24}Na	3.640 GBq	^{73}Se	15944.080 MBq	^{134}Ce	9.776 GBq
^{28}Mg	2248.800 MBq	^{74}As	9968.080 MBq	^{135}La	3.376 GBq
^{31}Si	9224.800 MBq	^{75}Ge	9.320 GBq	^{135}Ce	3.376 GBq
^{32}P	11426.400 MBq	^{75}Br	9.320 GBq	^{137}Ce	3.376 GBq
^{33}P	11167.200 MBq	^{77}Br	9.320 GBq	^{137m}Ce	3.376 GBq
^{34m}Cl	4.120 GBq	^{79}Kr	2.120 GBq	^{140}La	3.352 GBq
^{35}S	10109.600 MBq	^{81}Rb	10.520 GBq	^{143}Ce	3.360 GBq
^{42}K	9082.960 MBq	^{82}Sr	10.520 GBq	^{145}Eu	3.360 GBq
^{43}K	9.080 GBq	^{87m}Sr	9.320 GBq	^{146}Eu	3.360 GBq
^{43}Sc	12536.800 MBq	^{87}Y	9.320 GBq	^{147}Eu	3.360 GBq
^{44}Sc	10.520 GBq	^{97}Ru	10256.080 MBq	^{147}Gd	3.360 GBq
^{44m}Sc	10522.960 MBq	^{99}Rh	10872.080 MBq	^{149}Gd	3.360 GBq
^{45}Ti	10.520 GBq	^{99m}Rh	10.200 GBq	^{150m}Eu	3.360 GBq
^{47}Ca	9.080 GBq	^{100}Rh	4916.080 MBq	^{159}Gd	3.376 GBq
^{47}Sc	9109.600 MBq	^{100}Pd	5464.080 MBq	^{183}Ta	8.400 GBq
^{48}Sc	2.680 GBq	^{101}Pd	8792.080 MBq	^{186}Re	9.320 GBq
^{48}V	5335.500 MBq	^{103}Pd	9.776 GBq	^{187}W	8.400 GBq
^{48}Cr	9113.800 MBq	^{106m}Ag	5762.970 MBq	^{187}Os	12.680 GBq
^{49}Cr	9108.880 MBq	^{107}Cd	9804.880 MBq	^{197}Hg	12.680 GBq
^{52}Mn	17.495 GBq	^{110}Sn	10192.080 MBq	^{203}Bi	9.752 GBq
^{52}Fe	5224.080 MBq	^{111}In	13236.080 MBq	^{204}Bi	2.080 MBq
^{55}Fe	11.220 GBq	^{111}Sn	5788.880 MBq	^{205}Bi	3.344 GBq
^{55}Co	17.160 GBq	^{112}Ag	5762.960 MBq	^{206}Bi	3.344 GBq
^{56}Mn	9082.960 MBq	^{115}Cd	5778.960 MBq	^{18}F	123.800 GBq
^{56}Ni	10.020 GBq	^{119}Sb	12.680 GBq	^{7}Be	10.320 GBq
^{57}Ni	16.460 GBq	^{121}Te	11.880 GBq	^{51}Cr	7.500 GBq
^{59}Fe	5170.800 MBq	^{121}I	9.776 GBq	^{71}Ge	4.400 GBq
^{61}Co	5087.280 MBq	^{122}Xe	5.776 GBq	^{201}Tl	15.320 GBq

2. Radioactive Waste Management

2.1 Solid wastes

Table 5 shows the amounts of solid wastes at various properties and kinds generated in each quarter of fiscal 1996. Main wastes were combustible matter such as gloves and incombustible filters for exhaust air. Compressible wastes were generated mainly by the cyclotron maintenance.

2.2 Liquid waste

Liquid waste was almost waste water ("inorganic" in Table 6) generated with chemical experiments and operation of air conditioning units installed in each room of the first class radiation controlled area. Larger quantity of the waste water in summer season (2nd quarter) are mainly due to condensed drain from air by operating the units.

Category A waste water is treated by evaporation, and condensed water is reused in the controlled area. Only small ammounts of residue are generated by the evaporation because the radiation level is very low and the waste quality is very pure.

The evaporation residue and sludge are solidified by cement in a stainless steel drum. The residue and sludge of ca. 100 liter makes one cement solidify of 200 liter drum.

Table 5. Radioactive solid wastes generated in fiscal 1996.

Items \ Amounts	Amounts of generation in each periods (m^3)					Number of package /drum
	1st quarter	2nd quarter	3rd quarter	4th quarter	total	
Category A*	0.24	0.74	0.44	3.27	4.69	
1)Combustible	0.22	0.74	0.42	0.28	1.66	10**
2)Incombustible	0.02	0	0.02	2.99	3.03	0
Compressible	0.02	0	0.02	0.04	0.08	1**
Filters	0	0	0	2.93	2.93	27
Imcompressible	0	0	0	0.02	0.02	0
Ion exchange resin	0	0	0	0	0	0
(Cement solidify)	0	0	0	0	0	0
Category B*	0	0	0	0	0	
1)Incombustible	0	0	0	0	0	0

* defined by dose at the outer surface of container : (A) < 2 mSv/h ≦ (B)
** 200 liter drum

Table 6. Radioactive liquid waste generated in fiscal 1996.

Items \ Amounts	Amounts of generation in each periods (m^3)					Number of package /drum
	1st quarter	2nd quarter	3rd quarter	4th quarter	total	
Category A*	12.23	17.00	10.67	6.43	46.33	
1)Inorganic	12.23	17.00	10.67	6.33	46.23	treatment
2)Organic	0	0	0	0	0	0
Organic	0	0	0	0	0	0
Oil	0	0	0	0	0	0
3)Sludge	0	0	0	0.10	0.10	0
Category B*	0	0	0	0	0	
1)Inorganic	0	0	0	0	0	0
2)Organic	0	0	0	0	0	0
Organic	0	0	0	0	0	0
Oil	0	0	0	0	0	0
3)Sludge	0	0	0	0	0	0
Evaporation residue	0	0	0	0.20	0.20	0

* defined by concentrations in Bq/cm^3 (β, γ) : (A) < 3.7×10 ≦ (B) < 3.7×10^4

Appendix

Appendix 1. LIST OF PUBLICATIONS

A1.1. Publications in Journal

J01. A.Adachi, M.Inoue and I.Nakajima :
Effect of $^4He^{2+}$ beam-irradiation to pollen of *Nicotina Tabacum L.*
Rep. Soc. Crop Sci. Breed., Kinki **40**(1995)11.
C,T 2.7 61012/62020

J02. M.Asai, K.Kawade, H.Yamamoto, A.Osa, M.Koizumi and T.Sekine :
A five-HPGe detector system for $\gamma-\gamma$ angular correlation measurements of mass-separated short-lived nuclei.
Nucl. Instrum. Meth. **A**, (in press.)
C 6.4 61028

J03. M.Asano, M.Yoshida, H.Omichi, N.Nagaoka, H.Kubota, R.Katakai, N.Reber and R.Spohr :
Ion track pores in intelligent films.
Radiation **42** (1996) 61.
C 3.10 61020

J04. K.Furukawa, S.Ohno, H.Namba, M.Taguchi and R.Watanabe :
Radial dose distribution around a heavy ion's path.
Rad. Phys. Chem. **49**(1997)641.
C 2.5 61010

J05. M.Imamura, T.Murata, K.Akagi, Y.Tanaka, M.Imamura, K.Inoue, N.Mizuma, Y.Kobayasi, H.Watanabe, M.Hachiya, M.Akashi, Y.Furusawa, H.Yamanaka, S.Takahashi, T.Nakano, S.Nagaoka, T.Ohnishi, Y.Obiya and K.Harada :
Relationship between LET and RBE values for *Escherichia coli* determined using carbon ion beam from the TIARA cyclotron and HIMAC synchrotron.
J. Gen. Appl. Microbiol. **43** (1997) (in press.)
C 2.8 61013

J06. Y.Ishii, R.Tanaka and A.Isoya :
Low-energy ion source characteristics for producing an ultra-fine microbeam.
Nucl.Instrum.Meth. **B113**(1996)75.
O 8.12 off-line

J07. S.Ishiyama :
Long-life secondary battery of which discharge capacity can be controlled.
Jpn. Patent Kokai, **T.K.H-9-129235** (16 May 1997)
S 4.19 62028

J08. J.Isoya, H.Kanda and Y.Morita :
EPR identification of the $\langle 100 \rangle$-split $[B-N]^+$ interstitialcy in diamond.
Phy. Rev. **B** (1997) (in press.)
O 1.6 61021/62034

J09. J.Isoya, H.Kanda, I.Sakaguchi, Y.Morita and T.Ohshima :
ESR studies of high-energy phosphorus-ion implanted synthetic diamond crystals.
Radiat. Phy. Chem., (in press.)
T,I 1.6 61021/62034

J10. H.Itoh, A.Kawasuso, T.Ohshima, M.Yoshikawa, I.Nashiyama, S.Tanigawa, S.Misawa, H.Okumura and S.Misawa :
Intrinsic defects in cubic silicon carbide.
Phys. Stat. Sol. (a) **162**(1997) (in press.)
C,O 1.5 61002

J11. T.Iwai, N.Sekimura and F.A.Garner :
Void swelling behavior in ion-irradiated vanadium alloys.
J. Nucl. Mater. **239**(1996)157.
T,S,I 4.12 62015

J12. H.Kageyama, R.Takahashi, D.Hamaguchi, T.Awata, T.Nakae, A.Nishihata, K.Kawatsura, S.Arai, Y.Aoki, S.Yamamoto, H.Takeshita, P.Goppelt-Langer, H.Naramoto, T.Kamubara, M.Oura, T.Papp, Y.Kanai, Y.Awaya, Y.Horino, Y.Mokuno, A.Chayahara, A.Kinimura, N.Tsubouchi and K.Fujii :
High resolution L X-ray spectra of Fe and Cu induced by 0.75 MeV/u ion impact.
Int. J. PIXE, **5**(1995)203.
S,T 5.4 62031

J13. Y.Katano, T.Nakazawa, D.Yamaki, T.Aruga, K.Hojou and K.Noda :
Effects of dual and triple beam irradiation with O, He and H-ions on adamage structures in single crystal Al_2O_3.

Nucl.Instrum.Meth.B116(1996)230.
T,S,I 4.6 62009

J14. Y.Katano, T.Nakazawa, D.Yamaki, T.Aruga and K.Noda :
Microstructural evolution of single crystalline Al_2O_3 irradiated with singl and triple ion beams.
J. Nucl. Mater. **233-237** (1997) 1325.
T,S,I 4.6 62009

J15. K.Kawatsura, H.Kageyama, R.Takahashi, D.Hamaguchi, S.Arai, Y.Aoki, S.Yamamoto, H.Takehisa, H.Naramoto, T.Kambara, M.Oura, Y.Kanai and Y.Awaya :
Copper L X-ray spectra measured by a high resolution ion-induced X-ray spectrometer.
Rad. Phys. Chem. **49**(1997)617.
T,S 5.4 62031

J16. K.Kawatsura, T.Nakae, R.Takahashi, Y.Nakai, S.Arai, Y.Aoki, P.Goppelt-Langer, S.Yamamoto, H.Takeshita, H.Naramoto, Y.Horino, Y.Mokuno, T.Mitamura, M.Terasawa, H.Uchida and K.Koterazawa :
Analysis of radiation-induced segregation in type 304 stainless steel by PIXE and RBS channeling.
Nucl.Instrum.Meth. B118(1996)363.
S 5.4 62031

J17. Y.Kobayashi, M.Kikuchi, A.Tanaka and H.Watanabe :
Deinococcus radiodurans does not show RBE peak in LET response.
J. Radiat. Res. **37(4)**(1996)307.
C 2.3 61008

J18. H.Koizumi T.Ichikawa and H.Yoshida :
Radiation chemistry in alanine irradiated with γ-rays and ion-beams.
Appl. Radiat. Isot. **47**(1996)1205.
C 3.3 61034

J19. H.Koizumi T.Ichikawa, H.Yoshida, H.Namba, M.Taguchi and T.Kojima :
Radical formation in radiolysis of solid alanine by heavy ions.
Nucl.Instrum.Meth. B117(1996)431.
C 3.3 61034

J20. H.Koizumi T.Ichikawa, H.Yoshida, H.Shibata, S.Tagawa and Y.Yoshida :
Radical formation in radiolysis of solid alanine by proton and helium ions.
Nucl.Instrum.Meth.B117(1996)269.
C 3.3 61034

J21. M.Koizumi, A.Osa, T.Sekine and M.Kubota :
Development of a laser ion source with pulsed ion extraction.
Nucl.Instrum.Meth. B126(1997)100.
C 6.2 61025

J22. Y.Kojima, T.Ikuta, M.Asai, A. Taniguchi, M.Shibata, H.Yamamoto, and K.Kawade :
Measurement of response functions of HPGe detectors for monoenergetic electrons and positrons in an energy range of 6.0-9.0 MeV.
Nucl.Instrum.Meth. B126(1997)419.
C 6.4 61028

J23. H.Kudo, A.Sakamoto, S.Yamamoto, Y.Aoki, H.Naramoto, T.Inoue, M.Satoh, Y.Yamamoto, K.Umezawa and S.Seki :
Analysis of misoriented crystal structure by ion channeling observed using ion-induced secondary electrons.
Jpn. J. Appl. Phys. **35**(1996)L1538.
S 5.3 62030

J24. H.Kudo, A.Tanabe, T.Ishihara, S.Seki, Y.Aoki, S.Yamamoto, P.Goppelt-Langer, H.Takeshita and H.Naramoto :
Charge states of fast heavy ions in glancing collisions with aligned atoms in single crystals.
Nucl.Instrum.Meth. B115(1996)125.
S 5.3 62030

J25. H.Kudoh, T.Sasuga and T.Seguchi :
High energy ion irradation effects on mechanical property of polymeric materials.
Rad. Phys. Chem. **48**(1996)545.
C 3.8 61001

J26. H.Kudoh, T.Sasuga and T.Seguchi :
High energy ion irradation effects on polymer materials.
Am. Chem. Soc. Symposium Series, **620**(1996)2.
C 3.8 61001

J27. H.Kudoh, T.Sasuga, T.Seguchi and Y.Katsumura :
High energy ion irradation effects on polymer materials: 2. Proton irradiation effects on PMA and GFRP.

Polymer, 37(1996)4663.
C 3.8 61001

J28. H.Kudoh, T.Sasuga, T.Seguchi and Y.Katsumura :
High energy ion irradation effects on polymer materials: 3. The sensitivity of cellulose tri-acetate and poly(methylmethacrylate).
Polymer, 37(1996)2903.
C 3.8 61001

J29. H.Kudoh, T.Sasuga, T.Seguchi and Y.Katsumura :
High energy ion irradation effects on polymer materials: 4. Heavier ion irradiation effects on mechanical properties of polyethylene and polytetrafluoroethylene.
Polymer Communications, 37(1996) 3737.
C 3.8 61001

J30. N.Nakao, M.Nakao, H.Nakashima, Su.Tanaka, Y.Sakamoto, Y.Nakane, Sh.Tanaka and T.Nakamura :
Measurements and calculations of neutron energy spectra behind polyethylene shields bombarded by 40- and 65-MeV quasi-monoenergetic neutron sources.
J. Nucl. Sci. Tech. 34(1997)348.
C 7.5 61045

J31. N.Nakao, H.Nakashima, T.Nakamura, Sh.Tanaka, Su.Tanaka, K.Shin, M.Baba, Y.Sakamoto and Y.Nakane :
Transmission through shields of quasi-monoenergetic neutrons generated by 43- and 68-MeV Protons -I :
Concrete shielding experiment and calculation for practical application.
Nucl. Sci. Eng. 124 (1996) 228.
C 7.5 61045

J32. H.Nakashima, N.Nakao, Sh.Tanaka, T.Nakamura, K.Shin, Su.Tanaka, H.Takada, S.Meigo, Y.Nakane, Y.Sakamoto and M.Baba :
Transmission through shields of quasi-monoenergetic neutrons generated by 43- and 68-MeV protons -II :
Iron shielding experiment and analysis for investigating calculational method and cross-section data.
Nucl. Sci. Eng. 124 (1996) 243.
C 7.5 61045

J33. H.Nishimura, M.Inoue, A.Tanaka and H.Watanabe :
Pollen as a transporter of mutations induced by ion beams by ion beams in *Nicotiana tabacum L.*
Can. J. Bot. (1997) (in press.)
T 2.1 62019

J34. T.Ohnuki, N.Kozai, H.Isobe, T.Murakami, S.Yamamoto, Y.Aoki and H.Naramoto :
Sorption mechanism of europium by apatite using Rutherford back-scatering spectroscopy and resonant nuclear reaction analysis.
J. Nucl. Sci. & Tech. 34(1997)58.
T 5.11 62042

J35. H.Omichi, M.Asano, M.Yoshida, N.Nagaoka, H.Kubota, R.Katakai and R.Spohr :
Ion track pores in intelligent films.
Radiation, 22(2)(1996)61.
(in Japanese).
C 3.10 61020

J36. H.Omichi, M.Yoshida, M.Asano, R.Katakai, R.Spohr and J.Vetter :
Synthesis of environmentally responsive porous membranes by ion beam irradiation.
IONICS, 22(June-1996)27.
(in Japanese).
C 3.10 61020

J37. M.Saneyasu, M.Hasegawa, Z.Tang, M.Tabata, M.Fujinami, Y.Ito and S.Yamaguchi :
Positron trapping defects in neuron-irradiated vitreous and crystalline SiO_2.
Mater. Sci. Forum, (1997) (in press.)
C 5.9 61022

J38. S.Seki, K.Kanzaki, Y.Kunimi, Y.Yoshida, S.Tagawa, H.Kudoh, M.Sugimoto and T.Seguchi :
LET effects of ion beam irradiation on polysilanes.
Rad. Phys. Chem. (1997)(in press.)
C 3.2 61033

J39. S.Seki, H.Shibata, H.Ban, K.Ishigure and S.Tagawa :
Radiation effects of ion and electron beam on poly(methylphenylsilane).

Rad. Phys. Chem. **48**(1996)539.
O 3.2 61033

J40. M.Taguchi, Y.Aoki, H.Namba, R.Watanabe, Y.Matsumoto and H.Hiratsuka :
Fast fluorescence decay of naphthalene by Ar ion irradiation.
Nucl. Instrum. Meth. B(1997) (in press.)
C 2.5 61010

J41. M.Taguchi, H.Namba, Y.Aoki, S.Nagai and H.Hiratsuka :
Effect of fluence of He^+ ions of fluorescence intensity of triphenylmethyl radical.
Rad. Phys. Chem. **49**(1997)253.
C 3.6 61030

J42. M.Taguchi, H.Namba, Y.Aoki, R.Watanabe, Y.Matsumoto and H.Watanabe :
Specifications of EA-BRACHI (the experimental apparatus for basic study of radiation chemistry with heavy ions).
JAERI Tech. **96-046**(1996).
C 3.6 61030

J43. M.Taguchi, Y.Kobayashi, H.Watanabe, S.Yamasaki and K.Kiguchi :
Biological microbeam system for local irradiation of cells.
J. Radiat. Res. **37(4)**(1996)307.
C 2.3 61008

J44. S.Tajima, I.Takada, K.Mizuhashi, S.Uno, K.Ohkoshi, Y.Nakajima, Y.Saitoh, Y.Ishii and T.Kamiya :
TIARA electrostatic accelator facility.
JAERI Tech. **96-029** (1996).
T,S,I 8.9-8.11 62041

J45. A.Tanaka :
UV-B resistant mutations in *Arabidopsis thaliana.*
Kisokagaku Note **3**(2)(1996)31. (in Japanese).
C 2.2 61007

J46. A.Tanaka, N.Shikazono, Y.Yokota, H.Watanabe and S.Tano :
Effects of heavy ions on the germination and survival of *Arabidopsis thaliana.*
Int. J. Radiat. Biol. **72**(1996)121.
C 2.2 61007

J47. A.Tanaka, S.Tano, T.Chantes, Y.Yokota, N.Shikazono and H.Watanabe :
A new *Arabidopsis* mutant induced by ion beams affects flavonoid synthesis with spotted pigmentation in testa.
Genes Genet. Syst. (1997) (in press).
C 2.2 61007

J48. A.Tanaka, H.Watanabe, T.Shimizu, M.Inoue, M.Kikuchi, Y.Kobayashi and S.Tano :
Penetration controlled irradiation with ion beams for biological study.
Nucl. Instrum. Meth. B(1997) (in press.)
T 2.1 62019

J49. H.Tanimoto, H.Mizubayashi, H.Fujita and S.Okuda :
Anelastic study of nanocrystalline gold prepared by gas deposition method.
J. physique III (Paris) **6**, (1996) C8-199-202.
S 4.4 62007

J50. H.Tanimoto, H.Mizubayashi, H.Nishimura and S.Okuda :
A study of self-interstitial atom in W by means of low-temperature irradiations.
J. physique III (Paris) **6**, (1996) C8-285-288.
S 4.4 62007

J51. K.Umezawa, A.Takahashi, T.Yumura, S.Nakanishi and W.M.Gibson :
Initial stage of Pb adsorption on Ni(111) studied by LEED and ICISS.
Surface Science **365** (1996) 118.
T 5.8 62036

J52. A.Vazquez-Tello, T.Uozumi, M.Hidaka, Y.Kobayashi and H. Watanabe :
Effect of $^{12}C^{+5}$ ion beam irradiation on cell viability and plant regeneration in callus, protoplasts and cell suspensions of *Lavatera thuringiaca.*
Plant Cell Reports **16** (1996) 46.
C - 31020

J53. H.Watanabe :
Application of ion beams to development of gene resources.
RADIOISOTOPES, **44**(1995)824. (in Japanese).
T 2.1 62019

J54. H.Watanabe, Y.Kobayashi,

S.Yamasaki and K.Kiguchi :
Application of microprobe to local irradiation of biological systems.
Hoshasen, **23**(1)(1997)63.
(in Japanese).
C 2.4/2.9 61009/61014

J55. S.Yamamoto, H.Naramoto and Y.Aoki :
Analysis of hydrogen in Nb thin films and Nb/Cu multilayers, using ion beams.
J. Alloys and Compounds (1997)
(in press).
T,S 5.7 62024

J56. S.Yamamoto, H.Naramoto, K.Narumi, B.Tsuchiya and Y.Aoki :
Characterization of single-crystalline Nb film on sapphire by RBS/channeling technique.
submitted for J. Appl. Physics.
S 5.5 62022

J57. W.Yokota, M.Fukuda, S.Okumura, K.Arakawa, Y.Nakamura, T.Nara, T.Agematsu and I.Ishibori :
Performance and operation of a beam chopping system for a cyclotron with multiturn extraction.
Rev. Sci. Instrum. **68**(1997)1714.
C 8.3 61039

J58. W.Yokota, T.Nara, K.Arakawa, M.Ide and Y.Kamimura :
Metallic ion generation from ceramic rods by ECR ion source and thermodynamic feature of vaporization.
Nucl.Instrum.Meth. **B122**(1996)141.
O 8.4 off-line

J59. M.Yoshida :
Environment-sensitive ion-track membranes.
Radiation Chemistry **No.62**(1996) 2. (in Japanese).
C 3.10 61020

J60. M.Yoshida, M.Asano, A.Safranj, H.Omichi, R.Spohr, J.Vetter, and R.Katakai :
Novel thin film with cylindrical nanopores that open and close depending on temperature
- First successful synthesis -
Macromolecules, **29**(1996)8987.
C 3.10 61020

A1.2. Publications in Proceedings

C01. H.Abe, H.Naramoto, K.Hojou, S.Furuno and T.Tsukamoto :
Transmission electron microscope interfaced with ion accelerators and its application to materials science.
Proc. 7th Int. Symp. Adv. Nucl. En. Res. (Takasaki, March 1996)
JAERI-Conf 97-003 (1997) 365.
I 4.15 62026

C02. T.Agematsu, K.Arakawa and S.Okumura :
Develpoment of visual beam adjustment method for cyclotron.
Proc. 14th Int. Conf. Cyclotron and Their Applications (Cape Town, South Africa, Oct. 1995) 284.
C 8.1 61037

C03. J.Aoki, T.Hada, A.Pesce, T.Akutsu, S.Masuda, T.Igarashi and S.Baba :
An evaluation testing technique of single event effect using beam blanking SEM.
Proc. 7th Int. Symp. Adv. Nucl. En. Res. (Takasaki, March 1996)
JAERI-Conf 97-003 (1997) 230.
O,C 1.3 61004

C04. Y.Aoki, Nguyen T.My, S.Yamamoto, and H.Naramoto :
Ion irradiation effect of alumina and its luminescence.
Proc. 7th Int. Symp. Adv. Nucl. En. Res. (Takasaki, March 1996)
JAERI-Conf 97-003 (1997) 122.
I 4.14 62027

C05. K.Arakawa, Y.Nakamura, W.Yokota, T.Nara, T.Agematsu, S.Okumura, I.Ishibori and M.Fukuda :
Status report on TIARA-AVF cyclotron.
Proc. 14th Int. Conf. Cyclotron and Their Applications (Cape Town, South Africa, Oct. 1995) 54.
C 8.3-7 61039

C06. M.Fukuda, S.Okumura and K.Arakawa :
Analytical examination of a spiral beam scanning method for uniform irradiation.
Proc. 7th Int. Symp. Adv. Nucl. En.

Res. (Takasaki, March 1996)
JAERI-Conf 97-003 (1997) 441.
O 8.3-7 61039

C07. K.Furukawa, S.Ohno, H.Namba, M.Taguchi and R.Watanabe :
Radial dose distribution around an energetic heavy ion and an ion track structure model.
Proc. 7th Int. Symp. Adv. Nucl. En. Res. (Takasaki, March 1996)
JAERI-Conf 97-003 (1997) 289.
C,O 3.6 61030

C08. M.Gan, H.Naramoto, Y.Aoki, S.Yamamoto, J.Zeng and H.Takeshita :
Directional effect on coloration in LiF crystal by H^+ and H_2^+ ion bombardment.
Proc. 7th Int. Symp. Adv. Nucl. En. Res. (Takasaki, March 1996)
JAERI-Conf 97-003 (1997) 327.
S 5.5 62022

C09. S.Hamada, Y.Zhang, Y.Miwa and D.Yamaki :
Microstructural evolution in austenitic stainless steel irradiated with triple-beam.
Proc. 7th Int. Symp. Adv. Nucl. En. Res. (Takasaki, March 1996)
JAERI-Conf 97-003 (1997) 39.
T,S,I 4.5 62008

C10. H.Hase, M.Inoue, H.Watanabe and A.Tanaka :
Biological effects of $^4He^{2+}$ and $^{12}C^{5+}$ beam in *Nicotiana tabacum L.*
Proc. Ann. Meeting of Jpn. Soc. of Breeding 1996.
Breeding Sci. **46** ex.2(1996)103.
C 2.7 61012

C11. K.Hayashi, J.Saito, S.Kano, Y.Hirakawa, E.Yoshida, T.Seguchi and N.Kasai :
Nitrogen ion implantation of fast reactor materials for improvement in Na compatibility.
Proc. 12th Symp. Surface Layer Modification by Ion Implantation (Tokyo, Nov. 1996).
I 4.20 62038

C12. T.Hirao, T.Kamiya, T.Suda, T.Sakai, T.Hamano and I.Nashiyama :
Effect of ion position on single event transient current.
Proc. 5th Int. Conf. on Nuclear Microprobe Technol. and Applicatn. (Santafe, Oct. 1996).
T 1.4 62002

C13. T.Hirao, I.Nashiyama, T.Kamiya and T.Suda :
Study of transient current induced by heavy-ion microbeams in Si and GaAs.
Proc. 7th Int. Symp. Adv. Nucl. En. Res. (Takasaki, March 1996)
JAERI-Conf 97-003 (1997) 249.
T 1.4 62002

C14. T.Hirao, I.Nashiyama, T.Kamiya and T.Suda :
Measurement of charge collected from heavy-ion tracs in pn junction diodes.
Proc.2nd Int.Workshop on Radiation Effects of Semiconductor Devices for Space Application (Tokyo, March 1996).
T 1.4 62002

C15. T.Hirao, T.Nishijima :
Measurement of transient current and radiation damage induced by single-ion hits.
Proc. Radiat. Branch, Symp. of 57th Joint Conf. Applied Phys. (1996) Hoshasen, **23**(1)(1997)35.
T 1.4 62002

C16. Hisamitsu, O.Kawasaki, S.Matsuda and K.Tsukamoto :
Photoluminescence in large fluence radiation irradiated space silicon solar cells.
Proc. 7th Int. Symp. Adv. Nucl. En. Res. (Takasaki, March 1996)
JAERI-Conf 97-003 (1997) 237.
C,T 1.2 61005/62003

C17. M.Inoue and H.Watanabe :
The use of ion beam to overcome interspecific hybrid inviability in plants.
Proc. 7th Int. Symp. Adv. Nucl. En. Res. (Takasaki, March 1996)
JAERI-Conf 97-003 (1997) 59.
C,T 2.7 61012/62020

C18. I.Ishigaki :
Progress on research of materials science and biotechnology by ion beam application.
Proc. 7th Int. Symp. Adv. Nucl. En. Res. (Takasaki, March 1996)
JAERI-Conf 97-003 (1997) 3.
C,T,S,I - (TIARA-general)

C19. J.Isoya, H.Kanda, M.Akaishi, Y.Morita and T.Ohshima :
ESR studies of incorporation of phosphorus into high-pressure synthetic diamond.
Proc.5th Int.Conf. New Diamond Sci. and Technol., (Tours, Sept. 1996)
Diam. Relat. Mater. 6(1997)356.
T 1.6 61021/62034

C20. J.Isoya, H.Kanda, Y.Morita and T.Ohshima :
ESR studies of high-energy phosphorus-ion implanted synthetic diamond crystals.
Proc. 7th Int. Symp. Adv. Nucl. En. Res. (Takasaki, March 1996)
JAERI-Conf 97-003 (1997) 354.
T,I 1.6 61021/62034

C21. H.Itoh, A.Kawasuso, T.Ohshima, M.Yoshikawa and I.Nashiyama :
Study of defects in radiation tolerant semiconductor SiC.
Proc. 7th Int. Symp. Adv. Nucl. En. Res. (Takasaki, March 1996)
JAERI-Conf 97-003 (1997) 253.
O 1.5 61002

C22. T.Iwasaki, Y.Sakuya, T.Tabei, N.Hirakawa, Y.Sakamoto, H.Nakashima and Su.Tanaka :
Fission reaction rate distribution of ^{237}Np in polyethylene system for 65 MeV neutron.
Proc. Int. Conf. Future Nuclear Systems (Yokohama, Oct. 1997)
C 7.5 61045

C23. F.Kano, K.Fukuya, S.Hamada and Y.Miwa :
Effect of carbon on grain boundary segregation in stainless steels irradiated with Ni ions.
Proc. 4th Japan-China Symposium (Sapporo, Aug. 1996)
T 4.5 62008

C24. N.Kasai, T.Arakawa and T.Seguchi :
Heavy ion irradiation effects on optical properties of polymer materials.
Proc. 7th Int. Symp. Adv. Nucl. En. Res. (Takasaki, March 1996)
JAERI-Conf 97-003 (1997) 277.
T,C 3.8-9 61001/62001

C25. Y.Katano, T.Aruga, T.Nakazawa, D.Yamaki and K.Noda :
Cross-sectional observation of damage structures in Al_2O_3 irradiated with multiple beams of H, He and O-ions and after annealing at 1273 K.
Proc. 13th Int. Conf. of Ion Beam Analysis,(Lisbon, Aug. 1996)
Nucl.Instrum.Meth.B (1997)
(to be published)
T,S,I 4.6 62009

C26. Y.Katano, K.Hojou, T.Nakazawa, D.Yamaki, T.Aruga and K.Noda :
Cavity formation behaviors in single crystal Al_2O_3 irradiated with triple beams of O, He and H ions.
Proc. 9th Int.Conf.Radiat.Effects in Insulator (Knoxville, Sept.1996)
Nucl.Instrum.Meth.B (1997)
(to be published)
T,S,I 4.6 62009

C27. A.Kawasuso, H.Arai and S.Okada :
Vacancy-hydrogen interaction in proton-implanted Si studied by positron lifetime and infrared absorption measurements.
Proc. 11th Int. Conf. on Positron Annihilation (Kansas, May 1996)
Materials Sci. Forum (in press)
T 5.10 62025

C28. A.Kawasuso, S.Masuno, S.Okada, M.Hasegawa and M.Suezawa :
Internal positron source production with a cyclotron and vacancy study in silicon.
Proc. 7th Int. Symp. Adv. Nucl. En. Res. (Takasaki, March 1996)
JAERI-Conf 97-003 (1997) 476.
C 5.9 61022

C29. E.Kim, T.Nakamura, A.Konno, M.Imamura, N.Nakao, S.Shibata, Y.Uwamino, N.Nakanishi, Su.Tanaka, H.Nakashima and Sh.Tanaka :
Measurement of neutron spallation cross sections.
Proc. 1995 Symp. on Nucl. Deta (Tokai, Nov. 1995)
JAERI-Conf 96-008 (1996) 236.
C 7.4 61041

C30. E.Kim, T.Nakamura, M.Imamura, N.Nakao, S.Shibata, Y.Uwamino, N.Nakanishi and Su.Tanaka :
Measurement of neutron spallation cross section (2).
Proc. 1996 Symp. on Nucl. Deta (Tokai, Nov. 1996)
JAERI-Conf 97-005 (1997) 194.

C 7.4 61041

C31. Y.Kobayashi, M.Kikuchi, A.Tanaka, and H.Watanabe :
Deinococcus radiodurans does not show RBE peak in LET response.
Proc. 39th Ann. Meeting Japan Radiation Res. Soc.(Osaka, Nov. 1996) 249.
C 2.3 61008

C32. Y.Kobayashi, A.Tanaka, M.Kikuchi, J.P.Cao, T.Shimizu, G.Taucher-Scholz and H.Watanabe :
Influence of LET on repair of DNA damages in *Deinococcus radiodurans*.
Proc. 7th Int. Symp. Adv. Nucl. En. Res. (Takasaki, March 1996)
JAERI-Conf 97-003 (1997) 68.
C,T 2.3/2.1 61008/62019

C33. Y.Kobayashi, H.Watanabe, M.Taguchi, S.Yamasaki and K.Kiguchi :
Microbeam system for local irradiation of biological systems and effect of collimated beams on insect egg.
Proc. 12th Symp. on Microdosimetry (Oxford, Sept.-Oct.1996)(in press)
C 2.4/2.9 61009/61014

C34. H.Koizumi, T.Ichikawa, H.Yoshida H.Namba, M.Taguchi and T.Kojima :
Effect of radiation quality on radical formation in ion-irradiated solid alanine.
Proc. 7th Int. Symp. Adv. Nucl. En. Res. (Takasaki, March 1996)
JAERI-Conf 97-003 (1997) 286.
C 3.3 61034

C35. T.Kojima, H.Sunaga, H.Takizawa and H.Tachibana :
Study on dosimetry systems for a few tens MeV/u ion beams.
Proc. 7th Int. Symp. Adv. Nucl. En. Res. (Takasaki, March 1996)
JAERI-Conf 97-003 (1997) 492.
C 3.7 61040

C36. H.Kudo, A.Tanabe, T.Ishihara, S.Seki, K.Umezawa, S.Yamamoto, Y.Aoki, P.Goppelt-Langer, H.Takeshita and H.Naramoto :
Advamced ion beam analysis of materials using ion-induced fast electron.
Proc. 7th Int. Symp. Adv. Nucl. En. Res. (Takasaki, March 1996)
JAERI-Conf 97-003 (1997) 114.
T,O 5.3 62030

C37. H.Kudoh, T.Sasuga and T.Seguchi :
High energy ion irradiation effects on polymer material - LET dependence of G value of scission of polymethylmethacrylate(PMMA).
Proc. 7th Int. Symp. Adv. Nucl. En. Res. (Takasaki, March 1996)
JAERI-Conf 97-003 (1997) 273.
C 3.8 61001

C38. T.Kume, S.Matsuhashi, M.Shimazu, H.Ito, T.Fujimura, K.Adachi, H.Uchida, N.Shigeta, H.Matsuoka, A.Osa and T.Sekine :
Uptake and transport of positron-emitting tracer in plants.
Proc. 7th Int. Symp. Adv. Nucl. En. Res. (Takasaki, March 1996)
JAERI-Conf 97-003 (1997) 308.
C 2.11 61017

C39. S.Masuno, S.Okada and A.Kawasuso :
Construction of a pulsed MeV positron beam line.
Proc. 7th Int. Symp. Adv. Nucl. En. Res. (Takasaki, March 1996)
JAERI-Conf 97-003 (1997) 472.
O 5.10 62025

C40. K.Mizuhashi, S.Bunnak and S.Tajima :
Measurement of ion energy by the calorimeter method.
Proc. 9th Workshop on Tandem Accelerator and Technology (Tokai, July 1996) 88.
T,S,I 8.9-11 62041

C41. K.Morita, J.Yuhara, R.Ishigami, B.Tsuchiya, K.Soda, K.Saito, S.Yamamoto, P.Goppelt-Langer, Y.Aoki, H.Takeshita and H.Naramoto :
An in-situ RBS system for measuring nuclides adsorbed at the liquid-solid interface.
Proc. 7th Int. Symp. Adv. Nucl. En. Res. (Takasaki, March 1996)
JAERI-Conf 97-003 (1997) 411.
T 5.2 62018

C42. Y.Morita, S.Sasaki, T.Oshima, K.Kuroda and A.Ushirokawa :
Proton irradiation effects of amorphous silicon solar cell for solar power satellite.
Proc. 7th Int. Symp. Adv. Nucl. En. Res. (Takasaki, March 1996)

JAERI-Conf 97-003 (1997) 261.
C,T,O - 52006/41002

C43. Y.Nakamura, I.Ishibori, S.Okumura, T.Nara, W.Yokota, M.Fukuda, T.Agematsu, K.Mizuhashi and K.Arakawa :
Performance and constitution of the vacuum system in JAERI AVF cyclotron.
Proc. 14th Int. Conf. Cyclotron and Their Applications (Cape Town, South Africa, Oct. 1995) 276.
C 8.1-8.7 61037-9

C44. H.Naramoto, Y.Aoki, S.Yamamoto and H.Abe :
Comparison of damage growth and recovery in α-Al_2O_3 implanted with vanadium ions.
Proc. 10th Int. Conf. Ion Beam Modification of Materials (IBMM-96)
Nucl. Instrum. Meth. B127/128 (1997) 599.
S,I 5.5-6 62022/62023

C45. H.Naramoto, Y.Aoki, S.Yamamoto, P.Goppelt-Langer, M.Gan, J.Zeng and H.Takeshita :
On-site analysis of modified surface using dual beam system.
Proc. 7th Int. Symp. Adv. Nucl. En. Res. (Takasaki, March 1996)
JAERI-Conf 97-003 (1997) 117.
S,I 5.5 62022

C46. H.Naramoto, Y.Aoki, S.Yamamoto, K.Narumi and H.Abe :
Ion-beam-modified structure and some physical/chemical properties of sapphire.
Proc. Eng. Foundation Conf. on Modification of Ceramics and Semiconductors by ion bombardment (Castelvecchio Pascoli, May 1997), Mat. Sci. Eng.(1998) (to be published)
S,I 5.5 62022

C47. I.Nashiyama, T.Hirao, H.Itoh, and T.Ohshima :
Effect of ion beam irradiation on semiconductor devices.
Proc. 7th Int. Symp. Adv. Nucl. En. Res. (Takasaki, March 1996)
JAERI-Conf 97-003 (1997) 22.
C 1.1/1.5 61002/61003

C48. Y.Nauchi, M.Baba, T.Kiyosumi, T.Iwasaki, T.Sanami, S.Matsuyama, N.Hirakawa, S.Tanaka, S.Meigo, H.Nakashima, T.Nakamura, Y.Watanabe and M.Harada :
Measurement of double differential charged particle emissioin cross sections and development of a wide range charged particle spectrometer for ten's MeV neutrons.
Proc. 1996 Symp. on Nucl. Data, (Tokai, Nov. 1996)
JAERI-Conf. 97-005 (1997) 126.
C 7.3 61043

C49. Y.Nauchi, M.Baba, T.Sanami, T.Nakamura, S.Tanaka, S.Meigo, Y.Watanabe, M.Harada and H.Takada :
Measurement of (n,xp), (n,xd) double differential cross sections of Al and C for ten's MeV neutrons.
Proc. Int. Conf. on Nucl. Data for Science and Technology, (Trieste, May 1997) to be published.
C 7.3 61043

C50. N.Nemoto, T.Akutsu, I.Naitoh, S.Matsuda, H.Itoh, T.Agematsu, and I.Nashiyama :
Development of heavy-ion irradiation technique for single-event in semiconductor devices.
Proc. 7th Int. Symp. Adv. Nucl. En. Res. (Takasaki, March 1996)
JAERI-Conf 97-003 (1997) 234.
C 1.3 61004

C51. T.Ohnuki, N.Kozai, H.Isobe, T.Murakami, S.Yamamoto, Y.Aoki, and H.Naramoto :
RBS and RNRA studies on sorption of europium by apatite.
Proc. 7th Int. Symp. Adv. Nucl. En. Res. (Takasaki, March 1996)
JAERI-Conf 97-003 (1997) 377.
T,S 5.11 62042

C52. T.Ohshima, Y.Morita, I.Nashiyama, O.Kawasaki, T.Hisamatsu, Y.Yamamoto, S.Matsuda, T.Nakao and Y.Wakow :
Analysis on anomalous degradation in silicon solar cell designed for space use.
Proc. 7th Int. Symp. Adv. Nucl. En. Res. (Takasaki, March 1996)
JAERI-Conf 97-003 (1997) 256.
C,T,O 1.2 61005/62003

C53. H.Ohyama, J.Vanhellemont, Y.Takami,

K.Hayama, H.Sunaga, I.Nashiyama, Y. Uwatoko, J.Poormans and M.Caymax: Degradation of SiGe devices by proton irradiation.
Proc. 7th Int. Symp. Adv. Nucl. En. Res. (Takasaki, March 1996)
JAERI-Conf 97-003 (1997) 212.
C,O 1.5/1.1 61002/61003

C54. S.Okada, H.Sunaga, H.Kaneko, A.Kawasuso, S.Masuno, H.Takizawa and K.Yotsumoto :
Positron factory project.
Proc. 7th Int. Symp. Adv. Nucl. En. Res. (Takasaki, March 1996)
JAERI-Conf 97-003 (1997) 180.
- - (off-line)

C55. S.Okumura, M.Fukuda, I.Ishibori T.Agematsu, W.Yokota, T.Nara, Y.Nakamura and K.Arakawa :
Development of beam instruments at JAERI cyclotron facility.
Proc. 7th Int. Symp. Adv. Nucl. En. Res. (Takasaki, March 1996)
JAERI-Conf 97-003 (1997) 444.
C 8.2 61038

C56. H.Omichi, M.Yoshida, M.Asano, R.Katakai, R.Spohr and J.Vetter :
Synthesis of environmentally responsive organic materials by application of ion track holes in polymer films.
Proc. 7th Int. Symp. Adv. Nucl. En. Res. (Takasaki, March 1996)
JAERI-Conf 97-003 (1997) 44.
C 3.10 61020

C57. Y.Saitoh, K.Mizuhashi and S.Tajima :
Acceleration of B_n cluster to MeV energy.
Proc. 9th Workshop on Tandem Accelerator and Technology (Tokai, July 1996) 100.
T 8.10 62041

C58. Y.Saitoh and W.Yokota :
Characteristics of MINI ECR ion source.
Proc. 7th Int. Symp. Adv. Nucl. En. Res. (Takasaki, March 1996)
JAERI-Conf 97-003 (1997) 447.
- 8.4 off-line

C59. T.Sakai, T.Hamano, T.Suda, T.Hirao and T.Kamiya :
Development of noise-suppressed detector for single ion hit system.
Proc. 7th Int. Symp. Adv. Nucl. En. Res. (Takasaki, March 1996)
JAERI-Conf 97-003 (1997) 451.
T 1.4/8.8 62002/62039

C60. S.Seki, K.Kanzaki, S.Tagawa, Y.Yoshida, H.Kudoh, M.Sugimoto, T.Sasuga, T.Seguchi and H.Sibata :
LET effect of high energy ion beam irradiation on polysilanes.
Proc. 7th Int. Symp. Adv. Nucl. En. Res. (Takasaki, March 1996)
JAERI-Conf 97-003 (1997) 281.
C,O 3.2 61033

C61. S.Sekine :
Studies of radioisotope production with an AVF cyclotron in TIARA.
Proc. 7th Int. Symp. Adv. Nucl. En. Res. (Takasaki, March 1996)
JAERI-Conf 97-003 (1997) 86.
C 6.1 61024

C62. E.Simoen, J.Vanhellemont, A.Alaerys, C.Claeys, E.Gaubas, A.Kaniava, H.Ohyama, H.Sunaga, I.Nashiyama and W.Skorupa :
Proton irradiation effects in silicon devices.
Proc. 7th Int. Symp. Adv. Nucl. En. Res. (Takasaki, March 1996)
JAERI-Conf 97-003 (1997) 224.
C,O 1.5/1.1 61002/61003

C63. T.Sonoda, H.Abe, C.Kinoshita and H.Naramoto :
Formation and growth process of defect clusters in magnesia under ion irradiation.
Proc. 10th Int. Conf. Ion Beam Modification of Materials (IBMM-96)
Nucl.Instrum.Meth. **B127/128** (1997) 176.
I 4.15 62026

C64. M.Sugimoto, H.Kudoh, T.Sasuga, T.Seguchi, Y.Hama, K.Hamanaka and H.Matsumoto :
Distribution of products in polymer materials induced by ion-beam irradiation.
Proc. 7th Int. Symp. Adv. Nucl. En. Res. (Takasaki, March 1996)
JAERI-Conf 97-003 (1997) 269.
C 3.1 61032

C65. M.Taguchi, Y.Kobayashi, H.Watanabe, S.Yamasaki and K.Kiguchi :
Biological microbeam system for local irradiation of cells.
Proc. 39th Ann. Meeting, Japan

Radiation Res. Soc. (Osaka, Nov. 1996) 247.
C 2.4 61009

C66. S.Tajima, I.Takada, K.Mizuhashi, Y.Saitoh, S.Uno, K.Ohkoshi, Y.Ishii, Y.Nakajima and T.Sakai : Status of the TIARA electrostatic accelerators.
Proc. 9th Workshop on Tandem Accelerator and Technology (Tokai, July 1996) 10.
T,S,I 8.9-11 62041

C67. R.Takahashi, D.Hamaguchi, H.Kageyama, A.Nishihata, K.Kawatsura, S.Arai, Y.Aoki, S.Yamamoto, H.Takeshita, H.Naramoto, T.Kambara, M.Oura, Y.Kanai, Y.Awaya, Y.Horino, Y.Mokuno, A.Chayahara, A.Kinomura, N.Tsubouchi and K.Fujii :
Copper L X-ray spectra measured by a high resolution ion-induced X-ray spectrometer.
Proc. 7th Int. Symp. Adv. Nucl. En. Res. (Takasaki, March 1996)
JAERI-Conf 97-003 (1997) 345.
T,S 5.4 62031

C68. R.Takahashi, Y.Nakai, D.Hamaguchi, T.Nakae, A.Nishihata, T.Shiono, K.Kawatsura, S.Arai, Y.Aoki, S.Yamamoto, H.Takeshita, H.Naramoto Y.Horino, Y.Mokuno, K.Fujii and N.Masuda :
Radiation-induced effects in MgO single crystal by 200keV and 1 MeV Ni ion implantation.
Proc. 7th Int. Symp. Adv. Nucl. En. Res. (Takasaki, March 1996)
JAERI-Conf 97-003 (1997) 349.
S,T,I 5.4 62031

C69. R.Tanaka, T.Kamiya, T.Suda, T.Sakai, T.Hirao, Y.Kobayashi and H.Watanabe :
High energy ion hit technique to local area using microbeam.
Proc. 7th Int. Symp. Adv. Nucl. En. Res. (Takasaki, March 1996)
JAERI-Conf 97-003 (1997) 133.
C,T,S 2.4/8.8 61009/62039/62040

C70. A.Tanaka, T.Shimizu, M.Kikuchi, Y.Kobayashi, T.Yamashita and H.Watanabe :
Biological effect of penetration controlled irraduation with ion beams.
Proc. 7th Int. Symp. Adv. Nucl. En. Res. (Takasaki, March 1996)
JAERI-Conf 97-003 (1997) 323.
T 2.1 62019

C71. A.Tanaka, Y.Yokota, N.Shikazono, A. Sakamoto, H.Watanabe and S.Tano : Mutagenesis in *Arabidopsis* - Are ion beams useful to produce null mutant and novel mutant?
Abstr. 8th Int. Conf. on Arabidopsis Research (Madison, Wisconsin, June 1997) p.12.
C 2.2 61007

C72. S.Tano :
Heavy ion induced mutation in *Arabidopsis*.
Proc. 7th Int. Symp. Adv. Nucl. En. Res. (Takasaki, March 1996)
JAERI-Conf 97-003 (1997) 73.
C,O 2.2 61007

C73. B.Tsuchiya, S.Yamamoto, K.Narumi, Y.Aoki and H.Naramoto :
Ion irradiation effect of single-crystalline Cu/Nb film and sapphire.
Proc. 120th spring meeting, The Japan Institute of Metals (Tokyo, 1997)
S 5.6 62023

C74. B.Tsuchiya, S.Yamamoto, K.Narumi, Y.Aoki, H.Naramoto and K.Morita : Ion irradiation effect on single-crystalline Cu/Nb layer on sapphire.
Proc. 13th Int. Conf. on Ion Beam Analysis (Lisboa, Jul.-Aug. 1997) to be published in Nucl. Instr. Meth.(1998)
S,I 5.6 62023

C75. S.Yamamoto, P.Goppelt-Langer, H.Naramoto, Y.Aoki and H.Takesita : Ion beam analysis of multi-layered structure in Nb/Cu system.
Proc. 7th Int. Symp. Adv. Nucl. En. Res. (Takasaki, March 1996)
JAERI-Conf 97-003 (1997) 371.
T 5.7 62024

C76. S.Yamamoto, H.Naramoto, B.Tsuchiya and Y.Aoki :
Characterization of single-crystalline Cu/Nb multilayer films by ion beam analysis.
Proc. Int. Symp. Functinally Graded

materials (FGM'96) (Tsukuba, Oct. 1996)
S 5.7 62024

C77. S.Yamamoto, B.Tsuchiya, K.Narumi, and H.Naramoto :
Characterization of single-crystalline Cu/Nb multilayer by RBS/channeling.
Proc. 120th spring meeting, The Japan Institute of Metals (Tokyo, 1997)
S 5.7 62024

C78. K.Yasuda, R.Morisaki, C.Kinosita, H.Abe and H.Naramoto :
Concurrent irradiation effects with ionization and displacement on the formation of defect clusters in magnesium aluminate spinel.
Proc. 7th Int. Symp. Adv. Nucl. En. Res. (Takasaki, March 1996)
JAERI-Conf 97-003 (1997) 384.
I,O 4.15/4.16 62026/62032

C79. J.Zeng, H.Naramoto, Y.Aoki, Y.Yamamoto, M.Gan and H.Takeshita :
Thermal annealing behavior of niobium-implanted α-Al_2O_3 under reducing environment.
Proc. 7th Int. Symp. Adv. Nucl. En. Res. (Takasaki, March 1996)
JAERI-Conf 97-003 (1997) 207.
I 5.6 62023

Appendix 2. Type of Research Collaborations

Section of this Report	Research Program Number	Type of Research Collaborations*
1.1	61003	(JAERI)
1.2	61005/62003	Joint Res.
1.3	61004	Joint Res.
1.4	62002	(JAERI)
1.5	61002	(JAERI)
1.6	61021/62034	Coop.Res.Univ.
2.1	62019	(JAERI)
2.2	61007	(JAERI)
2.3	61008	(JAERI)
2.4	61009	(JAERI)
2.5	61010	(JAERI)
2.6	61011	(JAERI)
2.7	61012/62020	Coop.Res.Univ.
2.8	61013	Coop.Res.Univ.
2.9	61014	Coop.Res.Univ.
2.10	61016	Coop.Res.Univ.
2.11	61017	Joint Res. /& Coop.Res.Univ.
2.12	61018/62021	Joint Res.
3.1	61032	Proj.Res.Univ.
3.2	61033	Proj.Res.Univ.
3.3	61034	Proj.Res.Univ.
3.4	61031	(JAERI)
3.5	61035	Proj.Res.Univ.
3.6	61030	(JAERI)
3.7	61040	(JAERI)
3.8	61001	(JAERI)
3.9	62001	(JAERI)
3.10	61020	Coop.Res.Univ.
3.11	61036	Coop.Res.Univ.
4.1	62004	(JAERI)
4.2	62005	(JAERI)
4.3	62006	(JAERI)
4.4	62007	Coop.Res.Univ.
4.5	62008	(JAERI)
4.6	62009	(JAERI)
4.7	62010	(JAERI)
4.8	61006	(JAERI)
4.9	62011	(JAERI)
4.10	62012	(JAERI)
4.11	62014	Coop.Res.Univ.
4.12	62015	Coop.Res.Univ.
4.13	62016	Coop.Res.Univ.
4.14	62027	(JAERI)
4.15	62026	(JAERI)
4.16	62032	Proj.Res.Univ.
4.17	62037	Coop.Res.Univ.
4.18	62035	Coop.Res.Univ.
4.19	62028	(JAERI)
4.20	62038	Joint Res.
4.21	62029	(JAERI)
5.1	62017	Proj.Res.Univ.
5.2	62018	Proj.Res.Univ.
5.3	62030	Coop.Res.Univ.
5.4	62031	Proj.Res.Univ.
5.5	62022	(JAERI)
5.6	62023	(JAERI)
5.7	62024	(JAERI)
5.8	62036	Coop.Res.Univ.
5.9	61022	Coop.Res.Univ.
5.10	62025	(JAERI)
5.11	62042	(JAERI)
5.12	62044	Coop.Res.Univ.
6.1	61024	(JAERI)
6.2	61025	(JAERI)
6.3	61027	Coop.Res.Univ.
6.4	61028	Proj.Res.Univ.
6.5	61026	Coop.Res.Univ.
6.6	61029	Proj.Res.Univ.
6.7	(off-line)	Proj.Res.Univ.
7.1	61044	Proj.Res.Univ.
7.2	61042	Proj.Res.Univ.
7.3	61043	Proj.Res.Univ.
7.4	61041	Proj.Res.Univ.
7.5	61045	Proj.Res.Univ.
8.1	61037	(JAERI)
8.2	61038	(JAERI)
8.3	61039	(JAERI)
8.4	(off-line)	(JAERI)
8.5	61039	(JAERI)
8.6	61039	(JAERI)
8.7	61039	(JAERI)
8.8	62039/62040	(JAERI)
8.9	62041	(JAERI)
8.10	62041	(JAERI)
8.11	62041	(JAERI)
8.12	(off-line)	(JAERI)
8.13	62043	Coop.Res.Univ..
8.14	62045	Coop.Res.Univ.

* Joint Res. : Joint research with private company or governmental institution
Coop.Res.Univ. : Cooperative research with a university or universities #
Proj.Res.Univ. : The JAERI-Universities Joint Research Project #

For administration of these programs, we appreciate the cooperation of : Reasearch Center for Nuclear Science and Technology, The University of Tokyo.

Appendix 3. Organization and Personnel of TIARA (FY 1996)

1) Organization for the Research and Development of Advanced Radiation Technology

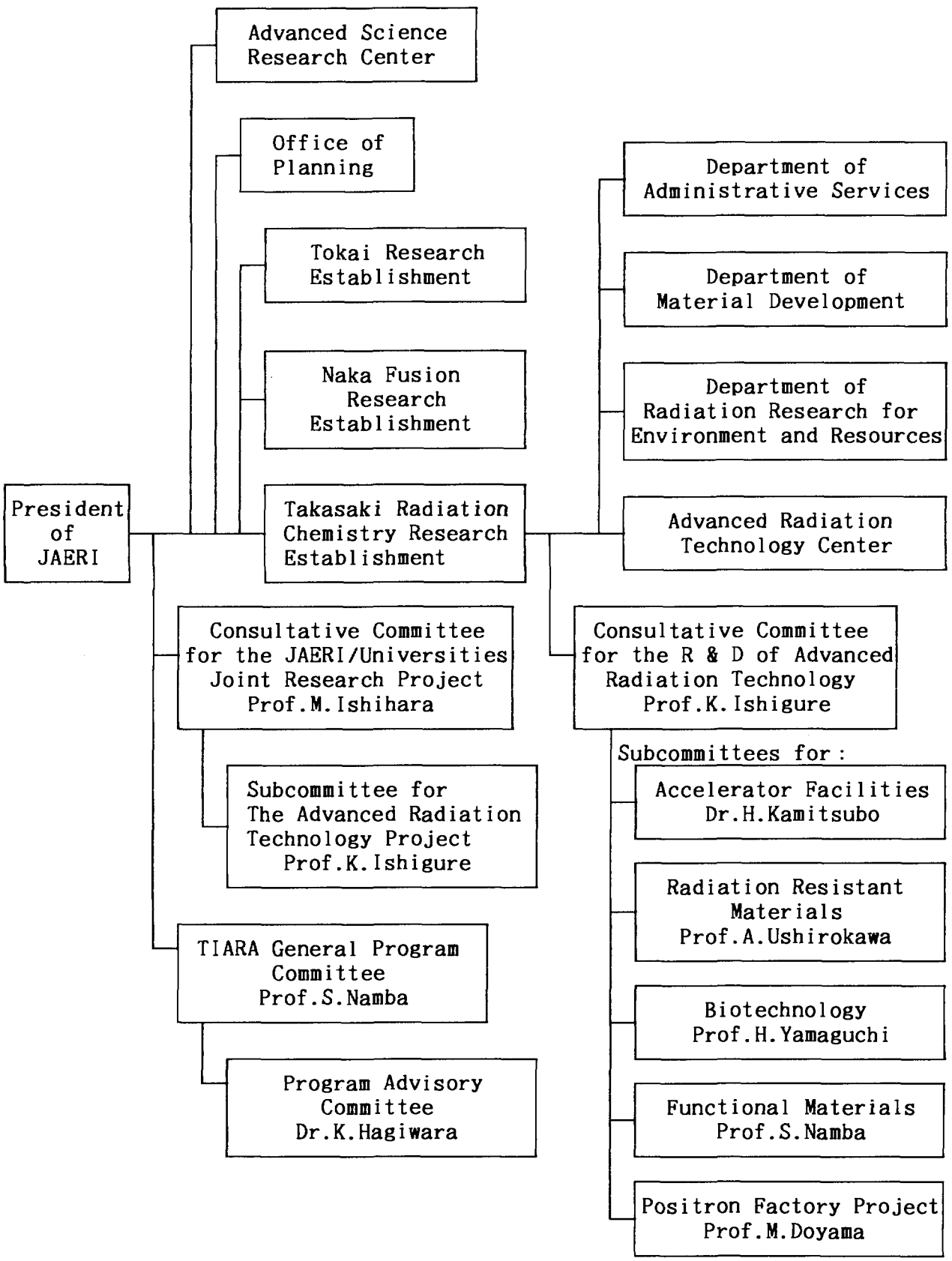

2) Personnel for the Administration, Operation and Control of TIARA

Advanced Radiation Technology Center

Director	R.Tanaka
Deputy Director	H.Omichi

Administration Division

General Manager	M.Sawahata
Staff Member	J.Kobayasi, H.Tonooka

Utilization and Coordination Division

General Manager	Y.Kusama
Staff Member	S.Tanaka, K.Nishimura, M.Hosono

Ion Accelerator Operation Division

General Manager	D.Nemoto

Group of Cyclotron Operation

Staff Member	K.Arakawa, Y.Nakamura, T.Nara, T.Agematsu, I.Ishibori, H.Tamura

Group of Electrostaic Accelerators Operation

Staff Member	S.Tajima, I.Takada, K.Mizuhashi, S.Uno, K.Ohkoshi, Y.Nakajima

Ion Beam Engineering Division

Head	S.Okada
Staff Member	T.Kojima, W.Yokota, H.Tachibana M.Fukuda, T.Kamiya, S.Okumura, Y.Saitoh, Y.Ishii, T.Sakai, A.Kawasuso, T.Suda, S.Masuno

Irradiation Service Division

General Manager	K.Yotsumoto
Staff Member	H.Sunaga, T.Kanazawa, T.Ookubo, H.Kaneko, Y.Haruyama, H.Takizawa

Department of Administrative Services

Safety Division

Staff Member	T.Furuta, T.Sakai

(Radiation Monitoring and Control in TIARA)

Utilities and Maintenance Division

Staff Member	K.Fukuda, J.Yoshii

(Radioactive Waste Management and Utility Control in TIARA)

国際単位系 (SI) と換算表

表 1　SI基本単位および補助単位

量	名称	記号
長さ	メートル	m
質量	キログラム	kg
時間	秒	s
電流	アンペア	A
熱力学温度	ケルビン	K
物質量	モル	mol
光度	カンデラ	cd
平面角	ラジアン	rad
立体角	ステラジアン	sr

表 2　SIと併用される単位

名称	記号
分，時，日	min，h，d
度，分，秒	°，′，″
リットル	l，L
トン	t
電子ボルト	eV
原子質量単位	u

1 eV = 1.60218 × 10^{-19} J

1 u = 1.66054 × 10^{-27} kg

表 5　SI接頭語

倍数	接頭語	記号
10^{18}	エクサ	E
10^{15}	ペタ	P
10^{12}	テラ	T
10^{9}	ギガ	G
10^{6}	メガ	M
10^{3}	キロ	k
10^{2}	ヘクト	h
10^{1}	デカ	da
10^{-1}	デシ	d
10^{-2}	センチ	c
10^{-3}	ミリ	m
10^{-6}	マイクロ	μ
10^{-9}	ナノ	n
10^{-12}	ピコ	p
10^{-15}	フェムト	f
10^{-18}	アト	a

表 3　固有の名称をもつSI組立単位

量	名称	記号	他のSI単位による表現
周波数	ヘルツ	Hz	s^{-1}
力	ニュートン	N	$m \cdot kg/s^2$
圧力，応力	パスカル	Pa	N/m^2
エネルギー，仕事，熱量	ジュール	J	N·m
工率，放射束	ワット	W	J/s
電気量，電荷	クーロン	C	A·s
電位，電圧，起電力	ボルト	V	W/A
静電容量	ファラド	F	C/V
電気抵抗	オーム	Ω	V/A
コンダクタンス	ジーメンス	S	A/V
磁束	ウェーバ	Wb	V·s
磁束密度	テスラ	T	Wb/m^2
インダクタンス	ヘンリー	H	Wb/A
セルシウス温度	セルシウス度	℃	
光束	ルーメン	lm	cd·sr
照度	ルクス	lx	lm/m^2
放射能	ベクレル	Bq	s^{-1}
吸収線量	グレイ	Gy	J/kg
線量当量	シーベルト	Sv	J/kg

表 4　SIと共に暫定的に維持される単位

名称	記号
オングストローム	Å
バーン	b
バール	bar
ガル	Gal
キュリー	Ci
レントゲン	R
ラド	rad
レム	rem

1 Å = 0.1 nm = 10^{-10} m

1 b = 100 fm^2 = 10^{-28} m^2

1 bar = 0.1 MPa = 10^5 Pa

1 Gal = 1 cm/s^2 = 10^{-2} m/s^2

1 Ci = 3.7 × 10^{10} Bq

1 R = 2.58 × 10^{-4} C/kg

1 rad = 1 cGy = 10^{-2} Gy

1 rem = 1 cSv = 10^{-2} Sv

(注)

1. 表1－5は「国際単位系」第5版，国際度量衡局 1985年刊行による。ただし，1 eVおよび1 uの値はCODATAの1986年推奨値によった。
2. 表4には海里，ノット，アール，ヘクタールも含まれているが日常の単位なのでここでは省略した。
3. barは，JISでは流体の圧力を表わす場合に限り表2のカテゴリーに分類されている。
4. EC閣僚理事会指令ではbar，barnおよび「血圧の単位」mmHgを表2のカテゴリーに入れている。

換算表

力

	N(=10^5 dyn)	kgf	lbf
	1	0.101972	0.224809
	9.80665	1	2.20462
	4.44822	0.453592	1

粘度　1 Pa·s(N·s/m^2) = 10 P(ポアズ)(g/(cm·s))

動粘度　1 m^2/s = 10^4 St(ストークス)(cm^2/s)

圧力

	MPa(=10 bar)	kgf/cm^2	atm	mmHg(Torr)	lbf/in^2(psi)
	1	10.1972	9.86923	7.50062 × 10^3	145.038
	0.0980665	1	0.967841	735.559	14.2233
	0.101325	1.03323	1	760	14.6959
	1.33322 × 10^{-4}	1.35951 × 10^{-3}	1.31579 × 10^{-3}	1	1.93368 × 10^{-2}
	6.89476 × 10^{-3}	7.03070 × 10^{-2}	6.80460 × 10^{-2}	51.7149	1

エネルギー・仕事・熱量

	J(=10^7 erg)	kgf·m	kW·h	cal(計量法)	Btu	ft·lbf	eV
	1	0.101972	2.77778 × 10^{-7}	0.238889	9.47813 × 10^{-4}	0.737562	6.24150 × 10^{18}
	9.80665	1	2.72407 × 10^{-6}	2.34270	9.29487 × 10^{-3}	7.23301	6.12082 × 10^{19}
	3.6 × 10^6	3.67098 × 10^5	1	8.59999 × 10^5	3412.13	2.65522 × 10^6	2.24694 × 10^{25}
	4.18605	0.426858	1.16279 × 10^{-6}	1	3.96759 × 10^{-3}	3.08747	2.61272 × 10^{19}
	1055.06	107.586	2.93072 × 10^{-4}	252.042	1	778.172	6.58515 × 10^{21}
	1.35582	0.138255	3.76616 × 10^{-7}	0.323890	1.28506 × 10^{-3}	1	8.46233 × 10^{18}
	1.60218 × 10^{-19}	1.63377 × 10^{-20}	4.45050 × 10^{-26}	3.82743 × 10^{-20}	1.51857 × 10^{-22}	1.18171 × 10^{-19}	1

1 cal = 4.18605 J(計量法)

= 4.184 J　(熱化学)

= 4.1855 J　(15 °C)

= 4.1868 J(国際蒸気表)

仕事率　1 PS(仏馬力)

= 75 kgf·m/s

= 735.499 W

放射能

Bq	Ci
1	2.70270 × 10^{-11}
3.7 × 10^{10}	1

吸収線量

Gy	rad
1	100
0.01	1

照射線量

C/kg	R
1	3876
2.58 × 10^{-4}	1

線量当量

Sv	rem
1	100
0.01	1

(86年12月26日現在)

TIARA Annual Report 1996